



NEUROPLASTICITY AND DEVELOPMENT EDITOR'S PICKS 2021

EDITED BY: Clive R. Bramham

PUBLISHED IN: Frontiers in Molecular Neuroscience



frontiers Research Topics



frontiers

Frontiers eBook Copyright Statement

The copyright in the text of individual articles in this eBook is the property of their respective authors or their respective institutions or funders. The copyright in graphics and images within each article may be subject to copyright of other parties. In both cases this is subject to a license granted to Frontiers.

The compilation of articles constituting this eBook is the property of Frontiers.

Each article within this eBook, and the eBook itself, are published under the most recent version of the Creative Commons CC-BY licence.

The version current at the date of publication of this eBook is CC-BY 4.0. If the CC-BY licence is updated, the licence granted by Frontiers is automatically updated to the new version.

When exercising any right under the CC-BY licence, Frontiers must be attributed as the original publisher of the article or eBook, as applicable.

Authors have the responsibility of ensuring that any graphics or other materials which are the property of others may be included in the CC-BY licence, but this should be checked before relying on the CC-BY licence to reproduce those materials. Any copyright notices relating to those materials must be complied with.

Copyright and source acknowledgement notices may not be removed and must be displayed in any copy, derivative work or partial copy which includes the elements in question.

All copyright, and all rights therein, are protected by national and international copyright laws. The above represents a summary only. For further information please read Frontiers' Conditions for Website Use and Copyright Statement, and the applicable CC-BY licence.

ISSN 1664-8714

ISBN 978-2-88971-068-3

DOI 10.3389/978-2-88971-068-3

About Frontiers

Frontiers is more than just an open-access publisher of scholarly articles: it is a pioneering approach to the world of academia, radically improving the way scholarly research is managed. The grand vision of Frontiers is a world where all people have an equal opportunity to seek, share and generate knowledge. Frontiers provides immediate and permanent online open access to all its publications, but this alone is not enough to realize our grand goals.

Frontiers Journal Series

The Frontiers Journal Series is a multi-tier and interdisciplinary set of open-access, online journals, promising a paradigm shift from the current review, selection and dissemination processes in academic publishing. All Frontiers journals are driven by researchers for researchers; therefore, they constitute a service to the scholarly community. At the same time, the Frontiers Journal Series operates on a revolutionary invention, the tiered publishing system, initially addressing specific communities of scholars, and gradually climbing up to broader public understanding, thus serving the interests of the lay society, too.

Dedication to Quality

Each Frontiers article is a landmark of the highest quality, thanks to genuinely collaborative interactions between authors and review editors, who include some of the world's best academicians. Research must be certified by peers before entering a stream of knowledge that may eventually reach the public - and shape society; therefore, Frontiers only applies the most rigorous and unbiased reviews. Frontiers revolutionizes research publishing by freely delivering the most outstanding research, evaluated with no bias from both the academic and social point of view. By applying the most advanced information technologies, Frontiers is catapulting scholarly publishing into a new generation.

What are Frontiers Research Topics?

Frontiers Research Topics are very popular trademarks of the Frontiers Journals Series: they are collections of at least ten articles, all centered on a particular subject. With their unique mix of varied contributions from Original Research to Review Articles, Frontiers Research Topics unify the most influential researchers, the latest key findings and historical advances in a hot research area! Find out more on how to host your own Frontiers Research Topic or contribute to one as an author by contacting the Frontiers Editorial Office: frontiersin.org/about/contact

NEUROPLASTICITY AND DEVELOPMENT EDITOR'S PICKS 2021

Topic Editor:

Clive R. Bramham, University of Bergen, Norway

Citation: Bramham, C. R., ed. (2021). Neuroplasticity and Development Editor's Picks 2021. Lausanne: Frontiers Media SA. doi: 10.3389/978-2-88971-068-3

Table of Contents

- 05** ***UBE3A: An E3 Ubiquitin Ligase With Genome-Wide Impact in Neurodevelopmental Disease***
Simon Jesse Lopez, David J. Segal and Janine M. LaSalle
- 13** ***Mitochondrial Calcium Transporters Mediate Sensitivity to Noise-Induced Losses of Hair Cells and Cochlear Synapses***
Xianren Wang, Yuanping Zhu, Haishan Long, Song Pan, Hao Xiong, Qiaojun Fang, Kayla Hill, Ruosha Lai, Hu Yuan and Su-Hua Sha
- 33** ***An Excitatory/Inhibitory Switch From Asymmetric Sensory Neurons Defines Postsynaptic Tuning for a Rapid Response to NaCl in *Caenorhabditis elegans****
Masahiro Kuramochi and Motomichi Doi
- 47** ***Impaired Cognitive Function and Altered Hippocampal Synaptic Plasticity in Mice Lacking Dermatan Sulfotransferase *Chst14/D4st1****
Qifa Li, Xuefei Wu, Xueyan Na, Biying Ge, Qiong Wu, Xuewen Guo, Michael Ntim, Yue Zhang, Yiping Sun, Jinyi Yang, Zhicheng Xiao, Jie Zhao and Shao Li
- 57** ***Neurocalcin Delta Knockout Impairs Adult Neurogenesis Whereas Half Reduction is Not Pathological***
Aaradhita Upadhyay, Seyyedmohsen Hosseinibarkooie, Svenja Schneider, Anna Kaczmarek, Laura Torres-Benito, Natalia Mendoza-Ferreira, Melina Overhoff, Roman Rombo, Vanessa Grysko, Min Jeong Kye, Natalia L. Kononenko and Brunhilde Wirth
- 72** ***CHRNA2 and Nocturnal Frontal Lobe Epilepsy: Identification and Characterization of a Novel Loss of Function Mutation***
Chiara Villa, Giulia Colombo, Simone Meneghini, Cecilia Gotti, Milena Moretti, Luigi Ferini-Strambi, Elisa Chisci, Roberto Giovannoni, Andrea Becchetti and Romina Combi
- 84** ***Loss of *Satb2* in the Cortex and Hippocampus Leads to Abnormal Behaviors in Mice***
Qiong Zhang, Ying Huang, Lei Zhang, Yu-Qiang Ding and Ning-Ning Song
- 96** ***Glycine Regulates Neural Stem Cell Proliferation During Development via *Lnx1*-Dependent Notch Signaling***
Abdelhamid Bekri, Meijiang Liao and Pierre Drapeau
- 103** ***Co-administration of Anti microRNA-124 and -137 Oligonucleotides Prevents Hippocampal Neural Stem Cell Loss Upon Non-convulsive Seizures***
Pascal Bielefeld, Marijn Schouten, Guido M. Meijer, Marit J. Breuk, Karlijne Geijtenbeek, Sedef Karayel, Alisa Tiaglik, Anna H. Vuuregge, Ruth A.L. Willems, Diede Witkamp, Paul J. Lucassen, Juan M. Encinas and Carlos P. Fitzsimons
- 116** ***BDNF Induced Translation of *Limk1* in Developing Neurons Regulates Dendrite Growth by Fine-Tuning *Cofilin1* Activity***
Sreenath Ravindran, Vijayalaxmi C. Nalavadi and Ravi S. Muddashetty

- 130** *The Autism and Angelman Syndrome Protein Ube3A/E6AP: The Gene, E3 Ligase Ubiquitination Targets and Neurobiological Functions*
Natasha Khatri and Heng-Ye Man
- 142** *Scn2a Haploinsufficiency in Mice Suppresses Hippocampal Neuronal Excitability, Excitatory Synaptic Drive, and Long-Term Potentiation, and Spatial Learning and Memory*
Wangyong Shin, Hanseul Kweon, Ryeonghwa Kang, Doyoun Kim, Kyungdeok Kim, Muwon Kang, Seo Yeong Kim, Sun Nam Hwang, Jin Yong Kim, Esther Yang, Hyun Kim and Eunjoon Kim
- 161** *Developmental Regulation of KCC2 Phosphorylation Has Long-Term Impacts on Cognitive Function*
Yvonne E. Moore, Leslie C. Conway, Heike J. Wobst, Nicholas J. Brandon, Tarek Z. Deeb and Stephen J. Moss
- 172** *The Orphan Cytokine Receptor CRLF3 Emerged With the Origin of the Nervous System and is a Neuroprotective Erythropoietin Receptor in Locusts*
Nina Hahn, Luca Büschgens, Nicola Schwedhelm-Domeyer, Sarah Bank, Bart R. H. Geurten, Pia Neugebauer, Bitu Massih, Martin C. Göpfert and Ralf Heinrich



UBE3A: An E3 Ubiquitin Ligase With Genome-Wide Impact in Neurodevelopmental Disease

Simon Jesse Lopez^{1,2,3,4}, David J. Segal^{2,3,4,5*} and Janine M. LaSalle^{1,2,3,4*}

¹Department of Medical Immunology and Microbiology, University of California, Davis, Davis, CA, United States, ²Genome Center, University of California, Davis, Davis, CA, United States, ³MIND Institute, University of California, Davis, Davis, CA, United States, ⁴Integrative Genetics and Genomics, University of California, Davis, Davis, CA, United States, ⁵Department of Biochemistry and Molecular Medicine, University of California, Davis, Davis, CA, United States

UBE3A is an E3 ubiquitin ligase encoded by an imprinted gene whose maternal deletion or duplication leads to distinct neurodevelopment disorders Angelman and Dup15q syndromes. Despite the known genetic basis of disease, how changes in copy number of a ubiquitin ligase gene can have widespread impact in early brain development is poorly understood. Previous studies have identified a wide array of UBE3A functions, interaction partners, and ubiquitin targets, but no central pathway fully explains its critical role in neurodevelopment. Here, we review recent UBE3A studies that have begun to investigate mechanistic, cellular pathways and the genome-wide impacts of alterations in UBE3A expression levels to gain broader insight into how UBE3A affects the developing brain. These studies have revealed that UBE3A is a multifunctional protein with important nuclear and cytoplasmic regulatory functions that impact proteasome function, Wnt signaling, circadian rhythms, imprinted gene networks, and chromatin. Synaptic functions of UBE3A interact with light exposures and mTOR signaling and are most critical in GABAergic neurons. Understanding the genome-wide influences of UBE3A will help uncover its role in early brain development and ultimately lead to identification of key therapeutic targets for UBE3A-related neurodevelopmental disorders.

Keywords: neurodevelopment, parental imprinting, human genetics and genomics, synapse, Angelman syndrome, autism (ASD)

OPEN ACCESS

Edited by:

Urs Albrecht,
Université de Fribourg, Switzerland

Reviewed by:

Toru Takumi,
RIKEN Brain Science Institute (BSI),
Japan

Dominic Landgraf,
Ludwig Maximilian University of
Munich, Germany

*Correspondence:

David J. Segal
djsegal@ucdavis.edu
Janine M. LaSalle
jmlasalle@ucdavis.edu

Received: 18 September 2018

Accepted: 05 December 2018

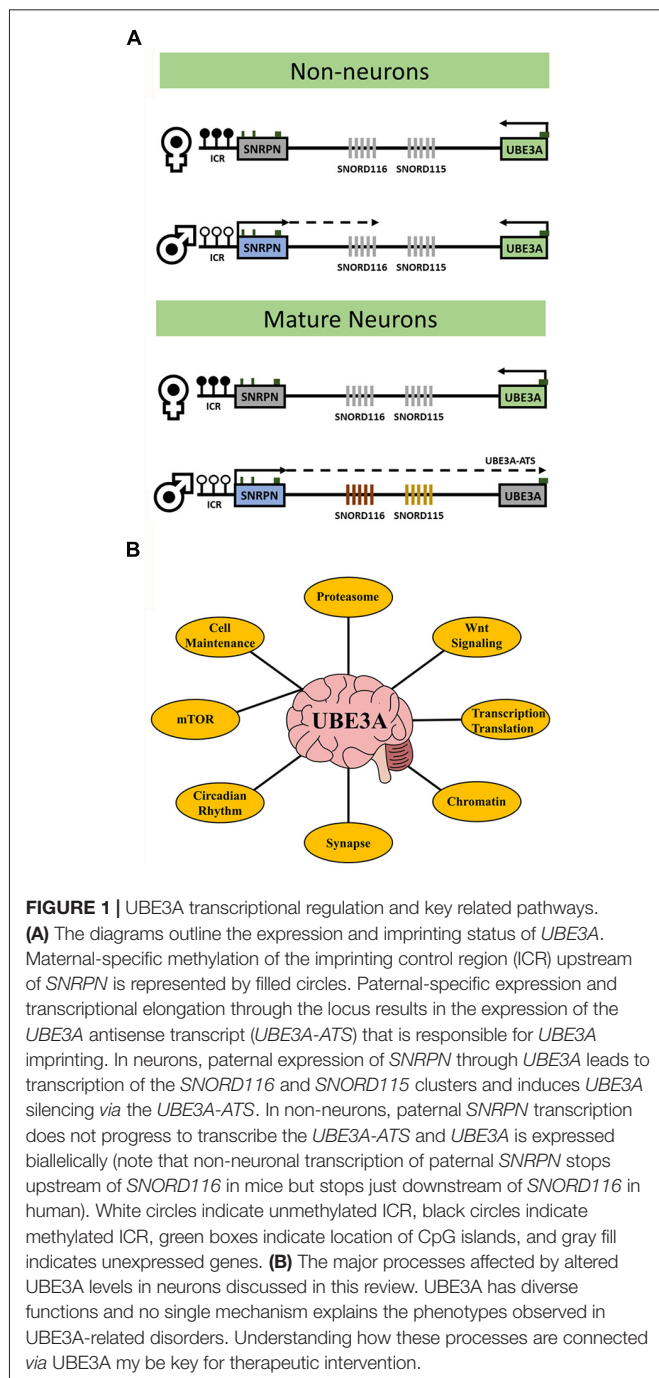
Published: 04 January 2019

Citation:

Lopez SJ, Segal DJ and LaSalle JM
(2019) UBE3A: An E3 Ubiquitin
Ligase With Genome-Wide Impact in
Neurodevelopmental Disease.
Front. Mol. Neurosci. 11:476.
doi: 10.3389/fnmol.2018.00476

INTRODUCTION TO UBE3A IMPRINTING AND ASSOCIATED DISEASES

UBE3A is an E3 ubiquitin ligase that targets proteins for proteasomal degradation. The UBE3A gene resides within the human 15q11.2-q13.3 locus that is parentally imprinted in neurons (**Figure 1A**) leading to the non-Mendelian inheritance patterns of three human neurodevelopmental disorders. Prader-Willi syndrome (PWS) results from 15q11.2-q13.3 paternal allele deletion whereas Angelman syndrome (AS) is caused by deletion of the maternal allele. In contrast, 15q11.2-q13.3 duplication (Dup15q) syndrome, a genetic cause of autism spectrum disorder (ASD), arises from duplications of the maternal allele. In neurons, UBE3A becomes silenced on the paternal allele due to the paternal-specific expression of an anti-sense transcript (*UBE3A-ATS*) originating from the unmethylated allele of *SNRPN*. UBE3A is the imprinted gene implicated in the maternal-specific effects of 15q11.2-q13.3 deletion or duplication disorders (LaSalle et al., 2015). However, a large population-based study recently demonstrated that paternal duplications of 15q11.2-q13.3 are



associated with increased risk of ASD or developmental delay (Isles et al., 2016). How paternal transcripts, including *UBE3A* or *UBE3A-ATS*, may contribute to this finding is currently unknown.

EVOLUTION OF PARENTAL IMPRINTING OF UBE3A WITHIN MAMMALS

How an E3 ubiquitin ligase contributes to the pathogenesis of neurodevelopmental disease is also poorly understood.

To gain functional insight into *UBE3A*, it is important to consider its evolutionary origin. The *UBE3A* gene predates the emergence of the nervous system but its imprinting was established relatively recently. After diversification of marsupials and placental mammals, multiple chromosomal rearrangements formed the domain controlling maternal expression of *UBE3A* from non-imprinted elements (Rapkins et al., 2006). Sequence data from an ancestral mammal were more similar to marsupials in chromatin arrangement suggesting that *UBE3A* imprinting evolved within mammalian radiation (Zhang et al., 2014). The ancestral non-imprinted *UBE3A* may explain its array of functions outside neurodevelopment while establishment of neuronal *UBE3A* imprinting coinciding with higher mammalian cognition may explain the link between them. The origin of *UBE3A* in ancient eukaryotes follows other human postsynaptic proteins that are also linked to neurogenetic disease (Bayés et al., 2011). Genomic imprinting, including that of *UBE3A*, may have evolved to regulate hibernation and sleep patterns to promote early mammalian survival at the Cretaceous–Paleogene boundary (Lovegrove et al., 2014; Tucci, 2016). The key events of *UBE3A* evolution likely included expression and localization at the synapse, colocalization with substrates essential in neurodevelopment, and acquisition of imprinting (Sato, 2017). *UBE3A* imprinting may have been critical for its neuronal role and understanding its establishment may pinpoint networks and pathways affected by *UBE3A*-associated disease.

CELLULAR LOCALIZATION OF UBE3A AND ITS ALTERNATIVELY SPLICED ISOFORMS

Immunohistochemical studies show *UBE3A* localization to both nuclear and cytoplasmic compartments of mature neurons. A proposed role for *UBE3A* in transcriptional regulation is consistent with nuclear localization (Nawaz et al., 1999; Bernassola et al., 2008; Pal et al., 2013). However, many reported *UBE3A* substrates are cytoplasmic proteins in the ubiquitin pathway. High-resolution light and electron microscopic immunocytochemistry of *UBE3A* has shown a broad neuronal distribution including both axon terminals and euchromatin-rich nuclear domains (Burette et al., 2017). Additionally, localization to the mitochondria supports the notion that *UBE3A* regulates oxidative metabolism (Su et al., 2011; Llewellyn et al., 2015). Strong localization to axon terminals indicates physiological significance of *UBE3A* for the function of individual synapses whereas its nuclear localization in euchromatin-rich domains indicates a role in mediating global neuronal physiology via transcription regulation. This suggests that *UBE3A* locally regulates individual synapses while also influencing global neuronal physiology through regulation of chromatin and transcription. Furthermore, recent evidence indicates sequence variation among *UBE3A*'s alternatively spliced isoforms helps to determine dendritic functions (Miao et al., 2013). Further study of individual isoforms, their localization, and subsequent roles will

be necessary to discriminate UBE3A's distinct functional localizations.

UBE3A and its interaction partners appear to integrate several cellular processes including translation, intracellular trafficking, and cytoskeleton regulation necessary for neuronal functions. Those interacting proteins discussed in this review are summarized in **Table 1**. Proteomic analysis of UBE3A binding proteins revealed that UBE3A binds to HERC2, another E3 ubiquitin ligase, in a complex of unknown function referred to as the HUN (HERC2, UBE3A, and NEURL4) complex (Martínez-Noël et al., 2012). Network analysis of UBE3A-associated proteins, including MCM6, SUGT1, EIF3C, and ASPP2, revealed that UBE3A-associated proteins are involved in several fundamental cellular processes including translation, DNA replication, intracellular trafficking, and centrosome regulation (Martínez-Noël et al., 2018). UBE3A could be involved in the regulation of these processes either directly or as a component of the HUN complex. Interaction with MCM6 might be relevant to the transcriptional activity of UBE3A since the MCM complex interacts with RNA polymerase

II and could facilitate transcription by remodeling chromatin (Yankulov et al., 1999). Binding of UBE3A to HERC2 and subsequent association with other DNA replication proteins also suggests a role of UBE3A in DNA replication and repair.

INTRACELLULAR PATHWAYS AND MECHANISTIC FUNCTIONS OF UBE3A

UBE3A is an E3 ubiquitin ligase that poly-ubiquitinates specific intracellular proteins for degradation by the ubiquitin-proteasome system (Huang et al., 1999). Recent proteomics studies indicate that UBE3A interacts with most of the components of the proteasome, the central organelle for intracellular protein degradation (Martínez-Noël et al., 2018; Ramirez et al., 2018). A ubiquitin proteomics approach identified 13 proteasome subunits or proteasome interacting proteins, including DDI1, showed increased ubiquitination in UBE3A over-expressing *Drosophila* photoreceptor cells (Ramirez et al., 2018). DDI1 was shown to be ubiquitinated by UBE3A, without

TABLE 1 | Summary of notable gene interactions with UBE3A and associated pathways outlined in this review.

Gene	Type of interaction	Functions and pathways	References
HERC2	HUN complex, E3 ubiquitin ligase activity	DNA replication and repair, proteasome degradation pathway	Vos et al. (2009); Zaaroor-Regev et al. (2010); Tomaš et al. (2011) and Martínez-Noël et al. (2012)
NEURL4	HUN complex	Centriolar homeostasis	Martínez-Noël et al. (2012)
HIF1AN	Direct interaction by co-immunoprecipitation	Oxygen sensor, negative regulator of NOTCH1	Martínez-Noël et al. (2012)
MAPK6	Indirect interaction via HERC2	MAP kinase cascade, Ser/Thr protein kinase	Martínez-Noël et al. (2012)
MCM6	Direct interaction by affinity purification mass spectrometry	MCM complex, transcription	Martínez-Noël et al. (2012)
SUGT1	Direct interaction by affinity purification mass spectrometry	Cell cycle regulation	Martínez-Noël et al. (2012)
EIF3C	Direct interaction by affinity purification mass spectrometry	Translation initiation	Martínez-Noël et al. (2012)
ASPP2	Direct interaction by affinity purification mass spectrometry	p53 family apoptosis and cell growth	Martínez-Noël et al. (2018)
DDI1	E3 ubiquitin ligase activity	Proteasomal shuttle component	Ramirez et al. (2018)
RPN10	E3 ubiquitin ligase activity	26S proteasome regulatory subunit	Lee et al. (2014)
UCHL5	Direct ubiquitination, non-degradation	26S proteasome regulatory subunit	Lee et al. (2014)
UBXN1	Direct ubiquitination, non-degradation	ER-associated protein degradation, innate immune response	Lee et al. (2014)
CTNNB1	Direct ubiquitination, non-degradation	Wnt signaling transduction	Kuslansky et al. (2016)
EDD	E3 ubiquitin ligase activity	Proteasome degradation pathway	Vos et al. (2009), Zaaroor-Regev et al. (2010) and Tomaš et al. (2011)
PSMD4	E3 ubiquitin ligase activity	Proteasome proteolytic activity	Martínez-Noël et al. (2012) and Tomaš and Banks (2015)
BMAL1	E3 ubiquitin ligase activity	Circadian clock dynamics	Gossan et al. (2014) and Shi et al. (2015)
ALDH1A2	E3 ubiquitin ligase activity	Retinoic acid synthesis	Xu et al. (2018)
SK2	E3 ubiquitin ligase activity	small-conductance potassium channel	Sun et al. (2015b)
mTOR	Direct interaction not confirmed	Cell cycle regulation	Tang et al. (2014) and Sun et al. (2015a)
TSC2	Direct interaction not confirmed	Negative regulator of mTOR	Sun et al. (2015a)
miR-134	Ube3a1 competitive binding	miR379–410 cluster co-translation	Valluy et al. (2015)
RING1B	E3 ubiquitin ligase activity	PRC1 complex	Dunaway et al. (2016)
H2A.Z	Indirect interaction via PRC1	Chromatin organization, constitutive heterochromatin	Dunaway et al. (2016)

being targeted for degradation, and expressed in the developing mouse brain with a significant peak at E16.5. UBE3A also interacts with HERC2 and EDD, ubiquitin ligase components of the proteasome degradation pathway (Vos et al., 2009; Zaaroor-Regev et al., 2010; Tomaić et al., 2011). Additionally, direct interaction between UBE3A and the proteasome itself has been observed (Uchiki et al., 2009; Lee et al., 2014). Although the function of UBE3A in the proteasome is still unclear, its association with PSMD4 suggests it might help control the proteolytic activity of the proteasome. AS-associated mutants were shown to strongly interact *via* PSMD4 with the proteasome, resulting in inhibition of the proteolytic activity of the proteasome (Tomaić and Banks, 2015). These data suggest that mutant, catalytically-inactive forms of UBE3A can cause functional deficits of the proteasome. Cellular stresses that increase polyubiquitinated protein levels also blocked UBE3A from ubiquitinating the proteasome and increased proteasome activity (Jacobson et al., 2014). This suggests the proteasome can detect global polyubiquitinated protein levels and that UBE3A is involved in adjusting proteasomal activity. This perturbation of overall proteasome function may be part of AS pathogenesis.

The interaction between the proteasome and UBE3A has also been shown to induce Wnt signaling, the group of signal transduction pathways that regulate cell fate determination, cell migration, and neural patterning during embryonic development. Wnt signals regulate adult neurogenesis as well as neural stem cell behavior during central nervous system development (Kléber and Sommer, 2004; Lie et al., 2005; Kuwabara et al., 2009). Abnormal Wnt signaling is also implicated in autism pathogenesis (De Rubeis et al., 2014; Ernst, 2016; Packer, 2016). Furthermore, a *de novo* autism-linked UBE3A mutant (UBE3AT485A) prevents UBE3A catalytic inhibition by disrupting protein kinase A (PKA) phosphorylation inhibition toward itself and other substrates (Yi et al., 2015). This disruption caused enhanced UBE3A activity with increased turnover of UBE3A substrates in patient-derived cells and excessive dendritic spine development with increased synapse number in the brain. UBE3AT485A protein ubiquitinated multiple proteasome subunits leading to reduced abundance and activity, while stabilizing nuclear β -catenin and stimulating canonical Wnt signaling compared to wild-type UBE3A. This indicates that UBE3A regulates Wnt signaling and that an autism-linked mutation enhanced its signaling effects, which is corroborated by other studies that place UBE3A within the Wnt signaling pathway (Lichtig et al., 2010; Sominsky et al., 2014; Kuslansky et al., 2016). These findings also suggest that PKA helps regulate UBE3A activity during postnatal neuronal maturation to ensure proper synaptic development. This model is further supported by observations that persistent PKA inhibition does not increase dendritic spine density in *Ube3a*-deficient neurons while overexpression of UBE3AT485A profoundly increased dendritic spine density *in vivo* (Yasuda et al., 2003; Lu et al., 2011).

The role of UBE3A in regulating circadian rhythms has also emerged as an important pathway in understanding

disease etiology. Ubiquitin-mediated turnover of circadian clock proteins was first observed in *Drosophila* and *Neurospora* (Naidoo et al., 1999; He and Liu, 2005). A link between neuronal imprinting of *UBE3A* and central clock components have been observed *via* regulation of BMAL1. UBE3A binds and degrades BMAL1 in a ubiquitin ligase-dependent manner suggesting that regulation of circadian dynamics *via* modulating BMAL1 turnover is an endogenous role of UBE3A (Gossan et al., 2014). Moreover, inactivation of UBE3A expression in AS-model mice increases BMAL1 in brain regions that control circadian behavior including enfeebled circadian activity and slowed molecular rhythms, including lengthened circadian period and reduced amplitude (Shi et al., 2015). Importantly, unsilencing the paternal allele restored functional circadian periodicity in neurons but did not alter periodicity in non-imprinted peripheral tissues. These findings constitute a mechanistic connection between circadian rhythmicity and sleep abnormalities in AS. The lengthened circadian period leads to delayed phase. This could explain why 75% of AS patients suffer from sleep disturbances, including short sleep duration and increased sleep onset latency (Smith et al., 1996; Pelc et al., 2008), one of the most stressful manifestations reported by AS families (Goldman et al., 2012).

SYNAPTIC ROLES FOR UBE3A

Of interest to the understanding of UBE3A in neurodevelopment is its effect on neuronal processes and synapses. Increased UBE3A dosage was shown to negatively regulate *ALDH1A2*, the rate-limiting enzyme of retinoic acid synthesis, leading to impaired post-synaptic homeostasis (Xu et al., 2018). The loss of UBE3A in adult AS model mice results in reduced spine density in the cerebellum and hippocampus (Dindot et al., 2008). These highlight the importance of proper UBE3A dosage in synapse formation and maintenance. During the first postnatal month, elimination of dendritic spines is higher in neurons of AS compared to wild-type mice. However, spine maintenance and density were indistinguishable for mice raised in darkness, suggesting that impaired experience-driven spine maintenance leads to decreased spine density in AS model mice (Kim et al., 2016). This demonstrates that light exposure is an important environmental factor that interacts with *UBE3A* mutation to reduce dendritic spine density and disrupt cortical circuitry. How this light-dependent synaptic change in the AS mouse model may influence UBE3A's impact on circadian factors, such as BMAL, is currently unknown.

Additionally, UBE3A has been shown to interact with small-conductance potassium channels (SKs), which are critical for learning and memory, rhythmic activity, and sleep (Adelman et al., 2012; Ohtsuki et al., 2012). UBE3A directly ubiquitinates SK2 in the C-terminal domain, facilitating endocytosis (Sun et al., 2015b). Postsynaptic SK2 levels are increased in UBE3A-deficient mice, resulting in decreased NMDA receptor activation and impairs long-term synaptic plasticity in the hippocampus. Importantly, synaptic plasticity and fear conditioned memory deficits in UBE3A-deficient mice were restored by blocking SK2. UBE3A loss in GABAergic neurons resulted in AS-like

increases in neocortical EEG delta power, enhanced susceptibility to seizures, and lead to accumulation of clathrin-coated vesicles (CCV) at the presynapse without decreasing GABAergic inhibition onto pyramidal neurons (Judson et al., 2016). Conversely, UBE3A loss in glutamatergic neurons fails to show the same phenotypes, despite impairing tonic inhibition onto pyramidal neurons supporting a role of UBE3A in GABAergic neuron circuit hyperexcitability in AS mice.

Finally, UBE3A has been shown to have an important interaction with the mTOR pathway, an intracellular signaling pathway important in regulating translation, cellular metabolism, and implicated in long-term synaptic plasticity and memory (Man et al., 2003; Sui et al., 2008). Studies in ASD human brain showed dendritic spine pruning defects and impaired mTOR-autophagy that was confirmed by mTOR overactivation causing spine pruning defects in ASD mouse models (Tang et al., 2014). Furthermore, these pruning defects and ASD-like behaviors were corrected after treatment with rapamycin, an inhibitor of mTOR. Additionally, neuronal autophagy further enabled spine elimination suggesting that developmental spine pruning requires mTOR-regulated autophagy and its activation corrects synaptic pathology and social behavior deficits in ASD models (Tang et al., 2014). Furthermore, imbalanced signaling, with increased mTORC1 and decreased mTORC2 activation, leads to UBE3A deficiency-induced cerebellum-dependent motor dysfunction (Sun et al., 2015a) and hippocampal synaptic plasticity and fear-conditioning memory deficits in an AS mouse model (Sun et al., 2016). Either mTORC1 inhibition or mTORC2 activation restored long-term potentiation (LTP) and actin polymerization in AS mice hippocampus. Decreased mTORC2 activity in AS mice was reversed by rapamycin, indicating that mTORC1 over-activation leads to reduced mTORC2 activity in AS mice. Increased mTORC1 could also increase Arc levels that stimulate AMPA receptor endocytosis leading to the LTP and learning deficits seen in AS mice (Sun et al., 2017). These demonstrate the importance of mTOR balance in AS, however the specific mechanistic link between UBE3A and mTOR and how it contributes to AS phenotypes is not yet understood.

MAMMALIAN NEURODEVELOPMENT AND IMPRINTING OF UBE3A

That UBE3A has distinct localization, expression and targeting patterns during different stages of mammalian development suggests the importance of timing in intervention for treatment of UBE3A-associated disorders. Particularly in AS, determining the time at which UBE3A reinstatement is able to rescue all pertinent phenotypes, including behavioral abnormalities, cellular dysfunction, and cognitive function, will be most crucial (Sell and Margolis, 2015). Cre-dependent, neuronal induction of maternal UBE3A during developmental timepoints identified distinct windows where UBE3A re-expression can rescue phenotypes in AS mice. Maternal UBE3A induction in adolescent mice restored motor deficits, however, *in utero* reinstatement was required to rescue anxiety, repetitive behavior, and epilepsy phenotypes (Silva-Santos et al., 2015). In contrast, hippocampal

synaptic plasticity could be restored in AS mice at any age. These findings indicate that therapeutic intervention early in development may be required to prevent most phenotypes associated with AS.

Another important factor in assessing UBE3A function is *UBE3A-ATS* transcribed in the opposite orientation to *UBE3A*. Transcription of *UBE3A-ATS*, or perhaps *UBE3A-ATS* itself, may introduce additional functions of both coding and non-coding UBE3A isoforms expressed in mammalian neurons. One hypothesis for why certain genes become imprinted is as a dosage-regulating mechanism. However, no correlation was found between imprinting status and expression levels of UBE3A after examination of cells and tissues among different species (Hillman et al., 2017). Alternatively, this study found that neuronal loss of paternal UBE3A protein levels during neurogenesis in mice were fully compensated by an accompanying increase in maternal UBE3A protein levels. Consistent with this finding, previous studies of mouse brain development as well as human tissues have shown UBE3A transcript level remain relatively constant (Kohama et al., 2011; Galiveti et al., 2014) and supports the emerging hypothesis that dosage compensation may not be a common reason explaining evolutionary selection of imprinted genes (Baran et al., 2015). These findings instead indicate that imprinting of UBE3A *via* the *UBE3A-ATS* may have been selected in mammals to more intricately regulate isoforms of UBE3A and not just overall expression levels.

Recently, *Ube3a1* RNA, a transcript encoding a truncated, catalytically inactive UBE3A protein, was shown to prevent dendrite growth and promote spine maturation in rat hippocampal neurons (Valluy et al., 2015). *Ube3a1* function was independent of its coding sequence and predicted to act as a long noncoding RNA (lncRNA) with a unique 3' untranslated region containing microRNA (miRNA) binding capabilities. *Ube3a1* knockdown increased activity of miR-134, which regulates plasticity, suggesting that *Ube3a1* lncRNA acts as a competing endogenous RNA, or "RNA sponge" for miR-134. In rat neurons, *Ube3a1* transcript sequestered miRNAs from the miR379–410 cluster, which contains miR-134, thereby regulating translation of miR379–410 targets in dendrites. During development, increased neuronal activity and subsequent increased *Ube3a1* RNA levels buffered miR379–410 activity allowing progression to spine maturation (Valluy et al., 2015). These findings indicate that *Ube3a1* lncRNA may help regulate the spatiotemporal control of mRNA translation within dendrites. Many questions remain about the regulation and function of *Ube3a1* including its imprinting pattern, if the paternally expressed *UBE3A-ATS* is required for *Ube3a1* expression, and its relevance in human AS.

Finally, we have begun to explore the chromatin-related genome-wide effects of UBE3A dysregulation in human brain and neurons. We previously observed that elevated UBE3A in Dup15q syndrome had widespread effects on the neuronal methylome that converged in the dysregulation of chromatin and synaptic gene pathways (Dunaway et al., 2016). This study identified many differentially methylated genes in Dup15q compared to control brains with functions in voltage-gated ion

channels, cell adhesion, signal transduction, and transcriptional regulation. Additionally, we observed a chromatin association between UBE3A and histone H2A.Z. UBE3A degrades RING1B, a known UBE3A target that monoubiquitinates histones H2A and H2A.Z, thereby regulating H2A.Z monoubiquitination. Additionally, we took a multi-layered genomics approach to identify the global effects of different UBE3A expression levels in human neuronal cell culture models revealing significant effects on DNA methylation leading to differentially methylated regions (DMRs) in genes involved in transcriptional regulation and brain development (Lopez et al., 2017). This revealed a significant effect of reduced UBE3A levels on the methylation of up to half of known imprinted genes, suggesting a role for UBE3A in a neuronal imprinted gene network. This provides strong support for a genome-wide, epigenomic function of UBE3A influencing DNA methylation and regulation of other imprinted genes in neurons.

SUMMARY

UBE3A has long been linked with ASD and is causal in AS etiology, however how UBE3A leads to disease phenotypes is not well understood. More recently, UBE3A genome-wide functions may enlighten additional gene pathways relevant to neurodevelopmental disorders (Table 1). Recent proteomics studies have uncovered a strong link between UBE3A and regulation of the proteasome and subsequent activation of

the Wnt signaling pathway in early brain development. Aberrant UBE3A expression has large influence on proper maintenance of circadian rhythmicity and increasing evidence shows this interaction to be key in the manifestation of AS and ASD phenotypes. Synaptic functions of UBE3A including neuronal excitability may be linked to the proper balance of mTOR signaling in developing neurons. Finally, the regulatory landscape of UBE3A may also be compounded by epigenetic functions such as regulation *via* the UBE3A-ATS and direct influences on chromatin dynamics and genome-wide DNA methylation including regulation of other imprinted genes. Understanding the functions of UBE3A in a neurodevelopmental context will improve the study of its associated disorders and may lead to enhanced therapeutic options at key targets and pathways (Figure 1B).

AUTHOR CONTRIBUTIONS

SL, JL, and DS all participated in the writing and editing of the manuscript.

FUNDING

This work was supported by NIH R56 NS076263 (JL) and R01 ES21707S1 (SL and JL), as well as the Foundation for Angelman Syndrome Therapeutics (DS).

REFERENCES

- Adelman, J. P., Maylie, J., and Sah, P. (2012). Small-conductance Ca^{2+} -activated K^{+} channels: form and function. *Annu. Rev. Physiol.* 74, 245–269. doi: 10.1146/annurev-physiol-020911-153336
- Baran, Y., Subramaniam, M., Biton, A., Tukiainen, T., Tsang, E. K., Rivas, M. A., et al. (2015). The landscape of genomic imprinting across diverse adult human tissues. *Genome Res.* 25, 927–936. doi: 10.1101/gr.192278.115
- Bayés, À., van de Lagemaat, L. N., Collins, M. O., Croning, M. D. R., Whittle, I. R., Choudhary, J. S., et al. (2011). Characterization of the proteome, diseases and evolution of the human postsynaptic density. *Nat. Neurosci.* 14, 19–21. doi: 10.1038/nn.2719
- Bernassola, F., Karin, M., Ciechanover, A., and Melino, G. (2008). The HECT family of E3 ubiquitin ligases: multiple players in cancer development. *Cancer Cell* 14, 10–21. doi: 10.1016/j.ccr.2008.06.001
- Burette, A. C., Judson, M. C., Burette, S., Phend, K. D., Philpot, B. D., and Weinberg, R. J. (2017). Subcellular organization of UBE3A in neurons. *J. Comp. Neurol.* 525, 233–251. doi: 10.1002/cne.24063
- De Rubeis, S., He, X., Goldberg, A. P., Poultney, C. S., Samocha, K., Cicek, A. E., et al. (2014). Synaptic, transcriptional and chromatin genes disrupted in autism. *Nature* 515, 209–215. doi: 10.1038/nature13772
- Dindot, S. V., Antalffy, B. A., Bhattacharjee, M. B., and Beaudet, A. L. (2008). The angelman syndrome ubiquitin ligase localizes to the synapse and nucleus and maternal deficiency results in abnormal dendritic spine morphology. *Hum. Mol. Genet.* 17, 111–118. doi: 10.1093/hmg/ddm288
- Dunaway, K. W., Islam, M. S., Coulson, R. L., Lopez, S. J., Vogel Ciernia, A., Chu, R. G., et al. (2016). Cumulative impact of polychlorinated biphenyl and large chromosomal duplications on DNA methylation, chromatin, and expression of autism candidate genes. *Cell Rep.* 17, 3035–3048. doi: 10.1016/j.celrep.2016.11.058
- Ernst, C. (2016). Proliferation and differentiation deficits are a major convergence point for neurodevelopmental disorders. *Trends Neurosci.* 39, 290–299. doi: 10.1016/j.tins.2016.03.001
- Galiveti, C. R., Raabe, C. A., Konthur, Z., and Rozhdestvensky, T. S. (2014). Differential regulation of non-protein coding RNAs from Prader-Willi Syndrome locus. *Sci. Rep.* 4:6445. doi: 10.1038/srep06445
- Goldman, S. E., Bichell, T. J., Surdyka, K., and Malow, B. A. (2012). Sleep in children and adolescents with angelman syndrome: association with parent sleep and stress. *J. Intellect. Disabil. Res.* 56, 600–608. doi: 10.1111/j.1365-2788.2011.01499.x
- Gossan, N. C., Zhang, F., Guo, B., Jin, D., Yoshitane, H., Yao, A., et al. (2014). The E3 ubiquitin ligase UBE3A is an integral component of the molecular circadian clock through regulating the BMAL1 transcription factor. *Nucleic Acids Res.* 42, 5765–5775. doi: 10.1093/nar/gku225
- He, Q., and Liu, Y. (2005). Degradation of the neurospora circadian clock protein FREQUENCY through the ubiquitin-proteasome pathway. *Biochem. Soc. Trans.* 33, 953–956. doi: 10.1042/BST0330953
- Hillman, P. R., Christian, S. G. B., Doan, R., Cohen, N. D., Konganti, K., Douglas, K., et al. (2017). Genomic imprinting does not reduce the dosage of UBE3A in neurons. *Epigenetics Chromatin* 10:27. doi: 10.1186/s13072-017-0134-4
- Huang, L., Kinnucan, E., Wang, G., Beaudenon, S., Howley, P. M., Huibregtse, J. M., et al. (1999). Structure of an E6AP-UbcH7 complex: insights into ubiquitination by the E2–E3 enzyme cascade. *Science* 286, 1321–1326. doi: 10.1126/science.286.5443.1321
- Isles, A. R., Ingason, A., Lowther, C., Walters, J., Gawlick, M., Stöber, G., et al. (2016). Parental origin of interstitial duplications at 15q11.2–q13.3 in schizophrenia and neurodevelopmental disorders. *PLoS Genet.* 12:e1005993. doi: 10.1371/journal.pgen.1005993
- Jacobson, A. D., MacFadden, A., Wu, Z., Peng, J., and Liu, C.-W. (2014). Autoregulation of the 26S proteasome by *in situ* ubiquitination. *Mol. Biol. Cell* 25, 1824–1835. doi: 10.1091/mbc.e13-10-0585
- Judson, M. C., Wallace, M. L., Sidorov, M. S., Burette, A. C., Gu, B., van Woerden, G. M., et al. (2016). GABAergic neuron-specific loss of Ube3a causes angelman syndrome-like EEG abnormalities and enhances seizure susceptibility. *Neuron* 90, 56–69. doi: 10.1016/j.neuron.2016.02.040

- Kim, H., Kunz, P. A., Mooney, R., Philpot, B. D., and Smith, S. L. (2016). Maternal loss of *Ube3a* impairs experience-driven dendritic spine maintenance in the developing visual cortex. *J. Neurosci.* 36, 4888–4894. doi: 10.1523/JNEUROSCI.4204-15.2016
- Kléber, M., and Sommer, L. (2004). Wnt signaling and the regulation of stem cell function. *Curr. Opin. Cell Biol.* 16, 681–687. doi: 10.1016/j.ccb.2004.08.006
- Kohama, C., Kato, H., Numata, K., Hirose, M., Takemasa, T., Ogura, A., et al. (2011). ES cell differentiation system recapitulates the establishment of imprinted gene expression in a cell-type-specific manner. *Hum. Mol. Genet.* 21, 1391–1401. doi: 10.1093/hmg/ddr577
- Kuslansky, Y., Sominsky, S., Jackman, A., Gamell, C., Monahan, B. J., Haupt, Y., et al. (2016). Ubiquitin ligase E6AP mediates nonproteolytic polyubiquitylation of β -catenin independent of the E6 oncoprotein. *J. Gen. Virol.* 97, 3313–3330. doi: 10.1099/jgv.0.000624
- Kuwabara, T., Hsieh, J., Muotri, A., Yeo, G., Warashina, M., Lie, D. C., et al. (2009). Wnt-mediated activation of NeuroD1 and retro-elements during adult neurogenesis. *Nat. Neurosci.* 12, 1097–1105. doi: 10.1038/nn.2360
- LaSalle, J. M., Reiter, L. T., and Chamberlain, S. J. (2015). Epigenetic regulation of UBE3A and roles in human neurodevelopmental disorders. *Epigenomics* 7, 1213–1228. doi: 10.2217/epi.15.70
- Lee, S. Y., Ramirez, J., Franco, M., Lectez, B., Gonzalez, M., Barrio, R., et al. (2014). Ube3a, the E3 ubiquitin ligase causing angelman syndrome and linked to autism, regulates protein homeostasis through the proteasomal shuttle Rpn10. *Cell. Mol. Life Sci.* 71, 2747–2758. doi: 10.1007/s00018-013-1526-7
- Lichtig, H., Gilboa, D. A., Jackman, A., Gonen, P., Levav-Cohen, Y., Haupt, Y., et al. (2010). HPV16 E6 augments Wnt signaling in an E6AP-dependent manner. *Virology* 396, 47–58. doi: 10.1016/j.virol.2009.10.011
- Lie, D.-C., Colamarino, S. A., Song, H.-J., Désiré, L., Mira, H., Consiglio, A., et al. (2005). Wnt signalling regulates adult hippocampal neurogenesis. *Nature* 437, 1370–1375. doi: 10.1038/nature04108
- Llewellyn, K. J., Nalbandian, A., Gomez, A., Wei, D., Walker, N., and Kimonis, V. E. (2015). Administration of CoQ10 analogue ameliorates dysfunction of the mitochondrial respiratory chain in a mouse model of angelman syndrome. *Neurobiol. Dis.* 76, 77–86. doi: 10.1016/j.nbd.2015.01.005
- Lopez, S. J., Dunaway, K., Islam, M. S., Mordaunt, C., Vogel Ciernia, A., Meguro-Horike, M., et al. (2017). UBE3A-mediated regulation of imprinted genes and epigenome-wide marks in human neurons. *Epigenetics* 12, 982–990. doi: 10.1080/15592294.2017.1376151
- Lovegrove, B. G., Lobban, K. D., and Levesque, D. L. (2014). Mammal survival at the cretaceous-paleogene boundary: metabolic homeostasis in prolonged tropical hibernation in tenrecs. *Proc. Biol. Sci.* 281:20141304. doi: 10.1098/rspb.2014.1304
- Lu, Y., Zha, X.-M., Kim, E. Y., Schachtele, S., Dailey, M. E., Hall, D. D., et al. (2011). A kinase anchor protein 150 (AKAP150)-associated protein kinase A limits dendritic spine density. *J. Biol. Chem.* 286, 26496–26506. doi: 10.1074/jbc.M111.254912
- Man, H.-Y., Wang, Q., Lu, W.-Y., Ju, W., Ahmadian, G., Liu, L., et al. (2003). Activation of PI3-kinase is required for AMPA receptor insertion during LTP of mEPSCs in cultured hippocampal neurons. *Neuron* 38, 611–624. doi: 10.1016/s0896-6273(03)00228-9
- Martínez-Noël, G., Galligan, J. T., Sowa, M. E., Arndt, V., Overton, T. M., Harper, J. W., et al. (2012). Identification and proteomic analysis of distinct UBE3A/E6AP protein complexes. *Mol. Cell. Biol.* 32, 3095–3106. doi: 10.1128/mcb.00201-12
- Martínez-Noël, G., Luck, K., Kühnle, S., Desbuleux, A., Szajner, P., Galligan, J. T., et al. (2018). Network analysis of UBE3A/E6AP-associated proteins provides connections to several distinct cellular processes. *J. Mol. Biol.* 430, 1024–1050. doi: 10.1016/j.jmb.2018.01.021
- Miao, S., Chen, R., Ye, J., Tan, G.-H., Li, S., Zhang, J., et al. (2013). The angelman syndrome protein Ube3a is required for polarized dendrite morphogenesis in pyramidal neurons. *J. Neurosci.* 33, 327–333. doi: 10.1523/JNEUROSCI.2509-12.2013
- Naidoo, N., Song, W., Hunter-Ensor, M., and Sehgal, A. (1999). A role for the proteasome in the light response of the timeless clock protein. *Science* 285, 1737–1741. doi: 10.1126/science.285.5434.1737
- Nawaz, Z., Lonard, D. M., Smith, C. L., Lev-Lehman, E., Tsai, S. Y., Tsai, M. J., et al. (1999). The angelman syndrome-associated protein, E6-AP, is a coactivator for the nuclear hormone receptor superfamily. *Mol. Cell. Biol.* 19, 1182–1189. doi: 10.1128/mcb.19.2.1182
- Ohtsuki, G., Piochon, C., Adelman, J. P., and Hansel, C. (2012). SK2 channel modulation contributes to compartment-specific dendritic plasticity in cerebellar purkinje cells. *Neuron* 75, 108–120. doi: 10.1016/j.neuron.2012.05.025
- Packer, A. (2016). Neocortical neurogenesis and the etiology of autism spectrum disorder. *Neurosci. Biobehav. Rev.* 64, 185–195. doi: 10.1016/j.neubiorev.2016.03.002
- Pal, P., Lochab, S., Kanaujiya, J. K., Kapoor, I., Sanyal, S., Behre, G., et al. (2013). E3 ubiquitin ligase E6AP negatively regulates adipogenesis by downregulating proadipogenic factor C/EBP α . *PLoS One* 8:e65330. doi: 10.1371/journal.pone.0065330
- Pelc, K., Cheron, G., Boyd, S. G., and Dan, B. (2008). Are there distinctive sleep problems in angelman syndrome? *Sleep Med.* 9, 434–441. doi: 10.1016/j.sleep.2007.07.001
- Ramirez, J., Lectez, B., Osinalde, N., Sivá, M., Elu, N., Aloria, K., et al. (2018). Quantitative proteomics reveals neuronal ubiquitination of Rngo/Ddi1 and several proteasomal subunits by Ube3a, accounting for the complexity of angelman syndrome. *Hum. Mol. Genet.* 27, 1955–1971. doi: 10.1093/hmg/ddy103
- Rapkins, R. W., Hore, T., Smithwick, M., Ager, E., Pask, A. J., Renfree, M. B., et al. (2006). Recent assembly of an imprinted domain from non-imprinted components. *PLoS Genet.* 2:e182. doi: 10.1371/journal.pgen.0020182
- Sato, M. (2017). Early origin and evolution of the angelman syndrome ubiquitin ligase gene *Ube3a*. *Front. Cell. Neurosci.* 11:62. doi: 10.3389/fncel.2017.00062
- Sell, G. L., and Margolis, S. S. (2015). From UBE3A to angelman syndrome: a substrate perspective. *Front. Neurosci.* 9:322. doi: 10.3389/fnins.2015.00322
- Shi, S.-Q., Bichell, T. J., Ihrie, R. A., and Johnson, C. H. (2015). Ube3a imprinting impairs circadian robustness in angelman syndrome models. *Curr. Biol.* 25, 537–545. doi: 10.1016/j.cub.2014.12.047
- Silva-Santos, S., van Woerden, G. M., Bruinsma, C. F., Mientjes, E., Jolfaei, M. A., Distel, B., et al. (2015). *Ube3a* reinstatement identifies distinct treatment windows in angelman syndrome model mice. *J. Clin. Invest.* 125, 2069–2076. doi: 10.1172/jci80554
- Smith, A., Wiles, C., Haan, E., McGill, J., Wallace, G., Dixon, J., et al. (1996). Clinical features in 27 patients with angelman syndrome resulting from DNA deletion. *J. Med. Genet.* 33, 107–112. doi: 10.1136/jmg.33.2.107
- Sominsky, S., Kuslansky, Y., Shapiro, B., Jackman, A., Haupt, Y., Rosin-Arbesfeld, R., et al. (2014). HPV16 E6 and E6AP differentially cooperate to stimulate or augment Wnt signaling. *Virology* 468, 510–523. doi: 10.1016/j.virol.2014.09.007
- Su, H., Fan, W., Coskun, P. E., Vesa, J., Gold, J.-A., Jiang, Y.-H., et al. (2011). Mitochondrial dysfunction in CA1 hippocampal neurons of the UBE3A deficient mouse model for angelman syndrome. *Neurosci. Lett.* 487, 129–133. doi: 10.1016/j.neulet.2009.06.079
- Sui, L., Wang, J., and Li, B.-M. (2008). Role of the phosphoinositide 3-kinase-Akt-mammalian target of the rapamycin signaling pathway in long-term potentiation and trace fear conditioning memory in rat medial prefrontal cortex. *Learn. Mem.* 15, 762–776. doi: 10.1101/lm.1067808
- Sun, J., Baudry, M., and Bi, X. (2017). Novel neurobiological roles of UBE3A. *Oncotarget* 8, 12548–12549. doi: 10.18632/oncotarget.15105
- Sun, J., Liu, Y., Tran, J., O'Neal, P., Baudry, M., and Bi, X. (2016). mTORC1-S6K1 inhibition or mTORC2 activation improves hippocampal synaptic plasticity and learning in angelman syndrome mice. *Cell. Mol. Life Sci.* 73, 4303–4314. doi: 10.1007/s00018-016-2269-z
- Sun, J., Liu, Y., Moreno, S., Baudry, M., and Bi, X. (2015a). Imbalanced mechanistic target of rapamycin C1 and C2 activity in the cerebellum of angelman syndrome mice impairs motor function. *J. Neurosci.* 35, 4706–4718. doi: 10.1523/JNEUROSCI.4276-14.2015
- Sun, J., Zhu, G., Liu, Y., Standley, S., Ji, A., Tunuguntla, R., et al. (2015b). UBE3A regulates synaptic plasticity and learning and memory by controlling SK2 channel endocytosis. *Cell Rep.* 12, 449–461. doi: 10.1016/j.celrep.2015.06.023
- Tang, G., Gudsnuk, K., Kuo, S.-H., Cotrina, M. L., Rosoklija, G., Sosunov, A., et al. (2014). Loss of mTOR-dependent macroautophagy causes autistic-like synaptic pruning deficits. *Neuron* 83, 1131–1143. doi: 10.1016/j.neuron.2014.07.040

- Tomać, V., and Banks, L. (2015). Angelman syndrome-associated ubiquitin ligase UBE3A/E6AP mutants interfere with the proteolytic activity of the proteasome. *Cell Death Dis.* 6:e1625. doi: 10.1038/cddis.2014.572
- Tomać, V., Pim, D., Thomas, M., Massimi, P., Myers, M. P., and Banks, L. (2011). Regulation of the human papillomavirus type 18 E6/E6AP ubiquitin ligase complex by the HECT domain-containing protein EDD. *J. Virol.* 85, 3120–3127. doi: 10.1128/jvi.02004-10
- Tucci, V. (2016). Genomic imprinting: a new epigenetic perspective of sleep regulation. *PLoS Genet.* 12:e1006004. doi: 10.1371/journal.pgen.1006004
- Uchiki, T., Kim, H. T., Zhai, B., Gygi, S. P., Johnston, J. A., O'Bryan, J. P., et al. (2009). The ubiquitin-interacting motif protein, S5a, is ubiquitinated by all types of ubiquitin ligases by a mechanism different from typical substrate recognition. *J. Biol. Chem.* 284, 12622–12632. doi: 10.1074/jbc.M900556200
- Valluy, J., Bicker, S., Aksoy-Aksel, A., Lackinger, M., Sumer, S., Fiore, R., et al. (2015). A coding-independent function of an alternative Ube3a transcript during neuronal development. *Nat. Neurosci.* 18, 666–673. doi: 10.1038/nn.3996
- Vos, R. M., Altreuter, J., White, E. A., and Howley, P. M. (2009). The ubiquitin-specific peptidase USP15 regulates human papillomavirus type 16 E6 protein stability. *J. Virol.* 83, 8885–8892. doi: 10.1128/jvi.00605-09
- Xu, X., Li, C., Gao, X., Xia, K., Guo, H., Li, Y., et al. (2018). Excessive UBE3A dosage impairs retinoic acid signaling and synaptic plasticity in autism spectrum disorders. *Cell Res.* 28, 48–68. doi: 10.1038/cr.2017.132
- Yankulov, K., Todorov, I., Romanowski, P., Licatalosi, D., Cilli, K., McCracken, S., et al. (1999). MCM proteins are associated with RNA polymerase II holoenzyme. *Mol. Cell. Biol.* 19, 6154–6163. doi: 10.1128/mcb.19.9.6154
- Yasuda, H., Barth, A. L., Stellwagen, D., and Malenka, R. C. (2003). A developmental switch in the signaling cascades for LTP induction. *Nat. Neurosci.* 6, 15–16. doi: 10.1038/nn985
- Yi, J. J., Berrios, J., Newbern, J. M., Snider, W. D., Philpot, B. D., Hahn, K. M., et al. (2015). An autism-linked mutation disables phosphorylation control of UBE3A. *Cell* 162, 795–807. doi: 10.1016/j.cell.2015.06.045
- Zaaroor-Regev, D., de Bie, P., Scheffner, M., Noy, T., Shemer, R., Heled, M., et al. (2010). Regulation of the polycomb protein Ring1B by self-ubiquitination or by E6-AP may have implications to the pathogenesis of angelman syndrome. *Proc. Natl. Acad. Sci. U S A* 107, 6788–6793. doi: 10.1073/pnas.1003108107
- Zhang, Y.-J., Yang, J.-H., Shi, Q.-S., Zheng, L.-L., Liu, J., Zhou, H., et al. (2014). Rapid birth-and-death evolution of imprinted snoRNAs in the Prader-Willi Syndrome locus: implications for neural development in euarchontoglires. *PLoS One* 9:e100329. doi: 10.1371/journal.pone.0100329

Conflict of Interest Statement: The authors declare that the research was conducted in the absence of any commercial or financial relationships that could be construed as a potential conflict of interest.

Copyright © 2019 Lopez, Segal and LaSalle. This is an open-access article distributed under the terms of the Creative Commons Attribution License (CC BY). The use, distribution or reproduction in other forums is permitted, provided the original author(s) and the copyright owner(s) are credited and that the original publication in this journal is cited, in accordance with accepted academic practice. No use, distribution or reproduction is permitted which does not comply with these terms.



Mitochondrial Calcium Transporters Mediate Sensitivity to Noise-Induced Losses of Hair Cells and Cochlear Synapses

Xianren Wang^{1,2†}, Yuanping Zhu^{1,3†}, Haishan Long¹, Song Pan¹, Hao Xiong¹, Qiaojun Fang¹, Kayla Hill¹, Ruosha Lai¹, Hu Yuan¹ and Su-Hua Sha^{1*}

¹Department of Pathology and Laboratory Medicine, Medical University of South Carolina, Charleston, SC, United States,

²Department of Otorhinolaryngology, The First Affiliated Hospital, Sun Yat-sen University, Guangzhou, China, ³Department of Otorhinolaryngology, Renmin Hospital of Wuhan University, Wuhan, China

OPEN ACCESS

Edited by:

Baojin Ding,
University of Louisiana at Lafayette,
United States

Reviewed by:

Elisabetta Ferraro,
University Hospital "Maggiore della
Carità" (UPO), Italy
Peter S. Steyger,
Oregon Health & Science University,
United States
Kelvin Y. Kwan,
Rutgers University, The State
University of New Jersey,
United States

*Correspondence:

Su-Hua Sha
shasu@usc.edu

[†]These authors have contributed
equally to this work

Received: 11 July 2018

Accepted: 04 December 2018

Published: 08 January 2019

Citation:

Wang X, Zhu Y, Long H, Pan S,
Xiong H, Fang Q, Hill K, Lai R, Yuan H
and Sha S-H (2019) Mitochondrial
Calcium Transporters Mediate
Sensitivity to Noise-Induced Losses
of Hair Cells and Cochlear Synapses.
Front. Mol. Neurosci. 11:469.
doi: 10.3389/fnmol.2018.00469

Mitochondria modulate cellular calcium homeostasis by the combined action of the mitochondrial calcium uniporter (MCU), a selective calcium entry channel, and the sodium calcium exchanger (NCLX), which extrudes calcium from mitochondria. In this study, we investigated MCU and NCLX in noise-induced hearing loss (NIHL) using adult CBA/J mice and noise-induced alterations of inner hair cell (IHC) synapses in MCU knockout mice. Following noise exposure, immunoreactivity of MCU increased in cochlear sensory hair cells of the basal turn, while immunoreactivity of NCLX decreased in a time- and exposure-dependent manner. Inhibition of MCU activity *via* MCU siRNA pretreatment or the specific pharmacological inhibitor Ru360 attenuated noise-induced loss of sensory hair cells and synaptic ribbons, wave I amplitudes, and NIHL in CBA/J mice. This protection was afforded, at least in part, through reduced cleavage of caspase 9 (CC9). Furthermore, MCU knockout mice on a hybrid genetic CD1 and C57/B6 background showed resistance to noise-induced seizures compared to wild-type littermates. Owing to the CD1 background, MCU knockouts and littermates suffer genetic high frequency hearing loss, but their IHCs remain intact. Noise-induced loss of IHC synaptic connections and reduction of auditory brainstem response (ABR) wave I amplitude were recovered in MCU knockout mice. These results suggest that cellular calcium influx during noise exposure leads to mitochondrial calcium overload *via* MCU and NCLX. Mitochondrial calcium overload, in turn, initiates cell death pathways and subsequent loss of hair cells and synaptic connections, resulting in NIHL.

Keywords: mitochondrial calcium uniporter (MCU), sensory hair cell, ribbon synapses, noise-exposure, auditory threshold shifts, mouse model

Abbreviations: ABR, auditory brainstem response; CaM, Ca²⁺-binding protein calmodulin; CC9, cleaved caspase 9; DAB, diaminobenzidine; EDTA, ethylenediaminetetraacetic acid; IHC, inner hair cell; MCU, mitochondrial calcium uniporter; mPTP, mitochondrial permeability transition pore; NCLX, sodium calcium exchanger; NIHL, noise-induced hearing loss; OBN, octave band noise; OC, organ of Corti; OHC, outer hair cell; PBS, phosphate buffered saline; PNH1, post noise exposure 1 h; PNH24, post noise exposure 24 h; PTS, permanent threshold shift; RIPA, radioimmunoprecipitation assay; RWN, round window niche; SGN, spiral ganglion neuron; SPL, sound pressure level.

INTRODUCTION

Dysfunctional buffering of calcium ions in mitochondria or the cytosol is associated with pathological conditions (Williams et al., 2013). Specifically, dysregulation of cytosolic calcium homeostasis appears to contribute to noise-induced hearing loss (NIHL). This notion is supported by a noise-dependent elevation of calcium levels in sensory hair cells (Maurer et al., 1993; Fridberger et al., 1998; Oliver et al., 2001) and the fact that calcium channel blockers protect from NIHL (Maurer et al., 1993; Fridberger et al., 1998; Heinrich et al., 1999; Oliver et al., 2001; Minami et al., 2004; Shen et al., 2007; Zuo et al., 2008). An elevation of intracellular Ca^{2+} levels after noise exposure can be deduced from an increase in the Ca^{2+} -binding protein calmodulin (CaM), a critical mediator of calcium signaling (Zuo et al., 2008). Such elevated calcium levels may contribute to sensory hair cell death, as noise exposure increases the phosphatase calcineurin (Minami et al., 2004) and triggers mitochondria-mediated cell death pathways (Vicente-Torres and Schacht, 2006).

Mitochondrial calcium has been postulated to regulate a wide range of processes involved in NIHL, including bioenergetics and cell death. The mitochondrial calcium uniporter (MCU) is an integral membrane protein located in the mitochondrial inner membrane. It is a major specific calcium channel for calcium uptake (Raffaello et al., 2012; Rizzuto et al., 2012). Excessive amounts of cellular calcium can rapidly enter the mitochondrial matrix through MCU (Raffaello et al., 2012; Rizzuto et al., 2012; Patron et al., 2013). MCU controls excitotoxicity (Qiu et al., 2013) and overexpression of MCU increases mitochondrial calcium uptake and sensitizes cells to apoptotic cell death (Patron et al., 2013). Excitotoxicity *via* an excess release of the neurotransmitter glutamate at inner hair cell (IHC) synapses has been linked to a loss of IHC connections to the auditory nerve (Puel et al., 1996). Glutamate overload results in a loss of function of type I afferent dendrites, and consequently the entry of Ca^{2+} triggers a cascade of metabolic events eventually leading to loss of function in type I spiral ganglion cells (SGCs). Furthermore, reduction of expression of the glutamate receptor AMPA reduces excitotoxicity in auditory neurons and correlates with auditory sensitivity (Chen et al., 2007, 2009). Conversely, extrusion of calcium from mitochondria is mediated primarily by a mitochondrial sodium calcium exchanger, encoded by the *NCLX* gene (Palty et al., 2012). Like MCU, *NCLX* is also localized in the mitochondrial inner membrane, where it regulates the mitochondrial calcium concentration and modulates intracellular calcium signaling. *NCLX* has been shown to be involved in neuronal death in a model of Parkinson disease (Gandhi et al., 2009; Palty et al., 2012).

While breakdown of calcium homeostasis appears to be crucial in the process leading to noise-induced sensory cell death and hearing loss, the role of mitochondrial calcium transporters and, particularly, the role of MCU and *NCLX* in the context of noise-induced hair cell death and hearing loss are unknown. We hypothesize that traumatic noise induces an increase in mitochondrial calcium *via* activation of MCU, thus stimulating

calcium uptake, coupled with a reduction in calcium extrusion from mitochondria *via* depression of sodium calcium exchanger (*NCLX*) activity, which together result in mitochondrial calcium overload. This then triggers the initial mitochondrial dependent cell death pathways leading to hair cell death and hearing loss. To investigate this idea, we first examined the contribution of MCU in noise-induced loss of outer hair cells (OHCs) and synaptic ribbons and the subsequent effect on NIHL by inhibition of MCU using siRNA silencing techniques and the pharmacological inhibitor Ru306, a cell-permeable specific inhibitor of MCU that binds MCU with high affinity and blocks mitochondrial calcium influx in adult CBA/J mice. We then examined the expression of MCU and *NCLX* in noise-exposed cochlear tissue with focus on the OHCs. Furthermore, we employed MCU knockout mice to investigate IHC synapses. These studies are the first to explore the role of mitochondrial transporters in the pathogenesis of noise-induced hair cell loss, cochlear synaptopathy, and NIHL.

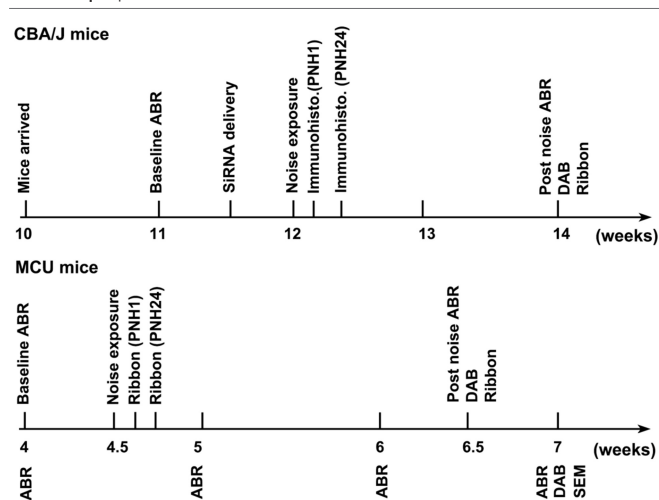
MATERIALS AND METHODS

Animals

Male CBA/J mice at 10 weeks of age were purchased from The Jackson Laboratory. All mice had free access to water and a regular mouse diet (Irradiated Lab Diet #5V75) and were kept at $22 \pm 1^\circ\text{C}$ under a standard 12:12 h light-dark cycle to acclimate for 1 week before the experiments. MCU heterozygous mice on a hybrid CD1 and C57/B6 background were purchased from the Texas A&M Institute of Genomic Medicine (Pan et al., 2013; Murphy et al., 2014). MCU knockout and wild-type littermates were bred in the animal facility of the Children's Research Institute (CRI) at the Medical University of South Carolina (MUSC). All mice were kept in the CRI animal facility at MUSC. All research protocols were approved by the Institutional Animal Care and Use Committee (IACUC) at MUSC. Animal care was under the supervision of the Division of Laboratory Animal Resources (DLAR) at MUSC. **Table 1** illustrates general experimental time line.

Noise Exposure

In this study, all CBA/J mice were exposed to 8–16 kHz at 101 dB sound pressure level (SPL) for 2 h and all MCU mice exposed to 2–8 kHz centered at 4 kHz for 2 h at 116 dB SPL unless otherwise stated. Unrestrained CBA/J male mice at 12 weeks of age (one mouse per stainless steel wire cage, approximately 9 cm^3) were exposed to 101 dB SPL to induce permanent threshold shifts (PTSs) with losses of IHC ribbons and OHCs, but not IHCs, or to 108 dB SPL to induce severe PTS with losses of IHC ribbons, OHCs, and IHCs by 14 days after the noise exposure. MCU knockout mice and wild-type littermates were first exposed to OBN centered at 4 kHz for 2 h at 118 dB and 116 dB SPL. Since the exposure to 118 dB SPL induced death in MCU wild-type littermates in our previous experiments, we selected 116 dB SPL for the experiments using MCU knockouts and littermates. Due to hereditary high-frequency hearing loss in the

TABLE 1 | Experimental time line.

CBA/J mice arrived at MUSC at the age of 10 weeks. Baseline auditory brainstem responses (ABRs) were measured at the age of 11 weeks. At the age of 12 weeks, mice were exposed to noise. Two weeks after the noise exposure (14 weeks), mice were euthanized for surface preparations for hair cell counts (left ear) and ribbon counts (right ear) after post-noise ABR measurements. siRNA was delivered 72 h before the noise exposure. For immunohistochemistry, mice were euthanized 1 h or 24 h after the completion of noise exposure. MCU knockout mice and littermates were generated from breeders and ABRs were measured initially at the ages of 4, 5, 6, and 7 weeks to observe hearing function and some mice were euthanized for assessment of hair cell pathology using myosin-VIIa labeling and DAB staining as well as scanning electron microscopy. For noise-exposed mice, baseline ABRs were measured at the age of 4.5 weeks. Two weeks after the noise exposure (6.5 weeks), mice were euthanized for surface preparations of hair cell counts (left ear) and ribbon counts (right ear) after the post-noise ABR measurements. Some mice were euthanized 1 h or 24 h after the completion of noise exposure to evaluate ribbon synapses additional time points.

CD1 strain, MCU knockouts and littermates were exposed at 4.5 weeks of age when hearing at 8 kHz remains intact. The sound exposure chamber was fitted with a loudspeaker (model 2450H; JBL) driven by a power amplifier (model XLS 202D; Crown Audio) fed from a CD player (model CD-200; Tascam TEAC American). Audio CD sound files were created and equalized with audio editing software (Audition 3; Adobe System Inc., San Jose, CA, USA). The background sound intensity of the environment surrounding the cages was 65 dB as measured with a sound level meter (model 1200; Quest Technologies). Sound levels for noise exposure are calibrated with a sound level meter at multiple locations within the sound chamber to ensure uniformity of the sound field and are measured before and after exposure to ensure stability. Control mice were kept in silence (without use of the loudspeaker) within the same chamber for 2 h.

Auditory Brainstem Response and Measurement of ABR Wave I Amplitudes

Auditory brainstem responses (ABRs) were measured in anesthetized mice before and 2 weeks after noise exposure. Mice were anesthetized with an intra-peritoneal (IP) injection of a mixture of ketamine (100 mg/kg) and xylazine (10 mg/kg), and then placed in a sound-isolated and electrically shielded booth (Acoustic Systems, Austin, TX, USA). Body temperature was monitored and maintained near 37°C with a heating pad.

Acoustic stimuli were delivered monaurally to a Beyer earphone attached to a customized plastic speculum inserted into the ear canal. Subdermal electrodes were inserted at the vertex of the skull (active), mastoid region under the left ear (reference), and mastoid region under the right ear (ground). ABRs were measured at 8, 16, and 32 kHz, as the system used is unable to test at lower frequencies such as 2 or 4 kHz. Tucker Davis Technology (TDT) System III hardware and SigGen/Biosig software (TDT, Alachua, FL, USA) were used to present the stimuli (15 ms duration tone bursts with 1 ms rise-fall time) and record the response. Up to 1,024 responses were averaged for each stimulus level. ABR wave I was used to determine ABR thresholds for each frequency. Thresholds were determined for each frequency by reducing the intensity in 10-dB increments and then in 5-dB steps near threshold until no organized responses were detected. Thresholds were estimated between the lowest stimulus level where a response was observed and the highest level without response. All ABR measurements were conducted by the same experimenter. The ABR thresholds were assigned by an expert who was blinded to the treatment conditions. The waveforms were saved and analyzed *post hoc* to measure the wave I amplitudes.

Drug Administration *via* Intra-Peritoneal Route to Mice

Ru360 (Calbiochem, 557440) was dissolved in 0.9% oxygenated saline (10 mg/mL Ru360) as a stock solution, aliquoted, and stored at -20°C . The stock solution was diluted with 0.9% oxygenated saline immediately before being injected into animals. Two concentrations of Ru360 (120 $\mu\text{g/kg}$ and 240 $\mu\text{g/kg}$) were tested in our preliminary study, based on the literature (Sanganahalli et al., 2013). The final selected concentration of Ru360 was 240 $\mu\text{g/kg}$ for use in this study. The mice used for the experiments designed to observe the evolution of ABR threshold shifts and hair cell counts were given five IP injections of Ru360 30 min before the noise exposure and 30 min, 4 h, 24 h, and 30 h after the end of noise exposure. Control animals received the same volume of 0.9% oxygenated saline on the same schedule. The mice used for immunohistochemistry to determine protein expression received only two IP injections of Ru360 at 30 min before and 30 min after the noise exposure.

Intra-Tympanic Delivery of MCU siRNA or MitoTracker *in vivo*

MCU siRNA (siMCU; Thermo Fisher, 103464) or siControl (Thermo Fisher, 4390843) was delivered locally *via* intra-tympanic application as previously described (Chen et al., 2013; Oishi et al., 2013). Briefly, after anesthesia, a retroauricular incision was made to approach the temporal bone. The otic bulla was identified ventral to the facial nerve and a shallow hole was made in the thin part of the otic bulla with a 30-G needle and enlarged with a dental drill to a diameter of 2 mm in order to visualize the round window. A customized sterile micro medical tube was inserted into the hole just above the round window niche (RWN) to slowly deliver 10 μL (0.6 μg) of pre-designed siRNA or MitoTracker (0.5 μM , Invitrogen, M7512) to completely fill the mouse RWN. After the siRNA

or MitoTracker was delivered, the hole was covered with the surrounding muscle. Finally, the skin incision was closed with tissue adhesive. The animal was allowed to rest in the surgical position for an additional hour after the procedure. Seventy-two hours after siRNA delivery, the animals were exposed to noise for 2 h. Based on our previous experiments, local intra-tympanic delivery of siRNA results in temporary elevation of thresholds that completely recovers to baseline by 72 h (Oishi et al., 2013; Zheng et al., 2014; Yuan et al., 2015). Therefore, noise exposure was performed at least 72 h after siRNA delivery. Forty-eight hours after MitoTracker delivery, control mice without noise exposure were euthanized for immunoassays to assess co-localization of MitoTracker with NCLX on surface preparations.

Surface Preparations and Myosin VIIa-DAB Staining of Cochlear Epithelia for Hair Cell Counts

This procedure was described in our previous reports (Chen F.-Q. et al., 2012; Zheng et al., 2014; Yuan et al., 2015). Briefly, 2 weeks after the end of noise exposure and after the final ABR measurement, the temporal bones were removed immediately following euthanasia and locally perfused gently with a solution of 4% paraformaldehyde in phosphate buffered saline, pH 7.4 (PBS) after removing the stapes and opening the oval and round windows and kept in this fixative overnight at 4°C. The cochleae were then rinsed in PBS. Before decalcification in a 4% solution of sodium EDTA (adjusted with HCl to pH 7.4), the apical and middle turns of the otic capsule were removed from each cochlea. The EDTA solution was changed daily for 3 days and maintained at 4°C. Following decalcification, the cochleae were placed in 3% hydrogen peroxide for 2.5 h to quench endogenous peroxidases. After incubation in a solution for blocking non-specific antibody binding overnight at 4°C, the tissues were incubated with a primary antibody (rabbit polyclonal anti-myosin VII, Proteus Bioscience, 25-6790) at a 1:100 dilution for 4 days at 4°C on a Nutator mixer, washed in PBS, and then incubated overnight at 4°C with secondary antibody (biotinylated goat anti-rabbit) at a 1:100 dilution. The specimens were rinsed again and then incubated in ABC solution (Vector Laboratories, PK-4001) overnight. Following another washing, the cochleae were incubated in DAB for 3 h, as necessary for sufficient staining intensity, followed by washing to stop the DAB reaction. Finally, the cochleae were micro-dissected under a microscope into apical, middle, and basal segments and mounted on slides with Fluoromount-G mounting medium. Images were taken with a Zeiss AxioCam MRC5 camera with Axioplan 2 imaging software with a Zeiss microscope for hair cell counts. Unless otherwise specified, all chemicals and reagents used were purchased from Sigma-Aldrich.

Mapping of frequencies as a function of distance along the length of the cochlear spiral was done using the ImageJ plugin. In addition, we also calculated with equation $[d = 156.5 - 82.5 \times \log(f)]$ from Müller's article (Müller et al., 2005). They are in agreement with literature (Viberg and Canlon, 2004).

Hair Cell Counts on Cochlear Epithelia From the Adult Mouse

Hair cells were counted from captured images using the 40×-magnification lens on the Zeiss microscope from the apex through the base of the DAB-stained surface preparations. The lengths of the cochlear epithelia were measured and recorded in millimeters. Both outer and IHCs were counted from the apex to the base of the mouse cochlear epithelium. Percentages of hair cell loss in each 0.5-mm length of epithelium were plotted as a function of the cochlear length as a cytochleogram (Chen F.-Q. et al., 2012; Zheng et al., 2014).

Immunocytochemistry for Cochlear Paraffin Sections

Following decalcification with 4% EDTA, each cochlea was transferred to 70% ethanol and embedded in paraffin for sectioning. Five-micrometer sections were routinely deparaffinized in xylene and rehydrated in alcohol. The sections were incubated with target retrieval solution (Dako, S2367) in a steamer (Oster, CKSTMD5-W) for 10 min and then 3% hydrogen peroxide solution for 10 min and protein block solution (Dako, 0909) for 20 min at room temperature. All primary antibodies were first optimized by titration with five different concentrations at two pH values (pH 6 and 9). Then primary antibodies (MCU at 1:200; Sigma-Aldrich, HPA016480) were applied and incubated overnight in a humid chamber at 4°C, followed by incubation with a biotinylated secondary antibody (Vector Laboratories, Torrance, CA, USA) for 30 min and ABC reagent (Vector Laboratories, Torrance, CA, USA) for 30 min. Immunocomplexes of horseradish peroxidase were visualized by DAB reaction, and sections were counterstained with hematoxylin before mounting.

Scanning Electron Microscope

Temporal bones of MCU mice at the age of 7 weeks were removed after cardio-vascular perfusion of anesthetized mice with a mixture of 4% paraformaldehyde and 2% glutaraldehyde in 0.1 M cold phosphate buffer, pH 7.4. The temporal bones were then locally perfused gently with the same fixative after removing the stapes and opening the oval and round windows and were kept in this fixative overnight at 4°C. The samples were washed with the phosphate buffer and decalcified with 4% EDTA, pH 7.4, for 72 h. After decalcification, each cochlea was dissected by removing the softened otic capsule, stria vascularis, Reissner's membrane, and tectorial membrane. The remaining tissues, including the modiolus and cochlear sensory epithelium were post fixed with 1% osmium tetroxide-1.5% ferrocyanide for 2 h in the dark, then dehydrated in increasing concentrations of ethanol from 70% to 100%, and dried with Hexamethyldisilazane until it evaporates. The specimens were micro-dissected by removing the modiolus and divided into three segments (apex, middle, and base). Each specimen was mounted on a scanning electron microscopy stub and sputter coated with 10 nm gold alloy. Cochlear epithelia were viewed and photographed with a JEOL 1510 scanning electron microscope (SEM).

Immunocytochemistry on Cochlear Surface Preparations

We have followed a procedure as previously described (Chen F.-Q. et al., 2012; Zheng et al., 2014; Yuan et al., 2015). Briefly, depending on the time points, mice were euthanized either 1 h or 24 h after completion of the exposure. The temporal bones were removed immediately following euthanasia, perfused locally with a fresh solution of 4% paraformaldehyde in PBS, pH 7.4, and kept in this fixative overnight at 4°C. The cochleae were then rinsed in PBS prior to decalcification with 4% EDTA. Following 72 h decalcification, each cochlea was dissected by removing the softened otic capsule, stria vascularis, Reissner's membrane, and tectorial membrane. The remaining tissue, including the modiolus and cochlear sensory epithelium, was permeabilized in fresh 3% Triton X-100 solution for 30 min at room temperature. The specimens were washed three times (10 min each) with PBS and blocked with 10% normal goat serum for 30 min at room temperature. The tissues were incubated at 4°C for 48 h with the following primary antibodies: MCU (1:50; Sigma-Aldrich, HPA016480), NCLX (1:50, Sigma-Aldrich, HPA040668), and cleaved caspase 9 (CC9; 1:50, Cell Signaling Technology, 9509). After three washings, the tissues were incubated with the Alexa-Fluor-594- or Alexa-Fluor-488-conjugated secondary antibody at a concentration of 1:200 at 4°C overnight in darkness. The specimens were then washed three times with PBS and incubated with Alexa Fluor 488 phalloidin at a concentration of 1:100 for 1 h in darkness at room temperature. After at least three final washes with PBS, the specimens were micro-dissected in PBS by removing the modiolus and divided into three segments (apex, middle, and base). Each segment was mounted on slides with Fluoro-gel with Tris buffer (Electron Microscopy Sciences, 17985-10). Control incubations were routinely processed without primary antibody treatments. Immunolabeled images were taken using a Zeiss laser confocal microscope (Zeiss LSM 880) or Leica SP5 confocal microscope.

Immunocytochemistry for Synaptic Ribbons on Cochlear Surface Preparations

Depending on the time points, CBA/J mice were euthanized at either 1 h or 14 days and MCU knockouts and littermates were euthanized at 1 h, 24 h, and 14 days, after completion of the exposure. The temporal bones were removed immediately following euthanasia, perfused locally with a fresh solution of 4% paraformaldehyde in PBS, pH 7.4 and fixed for 1 h at room temperature. After decalcification with 4% EDTA for 3 days, each cochlea was dissected by removing the softened otic capsule, stria vascularis, Reissner's membrane, and tectorial membrane. The remaining tissue, including the modiolus and cochlear sensory epithelium, was permeabilized in fresh 3% Triton X-100 solution for 30 min at room temperature. The specimens were washed three times (10 min each wash) with PBS and blocked with 10% normal goat serum for 30 min at room temperature and then incubated in darkness at 37°C overnight with primary monoclonal mouse anti-CtBP2 IgG1 at

1:200 (BD Biosciences, 612044) and monoclonal mouse anti-GluA2 IgG2a at 1:2,000 (Millipore, MAB397). After washing three times, the tissues were incubated with the Alexa-Fluor-594- and Alexa-Fluor-488-conjugated secondary antibody at a concentration of 1:1,000 at 37°C for 1 h in darkness. After washing three times, the tissues were re-incubated with Alexa-Fluor-conjugated secondary antibodies for an additional 1 h at 37°C to increase the immunolabeling for CtBP2 (Wan et al., 2014; Hill et al., 2016). Following three washings, the tissues were incubated in darkness at 4°C overnight with polyclonal rabbit anti-myosin VIIa at 1:200 (Proteus Biosciences, 25-6790). Then following washing steps, the tissues were incubated with Alexa Fluor 350-conjugated secondary antibody at a concentration of 1:200 at 4°C overnight in darkness. For all immunolabeling samples, after at least three final washes with PBS, the specimens were micro-dissected in PBS by removing the modiolus and divided into three segments (apex, middle, and base). Each segment was mounted on slides with Fluoro-gel with Tris buffer (Electron Microscopy Sciences, 17985-10). Immunolabeled images were taken with a 63×-magnification lens under identical Z-stack conditions using a Zeiss LSM 880 confocal microscope.

Quantification of the Immunofluorescence Signals From Outer Hair Cells of Surface Preparations

Immunohistochemistry is well accepted as a semi-quantitative methodology when used with careful consideration of the utility and semi-quantitative nature of these assays (Taylor and Levenson, 2006; Walker, 2006). The specificity of antibodies must be first detected by Western blot analysis. An antibody showing only a single band with the correct molecular weight was then used for immunolabeling on surface preparations and quantification of signaling in OHCs. The regions of interest were outlined within individual OHCs based on the counterstaining. The grayscale value was determined in only the hair cells to quantify the change in fluorescence intensity. This procedure provided quantitative measurements that are not confounded by protein expression in other cell types of the cochlea.

Immunolabeling for MCU, NCLX, and CC9 on surface preparations was quantified from original confocal images with 8-bit grayscale values, each taken with a 63×-magnification lens under identical conditions and equal parameter settings for laser gains and photomultiplier tube (PMT) gains within linear ranges of the fluorescence, using ImageJ software (National Institutes of Health, USA). The cochleae from the different groups were fixed and stained simultaneously with identical solutions and processed in parallel. All surface preparations were counterstained with Alexa Fluor 488 phalloidin for labeling OHC structure in order to identify the comparable parts of the OHCs in confocal images. The regions of interest of individual OHC cell bodies were outlined with the circle tool based on the phalloidin staining. The immunolabeling of MCU, NCLX, and CC9 in OHCs was measured in the upper-basal region of surface preparations, corresponding to sensitivity to 22–32 kHz,

in 0.12-mm segments, each containing about 60 OHCs. The intensity of the background fluorescence was subtracted and the average fluorescence per cell was then calculated. For each repetition, the relative grayscale values were determined by normalizing the ratio to control.

Quantification of the Immunolabeled Ribbons From Z Projections on Surface Preparations

We have followed a procedure as previously described (Hill et al., 2016). Immunofluorescence of CtBP2 on surface preparations was quantified from original confocal images, each taken with a 63 \times -magnification lens under identical Z-stack conditions in 0.25-mm intervals and equal parameter settings for laser gains and PMT gains. The z-stack images in each 0.12-mm segment (containing about 16 IHCs) were captured from cochlear surface preparations. The number of synaptic ribbon particles was counted using ImageJ software (National Institutes of Health, USA). Briefly, the background of the images was subtracted, the noise was despeckled once, and the threshold was set to isolate the immunolabeling of ribbon signals. The image was then converted to a binary file and the number of ribbon particles was counted using the 3D Object Counter and divided by the total number of IHC nuclei within the image. The number of functional synapses, identified by juxtaposed CtBP2 and GluA2, were manually counted by visualizing the presence of CtBP2 co-localization with GluA2.

Extraction of Total Cochlear Protein and Liver Protein

Cochlear or liver tissue was rapidly removed and dissected in ice-cold PBS containing completeTM mini EDTA-free protease inhibitor cocktail tablets (Roche Diagnostic, 11836170001) at pH 7.4. To extract total protein, tissue from two cochleae from one mouse or a small piece of liver was homogenized in ice-cold radioimmunoprecipitation assay (RIPA) lysis buffer (Sigma-Aldrich, R0278) plus Phosphatase Inhibitor Cocktails II and III, and Roche Protease Inhibitor (cocktail tablets) by using a glass/glass micro Tissue Grind pestle and vessel for 30 s. After 30 min on ice, tissue debris was removed by centrifugation at 15,000 \times g at 4°C for 10 min and the supernatants were retained as the total protein fractions. Protein concentrations were determined using the Bio-Rad Protein Assay dye reagent with bovine serum albumin as a protein standard.

Extraction of Protein From Formalin-Fixed Sensory Epithelia

We followed a procedure as previously described (Hill et al., 2016). Cochleae were rapidly removed and perfused with 4% paraformaldehyde and incubated for 2 h at room temperature (25°C). The cochleae were then rinsed in PBS and decalcified in a 4% solution of sodium EDTA for 3 days at 4°C, with the EDTA solution changed daily. Following decalcification, the micro-dissected sensory epithelia from three mice were placed

in 1.5-mL collection tubes with 100 μ L of extraction buffer EXB plus (Qproteome FFPE Tissue kit Qiagen, 37623) supplemented with β -mercaptoethanol. Glass micro grinder pestles were used to grind the tissue for 3 min. The tubes were sealed with a sealing clip and vortexed. The samples were incubated on ice for 5 min, followed by repeat vortexing. The tubes were then incubated for 20 min at 100°C on a heating block. After this incubation, the tubes were incubated for 2 h at 80°C with agitation at 750 rpm (Eppendorf) and then allowed to cool at 4°C for 1 min. Finally, the samples were centrifuged at 14,000 \times g at 4°C for 15 min. The supernatant containing the extracted proteins was transferred to a new tube. Protein concentrations were determined using the Bio-Rad RC DC protein assay (Invitrogen, 500-0119) with bovine serum albumin as a protein standard.

Cell Culture

HEI-OC1, an inner ear cell line, was provided by Dr. Kalinec, from UCLA, Los Angeles, CA, USA. The cell line was cultured on plastic culture dishes under permissive conditions (33°C, 10% CO₂) in high-glucose Dulbecco's Modified Eagle's Medium (DMEM; Gibco BRL, Gaithersburg, MD, USA) containing 10% fetal bovine serum (FBS; Gibco BRL) and 100 U/mL penicillin to proliferate.

Protein Extraction From Cultured Cells

HEI-OC1 cells were taken out of the incubator and treated with trypsin-EDTA (Thermo Fisher Scientific, 25200056) for 5 min. The trypsin was diluted with 10 mL of DMEM. The collected cells were transferred to a 15-mL conical tube (Corning, 430052) and centrifuged at 1,000 \times g for 5 min. After the medium was removed, the pellets of cells with 500 μ L medium were transferred to 1.5-mL Eppendorf tubes (Thermo Fisher Scientific, 05408133). The cells were washed with 1 mL of PBS (Invitrogen, 20012) and centrifuged again at 1,000 \times g for 5 min. After removing the PBS, 100 μ L of RIPA buffer was added to the cell pellets and the tubes were vortexed for 5 s and incubated for 20 min on ice. The RIPA buffer contained 860 μ L RIPA buffer base (Sigma-Aldrich, R0278), 100 μ L Protein Inhibitor Cocktail (Roche, 11836170001), 5 μ L PMSF (Sigma-Aldrich, P7626), 10 μ L Phosphatase Inhibitor Cocktail 2 (Sigma-Aldrich, P5726), 10 μ L Phosphatase Inhibitor Cocktail 3 (Sigma, P0044). The supernatants were collected in a clean, labeled tube and kept at -80°C after centrifugation.

Western Blot Analysis

Protein samples (30 μ g) were separated by SDS-PAGE. After electrophoresis, the proteins were transferred onto a nitrocellulose membrane (Pierce, USA) and blocked with 5% solution of nonfat dry milk in PBS-0.1% Tween 20 (PBS-T). The membranes were incubated with anti-MCU (1:1,000) or anti-NCLX (1:1,000) at 4°C overnight and then washed three times (10 min each) with PBS-T buffer. Membranes were incubated with an appropriate secondary antibody at a concentration of 1:2,500 for 1 h at room temperature. Following extensive washing of the membrane, the immunoblots were

visualized by SuperSignal® West Dura Extended Duration Substrate or Pierce® ECL Western Blotting Substrate (Thermo Fisher Scientific, Waltham, MA, USA). The membranes were then stripped and relabeled for GAPDH (1:10,000; Millipore, MAB374) at a concentration of 1:20,000 as a control for sample loading.

X-ray films of Western blots were scanned and analyzed using ImageJ software. The band densities were first normalized to the background. Next, the probing protein/GAPDH ratio was calculated from the band densities run on the same gel. Finally, the difference in the ratio of the control and experimental bands was tested for statistical significance.

Statistical Analysis

Data were analyzed using IBM SPSS Statistics Premium V21 and GraphPad software (GraphPad Software Inc.) for Windows. Biological sample sizes were determined based on the variability of measurements and the magnitude of the differences between groups, as well as experience from our previous studies, with stringent measurements of difference. Data of OHC loss along the length of the cochlear spiral were analyzed with repeated measures one-way analysis of variance (ANOVA) with Tukey's multiple comparisons using IBM SPSS Statistics. The rest analysis was done using GraphPad. Data with multiple comparisons were evaluated by one-way ANOVA with multiple comparisons. Differences for single-pair comparisons were analyzed using two-tailed unpaired Student's *t*-tests. Data for relative ratios of single-pair comparisons were analyzed with one-sample *t*-tests. The difference of death rate of MCU mice vs. wild-type littermates was analyzed using Chi-square test (and Fisher's exact test). A *p*-value < 0.05 was considered statistically significant. Data are presented as means ± SD or SEM based on the sample size and variability within groups. Sample sizes are indicated for each figure.

RESULTS

Inhibition of Mitochondrial Calcium Uniporter in CBA/J Mice by Pretreatment With siRNA or Ru360 Protects Against Noise-Induced Outer Hair Cell Loss and Permanent Hearing Loss

Based on our hypothesis, we first tested if inhibition of MCU could attenuate NIHL. Exposure of mice to the octave band noise (OBN; 8–16 kHz) induces loss of sensory hair cells following a base-to-apex gradient with losses beginning at the basal turn. Such a pattern of damage is similar to that seen in mice exposed to broadband noise (2–20 kHz) when examined 14 days after the completion of noise exposure (Figure 1A; Yuan et al., 2015; Hill et al., 2016). Using our lab's established technique for intra-tympanic delivery of siRNA into adult mouse cochleae (Oishi et al., 2013), we first determined the appropriate concentration of siMCU to be used in this study. The 0.6-μg concentration of siMCU was selected from preliminary experiments based on the assessment

of the efficacy from two concentrations (0.3 and 0.6 μg). Immunolabeling for MCU on cochlear surface preparations revealed 25% reduction of MCU in OHCs 72 h after 0.6-μg siRNA delivery compared to untreated controls (Supplementary Figures S1A,B). Additionally, Western blots with formalin-fixed sensory epithelium from pooled tissues also showed a significant 30% reduction in MCU band densities 72 h after siRNA delivery; Supplementary Figure S1C). Next, we found that pretreatment with siMCU reduced noise-induced OHC loss by 50% at 3.5–5.5 mm from the apex at 14 days after the exposure (Figure 1A). Noise-induced auditory threshold shifts were also significantly attenuated both at 16 and 32 kHz in the siMCU-pretreated group (Figure 1B).

Finally, we inhibited MCU with the specific inhibitor Ru360. Based on the literature, the doses of Ru360 used *in vivo* were tested at two concentrations (120 μg/kg and 240 μg/kg) in a preliminary study (Sanganahalli et al., 2013). CBA/J mice at 12 weeks of age tolerated Ru360 at either dose for five IP injections over 2 days without loss of body weight or changes in fur appearance. Ru360 also did not alter baseline hearing thresholds. However, treatment with Ru360 at 120 μg/kg did not significantly attenuate noise-induced auditory threshold shifts. We therefore chose the 240-μg/kg dose of Ru360 for assessment of a protective effect against NIHL. After treatment with Ru360 at 240 μg/kg, noise-induced auditory threshold shifts at both 16 and 32 kHz were significantly reduced (Figure 1C). Furthermore, treatment with Ru360 also reduced the extent of OHC loss by 50% at 3.5–5.5 mm from the apex 2 weeks after the noise exposure (Figure 1A). Additionally, we tested Ru360 treatment against a more severe noise damage paradigm (108 dB SPL for 2 h) that induced IHC loss at the basal turn at 4.5–5.5 mm from the apex (Figure 1D). Treatment with Ru360 almost completely blocked IHC loss (Figure 1D). Meanwhile, treatment with Ru360 also reduced OHC loss from the 108-dB exposure from 3–3.5 mm (*p* = 0.053), but not from 4–5.5 mm from the apex (Figure 1E). However, 108-dB-SPL-induced auditory threshold shifts were not significantly attenuated at 8, 16, or 32 kHz (Figure 1F). These results pointed out that blockade of MCU function can prevent moderate noise-induced permanent hearing loss, but not severe noise-induced permanent hearing loss.

Inhibition of Mitochondrial Calcium Uniporter in CBA/J Mice by Treatment With Ru360 or siRNA Reduces the Noise-Induced Loss of IHC Ribbons and ABR Peak I Amplitudes

To determine if blockade of MCU could attenuate noise-induced loss of IHC synaptic ribbons, ribbon numbers were counted and peak I amplitudes were measured 14 days after the completion of noise exposures. Based on our previous characterization of noise-induced loss of IHC pre-synaptic ribbons and ribbon synapses in CBA/J mice, we found significant reduction of ribbons juxtaposed with presynaptic ribbons (labeled with CtBP2) and glutamate receptors (labeled with GluA2) when examined 14 days after either noise exposure

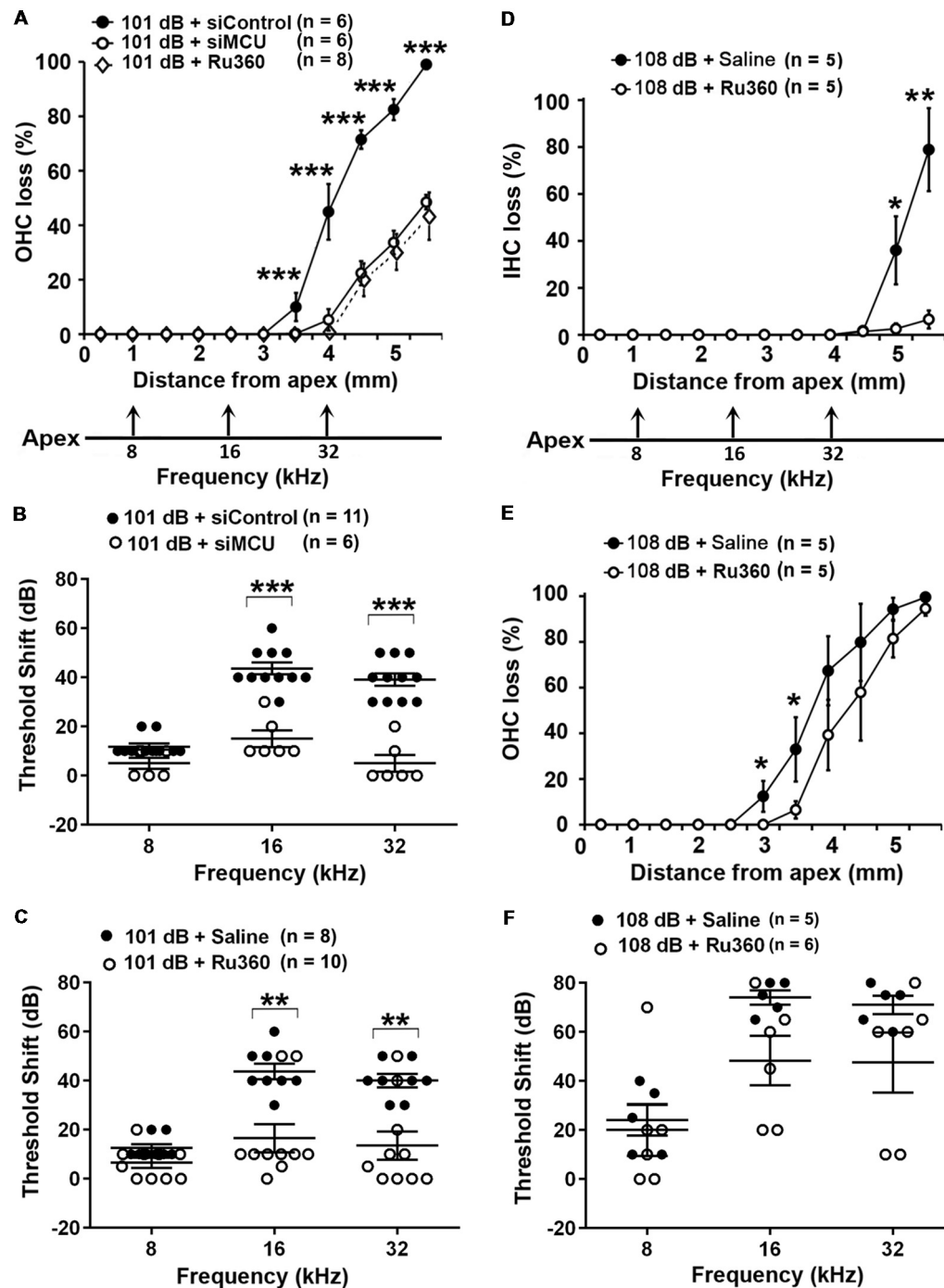


FIGURE 1 | Inhibition of mitochondrial calcium uniporter (MCU) *via* siRNA silencing or the pharmacological inhibitor Ru360 attenuated noise-induced hair cell loss and hearing loss. **(A)** Noise-induced outer hair cell (OHC) loss was reduced by siMCU pretreatment as well as by Ru360 treatment. The distance along the cochlear duct correlating with the frequencies of 8, 16, and 32 kHz is indicated. Data are presented as means \pm SD; *** p < 0.001. **(B)** Pretreatment with siMCU attenuated 101-dB-noise-induced auditory threshold shifts measured 14 days after the exposure. Data are presented as individual points and means \pm SD; *** p < 0.001. **(C)** Treatment with Ru360 also attenuated 101-dB-noise-induced auditory threshold shifts measured 14 days after the exposure. Data are presented as individual points and means \pm SD; ** p < 0.01. **(D)** Treatment with Ru360 attenuated 108-dB-noise-induced inner hair cell (IHC) loss. The distance along the cochlear duct correlating with the frequencies of 8, 16, and 32 kHz is indicated. Data are presented as means \pm SD; * p < 0.05, ** p < 0.01. **(E)** Treatment with Ru360 attenuated 108-dB-noise-induced OHC loss at 3 and 3.5 mm from the apex. Data are presented as means \pm SD; * p < 0.05. **(F)** Treatment with Ru360 did not attenuate 108-dB-noise-induced auditory threshold shifts measured 14 days after the exposure. Data are presented as individual points and means \pm SD; n in all figures indicates the number of mice per group; left cochlea was assessed per mouse.

condition (101 dB SPL or 108 dB SPL; Hill et al., 2016). In this study, we focused on presynaptic ribbons (labeled with CtBP2). Noise exposure decreased synaptic ribbons at areas corresponding to 8–32 kHz compared to age-matched unexposed controls (Saline). One-way ANOVA analysis of three groups (Control, 101-dB noise + Saline, and 101-dB noise + Ru360) showed a significant difference at 8 kHz, 16 kHz, 22 kHz, and 32 kHz, but not at 5 kHz (**Figures 2A,B**, detailed statistical values see **Supplementary Table S1**), while treatment with Ru360 significantly protected ribbons from damage by noise exposure at 8 kHz ($p = 0.0001$) and 16 kHz ($p = 0.003$), not at 5, 22, or 32 kHz (**Figures 2A,B**). Such protection of IHC synaptic ribbons matched age-matched mice without noise exposure particularly at lower frequencies (**Figure 2B**). Additionally, we also assessed CtBP2-labeled synaptic ribbons in the region of 16 kHz by treatment with siMCU or Ru360 examined 1 h after the completion of 101-dB or 108-dB noise exposure. The 101-dB exposure induced about 50% reduction, from 18 ribbons per IHC to 9, while pretreatment with siMCU reduced the loss of ribbons, bringing the average ribbon count up to 14 ribbons per IHC (**Supplementary Figures S2A,B**). The 108-dB exposure induced 66% reduction of ribbons, from 18 ribbons to 5 ribbons per IHC, whereas the treatment with Ru360 attenuated ribbon loss, restoring the ribbon number to 14 per IHC (**Figure 2C**). Furthermore, we assessed wave I amplitudes, which reflect the summed activity of auditory nerve fibers. Since loss of OHCs is a confounding factor affecting wave I amplitudes, we only measured at 16 kHz, which is one of the most sensitive frequencies of the auditory spectrum in mice, corresponding to a region where no OHC loss was found 14 days after the exposure. Noise exposure significantly diminished ABR wave I amplitudes from 30 dB to 100 dB SPL compared to age-matched mice without noise exposure (Saline control; detailed statistical values see **Supplementary Table S2**; Control vs. 101 dB noise). Treatment with Ru360 alone also elevated ABR wave I amplitudes at 70–100 dB SPL (detailed statistical values see **Supplementary Table S2**; Control vs. Ru360 only). Inhibition of MCU by treatment with Ru360 significantly reversed the noise-induced decrease in peak I amplitudes at sound intensities of 80, 90, and 100 dB SPL (**Figure 2D**, for detailed statistical values see **Supplementary Table S2**; 101 dB + Saline vs. 101 dB + Ru360).

Noise Trauma Increases Mitochondrial Calcium Uniporter in the Basal Turn of Outer Hair Cells of CBA/J Mice

Since inhibition of MCU activity by siRNA treatment and pharmacological inhibitor Ru360 attenuated noise-induced loss of ribbons and hair cells as well as NIHL, we further assessed the expression and localization of MCU in cochlear paraffin sections of CBA/J mice processed 1 h after completion of a noise exposure (OBN, 101 dB SPL). Immunohistochemistry revealed increased MCU labeling in OHCs of the organ of Corti (OC, insert enlarged images) and in the stria vascularis, but no obvious changes in spiral ganglion neurons (SGNs; **Figure 3A**). In order to quantify the immunolabeling for MCU in OHCs, we conducted immunohistochemistry on cochlear

surface preparations. MCU immunolabeling was stronger in OHCs of the basal turn when processed 1 h after noise exposure and was sustained until at least 24 h after the exposure. Quantification from original confocal images of the area of the basal turn corresponding to 22–32 kHz revealed that MCU in OHCs increased by 80% when examined at 1 h and 24 h after the exposure compared to age-matched controls (**Figures 3B,C**); although there was a larger variation at 24 h, there was no significant difference between the 1-h and 24-h time points. Furthermore, since the specificity of the MCU antibody from Sigma-Aldrich had only been confirmed in human tissue, we tested its applicability to mouse tissue by Western blots first using homogenates from HEI-OC1 cells, which showed a single band with a molecular weight at 30 kDa (**Supplementary Figure S2A**). We then used liver homogenates from MCU knockouts and wild-type littermates. A specific band for MCU was detected at 30 kDa in samples from MCU wild-type liver tissues, but not in MCU knockout mice (**Supplementary Figure S2B**). Additionally, immunoblots using total cochlear homogenates from CBA/J mice revealed no difference between the MCU band density of mice with and without noise exposure (**Figure 3D**).

Noise Trauma Depresses Mitochondrial Sodium Calcium Exchanger in the Basal Turn of Outer Hair Cells in a Time-Dependent and Noise-Intensity-Dependent Manner

Since NCLX plays an important role in extrusion of mitochondrial calcium, we also assessed NCLX in NIHL. First, we tested the localization of the NCLX antibody to mitochondria by co-localization of MitoTracker with NCLX immunolabeling on surface preparations using control CBA/J mice (**Figure 4A**). Quantification of the overlap coefficient of MitoTracker and NCLX immunolabeling in OHCs revealed 95% overlap. We then conducted immunolabeling for NCLX with surface preparations under 101-dB conditions for three time points (control without noise exposure, 1 h post noise exposure, and 24 h post noise exposure). Immunolabeling for NCLX in OHCs of the basal turn corresponding to 22–32 kHz appeared weaker when processed 1 h after and was further reduced at 24 h after the completion of the noise exposure (**Figure 4B**). Quantification of immunolabeling for NCLX from original confocal images in OHCs confirmed a reduction both 1 h after and 24 h after the exposure with significantly greater reduction at 24 h (50% reduction) than 1 h (10% reduction) after the noise exposure (**Figure 4C**). Furthermore, we confirmed that noise-diminished NCLX immunolabeling in OHCs was reduced significantly more under 108-dB-noise-exposure conditions (30% reduction) than 101-dB conditions (10% reduction) when processed 1 h post noise exposure (**Supplementary Figures S3A,B**). Finally, we evaluated the specificity of the NCLX antibody by immunoblotting using whole cochlear homogenates. Western blots showed a single NCLX band at 64 kDa (**Supplementary Figure S3C**) without

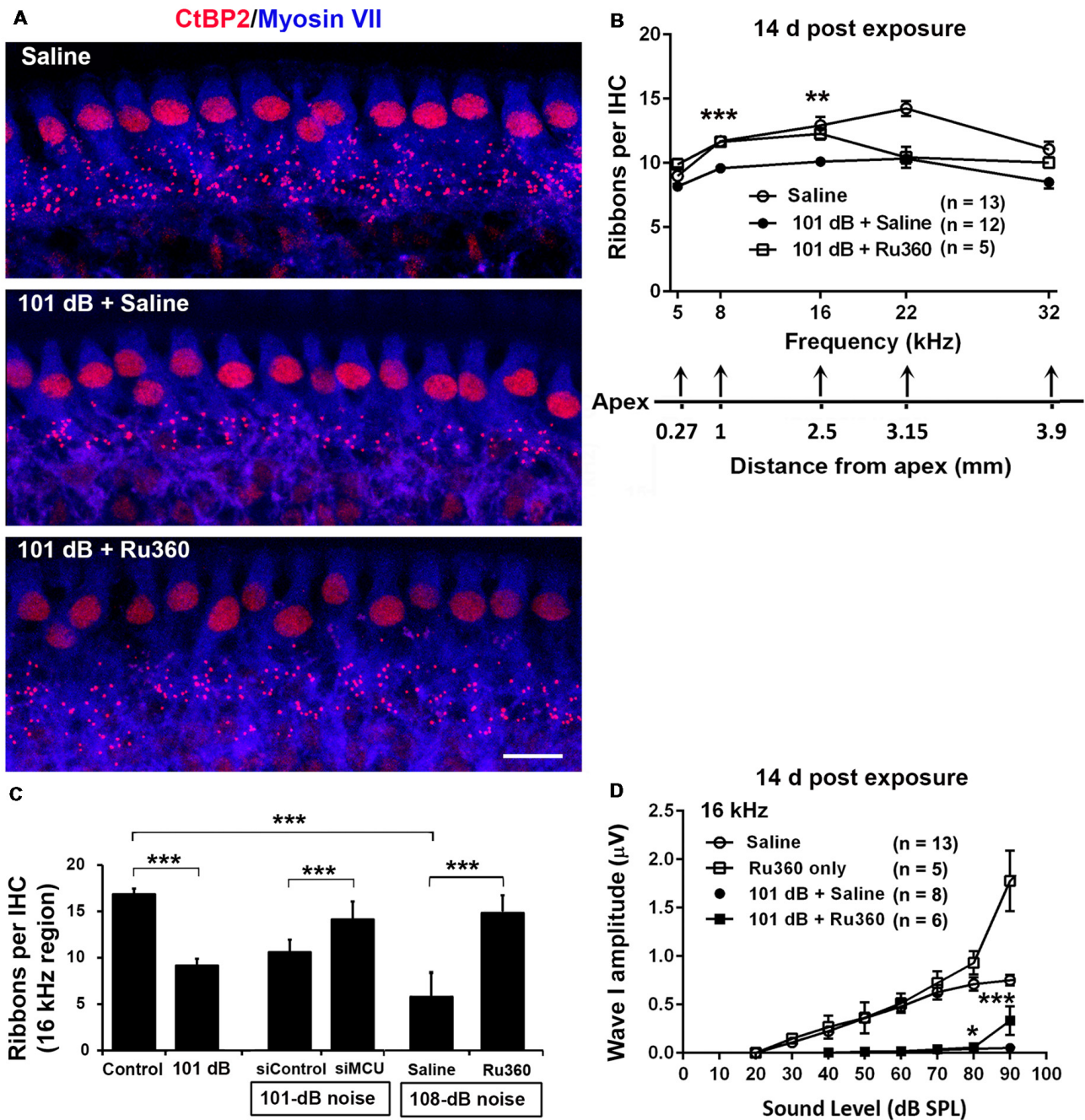


FIGURE 2 | Inhibition of MCU via Ru360 or siMCU attenuates noise-induced loss of synaptic ribbons and wave I amplitudes after the completion of noise exposure. **(A)** Representative images revealed immunolabeling for CtBP2 examined 14 days after noise exposure. Images are comprised of 40 Z-stack projections taken from the middle turn corresponding to sensitivity to 16 kHz. Blue: myosin-VIIa labeled IHCs, red: CtBP2-labeled synaptic ribbons and nuclei of IHCs; scale bar = 10 μ m. **(B)** Quantification of CtBP2-immunolabeled ribbon particles in IHCs corresponding to 5, 8, 16, 22, and 32 kHz showed significant reduction examined 14 days after noise exposure at all frequencies except 5 kHz (see **Supplementary Table S1** for detailed statistical values). Treatment with Ru360 prevented noise-induced synaptic ribbon loss at 8 and 16 kHz. The distance along the cochlear duct correlating with the frequency regions is indicated. Data are presented as means + SEM. $^{**}p < 0.01$, $^{***}p < 0.001$ for 101 dB + Saline vs. 101 dB + Ru360. **(C)** CtBP2-immunolabeled ribbon particles in IHCs at 16 kHz region also decrease examined 1 h after noise exposure that partially prevented with siMCU pretreatment; $n = 4$ mice per group with one cochlea used per mouse. Treatment with Ru360 also attenuated higher intensity noise sound pressure level (108-dB-SPL)-induced synaptic ribbon loss; $n = 6$ mice per group with one cochlea used per mouse. Data are presented as means + SD. $^{***}p < 0.001$. **(D)** Ru360 treatment alone increased wave I amplitudes at sound intensities of 90 dB SPL. Noise-reduced wave I amplitudes at sound intensities of 80 and 90 dB SPL were rescued by treatment with Ru360. Data are presented as means + SEM, $^{*}p < 0.05$, $^{***}p < 0.001$ corresponds to 101 dB + Saline vs. 101 dB + Ru360. In panels **(B,D)** n indicates the number of mice per group; the left cochlea was used from each mouse for these experiments.

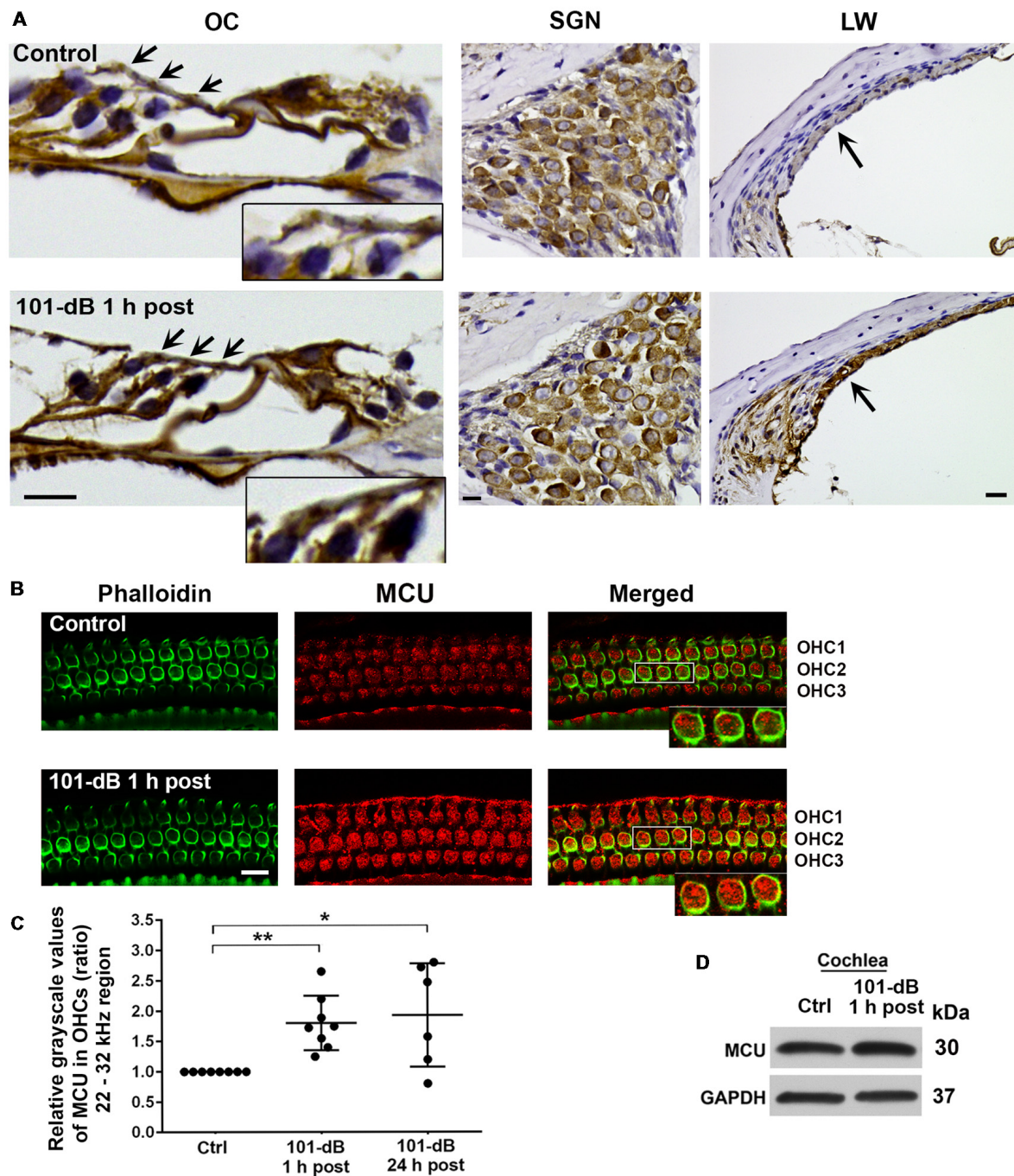


FIGURE 3 | Noise exposure increased immunolabeling for MCU in OHCs and the stria vascularis of the basal turn. **(A)** Paraffin sections of the adult CBA/J mouse inner ear revealed an increase in immunolabeling for MCU in DAB-stained OHCs (arrows and enlarged image inserts) in the organ of Corti (OC) and the stria vascularis (arrow) in the lateral wall, and no obvious change in spiral ganglion neurons (SGNs) examined 1 h after completion of the 101-dB noise exposure. These images were taken with 40 \times -magnification lens and are representative of five individual mice per group; scale bar = 10 μ m. **(B)** Representative images for MCU in OHCs of surface preparations stained with phalloidin when processed 1 h after completion of the noise exposure. An enlarged image of three OHCs better illustrates the immunolabeling for MCU. Images were taken from the area of the basal turn corresponding to 22–32 kHz; OHC1, 2, 3 indicate the three rows of OHCs, scale bar = 10 μ m. **(C)** Quantification of immunolabeling for MCU in OHCs in the 22–32 kHz region showed a significant increase when processed 1 h after and 24 h after completion of the exposure. Data are presented as individual points and means \pm SD; * p < 0.05, ** p < 0.001. Control: n = 8, 101-dB 1 h post: n = 8, 101-dB 24 h post: n = 6 with one cochlea from each mouse in the group. **(D)** Immunoblots using total cochlear homogenates of CBA/J mice revealed no difference in MCU band densities between control (Ctrl) and noise-exposed mice processed 1 h after completion of the noise exposure (101-dB 1 h post). GAPDH was used as a loading control; n = 8 mice per group.

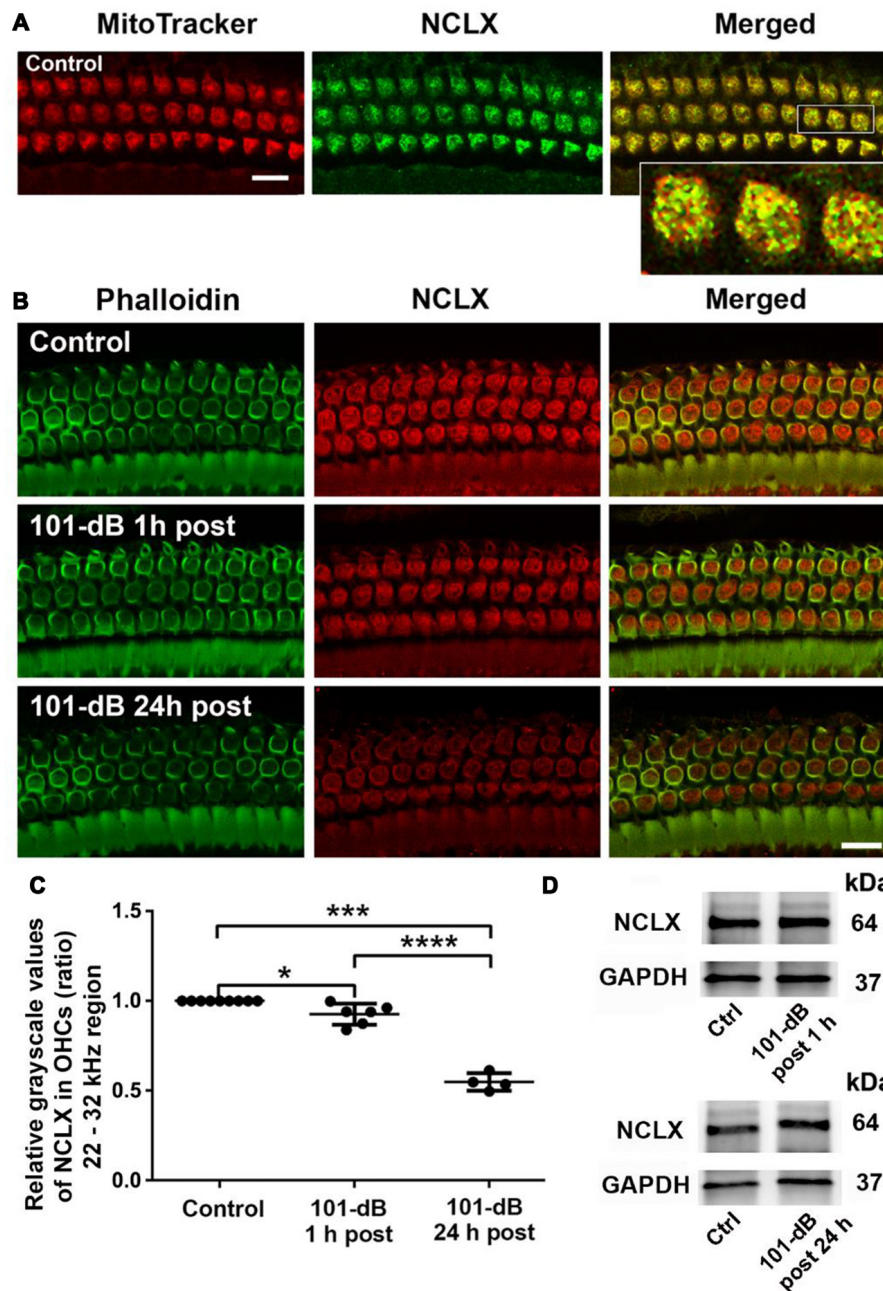


FIGURE 4 | Noise exposure decreased NCLX immunoreactivity in OHCs of the basal turn in a time-dependent and intensity-dependent manner. **(A)** Representative images of surface preparations revealed co-localization of NCLX (green) and MitoTracker (red) in OHCs (merged, yellow). An enlarged image of three OHCs better illustrates the co-localization; scale bar = 10 μ m, $n = 3$ per group with one cochlea used per mouse. **(B)** Representative images for NCLX in OHCs 1 h and 24 h after completion of the exposure. Green: phalloidin-stained OHCs. Images were taken from the 22–32 kHz region of the surface preparations using a Leica SP5 confocal microscope; scale bar = 10 μ m. **(C)** Quantitative analysis of NCLX immunolabeling in OHCs showed a significant decrease in a time-dependent manner. Data are presented as individual points and means \pm SD; * $p < 0.05$, *** $p < 0.001$, **** $p < 0.0001$. Control: $n = 9$, 101-dB 1 h post: $n = 6$, 101-dB 24 h post: $n = 4$ with one cochlea used per mouse. **(D)** Representative immunoblots of total cochlear homogenates from CBA/J mice showed no difference in NCLX band densities between control and noise exposed mice when examined 1 h and 24 h after completion of the exposure. GAPDH served as the sample loading control; $n = 6$ mice per group.

difference in the band density between mice exposed to noise at 101 dB or 108 dB SPL and un-exposed mice when processed 1 h after and 24 h after the completion of 101-dB noise exposure (Figure 4D). These results demonstrated that

depression of NCLX immunoreactivity in the basal turn of OHCs by noise exposure is time- and noise-intensity-dependent, suggesting decreased extrusion of calcium from mitochondria in OHCs.

Inhibition of Mitochondrial Calcium Uniporter in CBA/J Mice by Pretreatment With siRNA or Ru360 Reduces Noise-Induced Cleavage of Caspase 9 in the Basal Turn of Outer Hair Cells

Mitochondrial calcium overload initiates caspase-dependent cell death. Since noise exposure activates multiple cell death pathways, including apoptotic cell death (Zheng et al., 2014), we presumed that MCU inhibition diminishes mitochondrial calcium overload and should modulate apoptotic pathways. We inhibited MCU with the specific inhibitor Ru360 or with siRNA (siMCU). Based on the successful attenuation of noise-induced hair cell loss and hearing loss by treatment with Ru360 at 240 $\mu\text{g/kg}$, we used this dose for assessing inhibition of noise-activated CC9 in OHCs. According to our previously published results, CC9 was significantly elevated 1 h after noise exposure (Zheng et al., 2014); we therefore assessed CC9 at this time point. In agreement with our previous results, immunolabeling for CC9 in OHCs in the area of the basal turn corresponding to 22–32 kHz was significantly elevated after the noise exposure (Figures 5A,B). Such elevation of CC9 was significantly diminished by treatment

with Ru360 (Figure 5B). Additionally, pretreatment with siMCU attenuated the reduction of CC9 immunoreactivity by 35% compared to noise-exposed mice 1 h after the noise exposure (Figures 5C,D).

Impairment of Hearing at High Frequencies Is Found in Both MCU Knockout Mice and Their Wild-Type Littermates

To further determine the role of MCU in NIHL, we used MCU knockout mice on an outbred C57BL/6 with CD1 background (Murphy et al., 2014). Since the CD1 strain has sensorineural hearing impairment at high frequencies (Le Calvez et al., 1998), we measured ABRs weekly from 4 weeks to 7 weeks of age for both MCU knockouts and wild-type littermates. Thresholds at 8 kHz remained around 25 dB SPL from 4 weeks to 7 weeks, with sporadic impairment in both MCU knockouts and wild-type littermates without significant differences between MCU knockouts and wild-type littermates (Figure 6A). However, there were elevations in auditory thresholds at 16 kHz in both MCU knockouts and wild-type littermates with wide variations between individual mice. For example, some mice maintained almost normal auditory

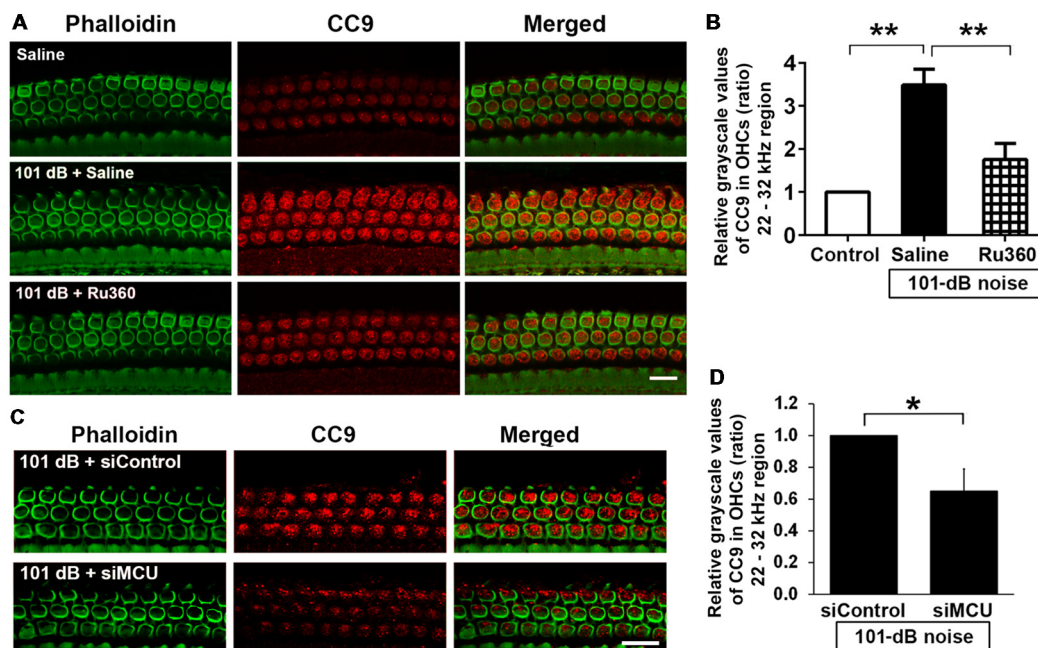


FIGURE 5 | Inhibition of MCU via the pharmacological inhibitor Ru360 or siMCU attenuated noise-induced increases in cleaved caspase 9 (CC9) in OHCs of the basal turn. **(A)** Representative images show an increase in immunoreactivity for CC9 (red) in OHCs stained with phalloidin 1 h after completion of the exposure (panel 2) compared to control mice without exposure (panel 1). Treatment with Ru360 attenuated noise-induced CC9 in OHCs (panel 3). Images were taken from the region of the surface preparations corresponding to sensitivity to 22–32 kHz using a Leica SP5 confocal microscope; scale bar = 10 μm . **(B)** Quantification of CC9 in OHCs confirmed a significant increase after noise exposure and attenuation of this increase with Ru360 treatment; $n = 4$ per group with one cochlea used per mouse. Data are presented as means + SD, $**p < 0.01$. **(C)** Representative images show that pretreatment with siMCU decreases immunoreactivity for CC9 (red) in OHCs stained with phalloidin (green) 1 h after completion of the exposure compared to siControl treatment. Images were taken from the region of the surface preparations corresponding to sensitivity to 22–32 kHz using a Zeiss confocal microscope; scale bar = 10 μm . **(D)** Pretreatment with siMCU also significantly reduced noise-increased immunolabeling for CC9 in OHCs compared to mice exposed to scrambled siRNA (siControl). Data are presented as means + SD, $n = 4$ per group with one cochlea used per mouse, $*p < 0.05$.

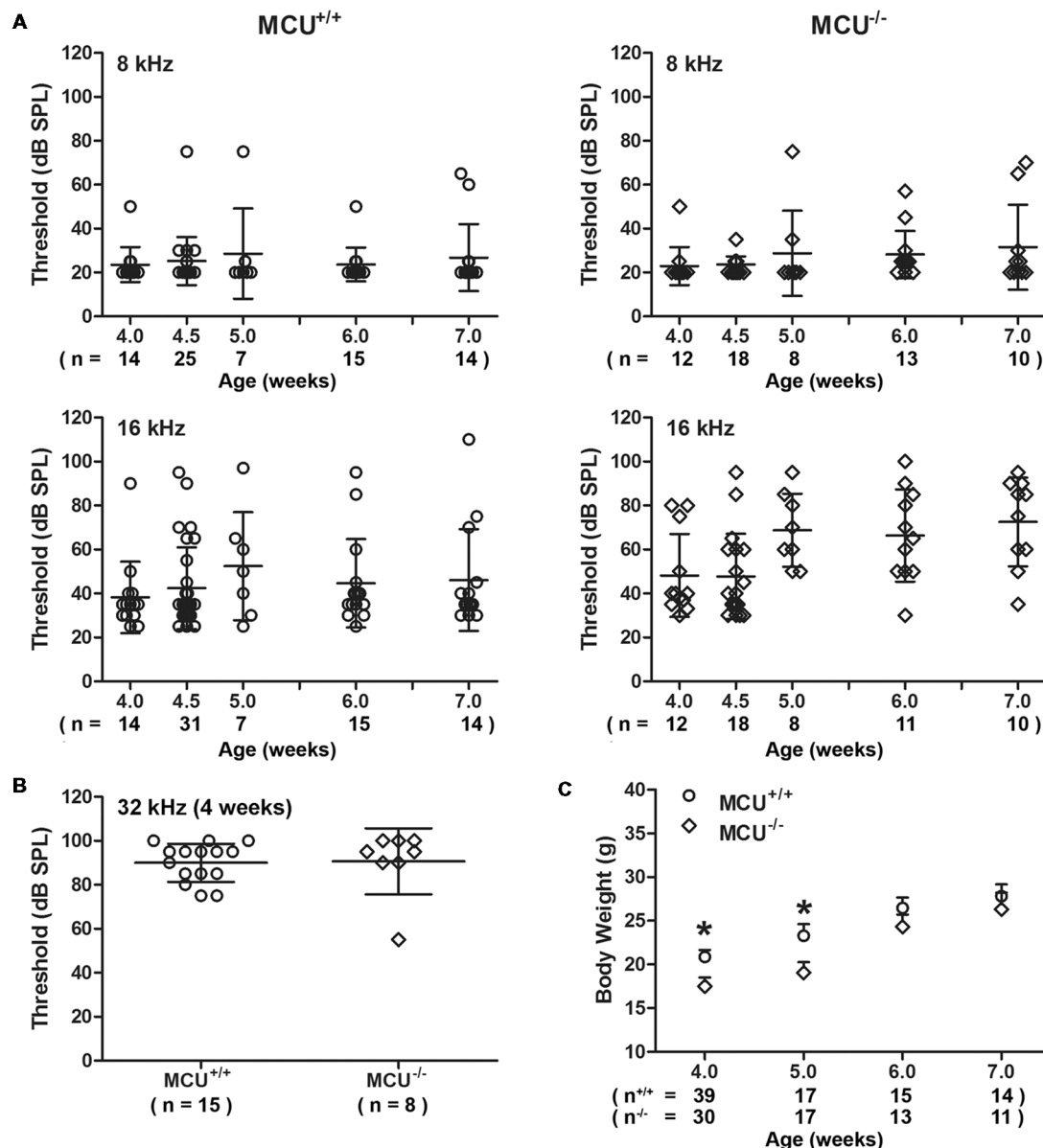


FIGURE 6 | MCU knockout mice (MCU^{-/-}) and wild-type littermates (MCU^{+/+}) on a hybrid CD1 and C57/B6 background had OHC loss in the basal turn and high-frequency hearing loss. **(A)** Auditory brainstem response (ABR) thresholds at 8 kHz were not significantly elevated and not different between MCU^{-/-} mice and MCU^{+/+} from weeks 4 to 7 weeks of age but displayed wide variations at 16 kHz. Data are presented as individual points and means \pm SD. **(B)** ABR thresholds at 32 kHz were greatly elevated in 4-week-old MCU^{-/-} and MCU^{+/+} mice without a significant difference between these two groups. Data are presented as individual points and means \pm SD. **(C)** Body weights of MCU^{-/-} mice were significantly lower than that of littermates at the age of 4–5 weeks, but were the same as wild-type littermates by 6 weeks. Data are presented as individual points and means \pm SEM, * $p < 0.05$. In panels **(A,B)** n indicates the number of mice per group with one cochlea used per mouse, n in panel **(C)** indicates the number of mice.

thresholds, while others were completely deaf at this frequency (Figure 6A). Furthermore, baseline auditory thresholds at 32 kHz were already elevated to around 90 dB SPL at 4 weeks of age (Figure 6B). DAB-stained myosin-VIIa-labeled cochlear surface preparations of both MCU knockouts and wild-type littermates showed intact IHCs from the apex through the base; however, severe OHC loss appeared in the basal turn

at 7 weeks of age (Supplementary Figure S4A), while OHCs in the apex appear normal by assays using both scanning electron-microscopy (Supplementary Figure S4B) and myosin-VIIa-labeled, DAB stained cochlear epithelia (Supplementary Figure S4A). Additionally, we observed that the body weights of MCU knockout mice were slightly lower than wild-type littermates at 4 and 5 weeks of age, and indistinguishable at 6 and

7 weeks of age (**Figure 6C**). These results indicate that knockout of the *MCU* gene alone did not alter auditory thresholds but highlight the fact that CD1 mice carry genetic hearing loss at high frequencies.

MCU Knockout Mice Are More Resistant to Acoustic Stress Than Wild-Type Littermates

Since the majority of MCU knockout and wild-type littermates showed baseline auditory thresholds around 30 dB SPL at 8 kHz, we first exposed both MCU knockouts and wild-type littermates at the age of 4.5 weeks with baseline auditory thresholds of less than 30 dB SPL at 8 kHz to OBN centered at 4 kHz and intensities of 118 or 116 dB SPL for 2 h in order to set up appropriate noise exposure conditions. Surprisingly, sudden death occurred in the MCU wild-type littermates during the noise exposure, with a death rate of 40% (2/5) at 118 dB SPL and 7.5% (6/80) at 116 dB SPL. No MCU knockout mice (five knockout mice at 118 dB, 65 knockout mice at 116 dB SPL) died under either noise exposure condition, indicating that mice with knockout of the *MCU* gene are significantly resistant to general noise stress at 116 dB SPL ($p = 0.033$). We therefore chose the 116-dB SPL noise condition for further study. MCU knockouts and wild-type littermates were exposed to OBN at 116 dB SPL for 2 h at the age of 4.5 weeks. Two weeks after the noise exposure, permanent auditory threshold shifts at 8 kHz were noted in both MCU knockouts and wild-type littermates compared to non-noise-exposed age-matched control mice (**Supplementary Figure S4C**). MCU knockouts had average threshold shifts of 33 ± 8 dB, and those of wild-type littermates were 39 ± 11 dB with no statistical difference between these groups. Furthermore, this intensity of noise exposure did not induce OHC loss in the apex of the cochlear spiral. These results indicate that MCU knockouts were resistant to noise-induced seizures and noise exposure was unable to induce loss of OHCs in the apical region.

MCU Knockout Mice Have Recovery of IHC Synaptic Ribbons After Noise Exposure and Attenuation of Noise-Diminished Wave I Amplitudes

Since IHCs are intact along the entire cochlear spiral of MCU knockouts and littermates, we determined if knockout of the *MCU* gene could attenuate noise-induced loss of synapses in IHCs. First, we compared the number of presynaptic ribbons and functional synapses in MCU knockouts and wild-type littermates without noise exposure 14 days after the completion of 116 dB SPL noise exposure. Functional synapses were assessed as juxtaposed presynaptic ribbons (CtBP2-labeled) and postsynaptic glutamate receptors (GluA2-labeled). Knockout of *MCU* alone did not impact the synapses (**Figures 7A,B**, upper panels, and **Figure 7C**). After noise exposure, no obvious separation of the immunolabeling for CtBP2 and GluA2 was observed in either group (**Figures 7A,B**, lower panels). Additionally, some of the CtBP2 and GluA2 signals surrounded the nuclei or were even above the nuclei of IHCs

in the MCU knockout mice regardless of noise exposure, but the majority of CtBP2 and GluA2 were located below the IHC nuclei (**Figure 7B**). A severe reduction in functional synapses was evident after noise exposure in wild-type mice from the apex to the base as measured at areas corresponding to 5, 8, 16, 22, and 32 kHz (for detailed statistical values see **Supplementary Table S3**). By contrast, MCU knockout mice had no significant loss of synapses 14 days after noise exposure compared to age-matched MCU knockouts without noise exposure. Further comparison of noise-exposed MCU knockouts to noise-exposed wild-type littermates showed that MCU knockouts were significantly resistant to noise-induced loss of synapses at the regions corresponding to 8, 22, and 32 kHz, but was not different in the 5- and 16-kHz regions (**Figure 7D**; for detailed statistical values see **Supplementary Table S4**). To further determine if the MCU knockouts are resistant to noise damage or have recovery of IHC ribbon synapses, we assessed ribbons at 1 h and 24 h after the completion of 116-dB noise exposure in both MCU knockouts and their littermates. Noise-induced loss of ribbons was not statistically different between groups when examined at 1 h and 24 h after the completion of exposure (**Figures 7E,F**). These results indicate that MCU knockouts had recovery of noise-induced loss of ribbon synapses.

In addition, we evaluated ABR wave I amplitudes (8 kHz) as functional markers for synaptic integrity. Knockout of the *MCU* gene alone (without noise exposure) did not alter wave I amplitudes (**Figure 8A**). In agreement with our previous reports and those of others (Kujawa and Liberman, 2009; Wan et al., 2014; Hill et al., 2016), noise exposure reduced wave I amplitudes in wild-type littermates at sound stimulation levels from 50 dB to 100 dB SPL (for detailed statistical values see **Supplementary Table S5**). By contrast, noise exposure did not significantly reduce wave I amplitude levels in MCU knockout mice at sound stimulation levels of 90 dB and 100 dB SPL (**Figure 8B**).

DISCUSSION

The salient finding of this study is that inhibition of MCU *via* pretreatment with MCU siRNA or the selective MCU inhibitor Ru360 reduced PTS-noise-induced losses of IHC synaptic ribbons, OHCs, and wave I amplitudes, as well as NIHL in adult CBA/J mice. Finally, MCU knockout mice with intact IHCs are resistant to noise-induced seizures and have the capacity for recovery of IHC synapses after extremely high noise exposure.

Mitochondrial Transporters Are Important Modulators of Noise-Induced Cochlear Synaptopathy, Hair Cell Death, and Functional Deficits in CBA/J Mice

While mitochondrial calcium uptake by MCU under stress is a means to maintain cytosolic calcium homeostasis (Boitier et al., 1999; Kirichok et al., 2004; Chaudhuri et al., 2013), it may lead to pathologically high mitochondrial calcium, triggering cell death (Mattson, 2007; Celsi et al., 2009). The

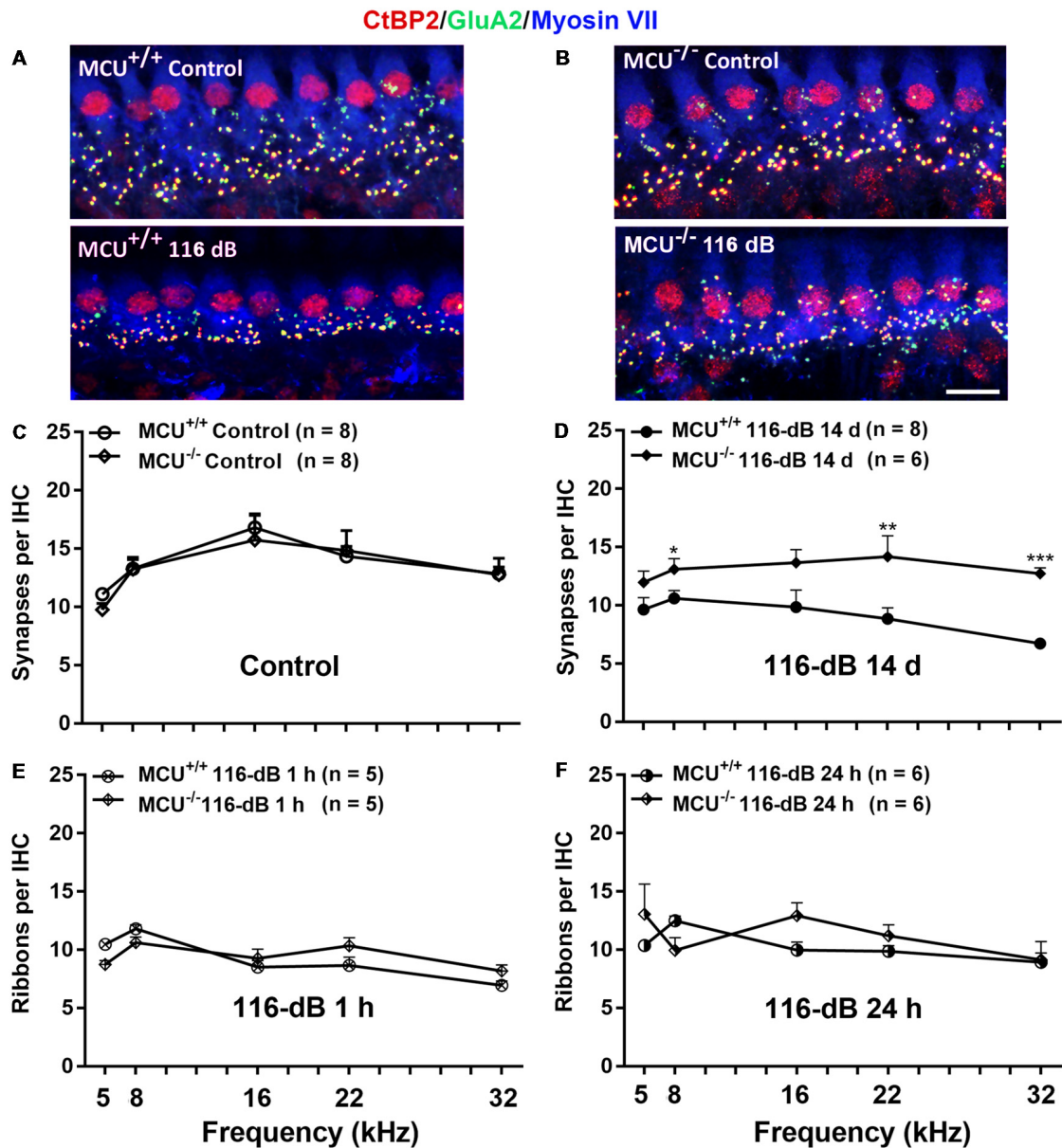


FIGURE 7 | Noise-induced losses of synapses were attenuated in MCU knockout mice at 14 days after the completion of noise exposure. **(A,B)** Representative images of immunolabeling for IHC synapses in the apical region corresponding to 8 kHz of MCU^{+/+} or MCU^{-/-} mice examined 14 days after the noise exposure. The images were projected from Z sections. Red: CtBP2, green: GluA2, blue: myosin-VIIa-labeled IHCs; scale bar = 10 μ m. **(C)** The number of synapses per IHC was similar between MCU^{+/+} and MCU^{-/-} mice without noise exposure. **(D)** The number of synapses had recovered significantly in MCU knockout mice but not in littermates when examined 14 days after the noise exposure. **(E)** Noise-induced loss of ribbons was also similar between MCU^{-/-} mice and littermates when examined 1 h after the completion of noise exposure. **(F)** Ribbons were not different between MCU^{-/-} mice and MCU^{+/+} when examined 24 h after the completion of noise exposure. Data are shown as means \pm SEM in panels **(C–F)**, *n* indicates the number of mice with one cochlea used per mouse, **p* < 0.05, ***p* < 0.01, ****p* < 0.001.

hypothesis that excessive mitochondrial calcium due to increased MCU expression and decreased NCLX contributes to OHC death is clearly supported by the reduction of noise-induced OHC loss and protection against NIHL after treatment with siMCU or the selective inhibitor Ru360 in CBA/J mice. In addition to protecting hair cells, MCU inhibition reduced the extent of

noise-induced IHC synaptic ribbon loss, thereby preventing the decline of ABR peak I amplitudes. These results implicate MCU as an important mediator affecting cochlear synaptopathy, hair cell death, and functional deficits. Such an action is in line with previous reports in cortical and hippocampal neurons in which the inhibition of MCU *via* knockdown exerted a

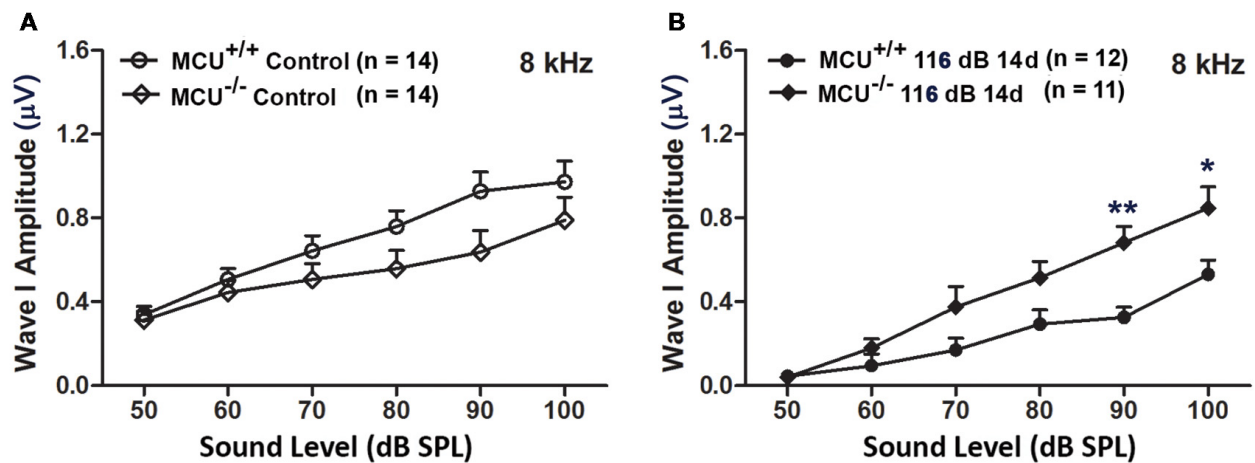


FIGURE 8 | MCU knockout mice were resistant to reduction in their ABR wave I amplitudes at 8 kHz measured 14 days after noise exposure. **(A)** There was no significant difference in wave I amplitudes between MCU^{-/-} and MCU^{+/+} mice without noise exposure. **(B)** MCU knockouts were significantly resistant to reduction in ABR wave I amplitudes after noise in comparison to wild-type littermates at sound intensities of 90 and 100 dB SPL. Data are shown as means \pm SEM, * $p < 0.05$, ** $p < 0.01$. n indicates the number of mice; one cochlea was used per mouse.

neuroprotective effect from NMDA-induced excitotoxicity (Qiu et al., 2013) and a recent report on transcriptional repression of MCU reducing excitotoxicity (Depp et al., 2018). Likewise, Ru360 treatment has also been shown to reduce pathological mitochondrial calcium uptake in various cell types, including cochlear supporting cells such as Claudius' and Deiters' cells of neonatal rat cochlear explants (Mann et al., 2009). It is interesting that reduction of MCU by local intra-tympanic application of siMCU prior to noise exposure showed similar effects as that of Ru360 treatment. We believe that Ru360 treatment only partially inhibits MCU channel function in CBA/J mice. Likewise, treatment with siMCU also decreases MCU in OHCs. Such a decrease might also partially influence MCU function. However, the detailed mechanisms on how reduction of MCU expression decreases channel function needs further investigation.

The downstream mechanisms by which MCU can protect against hair cell loss remain speculative. Mitochondrial calcium overload and over production of reactive oxygen species (ROS) have been associated with necrotic and apoptotic cell death pathways *via* a sustained opening of the mitochondrial permeability transition pore (mPTP), resulting in collapse of mitochondrial membrane potential, and release of cytochrome C (Szalai et al., 1999; Nicotera et al., 2003; Rizzuto et al., 2012). Conversely, blockade of the mPTP, reduction of mitochondrial calcium uptake and inhibition of ROS production can serve a protective role against mitochondria-mediated cell death in neuronal cells and in NIHL (Baines et al., 2005; Sha and Schacht, 2017). Supporting such a concept for noise trauma, our current results show inhibition of MCU *via* siMCU or Ru360 treatment significantly reduced the CC9 in OHCs, an essential downstream step in the activation of intrinsic mitochondria-dependent apoptotic pathways. Still, treatment with Ru360 was insufficient to protect from severe PTS-NIHL (108-dB, SPL) in CBA/J mice,

suggesting that such a high-level exposure may trigger additional cell death pathways and that pharmacological protection must be directed at multiple targets. Of note, our previous report showed that inhibition of noise-induced apoptosis in OHCs shifts the predominant cell death pathway to necrosis under such severe PTS noise exposure (Zheng et al., 2014).

Noise exposure, especially higher intensities, decreases capillary blood flow and causes local vasoconstriction, resulting in ischemia (Quirk and Seidman, 1995; Miller et al., 2003). Such ischemia depletes ATP levels within inner ear structures, including sensory hair cells and the stria vascularis (Nagashima et al., 2011; Chen F.-Q. et al., 2012). In support of transient cellular ATP depletion in sensory hair cells, a homeostatic energy sensor, adenosine monophosphate-activated protein kinase (AMPK), is activated after noise exposure known to induce permanent hearing loss (Hill et al., 2016). Noise exposure, especially higher intensities, triggers elevation of intracellular Ca^{2+} levels, followed by rapid Ca^{2+} entry into the mitochondrial matrix *via* MCU (Chen Q. et al., 2012). The enhanced MCU function following noise exposure may initially be an adaptive response to stress, trapping excessive amounts of intracellular Ca^{2+} in mitochondria to maintain Ca^{2+} homeostasis in the cytosol, while the initial increased mitochondrial calcium levels stimulate mitochondria to generate ATP (Clapham, 2007). However, prolonged Ca^{2+} uptake eventually leads to mitochondrial Ca^{2+} overload, resulting in collapse of the mitochondrial membrane potential, uncoupling of oxidative phosphorylation in the respiratory chain, and over-production of ROS. It is well known that oxidative imbalance contributes to sensory hair cell death after inner ear trauma including noise-induced, ototoxic drug-induced, and age-related hearing loss (Jiang et al., 2007; Oishi and Schacht, 2011; Chen et al., 2013). While MCU controls uptake of mitochondrial calcium, extrusion of calcium from mitochondria is mediated primarily

by a mitochondrial sodium calcium exchanger (NCLX), encoded by the *NCLX* gene (Palty et al., 2012). Like MCU, NCLX is localized to the mitochondrial inner membrane, where it regulates mitochondrial calcium concentrations and shapes intracellular calcium signaling. Under normal physiological conditions, mitochondrial calcium uptake and release are in equilibrium. NCLX has been shown to be involved in neuronal death in a model of Parkinson disease (Gandhi et al., 2009; Palty et al., 2012). Noise exposure decreased NCLX expression in OHCs in a time- and intensity-dependent manner, indicating alteration of NCLX function. Although the detailed mechanisms of decreased NCLX function in sensory hair cells after noise exposure need to be investigated further, the noise-induced decrease in NCLX in OHCs seems to act as a deleterious complement to the increase in MCU and further augments mitochondrial calcium overload.

In addition, we need to review our negative results by Western analysis. Noise-induced loss of sensory hair cells in mice does not map to the frequencies of noise exposure. Regardless of whether mice are exposed to the OBN (8–16 kHz) or broadband noise (2–20 kHz), noise-induced loss of sensory hair cells follows a base-to-apex gradient with losses of sensory hair cells beginning at the basal turn of the cochlear spiral and the changes in molecular signals in OHCs also showed a similar pattern (Yuan et al., 2015; Hill et al., 2016). Due to the limitation of mouse cochlear tissues by Western blot analysis being assessed in whole cochlear homogenates that contain all three turns of the cochlear spiral (apex, middle, and basal turn) and multiple cochlear cell types, changes in specific regions are muted when assessed by Western blot. Therefore, changes in MCU or NCLX only in the cochlear sensory hair cells of the basal turn might be diluted by other cochlear cell types resulting in unchanged total MCU or NCLX by Western blot.

Noise-Induced Loss of Inner Hair Cell Synapses Is Reversed in MCU Knockout Mice

The fact that MCU knockout mice are viable indicates compensatory or alternative pathways for the entry of mitochondrial calcium. The scientists who originally generated MCU knockout mice reported that mitochondrial calcium levels are reduced but not absent in the MCU knockout mice (Murphy et al., 2014). This supports the studies from another group showing that other MCU-independent mitochondrial calcium channels, such as transient receptor potential channels, are also responsible for mitochondrial calcium uptake (Feng et al., 2013).

The observed basic hearing characteristics of MCU knockout and wild-type littermates are in agreement with what is known of the well-documented CD1 strain, which has sensorineural hearing loss at high frequencies correlating to the basal turn (Le Calvez et al., 1998), but not at low frequencies, such as 8 kHz, and OHCs at apical turn remain intact. Furthermore, IHCs also remain intact along the entire cochlear spiral. Based on this feature, high-intensity noise exposure (116-dB SPL OBN centered at 4 kHz) was imposed on MCU knockout and wild-type littermates in order to induce OHC loss at the apex; this is

the highest noise intensity that MCU wild-type mice survived. Unfortunately, such high noise intensity is unable to induce OHC loss at the apex, although we observe moderate hearing impairment at 8 kHz 14 days after the noise exposure. The mammalian cochlea has a tonotopic organization producing an exponential frequency map (Müller et al., 2005). The different vulnerability of OHCs to inner ear damage is a well-documented phenomenon, although the detailed mechanism is unknown (Sha and Schacht, 2017). It has been suggested that the ability of plasma membrane calcium ATPase (PMCA2) to extrude calcium load through mechanotransducer channels is limited in the OHC basal turn, causing cytosolic calcium overload and leading to high-frequency hearing loss (Chen Q. et al., 2012). Additionally, OHCs in the basal turn are more susceptible to free radical damage (Sha et al., 2001). Furthermore, stiffness of the basilar membrane is different between base and apex (Liu et al., 2015). Recently, it has been suggested that there is a high-pass filter at the cochlear apex, where the mechanical turning curves are less aligned with the nerve fiber tuning curves (Fettiplace, 2017).

Since IHCs are intact along the whole cochlear spiral, we have focused our investigation on noise-induced changes in ribbon synapses using MCU knockouts and wild-type littermates. In line with our observations in CBA/J mice, high-intensity noise exposure induces loss of ribbon synapses in MCU wild-type littermates without significant recovery by 14 days after the exposure (Hill et al., 2016). However, MCU knockouts suffer only temporary damage rather than permanent noise-induced IHC synapse loss, allowing IHC synapses to fully recover and protect against the decline of ABR wave I amplitudes. These results are compatible with our data from treatment with siMCU and Ru360 showing protection against noise-induced loss of ribbon synapses in CBA/J mice, indicating MCU as an important mediator affecting cochlear synaptopathy. In the current study, there is no evidence of retraction of peripheral nerve endings from the CtBP2 puncta when examined 14 days after the exposure. While such retraction is reported in the literature (Shi et al., 2013; Liberman et al., 2015), the majority of CtBP2 puncta were co-localized with GluA2. The CtBP2 and GluA2 signals surrounding or above the nuclei of IHC in the MCU knockout mice cannot be attributed to an effect of noise exposure, as such scenario occurred regardless of noise exposure. Additionally, the majority of CtBP2 and GluA2 were located below the IHC nuclei. The detailed downstream mechanisms by which knockout of the *MCU* gene can protect against IHC synapse loss and the plasticity of ribbon synapses after noise damage require further investigation. As we have discussed above, noise-induced mitochondrial calcium overload may lead to overproduction of ROS, which is associated with noise-induced ribbon loss (Fetoni et al., 2013). Furthermore, recovery of noise-induced loss of ribbon synapses in MCU knockout mice is in line with the excitotoxicity theory, as transcriptional repression of MCU reduces excitotoxicity (Depp et al., 2018).

In summary, our results establish for the first time that noise-induced elevation of MCU and reduction of NCLX immunoreactivity in sensory hair cells may facilitate NIHL by mediating the loss of IHC synaptic ribbons and OHCs. The upregulation of MCU and decrease in NCLX in OHCs of the

basal turn after noise exposure is most likely a response to increased intracellular calcium levels. Agents that inhibit MCU activity reduce the extent of mitochondrial calcium overload and, subsequently, decrease the induction of apoptotic pathways associated with hair cell loss.

AUTHOR CONTRIBUTIONS

XW, HL, HX, RL, KH and HY performed research in CBA/J mice. YZ performed research in MCU KO mice. SP and QF performed research in CBA/J and MCU KO mice. KH performed research in OC-1 cells. S-HS designed research, analyzed the data and wrote the article. All authors have reviewed the contents of the manuscript, approve of its contents, and validate the accuracy of the data.

FUNDING

The research project described was supported by grant R01 DC009222 from the National Institute on Deafness and

Other Communication Disorders, National Institutes of Health. This work was conducted in the WR Building at MUSC in renovated space supported by grant C06 RR014516. Animals were housed in MUSC CRI animal facilities supported by grant C06 RR015455 from the Extramural Research Facilities Program of the National Center for Research Resources.

ACKNOWLEDGMENTS

We thank Dr. Jochen Schacht for his valuable comments on the manuscript. We also thank Dr. Yuan Shao in the MUSC Biorepository & Tissue Analysis Shared Resource for technical assistance with cochlear paraffin sections and Andra Talaska for proofreading of the manuscript.

SUPPLEMENTARY MATERIAL

The Supplementary Material for this article can be found online at: <https://www.frontiersin.org/articles/10.3389/fnmol.2018.00469/full#supplementary-material>

REFERENCES

- Baines, C. P., Kaiser, R. A., Purcell, N. H., Blair, N. S., Osinska, H., Hambleton, M. A., et al. (2005). Loss of cyclophilin D reveals a critical role for mitochondrial permeability transition in cell death. *Nature* 434, 658–662. doi: 10.1038/nature03434
- Boitier, E., Rea, R., and Duchen, M. R. (1999). Mitochondria exert a negative feedback on the propagation of intracellular Ca^{2+} waves in rat cortical astrocytes. *J. Cell Biol.* 145, 795–808. doi: 10.1083/jcb.145.4.795
- Celsi, F., Pizzo, P., Brini, M., Leo, S., Fotino, C., Pinton, P., et al. (2009). Mitochondria, calcium cell death: a deadly triad in neurodegeneration. *Biochim. Biophys. Acta* 1787, 335–344. doi: 10.1016/j.bbmbio.2009.02.021
- Chaudhuri, D., Sancak, Y., Mootha, V. K., and Clapham, D. E. (2013). MCU encodes the pore conducting mitochondrial calcium currents. *Elife* 2:e00704. doi: 10.7554/elif00704
- Chen, Z., Kujawa, S. G., and Sewell, W. F. (2007). Auditory sensitivity regulation via rapid changes in expression of surface AMPA receptors. *Nat. Neurosci.* 10, 1238–1240. doi: 10.1038/nn1974
- Chen, Q., Mahendrasingam, S., Tickle, J. A., Hackney, C. M., Furness, D. N., and Fettiplace, R. (2012). The development, distribution density of the plasma membrane calcium ATPase 2 calcium pump in rat cochlear hair cells. *Eur. J. Neurosci.* 36, 2302–2310. doi: 10.1111/j.1460-9568.2012.08159.x
- Chen, Z., Peppi, M., Kujawa, S. G., and Sewell, W. F. (2009). Regulated expression of surface AMPA receptors reduces excitotoxicity in auditory neurons. *J. Neurophysiol.* 102, 1152–1159. doi: 10.1152/jn.00288.2009
- Chen, F.-Q., Zheng, H.-W., Hill, K., and Sha, S.-H. (2012). Traumatic noise activates Rho-family GTPases through transient cellular energy depletion. *J. Neurosci.* 32, 12421–12430. doi: 10.1523/jneurosci.6381-11.2012
- Chen, F. Q., Zheng, H. W., Schacht, J., and Sha, S. H. (2013). Mitochondrial peroxiredoxin 3 regulates sensory cell survival in the cochlea. *PLoS One* 8:e61999. doi: 10.1371/journal.pone.0061999
- Clapham, D. E. (2007). Calcium signaling. *Cell* 131, 1047–1058. doi: 10.1016/j.cell.2007.11.028
- Depp, C., Bas-Orth, C., Schroeder, L., Hellwig, A., and Bading, H. (2018). Synaptic activity protects neurons against calcium-mediated oxidation contraction of mitochondria during excitotoxicity. *Antioxid. Redox Signal.* 29, 1109–1124. doi: 10.1089/ars.2017.7092
- Feng, S., Li, H., Tai, Y., Huang, J., Su, Y., Abramowitz, J., et al. (2013). Canonical transient receptor potential 3 channels regulate mitochondrial calcium uptake. *Proc. Natl. Acad. Sci. U S A* 110, 11011–11016. doi: 10.1073/pnas.1309531110
- Fetoni, A. R., De Bartolo, P., Eramo, S. L., Rolesi, R., Paciello, F., Bergamini, C., et al. (2013). Noise-induced hearing loss (NIHL) as a target of oxidative stress-mediated damage: cochlear cortical responses after an increase in antioxidant defense. *J. Neurosci.* 33, 4011–4023. doi: 10.1523/JNEUROSCI.2282-12.2013
- Fettiplace, R. (2017). Hair cell transduction, tuning synaptic transmission in the mammalian cochlea. *Compr. Physiol.* 7, 1197–1227. doi: 10.1002/cphy.c160049
- Fridberger, A., Flock, A., Ulfendahl, M., and Flock, B. (1998). Acoustic overstimulation increases outer hair cell Ca^{2+} concentrations causes dynamic contractions of the hearing organ. *Proc. Natl. Acad. Sci. U S A* 95, 7127–7132. doi: 10.1073/pnas.95.12.7127
- Gandhi, S., Wood-Kaczmar, A., Yao, Z., Plun-Favreau, H., Deas, E., Klupsch, K., et al. (2009). PINK1-associated Parkinson's disease is caused by neuronal vulnerability to calcium-induced cell death. *Mol. Cell* 33, 627–638. doi: 10.1016/j.molcel.2009.02.013
- Heinrich, U. R., Maurer, J., and Mann, W. (1999). Ultrastructural evidence for protection of the outer hair cells of the inner ear during intense noise exposure by application of the organic calcium channel blocker diltiazem. *ORL J. Otorhinolaryngol. Relat. Spec.* 61, 321–327. doi: 10.1159/000027693
- Hill, K., Yuan, H., Wang, X., and Sha, S. H. (2016). Noise-induced loss of hair cells cochlear synaptopathy are mediated by the activation of AMPK. *J. Neurosci.* 36, 7497–7510. doi: 10.1523/JNEUROSCI.0782-16.2016
- Jiang, H., Talaska, A. E., Schacht, J., and Sha, S. H. (2007). Oxidative imbalance in the aging inner ear. *Neurobiol. Aging* 28, 1605–1612. doi: 10.1016/j.neurobiolaging.2006.06.025
- Kirichok, Y., Krapivinsky, G., and Clapham, D. E. (2004). The mitochondrial calcium uniporter is a highly selective ion channel. *Nature* 427, 360–364. doi: 10.1038/nature02246
- Kujawa, S. G., and Liberman, M. C. (2009). Adding insult to injury: cochlear nerve degeneration after “temporary” noise-induced hearing loss. *J. Neurosci.* 29, 14077–14085. doi: 10.1523/JNEUROSCI.2845-09.2009
- Le Calvez, S., Avan, P., Gilain, L., and Romand, R. (1998). CD1 hearing-impaired mice. I: distortion product otoacoustic emission levels, cochlear function and morphology. *Hear. Res.* 120, 37–50. doi: 10.1016/s0378-5955(98)00050-1
- Liberman, L. D., Suzuki, J., and Liberman, M. C. (2015). Dynamics of cochlear synaptopathy after acoustic overexposure. *J. Assoc. Res. Otolaryngol.* 16, 205–219. doi: 10.1007/s10162-015-0510-3
- Liu, Y., Gracewski, S. M., and Nam, J. H. (2015). Consequences of location-dependent organ of corti micro-mechanics. *PLoS One* 10:e0133284. doi: 10.1371/journal.pone.0133284
- Mann, Z. F., Duchon, M. R., and Gale, J. E. (2009). Mitochondria modulate the spatio-temporal properties of intra- and intercellular Ca^{2+} signals in cochlear supporting cells. *Cell Calcium* 46, 136–146. doi: 10.1016/j.ceca.2009.06.005
- Mattson, M. P. (2007). Calcium and neurodegeneration. *Aging Cell* 6, 337–350. doi: 10.1111/j.1474-9726.2007.00275.x

- Maurer, J., Heinrich, U. R., and Mann, W. (1993). Morphologic damage and changes of intracellular calcium-binding sites after acute noise trauma in the organ of Corti of the guinea pig. *ORL J. Otorhinolaryngol. Relat. Spec.* 55, 7–12. doi: 10.1159/000276345
- Miller, J. M., Brown, J. N., and Schacht, J. (2003). 8-iso-prostaglandin F_{2α}, a product of noise exposure, reduces inner ear blood flow. *Audiol. Neurotol.* 8, 207–221. doi: 10.1159/000071061
- Minami, S. B., Yamashita, D., Schacht, J., and Miller, J. M. (2004). Calcineurin activation contributes to noise-induced hearing loss. *J. Neurosci. Res.* 78, 383–392. doi: 10.1002/jnr.20267
- Müller, M., von Hünenbein, K., Hoidis, S., and Smolders, J. W. (2005). A physiological place-frequency map of the cochlea in the CBA/J mouse. *Hear. Res.* 202, 63–73. doi: 10.1016/j.heares.2004.08.011
- Murphy, E., Pan, X., Nguyen, T., Liu, J., Holmström, K. M., and Finkel, T. (2014). Unresolved questions from the analysis of mice lacking MCU expression. *Biochem. Biophys. Res. Commun.* 449, 384–385. doi: 10.1016/j.bbrc.2014.04.144
- Nagashima, R., Yamaguchi, T., Kuramoto, N., and Ogita, K. (2011). Acoustic overstimulation activates 5'-AMP-activated protein kinase through a temporary decrease in ATP level in the cochlear spiral ligament prior to permanent hearing loss in mice. *Neurochem. Int.* 59, 812–820. doi: 10.1016/j.neuint.2011.08.015
- Nicotera, T. M., Hu, B. H., and Henderson, D. (2003). The caspase pathway in noise-induced apoptosis of the chinchilla cochlea. *J. Assoc. Res. Otolaryngol.* 4, 466–477. doi: 10.1007/s10162-002-3038-2
- Oishi, N., Chen, F. Q., Zheng, H. W., and Sha, S. H. (2013). Intra-tympanic delivery of short interfering RNA into the adult mouse cochlea. *Hear. Res.* 296, 36–41. doi: 10.1016/j.heares.2012.10.011
- Oishi, N., and Schacht, J. (2011). Emerging treatments for noise-induced hearing loss. *Expert Opin. Emerg. Drugs* 16, 235–245. doi: 10.1517/14728214.2011.552427
- Oliver, D., Ludwig, J., Reisinger, E., Zoellner, W., Ruppersberg, J. P., and Fakler, B. (2001). Memantine inhibits efferent cholinergic transmission in the cochlea by blocking nicotinic acetylcholine receptors of outer hair cells. *Mol. Pharmacol.* 60, 183–189. doi: 10.1124/mol.60.1.183
- Palty, R., Hershfinkel, M., and Sekler, I. (2012). Molecular identity and functional properties of the mitochondrial Na⁺/Ca²⁺ exchanger. *J. Biol. Chem.* 287, 31650–31657. doi: 10.1074/jbc.r112.355867
- Pan, X., Liu, J., Nguyen, T., Liu, C., Sun, J., Teng, Y., et al. (2013). The physiological role of mitochondrial calcium revealed by mice lacking the mitochondrial calcium uniporter. *Nat. Cell Biol.* 15, 1464–1472. doi: 10.1038/ncb2868
- Patron, M., Raffaello, A., Granatiero, V., Tosatto, A., Merli, G., De Stefani, D., et al. (2013). The mitochondrial calcium uniporter (MCU): molecular identity and physiological roles. *J. Biol. Chem.* 288, 10750–10758. doi: 10.1074/jbc.R112.420752
- Puel, J. L., d'Aldin, C. G., Saffiende, S., Eybalin, M., and Pujol, R. (1996). "Excitotoxicity and plasticity of IHC-auditory nerve contributes to both temporary and permanent threshold shift," in *Scientific Basis of Noise-Induced Hearing Loss*, eds A. Axelsson, H. M. Borchgrevink, R. P. Hamernik, P. A. Hellström, D. Henderson and R. J. Salvi (New York, NY: Thieme Press), 36–42.
- Qiu, J., Tan, Y. W., Hagenston, A. M., Martel, M. A., Kneisel, N., Skehel, P. A., et al. (2013). Mitochondrial calcium uniporter Mcu controls excitotoxicity and is transcriptionally repressed by neuroprotective nuclear calcium signals. *Nat. Commun.* 4:2034. doi: 10.1038/ncomms3034
- Quirk, W. S., and Seidman, M. D. (1995). Cochlear vascular changes in response to loud noise. *Am. J. Otol.* 16, 322–325.
- Raffaello, A., De Stefani, D., and Rizzuto, R. (2012). The mitochondrial Ca²⁺ uniporter. *Cell Calcium* 52, 16–21. doi: 10.1016/j.ceca.2012.04.006
- Rizzuto, R., De Stefani, D., Raffaello, A., and Mammucari, C. (2012). Mitochondria as sensors and regulators of calcium signalling. *Nat. Rev. Mol. Cell Biol.* 13, 566–578. doi: 10.1038/nrm3412
- Sanganahalli, B. G., Herman, P., Hyder, F., and Kannurpatti, S. S. (2013). Mitochondrial calcium uptake capacity modulates neocortical excitability. *J. Cereb. Blood Flow Metab.* 33, 1115–1126. doi: 10.1038/jcbfm.2013.61
- Sha, S. H., and Schacht, J. (2017). Emerging therapeutic interventions against noise-induced hearing loss. *Expert Opin. Investig. Drugs* 26, 85–96. doi: 10.1080/13543784.2017.1269171
- Sha, S. H., Taylor, R., Forge, A., and Schacht, J. (2001). Differential vulnerability of basal and apical hair cells is based on intrinsic susceptibility to free radicals. *Hear. Res.* 155, 1–8. doi: 10.1016/s0378-5955(01)00224-6
- Shen, H., Zhang, B., Shin, J. H., Lei, D., Du, Y., Gao, X., et al. (2007). Prophylactic and therapeutic functions of T-type calcium blockers against noise-induced hearing loss. *Hear. Res.* 226, 52–60. doi: 10.1016/j.heares.2006.12.011
- Shi, L., Liu, L., He, T., Guo, X., Yu, Z., Yin, S., et al. (2013). Ribbon synapse plasticity in the cochleae of Guinea pigs after noise-induced silent damage. *PLoS One* 8:e81566. doi: 10.1371/journal.pone.0081566
- Szalai, G., Krishnamurthy, R., and Hajnóczky, G. (1999). Apoptosis driven by IP₃-linked mitochondrial calcium signals. *EMBO J.* 18, 6349–6361. doi: 10.1093/emboj/18.22.6349
- Taylor, C. R., and Levenson, R. M. (2006). Quantification of immunohistochemistry—issues concerning methods, utility and semiquantitative assessment II. *Histopathology* 49, 411–424. doi: 10.1111/j.1365-2559.2006.02513.x
- Viberg, A., and Canlon, B. (2004). The guide to plotting a cochleogram. *Hear. Res.* 197, 1–10. doi: 10.1016/j.heares.2004.04.016
- Vicente-Torres, M. A., and Schacht, J. (2006). A BAD link to mitochondrial cell death in the cochlea of mice with noise-induced hearing loss. *J. Neurosci. Res.* 83, 1564–1572. doi: 10.1002/jnr.20832
- Walker, R. A. (2006). Quantification of immunohistochemistry—issues concerning methods, utility and semiquantitative assessment I. *Histopathology* 49, 406–410. doi: 10.1111/j.1365-2559.2006.02514.x
- Wan, G., Gómez-Casati, M. E., Gigliello, A. R., Liberman, M. C., and Corfas, G. (2014). Neurotrophin-3 regulates ribbon synapse density in the cochlea and induces synapse regeneration after acoustic trauma. *Elife* 3:e03564. doi: 10.7554/elife.03564
- Williams, G. S., Boyman, L., Chikando, A. C., Khairallah, R. J., and Lederer, W. J. (2013). Mitochondrial calcium uptake. *Proc. Natl. Acad. Sci. U S A* 110, 10479–10486. doi: 10.1073/pnas.1300410110
- Yuan, H., Wang, X., Hill, K., Chen, J., Lemasters, J., Yang, S. M., et al. (2015). Autophagy attenuates noise-induced hearing loss by reducing oxidative stress. *Antioxid. Redox Signal.* 22, 1308–1324. doi: 10.1089/ars.2014.6004
- Zheng, H. W., Chen, J., and Sha, S. H. (2014). Receptor-interacting protein kinases modulate noise-induced sensory hair cell death. *Cell Death Dis.* 5:e1262. doi: 10.1038/cddis.2014.177
- Zuo, H., Cui, B., She, X., and Wu, M. (2008). Changes in Guinea pig cochlear hair cells after sound conditioning and noise exposure. *J. Occup. Health* 50, 373–379. doi: 10.1539/joh.l8032

Conflict of Interest Statement: The authors declare that the research was conducted in the absence of any commercial or financial relationships that could be construed as a potential conflict of interest.

Copyright © 2019 Wang, Zhu, Long, Pan, Xiong, Fang, Hill, Lai, Yuan and Sha. This is an open-access article distributed under the terms of the Creative Commons Attribution License (CC BY). The use, distribution or reproduction in other forums is permitted, provided the original author(s) and the copyright owner(s) are credited and that the original publication in this journal is cited, in accordance with accepted academic practice. No use, distribution or reproduction is permitted which does not comply with these terms.



An Excitatory/Inhibitory Switch From Asymmetric Sensory Neurons Defines Postsynaptic Tuning for a Rapid Response to NaCl in *Caenorhabditis elegans*

Masahiro Kuramochi[†] and Motomichi Doi^{*}

OPEN ACCESS

Edited by:

Jaewon Ko,
Daegu Gyeongbuk Institute of
Science and Technology (DGIST),
South Korea

Reviewed by:

Seok-Kyu Kwon,
Korea Institute of Science and
Technology (KIST), South Korea
Kyuhyung Kim,
Daegu Gyeongbuk Institute of
Science and Technology (DGIST),
South Korea

*Correspondence:

Motomichi Doi
doi-m@aist.go.jp

[†]Present address:

Masahiro Kuramochi,
Graduate School of Frontier
Sciences, The University of Tokyo,
AIST-UTokyo Advanced
Operando-Measurement Technology
Open Innovation Laboratory
(OPERANDO-OIL), National Institute
of Advanced Industrial Science and
Technology (AIST), Kashiwa, Japan

Received: 02 September 2018

Accepted: 12 December 2018

Published: 09 January 2019

Citation:

Kuramochi M and Doi M (2019) An
Excitatory/Inhibitory Switch From
Asymmetric Sensory Neurons
Defines Postsynaptic Tuning for a
Rapid Response to NaCl in
Caenorhabditis elegans.
Front. Mol. Neurosci. 11:484.
doi: 10.3389/fnmol.2018.00484

Molecular Neurobiology Research Group and DAILAB, Biomedical Research Institute, National Institute of Advanced Industrial Science and Technology (AIST), Tsukuba, Japan

The neural networks that regulate animal behaviors are encoded in terms of neuronal excitation and inhibition at the synapse. However, how the temporal activity of neural circuits is dynamically and precisely characterized by each signaling interaction *via* excitatory or inhibitory synapses, and how both synaptic patterns are organized to achieve fine regulation of circuit activities is unclear. Here, we show that in *Caenorhabditis elegans*, the excitatory/inhibitory switch from asymmetric sensory neurons (ASEL/R) following changes in NaCl concentration is required for a rapid and fine response in postsynaptic interneurons (AIBs). We found that glutamate released by the ASEL neuron inhibits AIBs *via* a glutamate-gated chloride channel localized at the distal region of AIB neurites. Conversely, glutamate released by the ASER neuron activates AIBs *via* an AMPA-type ionotropic receptor and a G-protein-coupled metabotropic glutamate receptor. Interestingly, these excitatory receptors are mainly distributed at the proximal regions of the neurite. Our results suggest that these convergent synaptic patterns can tune and regulate the proper behavioral response to environmental changes in NaCl.

Keywords: synapse integration, *C. elegans*, salt-chemotaxis behavior, Ca^{2+} imaging, glutamate

INTRODUCTION

Neuronal circuit activity is modulated by a balanced and well-organized combination of excitatory and inhibitory signals. The circuit dynamics are temporally and spatially regulated by rate of synaptic transmission and are intrinsic for the brain functions that regulate numerous animal behaviors. Such behavioral responses to sensory stimuli are dynamic and finely tuned largely as a result of the interactions between excitatory and inhibitory signals. In the vertebrate visual system, the responses of ON and OFF bipolar neurons are finely tuned by photoreceptor neurons *via* both excitatory and inhibitory synapses, and these bipolar neurons then transmit visual information to upper layer ganglion cells (Schiller et al., 1986). An information stream to discriminate between brightness and contrast in the retina has also been proposed to be strictly regulated by excitatory and inhibitory signals (Molnar et al., 2009). In an analogous fashion, even robotic control systems integrate positive and negative signals to finely regulate dynamic

operations with quick and precise movements (Brooks, 1986). This strategy of using positive and negative signaling to finely regulate systems is thus widely adopted from machines to multicellular organisms. However, how each positive (excitatory) and negative (inhibitory) synapse in the animal brain contributes to the overall temporal activity of circuits, and how both types of synapse are organized in a certain circuit to regulate activity at the single neuron level is unclear.

The nematode *Caenorhabditis elegans* is an accessible and valuable model to characterize neural circuit dynamics at the cellular network level and the subcellular synaptic level. As such, the synaptic connectivity of the whole *C. elegans* nervous system has been identified (White et al., 1986). Worms can execute various behaviors, from simple withdrawal reflexes, thermotaxis and chemotaxis, to more the complex associative learning and memory, despite having a small nervous system of only 302 neurons (Mori and Ohshima, 1995; Wicks and Rankin, 1995; Nuttley et al., 2002; Kunitomo et al., 2013). A combination of genetic manipulation, laser ablation, calcium imaging and optogenetic techniques have been used to map the neural circuits regulating these behaviors in worms, and determine the neuronal dynamics underlying these behaviors at the cellular level. In particular, calcium imaging is often used to monitor brain-wide activity at the cellular resolution level (Prevedel et al., 2014; Kato et al., 2015).

The salt-chemotaxis behavior exhibited by *C. elegans* is regulated by a pair of chemosensory ASE neurons (ASEL and ASER) and their postsynaptic interneurons. ASEL and ASER both detect changes in NaCl concentration, yet produce opposite responses to the NaCl change. ASEL is activated by increases in NaCl concentration, whereas ASER is activated by decreases in NaCl concentration (Suzuki et al., 2008). Furthermore, these neurons have distinct functions in mediating chemotaxis behavior: ASEL activation promotes forward run probability, whereas ASER activation promotes turn probability (Suzuki et al., 2008; Thiele et al., 2009). Despite these asymmetric properties, both neurons probably use glutamate as a neurotransmitter, based on the expression of the vesicular glutamate transporter EAT-4 (Serrano-Saiz et al., 2013) and connect to several of the same interneurons, including AIB and AIY interneurons (White et al., 1986). The AIB interneurons regulate the reversal/turn behavior and communicate with both ASEL and R sensory neurons via chemical synapses. These findings provoke an intriguing question as to what synaptic signaling mechanism exists between the same interneurons that can generate opposing behavioral outputs as a result of asymmetric responses in the receiving sensory neuron using the same transmitter (glutamate).

Kunitomo et al. (2013) reported that AIB interneurons are activated by the decrease of NaCl concentration, possibly dependent on the synchronous activation of the ASER neuron. On the other hand, these AIB are inhibited when ASEL is activated (Wang et al., 2017). These findings suggest that switch from excitatory by ASER to inhibitory by ASEL or vice versa may precisely regulate the AIB activity and affect forward and backward locomotion in salt chemotaxis.

However, it is not clear whether such excitatory/inhibitory switch is really involved in the ASE-AIB synaptic circuit, and how this switch is regulated in molecular level. Here we show that in the *C. elegans* salt-chemotaxis circuit, the excitatory/inhibitory switch from asymmetric sensory neurons defines postsynaptic tuning and smooth transition of activity to changes in NaCl concentration. We also show that glutamate released by the ASEL inhibits postsynaptic AIBs through a glutamate-gated chloride channel and an unidentified receptor, whereas glutamate released by the ASER activates AIBs via AMPA-type ionotropic and G-protein-coupled metabotropic glutamate receptors. Furthermore, each excitatory or inhibitory synapse is located on distinct regions of the postsynaptic AIB neurite. These results suggest that excitatory/inhibitory signaling from asymmetric sensory neurons is integral to the salt-chemotaxis neural circuit to achieve rapid and fine responses in postsynaptic neurons for suitable behavioral decisions.

MATERIALS AND METHODS

Strains

Worms were cultivated on standard NGM agar plates seeded with *E. coli* OP50 at room temperature (~22°C). The Bristol N2 was used as wild-type strain, and other mutant strains and transgenic strains used in this study are listed in **Supplementary Table S1**.

Molecular Biology and Transgenic Animals

Standard methods for molecular biology were used to construct plasmid DNAs. For the expression of the calcium indicator protein G-GECO1.2 (a kind gift from Takeshi Ishihara) or GCaMP6 (kind gift from Junichi Nakai), each coding sequence was inserted between the AgeI and EcoRI sites of the pPD95.79 vector (kind gift from Andy Fire). Then, the promoter region for cell-specific expression of the cDNAs was inserted between the SphI and XmaI sites of the resulting pPD95.79/G-GECO1.2 or pPD95.79/GCaMP6 plasmids. We used the following promoters for cell-specific expression: *gcy-5* for ASER, *gcy-7* for ASEL, and *npr-9* for AIB. To generate plasmid DNAs for cell-specific UNC-13 expression, the full-length *unc-13* cDNA fragment was amplified by overlapping PCR fusion using the following primers:

- 5'CCGGGATGCCACGCCGACGGAACGAAA3'
- 5'GTGTCCTTCGTTTGGTCTTTCCAACTTGAG3'
- 5'CTCAAGTTGGAAAGACCAAACGAAGGACAC3'
- 5'CAGGCGTCTTGCATCGTTTCTTTTG3'
- 5'CAAAAGAAACGATGCAAGACGCCTG3'
- 5'GCATTCGGCAGTTGTTTCAATAGAGCC3'
- 5'GGCTCTATTGAAACAACGCGGAATGC3'.

The resulting full-length UNC-13 cDNA fragment was inserted between the XmaI and KpnI sites of the pPD95.79 Vector. Then, each promoter sequence for ASEL or ASER was inserted between the SphI and XmaI sites of the pPD95.79/UNC-13 plasmid DNA. To generate a *tetanus*

toxin expression plasmid, the *TeTx::mCherry* fragment from *Pttx-3::TeTx::mCherry* (a kind gift from Sreekanth Chalasani) was exchanged with the GCaMP6 sequence of the *Pgcy-5::GCaMP6* plasmid DNA. For the expression of the glutamate-gated chloride channel *glc-3*, the *glc-3* cDNA fragment was amplified by PCR fusion using the following primers:

- 5'ATGCGGATCCATGAGTCTCCGTTCACTTCTCAAT3' and
- 5'TTCTACCGGTACCTTGGCTTCCGGTGCGTGATATTGT3'.

The resulting full-length *glc-3* cDNA was inserted between the BamHI and KpnI sites of the pPD95.79/Venus Vector. Then, the *npr-9* promoter region was inserted between the SphI and BamHI sites of the pPD95.79/*glc-3* plasmid DNA. For the expression of an AMPA-type ionotropic glutamate receptor *glr-1*, the *glr-1::GFP* fragment was excised by KpnI and EcoRV digestion from the *Pttx-3::glr-1::GFP* plasmid (a kind gift from Takaaki Hirotsu), and then inserted into the *Pgcy-7::R-GECO1* plasmid DNA. Finally, the *npr-9* promoter region was inserted between the KpnI and ApaI sites. For the rescue experiments of *glc-3* or *glr-1* mutants, Venus or GFP sequence was removed from each expression plasmid DNA by using in-Fusion reaction (Takara), respectively.

For the generation of transgenic animals, the resulting plasmid DNAs were injected into N2 (Bristol) or mutant animals using a standard microinjection method (Mello et al., 1991). Details of the strains used in this study are listed in **Supplementary Table S1**.

Calcium Imaging

Calcium imaging was performed as described previously (Kuramochi and Doi, 2017). Adult transgenic worms were used for imaging. Worms were immobilized in a microfluidic device fabricated from polydimethylsiloxane (PDMS; Chronis et al., 2007). The microfluidic device was set on an inverted fluorescent microscope (Olympus IX71), and time-lapse images were captured (10 frames/s) using an ORCA-Flash 4.0 CCD camera (Hamamatsu Photonics) controlled by HCLImage software (Hamamatsu Photonics). Recordings started within 5 min after removal from food. The following buffers for calcium imaging were used: 5 mM KPO₄ (pH 6.0), 1 mM CaCl₂, 1 mM MgSO₄, including 0 or 50 mM NaCl for the stimulation. All the buffers were adjusted to 350 mOsmol/L H₂O with glycerol (Oda et al., 2011). The patterns of salt stimulation were automated using the Perfusion Valve Controller System VC-6M (Warner Instruments) and Arduino microcontroller to control solenoid valves (Arduino SRL) with a pre-generated sequence. We used $\Delta F/F_0$ to indicate fluorescence intensity change. F_0 was defined as the average fluorescence in a 5 s window before stimulation. After background subtraction, the total fluorescence intensity was measured from individual regions of interest (ROIs) in each neuron. An animal was imaged twice, with a 30 s interval between the first and second observation. For the comparison of $\Delta F/F_0$ among genotypes, “response ($\Delta F/F_0$)” was calculated using the average fluorescence in a 20 s window when NaCl concentration

is decreased or in a 10 s window when NaCl concentration is increased.

Confocal Microscopy and Synapse Observation

L4 larvae were mounted on a 1.5% agarose pad with 20 mM sodium azide in M9 solution for anesthesia. Images were acquired on an inverted confocal microscope (Nikon A1, Nikon) with a 60× objective lens, and were analyzed by NIS-Elements C/NIS-Elements C-ER and ImageJ software, respectively. The Z-stack image was acquired from the whole animals expressing each fluorescent fusion proteins. Co-localization between GLR-1 or GLC-3 GFP fusion proteins and a presynaptic mCherry::RAB-3 fusion protein was quantified by counting the number of GFP pixels overlapping with mCherry signal in a single z-axis frame. The number of pixels in each frame of Z-scan was averaged in each animal and used for quantitative analyses.

Statistical Methods

All data, except for the ASE activity, did not show gaussian distribution based on the Shapiro–Wilk test. Thus, a non-parametric Wilcoxon rank sum test was used to evaluate the median difference in calcium response.

RESULTS

Calcium Responses in Presynaptic Sensory ASE and Postsynaptic AIB Neurons Following Changes in NaCl Concentration

C. elegans detect NaCl concentration gradients *via* the ASEL and ASER sensory neurons and move to a preferential NaCl condition by using several behavioral strategies (Pierce-Shimomura et al., 1999; Iino and Yoshida, 2009). Both ASEL/R have synaptic connections to downstream first-layer interneurons including AIB neurons (**Figure 1A**). To understand the role of presynaptic excitatory/inhibitory switch in postsynaptic responses of AIB neurons, we recorded fluorescent changes of the genetically-encoded calcium indicator G-GECO1.2 (Zhao et al., 2011) that is specifically expressed in either pre- or postsynaptic neurons. Consistent with previous reports (Suzuki et al., 2008), the ASEL neuron did not show any response to a downstep in NaCl concentration (from 50 mM to 0 mM NaCl), whereas the ASER neuron showed a large, long-lasting response to the downstep (**Figure 1B**). Conversely, the ASEL neuron showed a fast calcium response to an upstep in NaCl (0 mM to 50 mM), and its response immediately decayed to the steady state level. The ASER calcium response decayed immediately after an upstep in NaCl concentration (**Figure 1D**). The AIB neurons showed a similar response pattern as the ASER: their responses rose slowly after a downstep in NaCl concentration, and after the peak level, slowly decayed during the exposure to 0 mM NaCl (**Figure 1B**). In response to an upstep in NaCl concentration, the AIB calcium level immediately decayed to the steady-state level (**Figure 1D**). Thus, as shown in previous report (Kunitomo et al., 2013; Wang et al.,

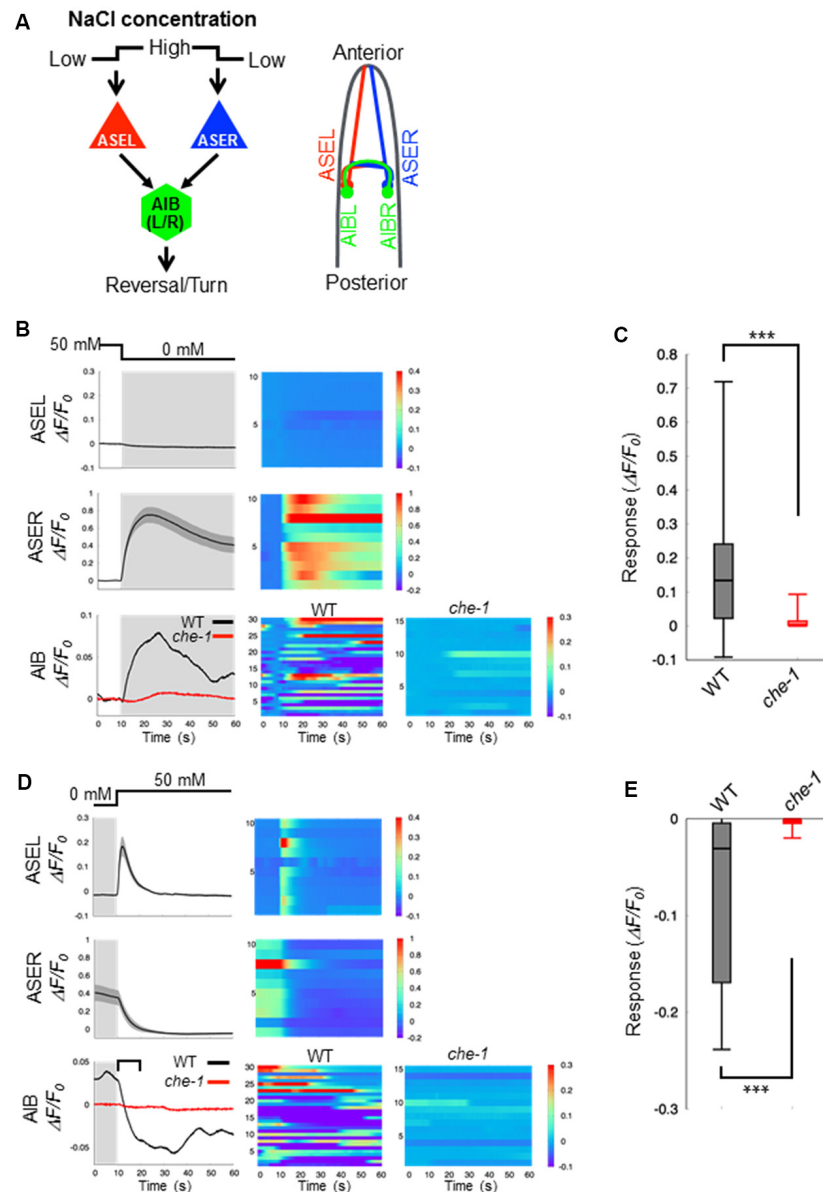


FIGURE 1 | Calcium dynamics in ASEL, ASER and AIB neurons in response to changes in NaCl concentration. **(A)** Simplified synaptic connections between ASE sensory neurons (ASEL and ASER) and AIB interneurons. Both ASE neurons respond to changes in NaCl concentration and connect to several interneurons, including AIB. AIB neurons trigger reversal and turning behaviors. **(B)** Calcium dynamics of ASEL, ASER and AIB neurons in response to a downstep in NaCl concentration from 50 mM to 0 mM. Averaged calcium responses to changes in NaCl concentration (left) and heatmap traces of individual worms (right). The black line indicates the calcium responses in wild-type animals ($n = 10$), and the red line indicates the calcium responses in *che-1(p679)* mutants ($n \geq 15$). Shaded areas indicate the SEM. **(C)** Quantitative analysis of the maximum calcium responses in AIB neurons during a downstep in NaCl concentration in the wild type (gray) and *che-1* mutants (red). The error bars indicate the SEM; *** $p < 0.001$; Wilcoxon rank sum test. **(D)** Calcium dynamics of ASEL, ASER and AIB neurons in response to an upstep in NaCl concentration from 0 mM to 50 mM. Averaged calcium responses to changes in NaCl concentration (left) and heatmap traces of individual worms (right). The black line indicates the calcium responses in the wild-type worms ($n = 10$), and the red line indicates the calcium responses in *che-1(p679)* mutants ($n \geq 15$). The shaded areas indicate SEM. **(E)** Quantitative analysis of the maximum calcium responses in AIB neurons during the first 10 s (blanket in **D**) after an upstep in NaCl concentration in wild type (gray) and *che-1(p679)* mutants (red). The error bars indicate the SEM; *** $p < 0.001$; Wilcoxon rank sum test.

2017), AIB neurons show similar neuronal responses to both up and down changes in NaCl concentration as the ASER neuron.

Sensory neurons, including AFD, ASE, ASH, ASJ, AWB, and AWC, are thought to function as salt-sensing neurons

(Thiele et al., 2009; Zaslaver et al., 2015), and AIB interneurons receive synaptic inputs from many sensory neurons. To examine whether the AIB neuronal responses to changes in NaCl concentration are regulated by ASE neuronal activity specifically, we recorded the AIB response in *che-1(p679)* mutant worms that

specifically lacks ASE neurons (Chang et al., 2003; Uchida et al., 2003). Here we found that the AIB neurons in *che-1* mutants showed no significant calcium response to either a downstep or upstep in NaCl concentration (Figures 1B–E). These results indicate that ASE neurons strongly affect AIB activity in response to NaCl concentration changes; other sensory neurons probably have a weak or no effect on AIB activity as they could not compensate for a loss of ASE neurons.

ASEL Inhibits AIB Activity Whereas ASER Stimulates AIB Activity

Our results suggest that ASE neurons are the main regulators of AIB activity during salt-chemotaxis. To confirm the role of each ASE neuron in the AIB response to changes in NaCl concentration, we analyzed the neurotransmission from the ASEL or the ASER neuron to AIBs. First, we monitored AIB responses to changes in NaCl concentration in the synaptic transmission-defective mutant *unc-13* (Richmond et al., 1999). *unc-13* encodes a protein required for vesicle priming at the presynapse and mutations in this gene cause severe defects in neurotransmitter release. The AIB neurons in *unc-13(e312)* mutants did not show any response to either a downstep or upstep in NaCl concentration (Figures 2A–F). Therefore, together with our findings in the *che-1* mutant, these results suggest that synaptic transmission from ASE neurons is required to regulate AIB activity when NaCl concentrations change.

We further examined how the two distinct ASEL and ASER neuronal responses to changes in NaCl concentration cooperatively modulate AIB activity. To answer this question, we monitored AIB responses when only ASEL or ASER synaptic transmission was functional. To this aim, UNC-13 protein was specifically expressed in either ASEL or ASER neurons in the *unc-13(e312)* mutant background to recover synaptic transmission from one of these neurons. We then monitored AIB calcium responses in these cell-specific synaptic rescue worms. With regards to ASER function, we found that ASER activates AIBs only when the NaCl concentration is decreased. In worms in which transmission from the ASER was rescued by cell-specific expression of UNC-13 in the ASER neuron, we observed that the calcium response in AIB neurons increased just after the NaCl concentration is decreased (Figures 2A–C). However, a strong inactivation following an increase in NaCl concentration was not observed in this rescue animal. These results suggest that the ASER neuron may activate AIBs when NaCl decreases, but likely has no inhibitory effect on AIB activity when NaCl increases. To further confirm these results, we also monitored AIB activity in transgenic worms in which the tetanus toxin light chain from *Clostridium tetani* (*TeTx*) was expressed in a cell-specific manner to block synaptic transmission. *TeTx* expression reduces presynaptic vesicle release by cleaving synaptobrevin/VAMP protein, a core component required for synaptic vesicle fusion (Schiavo et al., 1992). The transgenic worms expressing *TeTx* specifically in the ASER elicited a significantly weaker calcium response in AIBs during a downstep of in NaCl concentration compared to control worms (Figures 2G–I). Therefore, we conclude that the ASER signal

probably excites AIB neurons when the NaCl concentration decreases.

With regards to ASEL function, we found that ASEL signaling provides an inhibitory signal to inactivate AIB activity. AIB neurons were rapidly inactivated during an upstep in NaCl concentration, and this inactivation was also observed when the synaptic transmission from the ASEL neuron was specifically rescued upon expressing UNC-13 in the ASEL neuron of *unc-13* mutants (Figures 2D–F). Conversely, AIB activation in response to a downstep in NaCl concentration was not observed in this transgenic worm, suggesting that the ASEL may not have an excitatory role in AIB activation. Therefore, we conclude that the ASEL signal likely inactivates AIBs in response to ASEL transient activity when NaCl concentrations increase.

Distinct Glutamatergic Signals From ASEL and ASER Neurons Affect AIB Neuronal Activity

Thus far, we have shown that ASEL and ASER activities have opposing effects on AIB activity in response to changes in NaCl concentration (Figures 1B,D). Both ASEL and ASER neurons connect to AIB neurons *via* chemical synapses and probably release glutamate as a neurotransmitter (Serrano-Saiz et al., 2013). To test how glutamate delivers both as an excitatory and inhibitory signal to AIBs, we monitored the AIB calcium response in the *eat-4(ky5)* mutant. *eat-4* encodes a vesicular glutamate transporter in *C. elegans*, and mutations in this gene cause lack or decrease of glutamate in synaptic vesicles (Lee et al., 1999). We found that *eat-4(ky5)* mutants did not show a clear AIB response to either an increase or decrease in NaCl concentration (Figure 3). These results suggest that the glutamate signal from each ASE neuron likely generates both excitation and inhibition in AIBs.

AMPA-type ionotropic glutamate receptors can act as excitatory postsynaptic receptors for odor-evoked responses in AIB neurons (Chalasani et al., 2007). As such, we questioned whether the same AMPA-type glutamate receptors also mediate AIB activity in response to changes in NaCl concentration. Here, we used *glr-1* mutants in which expression of the non-NMDA glutamate receptor is disrupted. In *glr-1(n2461)* mutants, the averaged AIB calcium response was weaker than that elicited in wild-type worms but higher than that in *eat-4* mutant worms (Figures 3A–C). Although several studies have reported that AMPA-type excitatory receptors might modulate AIB activity *via* glutamate release (Chalasani et al., 2007; Piggott et al., 2011), we conclude that both GLR-1 and other receptors coordinately contribute to AIB neuronal excitation during exposure to decreases in NaCl concentration. This lower calcium responses in AIB neurons of *glr-1* mutants was rescued by the AIB-specific expression of GLR-1 receptor, suggesting the cell-autonomous regulation of AIB neuronal activity by GLR-1 (Supplementary Figure S1). GLR-1 is not required for inactivation in response to increase of NaCl concentration because *glr-1* mutant animals showed similar calcium responses with wild-type animals upon increase of NaCl concentration (Supplementary Figure S2).

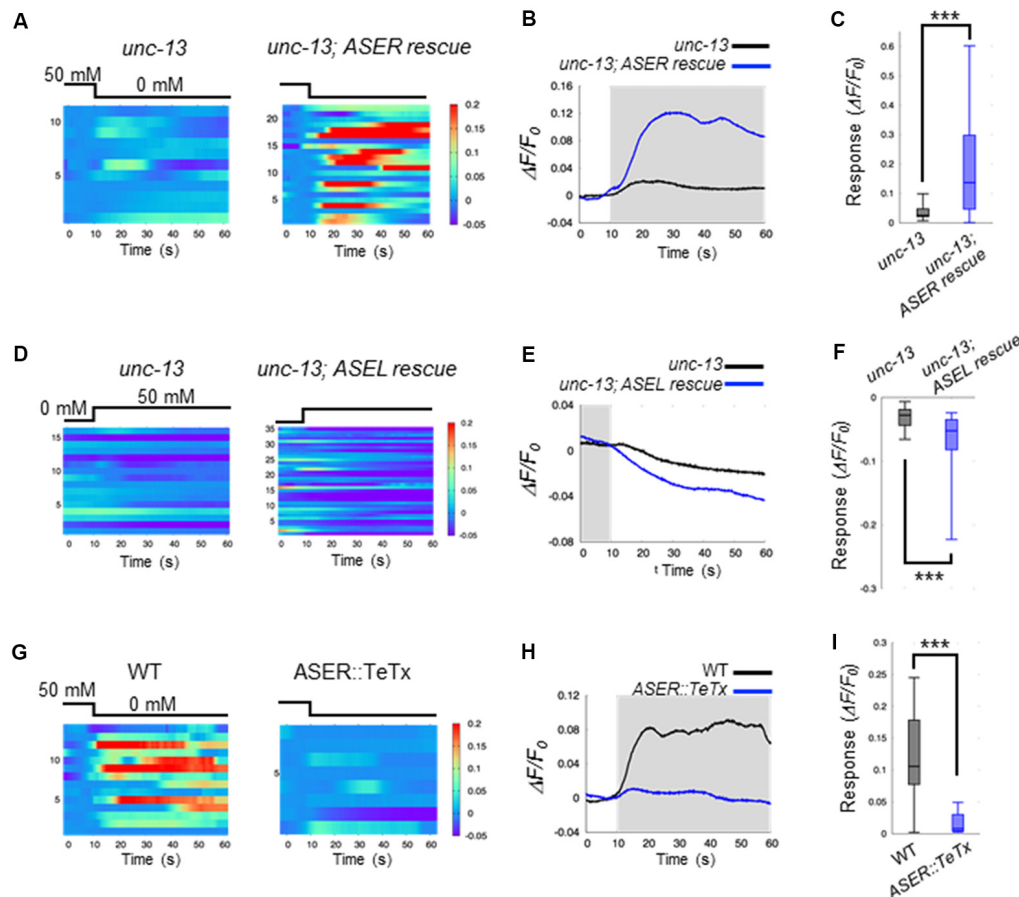


FIGURE 2 | ASEL inhibits AIB whereas ASER stimulates AIB. **(A)** Heatmap traces of the AIB response to a downstep in NaCl concentration in *unc-13* mutants and ASER-specific UNC-13 rescue worms on a *unc-13* mutant background. **(B)** Averaged calcium responses in **(A)**. The shaded area indicates the period corresponding to 0 mM NaCl. **(C)** Quantitative analysis of the maximum calcium responses during a downstep in NaCl concentration in **(A)**. The error bars indicate the SEM; *** $p < 0.001$; Wilcoxon rank sum test. **(D)** Heatmap traces for AIB responses to an upstep in NaCl concentration in *unc-13* mutants and ASEL-specific UNC-13 rescue worms on an *unc-13* mutant background. **(E)** Averaged calcium responses in **(D)**. The shaded area indicates the period corresponding to 0 mM NaCl. **(F)** Quantitative analysis of the minimum calcium responses in AIBs during the first 10 s after an upstep in NaCl concentration. The error bars indicate the SEM; *** $p < 0.001$; Wilcoxon rank sum test. **(G)** Heatmap traces for the AIB responses in wild-type and transgenic worms expressing *TeTx* specifically in the ASER neuron. **(H)** Averaged calcium responses in **(G)**. **(I)** Quantitative analysis of the maximum calcium responses during a downstep in NaCl concentration in **(G)**. The error bars indicate the SEM; *** $p < 0.001$; Wilcoxon rank sum test.

The metabotropic G-protein-coupled glutamate receptors (encoded by three *mgl* genes *mgl-1*, *mgl-2* and *mgl-3*) are thought to be expressed in AIB interneurons and act as excitatory postsynaptic receptors (Dillon et al., 2006). We next studied whether these metabotropic glutamate receptors contribute to AIB activity using *mgl-1(tm1811)*, *mgl-2(tm355)*, and their double mutant worms. Here, we found that the calcium responses in AIB neurons of the double mutants rose slowly to a peak following a downstep in NaCl concentration. On the other hand, the calcium responses in wild-type animals rose rapidly to a peak within 20 s after a downstep in NaCl concentration (**Figures 3D,E**). Furthermore, *glr-1*, *mgl-1* and *mgl-2* triple mutant animals showed significantly lower calcium responses than *mgl-1*; *mgl-2* double mutant animals after a downstep in NaCl concentration (**Figures 3D,E**). These results suggest that both AMPA-type and metabotropic glutamate receptors are

required for rapid AIB neuronal activity after a downstep in NaCl concentration.

As for inhibitory synaptic signaling *via* glutamate, a glutamate-gated chloride ion channel (encoded by four *glc* genes and two *avr* genes in *C. elegans*) can act as an inhibitory postsynaptic receptor (Cully et al., 1994; Hart et al., 1995; Maricq et al., 1995; Yates et al., 2003; Dillon et al., 2006). Mutations in *glc-3*, a subunit of the glutamate-gated chloride ion channel, can cause decreased activity of the glutamate-gated chloride ion channel (Cully et al., 1994). We hypothesized that the ASEL neuron may inhibit AIB activity *via* this glutamate-gated chloride ion channel on AIB neurites. To test this hypothesis, we examined the calcium response in AIB neurons of *glc-3(ok321)* mutants during an increase in NaCl concentration. We found that AIB responses in *glc-3(ok321)* mutants showed a slightly slower

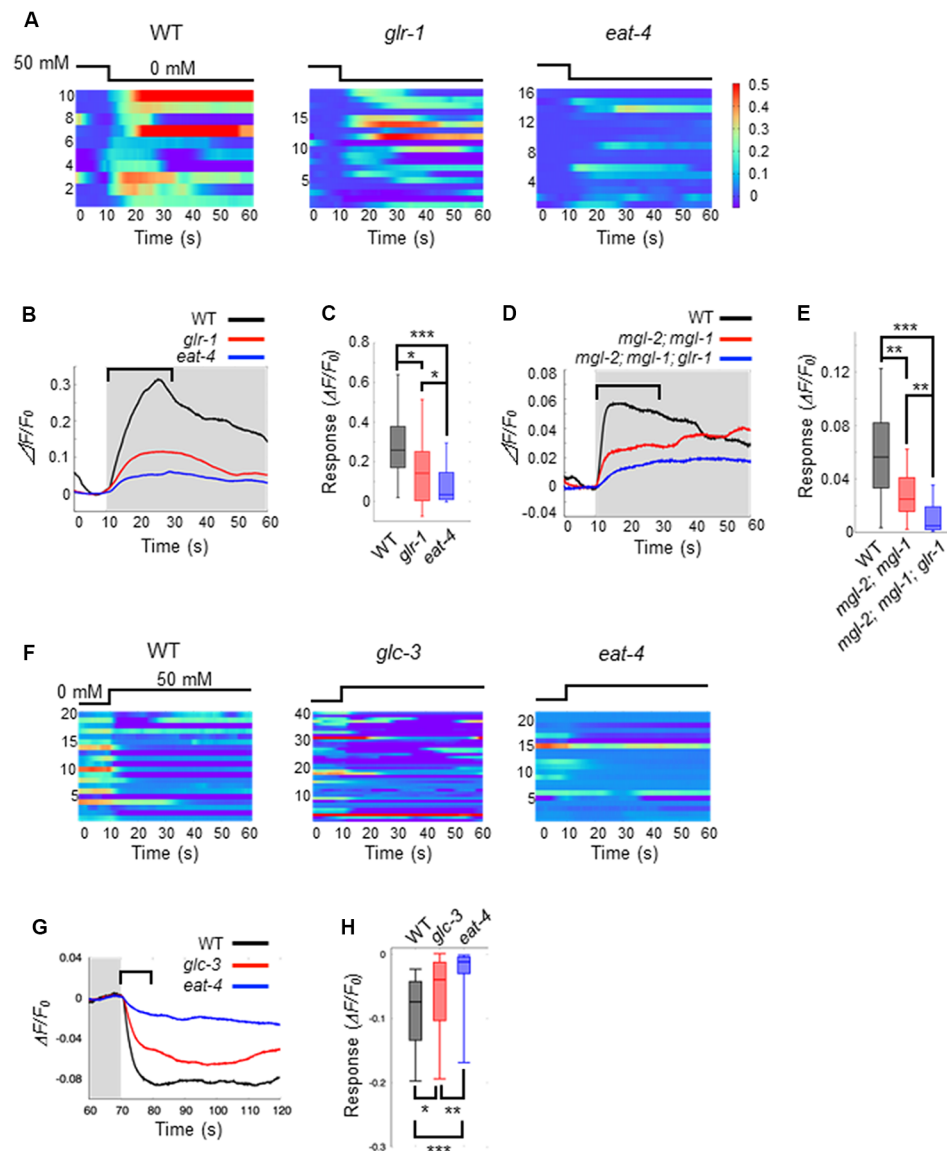


FIGURE 3 | Glutamate released by ASE neurons and its receptors on AIB neurons elicit AIB excitation and inhibition. **(A)** Heatmap traces for AIB responses to a downstep in NaCl concentration in wild-type, *glr-1*(*n2461*) and *eat-4*(*ky5*) mutants. **(B)** Averaged calcium responses to a downstep in NaCl concentration in **(A)**. The shaded area indicates the period of 0 mM NaCl. A 20 s window used for analysis is shown by a blanket. **(C)** Quantitative analysis of the maximum calcium responses during 20 s of a downstep in NaCl concentration in **(A)**. The error bars indicate the SEM; * $p < 0.05$; *** $p < 0.001$; Wilcoxon rank sum test with Bonferroni correction. **(D)** Averaged calcium responses to a downstep in NaCl concentration in wild-type (black), *mgl-2*(*tm355*); *mgl-1*(*tm1811*) double mutants (red) and *mgl-2*; *mgl-1*; *glr-1* triple mutants (blue) expressing GCaMP6 ($n \geq 18$). **(E)** Quantitative analysis of the maximum calcium responses during 20 s of a downstep in NaCl concentration in **(D)**. The error bars indicate the SEM; ** $p < 0.01$, *** $p < 0.001$; Wilcoxon rank sum test with Bonferroni correction. **(F)** Heatmap traces for AIB responses to an upstep in NaCl concentration in wild-type, *glc-3*(*ok321*) and *eat-4*(*ky5*) mutants. **(G)** Averaged calcium responses to an upstep in NaCl concentration in **(F)**. The shaded area indicates the period of 0 mM NaCl. A 10 s window used for analysis is shown by a blanket. **(H)** Quantitative analysis of the minimum calcium responses during the 10 s of an upstep in NaCl concentration (blanket in **G**). The error bars indicate the SEM; * $p < 0.05$, ** $p < 0.01$, *** $p < 0.001$; Wilcoxon rank sum test with Bonferroni correction.

decay in activity than the responses in wild-type animals. However, AIB activity returned to baseline faster in *glc-3*(*ok321*) mutants than *eat-4* mutants (where glutamate in synaptic vesicles is lost; **Figures 3F–H**). This slower inactivation was rescued by the AIB-specific expression of GLC-3, suggesting the cell-autonomous function of GLC-3 in AIB neurons

(**Supplementary Figure S1**). These results suggest that the glutamate-gated chloride ion channel is required for AIB neuronal inactivation in response to an increase in NaCl concentration. The GLC-3 channel does not function for the fast excitation of AIB neurons when NaCl concentration is decreased (**Supplementary Figure S2**).

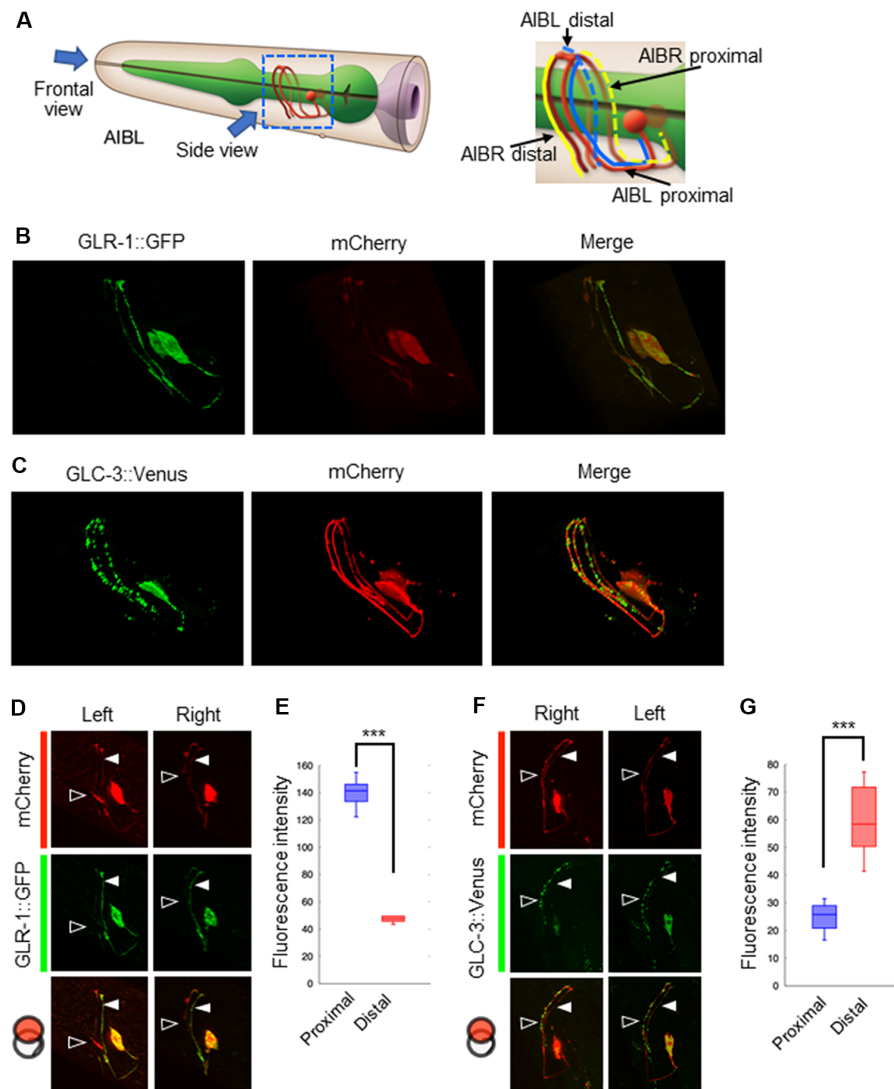


FIGURE 4 | Localization patterns of the AMPA-type glutamate receptor and the glutamate-gated chloride ion channel on AIB neurites. **(A)** Left: schematic cartoon showing the morphology of AIBL neurons, modified from worm atlas (<http://www.wormatlas.org>). Each arrow indicates the direction for frontal-view observation or side-view observation, respectively. Right: blue and yellow lines indicate the AIBL or AIBR neurite respectively. From left-side view, both the proximal AIBL neurite and the distal AIBR neurite can be clearly observed. **(B)** The localization patterns of the AMPA-type glutamate receptor on the AIB neurites. The GFP-fused GLR-1 is expressed specifically in the AIB neurons indicated by the mCherry marker. **(C)** The localization patterns of the glutamate-gated chloride ion channel on the AIB neurites. The Venus-fused GLC-3 is expressed in the AIB neurons indicated by the mCherry marker. **(D)** One-side images for the localization of the GLR-1::GFP fusion protein in AIB neurons. Left images show the localization patterns of the fluorescent proteins in both the AIBL proximal neurite and AIBR distal neurite from each neuronal cell body. Right images show the localization patterns of the fusion proteins in both the AIBR proximal neurite and the AIBL distal neurite from each neuronal cell body. Open and closed arrowheads mark each distal or proximal neurite, respectively. **(E)** The averaged fluorescence intensity of the GLR-1::GFP fusion protein in the proximal or distal region of AIB neurons, respectively. *** $p < 0.001$, Wilcoxon rank sum test ($n = 11$). **(F)** One-side images for the localization patterns of the GLC-3::Venus fusion protein in AIB neurons. Right images show the localization patterns of the fluorescent proteins in both the AIBR proximal neurite and AIBL distal neurite from each neuronal cell body. Left images show the localization patterns of the fusion proteins in both the AIBL proximal neurite and the AIBR distal neurite from each neuronal cell body. Open and closed arrowheads mark each distal or proximal neurite, respectively. **(G)** The averaged fluorescence intensity of GLC-3::Venus fusion protein in the proximal or distal region of AIB neurons. *** $p < 0.001$, Wilcoxon rank sum test ($n = 13$).

The AMPA-Type Glutamate Receptor and the Glutamate-Gated Chloride Channel Are Differentially Localized on the AIB Neurite

Our results suggest that glutamate released by the ASER neuron generates an excitatory response in AIB neurons,

probably *via* AMPA-type and metabotropic G-protein-coupled glutamate receptors. Conversely, glutamate released by the ASEL neuron may cause AIB inhibition *via* the glutamate-gated chloride ion channel. Because both neurons use glutamate as a transmitter, we wondered whether each synaptic site

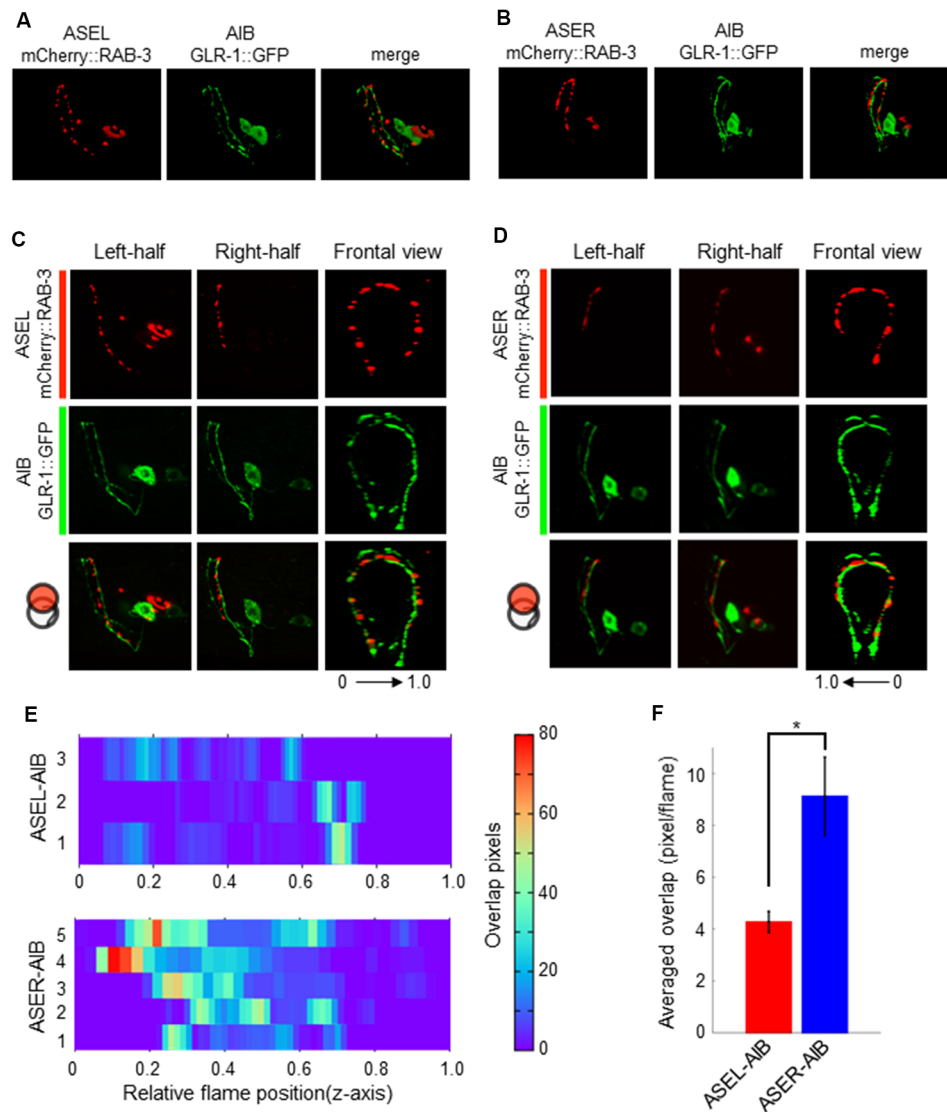


FIGURE 5 | The localization patterns of the presynaptic protein RAB-3 in ASEL/R neurons and the postsynaptic AMPA-type glutamate receptors in AIB neurons. **(A)** The localization patterns of RAB-3 in the ASEL and the AMPA-type glutamate receptor GLR-1 in the AIB. **(B)** The localization patterns of RAB-3 in the ASER and the AMPA-type glutamate receptor GLR-1 in the AIB. **(C)** One-side images from left or right, and frontal images for the localization patterns of mCherry::RAB-3 on ASEL and GLR-1::GFP on the AIB. The left-half images show the co-localization pattern of mCherry::RAB-3 on the proximal ASEL and GLR-1::GFP in both the AIBL proximal neurite and AIBR distal neurite. The right side shows the co-localization pattern of mCherry::RAB-3 on the distal ASEL and GLR-1::GFP in both the AIBR proximal neurite and AIBL distal neurite. 0–1.0 shows the corresponding Z-axis frame position in (E). **(D)** One-side images from left or right, and frontal images for the localization patterns of mCherry::RAB-3 on ASER and GLR-1::GFP on AIB. The left-side images show the co-localization pattern of mCherry::RAB-3 on the distal ASEL and GLR-1::GFP in both the AIBL proximal neurite and AIBR distal neurite. The right side shows the co-localization pattern of mCherry::RAB-3 on the proximal ASER and GLR-1::GFP in both the AIBR proximal neurite and AIBL distal neurite. 0–1.0 shows the corresponding Z-axis frame position in (E). **(E)** Heatmap images of colocalization between mCherry (RAB-3) and GFP (GLR-1). Each colored line represents the overlap between green and red fluorescence in single slice image from Z-stack acquisition of corresponding transgenic worms. Numbers in left indicate individual animals. 0–1.0 is the relative flame position in full Z-stack image. **(F)** Quantification of overlap position in (E). The number of overlapped pixels in each z-axis frame are averaged. The error bars indicate the SEM; * $p < 0.05$; Wilcoxon rank sum test.

(or receptor) is randomly located on the AIB neurites or any positional arrangements exist. To answer this question, we analyzed the localization patterns of both the AMPA-type glutamate receptor GLR-1 and the glutamate-gated chloride ion channels GLC-3 on the postsynaptic AIB neurite. Because the process of each AIB neuron runs around the nerve ring

from ventral to dorsal at the side of cell body and comes back to ventral at opposite side, we divided the neurite into two regions; “proximal region” which is the neurite from the cell body to dorsal midline, and “distal region” from dorsal midline to the tip of neurite (Figure 4A). In the transgenic animals expressing a GLR-1::GFP fusion protein

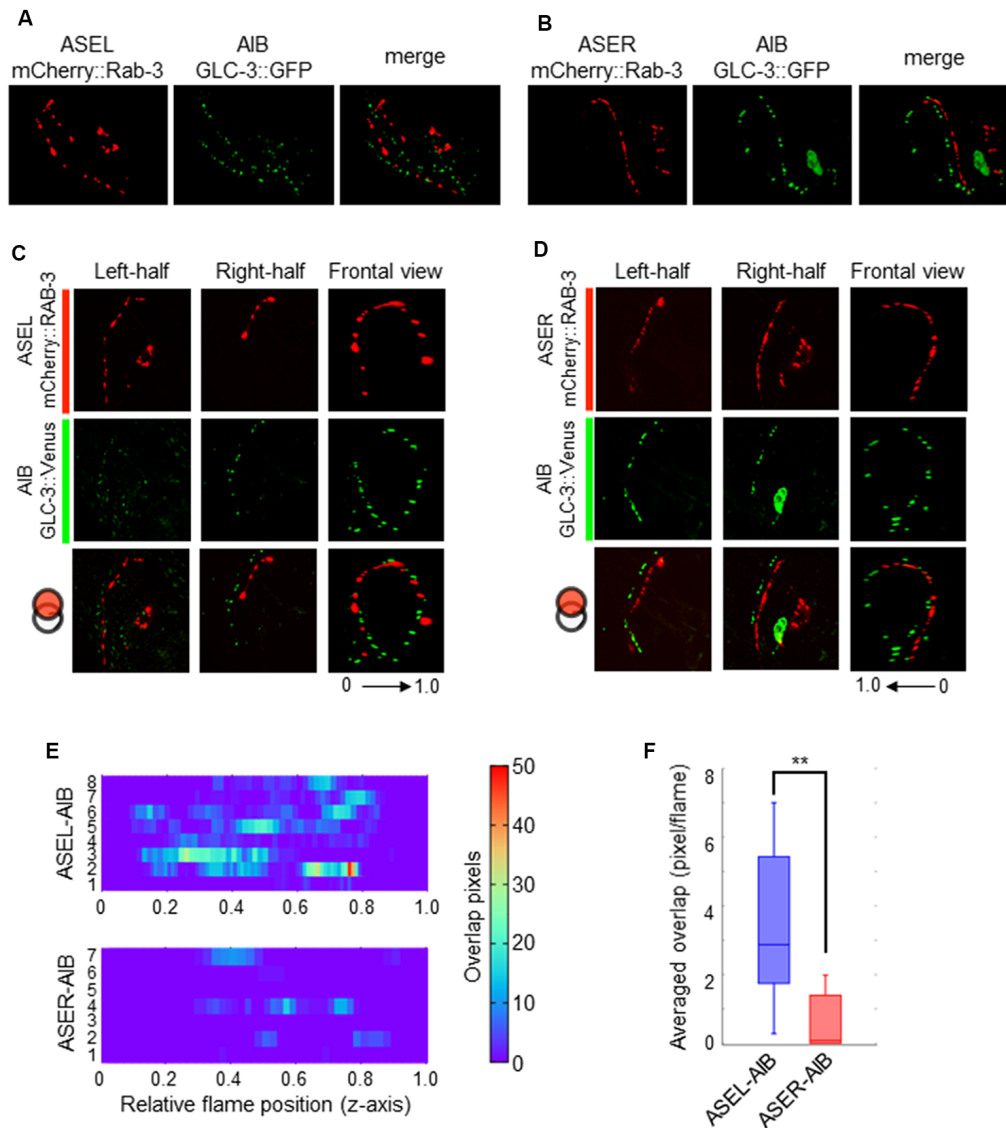


FIGURE 6 | The localization patterns of the presynaptic protein RAB-3 in ASEL/R neurons and the postsynaptic glutamate-gated chloride ion channel in AIB neurons. **(A)** The localization patterns of RAB-3 in the ASEL and the glutamate-gated chloride channel GLC-3 in the AIB. **(B)** The localization patterns of RAB-3 in the ASER and the glutamate-gated chloride channel GLC-3 in the AIB. **(C)** One-side images from left or right, and frontal images for the localization patterns of mCherry::RAB-3 on the ASEL and GLC-3::Venus on the AIB. The left-half images show the co-localization pattern of mCherry::RAB-3 on the proximal ASEL and GLC-3::Venus in both the AIBL proximal neurite and AIBR distal neurite. The right side shows the co-localization pattern of mCherry::RAB-3 on the distal ASEL and GLC-3::Venus in both the AIBL proximal neurite and AIBR distal neurite. **(D)** One-side images from left or right, and frontal images for the localization patterns of mCherry::RAB-3 on the ASER and GLC-3::Venus on the AIB. The left-half images show the co-localization pattern of mCherry::RAB-3 on the distal ASER and GLC-3::Venus in both the AIBL proximal neurite and AIBR distal neurite. The right side shows the co-localization pattern of mCherry::RAB-3 on the proximal ASER and GLC-3::Venus in both the AIBL proximal neurite and AIBR distal neurite. **(E)** Heatmap images of colocalization between mCherry (RAB-3) and GFP (GLR-1). Each colored line represents the overlap between green and red fluorescence in single slice image from Z-stack acquisition of corresponding transgenic worms. Numbers in left indicate individual animals. 0–1.0 is the relative flame position in full Z-stack image. **(F)** Quantification of overlap between RAB-3 on the ASEL or ASER and GLC-3 on the AIBs. The number of overlapped pixels in each frame are averaged. The error bars indicate the SEM; ** $p < 0.01$; Wilcoxon rank sum test.

specifically in the AIB, the GFP signal seemed to be localized uniformly across the neurite due to many small puncta (Figure 4B and see below for further observation). In the transgenic worms expressing a GLC-3::Venus in the AIB, however, the Venus signal was observed as several size of puncta (Figure 4C). Furthermore, we found that the GLR-1

fusion protein predominantly localized to the proximal region of the AIB cell body (Figures 4D,E), whereas the GLC-3 fusion protein was predominantly localized distal to the AIB cell body (Figures 4F,G). Thus, the localization patterns of GLR-1::GFP and GLC-3::Venus were strikingly different on the AIB neurite.

Coordinated Synapse Formation Between ASE-to-AIB May Fine-Tune Postsynaptic Responses to Opposing Excitatory and Inhibitory Signals

Although the AMPA-type glutamate receptor and the glutamate-gated chloride ion channel seem to be localized at distinct regions on the AIB neurite, we could not confirm whether each receptor really localizes at distinct regions on the neurite due to the localization of many fluorescent puncta on the neurite. We also could not confirm whether those localizations really corresponded to their specific functions as inhibitory (with ASEL) or excitatory (with ASER) synapses. To investigate these questions, we first observed the co-localization of a presynaptic vesicle-associated protein, RAB-3, on the ASEL or ASER and the postsynaptic GLR-1 on the AIB (**Figures 5A,B**). The positions of mCherry::RAB-3 on the ASEL and GLR-1::GFP on the AIB neurite were not well-correlated with each other, only a few GFP puncta overlapped with the mCherry signal on the ASEL neurite (**Figures 5C,E,F**). On the other hand, the positions of that on the ASER and that on the AIB neurite closely localized each other (**Figures 5D–F**). Especially, many synapses of the ASER localize to the proximal region of the AIB neurite (**Figure 5E**). The overlap between ASER and AIB was significantly larger than that between ASEL and AIB (**Figure 5F**). These results suggest that the AMPA-type glutamate receptor GLR-1 on the AIB predominantly localize on the proximal neurite to form synapses with the ASER and can receive excitatory glutamate signals from it.

Contrary to the ASER-to-AIB excitatory signal, our calcium imaging data showed that ASEL glutamatergic signaling inhibits AIB activity (**Figure 3**). We thus hypothesized that the ASEL and AIB may form inhibitory synapses, and that both the presynaptic and postsynaptic components of the synapse can closely localize with each other. To prove this, we observed the localization pattern of mCherry::RAB-3 on ASEL and ASER neurites and GLC-3::Venus on AIB neurites. We found that the puncta of mCherry::RAB-3 on the ASEs were mainly facing the proximal region of the AIB neurons whereas the puncta of GLC-3::Venus were localized strongly on the distal region of AIB neurons (**Figures 4G, 6A,B**). These results suggest that the presynaptic sites labeled by mCherry::RAB-3 on ASE neurons and postsynaptic GLC-3 accumulation on AIB neurons are distantly located, compared to the sites of RAB-3 on the ASE neurons and postsynaptic GLR-1 on the AIB (**Figures 5A,B**). So, we found that only a small number of mCherry::RAB-3 puncta on the ASEL was closely aligned with the GLC-3::Venus on the AIB (**Figures 6C,E**). On the other hand, mCherry::RAB-3 on the ASER was distinct from the distribution of GLC-3::Venus on the AIB, few overlap was observed (**Figures 6D,E**). The averaged overlap between ASEL and AIB was significantly larger than those between ASER and AIB (**Figures 6E,F**). These results suggest that a few but clear synapses are formed between the ASEL and AIB, and at those synapses, the glutamate-gated chloride ion channel GLC-3 on the AIB receives inhibitory glutamate signals from the ASEL.

DISCUSSION

In this study, we show that the excitatory/inhibitory switch from asymmetric sensory neurons defines smooth and fine transitions of responses to changes in salt concentration in *C. elegans* postsynaptic neurons. Previous studies have indicated that the ASER neuron stimulates AIBs (Kunitomo et al., 2013), whereas the ASEL neuron inhibits AIBs (Wang et al., 2017), though molecular components in these neuronal regulations has not been revealed. Our results on excitatory/inhibitory signaling patterns are consistent with these previous studies. Based on the expression of EAT-4 vesicular glutamate transporter in these two neurons, it is highly possible that these neurons release glutamate as transmitter. By using several presynaptic and postsynaptic mutants, we confirmed that glutamate from the ASEL neuron is really required to inhibit AIBs *via* a glutamate-gated chloride channel, whereas glutamate from the ASER neuron activates AIBs *via* two types of glutamate receptors. Furthermore, we found a differential distribution of each excitatory or inhibitory receptor on AIB neurites: excitatory synapses are mainly located proximal to the AIB cell body but inhibitory synapses are distal to the AIB cell body. These results suggest that the two glutamatergic signals govern fine, single-cell activity in response to environmental stimuli, and that a unique mechanism for excitatory/inhibitory transformation exists for circuit dynamics in animal behavioral strategy.

For ASER-to-AIB signaling, we show that glutamate and its receptors mediate activation of AIB neurons during a downstep in NaCl concentration. Several glutamate receptors are expressed in AIB neurons. For example, GLR-1 receptors operate as an excitatory receptor during odor-evoked behaviors, and *glr-1* mutants show a lack of AIB excitation by odor stimulation and defective odor-evoked chemotaxis (Chalasani et al., 2007). As such, we suspected that GLR-1 might also function as an excitatory receptor to receive glutamate from the ASER during decreases in NaCl concentration (**Figure 3**). The calcium response in the AIB neurons of *glr-1* mutants was decreased compared to wild-type, but not completely lost as observed in *eat-4* mutant animals. Supporting our results, the salt-chemotaxis behavior of *glr-1* mutants is comparable to that of wild-type animals (Kano et al., 2008). Thus, the contribution of the GLR-1 receptor in AIB excitation is not sufficient for mediating salt-chemotaxis behavior. The AMPA-type glutamate receptor functions in a heteromeric complex with several GLR subunits such as GLR-1/GLR-2 in osmotic avoidance response (Mellem et al., 2002); disrupting the single AMPA-type glutamate receptor subunit might not be effective in abolishing the glutamatergic signal for the salt-chemotaxis. Furthermore, other glutamate-gated cation channels (except for AMPA-type glutamate receptors) may also affect AIB excitation. Consistent with this hypothesis, AIB responses in *mgl-2; mgl-1* double mutants decreased the initial activation of response during the decrease in NaCl concentration, and triple mutants with *glr-1* further decreased its activation (**Figures 3D,E**). Thus, the metabotropic glutamate receptors probably contribute to initial AIB activity in initial phase of

detecting a downstep in NaCl. Further analyses will reveal the exact postsynaptic components for the excitatory synapses in AIBs.

We also showed that activated AIBs are rapidly inactivated when NaCl concentration increases, suggesting the receipt of an inhibitory signal at this point. Four *glc* genes and two *avr* genes in the *C. elegans* genome are associated with glutamate-evoked inactivation of neuronal cells. Mutations in the *avr-14* gene cause a lack or decrease in glutamate-evoked current in AIB neurons (Summers et al., 2015). In this study, we showed that a mutation in *glc-3* causes weaker inhibition of AIBs during increases in NaCl than that of wild-type animals, suggesting that at least GLC-3 is involved in the inhibitory synaptic transmission between ASEL and AIBs. However, *eat-4* mutant animals showed even weaker inhibition of AIBs, therefore, suggesting that several other glutamate-gated chloride ion channels might be expressed on AIBs and function as inhibitory receptors.

Interestingly, we showed that AIB neurons are weakly activated by a downstep in NaCl concentration, even in *eat-4* mutants (Figure 3). This weak activation was not observed in *che-1* mutants that lack ASE sensory activity (Figure 1). On the other hand, a previous study reported that the AIB response to odor stimulation, which is mainly received by AWC sensory neurons and transmitted to AIB neurons, was almost fully lost in *eat-4* mutants (Chalasani et al., 2007). Based on this discrepancy, we hypothesize that not only glutamate but also other signals from ASEs may affect AIB activity. A neuropeptide may be a candidate signaling molecule because ASEs release an insulin-like peptide, and this peptide can activate surrounding neurons expressing DAF-2 receptors (Leinwand and Chalasani, 2013). AIB neurons may also be regulated by this peptidic signaling, either directly or indirectly. Furthermore, non-glutamatergic signaling may also downregulate AIB activity upon increases in NaCl concentration. Compared to a lack of response in *che-1* mutants, slight inactivation was observed in *eat-4* mutants (compare Figures 1C, 3G). The ASEL neuron releases insulin during increases in NaCl concentration, suggesting that the same peptide may be used to inactivate AIB (Leinwand and Chalasani, 2013).

We also examined the relationship between synapse formation on AIBs and its significance for their activities. On the AIB neurons, the proximal neurites receive synaptic inputs from both sensory and upper-layer interneurons, whereas the distal neurites receive synaptic inputs from lower-layer interneurons and motor neurons (White et al., 1986). This clear segregation of sites of synaptic input is likely associated with the fine regulation of neuronal activity. A previous study reported that each type of glutamate receptor shows a different distribution pattern along the AIB neurite (Summers et al., 2015). Consistent with this result, we found that the localization patterns of GLR-1 and those of GLC-3 are strikingly different on the AIB neurite: GLR-1 receptors are localized predominantly at the proximal region, whereas GLC-3 receptors are localized at the distal region. These distinct localization patterns of excitatory and inhibitory receptors in one neurite is likely important for AIB activity and function. Although we have not determined the exact role for excitatory and

inhibitory signaling in AIB tuning, a lack in inhibitory signal from the ASEL neuron abolished the rapid AIB inactivation when NaCl concentration increased. We believe that this rapid inactivation is probably required to sense subtle changes in sensory signals and to control precise chemotaxis behaviors to different salt concentrations. As well as salt-chemotaxis neurons ASE, other sensory neurons such as ASH and AWC form chemical synapses at the proximal region of the AIB neurite (White et al., 1986), and these synapses stimulate AIBs via EAT-4-dependent glutamatergic signaling (Chalasani et al., 2007; Piggott et al., 2011). To understand the meaning of these unbalanced synaptic inputs on a specific postsynaptic target cell, further experiments that monitor developmental stage-specific synapse formation and/or elimination between these sensory neurons and AIB neurons, are required. We believe that these analyses may answer how a sensory-evoked AIB excitation might govern reversal behavior in the worm, whereas feedback from interneurons and motor neurons for AIB inhibition might promote forward movement. We also believe that our study provides a framework for sensorimotor integration system at cellular resolution.

Information processing in the *C. elegans* salt-chemotaxis circuit is similar to the thermotaxis circuit that is composed of the AFD and AWC thermosensory neurons and AIY interneurons. The AFD-glutamatergic signal strongly inhibits AIY activity via GLC-3 receptors. By contrast, the AWC-glutamatergic signal weakly activates AIY via unknown receptors (Ohnishi et al., 2011). In addition, AWC neurons, which can sense both temperature and odor, regulate the activity of two classes of postsynaptic interneurons via glutamatergic signaling. This AWC signal inhibits AIY via GLC-3 inhibitory glutamate receptors, whereas activates AIBs via GLR-1 excitatory glutamate receptors (Chalasani et al., 2007). The same glutamate neurotransmitter from AWC sensory neurons is used to regulate distinct types of postsynaptic glutamate receptors in different classes of interneurons. However, the significance of this neural mechanism by which the same synaptic transmitter from one presynaptic neuron can generate an opposite postsynaptic neuronal-state is still poorly understood (Ohnishi et al., 2011; Wang et al., 2017). Here we provide a similar but more compact neural signaling mechanism, which may be important in regulating opposing behavioral states.

Our data suggest that the activity of individual neurons can be finely tuned by dynamic synaptic inputs by one neurotransmitter, which is transformed into either an excitatory or inhibitory signal via distinct receptors in single postsynaptic cells. This simple but well-organized neural mechanism may be converged to achieve numerous behavioral outcomes using only a limited number of neuronal cells in *C. elegans*. By employing these mechanisms, *C. elegans* can detect complex and dynamic environmental changes by its sensory system, and this paradigm can quickly enable the production of a suitable behavior. The identification of these converged neuronal mechanisms in *C. elegans*, from sensory neurons to first-layer interneurons, provides a novel insight into the more complex information processing in other neural circuits. Further studies

on the ASEs circuits in *C. elegans* are now warranted to improve our understanding of the relationship between sensory inputs and synaptic regulation for fine-tuned responses in postsynaptic neurons, such as AIBs.

AUTHOR CONTRIBUTIONS

MK and MD designed the experiments and wrote the article. MK performed all the experiments and analyzed the data.

FUNDING

Some strains were provided by the CGC which is funded by NIH Office of Research Infrastructure Programs (P40OD010440). This study was supported by Grant-in-Aid for JSPS Research Fellow 16J00633 to MK, and for Scientific Research on Innovative Areas 21115522 from the Ministry of

Education, Culture, Sports, Science and Technology (MEXT) to MD.

ACKNOWLEDGMENTS

We would like to thank Y. Iino, H. Kunitomo and H. Sato for providing the calcium imaging techniques and for sharing plasmid DNAs, T. Ishihara and T. Teramoto, T. Hirotsu, J. Nakai and S. Chalasani for sharing plasmid DNAs. We also thank M. Sato, X. Wang and S. Tsukakoshi for technical assistance and Y. Shinkai and other members in AIST for critical discussion.

SUPPLEMENTARY MATERIAL

The Supplementary Material for this article can be found online at: <https://www.frontiersin.org/articles/10.3389/fnmol.2018.00484/full#supplementary-material>

REFERENCES

- Brooks, R. A. (1986). A Robust layered control system for a mobile robot. *IEEE J. Robotics Autom.* 2, 14–23. doi: 10.1109/jra.1986.1087032
- Chalasani, S. H., Chronis, N., Tsunozaki, M., Gray, J. M., Ramot, D., Goodman, M. B., et al. (2007). Dissecting a circuit for olfactory behaviour in *Caenorhabditis elegans*. *Nature* 450, 63–70. doi: 10.1038/nature06292
- Chang, S., Johnston, R. J. Jr., and Hobert, O. (2003). A transcriptional regulatory cascade that controls left/right asymmetry in chemosensory neurons of *C. elegans*. *Genes Dev.* 17, 2123–2137. doi: 10.1101/gad.1117903
- Chronis, N., Zimmer, M., and Bargmann, C. I. (2007). Microfluidics for *in vivo* imaging of neuronal and behavioral activity in *Caenorhabditis elegans*. *Nat. Methods* 4, 727–731. doi: 10.1038/nmeth1075
- Cully, D. F., Vassilatis, D. K., Liu, K. K., Pareiss, P. S., Van der Ploeg, L. H., Schaeffer, J. M., et al. (1994). Cloning of an avermectin-sensitive glutamate-gated chloride channel from *Caenorhabditis elegans*. *Nature* 371, 707–711. doi: 10.1038/371707a0
- Dillon, J., Hopper, N. A., Holden-Dye, L., and O'Connor, V. (2006). Molecular characterization of the metabotropic glutamate receptor family in *Caenorhabditis elegans*. *Biochem. Soc. Trans.* 34, 942–948. doi: 10.1042/BST0340942
- Hart, A. C., Sims, S., and Kaplan, J. M. (1995). Synaptic code for sensory modalities revealed by *C. elegans* GLR-1 glutamate receptor. *Nature* 378, 82–85. doi: 10.1038/378082a0
- Iino, Y., and Yoshida, K. (2009). Parallel use of two behavioral mechanisms for chemotaxis in *Caenorhabditis elegans*. *J. Neurosci.* 29, 5370–5380. doi: 10.1523/JNEUROSCI.3633-08.2009
- Kano, T., Brockie, P. J., Sassa, T., Fujimoto, H., Kawahara, Y., Iino, Y., et al. (2008). Memory in *Caenorhabditis elegans* is mediated by NMDA-type ionotropic glutamate receptors. *Curr. Biol.* 18, 1010–1015. doi: 10.1016/j.cub.2008.05.051
- Kato, S., Kaplan, H. S., Schrödel, T., Skora, S., Lindsay, T. H., Yemini, E., et al. (2015). Global brain dynamics embed the motor command sequence of *Caenorhabditis elegans*. *Cell* 163, 656–669. doi: 10.1016/j.cell.2015.09.034
- Kunitomo, H., Sato, H., Iwata, R., Satoh, Y., Ohno, H., Yamada, K., et al. (2013). Concentration memory-dependent synaptic plasticity of a taste circuit regulates salt concentration chemotaxis in *Caenorhabditis elegans*. *Nat. Commun.* 4:2210. doi: 10.1038/ncomms3210
- Kuramochi, M., and Doi, M. (2017). A computational model based on multi-regional calcium imaging represents the spatio-temporal dynamics in a *Caenorhabditis elegans* sensory neuron. *PLoS One* 12:e0168415. doi: 10.1371/journal.pone.0168415
- Lee, R. Y., Sawin, E. R., Chalfie, M., Horvitz, H. R., and Avery, L. (1999). EAT-4, a homolog of a mammalian sodium-dependent inorganic phosphate cotransporter, is necessary for glutamatergic neurotransmission in *Caenorhabditis elegans*. *J. Neurosci.* 19, 159–167. doi: 10.1523/jneurosci.19-01-00159.1999
- Leinwand, S. G., and Chalasani, S. H. (2013). Neuropeptide signaling remodels chemosensory circuit composition in *Caenorhabditis elegans*. *Nat. Neurosci.* 16, 1461–1467. doi: 10.1038/nn.3511
- Maricq, A. V., Peckol, E., Driscoll, M., and Bargmann, C. I. (1995). Mechanosensory signalling in *C. elegans* mediated by the GLR-1 glutamate receptor. *Nature* 378, 78–81. doi: 10.1038/378078a0
- Mellem, J. E., Brockie, P. J., Zheng, Y., Madsen, D. M., and Maricq, A. V. (2002). Decoding of polymodal sensory stimuli by postsynaptic glutamate receptors in *C. elegans*. *Neuron* 36, 933–944. doi: 10.1016/s0896-6273(02)01088-7
- Mello, C. C., Kramer, J. M., Stinchcomb, D., and Ambros, V. (1991). Efficient gene transfer in *C. elegans*: extrachromosomal maintenance and integration of transforming sequences. *EMBO J.* 10, 3959–3970. doi: 10.1002/j.1460-2075.1991.tb04966.x
- Molnar, A., Hsueh, H. A., Roska, B., and Werblin, F. S. (2009). Crossover inhibition in the retina: circuitry that compensates for nonlinear rectifying synaptic transmission. *J. Comput. Neurosci.* 27, 569–590. doi: 10.1007/s10827-009-0170-6
- Mori, I., and Ohshima, Y. (1995). Neural regulation of thermotaxis in *Caenorhabditis elegans*. *Nature* 376, 344–348. doi: 10.1038/376344a0
- Nuttley, W. M., Atkinson-Leadbetter, K. P., and Van Der Kooy, D. (2002). Serotonin mediates food-odor associative learning in the nematode *Caenorhabditis elegans*. *Proc. Natl. Acad. Sci. U S A* 99, 12449–12454. doi: 10.1073/pnas.192101699
- Oda, S., Tomioka, M., and Iino, Y. (2011). Neuronal plasticity regulated by the insulin-like signaling pathway underlies salt chemotaxis learning in *Caenorhabditis elegans*. *J. Neurophysiol.* 106, 301–308. doi: 10.1152/jn.01029.2010
- Ohnishi, N., Kuhara, A., Nakamura, F., Okochi, Y., and Mori, I. (2011). Bidirectional regulation of thermotaxis by glutamate transmissions in *Caenorhabditis elegans*. *EMBO J.* 30, 1376–1388. doi: 10.1038/emboj.2011.13
- Pierce-Shimomura, J. T., Morse, T. M., and Lockery, S. R. (1999). The fundamental role of pirouettes in *Caenorhabditis elegans* chemotaxis. *J. Neurosci.* 19, 9557–9569. doi: 10.1523/JNEUROSCI.19-21-09557.1999
- Piggott, B. J., Liu, J., Feng, Z., Wescott, S. A., and Xu, X. Z. (2011). The neural circuits and synaptic mechanisms underlying motor initiation in *C. elegans*. *Cell* 147, 922–933. doi: 10.1016/j.cell.2011.08.053
- Prevedel, R., Yoon, Y. G., Hoffmann, M., Pak, N., Wetzstein, G., Kato, S., et al. (2014). Simultaneous whole-animal 3D imaging of neuronal activity using light-field microscopy. *Nat. Methods* 11, 727–730. doi: 10.1038/nmeth.2964

- Richmond, J. E., Davis, W. S., and Jorgensen, E. M. (1999). UNC-13 is required for synaptic vesicle fusion in *C. elegans*. *Nat. Neurosci.* 2, 959–964. doi: 10.1038/14755
- Schiavo, G., Benfenati, F., Poulain, B., Rossetto, O., Polverino de Laureto, P., DasGupta, B. R., et al. (1992). Tetanus and botulinum-B neurotoxins block neurotransmitter release by proteolytic cleavage of synaptobrevin. *Nature* 359, 832–835. doi: 10.1038/359832a0
- Schiller, P. H., Sandell, J. H., and Maunsell, J. H. (1986). Functions of the ON and OFF channels of the visual system. *Nature* 322, 824–825. doi: 10.1038/322824a0
- Serrano-Saiz, E., Poole, R. J., Felton, T., Zhang, F., De La Cruz, E. D., and Hobert, O. (2013). Modular control of glutamatergic neuronal identity in *C. elegans* by distinct homeodomain proteins. *Cell* 155, 659–673. doi: 10.1016/j.cell.2013.09.052
- Summers, P. J., Layne, R. M., Ortega, A. C., Harris, G. P., Bamber, B. A., and Komuniecki, R. W. (2015). Multiple sensory inputs are extensively integrated to modulate nociception in *C. elegans*. *J. Neurosci.* 35, 10331–10342. doi: 10.1523/JNEUROSCI.0225-15.2015
- Suzuki, H., Thiele, T. R., Faumont, S., Ezcurra, M., Lockery, S. R., and Schafer, W. R. (2008). Functional asymmetry in *Caenorhabditis elegans* taste neurons and its computational role in chemotaxis. *Nature* 454, 114–117. doi: 10.1038/nature06927
- Thiele, T. R., Faumont, S., and Lockery, S. R. (2009). The neural network for chemotaxis to tastants in *Caenorhabditis elegans* is specialized for temporal differentiation. *J. Neurosci.* 29, 11904–11911. doi: 10.1523/JNEUROSCI.0594-09.2009
- Uchida, O., Nakano, H., Koga, M., and Ohshima, Y. (2003). The *C. elegans* che-1 gene encodes a zinc finger transcription factor required for specification of the ASE chemosensory neurons. *Development* 130, 1215–1224. doi: 10.1242/dev.00341
- Wang, L., Sato, H., Satoh, Y., Tomioka, M., Kunitomo, H., and Iino, Y. (2017). A gustatory neural circuit of *Caenorhabditis elegans* generates memory-dependent behaviors in Na⁺ chemotaxis. *J. Neurosci.* 37, 2097–2111. doi: 10.1523/JNEUROSCI.1774-16.2017
- White, J. G., Southgate, E., Thomson, J. N., and Brenner, S. (1986). The structure of the nervous system of the nematode *Caenorhabditis elegans*. *Philos. Trans. R. Soc. Lond. B Biol. Sci.* 314, 1–340. doi: 10.1098/rstb.1986.0056
- Wicks, S. R., and Rankin, C. H. (1995). Integration of mechanosensory stimuli in *Caenorhabditis elegans*. *J. Neurosci.* 15, 2434–2444. doi: 10.1523/jneurosci.15-03-02434.1995
- Yates, D. M., Portillo, V., and Wolstenholme, A. J. (2003). The avermectin receptors of *Haemonchus contortus* and *Caenorhabditis elegans*. *Int. J. Parasitol.* 33, 1183–1193. doi: 10.1016/s0020-7519(03)00172-3
- Zaslaver, A., Liani, I., Shtangel, O., Ginzburg, S., Yee, L., and Sternberg, P. W. (2015). Hierarchical sparse coding in the sensory system of *Caenorhabditis elegans*. *Proc. Natl. Acad. Sci. U S A* 112, 1185–1189. doi: 10.1073/pnas.1423656112
- Zhao, Y., Araki, S., Wu, J., Teramoto, T., Chang, Y. F., Nakano, M., et al. (2011). An expanded palette of genetically encoded Ca²⁺ indicators. *Science* 333, 1888–1891. doi: 10.1126/science.1208592

Conflict of Interest Statement: The authors declare that the research was conducted in the absence of any commercial or financial relationships that could be construed as a potential conflict of interest.

The reviewer KK and handling editor declared their shared affiliation at time of review.

Copyright © 2019 Kuramochi and Doi. This is an open-access article distributed under the terms of the Creative Commons Attribution License (CC BY). The use, distribution or reproduction in other forums is permitted, provided the original author(s) and the copyright owner(s) are credited and that the original publication in this journal is cited, in accordance with accepted academic practice. No use, distribution or reproduction is permitted which does not comply with these terms.



Impaired Cognitive Function and Altered Hippocampal Synaptic Plasticity in Mice Lacking Dermatan Sulfotransferase Chst14/D4st1

Qifa Li^{1†}, Xuefei Wu^{1†}, Xueyan Na¹, Biying Ge², Qiong Wu¹, Xuwen Guo¹, Michael Ntim¹, Yue Zhang¹, Yiping Sun¹, Jinyi Yang³, Zhicheng Xiao^{4*}, Jie Zhao^{2*} and Shao Li^{1*}

OPEN ACCESS

Edited by:

Jaewon Ko,
Daegu Gyeongbuk Institute of
Science and Technology (DGIST),
South Korea

Reviewed by:

Se-Young Choi,
Seoul National University,
South Korea
Sajikumar Sreedharan,
National University of Singapore,
Singapore

*Correspondence:

Zhicheng Xiao
zhicheng.xiao@monash.edu
Jie Zhao
zhaoj@dmu.edu.cn
Shao Li
lishao89@dmu.edu.cn

[†]These authors have contributed
equally to this work

Received: 10 June 2018

Accepted: 21 January 2019

Published: 11 February 2019

Citation:

Li Q, Wu X, Na X, Ge B, Wu Q,
Guo X, Ntim M, Zhang Y, Sun Y,
Yang J, Xiao Z, Zhao J and Li S
(2019) Impaired Cognitive Function
and Altered Hippocampal Synaptic
Plasticity in Mice Lacking Dermatan
Sulfotransferase Chst14/D4st1.
Front. Mol. Neurosci. 12:26.
doi: 10.3389/fnmol.2019.00026

¹Liaoning Provincial Key Laboratory of Cerebral Diseases, Department of Physiology, Dalian Medical University, Dalian, China, ²National-Local Joint Engineering Research Center for Drug-Research and Development (R & D) of Neurodegenerative Diseases, Dalian Medical University, Dalian, China, ³Department of Urology, Dalian Friendship Hospital, Dalian, China, ⁴Department of Anatomy and Developmental Biology, Monash University, Melbourne, VIC, Australia

Chondroitin sulfate (CS) and dermatan sulfate (DS) proteoglycans (PGs) are major extracellular matrix (ECM) components of the central nervous system (CNS). A large body of evidence has shown that CSPGs/DSPGs play critical roles in neuronal growth, axon guidance, and plasticity in the developing and mature CNS. It has been proposed that these PGs exert their function through specific interaction of CS/DS chains with its binding partners in a manner that depends on the sulfation patterns of CS/DS. It has been reported that dermatan 4-O-sulfotransferase-1 (Chst14/D4st1) specific for DS, but not chondroitin 4-O-sulfotransferase-1 (Chst11/C4st1) specific for CS, regulates proliferation and neurogenesis of neural stem cells (NSCs), indicating that CS and DS play distinct roles in the self-renewal and differentiation of NSCs. However, it remains unknown whether specific sulfation profiles of DS has any effect on CNS plasticity. In the present study, Chst14/D4st1-deficient (*Chst14*^{-/-}) mice was employed to investigate the involvement of DS in synaptic plasticity. First, behavior study using Morris Water Maze (MWM) showed that the spatial learning and memory of *Chst14*^{-/-} mice was impaired when compared to their wild type (WT) littermates. Corroborating the behavior result, long-term potentiation (LTP) at the hippocampal CA3-CA1 connection was reduced in *Chst14*^{-/-} mice compared to the WT mice. Finally, the protein levels of N-Methyl-D-aspartate (NMDA) receptor, α -amino-3-hydroxy-5-methyl-4-isoxazolepropionic acid (AMPA) receptor, postsynaptic density 95 (PSD95), growth associated protein 43 (GAP-43), synaptophysin (SYN) and N-ethylmaleimide sensitive factor (NSF) which are important in synaptic plasticity were examined and Chst14/D4st1 deficiency was shown to significantly reduce the expression of these proteins in the hippocampus. Further studies revealed that Akt/mammalian target rapamycin (mTOR) pathway proteins, including protein kinase B (p-Akt), p-mTOR and p-S6, were significantly lower in *Chst14*^{-/-} mice, which might contribute to the decreased protein expression.

Together, this study reveals that specific sulfation of DS is critical in synaptic plasticity of the hippocampus and learning and memory, which might be associated with the changes in the expression of glutamate receptors and other synaptic proteins through Akt/mTOR pathway.

Keywords: dermatan sulfate, *Chst14/D4st1*, synaptic plasticity, learning and memory, LTP

INTRODUCTION

Proteoglycans (PGs) are important components of the extracellular matrix (ECM) formed by covalent attachments of glycosaminoglycans (GAGs) to serine residues of core proteins (Bian et al., 2011). GAGs are linear polysaccharides consisting of repeated disaccharide units which can be sulfated at different positions to create a vast structural microheterogeneity of chains with different function, for instance, dermatan sulfate (DS), chondroitin sulfate (CS) and heparan sulfate (HS). PGs are known to contribute to normal embryonic and postnatal development and tissue homeostasis by ensuring tissue stability and signaling functions, such as cell migration, proliferation and survival. GAGs can be classified into two types, one is galactosaminoglycans with CS and DS, the other one is glucosaminoglycans represented by HS (Dündar et al., 2009; Krichen et al., 2017; Ramachandra et al., 2017; Soares da Costa et al., 2017).

CSPG/DSPG are major ECM components of the central nervous system (CNS) and have the potential to interact with a wide range of growth factors and neurotrophic factors that influence neuronal migration, axon guidance, neurite outgrowth and synaptic plasticity (Miller and Hsieh-Wilson, 2015; Miyata and Kitagawa, 2015). It has been proposed that CSPG/DSPG exert their function through specific interaction of CS/DS chains with its binding partners in a manner that depends on the sulfation patterns of CS/DS, e.g., the participation of CS/DS in neurosphere formation (Von Holst et al., 2006). Chondroitinase ABC (ChaseABC), which unselectively degrades CS and DS and has been used in a lot of studies to investigate the function of CS/DS. Thus, it is difficult to discern the function of DS and CS which might actually be different. Treatment of neural stem cells (NSCs) from the embryonic mouse telencephalon with ChaseABC resulted in diminished proliferation and impaired neuronal differentiation of NSCs (Sirko et al., 2007). However, dermatan 4-O-sulfotransferase-1 (*Chst14/D4st1*) that is specific for DS, but not chondroitin 4-O-sulfotransferase-1 (*Chst11/C4st1*) specific for CS, regulates proliferation and neurogenesis of NSCs (Bian et al., 2011). This indicates that CS and DS play distinct roles in the self-renewal and differentiation of NSCs. It is still unclear whether specific sulfation profiles of DS has any effect on CNS plasticity.

In terms of the structure, DS is a copolymer which consists of alternating disaccharide units of l-iduronic acid (IdoUA) and N-acetyl-d-galactosamine (GalNAc) with 50–200 repeats (Mizumoto et al., 2017). DS chains can be sulfated at the hydroxy groups of C-2 on IdoUA and the C-4 positions of GalNAc residues by various sulfotransferases. There are

three major sulfotransferases which take part in this process and have different substrate specificities (Mitsunaga et al., 2006). *C4st1* preferably sulfates a GalNAc flanked by two GlcA residues while *Chst14/D4st1* prefers two flanking IdoA residues. *C4st2* can equally sulfate both substrates (Pacheco et al., 2009). Among the three sulfotransferases, *Chst14/D4st1* is a key and specific enzyme that cannot be replaced by other sulfotransferases in the process of synthesizing DSs (Bian et al., 2011). *Chst14/D4st1*-deficient (*Chst14*^{-/-}) mice are useful for studying the functions of specific sulfation profile of DS.

In the current study, we investigated the role of DS sulfation in synaptic plasticity as well as learning and memory using *Chst14*^{-/-} mice. Our data showed that *Chst14/D4st1* deficiency resulted in impaired spatial learning and memory as well as long-term potentiation (LTP). We also found that the protein levels of α -amino-3-hydroxy-5-methyl-4-isoxazolepropionic acid (AMPA) receptor subunit GluA1, N-Methyl-D-Aspartate (NMDA) receptor subunit NR2B, postsynaptic density protein 95 (PSD95), growth-associated protein 43 (GAP-43), synaptophysin (SYN) and N-ethylmaleimide sensitive factor (NSF) protein kinase B (p-Akt) and p-S6 were decreased in *Chst14*^{-/-} mice. Our results suggest that specific sulfation profile of DS is indispensable for synaptic plasticity that might be associated with downregulation of synaptic proteins through Akt/mammalian target rapamycin (mTOR) signaling pathway.

MATERIALS AND METHODS

Animals

Mice (C57BL/6J) were kept in the conventional housing unit under standard conditions (five per cage, 24°C, 45%–65% humidity, 12 h light/dark cycle), with free accessing to food and water. This study was carried out in accordance with the recommendations of National Institute of Health Guide for the Care and Use of Laboratory Animals (NIH Publications No. 80-23) revised 1996. All experimental protocols were approved by the Institutional Ethics Committee of the Dalian Medical University, and all efforts were made to minimize the number of animals used and their suffering.

Morris Water Maze

The protocol used was described by Morris (1984). The Morris Water Maze (MWM) apparatus consisted of a tank which is 120 cm in diameter, 60 cm in height and was divided into four quadrants. The tank was filled with water (temperature, 25 ± 1°C) until the platform (10 cm in diameter) was submerged 1 cm below the water. Four visual cues were placed on the walls of the tank (in each quadrant) as spatial references for mice to determine their navigation path. Above the center of the pool,

a camera was used to detect the position of the animals and Ethosvision software was used to record the real time data. Before the experiment, the animals (3–4 months old) were placed in the pool without any platform for 30 s to let the animals get familiar with the environment. In the hidden platform acquisition test, animals were trained four trials per day for five consecutive days. The starting positions were done in the quadrants and alternated on each trial. The duration of a trial was 90 s, after which mouse was manually guided to the platform and allowed to stay on it for 10 s if it could not find it. Otherwise, it was allowed to remain on the platform for 10 s before the next trial. One day after the last trial, we removed the platform and performed the probe test. The escape latency and path length were measured, and the numbers of platform-site crossovers were recorded. The results are expressed as mean \pm standard error of the mean (SEM).

Electrophysiological Recordings

Hippocampi were dissected from the brain of 3–4 months old mice and acute 300 μ m thick slices were prepared using a vibratome (LEICA VT1200S) in cold artificial cerebrospinal fluid (ACSF, 4°C) bubbled with 95% O₂ and 5% CO₂ containing: 110 mM NaCl, 2.5 mM KCl, 1.5 mM MgSO₄·2H₂O, 2.5 mM CaCl₂, 1.25 mM NaH₂PO₄, 26 mM NaHCO₃ and 10 mM D-glucose (pH 7.3). Prior to stimulation, hippocampal slices were maintained at room temperature in ACSF for at least 1 h before being removed to a submersion-recording chamber and was continually perfused with oxygenated ACSF at the rate of 1–2 mL per minute. Test stimuli were delivered at 0.033 Hz (0.2 ms duration) through concentric bipolar electrodes, placed in the CA1 area of the hippocampal slice to stimulate Schaffer Collateral (SC) pathway. Field excitatory postsynaptic potentials (fEPSPs) were recorded from the stratum radiatum of CA1 using glass microelectrodes filled with 3 M NaCl solution (resistance 2–5 M Ω). After baseline was recorded for 30 min at an intensity that was set to 40%–50% of the maximal response, LTP was induced using high frequency stimulation (four 100 Hz and 1 s trains delivered 20 s apart).

The data were acquired with an Axon multiclamp 700 B amplifier, filtered at 0.1e5 KHz, and digitized at 10 KHz, and analyzed offline by pClamp10.3 software (Molecular Devices Corp, USA).

Input-output (I/O) curves were established by single-pulse stimulation of the SCs region in order to evaluate synaptic efficacy by adjusting the stimulus intensity between by steps 0.05–1.0 mA. Stimulus pulses were delivered at 0.033 Hz and five responses at each current intensity were averaged.

Presynaptic function was explored by using paired-pulse facilitation (PPF) paradigm with inters-stimulus intervals (ISIs) ranging from 25, 50, 75, 100, 125, 150 and 200 ms. Facilitation was measured as a ratio of the second pulse-evoked EPSP slope to the first evoked, averaged over five responses per pulse pair.

Western Blot

Hippocampi were homogenized in RIPA buffer with 1% cocktail. The lysates were centrifuged at 12,000 rpm for 30 min at 4°C and the supernatants were collected. Proteins were separated

by 10% SDS-PAGE gel and transferred onto PVDF membranes (Millipore, Billerica, MA, USA). Then the membranes were blocked in 5% nonfat dried milk for 1 h at room temperature and incubated overnight at 4°C with primary antibodies: GluA1 (1:1,000, Abcam, ab31232), NR1 (1:500, BD Pharmingen, 556308), NR2A (1:500, Millipore, MAB5216), NR2B (1:1,000, Abcam, ab93610), PSD95 (1:1,000, Abcam, ab2723), GAP-43 (1:1,000, Millipore, AB5220), NSF (1:500, Cell Signaling Technology, 2145S), SYN (1:1,000, Millipore, MAB5258-I), p-S6 (1:1,000, Cell Signaling Technology, 4858), p-Akt (1:1,000, Cell Signaling Technology, 4060), p-mTOR (1:1,000, Cell Signaling Technology, 5536), actin (1:2,000, Abcam, ab6276). After being washed three times with TBST, the membranes were incubated with the HRP-conjugated secondary antibodies for 1 h at room temperature, and then detected by enhanced chemiluminescence (ECL, Bioutil). Protein bands were quantified and analyzed with ImageJ. For some proteins including GluA1, NR1, GAP-43, PSD95 and β -actin, immunoblots were performed on the different parts of PVDF membrane from the same gel, thus their bands were normalized to the same β -actin bands, although the protein levels were expressed separately in results, which is the case of NR1, GluA1, PSD95 and GAP-43 in **Figure 3**.

Statistical Analyses

All statistical analyses were performed using SPSS18.0. Data are presented as the mean \pm SEM. Data between multiple groups were analyzed by one- or two-way analysis of variance followed by Fischer protected least significant difference *post hoc* tests. Unpaired *t*-test was used to analyze differences between two groups. *p* Value < 0.05 was considered as the significance level for all analyses (**p* < 0.05, ***p* < 0.01).

RESULTS

Chst14^{-/-} Mice Show Deficits in Spatial Learning and Memory

As DS plays an important role in self-renewal and differentiation of NSCs, we investigated whether DS has any effect on learning and memory using the MWM test. In the test, mice were trained for 5 days with a hidden platform. During each trial, the escape latency was measured as an index of the spatial learning ability. During the first 2 days, we found no significant differences between the two groups. However, *Chst14*^{-/-} mice showed much higher escape latencies during 3–5 days of training trial compared to wild type (WT) mice (**Figure 1A**). To eliminate the influence of swimming speed, we normalized the escape latencies in the first trial of each group to 1.0. The relative escape latencies in the subsequent trial days were then quantified to that in the first trial (**Figure 1B**). This could enable us to compare the spatial learning ability of each group taking into consideration their differences in swimming speed. As shown in **Figure 1B**, compared with WT mice, *Chst14*^{-/-} mice failed to show a learning trend indicated by the shortening escape latencies as days of training passed. Consistently, the swimming length of *Chst14*^{-/-} mice was

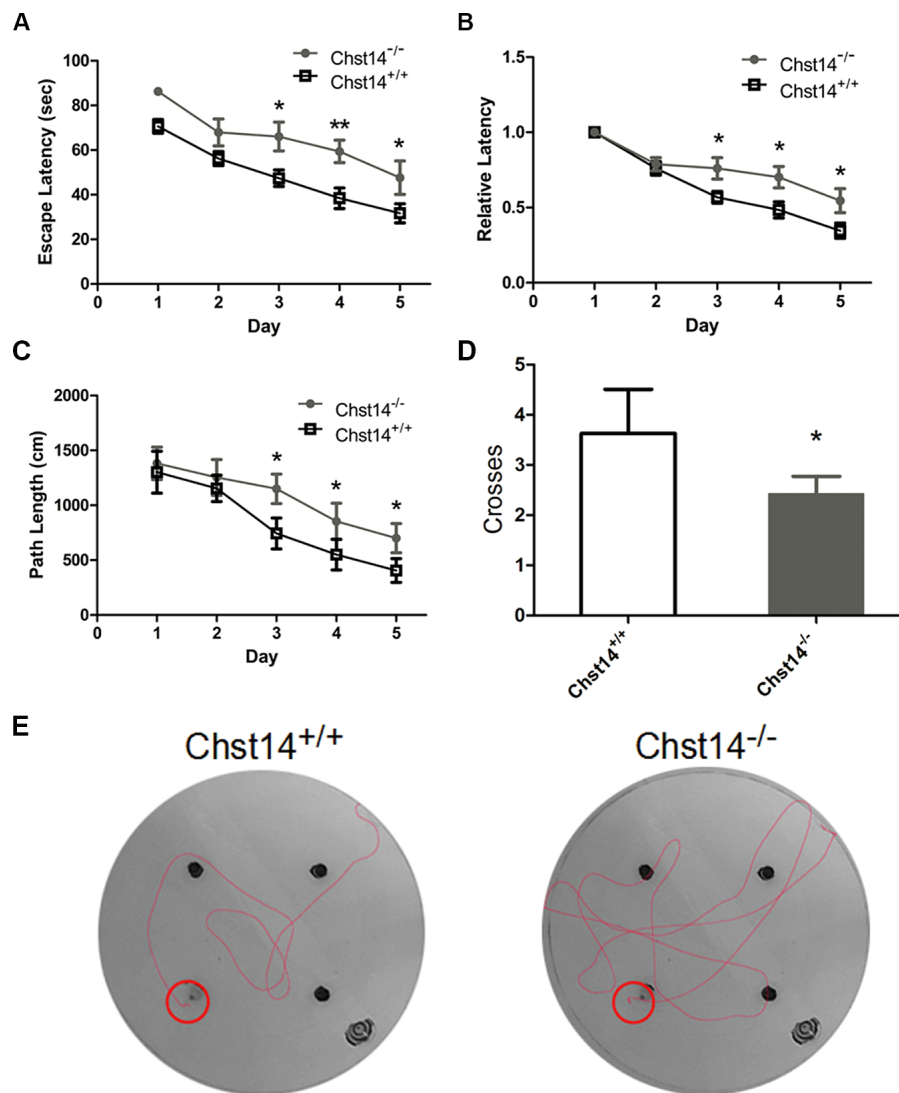


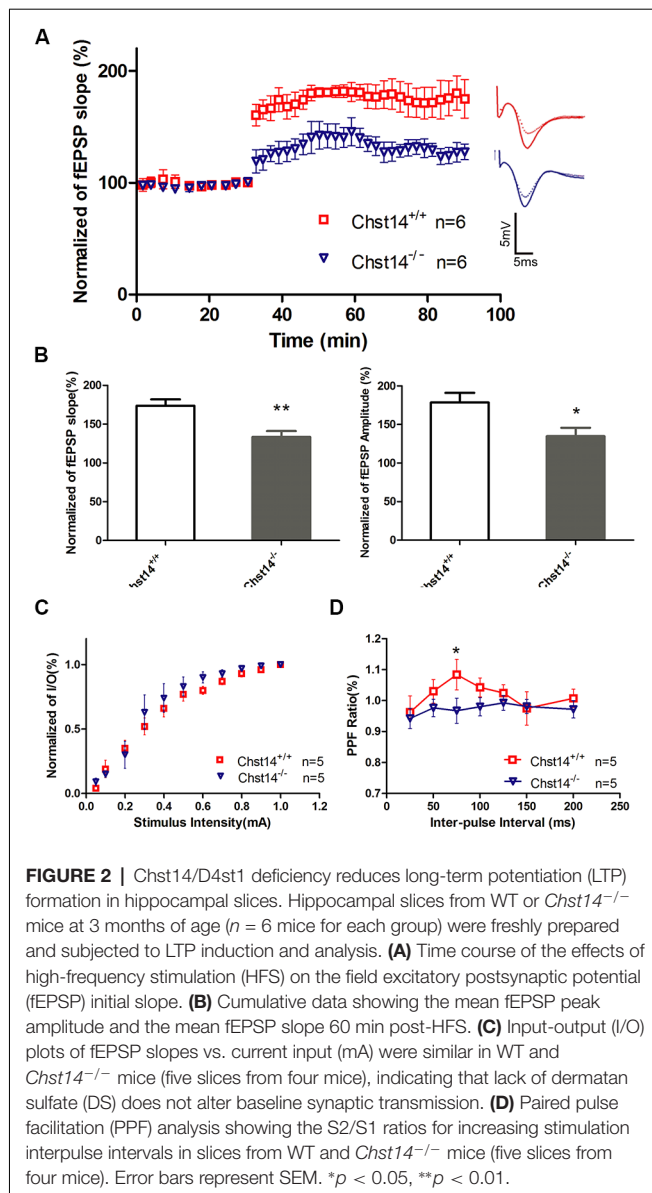
FIGURE 1 | *Chst14*/D4st1 deficiency leads to impaired spatial learning and memory. Morris Water Maze (MWM) tests were performed on wild type (WT; $n = 16$) or *Chst14*^{-/-} mice ($n = 12$) and animal behaviors were recorded and analyzed. **(A)** The escape latencies in each group of the mice were analyzed. **(B)** The escape latencies of each group of mice on the first day were normalized to 1.0. The relative escape latencies in the subsequent days to that of the first day were calculated. **(C)** The average distances that the mice spent to find the platform. **(D)** The times that each group of mice swam across the target sites after retrieval of the platform. **(E)** Representative images of the path that the mice swam along to find the platform. Data are presented as mean \pm standard error of the mean (SEM) in each group. * $p < 0.05$, ** $p < 0.01$.

increased compared with WT mice (**Figure 1C**). In the probe test, the number of platform crossing were measured to evaluate spatial memory ability. *Chst14*^{-/-} mice showed a significantly decreased number of platform crossing (**Figure 1D**). These results demonstrate that *Chst14* deletion results in impaired learning and memory.

***Chst14*^{-/-} Mice Manifest Impaired LTP**

It is well known that the hippocampus plays important roles in long-term memory (Luo et al., 2011). Synaptic loss and synaptic abnormalities are strongly correlated with cognitive impairment. LTP is a very important form of synaptic plasticity

and is the most extensively studied cellular model for learning and memory (Petrovic et al., 2017). To investigate whether the behavioral deficits in *Chst14*^{-/-} mice were associated with altered hippocampal synaptic plasticity, LTP was induced by high-frequency stimulation (HFS; four 100 Hz and 1 s trains were delivered 20 s apart) at SC-CA1 synapses in hippocampal slices of 3-month-old *Chst14*^{-/-} and WT mice (Zhao et al., 2015). **Figure 2A** shows the changes in fEPSPs slope before and after HFS in different mice. As shown in the **Figure 2B**, LTP was significantly attenuated in *Chst14*^{-/-} mice, as indicated by the decreased fEPSP slope ($173.75\% \pm 8.12\%$ vs. $133.41\% \pm 7.66\%$) and amplitude ($178.50\% \pm 12.56\%$ vs.



134.76% \pm 11.029%) compared with WT mice. There was no difference between WT and *Chst14*^{-/-} mice on baseline responses in a control pathway (Supplementary Figure S1). This is consistent with the observation in learning and memory in *Chst14*^{-/-} mice. These data confirm that *Chst14* plays an important role in synaptic plasticity. To examine whether the properties of basic synaptic transmission at SC-CA1 synapses is altered in *Chst14*^{-/-} mice, input-output curves were obtained by measuring the post-synaptic potential slope with varying stimulus intensities (0.05–1.0 mA). Data were normalized using 100% as the highest amplitude (average of five selected sweeps in each stimulation intensity) of the fEPSP. *Chst14*^{-/-} mice showed no significant change in the input-output curve compared to WT littermates (Figure 2C). This indicates that DS does not affect the basal synaptic response. PPF was obtained after the I/O curve measurements to determine the probability of synaptic

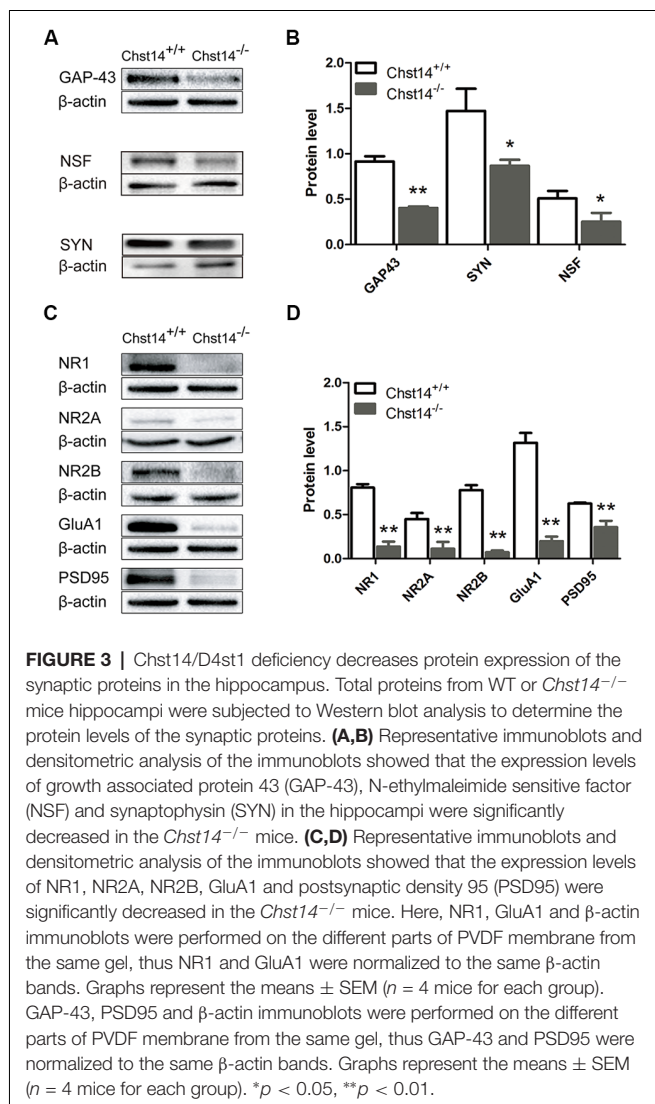
vesicle release, and this was measured by paired pulses at intervals between 25 and 200 ms. As shown in Figure 2D, the basal PPF at a 75-ms inter-stimulus interval was significantly decreased in *Chst14*^{-/-} mice compared WT littermates. This finding suggests that DS may interfere with probability of synaptic vesicle release from the pre-synaptic terminals.

The Synaptic Proteins Are Decreased in *Chst14*^{-/-} Mice

It is known that both presynaptic and postsynaptic mechanisms are involved in LTP (Nicoll and Malenka, 1995). As synaptic proteins are critical for synaptic transmission, it is of interest to see whether *Chst14/D4st1* deficiency has any effect on expressions of proteins that are involved in synaptic plasticity.

GAP-43 is neuron-specific and found in high concentrations in growth cones. It plays an important role in the process of learning and memory (Li et al., 2016; Moghimi et al., 2016). As a marker of synaptic activity, SYN is the main membrane protein of presynaptic vesicles involved in vesicle formation and exocytosis (Valtorta et al., 2004). Meanwhile, the function of NSF is essential for a highly dynamic response before synaptic vesicles fuse with presynaptic plasma membranes to release neurotransmitters (Kuner et al., 2008). The results show that GAP-43, NSF and SYN were decreased in the hippocampus of *Chst14*^{-/-} mice (Figures 3A,B), supporting dysfunction of presynaptic membrane.

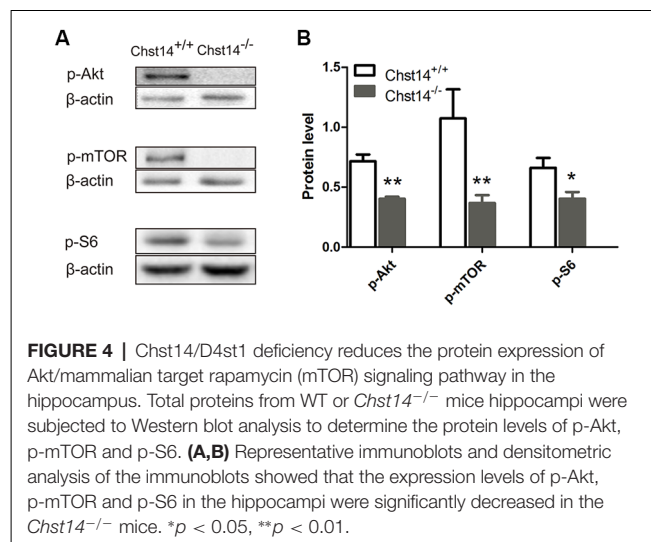
For postsynaptic proteins, we first examined NMDA and AMPA receptors that play major roles in hippocampus-dependent learning and memory as well as LTP (Cull-Candy et al., 2001; Tu and Kuo, 2015). NMDA receptors are heterotetramer formed by two glycine-binding NR1 subunits and two glutamate-binding NR2 subunits (NR2A, NR2B, NR2C and NR2D). NR2A or NR2B combined with NR1 are the major forms of NMDA receptors and play important roles in synaptic plasticity in the adult brain (Sachser et al., 2017). Accordingly, we determined the protein expression of NMDA subunits NR1, NR2A and NR2B in the hippocampus of WT and *Chst14*^{-/-} mice. The results show that the protein expression levels of NR1, NR2A and NR2B (Figure 3) were decreased in the hippocampus of *Chst14*^{-/-} mice compared with WT mice. AMPA receptors are heterotetramers composed of various subunits (GluA1–4) usually permeable to Na⁺ and K⁺ (Sachser et al., 2017). They are widely expressed in the brain with different functions. During the induction of LTP, the recruitment of GluA1-containing AMPA receptors to the post-synaptic membrane is a critical step (Panja and Bramham, 2014). Hence, we also measured the protein expression levels of GluA1 from the hippocampus of WT and *Chst14*^{-/-} mice (Figures 3C,D). It was significantly decreased in the hippocampus of *Chst14*^{-/-} mice compared with WT mice. PSD95 plays a key role to determine the PSD size and synaptic strength in neuronal development, experience-dependent plasticity, like LTP and LTD (Holahan et al., 2007). In this study, it was shown that the protein expression level of PSD95 was decreased significantly in the hippocampus of *Chst14*^{-/-} mice compared with WT mice (Figures 3C,D). These results suggested that DS may affect



synaptic transmission through regulating the expression of postsynaptic proteins in the hippocampus.

The Protein Levels of the Akt/mTOR Signaling Pathway Are Decreased in *Chst14*^{-/-} Mice

The above results have shown significant down-regulation of both presynaptic and postsynaptic proteins, we then tried to explore the signaling pathways of DS affecting protein expression. In previous reports, the Akt/mTOR pathway plays an important role in protein synthesis (Chen et al., 2016). Ribosomal protein S6 is essential for protein translation and is acutely phosphorylated by S6K, an established downstream target of mTOR (Sawicka et al., 2016). Our results showed that p-Akt, p-mTOR and p-S6 were decreased in the *Chst14*^{-/-} mice (Figure 4), suggesting that Akt/mTOR pathway may contribute to decreased protein synthesis in *Chst14*^{-/-} mice. There was no difference between trained and untrained animals (Supplementary Figure S2).



DISCUSSION

As DS-specific sulfotransferase *Chst14* regulates proliferation and neurogenesis of NSCs (Bian et al., 2011), it is rational to see whether *Chst14* plays a role in the adult CNS function such as synaptic plasticity. In the present study, we investigated the changes of spatial learning/memory and LTP as well as expression of several proteins that are associated with synaptic plasticity in *Chst14*^{-/-} mice.

In order to study whether *Chst14/D4st1* deficiency affects learning and memory, MWM test was used in the present study to evaluate spatial learning and memory ability in mice through the training trial and probe trial. When animals have problems in finding the platform in the water maze, it indicates their inability to remember the spatial information which was supposed to have been acquired during the training days, reflecting deficits in hippocampal-dependent spatial cognition (Kim et al., 2016). In our study, it was shown that the spatial learning and memory was impaired in *Chst14*^{-/-} mice (Figure 1). Synaptic plasticity is considered the basis of learning and memory (Gu et al., 2016). As a physiological pattern of synaptic plasticity, LTP is correlated with hippocampal-dependent memory (Yang et al., 2017). Here, LTP from SCs to hippocampal CA1 region was measured after MWM test. Our results indicated that LTP induction was dampened in *Chst14*^{-/-} mice (Figures 2A,B), which probably could explain their performance in the behavioral test. In order to assess the differences that potentially exist in baseline synaptic responsiveness, the I/O function was measured in this study. However, we noted there was no difference in synaptic transmission at baseline between WT and *Chst14*^{-/-} mice (Figure 2C). PPF is a phenomenon of short-term plasticity whereby a second synaptic response is enhanced by a preceding stimulation of similar intensity. This phenomenon determines the probability of vesicle release and is usually increased due to increased calcium entry into presynaptic terminals (Shang et al., 2016). In our data, we report of decrease in PPF function in *Chst14*^{-/-} mice which may indicate that the probability

of presynaptic glutamate release was decreased in *Chst14*^{-/-} mice.

As changes in synaptic proteins or receptors associated with learning and memory may be the structural basis for the defect in synaptic functions, we examined the levels of these proteins in presynaptic and postsynaptic membranes, respectively. GAP-43, a nervous system-specific protein enriched at presynaptic nerve terminals, is thought to be involved in axonal outgrowth and plasticity in synaptic connections (Kristjansson et al., 1982). It can be phosphorylated by protein kinase C (PKC; De Graan et al., 1990) and its phosphorylation level is directly related to LTP and learning and memory (Gianotti et al., 1992; Young et al., 2000). In GAP-43 heterozygous knockdown mice, hippocampal-dependent memory is reported to be impaired (Rekart et al., 2005). Overexpression of GAP-43 has been shown to increase LTP in dentate gyrus and improve learning in an 8-arm radial maze (Routtenberg et al., 2000). Involvement of GAP-43 in learning and memory has been proposed in two ways. First, GAP-43 is located in the presynaptic terminal and can directly interact with components that regulate the release of neurotransmitters including soluble NSF attachment protein (SNARE) complex proteins to modulate presynaptic neurotransmitter release (Haruta et al., 1997). Second, PKC in presynaptic terminal can be activated by a NMDA-dependent postsynaptic retrograde signal. The phosphorylated GAP-43 then interacts with calcium-sensing proteins of the EPM (exocytotic protein machine) to enhance the release of neurotransmitters when intraterminal calcium is raised sufficiently (Routtenberg et al., 2000). NSF plays a key role in eukaryotic trafficking and is essential for maintaining pools of fusion-ready individual SNARE proteins that mediate membrane fusion in a variety of cellular processes, including neurotransmitter release, protein transport, and hormone secretion (Zhao and Brunger, 2016). As one of the most abundant synaptic vesicle proteins, SYN can interact with synaptobrevin which is a key SNARE protein and is involved in neurotransmitter release (Egbujo et al., 2016). Hence, the decrease in protein expression levels of GAP-43, NSF and SYN in *Chst14*^{-/-} mice (Figures 3A,B) might result in weakened release of presynaptic neurotransmitters followed by affected learning and memory.

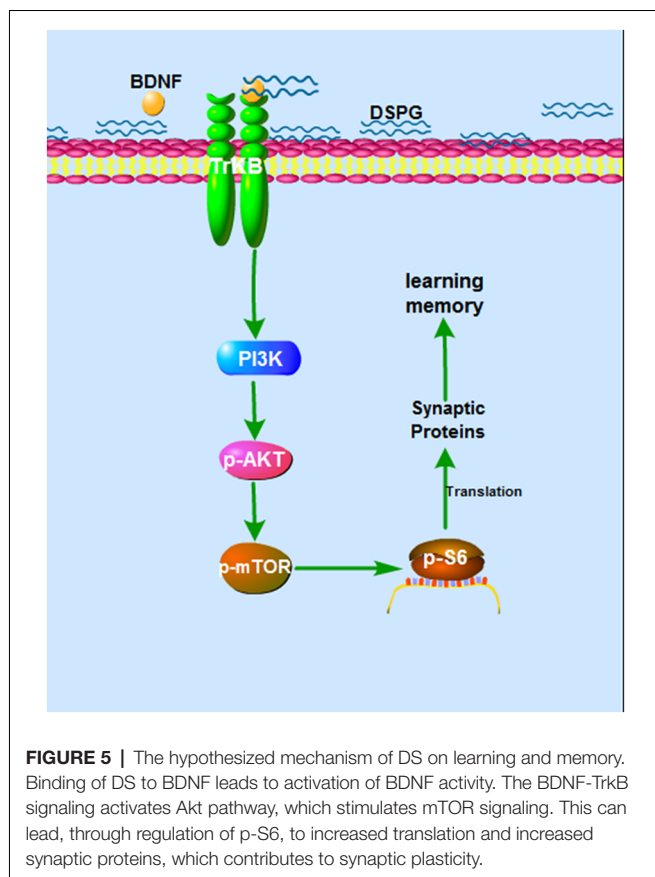
Glutamate receptors are the most important receptors for excitatory amino acids in CNS. They have been shown to be crucial for the formation of synapses, synaptic plasticity as well as learning and memory (Yan et al., 2014). NMDA and AMPA receptors, two important ionotropic glutamate receptors, have been proven to participate in regulating many important functions in the CNS such as LTP and the development of neural plasticity (Cull-Candy et al., 2001; Tu and Kuo, 2015). Extensive research effort including gene knockout, agonists and antagonists have been used in identifying the roles of NMDA/AMPA receptors in LTP. For instance, the NMDA receptor antagonist (2R)-amino-5-phosphonovaleric acid (APV) has been reported to block LTP induction (Bourne et al., 2013). NR2B-overexpressing mice show increased LTP (Cui et al., 2011). In adult GluA1^{-/-} mice, the induction of LTP failed (Zamanillo et al., 1999). During the initial phase

of LTPGluA2-lacking AMPA receptors increase at CA1 SC synapses through an insertion from the intracellular pools (Rozov et al., 2012). Thus, alterations in the expression of hippocampal NMDA and AMPA receptors have been proposed to impact synaptic plasticity and learning and memory. Our results showed that *Chst14* deficiency led to a strong reduction in the hippocampal expression of the NMDA subunit NR1, NR2A, NR2B and the AMPA subunit GluA1 (Figures 3C,D).

In addition to these receptors in the post-synaptic membrane, we also checked the expression of PSD95. PSD95 is highly enriched in the PSD and is the most widely studied in synaptic plasticity among the four PSD-MAGUKs (PSD95-like membrane associated guanylate kinases) family members (Chen et al., 2005). It interacts with the subunits of NMDA/AMPA receptors to affect the stability of these receptors and their participation in synaptic plasticity. During early development of the brain, NR2B-to NR2A-subunit switch can be found in most regions and can promote synaptic maturation (Dumas, 2005). In this process, PSD95/NR2A complexes do replace synapse-associated protein 102 (SAP102)/NR2B complexes indicating PSD95 is a developmental regulator of NMDA receptor (Coley and Gao, 2018). In the hippocampus of PSD95^{-/-} mice, the protein level of GluA1 is significantly decreased (Béique et al., 2006), prompting that the downregulation of PSD95 affects synaptic function. Furthermore, overexpressing PSD95 in hippocampal neurons causes an increase of AMPA receptor and dendritic spine density (El-Husseini et al., 2000). In *Chst14*^{-/-} mice, downregulation of PSD95 may attenuate the regulation of PSD95 on NMDA/AMPA receptors, affecting receptor function and synapse development.

Together, our study suggests that specific sulfation profile of DS promotes the synaptic plasticity in the hippocampus and enhances spatial learning and memory. Both presynaptic and postsynaptic changes in protein expression might contribute to the synaptic defect caused by *Chst14*/D4st1 deficiency. Since *Chst14* deficiency does not affect the volume and thickness of the motor cortex, the volume of CA1/dentate gyrus regions of hippocampus and the density of neurons and astrocytes in these brain regions (Bian et al., 2011), the reduction of synaptic proteins observed here is probably due to regulation on protein expression by DSPG, but not the consequence of reduced number of mature neurons.

Previous reports have shown that PGs can participate in learning and memory in different ways. Biglycan, a neurotrophic brain-derived CS proteoglycan, was found to facilitate learning when injected into the posterior part of the ventral pallidum (De Souza Silva et al., 2002). Meanwhile CSPG is known to act as major inhibitors of the structural and functional plasticity of neural circuits which might be due to interaction of CS with some growth factors and neurotrophic factors (Miyata and Kitagawa, 2015; Mizumoto et al., 2015; Ohtake et al., 2016). Both Crtl1-deficient mice and chondroitinase ABC-treated WT mice show an enhanced long-term object recognition memory in the perirhinal cortex (Romberg et al.,



2013). Compared with CS, DS involves a variety of biological processes due to the existence of IdoUA whose pyranose ring tends to form various conformations, causing interaction with various partners to perform different functions (Nandini et al., 2005). DSPGs can regulate biological processes at or near the cell surface through binding several growth factors, cytokines, chemokines, and adhesion molecules. As the co-receptors of various growth factors, DSPGs are involved in migration and intracellular signal transduction by linking the external environment with intracellular signal transduction (Malmström et al., 2012). For instance, the interaction between DS chain and fibroblast growth factor (FGF)-7 can promote the binding of FGF-7 to a FGF receptor and the cell proliferation (Hashiguchi et al., 2010). Similarly, HS PGs have been suggested to modulate the activities of heparin-binding growth factors (Villena and Brandan, 2004). Previous study also showed that the binding affinity of BDNF to DS was higher than HS (Nandini et al., 2005), suggesting that DS may affect downstream signaling pathway of BDNF after binding to it.

As a member of the neurotrophin family, BDNF is found to be involved in various biological processes in the CNS ranging from neurogenesis to synaptic plasticity and cognition (Guo et al., 2018; Sonal and Raghavan, 2018). The maintenance of hippocampal LTP requires synthesis of new proteins. Local protein synthesis maintains an appropriate level of synaptic strength in cortical and hippocampal neurons,

which is related to homeostatic synaptic plasticity (Miller et al., 2014). Binding with its TrkB tyrosine kinase receptor, BDNF stimulates the activation of many signaling pathways, including PI3K/Akt signaling pathway, to promote protein translation. Akt activates mammalian target rapamycin (mTOR), which induces the phosphorylation of p70 ribosomal S6 kinase (p70S6K). Then activated p70S6K induces phosphorylation of small ribosomal protein 6 (S6) whose phosphorylation state correlates with translational rates. mTOR, p70S6K and S6 regulated by Akt pathways are crucial in the regulation of protein translation initiation (García-Gutiérrez et al., 2013). Phosphorylation of S6 leads to increased translation of mRNA such as CaMKII α , NR1, GluR1, PSD95, synapsin I, all of which have been demonstrated to play core roles in synaptic plasticity (Aakalu et al., 2001; Schratt et al., 2004, 2006).

In the current study, we examined the protein levels of BDNF-PI3K/Akt-mTOR pathway, showing that p-Akt, p-mTOR and p-S6 were all decreased in the *Chst14*^{-/-} mice (Figure 4), which may contribute to at least partially to downregulation of synaptic proteins caused by *Chst14*/D4st1 deficiency. However, this hypothesis (Figure 5) need to be verified by further investigation, for instance, examining whether activation of this pathway can ameliorate the defect in synaptic function and protein expression of *Chst14*^{-/-} mice.

CONCLUSION

In summary, our findings suggest that specific DS sulfation is critical for synaptic plasticity and learning and memory in the hippocampus, which might be associated with regulation on presynaptic and postsynaptic protein expression by DSPG.

AUTHOR CONTRIBUTIONS

SL, ZX and JZ contributed to the conception and design of the project. QL, QW, BG, XN, YS and XG contributed to the experiments. QL, YZ and XW analyzed and interpreted the data. QL, XW, MN, JY and SL wrote and revised the manuscript.

FUNDING

This work was supported by grants from The National Sciences Foundation of China (81571061, 81671061), Natural Science Foundation of Liaoning province of China (2015020672, 201602218) and Scientific Study Project for Institutes of Higher Learning, Ministry of Education, Liaoning Province (LZ2017001, LZ2016002).

SUPPLEMENTARY MATERIAL

The Supplementary Material for this article can be found online at: <https://www.frontiersin.org/articles/10.3389/fnmol.2019.00026/full#supplementary-material>

REFERENCES

- Aakalu, G., Smith, W. B., Nguyen, N., Jiang, C., and Schuman, E. M. (2001). Dynamic visualization of local protein synthesis in hippocampal neurons. *Neuron* 30, 489–502. doi: 10.1016/S0896-6273(01)00295-1
- Béique, J. C., Lin, D. T., Kang, M. G., Aizawa, H., Takamiya, K., and Huganir, R. L. (2006). Synapse-specific regulation of AMPA receptor function by PSD-95. *Proc. Natl. Acad. Sci. U S A* 103, 19535–19540. doi: 10.1073/pnas.0608492103
- Bian, S., Akyüz, N., Bernreuther, C., Loers, G., Laczynska, E., Jakovcevski, L., et al. (2011). Dermatan sulfotransferase *Chst14/D4st1*, but not chondroitin sulfotransferase *Chst11/C4st1*, regulates proliferation and neurogenesis of neural progenitor cells. *J. Cell Sci.* 124, 4051–4063.
- Bourne, J. N., Chirillo, M. A., and Harris, K. M. (2013). Presynaptic ultrastructural plasticity along CA3→CA1 axons during long-term potentiation in mature hippocampus. *J. Comp. Neurol.* 521, 3898–3912. doi: 10.1002/cne.23384
- Chen, C. H., Sung, C. S., Huang, S. Y., Feng, C. W., Hung, H. C., Yang, S. N., et al. (2016). The role of the PI3K/Akt/mTOR pathway in glial scar formation following spinal cord injury. *Exp. Neurol.* 278, 27–41. doi: 10.1016/j.expneurol.2016.01.023
- Chen, X., Vinade, L., Leapman, R. D., Petersen, J. D., Nakagawa, T., Phillips, T. M., et al. (2005). Mass of the postsynaptic density and enumeration of three key molecules. *Proc. Natl. Acad. Sci. U S A* 102, 11551–11556. doi: 10.1073/pnas.0505359102
- Coley, A. A., and Gao, W. J. (2018). PSD95: A synaptic protein implicated in schizophrenia or autism? *Prog. Neuropsychopharmacol. Biol. Psychiatry* 82, 187–194. doi: 10.1016/j.pnpbp.2017.11.016
- Cui, Y., Jin, J., Zhang, X., Xu, H., Yang, L., Du, D., et al. (2011). Forebrain NR2B overexpression facilitating the prefrontal cortex long-term potentiation and enhancing working memory function in mice. *PLoS One* 6:e20312. doi: 10.1371/journal.pone.0020312
- Cull-Candy, S., Brickley, S., and Farrant, M. (2001). NMDA receptor subunits: diversity, development and disease. *Curr. Opin. Neurobiol.* 11, 327–335. doi: 10.1016/S0959-4388(00)00215-4
- De Graan, P. N., Oestreicher, A. B., De Wit, M., Kroef, M., Schrama, L. H., and Gispen, W. H. (1990). Evidence for the binding of calmodulin to endogenous B-50 (GAP-43) in native synaptosomal plasma membranes. *J. Neurochem.* 55, 2139–2141. doi: 10.1111/j.1471-4159.1990.tb05808.x
- De Souza Silva, M. A., Jezek, K., Weth, K., Müller, H. W., Huston, J. P., Brandao, M. L., et al. (2002). Facilitation of learning and modulation of frontal cortex acetylcholine by ventral pallidal injection of heparin glucosaminoglycan. *Neuroscience* 113, 529–535. doi: 10.1016/S0306-4522(02)00184-7
- Dumas, T. C. (2005). Developmental regulation of cognitive abilities: modified composition of a molecular switch turns on associative learning. *Prog. Neurobiol.* 76, 189–211. doi: 10.1016/j.pneurobio.2005.08.002
- Dündar, M., Müller, T., Zhang, Q., Pan, J., Steinmann, B., Vodopitzi, J., et al. (2009). Loss of dermatan-4-sulfotransferase 1 function results in adducted thumb-clubfoot syndrome. *Am. J. Hum. Genet.* 85, 873–882. doi: 10.1016/j.ajhg.2009.11.010
- Egbujo, C. N., Sinclair, D., and Hahn, C. G. (2016). Dysregulations of synaptic vesicle trafficking in schizophrenia. *Curr. Psychiatry Rep.* 18:77. doi: 10.1007/s11920-016-0710-5
- El-Husseini, A. E., Schnell, E., Chetkovich, D. M., Nicoll, R. A., and Bredt, D. S. (2000). PSD-95 involvement in maturation of excitatory synapses. *Science* 290, 1364–1368. doi: 10.1126/science.290.5495.1364
- García-Gutiérrez, M. S., Ortega-Álvarez, A., Busquets-García, A., Pérez-Ortiz, J. M., Caltanum, L., Ricatti, M. J., et al. (2013). Synaptic plasticity alterations associated with memory impairment induced by deletion of CB2 cannabinoid receptors. *Neuropharmacology* 73, 388–396. doi: 10.1016/j.neuropharm.2013.05.034
- Gianotti, C., Nunzi, M. G., Gispen, W. H., and Corradetti, R. (1992). Phosphorylation of the presynaptic protein B-50 (GAP-43) is increased during electrically induced long-term potentiation. *Neuron* 8, 843–848. doi: 10.1016/0896-6273(92)90198-m
- Gu, X. H., Xu, L. J., Liu, Z. Q., Wei, B., Yang, Y. J., Xu, G. G., et al. (2016). The flavonoid baicalein rescues synaptic plasticity and memory deficits in a mouse model of Alzheimer's disease. *Behav. Brain Res.* 311, 309–321. doi: 10.3389/fneur.2016.00141
- Guo, W., Nagappan, G., and Lu, B. (2018). Differential effects of transient and sustained activation of BDNF-TrkB signaling. *Dev. Neurobiol.* 78, 647–659. doi: 10.1002/dneu.22592
- Haruta, T., Takami, N., Ohmura, M., Misumi, Y., and Ikehara, Y. (1997). Ca²⁺-dependent interaction of the growth-associated protein GAP-43 with the synaptic core complex. *Biochem. J.* 325, 455–463.
- Hashiguchi, T., Mizumoto, S., Yamada, S., and Sugahara, K. (2010). Analysis of the structure and neuritogenic activity of chondroitin sulfate/dermatan sulfate hybrid chains from porcine fetal membranes. *Glycoconj. J.* 27, 49–60. doi: 10.1007/s10719-009-9253-x
- Holahan, M. R., Honegger, K. S., Tabatadze, N., and Routtenberg, A. (2007). GAP-43 gene expression regulates information storage. *Learn. Mem.* 14, 407–415. doi: 10.1101/lm.581907
- Kim, S., Kim, T., Lee, H. R., Jang, E. H., Ryu, H. H., Kang, M., et al. (2016). Impaired learning and memory in CD38 null mutant mice. *Mol. Brain* 9:16. doi: 10.1186/s13041-016-0195-5
- Krichen, F., Volpi, N., Sila, A., Maccari, F., Mantovani, V., Galeotti, F., et al. (2017). Purification, structural characterization and antiproliferative properties of chondroitin sulfate/dermatan sulfate from tunisian fish skins. *Int. J. Biol. Macromol.* 95, 32–39. doi: 10.1016/j.ijbiomac.2016.10.108
- Kristjansson, G. I., Zwiers, H., Oestreicher, A. B., and Gispen, W. H. (1982). Evidence that the synaptic phosphoprotein B-50 is localized exclusively in nerve tissue. *J. Neurochem.* 39, 371–378. doi: 10.1111/j.1471-4159.1982.tb03958.x
- Kuner, T., Li, Y., Gee, K. R., Bonewald, L. F., and Augustine, G. J. (2008). Photolysis of a caged peptide reveals rapid action of N-ethylmaleimide sensitive factor before neurotransmitter release. *Proc. Natl. Acad. Sci. U S A* 105, 347–352. doi: 10.1073/pnas.0707197105
- Li, D., Huang, Y., Cheng, B., Su, J., Zhou, W. X., and Zhang, Y. X. (2016). Streptozotocin induces mild cognitive impairment at appropriatedoses in mice as determined by long-term potentiation and the morris water maze. *J. Alzheimers Dis.* 54, 89–98. doi: 10.3233/JAD-150979
- Luo, Y. Y., Zhu, D. M., and Ruan, D. Y. (2011). Galantamine rescues lead-impaired synaptic plasticity in rat dentate gyrus. *Toxicology* 289, 45–51. doi: 10.1016/j.tox.2011.07.007
- Malmström, A., Bartolini, B., Thelin, M. A., Pacheco, B., and Maccarana, M. (2012). Iduronic acid in chondroitin/dermatan sulfate: biosynthesis and biological function. *J. Histochem. Cytochem.* 60, 916–925. doi: 10.1369/0022155412459857
- Morris, R. (1984). Developments of a water-maze procedure for studying spatial learning in the rat. *J. Neurosci. Methods* 11, 47–60. doi: 10.1016/0165-0270(84)90007-4
- Miller, O. H., Yang, L., Wang, C. C., Hargroder, E. A., Zhang, Y., Delpire, E., et al. (2014). GluN2B-containing NMDA receptors regulate depression-like behavior and are critical for the rapid antidepressant actions of ketamine. *Elife* 3:e03581. doi: 10.7554/eLife.03581
- Miller, G. M., and Hsieh-Wilson, L. C. (2015). Sugar-dependent modulation of neuronal development, regeneration, and plasticity by chondroitin sulfate proteoglycans. *Exp. Neurol.* 274, 115–125. doi: 10.1016/j.expneurol.2015.08.015
- Mitsunaga, C., Mikami, T., Mizumoto, S., Fukuda, J., and Sugahara, K. (2006). Chondroitin sulfate/dermatan sulfate hybrid chains in the development of cerebellum spatiotemporal regulation of the expression of critical disulfated disaccharides by specific sulfotransferases. *J. Biol. Chem.* 281, 18942–18952. doi: 10.1074/jbc.M510870200
- Miyata, S., and Kitagawa, H. (2015). Mechanisms for modulation of neural plasticity and axon regeneration by chondroitin sulphate. *J. Biochem.* 157, 13–22. doi: 10.1093/jb/mvu067
- Mizumoto, S., Koshio, T., Hatamochi, A., Honda, T., Yamaguchi, T., Okamoto, N., et al. (2017). Defect in dermatan sulfate in urine of patients with Ehlers-Danlos syndrome caused by a CHST14/D4ST1 deficiency. *Clin. Biochem.* 50, 670–677. doi: 10.1016/j.clinbiochem.2017.02.018
- Mizumoto, S., Yamada, S., and Sugahara, K. (2015). Molecular interactions between chondroitin-dermatan sulfate and growth factors/receptors/matrix proteins. *Curr. Opin. Struct. Biol.* 34, 35–42. doi: 10.1016/j.sbi.2015.06.004
- Moghimi, M., Parvardeh, S., Zanjani, T. M., and Ghafghazi, S. (2016). Protective effect of α -terpineol against impairment of hippocampal synaptic plasticity and spatial memory following transient cerebral ischemia in rats. *Iran. J. Basic Med. Sci.* 19, 960–969.

- Nandini, C. D., Itoh, N., and Sugahara, K. (2005). Novel 70-kDa chondroitin sulfate/dermatan sulfate hybrid chains with a unique heterogeneous sulfation pattern from shark skin, which exhibit neurotogenic activity and binding activities for growth factors and neurotrophic factors. *J. Biol. Chem.* 280, 4058–4069. doi: 10.1074/jbc.m412074200
- Nicoll, R. A., and Malenka, R. C. (1995). Contrasting properties of two forms of long-term potentiation in the hippocampus. *Nature* 377, 115–118. doi: 10.1038/377115a0
- Ohtake, Y., Wong, D., Abdul-Muneer, P. M., Selzer, M. E., and Li, S. X. (2016). Two PTP receptors mediate CSPG inhibition by convergent and divergent signaling pathways in neurons. *Sci. Rep.* 6:37152. doi: 10.1038/srep37152
- Pacheco, B., Maccarana, M., and Malmström, A. (2009). Dermatan 4-O-sulfotransferase 1 is pivotal in the formation of iduronic acid blocks in dermatan sulfate. *Glycobiology* 19, 1197–1203. doi: 10.1093/glycob/cwp110
- Panja, D., and Bramham, C. R. (2014). BDNF mechanisms in late LTP formation: A synthesis and breakdown. *Neuropharmacology* 76, 664–676. doi: 10.1016/j.neuropharm.2013.06.024
- Petrovic, M. M., Viana da Silva, S., Clement, J. P., Vyklicky, L., Mulle, C., González-González, I. M., et al. (2017). Metabotropic action of postsynaptic kainate receptors triggers hippocampal long-term potentiation. *Nat. Neurosci.* 20, 529–539. doi: 10.1038/nn.4505
- Ramachandra, R., Namburi, R. B., Dupont, S. T., Ortega-Martinez, O., van Kuppevelt, T. H., Lindahl, U., et al. (2017). A potential role for chondroitin sulfate/dermatan sulfate in arm regeneration in *Amphibia* *filiformis*. *Glycobiology* 27, 438–449. doi: 10.1093/glycob/cwx010
- Rekart, J. L., Meiri, K., and Routtenberg, A. (2005). Hippocampal-dependent memory is impaired in heterozygous GAP-43 knockout mice. *Hippocampus* 15, 1–7. doi: 10.1002/hipo.20045
- Romberg, C., Yang, S., Melani, R., Andrews, M. R., Horner, A. E., Spillantini, M. G., et al. (2013). Depletion of perineuronal nets enhances recognition memory and long-term depression in the perirhinal cortex. *J. Neurosci.* 33, 7057–7065. doi: 10.1523/JNEUROSCI.6267-11.2013
- Routtenberg, A., Cantalopos, I., Zaffuto, S., Serrano, P., and Namgung, U. (2000). Enhanced learning after genetic overexpression of a brain growth protein. *Proc. Natl. Acad. Sci. U S A* 97, 7657–7662. doi: 10.1073/pnas.97.13.7657
- Rozov, A., Zivkovic, A. R., and Schwarz, M. K. (2012). Homer1 gene products orchestrate Ca²⁺-permeable AMPA receptor distribution and LTP expression. *Front. Synaptic Neurosci.* 4:4. doi: 10.3389/fnsyn.2012.00004
- Sachser, R. M., Haubrich, J., Lunardi, P. S., and de Oliveira Alves, L. (2017). Forgetting of what was once learned: Exploring the role of postsynaptic ionotropic glutamate receptors on memory formation, maintenance, and decay. *Neuropharmacology* 112, 94–103. doi: 10.1016/j.neuropharm.2016.07.015
- Sawicka, K., Pyronneau, A., Chao, M., Bennett, M. V., and Zukin, R. S. (2016). Elevated ERK/p90 ribosomal S6 kinase activity underlies audiogenic seizure susceptibility in fragile X mice. *Proc. Natl. Acad. Sci. U S A* 113, E6290–E6297. doi: 10.1073/pnas.1610812113
- Schratt, G. M., Nigh, E. A., Chen, W. G., Hu, L., and Greenberg, M. E. (2004). BDNF regulates the translation of a select group of mRNAs by a mammalian target of rapamycin-phosphatidylinositol 3-kinase-dependent pathway during neuronal development. *J. Neurosci.* 24, 7366–7377. doi: 10.1523/JNEUROSCI.1739-04.2004
- Schratt, G. M., Tuebing, F., Nigh, E. A., Kane, C. G., Sabatini, M. E., Kiebler, M., et al. (2006). A brain-specific microRNA regulates dendritic spine development. *Nature* 439, 283–289. doi: 10.1038/nature04367
- Shang, Y., Wang, X., Shang, X., Zhang, H., Liu, Z., Yin, T., et al. (2016). Repetitive transcranial magnetic stimulation effectively facilitates spatial cognition and synaptic plasticity associated with increasing the levels of BDNF and synaptic proteins in Wistar rats. *Neurobiol. Learn. Mem.* 134, 369–378. doi: 10.1016/j.nlm.2016.08.016
- Sirko, S., von Holst, A., Wizenmann, A., Götz, M., and Faissner, A. (2007). Chondroitin sulfate glycosaminoglycans control proliferation, radial glia cell differentiation and neurogenesis in neural stem/progenitor cells. *Development* 134, 2727–2738. doi: 10.1242/dev.02871
- Soares da Costa, D., Reis, R. L., and Pashkuleva, I. (2017). Sulfation of Glycosaminoglycans and Its Implications in Human Health and Disorders. *Annu. Rev. Biomed. Eng.* 19, 1–26. doi: 10.1146/annurev-bioeng-071516-044610
- Sonal, A., and Raghavan, V. (2018). Brain derived neurotrophic factor (BDNF) and suicidal behavior: A review of studies from Asian countries. *Asian J. Psychiatr.* 33, 128–132. doi: 10.1016/j.ajp.2018.03.004
- Tu, Y. C., and Kuo, C. C. (2015). The differential contribution of GluN1 and GluN2 to the gating operation of the NMDA receptor channel. *Pflugers Arch.* 467, 1899–1917. doi: 10.1007/s00424-014-1630-z
- Valtorta, F., Pennuto, M., Bonanomi, D., and Benfenati, F. (2004). Synaptophysin: leading actor or walk-on role in synaptic vesicle exocytosis? *Bioessays* 26, 445–453. doi: 10.1002/bies.20012
- Villena, J., and Brandan, E. (2004). Dermatan sulfate exerts an enhanced growth factor response on skeletal muscle satellite cell proliferation and migration. *J. Cell Physiol.* 198, 169–178. doi: 10.1002/jcp.10422
- Von Holst, A., Sirko, S., and Faissner, A. (2006). The unique 473HD-Chondroitinsulfate epitope is expressed by radial glia and involved in neural precursor cell proliferation. *J. Neurosci.* 26, 4082–4094. doi: 10.1523/jneurosci.0422-06.2006
- Yan, Y. G., Zhang, J., Xu, S. J., Luo, J. H., Qiu, S., and Wang, W. (2014). Clustering of surface NMDA receptors is mainly mediated by the C-terminus of GluN2A in cultured rat hippocampal neurons. *Neurosci. Bull.* 30, 655–666. doi: 10.1007/s12264-014-1450-8
- Yang, J., Yao, Y., Wang, L., Yang, C., Wang, F., Guo, J., et al. (2017). Gastrin-releasing peptide facilitates glutamatergic transmission in the hippocampus and effectively prevents vascular dementia induced cognitive and synaptic plasticity deficits. *Exp. Neurol.* 287, 75–83. doi: 10.1007/s12264-014-1450-8
- Young, E. A., Owen, E. H., Meiri, K. F., and Wehner, J. M. (2000). Alterations in hippocampal GAP-43 phosphorylation and protein level following contextual fear conditioning. *Brain Res.* 860, 95–103. doi: 10.1016/S0006-8993(00)02021-7
- Zamanillo, D., Sprengel, R., Hvalby, O., Jensen, V., Burnashev, N., Rozov, A., et al. (1999). Importance of AMPA receptors for hippocampal synaptic plasticity but not for spatial learning. *Science* 284, 1805–1811. doi: 10.1126/science.284.5421.1805
- Zhao, M. L., and Brunger, A. T. (2016). Recent advances in deciphering the structure and molecular mechanism of the AAA plus ATPase N-ethylmaleimide-sensitive factor (NSF). *J. Mol. Biol.* 428, 1912–1926. doi: 10.1016/j.jmb.2015.10.026
- Zhao, Y. G., Sun, L., Miao, G., Ji, C., Zhao, H., Sun, H., et al. (2015). The autophagy gene Wdr45/Wipi4 regulates learning and memory function and axonal homeostasis. *Autophagy* 11, 881–890. doi: 10.1080/15548627.2015.1047127

Conflict of Interest Statement: The authors declare that the research was conducted in the absence of any commercial or financial relationships that could be construed as a potential conflict of interest.

Copyright © 2019 Li, Wu, Na, Ge, Wu, Guo, Ntim, Zhang, Sun, Yang, Xiao, Zhao and Li. This is an open-access article distributed under the terms of the Creative Commons Attribution License (CC BY). The use, distribution or reproduction in other forums is permitted, provided the original author(s) and the copyright owner(s) are credited and that the original publication in this journal is cited, in accordance with accepted academic practice. No use, distribution or reproduction is permitted which does not comply with these terms.



Neurocalcin Delta Knockout Impairs Adult Neurogenesis Whereas Half Reduction Is Not Pathological

Aaradhita Upadhyay^{1,2,3}, Seyyedmohsen Hosseinibarkooie^{1,2,3}, Svenja Schneider^{1,2,3}, Anna Kaczmarek^{1,2,3}, Laura Torres-Benito^{1,2,3}, Natalia Mendoza-Ferreira^{1,2,3}, Melina Overhoff^{3,4}, Roman Rombo^{1,2,3}, Vanessa Grysko^{1,2,3}, Min Jeong Kye¹, Natalia L. Kononenko^{3,4*} and Brunhilde Wirth^{1,2,3,5*}

¹Institute of Human Genetics, University of Cologne, Cologne, Germany, ²Center for Molecular Medicine Cologne, University of Cologne, Cologne, Germany, ³Institute for Genetics, University of Cologne, Cologne, Germany, ⁴Excellence Cluster on Cellular Stress Responses in Aging Associated Diseases (CECAD), University of Cologne, Cologne, Germany, ⁵Center for Rare Diseases Cologne, University Hospital of Cologne, Cologne, Germany

OPEN ACCESS

Edited by:

Ashok K. Shetty,
Texas A&M University College of
Medicine, United States

Reviewed by:

Alla B. Salmina,
Krasnoyarsk State Medical University
named after Prof.
V. F. Voyno-Yasenetski, Russia
Di Lang,
University of Wisconsin-Madison,
United States
Diego Minciacci,
Università degli Studi di Firenze, Italy
Annalisa Buffo,
University of Turin, Italy

*Correspondence:

Natalia L. Kononenko
n.kononenko@uni-koeln.de
Brunhilde Wirth
brunhilde.wirth@uk-koeln.de

Received: 14 August 2018

Accepted: 21 January 2019

Published: 12 February 2019

Citation:

Upadhyay A, Hosseinibarkooie S, Schneider S, Kaczmarek A, Torres-Benito L, Mendoza-Ferreira N, Overhoff M, Rombo R, Grysko V, Kye MJ, Kononenko NL and Wirth B (2019) Neurocalcin Delta Knockout Impairs Adult Neurogenesis Whereas Half Reduction Is Not Pathological. *Front. Mol. Neurosci.* 12:19. doi: 10.3389/fnmol.2019.00019

Neurocalcin delta (NCALD) is a brain-enriched neuronal calcium sensor and its reduction acts protective against spinal muscular atrophy (SMA). However, the physiological function of NCALD and implications of NCALD reduction are still elusive. Here, we analyzed the ubiquitous *Ncald* knockout in homozygous (*Ncald*^{KO/KO}) and heterozygous (*Ncald*^{KO/WT}) mice to unravel the physiological role of NCALD in the brain and to study whether 50% NCALD reduction is a safe option for SMA therapy. We found that *Ncald*^{KO/KO} but not *Ncald*^{KO/WT} mice exhibit significant changes in the hippocampal morphology, likely due to impaired generation and migration of newborn neurons in the dentate gyrus (DG). To understand the mechanism behind, we studied the NCALD interactome and identified mitogen-activated protein kinase kinase kinase 10 (MAP3K10) as a novel NCALD interacting partner. MAP3K10 is an upstream activating kinase of c-Jun N-terminal kinase (JNK), which regulates adult neurogenesis. Strikingly, the JNK activation was significantly upregulated in the *Ncald*^{KO/KO} brains. Contrary, neither adult neurogenesis nor JNK activation were altered by heterozygous *Ncald* deletion. Taken together, our study identifies a novel link between NCALD and adult neurogenesis in the hippocampus, possibly via a MAP3K10-JNK pathway and emphasizes the safety of using NCALD reduction as a therapeutic option for SMA.

Keywords: neurocalcin delta, neuronal calcium sensor, adult neurogenesis, MAP3K10, pJNK activation, spinal muscular atrophy, survival motor neuron

INTRODUCTION

Neurocalcin delta (NCALD) is a brain-enriched highly conserved neuronal calcium sensor protein (Wang et al., 2001; Di Sole et al., 2012). Recently, we have shown that reduced NCALD levels protect against spinal muscular atrophy (SMA) in individuals carrying homozygous deletion of *SMN1* and only four *SMN2* copies (Riessland et al., 2017). In that study, five *SMN1*-deleted individuals from a large SMA family were asymptomatic while two were symptomatic. Asymptomatic individuals showed a reduction of NCALD of approximately 50% in fibroblast and almost 80% in lymphoblastoid cell lines in comparison to affected individuals (Riessland et al., 2017).

SMA is one of the most common autosomal recessive disorders in humans and the most common genetic cause of early childhood lethality (Mercuri et al., 2018b). Usually, four *SMN2* copies in the presence of homozygous deletion of *SMN1* result in mild type III SMA (Wirth et al., 2006). The most severely affected cells in SMA patients are spinal motor neurons (MNs), whose loss causes muscle weakness and atrophy (Finkel et al., 2018; Mercuri et al., 2018b). Moreover, we found that reduced NCALD levels ameliorate MN defects also in genetically modified SMA animal models (worm, zebrafish and mice), indicating that NCALD reduction acts SMA protective across species (Riessland et al., 2017). Strategies to treat SMA include the splicing modulation of the *SMN2* copy gene or gene replacement therapy (Finkel et al., 2017; Mendell et al., 2017). Recently, Nusinersen, an antisense oligonucleotide (ASO) that restores the *SMN2* splicing has been approved by the US Food and Drug Administration (FDA) and European Medicines Agency (EMA) as a first drug treatment for SMA (Finkel et al., 2017; Hoy, 2017). However, since 60% of SMA patients usually carry only two *SMN2* copies and develop the severe form of SMA, augmenting the *SMN* level solely *via* splice correction molecules seems to be insufficient to cure SMA (Finkel et al., 2017; Mercuri et al., 2018a). Therefore, targeting additional *SMN*-independent pathways that support the MN function—such as NCALD reduction—are urgently needed (Wirth et al., 2015).

While acting protective in SMA, NCALD reduction has also been associated with various neurological disorders. NCALD levels are downregulated in the brains of patients with Alzheimer's disease (Shimohama et al., 1996; Miller et al., 2013) and in a genetic mouse model of schizophrenia (Vercauteren et al., 2007). Additionally, single nucleotide polymorphisms (SNPs) in *NCALD* have been associated with autism and bipolar disorder (Ben-David et al., 2011; Xu et al., 2014).

NCALD is a member of visinin-like proteins (VSNLs) subfamily of neuronal calcium sensors, which includes the additional four members VILIP1, VILIP2, VILIP3 and hippocalcin (Braunewell and Klein-Szanto, 2009). Depending on their location within the cell and interactions with other proteins, VSNLs transduce the Ca^{2+} signals into specific cellular changes (Burgoyne, 2007; Braunewell and Klein-Szanto, 2009). NCALD, like the other VSNLs, possesses three functional EF hand motifs, which upon Ca^{2+} binding cause the extrusion of myristoyl chain and enables NCALD for insertion into the biological membranes. Cytoplasmic myristoylated NCALD can interact with outer mitochondrial membrane and endoplasmic reticulum (ER; Iino et al., 1995; Ladant, 1995). Furthermore, NCALD has been reported to interact with microsomal cytochrome b5 (Cyb5) on the ER membrane and modulate NADH-dependent microsomal electron transport pathway (Oikawa et al., 2016).

Moreover, NCALD has been found to interact with actin and clathrin, both proteins essential for endocytosis (Ivings et al., 2002; Riessland et al., 2017). Accordingly, NCALD is implicated in the regulation of multiple endocytosis-dependent neuronal functions, like neurotransmitter release, axonal growth and branching (Vercauteren et al., 2007; Yamatani et al., 2010; Riessland et al., 2017). In MN-like

cells, calcium influx is reduced which facilitates the binding of NCALD to clathrin. Consequently, NCALD reduction releases clathrin and thus, allows its function in vesicle coating restoring impaired endocytosis in SMA (Riessland et al., 2017).

In conclusion, NCALD reduction acts protective in SMA and at the same time is associated with various neurological diseases. Hence, this study aims to provide an insight into the pathophysiology of homozygous and heterozygous *Ncald* deletion in the brain. To understand the function of NCALD in the brain and to unravel the physiological consequences of its reduction for SMA therapy, we characterized the NCALD depletion in the mouse central nervous system (CNS), using conventional *Ncald* knockout mice from Jackson laboratory (Stock No 018575).

MATERIALS AND METHODS

Mouse Experiments

All animal procedures were conducted in accordance with European, national and institutional guidelines and protocols, and were approved by the responsible government authority: Landesamt für Natur, Umwelt und Verbraucherschutz NRW (Animal Licence: LANUV NRW under the reference number 84-02.04.2014.A 126). Homozygous *Ncald*^{KO/KO} and heterozygous *Ncald*^{KO/WT} [B6N(Cg)-*Ncald*^{tm1.1(KOMP)Vlcr/J}, Stock Number: 018575] animals were acquired from Jackson Laboratory. Animals used for all experiments were provided food and water *ad libitum* and were caged in small groups on a 12 h light/ dark cycle. These animals were genotyped using following primers: *mmu Ncald*WTfw: 5'-TTTCCCTTACGGG GATGCT-3'; *mmu Ncald*WTrev: 5'-AGCATTCTGCCTTG CTGAT-3'; *mmu Ncald*KOfw: 5'-CGGTCGCTACCATTAC-3'; *mmu Ncald*KOrev: 5'-GCATGTGTGACAACAG-3'.

Western Blot Analysis

Tissues were lysed in ice cold RIPA buffer (Sigma) together with protease (Complete Mini, Roche) and phosphatase inhibitors (Thermo scientific, Waltham, MA, USA). For further analysis, the following primary antibodies were used; anti-NCALD (1:1,000, 12925-1-AP, Proteintech), anti-beta-actin (1:2,500, A5316, Sigma), anti-GAPDH (1:5,000 G-9295, Sigma), anti-myelin basic protein (anti-MBP; 1:1,000 SMI94, Covance), anti-MAP3K10 (1:500, NBP1-87737, Novus Biologicals), anti-pJNK (1:500, sc-6254, Santa Cruz), anti-JNK (1:1,000, #9252, Cell signaling). Chemiluminescence signal was detected with HRP conjugated-secondary antibodies and Chemiluminescence reagent (Thermo Scientific, Waltham, MA, USA) according to manufacturer's protocol.

Nissl Staining

A freezing microtome was used for cutting 40 μm thick consecutive horizontal brain sections. 0.2% gelatin solution in 250 mM Tris-HCl was used for mounting the sections and left overnight at 40°C heating plate for drying. For further staining the sections were first rehydrated for 1 min in water and then stained in 0.1% cresyl violet solution

for approximately 8 min. Following this, the sections were washed three times in water (2 min each) and an ascending ethanol series (50%, 70%, 80%, 90%) was used for dehydration. Sections were finally destained with 96% ethanol and 0.5% acetic acid solution and washed twice in 100% ethanol (2 min each). Subsequently, the sections were incubated in xylene for at least 2 min or until they were mounted using Entellan.

Immunohistochemical Analysis of Brain Sections

Mice were sacrificed at P14, P30 or 4 months by ketamine/xylazine overdose followed by transcardial perfusion with saline solution (0.85% NaCl, 0.025% KCl, 0.02% NaHCO₃, pH 6.9, 0.01% heparin, body temperature) and ice cold 4% paraformaldehyde (PFA) freshly depolymerized in 1×phosphate-buffered saline (PBS), pH 7.4. The fixed brains were carefully isolated from the skull and were further stored overnight in the same ice-cold 4% PFA solution as used for transcardial perfusion. For further storage and cryoprotection, the brains were transferred to a mixture of 20% glycerol and 2% dimethylsulfoxide in 0.1 M phosphate buffer. Consecutive horizontal sections (40 μm) were collected in six series using a freezing microtome. Corresponding brain sections from wildtype (WT) and *Ncald*^{KO/KO} littermates (gender matched) were stained simultaneously for further immunohistochemical analysis as previously described (Kononenko et al., 2017). The following antibodies were used: anti-NCALD (1:100, 12925-1-AP, Proteintech), anti-NeuN (1:500, EPR 12763, Abcam), anti-TBR1 (1:500, ab31940), anti-CUX1 (1:200 sc-13024, Santa Cruz), anti-glial fibrillary acidic protein (anti-GFAP; 1:500, G3893, Sigma), anti-Ki-67 (1:500, ab15580 Abcam), anti-DCX (1:500, AB2253, Merck), anti-adenomatous polyposis coli (anti-APC; 1:500, OP80, Merck), anti-MBP (1:1,000 SMI94, Covance).

Hippocampal Neuronal Culture and Sholl Analysis

Hippocampi were isolated from P1–P5 postnatal mice and the neurons were cultured as described previously (Kononenko et al., 2013). Calcium phosphate transfection procedure was used to transfect the cultured hippocampal neurons at DIV 6–8 with eGFP plasmid as previously described (Threadgill et al., 1997). Neurons were fixed using 4% PFA on DIV 14–15 and were additionally immunostained with anti-GFP (1:5,000, ab13970, Abcam) antibody. Neurons were then imaged with AxioImager M2 fluorescence microscope (Zeiss) appended with ApoTome.2 which allowed virtual confocality. Single cells captured with soma in the center of the image were then subjected to Sholl analysis using ImageJ Sholl Analysis Macro (Gensel et al., 2010). Dendritic branching was determined by adding the total number of intersections within 220 μm from the cell body.

Primary Motor Neuron Culture

E13.5 mouse embryos were used for dissecting spinal cords (Hosseiniabarkooie et al., 2016). Trypsin (Worthington) and

DNase (Sigma) mixture was used for isolating neurons. These singularized neurons were sieved and plated on poly-D-lysine/laminin (Sigma) coated coverslips. Neurobasal medium along with B27 supplement, 2 mM L-glutamine, 1× pen-strep (Invitrogen, Carlsbad, CA, USA) containing 50 ng/μl BDNF, 50 ng/μl GDNF and 50 ng/μl CNTF (Peprotech) was used as culture medium at 37°C in a humidified incubator with 5% CO₂ add space after 5%). Along with axonal length (longest neurite), we have also analyzed primary branching and secondary branching (branches from the longest neurite were considered primary whereas branches from the primary branches were considered secondary) of these MNs.

Immunocytochemistry for Cultured Neurons

On DIV 14 the neurons on coverslips were fixed using 4% PFA in PBS at RT for 15 min and washed three times with 1×PBS at room temperature. After blocking with PBS containing 5% normal goat serum (NGS) and 0.3% Saponin for 1 h, neurons were incubated for 1 h with following primary antibodies anti-NCALD (1:600, 12925-1-AP), anti-VGLUT1 (1:300, 131004, Synaptic Systems), anti-VGAT (1:300, 135011, Synaptic Systems), anti-TAU (1:800, sc-390476, Santa Cruz) and anti-Choline Acetyltransferase (anti-CHAT; 1:500, AB144P, Millipore, Burlington MA, USA) diluted in blocking solution. Coverslips with neurons were then rinsed three times with PBS and incubated for 30 min with corresponding secondary antibodies (diluted 1:1,000 in PBS containing 0.3% Saponin and 5% NGS). Subsequently, coverslips with neurons were washed three times in 1×PBS and mounted using Immumount. A random stretch of neurites with certain observable puncta with co-localization (yellow) signal was chosen. A line was drawn on this stretch and ImageJ plot profile function was used for each channel individually to calculate the intensity plot along the line. Intensity values were plotted against the XY value on the line for each channel in GraphPad Prism 6 software. Subsequently, the plots for NCALD and each synaptic marker were superimposed. The asterisks represent overlapping peaks of each channel, thus showing the co-localization.

Confocal Microscopy

Confocal imaging was performed using a commercial Leica SP8 TCS microscope (Leica Microsystems) equipped with four laser lines 405 nm, 488 nm, 552 nm and 638 nm. Samples within each independent experiment were acquired with equal settings. Images were acquired with an HC PL APO 20×/0.75 CS2 or HC PL APO 63×/1.40 CS2 (oil) objectives (Leica Microsystems), a scanning format of 1,024 × 1,024, eight-bit sampling, and 1 zoom, yielding a pixel dimension of 567.62 × 567.62 or 90.09 nm × 90.09 nm in the *x* and *y* dimensions, respectively.

Co-immunoprecipitation

The brain and spinal cord samples were collected at P30 and P14, respectively (From both WT and *Ncald*^{KO/KO} mice). The

tissue samples were homogenized and lysed in NP40-based lysis buffer (50 mM Tris-HCl, 1% NP40, 100 mM NaCl, 2 mM MgCl₂ including protease inhibitor). Ten microliter of Control rabbit IgG (SantaCruz) and NCALD polyclonal antibody were used for immunoprecipitation using protein A paramagnetic MicroBeads (Miltenyi) following the manufacturer's instruction. Finally, the IP columns were washed at least six times with lysis buffer. The bound fraction of proteins was directly used for further mass spectrometry analysis.

Mass Spectrometry and Data Analysis

All samples were analyzed on a Q-Exactive Plus (Thermo Scientific, Waltham, MA, USA) mass spectrometer coupled to an EASY nLC 1,000 UPLC (Thermo Scientific, Waltham, MA, USA). Peptides were loaded with solvent A (0.1% formic acid in water) onto an in-house packed analytical column (50 cm × 75 μm I.D., filled with 2.7 μm Poroshell EC120 C18, Agilent). Peptides were chromatographically separated at a constant flow rate of 250 nL/min using the following gradient: 5–30% solvent B (0.1% formic acid in 80% acetonitrile) within 66 min, 30–50% solvent B within 13 min, followed by washing and column equilibration. The mass spectrometer was operated in data-dependent acquisition mode. The MS1 survey scan was acquired from 300 to 1,750 m/z at a resolution of 70,000. The top 10 most abundant peptides were isolated within a 1.8 Th window and subjected to HCD fragmentation at a normalized collision energy of 27%. The AGC target was set to 5e5 charges, allowing a maximum injection time of 120 ms. Product ions were detected in the Orbitrap at a resolution of 35,000. Precursors were dynamically excluded for 20 s.

All mass spectrometric raw data were processed with Maxquant (version 1.5.3.8) using default parameters. Briefly, MS2 spectra were searched against the Uniprot MOUSE.fasta (downloaded at: 18.47.2017) database, including a list of common contaminants. False discovery rates on protein and PSM level were estimated by the target-decoy approach to 1% (Protein FDR) and 1% (PSM FDR) respectively. The minimal peptide length was set to seven amino acids and carbamidomethylation at cysteine residues was considered as a fixed modification. Oxidation (M) and Acetyl (Protein N-term) were included as variable modifications. The match-between runs option was enabled. LFQ quantification was enabled using default settings.

Statistical Analysis

Statistical significance was calculated from independent experiments (*n*) for analysis of all experiments. A two-tailed unpaired student's *t*-test was used to evaluate the statistical significance between two groups for all normally distributed raw data. The statistical significance between more than two groups for all normally distributed raw data was evaluated using one-way analyses of variance (ANOVA; Tukey *post hoc* test was used to determine the statistical significance between the groups). Significant differences were accepted at *p* < 0.05. For box plots the median divides the box, while the upper boundary of the box corresponds to the third quartile and the lower

boundary corresponds to the first quartile. The minimum and the maximum values extend as bars from the bottom and top of the box.

RESULTS

Homozygous Loss of *Ncald* Alters Gross Morphology of the Brain

In order to gain an in-depth understanding of NCALD function in the brain, we acquired the heterozygous *Ncald* knockout (*Ncald*^{KO/WT}) animals from the Jackson Laboratories [Bl6N(Cg)-*Ncald*^{tm1.1(KOMP)Vlcg/J}, Stock Number: 018575]. After crossing the heterozygous parents, we obtained 25% *Ncald*^{KO/KO}, 50% *Ncald*^{KO/WT} and 25% *Ncald*^{WT/WT} mice, according to the Mendelian inheritance. *Ncald*^{KO/KO} mice were fertile (with lower fertility rate) and showed normal survival (data not shown). We observed more than a half of NCALD reduction in *Ncald*^{KO/WT} and a complete absence of NCALD in *Ncald*^{KO/KO} animals in the brain (Figure 1A). Furthermore, *Ncald*^{KO/KO} animals revealed significantly reduced body weight compared to their WT littermates (Figure 1B). Since NCALD is highly abundant in neurons, we next analyzed the gross morphology of NCALD deficient brains (Figure 1B). We found that *Ncald*^{KO/KO} animals have significantly smaller brains compared to WT littermates, however when normalized to reduced body weight the reduction in brain weight was not significant (Figure 1B). Interestingly, neither the body weight nor the brain weight or morphology were altered by the heterozygous *Ncald* knockout (Supplementary Figures S1A–C).

Next, we used the Nissl staining on consecutive 40 μm thin sections to characterize the brain morphology of *Ncald*^{KO/KO} mice at 2 weeks (P14), 1 month (P30) and 4-months of age (adult). We found that although no significant changes in brain weight and gross morphology could be detected at P14 (Supplementary Figures S2A,B) and P30 (Supplementary Figures S2C,D), adult *Ncald*^{KO/KO} brains exhibited significantly enlarged lateral ventricles and disturbed hippocampal morphology, which was accompanied by a significantly reduced subgranular zone length (SGZ; Figures 2A–D). Interestingly, this SGZ reduction was proportional to the hippocampal volume, indicating that *Ncald*^{KO/KO} brains possess smaller hippocampi in general. These morphological changes in *Ncald*^{KO/KO} animals could either indicate a brain maturation defect occurring during the adolescence or be a sign of a progressive neurodegeneration, which would get more severe later in the adulthood. To answer this question we analyzed the brain morphology of 1.5 years *Ncald*^{KO/KO} animals and older. However, we did not detect any severe exacerbation of the phenotype in old *Ncald*^{KO/KO} animals compared to the adult mice (data not shown). *Ncald*^{KO/KO} brains also revealed no signs of astrogliosis, marked by immunostaining for GFAP (Pekny and Pekna, 2014; Supplementary Figure S3A). Furthermore, neither overall neuronal cell density nor neuronal complexity *per se* were altered by the homozygous *Ncald* knockout in mice (Supplementary Figures S3B,C). Taken together, our data point

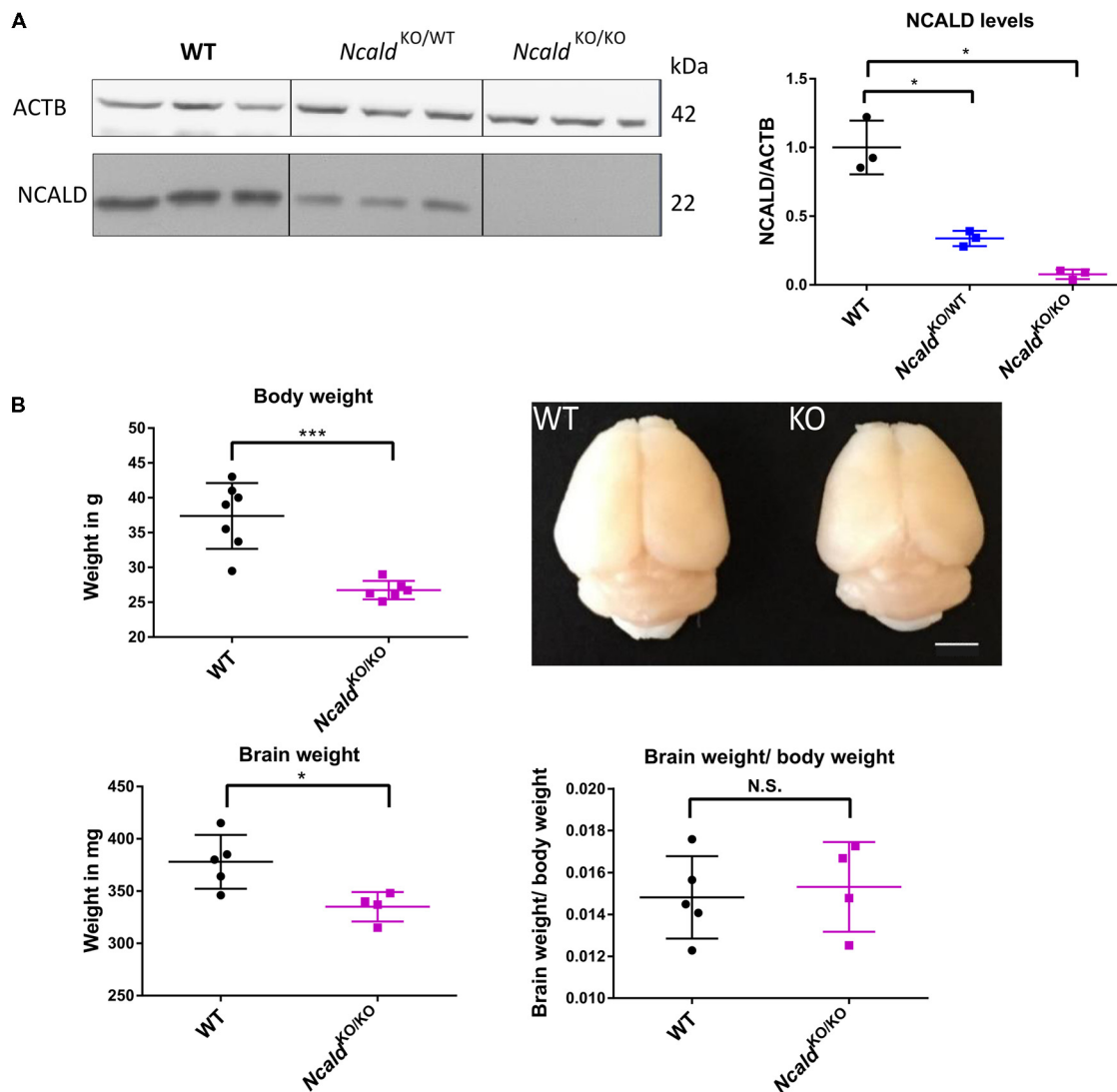


FIGURE 1 | Neurocalcin delta (*Ncald*)^{KO/KO} animals weight less and have smaller brains than wildtype (WT) littermates. **(A)** Western blot analysis of brain lysates from WT, *Ncald*^{KO/WT} and *Ncald*^{KO/KO} mice showing a significant reduction of NCALD in *Ncald*^{KO/WT} animals and absence of NCALD in *Ncald*^{KO/KO} animals; **P* > 0.05. **(B)** Body weight of 5-month-old *Ncald*^{KO/KO} males is significantly reduced (*N* = 6) compared to their WT littermates (*N* = 7); *P* < 0.05. Representative images of 4-month-old *Ncald*^{KO/KO} (*N* = 4) and WT (*N* = 5) littermate brains and dot plot quantifications, indicating significantly smaller brains, but no significant changes in brain-to-body mass ratio in *Ncald*^{KO/KO} animals compared to WT littermates; scale bar 100 pixels; **P* < 0.05; ****P* < 0.005; N.S. = not significant. Uncropped Western blots are included in **Supplementary Data Sheet 8**.

to brain maturation defects in the adult *Ncald*^{KO/KO} mice and suggest that NCALD has a specific role during postnatal brain maturation.

NCALD Is Highly Elevated Postnatally and Regulates Neurogenesis in the Adult Mouse Brain

To address the role of NCALD in brain maturation, we first analyzed NCALD levels in the WT mouse brain at various developmental time points (E16, P1 and P10–P14). We found that NCALD is present at very low levels during the embryonic stages and increases dramatically at P10–P14

(Figure 3A and Supplementary Figure S1D). In the adult brain, NCALD was found to be present throughout the brain, but was particularly enriched at multiple sites including hippocampal regions, dentate gyrus (DG) and CA3 as well as in the presubiculum (PreS; Figure 3B). Immunostaining of *Ncald*^{KO/KO} brain with NCALD antibody failed to show any signal (data not shown), demonstrating the specificity of the antibody. In cultured hippocampal neurons NCALD was co-localized with the excitatory vesicular glutamate transporter 1 (VGLUT1) and inhibitory vesicular GABA transporter (VGAT) presynaptic markers, indicating the presence of NCALD at presynaptic terminals (Figure 3C).

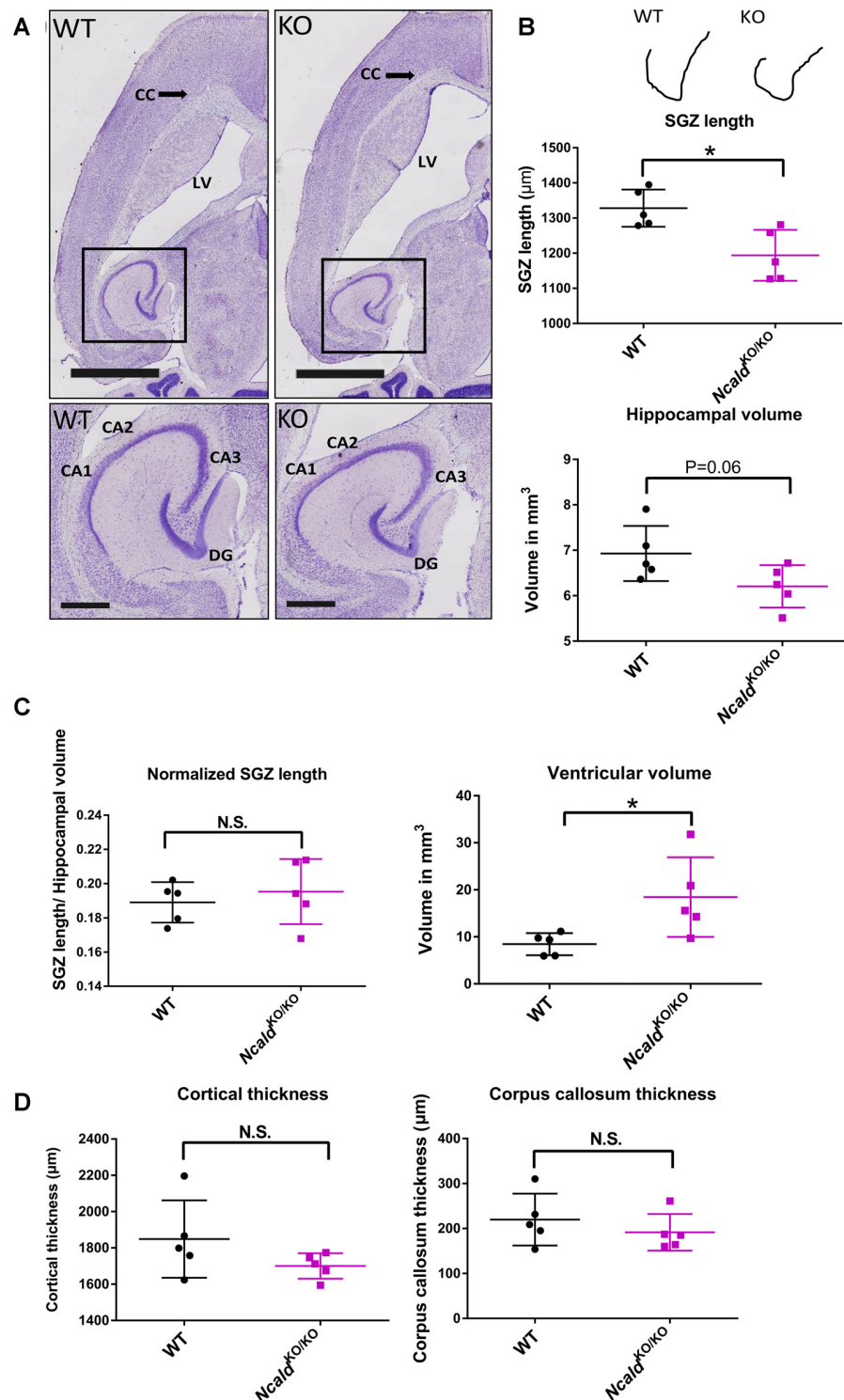


FIGURE 2 | *Ncald^{KO/KO}* mice exhibit abnormal brain gross morphology when compared to WT littermates. **(A)** Representative examples of Nissl-stained 4-month-old *Ncald^{KO/KO}* and WT brains; scale bars 2 mm and 500 μm (magnified inset). **(B)** Schematic illustration of a tracing line used to manually measure the subgranular zone (SGZ) length on Nissl-stained consecutive brain section. Dot plots representing a reduction in the SG length (SGL) of the dentate gyrus (DG) and a strong tendency towards a smaller hippocampal volume in *Ncald^{KO/KO}* mice compared to WT littermates; $N = 5$; $*P < 0.05$. **(C)** Dot plots representing no significant difference in the SGL, when normalized to the hippocampal volume and significantly increased volume of lateral ventricles in *Ncald^{KO/KO}* mice compared to WT littermates; $N = 5$; $*P < 0.05$; N.S. = not significant. **(D)** Dot plots representing unaltered cortical thickness and corpus callosum thickness in the *Ncald^{KO/KO}* animals in comparison to WT littermates; $N = 5$; N.S. = not significant.

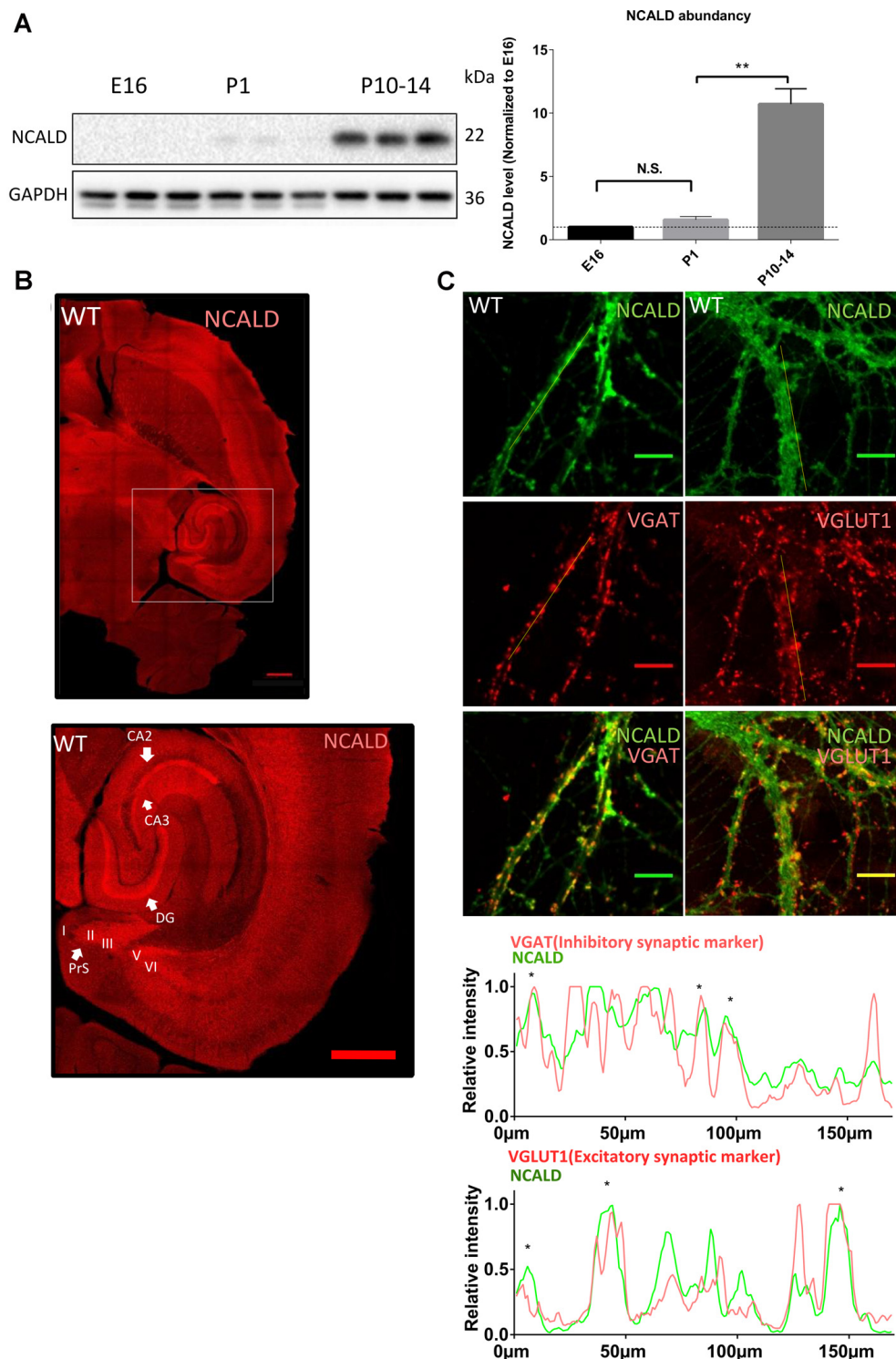


FIGURE 3 | NCALD is enriched postnatally and in presynaptic terminals. **(A)** Western blot analysis of NCALD levels in brain lysates derived from the embryonic stage 16 (E16), postnatal day 1 (P1) and postnatal day 14 (P14) WT mice. Dot plots quantification reveals a 10-fold increase in the NCALD level in P10–14 brains; $**P < 0.01$; N.S. = not significant. **(B)** Representative confocal images of a WT brain immunostained for the NCALD, showing high protein expression in the forebrain and the midbrain and its abundance in the hippocampal and parahippocampal regions (magnified area); scale bar 500 μ m. **(C)** Representative confocal images of cultured WT hippocampal neurons stained with NCALD antibody (green) and co-stained with synaptic markers VGLUT1 and VGAT (red), showing NCALD enrichment in the presynaptic terminals; scale bar 10 μ m. Dotted white lines indicate areas taken for line plot analysis, where fluorescent signal for each channel is plotted relative to the distance. Asterisks in line plots represent the colocalization of NCALD with either VGLUT or VGAT. Uncropped Western blots are included in **Supplementary Data Sheet 8**.

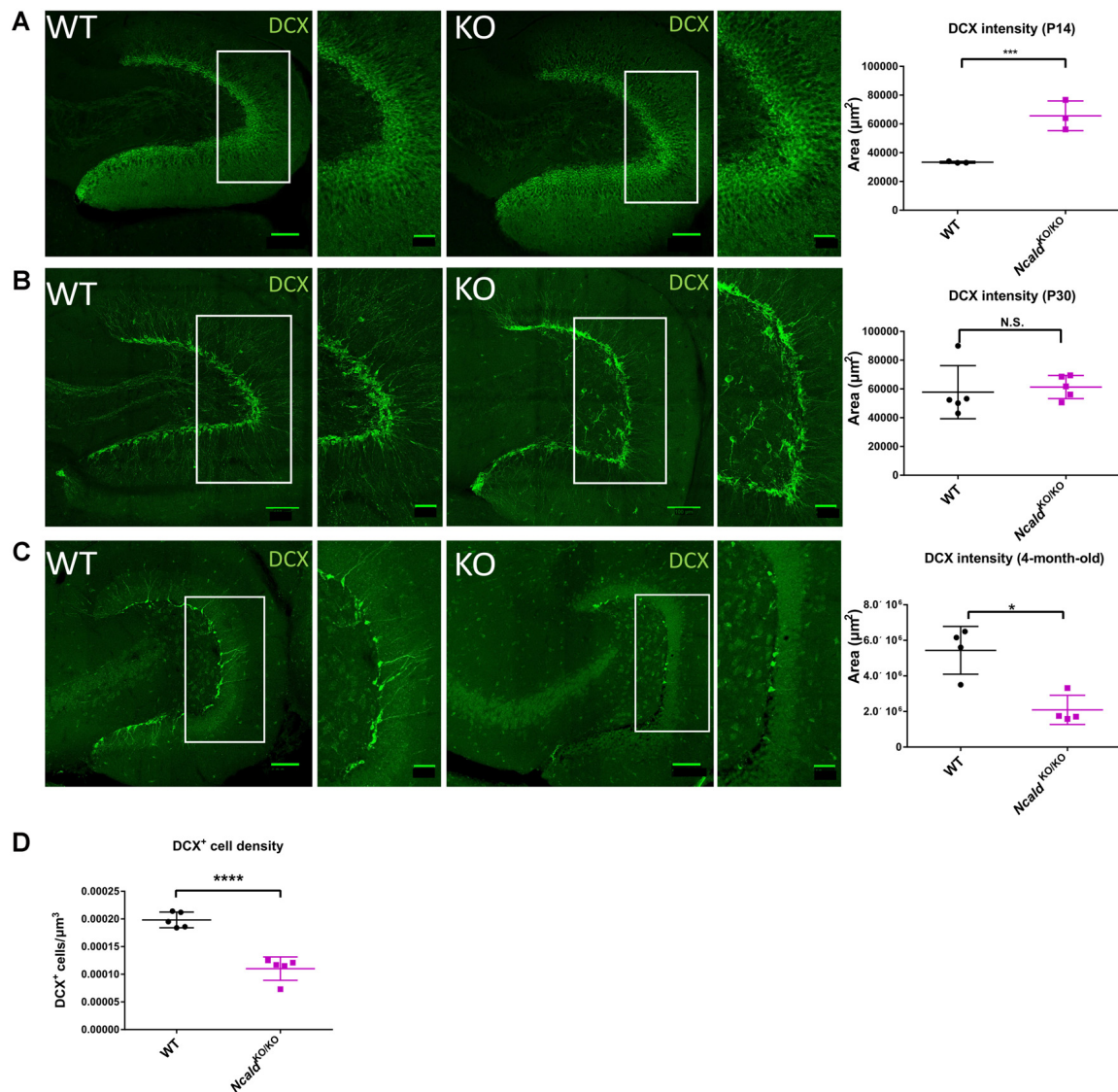


FIGURE 4 | Disturbed adult neurogenesis in the hippocampus of *Ncald*^{KO/KO} mice. **(A)** Immunofluorescent analysis of doublecortin (DCX) positive neurons in the DG of P14 WT and *Ncald*^{KO/KO} animals; scale bars 100 μm and 40 μm (magnified insert); *N* = 3; ****P* < 0.005. **(B)** Immunofluorescent analysis of DCX⁺ neurons in the DG of WT and *Ncald*^{KO/KO} animals at P30; scale bars 100 μm and 40 μm (magnified insert); *N* = 5; N.S. = not significant. **(C)** Immunofluorescent analysis of DCX⁺ neurons in the DG of 4-month-old WT and *Ncald*^{KO/KO} animals. DCX intensity is significantly lower in mice deficient for NCLAD; scale bar 100 μm and 40 μm (magnified insert); *N* = 5; **P* < 0.05. **(D)** Dot plot analysis indicating a significant decrease in the DCX⁺ cell density in 4-month-old *Ncald*^{KO/KO} animals compared to WT controls; *N* = 5; *****P* < 0.0001.

Since NCALD is strongly enriched in the hippocampus (Figure 3B) and homozygous *Ncald* knockout brains reveal defects in the architecture of the DG (Figure 2), we speculated that NCALD might be specifically involved in the regulation of the hippocampal morphology in the mouse brain. Since, defects in the hippocampal morphology in the adult *Ncald*^{KO/KO} animals can be associated with impaired postnatal neurogenesis, we first examined the overall cell proliferation in the DG using Ki-67, a protein only expressed in actively dividing cells (Scholzen and Gerdes, 2000), and found no general defect in cell proliferation (Supplementary Figure S5B). Following this, we analyzed newly

generated neurons in the DG of *Ncald*^{KO/KO} animals and their control littermates by using Doublecortin (DCX) antibody, which labels newly generated granule cells undergoing migration (Couillard-Despres et al., 2005). We observed that the DCX intensity was significantly increased in *Ncald*^{KO/KO} mice at P14 whereas it was unaltered by homozygous *Ncald* deletion in the DG of P30 animals (Figures 4A,B). In contrast, in the DG of adult *Ncald*^{KO/KO} animals, we observed a significant reduction of DCX intensity as well as DCX⁺ neuronal density when compared to WT littermates (Figures 4C,D). Moreover, those few DCX⁺ neurons, which were present in the *Ncald*^{KO/KO} DG showed a

tangential orientation instead of integration in the granule cell layer pointing towards a possible migration defect (**Figure 4C**).

To investigate this possibility, we analyzed the cortical layering in the 4-month-old *Ncald*^{KO/KO} animals. Improper organization of six cortical layers might be a consequence of the defects in neuronal migration, originating prenatally or early postnatally (Molyneaux et al., 2007). Immunohistochemical analysis of superficial and deep cortical layers stained with T-Box, Brain 1 (TBR1) and Cut Like Homeobox 1 (CUX1) antibodies revealed no alteration of cortical structure in *Ncald*^{KO/KO} animals (**Supplementary Figures S4A,B**), which suggests that NCALD does not regulate cortical layering. Taking into consideration a significant loss of DCX⁺ neurons in the adult *Ncald*^{KO/KO} animals, we also analyzed the heterozygous *Ncald*^{KO/WT} brains. We found that the DCX⁺ neuronal density as well as the DCX intensity was not significantly altered in *Ncald*^{KO/WT} brains, indicating that heterozygous *Ncald* knockout does not affect adult neurogenesis (**Supplementary Figure S4C**). Considering the possibility of degeneration of the DCX⁺ neurons, we immunostained *Ncald*^{KO/KO} brains for cleaved caspase 3 (an apoptotic marker), but we did not detect any apoptotic cell deaths in neurons lacking NCALD (data not shown).

To further investigate at which stage of adult neurogenesis NCALD regulates the DG granule cell function, we first quantified all the proliferating cells in the DG using the Ki-67 antibody as a cell-proliferating marker (**Supplementary Figure S5A**). However, we did not find any significant difference in the number of proliferating cells in adult *Ncald*^{KO/KO} compared to WT mice (**Supplementary Figure S5B**). Next, to label neural stem cells type 1 and type 2 we used GFAP and Nestin antibodies in combination with Ki-67, while type 3 neuronal stem cells were identified as being positive for Ki-67 along with DCX (**Supplementary Figure S5A**, and Sibbe et al., 2015). However, we did not observe any significant differences in the percentages of type1, 2 or 3 population of proliferating neuroblasts in *Ncald*^{KO/KO} compared to WT mice (**Supplementary Figures S5C,D**). Taken together, these data indicate that NCALD is not involved in neuroblast proliferation and likely regulates the DG granule cell function at the stage of neuronal maturation.

NCALD Regulates Myelination in the Mouse Brain

Myelination is another important postnatal developmental event in the mouse brain (O'Rourke et al., 2014). Therefore, we next examined the myelination upon NCALD depletion by analyzing the levels of MBP in the 1-month-old *Ncald*^{KO/KO} animals. By using both immunohistochemistry and Western blotting, we found that MBP levels were significantly lower in brains lacking NCALD (**Supplementary Figure S6A**). Since the defects in the myelination could originate from a direct role of NCALD in oligodendrocytes, we analyzed the NCALD expression levels in oligodendrocytes by immunostaining with anti-APC antibody, an oligodendrocyte-specific marker (Lang et al., 2013). Co-localization analysis showed that NCALD is

absent from these cells (**Supplementary Figure S6B**), indicating that NCALD does not function directly in oligodendrocytes.

To analyze if MBP reduction observed at P30 is a result of delayed myelination, we quantified the levels of MBP also at P14 and adult brains of *Ncald*^{KO/KO} mice (**Supplementary Figures S6C–E**). Indeed, we found no significant reduction in the MBP levels in adult brains, pointing towards a possible myelination delay in the 1-month-old *Ncald*^{KO/KO} animals. Since, it is known that the decreased myelination can be a consequence of reduced number of axons, we also analyzed the levels of neurofilament, an axonal marker in *Ncald*^{KO/KO} brain (**Supplementary Figures S6C–E**). We found no significant difference in the neurofilament levels ruling out decreased number of axons as the cause for the myelination defect observed in the *Ncald*^{KO/KO} brain.

NCALD Regulates JNK Pathway

In order to unveil the mechanism underlying the morphological defects observed in the brain upon *Ncald* knockout, the interactome of NCALD was investigated using mass spectrometry (LC-MS) analysis of WT and *Ncald*^{KO/KO} brain samples at P30. Three different IPs were performed in triplicates with the following groups: (1) three IPs with NCALD antibody using WT brain lysate; (2) three IPs with NCALD antibody using *Ncald*^{KO/KO} brain lysates; and (3) three independent negative IPs (beats only) with WT lysates. The mass spectrometry result confirmed the absence of NCALD in the brain of *Ncald* knockout samples. The final list of identified proteins was based on the fact that the candidate was present only in the WT NCALD IPs (group 1) but absent from all IPs of groups 2 and 3. Only three proteins met these criteria (**Figure 5A**). Due to the highest number of identified peptides for MAP3K10 this protein was selected for further analysis. We first confirmed the interaction of MAP3K10 and NCALD in the brain by co-immunoprecipitation using the MAP3K10 antibody (**Figure 5A**).

MAP3K10 functions as a part of the MAP kinase pathway, upstream of two major MAPKs, namely JNK and P38 (Hirai et al., 1997). JNK is known to regulate various cellular processes, including apoptosis, neuronal differentiation, axonal growth and branching. Additionally, JNK has recently been reported to regulate the adult neurogenesis (Coffey, 2014; Mohammad et al., 2018; **Figure 5B**). Taking into account the impaired adult neurogenesis in *Ncald*^{KO/KO} animals, we evaluated the JNK and pJNK level in adult NCALD-depleted brains by Western blotting. We found that in *Ncald*^{KO/KO} brains the phosphorylation of JNK (pThr 183 and pTyr 185) was significantly upregulated compared to wildtype littermates (**Figure 5C**). At the same time, the phosphorylation of JNK in heterozygous *Ncald* knockout brains was not altered (**Supplementary Figure S7A**). These data suggest a specific role for NCALD in the MAP3K10-regulated JNK activation. These findings, together with the fact that alterations in the JNK pathway have already been reported in SMA (Genabai et al., 2015), prompted us to subject the spinal cord lysates from *Ncald*^{KO/KO} and WT animals to LC/MS analysis. Our results from the spinal cord confirmed the data obtained from the brain and revealed the MAP3K10 as one of the top interaction partners of NCALD (data not shown). However, we did not

find any significant differences in p-JNK in the spinal cord from *Ncald*^{KO/KO} animals, suggesting a brain-confined modulation of JNK pathway by NCALD (Supplementary Figure S7B).

Heterozygous and Homozygous *Ncald* Knockout Increases Axonal Length

Finally, since NCALD reduction has been shown to act protective in MNs derived from the spinal cord of SMA transgenic mice (Riessland et al., 2017), we analysed the effect of NCALD deficiency on MN morphology in *Ncald*^{KO/WT} and *Ncald*^{KO/KO} mice. We examined the morphology of cultured MNs with a MN specific marker ChAT as well as microtubule stabilising protein TAU. In accordance with our previous findings (Riessland et al., 2017), we found that both 50% reduction and a complete deletion of NCALD significantly increased the length of MN axons compared to controls (Figure 6). Interestingly, *Ncald*^{KO/KO} MNs had significantly shorter axons when compared to MNs isolated from *Ncald*^{KO/WT} mice. Since this phenotype in *Ncald*^{KO/KO} mice was accompanied by a strong, but not significant increase in a number of secondary branches, we reason that decreased axonal length in *Ncald*^{KO/KO} neurons results from their increased secondary branching (Figure 6). On other hand, we found that in *Ncald*^{KO/WT} and *Ncald*^{KO/KO} hippocampal neurons axonal length was not altered (Supplementary Figure S7C).

DISCUSSION

The main findings of this study are: (1) NCALD is especially abundant in certain regions of the hippocampus like DG and CA3 as well as in the PreS; (2) homozygous loss of *Ncald* impairs hippocampal morphology with reduction in subgranular zone length and causes enlargement of lateral ventricles in 4-month-old mice; (3) NCALD levels increase dramatically during the early postnatal stages between P10 and P14; (4) adult *Ncald*^{KO/KO} animals reveal severe changes in the adult neurogenesis in the DG; (5) NCALD interacts with MAP3K10 and regulates the JNK pathway in the brain; and (6) none of the deleterious phenotypes found in homozygous *Ncald* knockout mice are observed in heterozygous *Ncald* knockout animals, while NCALD reduction is sufficient to increase the axonal length of MN; this indicates that half reduction of NCALD is safe to be used as a potential SMN-independent therapy for SMA patients.

Physiological Significance of NCALD in Postnatal Brain Development and Adult Neurogenesis

We found that NCALD levels are steadily increasing at postnatal stages until P14. Moreover, we found that homozygous *Ncald* knockout significantly increases the intensity of DCX (a marker for newly differentiated and immature cells) in the early adolescent (P14) brain. These data are in agreement with our previous finding, where NCALD reduction in cultured MN-like cells has been shown to promote their early differentiation (Riessland et al., 2017). In contrast to the P14, we found that the loss of NCALD in the adult DG significantly decreases the DCX intensity as well as the DCX⁺ cell number. The transition of immature DCX positive cells to mature granule

cells is most pronounced during P7–P28, hence it is a crucial stage for the formation of the SGZ (Radic et al., 2017). Furthermore, the full electrophysiological maturation of new granule cells progresses over the period of ca. 3–7 weeks after cell division (Overstreet-Wadiche and Westbrook, 2006; Zhao et al., 2006). Therefore, potential effects of NCALD loss on brain morphology would arise earliest at 7 week-of age. This is strongly in line with our observations, where no significant changes in the hippocampus could be detected in P30 animals, however they were prominent in adult *Ncald* knockout mice. Additionally, we found that NCALD depletion does not affect the proliferation of various types of neuroblasts in the adult DG. However, future studies using the BrdU incorporation method are required to fine-tune the onset of these aberrations and reinforce our findings. Moreover, it has been shown that adult neurogenesis can directly regulate the volume and morphology of the hippocampus (Fuss et al., 2014; Baptista and Andrade, 2018). Therefore, the loss of adult neurogenesis observed in adult *Ncald* knockout animals could be an accumulated loss of DCX⁺ immature neurons, which were not able to integrate into the granule layer. Interestingly, in a recent database of RNA expression profiles during adult neurogenesis, *Ncald* expression has been shown to specifically increase at the immature granule cell stage (Hochgerner et al., 2018). These data corroborate our finding that adult *Ncald*^{KO/KO} animals show a significant reduction specifically in immature granule cell population of neurons (Figures 4C,D) and points towards a stage specific role of NCALD in the adult neurogenesis.

We show that the changes in adult neurogenesis observed in *Ncald*^{KO/KO} mice are accompanied by hyperactivation of the JNK pathway in the brain of NCALD depleted animals. These data are in agreement with the recent study showing that JNK acts as a negative regulator of adult neurogenesis (Mohammad et al., 2018). Considering that the gradient regulation of JNK pathway during the embryonic development of the brain has been implicated in the migration and maturation of neurons (Hirai et al., 2002), JNK activation could well be the mechanism responsible for the aberrant migration of newborn neurons in adult *Ncald*^{KO/KO} animals. Therefore, further rescue studies of adult neurogenesis defects in *Ncald*^{KO/KO} animals treated with blood-brain barrier permeable JNK inhibitor (Mohammad et al., 2018) as well as by targeted overexpression of *Ncald* can deepen our understanding of NCALD function.

Implications of NCALD in Other Physiological Functions

Most of the NCALD-enriched brain regions described in the current study have already been reported (Girard et al., 2015), except for the PreS. PreS is a part of the parahippocampal region (Witter et al., 2000) which has been strongly implicated in spatial navigation (Boccaro et al., 2010). Thus, we suggest that spatial navigation might be disturbed by NCALD loss in the adult mice, however this hypothesis needs to be tested in future experiments.

Although NCALD has been previously implicated in synaptic function (Kedracka-Krok et al., 2015), our study provides the first direct evidence of NCALD localization at synaptic boutons of hippocampal neurons *via* colocalization of NCALD

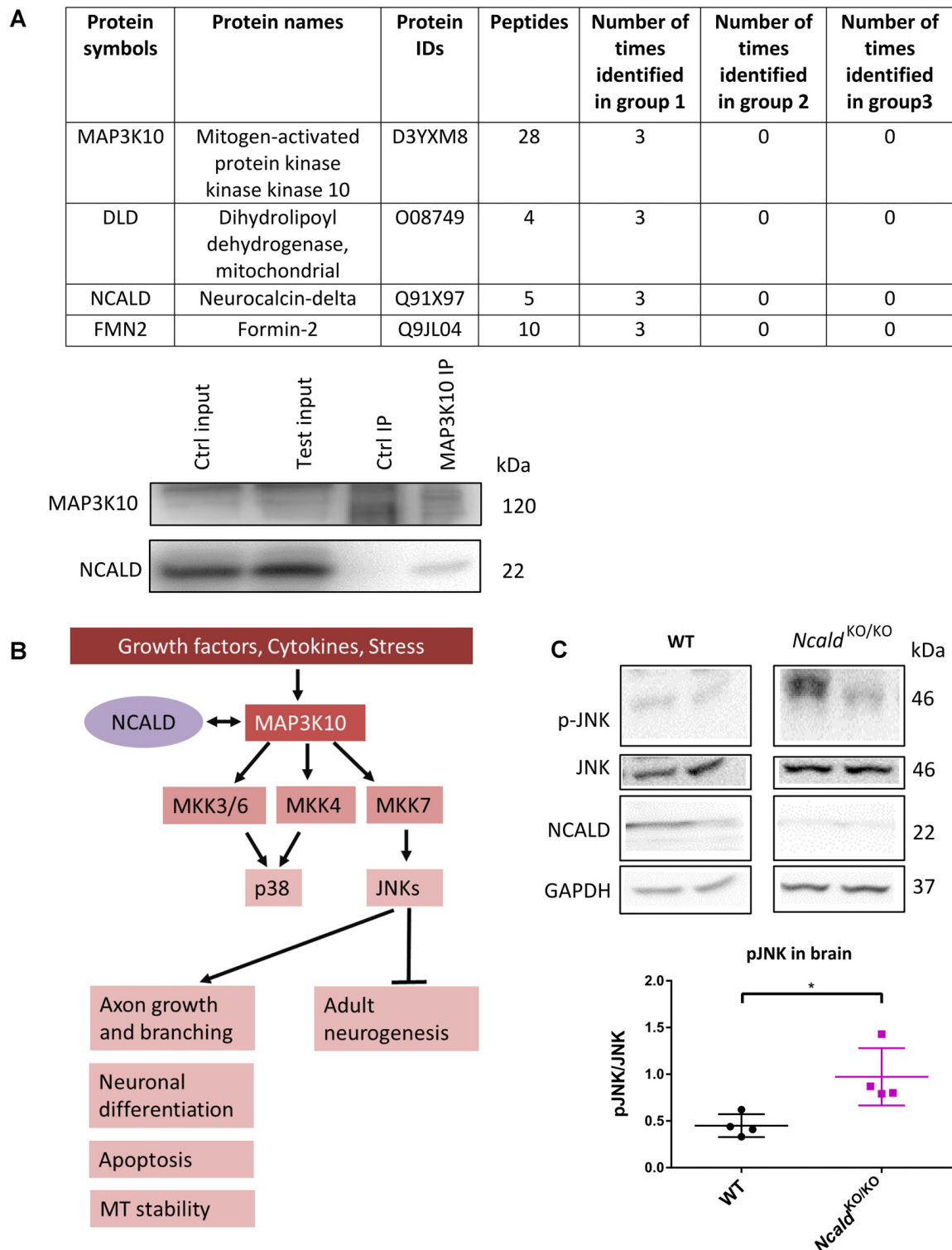


FIGURE 5 | MAP3K10 interacts with NCALD and the downstream JUN N-terminal kinase (JNK) pathway is misregulated in *Ncald*^{KO/KO} brains. **(A)** Proteins identified to be present in all WT but not in *Ncald*^{KO/KO} or negative control (beads only) brain lysates at P30. NCALD was immunoprecipitated using an NCALD-specific antibody and peptides were identified by mass spectrometry. Interaction between MAP3K10 and NCALD was confirmed by co-immunoprecipitation analysis. **(B)** Schematic illustration of MAP3K10-dependent regulation of JNK and P38 signaling pathways (modified from Hirai et al., 1997). **(C)** Representative Western blots and dot plots analysis showing a significant increase in JNK signaling in 4-month-old *Ncald*^{KO/KO} brain lysates compared WT controls. For quantification, pJNK levels were normalized to the total JNK levels; *N* = 4; **P* < 0.05. Uncropped Western blots are included in **Supplementary Data Sheet 8**.

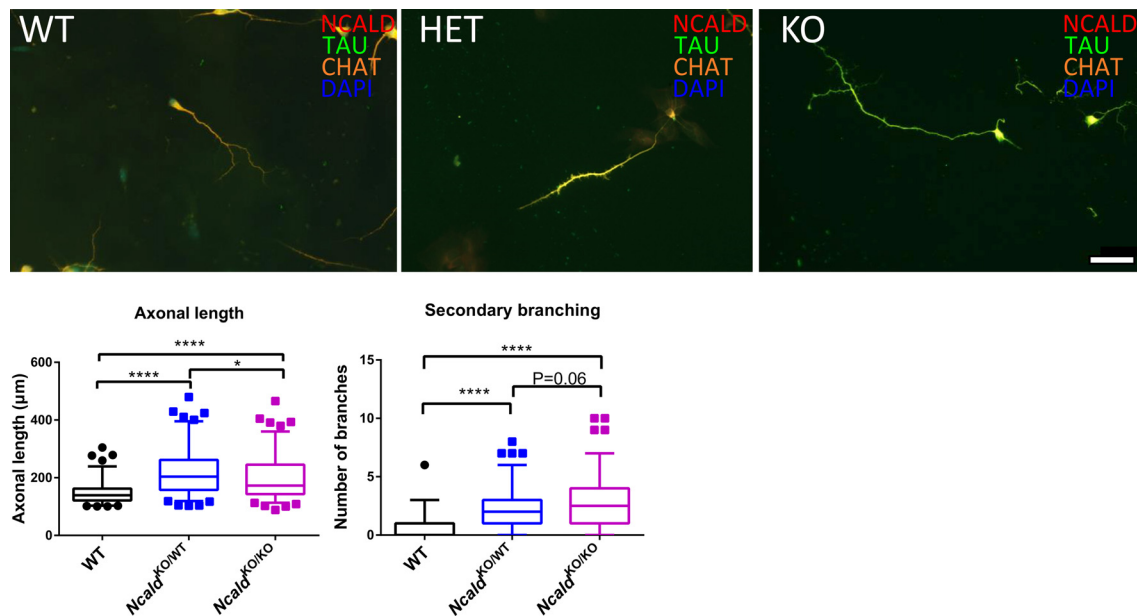


FIGURE 6 | Heterozygous and homozygous *Ncald* deletion results in longer axons in spinal motor neurons (MNs). Cultured MNs isolated from WT, *Ncald*^{KO/WT} and *Ncald*^{KO/KO} E13.5 mouse embryos were stained with NCALD, TAU and Choline acetyltransferase (CHAT) antibodies. Nuclei were labeled with DAPI; scale bar 50 μm. Dot plot analysis reveals a statistically significant increase in the average axon length and secondary axonal branching in *Ncald*^{KO/WT} and *Ncald*^{KO/KO} neurons compared to WT; $N = 108, 104, 105$; **** $P < 0.0001$; * $P < 0.05$. Twenty-five to Seventy-five percent values covered by each box plot, line represents median and dotted outliers at <5% and >95% CI.

with VGLUT1, an excitatory synaptic marker and VGAT, an inhibitory synaptic marker.

NCALD in Neurodevelopmental Diseases

Multiple studies indicate the importance of hippocampal shape and morphology in cognitive functions (Smith et al., 2012; Voineskos et al., 2015). Smaller hippocampi, as well as severe morphological disturbances in hippocampal shape observed in *Ncald*^{KO/KO} animals implicate NCALD function in cognition. Indeed, NCALD has been associated with schizophrenia (Vercauteren et al., 2007) and autism (Ben-David et al., 2011), both representing neurodevelopmental disorders associated with cognitive loss and characterized by enlargement of lateral ventricles both in human patients (Movsas et al., 2013) and genetic mouse models (Pletnikov et al., 2008). A similar ventricle enlargement phenotype, as well as impairment in postnatal development has been observed for *Ncald*^{KO/KO} mice in the current study. Moreover, phenotypic data available at the International Mouse Phenotyping Consortium platform indicate that *Ncald*^{KO/KO} mice are hyperactive and anxious and exhibit severe reduction of body mass,¹ similar to what we observed in our *Ncald*^{KO/KO} animals. Henceforth, a detailed study of NCALD function in the pathophysiology of schizophrenia, autism, depression, stress-related disorders like bipolar disorder and anxiety, as well as a comprehensive analysis cognitive behavior of *Ncald*^{KO/KO} animals have a potential to reveal a disease mouse model for neurodevelopmental disorders with subtle

behavioral symptoms, thereby improving our understanding of such disorders.

Can NCALD Reduction be Used for Future SMN-Independent SMA Therapy?

SMA therapeutics reached a very important milestone in the last 2 years, with the FDA and EMA approval of Nusinersen for treatment of SMA patients outside the clinical trial (Scoto et al., 2017). Nusinersen is a modified ASO which binds to the SMN2 pre-mRNA at an intronic splice silencer site, whereby it disrupts the interaction with negative splicing factors. This in turn promotes the inclusion of exon 7 in the SMN2 mRNA thereby enhancing the SMN protein levels (Rigo et al., 2014). Nusinersen has shown significant benefits in the progress of SMA patients, however it could not fully revert the normal motor functions in patients (Talbot and Tizzano, 2017). Specifically, in case of type I SMA patients, who usually have only two SMN2 copy and some even only one (Feldkötter et al., 2002), increasing the SMN level via one or two SMN2 copies may not be sufficient to fully counteract SMA pathology. Therefore, there is a need for SMN-independent therapies, which can work in combination with Nusinersen or other SMN-dependent therapies (Finkel et al., 2017; Mendell et al., 2017).

We have already published the therapeutic importance of NCALD reduction in the context of SMA (Riessland et al., 2017). Supporting our previous studies here, we show that reduction of NCALD even by 50%, such as in *Ncald*^{KO/WT} mice has no systemic consequences for the animal physiology. Furthermore,

¹<http://www.mousephenotype.org/>

we found that NCALD reduction in *Ncald*^{KO/WT} MNs increases the axonal length independent of SMA.

JNK Pathway in SMA

We observed that *Ncald*^{KO/KO} can alter JNK phosphorylation in the brain but not in the spinal cord (Figure 5C and Supplementary Figure S7B). Although both the spinal cord and the brain are the part of the CNS, there are significant variations in their metabolic, functional and defense mechanisms (Panov et al., 2011). These variations could underlie the neuronal type-specific response of JNK signaling pathway to the NCALD depletion in either brain or spinal cord. Moreover, we found that while *Ncald*^{KO/KO} significantly upregulated the JNK phosphorylation (Figure 5C), half reduction (*Ncald*^{KO/WT}) has no effect on the JNK activation (Supplementary Figure S7A), suggesting its safe use in SMA therapy.

Interestingly, increased JNK phosphorylation has also been detected in the spinal cord of SMA mice, which however is linked to reduced SMN levels and cellular stress response in spinal cord MNs (Genabai et al., 2015). Consequently, inhibition of JNK in SMA mice by using the D-JNKI1 inhibitor ameliorated the SMA pathology (Schellino et al., 2018). We speculate that different signaling pathways operate to regulate JNK signaling in SMA disease mouse model and in *Ncald* knockout condition. In this scenario, cellular stress response causes JNK activation in SMA mice, whereas *Ncald* knockout leads to the loss of MAP3K10–NCALD interaction, which causes the increased JNK phosphorylation in the brain.

Taken together, our study identifies a novel link between NCALD and adult neurogenesis in the hippocampus, possibly via

MAP3K10–JNK pathway and establishes the safety of NCALD reduction as viable option for a combinatorial therapy to treat SMA.

AUTHOR CONTRIBUTIONS

AU, BW and NK designed the project and wrote the manuscript and co-authors read and confirmed the finally submitted manuscript. AU carried out all experiments with the help of SH, SS, AK, LT-B, NM-F, MO, RR, VG, MK and NK. SH carried out the mass spectrometry and proteomics analysis. BW and NK supervised the project.

FUNDING

This work was supported by grants from the Deutsche Forschungsgemeinschaft (Wi-945/14-2, Wi 945/17-1; RTG 1960 to BW and KO5091/2-1 to NK), CMMC C16 (to BW), CECAD (Exc 229 to NK) and Fritz Thyssen Foundation (Az. 10.18.1.036 MN to NK).

ACKNOWLEDGMENTS

We thank the proteomics and imaging facility at the CECAD.

SUPPLEMENTARY MATERIAL

The Supplementary Material for this article can be found online at: <https://www.frontiersin.org/articles/10.3389/fnmol.2019.00019/full#supplementary-material>

REFERENCES

- Baptista, P., and Andrade, J. P. (2018). Adult hippocampal neurogenesis: regulation and possible functional and clinical correlates. *Front. Neuroanat.* 12:44. doi: 10.3389/fnana.2018.00044
- Ben-David, E., Granot-HersHKovitz, E., Monderer-Rothkoff, G., Lerer, E., Levi, S., Yaari, M., et al. (2011). Identification of a functional rare variant in autism using genome-wide screen for monoallelic expression. *Hum. Mol. Genet.* 20, 3632–3641. doi: 10.1093/hmg/ddr283
- Boccara, C. N., Sargolini, F., Thoresen, V. H., Solstad, T., Witter, M. P., Moser, E. I., et al. (2010). Grid cells in pre- and parasubiculum. *Nat. Neurosci.* 13, 987–994. doi: 10.1038/nn.2602
- Braunewell, K. H., and Klein-Szanto, A. J. (2009). Visinin-like proteins (VSNLs): interaction partners and emerging functions in signal transduction of a subfamily of neuronal Ca²⁺-sensor proteins. *Cell Tissue Res.* 335, 301–316. doi: 10.1007/s00441-008-0716-3
- Burgoyne, R. D. (2007). Neuronal calcium sensor proteins: generating diversity in neuronal Ca²⁺ signalling. *Nat. Rev. Neurosci.* 8, 182–193. doi: 10.1038/nrn2093
- Coffey, E. T. (2014). Nuclear and cytosolic JNK signalling in neurons. *Nat. Rev. Neurosci.* 15, 285–299. doi: 10.1038/nrn3729
- Couillard-Despres, S., Winner, B., Schaubeck, S., Aigner, R., Vroemen, M., Weidner, N., et al. (2005). Doublecortin expression levels in adult brain reflect neurogenesis. *Eur. J. Neurosci.* 21, 1–14. doi: 10.1111/j.1460-9568.2004.03813.x
- Di Sole, F., Vадnagara, K., Moe, O. W., and Babich, V. (2012). Calcineurin homologous protein: a multifunctional Ca²⁺-binding protein family. *Am. J. Physiol. Renal Physiol.* 303, F165–F179. doi: 10.1152/ajprenal.00628.2011
- Feldkötter, M., Schwarzer, V., Wirth, R., Wienker, T. F., and Wirth, B. (2002). Quantitative analyses of SMN1 and SMN2 based on real-time lightCycler PCR: fast and highly reliable carrier testing and prediction of severity of spinal muscular atrophy. *Am. J. Hum. Genet.* 70, 358–368. doi: 10.1086/338627
- Finkel, R. S., Mercuri, E., Darras, B. T., Connolly, A. M., Kuntz, N. L., Kirschner, J., et al. (2017). Nusinersen versus sham control in infantile-onset spinal muscular atrophy. *N. Engl. J. Med.* 377, 1723–1732. doi: 10.1056/NEJMoa1702752
- Finkel, R. S., Mercuri, E., Meyer, O. H., Simonds, A. K., Schroth, M. K., Graham, R. J., et al. (2018). Diagnosis and management of spinal muscular atrophy: part 2: pulmonary and acute care; medications, supplements and immunizations; other organ systems; and ethics. *Neuromuscul. Disord.* 28, 197–207. doi: 10.1016/j.nmd.2017.11.004
- Fuss, J., Biedermann, S. V., Falfan-Melgoza, C., Auer, M. K., Zheng, L., Steinle, J., et al. (2014). Exercise boosts hippocampal volume by preventing early age-related gray matter loss. *Hippocampus* 24, 131–134. doi: 10.1002/hipo.22227
- Genabai, N. K., Ahmad, S., Zhang, Z., Jiang, X., Gabaldon, C. A., and Gangwani, L. (2015). Genetic inhibition of JNK3 ameliorates spinal muscular atrophy. *Hum. Mol. Genet.* 24, 6986–7004. doi: 10.1093/hmg/ddv401
- Gensel, J. C., Schonberg, D. L., Alexander, J. K., Mctigue, D. M., and Popovich, P. G. (2010). Semi-automated Sholl analysis for quantifying changes in growth and differentiation of neurons and glia. *J. Neurosci. Methods* 190, 71–79. doi: 10.1016/j.jneumeth.2010.04.026
- Girard, F., Venail, J., Schwaller, B., and Celio, M. R. (2015). The EF-hand Ca(2+)-binding protein super-family: a genome-wide analysis of gene expression patterns in the adult mouse brain. *Neuroscience* 294, 116–155. doi: 10.1016/j.neuroscience.2015.02.018
- Hirai, S., Katoh, M., Terada, M., Kyriakis, J. M., Zon, L. I., Rana, A., et al. (1997). MST/MLK2, a member of the mixed lineage kinase family, directly phosphorylates and activates SEK1, an activator of c-Jun N-terminal kinase/stress-activated protein kinase. *J. Biol. Chem.* 272, 15167–15173. doi: 10.1074/jbc.272.24.15167

- Hirai, S., Kawaguchi, A., Hirasawa, R., Baba, M., Ohnishi, T., and Ohno, S. (2002). MAPK-upstream protein kinase (MUK) regulates the radial migration of immature neurons in telencephalon of mouse embryo. *Development* 129, 4483–4495.
- Hochgerner, H., Zeisel, A., Lönnerberg, P., and Linnarsson, S. (2018). Conserved properties of dentate gyrus neurogenesis across postnatal development revealed by single-cell RNA sequencing. *Nat. Neurosci.* 21, 290–299. doi: 10.1038/s41593-017-0056-2
- Hosseini-Barkoobi, S., Peters, M., Torres-Benito, L., Rastetter, R. H., Hupperich, K., Hoffmann, A., et al. (2016). The power of human protective modifiers: PLS3 and CORO1C unravel impaired endocytosis in spinal muscular atrophy and rescue SMA phenotype. *Am. J. Hum. Genet.* 99, 647–665. doi: 10.1016/j.ajhg.2016.07.014
- Hoy, S. M. (2017). Nusinersen: first global approval. *Drugs* 77, 473–479. doi: 10.1007/s40265-017-0711-7
- Iino, S., Kobayashi, S., Okazaki, K., and Hidaka, H. (1995). Neurocalcin-immunoreactive receptor cells in the rat olfactory epithelium and vomeronasal organ. *Neurosci. Lett.* 191, 91–94. doi: 10.1016/0304-3940(95)11568-2
- Ivings, L., Pennington, S. R., Jenkins, R., Weiss, J. L., and Burgoyne, R. D. (2002). Identification of Ca^{2+} -dependent binding partners for the neuronal calcium sensor protein neurocalcin delta: interaction with actin, clathrin and tubulin. *Biochem. J.* 363, 599–608. doi: 10.1042/0264-6021.3630599
- Kedracka-Krok, S., Swiderska, B., Jankowska, U., Skupien-Rabian, B., Solich, J., Buczak, K., et al. (2015). Clozapine influences cytoskeleton structure and calcium homeostasis in rat cerebral cortex and has a different proteomic profile than risperidone. *J. Neurochem.* 132, 657–676. doi: 10.1111/jnc.13007
- Kononenko, N. L., Claßen, G. A., Kuijpers, M., Puchkov, D., Maritzen, T., Tempes, A., et al. (2017). Retrograde transport of TrkB-containing autophagosomes via the adaptor AP-2 mediates neuronal complexity and prevents neurodegeneration. *Nat. Commun.* 8:14819. doi: 10.1038/ncomms14819
- Kononenko, N. L., Diril, M. K., Puchkov, D., Kintscher, M., Koo, S. J., Pfuhl, G., et al. (2013). Compromised fidelity of endocytic synaptic vesicle protein sorting in the absence of stonin 2. *Proc. Natl. Acad. Sci. U S A* 110, E526–E535. doi: 10.1073/pnas.1218432110
- Ladant, D. (1995). Calcium and membrane binding properties of bovine neurocalcin delta expressed in *Escherichia coli*. *J. Biol. Chem.* 270, 3179–3185.
- Lang, J., Maeda, Y., Bannerman, P., Xu, J., Horiuchi, M., Pleasure, D., et al. (2013). Adenomatous polyposis coli regulates oligodendroglial development. *J. Neurosci.* 33, 3113–3130. doi: 10.1523/jneurosci.3467-12.2013
- Mendell, J. R., Al-Zaidy, S., Shell, R., Arnold, W. D., Rodino-Klapac, L. R., Prior, T. W., et al. (2017). Single-dose gene-replacement therapy for spinal muscular atrophy. *N. Engl. J. Med.* 377, 1713–1722. doi: 10.1056/NEJMoa1706198
- Mercuri, E., Darras, B. T., Chiriboga, C. A., Day, J. W., Campbell, C., Connolly, A. M., et al. (2018a). Nusinersen versus sham control in later-onset spinal muscular atrophy. *N. Engl. J. Med.* 378, 625–635. doi: 10.1056/NEJMoa1710504
- Mercuri, E., Finkel, R. S., Muntoni, F., Wirth, B., Montes, J., Main, M., et al. (2018b). Diagnosis and management of spinal muscular atrophy: part 1: recommendations for diagnosis, rehabilitation, orthopedic and nutritional care. *Neuromuscul. Disord.* 28, 103–115. doi: 10.1016/j.nmd.2017.11.005
- Miller, J. A., Woltjer, R. L., Goodenbour, J. M., Horvath, S., and Geschwind, D. H. (2013). Genes and pathways underlying regional and cell type changes in Alzheimer's disease. *Genome Med.* 5:48. doi: 10.1186/gm452
- Mohammad, H., Marchisella, F., Ortega-Martinez, S., Hollos, P., Eerola, K., Komulainen, E., et al. (2018). JNK1 controls adult hippocampal neurogenesis and imposes cell-autonomous control of anxiety behaviour from the neurogenic niche. *Mol. Psychiatry* 23:487. doi: 10.1038/mp.2017.21
- Molyneux, B. J., Arlotta, P., Menezes, J. R., and Macklis, J. D. (2007). Neuronal subtype specification in the cerebral cortex. *Nat. Rev. Neurosci.* 8, 427–437. doi: 10.1038/nrn2151
- Movsas, T. Z., Pinto-Martin, J. A., Whitaker, A. H., Feldman, J. F., Lorenz, J. M., Korzeniewski, S. J., et al. (2013). Autism spectrum disorder is associated with ventricular enlargement in a low birth weight population. *J. Pediatr.* 163, 73–78. doi: 10.1016/j.jpeds.2012.12.084
- Oikawa, K., Otero, G. L., Nafez, S., Ge, N., Zhang, D., Kobayashi, H., et al. (2016). Visinin-like protein-3 modulates the interaction between cytochrome b_5 and NADH-cytochrome b_5 reductase in a Ca^{2+} -dependent manner. *Cell Biochem. Biophys.* 74, 449–457. doi: 10.1007/s12013-016-0753-6
- O'Rourke, M., Gasperini, R., and Young, K. M. (2014). Adult myelination: wrapping up neuronal plasticity. *Neural Regen. Res.* 9, 1261–1264. doi: 10.4103/1673-5374.137571
- Overstreet-Wadiche, L. S., and Westbrook, G. L. (2006). Functional maturation of adult-generated granule cells. *Hippocampus* 16, 208–215. doi: 10.1002/hipo.20152
- Panov, A. V., Kubalik, N., Zinchenko, N., Ridings, D. M., Radoff, D. A., Hemendinger, R., et al. (2011). Metabolic and functional differences between brain and spinal cord mitochondria underlie different predisposition to pathology. *Am. J. Physiol. Regul. Integr. Comp. Physiol.* 300, R844–R854. doi: 10.1152/ajpregu.00528.2010
- Pekny, M., and Pekna, M. (2014). Astrocyte reactivity and reactive astrogliosis: costs and benefits. *Physiol. Rev.* 94, 1077–1098. doi: 10.1152/physrev.00041.2013
- Pletnikov, M. V., Ayhan, Y., Xu, Y., Nikolskaia, O., Ovanesov, M., Huang, H., et al. (2008). Enlargement of the lateral ventricles in mutant DISC1 transgenic mice. *Mol. Psychiatry* 13:115. doi: 10.1038/sj.mp.4002144
- Radic, T., Friess, L., Vijikumar, A., Jungenitz, T., Deller, T., and Schwarzscher, S. W. (2017). Differential postnatal expression of neuronal maturation markers in the dentate gyrus of mice and rats. *Front. Neuroanat.* 11:104. doi: 10.3389/fnana.2017.00104
- Riessland, M., Kaczmarek, A., Schneider, S., Swoboda, K. J., Lohr, H., Bradler, C., et al. (2017). Neurocalcin delta suppression protects against spinal muscular atrophy in humans and across species by restoring impaired endocytosis. *Am. J. Hum. Genet.* 100, 297–315. doi: 10.1016/j.ajhg.2017.01.005
- Rigo, F., Chun, S. J., Norris, D. A., Hung, G., Lee, S., Matson, J., et al. (2014). Pharmacology of a central nervous system delivered 2'-O-methoxyethyl-modified survival of motor neuron splicing oligonucleotide in mice and non-human primates. *J. Pharmacol. Exp. Ther.* 350, 46–55. doi: 10.1124/jpet.113.212407
- Schellino, R., Boido, M., Borsello, T., and Vercelli, A. (2018). Pharmacological c-Jun NH2-terminal kinase (JNK) pathway inhibition reduces severity of spinal muscular atrophy disease in mice. *Front. Mol. Neurosci.* 11:308. doi: 10.3389/fnmol.2018.00308
- Scholzen, T., and Gerdes, J. (2000). The Ki-67 protein: from the known and the unknown. *J. Cell. Physiol.* 182, 311–322. doi: 10.1002/(SICI)1097-4652(200003)182:3<311::AID-JCP1>3.0.CO;2-9
- Scoto, M., Finkel, R. S., Mercuri, E., and Muntoni, F. (2017). Therapeutic approaches for spinal muscular atrophy (SMA). *Gene Ther.* 24, 514–519. doi: 10.1038/gt.2017.45
- Shimohama, S., Chachin, M., Taniguchi, T., Hidaka, H., and Kimura, J. (1996). Changes of neurocalcin, a calcium-binding protein, in the brain of patients with Alzheimer's disease. *Brain Res.* 716, 233–236. doi: 10.1016/0006-8993(96)00070-4
- Sibbe, M., Kuner, E., Althof, D., and Frotscher, M. (2015). Stem- and progenitor cell proliferation in the dentate gyrus of the reeler mouse. *PLoS One* 10:e0119643. doi: 10.1371/journal.pone.0119643
- Smith, G. N., Thornton, A. E., Lang, D. J., Macewan, G. W., Ehmann, T. S., Kopala, L. C., et al. (2012). Hippocampal volume and the brain-derived neurotrophic factor Val66Met polymorphism in first episode psychosis. *Schizophr. Res.* 134, 253–259. doi: 10.1016/j.schres.2011.11.022
- Talbot, K., and Tizzano, E. F. (2017). The clinical landscape for SMA in a new therapeutic era. *Gene Ther.* 24, 529–533. doi: 10.1038/gt.2017.52
- Threadgill, R., Bobb, K., and Ghosh, A. (1997). Regulation of dendritic growth and remodeling by Rho, Rac, and Cdc42. *Neuron* 19, 625–634. doi: 10.1016/s0896-6273(00)80376-1
- Vercauteren, F. G., Flores, G., Ma, W., Chabot, J. G., Geenen, L., Clerens, S., et al. (2007). An organelle proteomic method to study neurotransmission-related proteins, applied to a neurodevelopmental model of schizophrenia. *Proteomics* 7, 3569–3579. doi: 10.1002/pmic.200700379
- Voineskos, A. N., Winterburn, J. L., Felsky, D., Pipitone, J., Rajji, T. K., Mulsant, B. H., et al. (2015). Hippocampal (subfield) volume and shape in relation to cognitive performance across the adult lifespan. *Hum. Brain Mapp.* 36, 3020–3037. doi: 10.1002/hbm.22825

- Wang, W., Zhou, Z., Zhao, W., Huang, Y., Tang, R., Ying, K., et al. (2001). Molecular cloning, mapping and characterization of the human neurocalcin delta gene (NCALD). *Biochim. Biophys. Acta* 1518, 162–167. doi: 10.1016/s0167-4781(00)00290-6
- Wirth, B., Barkats, M., Martinat, C., Sendtner, M., and Gillingwater, T. H. (2015). Moving towards treatments for spinal muscular atrophy: hopes and limits. *Expert Opin. Emerg. Drugs* 20, 353–356. doi: 10.1517/14728214.2015.1041375
- Wirth, B., Brichta, L., Schrank, B., Lochmuller, H., Blick, S., Baasner, A., et al. (2006). Mildly affected patients with spinal muscular atrophy are partially protected by an increased SMN2 copy number. *Hum. Genet.* 119, 422–428. doi: 10.1007/s00439-006-0156-7
- Witter, M. P., Wouterlood, F. G., Naber, P. A., and Van Haeften, T. (2000). Anatomical organization of the parahippocampal-hippocampal network. *Ann. N. Y. Acad. Sci.* 911, 1–24. doi: 10.1111/j.1749-6632.2000.tb06716.x
- Xu, W., Cohen-Woods, S., Chen, Q., Noor, A., Knight, J., Hosang, G., et al. (2014). Genome-wide association study of bipolar disorder in Canadian and UK populations corroborates disease loci including SYNE1 and CSMD1. *BMC Med. Genet.* 15:2. doi: 10.1186/1471-2350-15-2
- Yamatani, H., Kawasaki, T., Mita, S., Inagaki, N., and Hirata, T. (2010). Proteomics analysis of the temporal changes in axonal proteins during maturation. *Dev. Neurobiol.* 70, 523–537. doi: 10.1002/dneu.20794
- Zhao, C., Teng, E. M., Summers, R. G. Jr., Ming, G. L., and Gage, F. H. (2006). Distinct morphological stages of dentate granule neuron maturation in the adult mouse hippocampus. *J. Neurosci.* 26, 3–11. doi: 10.1523/jneurosci.3648-05.2006

Conflict of Interest Statement: The authors declare that the research was conducted in the absence of any commercial or financial relationships that could be construed as a potential conflict of interest.

Copyright © 2019 Upadhyay, Hosseinibarkoie, Schneider, Kaczmarek, Torres-Benito, Mendoza-Ferreira, Overhoff, Rombo, Grysko, Kye, Kononenko and Wirth. This is an open-access article distributed under the terms of the Creative Commons Attribution License (CC BY). The use, distribution or reproduction in other forums is permitted, provided the original author(s) and the copyright owner(s) are credited and that the original publication in this journal is cited, in accordance with accepted academic practice. No use, distribution or reproduction is permitted which does not comply with these terms.



CHRNA2 and Nocturnal Frontal Lobe Epilepsy: Identification and Characterization of a Novel Loss of Function Mutation

Chiara Villa^{1†}, Giulia Colombo^{2†}, Simone Meneghini², Cecilia Gotti³, Milena Moretti⁴, Luigi Ferini-Strambi^{5*}, Elisa Chisci¹, Roberto Giovannoni^{1‡}, Andrea Becchetti² and Romina Combi^{1*}

¹ School of Medicine and Surgery, University of Milano – Bicocca, Monza, Italy, ² Department of Biotechnology and Biosciences, University of Milano – Bicocca, Milan, Italy, ³ CNR, Institute of Neuroscience, Milan, Italy, ⁴ Department of Medical Biotechnology and Translational Medicine, University of Milan, Milan, Italy, ⁵ Department of Clinical Neurosciences, San Raffaele Scientific Institute, Sleep Disorders Center, Vita-Salute San Raffaele University, Milan, Italy

OPEN ACCESS

Edited by:

Antoine Taly,
Centre National de la Recherche
Scientifique (CNRS), France

Reviewed by:

Pierre-Jean Corringer,
Institut Pasteur, France
Fabio Marti,
Institut National de la Santé et de la
Recherche Médicale (INSERM),
France

*Correspondence:

Luigi Ferini-Strambi
ferinistrambi.luigi@hsr.it
Romina Combi
romina.combi@unimib.it

[†] These authors have contributed
equally to this work

*Present address:

Roberto Giovannoni,
Genetics Unit, Department of Biology,
University of Pisa, Pisa, Italy

Received: 05 September 2018

Accepted: 17 January 2019

Published: 12 February 2019

Citation:

Villa C, Colombo G, Meneghini S,
Gotti C, Moretti M, Ferini-Strambi L,
Chisci E, Giovannoni R, Becchetti A
and Combi R (2019) CHRNA2
and Nocturnal Frontal Lobe Epilepsy:
Identification and Characterization of a
Novel Loss of Function Mutation.
Front. Mol. Neurosci. 12:17.
doi: 10.3389/fnmol.2019.00017

Mutations in genes coding for subunits of the neuronal nicotinic acetylcholine receptor (nAChR) have been involved in familial sleep-related hypermotor epilepsy (also named autosomal dominant nocturnal frontal lobe epilepsy, ADNFLE). Most of these mutations reside in *CHRNA4* and *CHRNA2* genes, coding for the $\alpha 4$ and $\beta 2$ nAChR subunits, respectively. Two mutations with contrasting functional effects were also identified in the *CHRNA2* gene coding for the $\alpha 2$ subunit. Here, we report the third mutation in the *CHRNA2*, found in a patient showing ADNFLE. The patient was examined by scalp EEG, contrast-enhanced brain magnetic resonance imaging (MRI), and nocturnal video-polysomnographic recording. All exons and the exon-intron boundaries of *CHRNA2*, *CHRNA4*, *CHRNA2*, *CRH*, *KCNT1* were amplified and Sanger sequenced. In the proband, we found a c.754T>C (p.Tyr252His) missense mutation located in the N-terminal ligand-binding domain and inherited from the mother. Functional studies were performed by transient co-expression of $\alpha 2$ and $\alpha 2^{\text{Tyr252His}}$, with either $\beta 2$ or $\beta 4$, in human embryonic kidney (HEK293) cells. Equimolar amounts of subunits expression were obtained by using F2A-based multi-cistronic constructs encoding for the genes relative to the nAChR subunits of interest and for the enhanced green fluorescent protein. The mutation reduced the maximal currents by approximately 80% in response to saturating concentrations of nicotine in homo- and heterozygous form, in both the $\alpha 2\beta 4$ and $\alpha 2\beta 2$ nAChR subtypes. The effect was accompanied by a strong right-shift of the concentration-response to nicotine. Similar effects were observed using ACh. Negligible effects were produced by $\alpha 2^{\text{Tyr252His}}$ on the current reversal potential. Moreover, binding of (\pm)-[³H]Epibatidine revealed an approximately 10-fold decrease of both K_d and B_{max} (bound ligand in saturating conditions), in cells expressing $\alpha 2^{\text{Tyr252His}}$. The reduced B_{max} and whole-cell currents were not caused by a decrease in mutant receptor expression, as minor effects were produced by $\alpha 2^{\text{Tyr252His}}$ on the level of transcripts and the membrane expression of $\alpha 2\beta 4$ nAChR. Overall, these results suggest

that $\alpha 2^{\text{Tyr252His}}$ strongly reduced the number of channels bound to the agonist, without significantly altering the overall channel expression. We conclude that mutations in *CHRNA2* are more commonly linked to ADNFLE than previously thought, and may cause a loss-of-function phenotype.

Keywords: ADNFLE, ADSHE, genetics, frontal lobe epilepsy, nicotinic receptor, patch-clamp

INTRODUCTION

ADNFLE, also known as autosomal dominant sleep-related hypermotor epilepsy (ADSHE) (Tinuper et al., 2016) is a familial idiopathic focal epilepsy with increased nocturnal instability (Sansoni et al., 2013), characterized by a wide spectrum of brief stereotyped hypermotor seizures, mostly occurring during non-rapid eye movement (non-REM) sleep. About the 80% of individuals develop ADNFLE in the first two decades of life and mean age of onset is 10 years (Nobili et al., 2014; Tinuper et al., 2016). Within a family, the manifestation of the disorder may vary considerably, and no clear difference between sexes is observed.

ADNFLE was the first epilepsy to be recognized as a channelopathy, i.e., a disease resulting from ion channel dysfunction, after the identification of the first mutation in the *CHRNA4* gene, coding for the $\alpha 4$ nAChR subunit (Steinlein et al., 1995). Subsequently, evidence has grown about the role of nAChRs in the pathophysiology of ADNFLE (Ferini-Strambi et al., 2012). Nonetheless, mutations in nAChR genes are rare and the involvement of other genes implicated in ADNFLE has been recognized since 2005 (Combi et al., 2005b). In fact, mutations were also found in *KCNT1* (coding for a sodium-dependent K^+ channel) (Heron et al., 2012) as well as in genes not coding for ion channels, such as *CRH* (corticotropin-releasing hormone) (Combi et al., 2005a) and *DEPDC5* (Disheveled, Egl-10 and Pleckstrin Domain-containing protein 5) (Ishida et al., 2013).

The nAChR is a pentameric ion channel formed by various combinations of α and β subunits, which determine the physiological and pharmacological properties of each subtype (Dani and Bertrand, 2007). Most ADNFLE mutations of the nAChR were found in the genes coding the $\alpha 4$ (Steinlein et al., 1995), and $\beta 2$ (De Fusco et al., 2000; Phillips et al., 2001) subunits, in agreement with the prevalence of the $\alpha 4\beta 2$ subtype in the mammalian brain (Zoli et al., 2015). When expressed in *Xenopus laevis* oocytes or mammalian cell lines, mutant subunits tend to confer a gain-of-function phenotype, especially in the simulated heterozygote, because of increased receptor's sensitivity to the agonist or other kinetic alterations (Becchetti et al., 2015). Several hypotheses concerning the nAChR-dependent pathogenetic mechanism have been proposed (Nobili et al., 2014). These are difficult to demonstrate considering that nAChRs are expressed in the brain at pre-, post-, and extra-synaptic locations (Dani and Bertrand, 2007), and they regulate both excitatory and inhibitory transmission (Becchetti et al., 2015). In prefrontal regions, heteromeric nAChRs exert a widespread stimulatory effect on glutamatergic transmission (Vidal and Changeux, 1993; Lambe et al., 2003; Aracri et al., 2013). These receptors also regulate GABAergic interneurons (Porter et al., 1999; Alkondon

et al., 2000; Couey et al., 2007) although the expression of heteromeric nAChRs in these cells is more variable, depending on neuronal subtype and age (Porter et al., 1999; Couey et al., 2007; Aracri et al., 2010, 2017).

Understanding the nAChR-dependent pathogenesis of ADNFLE is made even more complex by the involvement of *CHRNA2*. Two mutations with opposite effects on the channel functioning were previously reported in the *CHRNA2* gene, coding for the nAChR $\alpha 2$ subunit. In particular, the p.Ile279Asn increases the receptor sensitivity to the agonists (Aridon et al., 2006), whereas the p.Ile297Phe mutation presents a strongly decreased current density as compared to the WT, but scarce alteration of the conductive properties and the sensitivity to nicotine (Conti et al., 2015). Mutations in the *CHRNA2* are rare in the Italian ADNFLE population (Combi et al., 2009). Hence, it is important to determine whether *CHRNA2* mutations can be a significant etiologic factor in sleep-related hypermotor epilepsy, and what is the prevalent pathogenetic mechanism. Here, we report the third *CHRNA2* mutation detected in an ADNFLE patient, showing a loss of function effect when expressed in human cell lines.

MATERIALS AND METHODS

Sample Composition and Genetic Analysis

The de-identified DNA of three individuals (one affected by NFLE and his parents) was isolated from leftover venous blood samples. Clinical samples and data were collected according to Italian authority laws on privacy protection (G.U. n. 72 26/03/2012) and genetic data (G.U. n. 159 11/07/2011), in compliance with the General Data Protection Regulation (EU Directive 2016/679) and with written consent from all subjects. The patient (>18 years old) and his parents signed a written informed consent form for the use of their biological materials for genetic and clinical research in accordance with the Helsinki declaration. No sensitive data are included in the manuscript.

A video-polysomnographic analysis allowed a correct diagnosis of NFLE.

Polymerase chain reactions (PCRs) were performed directly on 50–100 ng of genomic DNA in a 25 μL volume. Each reaction was performed using the PCR Master Mix (Promega, Madison, WI, United States). PCRs were carried out on Mastercycler Ep Gradient thermomodules (Eppendorf, Milan, Italy) under standard conditions. Primers used for amplification and sequencing reactions (Life Technologies, Inchinnan, Paisley, United Kingdom) were designed using the Oligo 6.0 software

(Molecular Biology Insights Inc., Cascade, CO, United States) on the basis of the genomic sequences of known genes and can be provided upon request. Sequencing was carried out directly on both strands of purified PCR products by using the BigDye Terminator Cycle Sequencing kit v1.1 and an automated ABI-3130 DNA sequencer (Applied Biosystems, Foster City, CA, United States). ChromasPro v1.34 (Technelysium Pty Ltd.) software was used for mutation detection. The pathogenicity was predicted using PolyPhen-2¹, SIFT², and MutationTaster³ bioinformatic tools.

Plasmid Constructs and Expression Vectors

Four F2A system-based tricistronic vectors for the expression of either the $\alpha 2/\beta 2$ or the $\alpha 2/\beta 4$ receptors, both in the presence or absence of the *CHRNA2* mutation were obtained following a strategy similar to those previously reported by Ryan and Drew (1994). To facilitate detection of the transfected cells, each vector also encoded for the e-GFP (enhanced green fluorescent protein) as a valuable reporter molecule. Briefly, the e-GFP coding sequence (CDS) was amplified without the stop codon and cloned into a *Bam*HI/*Bgl*II-digested pCX plasmid, to produce the pCX-eGFP (deltaTAG) vector. The first F2A sequence (F2A1), obtained as previously described (De Giorgi et al., 2015), was ligated by directional cloning downstream the eGFP sequence into the pCX-eGFP (deltaTAG) plasmid. The *CHRNA2* CDS (NCBI: NM_000742.3) was PCR-amplified removing the stop codon and cloned downstream the F2A1 sequence. The second F2A sequence (F2A2) was first amplified and then ligated in frame downstream the *CHRNA2* sequence in order to obtain the pCX-eGFP-F2A1-*CHRNA2*(WT)-F2A2 plasmid. Finally, the CDS of either *CHRNA2* (NCBI: NM_000748.2) or *CHRNA4* (NCBI: NM_000750.4) sequences were PCR-amplified including the stop codon and cloned into the *Afl*III-linearized pCX-eGFP-F2A1-*CHRNA2*(WT)-F2A2 plasmid acceptor downstream the F2A2 sequence generating the final constructs, named pCX-eGFP-F2A1-*CHRNA2*(WT)-F2A2-*CHRNA2* and pCX-eGFP-F2A1-*CHRNA2*(WT)-F2A2-*CHRNA4*, respectively. For each PCR amplification, specific restriction sites were added at the 5'-end of both sequences to allow the directional cloning and each PCR product was firstly cloned into a pGEM T-Easy vector (Promega) as intermediate plasmid.

The p.Tyr252His (c.754T>C) *CHRNA2* mutation was introduced by Quick Change II XL Site Directed Mutagenesis Kit (Stratagene, La Jolla, CA, United States) into both pCX-eGFP-F2A1-*CHRNA2*(WT)-F2A2-*CHRNA2* and pCX-eGFP-F2A1-*CHRNA2*(WT)-F2A2-*CHRNA4* constructs, in order to obtain pCX-eGFP-F2A1-*CHRNA2*(MUT)-F2A2-*CHRNA2* and pCX-eGFP-F2A1-*CHRNA2*(MUT)-F2A2-*CHRNA4* plasmids, respectively. All the intermediate and final constructs were verified by sequencing analyses performed on both strands using an automated ABI-3130 DNA sequencer (Applied Biosystems, Foster City, CA, United States). All plasmids were

purified using the QIAGEN Plasmid Maxiprep kit (QIAGEN, Hilden, Germany) following the suggested protocol and resuspended in water.

Culture and Transfection Procedure

Plasmids expressing wild-type (WT) or mutant $\alpha 2\beta 2$ or $\alpha 2\beta 4$ were transiently transfected in HEK293 cells (TsA subclone; American Type Culture Collection) as reported (Conti et al., 2015). In brief, cells were cultured in DMEM high glucose (Dulbecco's modified Eagle medium high glucose; HyClone Laboratories, Logan, UT, United States) supplemented with 10% fetal calf serum (HyClone) and 2 mM L-glutamine, at 37°C and 5% CO₂. For patch-clamp experiments, cells were seeded onto 35-mm culture dishes. Transfection was carried out with Lipofectamine 2000 (Life Technologies). To simulate the heterozygous state, equal amounts of WT and mutant plasmids were cotransfected. The DNA concentration in the transfection mixture was 1.33 ng/ μ L. Cells were incubated with the transfection mixture for 5 h, at 37°C, and kept at 30°C in 5% CO₂ during the 24 h preceding the electrophysiological recordings, to enhance the surface receptor density (Cooper et al., 1999).

Patch-Clamp Recording

Chemicals and drugs for intra- and extracellular solutions were purchased from Sigma-Aldrich. The extracellular solution contained (mM): NaCl 130, KCl 5, CaCl₂ 2, MgCl₂ 2, HEPES 10, and D-glucose 5 (pH 7.3). Patch pipettes contained (mM): K-gluconate 140, KCl 5, MgCl₂ 1, BAPTA-KOH 0.5, HEPES 10, NaGTP 0.3, and MgATP 2 (pH 7.3). Stock solutions of nicotine (10 mM) were prepared weekly in our extracellular solution and kept refrigerated; acetylcholine (10 mM) and atropine (1 mM) were dissolved in extracellular solution, aliquoted and frozen until usage. Extracellular solutions with the appropriate agonist concentration were prepared daily; pH was always checked after nicotine addition.

Whole-cell currents were registered 36–72 h after transfection, with an Axopatch 200B amplifier (Molecular Devices, Sunnyvale, CA, United States), at room temperature. Micropipettes (3–5 M Ω) were pulled from borosilicate capillaries (Corning Inc., NY, United States) with a P-97 Flaming/Brown Puller (Sutter Instruments, Novato, CA, United States). Cell capacitance and series resistance (up to 75%) were always compensated. When necessary, the cell capacitance value thus measured was used to calculate the cell current density (i.e., the peak whole-cell current at a given V_m and agonist concentration was divided by the cell capacitance). Because the cell capacitance is proportional to the cell surface area, the calculated values are proportional to the current per unit area. Fluorescent cells were identified with an inverted Eclipse TE200 microscope (Nikon) equipped with a TE-FM epifluorescence attachment. Currents were low-pass-filtered at 2 kHz and acquired online at 10–20 kHz with pClamp nine hardware and software (Molecular Devices). Drugs were applied with an RSC-160 Rapid Solution Changer (Bio-Logic Science Instruments, Claix, France).

Patch-clamp data were analyzed with OriginPro 9 (OriginLab), as previously described (Brusco et al., 2015). Theoretical curves best fitting the data were calculated by a

¹<http://genetics.bwh.harvard.edu/pph2/>

²<http://sift.jcvi.org/>

³<http://www.mutationtaster.org/>

Levenberg-Marquardt algorithm. The concentration-response data were fitted by using a two-components Hill-type equation (Covernton and Connolly, 2000), as follows:

$$\frac{I_L}{I_{\max}} = \frac{A}{1 + \left(\frac{EC_{50\text{high}}}{[L]}\right)^{nH1}} + \frac{1 - A}{1 + \left(\frac{EC_{50\text{low}}}{[L]}\right)^{nH2}} \quad (1)$$

where I_{\max} is the maximal current, I_L is the current at a given concentration L of agonist, A is the fraction of receptors in the high-affinity state; $EC_{50\text{high}}$ and $EC_{50\text{low}}$ are the agonist concentrations producing the half-maximal effect for the high and low affinity components, respectively; $nH1$ and $nH2$ are the Hill coefficients for the two components.

cDNA Synthesis and Real-Time Quantitative PCR

Total RNA was isolated from cultured cells using Direct-zol RNA MiniPrep (Zymo Research) and eluted in water. One microgram of the total extracted amount of RNA was subsequently treated with DNase I and reverse-transcribed using SuperScript VILO cDNA Synthesis Kit (Invitrogen). The first-strand cDNA was used as a template for real-time PCR (RT-PCR) using a human *CHRNA2* specific primer pair (Fw 5'-GCTAAAACAGGAGTGGAGCG-3' and Rv 5'-TCGAAGGGGAAGAAGGTGAC-3') and EvaGreen fluorescent dye (Bio-Rad). PCR reaction was performed using a CFX96 Real-time system (Bio-Rad) sequence detector. Data, normalized to eGFP transcript levels, are expressed as fold change value respect to the untransfected cells according to the $2^{-[\Delta\Delta C(q)]}$ algorithm.

Western Blotting

The anti- $\alpha 2$ and $\beta 4$ Abs were produced in rabbits immunized with the human peptides CHPLRLKLSPSYHWLESNVDA EEREV ($\alpha 2$) and GPDSSPARAFPPSKSCVTKEATATSP ($\beta 4$), respectively, affinity purified and characterized as previously described (Mazzo et al., 2013).

SDS-PAGE and blotting were carried out by standard procedures. In brief, 20 μg of proteins obtained from HEK 293 cells transfected with $\alpha 2\beta 4$, $\alpha 2^{\text{Tyr252His}}\beta 4$, or from non-transfected HEK293 cells were loaded separated by means of SDS-polyacrylamide gel electrophoresis using 9% acrylamide, and electrophoretically transferred to nitrocellulose membranes with 0.45 mm pores (Schleicher and Schull, Dassel, Germany). The blots were blocked overnight in 4% non-fat milk in Tris-buffered saline, washed in a buffer containing 4% non-fat milk and 0.3% Tween 20 in Tris-buffered saline, and incubated for 2 h with the primary antibody at the concentration of 5 $\mu\text{g}/\text{ml}$. They were then incubated for 1 h with the appropriate secondary antibody (anti-rabbit Ly-Cor IRDye800RD). After washing, the membranes were dried overnight in the dark at room temperature. The IR signal was measured using an Odyssey CLx – Infrared Imaging System. The signal intensity of the Western blot bands was quantified using iStudio software.

Radioligand Binding Assays

(\pm)-[^3H]Epibatidine (specific activity of 56–60 Ci/mmol) was purchased from Perkin Elmer (Boston, MA, United States). Non-radioactive epibatidine was purchased from Sigma-Aldrich. Saturation experiments were performed by incubating aliquots of membranes from HEK293 cells expressing $\alpha 2\beta 4$ or $\alpha 2^{\text{Tyr252His}}\beta 4$ nAChR with 0.01–5 nM concentrations of (\pm)-[^3H]Epibatidine (Perkin Elmer) overnight at 4°C. Non-specific binding was determined in parallel by incubation in the presence of 100 nM unlabeled epibatidine. After incubation, the samples were filtered on GFC filters soaked in 0.5% polyethyleneimine and washed with 15 mL ice-cold phosphate buffered saline (PBS) and the filters were counted for radioactivity in a β counter.

Statistical Analysis

Data are generally given as mean values \pm standard error of the mean, with n representing the number of experiments (tested cells, in the case of patch-clamp experiments). Statistical comparisons between two populations of data were carried out with a Student's t -test for unpaired samples, after checking for data normality (Kolmogorov–Smirnov test) and variance homogeneity (F -test). The Welch correction was applied in case of non-homogeneous variances. Multiple comparisons were carried out with one-way ANOVA, followed by Tukey *post hoc* test, after checking for data normality (Kolmogorov–Smirnov test) and variance homogeneity (Brown–Forsythe test). The level of statistical significance was set at $p < 0.05$. Data from saturation binding assays were evaluated by saturation binding curve-fitting procedures using GraphPad Prism version 6 (GraphPad Software, Inc., CA, United States).

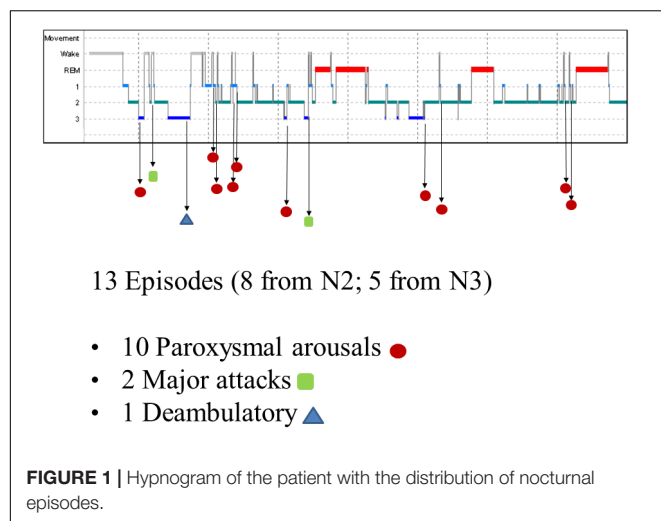
RESULTS

Clinical and Neurophysiological Studies in the Proband Carrying the p.Tyr252His *CHRNA2* Mutation

A 19-year-old right-handed man was referred for nocturnal episodes with abnormal motor-behavioral phenomena occurring several times every night. The episodes started at the age of 13 years. The majority of episodes were characterized by sudden vocalization with grunting followed by dystonic posturing; sometimes (2–3 episodes for week) a deambulatory behavior was reported. There was a family history of nocturnal confusional arousals in the mother during her adolescence: confusional arousal episodes occurred in the first part of the night (1–5 episodes for week, from age 13 to 16 years), in these episodes (5–20 s in duration) the mother sat up in bed and looked around in a confused manner.

Scalp EEG monitoring during wakefulness as well as the contrast-enhanced brain magnetic resonance imaging (MRI) were normal. Neurological examination was also normal.

The nocturnal video-PSG recording showed 13 episodes, 8 in stage N2 and 5 in stage N3. Ten of these were classified



as paroxysmal arousals, characterized by sudden arousals (5–8 s in duration) with stereotyped movements of arms and vocalization. Two episodes (16 and 19 s in duration, respectively) characterized by asymmetric dystonic posturing were classified as major attacks. The last episode was a deambulatory behavior with frightened expression and fear. **Figure 1** shows the hypnogram with the distribution of nocturnal attacks registered in one night.

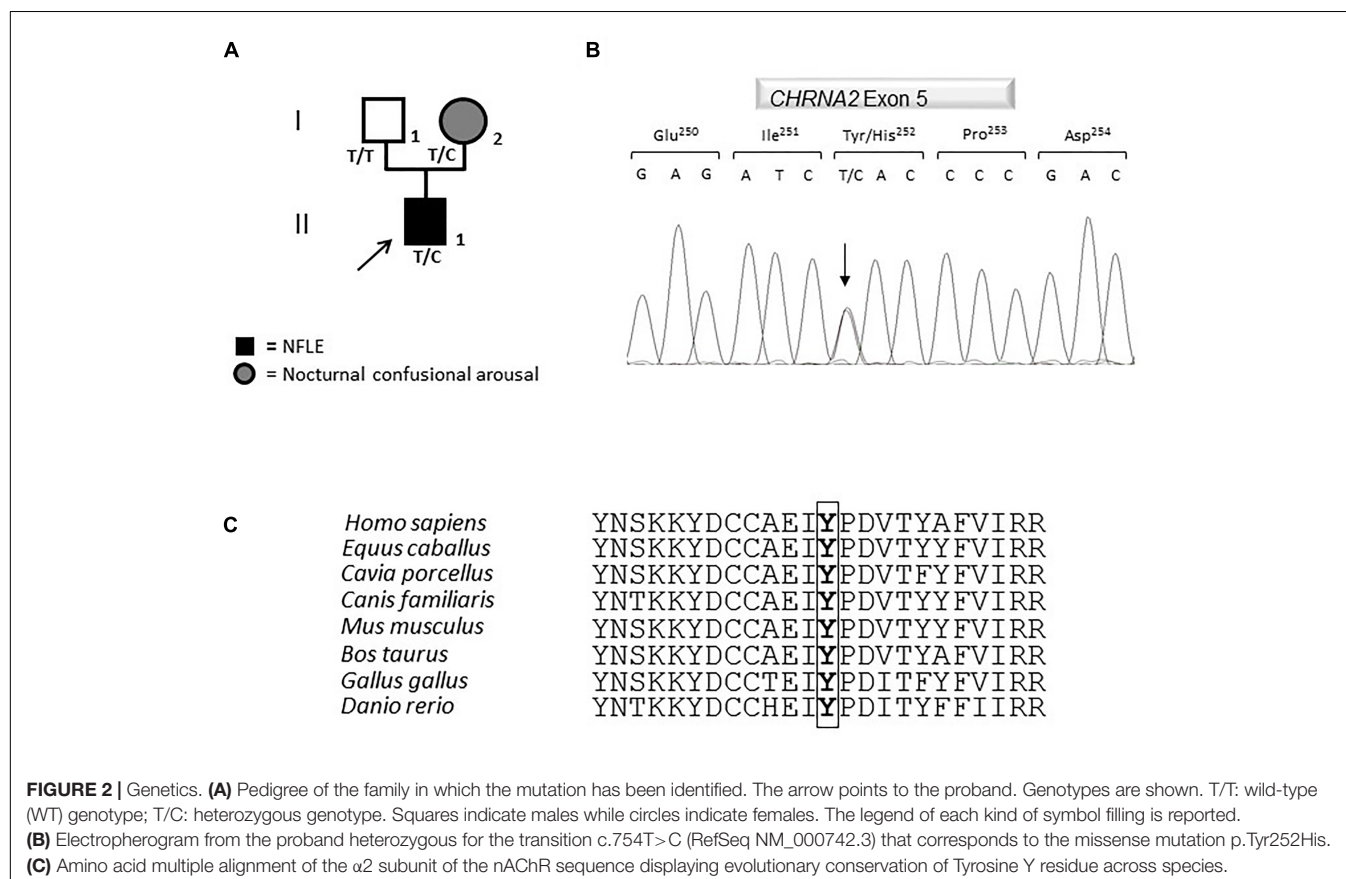
The EEG before, during and after the episodes did not show any epileptiform activity, but in eight episodes showed ictal rhythmic slow activity over anterior areas. A marked reduction of the nocturnal episodes was observed with the administration of carbamazepine (600 mg/day, single bedtime dose).

Mutation Screening

The coding region, intron-exon boundaries and UTRs of *CHRNA4*, *CHRNA2*, *CHRNA2*, *CRH*, *KCNT1* genes previously associated with ADNFLE were amplified and Sanger sequenced. This work revealed that the proband is a heterozygote for a missense mutation in the *CHRNA2* gene (**Figure 2A**). Nucleotide numbering from here onward is according to cDNA position (GenBank accession number NM_000742.3 starting from the first nucleotide of the ATG start codon).

The mutation consists of a T>C transition at cDNA position 754 (c.754T>C), which leads to a non-conservative Tyr to His change at position 252 (p.Tyr252His, according to the Human Genome Variation guidelines) in the $\alpha 2$ subunit of the nAChR. Electropherograms of exon five encompassing the mutation are shown in **Figure 2B**. The variation was not reported yet and it was located in the N-terminal domain, in a highly conserved region (**Figure 2C**) involved in the acetylcholine binding.

A segregation analysis was performed and the mutation was found in the heterozygous state also in the affected proband's mother, while it was absent in the healthy father



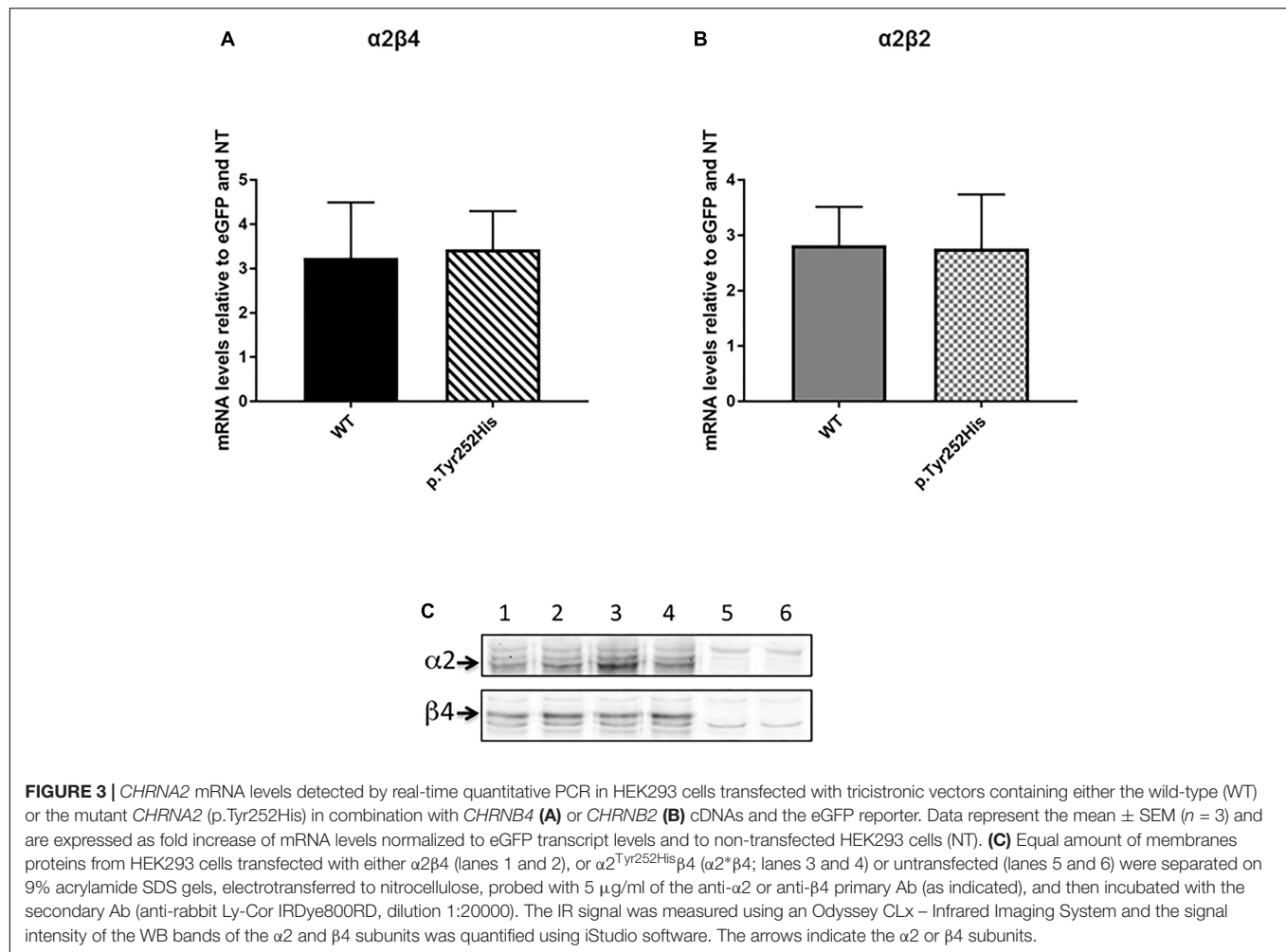


FIGURE 3 | *CHRNA2* mRNA levels detected by real-time quantitative PCR in HEK293 cells transfected with tricistronic vectors containing either the wild-type (WT) or the mutant *CHRNA2* (p.Tyr252His) in combination with *CHRNA4* (A) or *CHRNA2* (B) cDNAs and the eGFP reporter. Data represent the mean \pm SEM ($n = 3$) and are expressed as fold increase of mRNA levels normalized to eGFP transcript levels and to non-transfected HEK293 cells (NT). (C) Equal amount of membranes proteins from HEK293 cells transfected with either $\alpha 2\beta 4$ (lanes 1 and 2), or $\alpha 2^{Tyr252His}\beta 4$ ($\alpha 2^*\beta 4$; lanes 3 and 4) or untransfected (lanes 5 and 6) were separated on 9% acrylamide SDS gels, electrotransferred to nitrocellulose, probed with 5 μ g/ml of the anti- $\alpha 2$ or anti- $\beta 4$ primary Ab (as indicated), and then incubated with the secondary Ab (anti-rabbit Ly-Cor IRDye800RD, dilution 1:20000). The IR signal was measured using an Odyssey CLx – Infrared Imaging System and the signal intensity of the WB bands of the $\alpha 2$ and $\beta 4$ subunits was quantified using iStudio software. The arrows indicate the $\alpha 2$ or $\beta 4$ subunits.

(Figure 2A). The mother reported to have been affected by nocturnal confusional arousal in her adolescence but no clinical examinations are available to evaluate the existence of an undiagnosed NFLE phenotype.

Since the mutation had never been studied from a functional point of view, we performed a bioinformatic analysis using Polyphen-2, SIFT or MutationTaster, in order to predict its possible effect on the channel functionality. The p.Tyr252His was predicted to be probably damaging by all these tools. This would be related to the fact that the mutation causes the substitution in an important functional domain of a polar but not charged amino acid with an aromatic R group (the Tyr) with another (the His) with a positively charged R group. Because the mutation was not reported yet, we decided to study its effects on the channel properties.

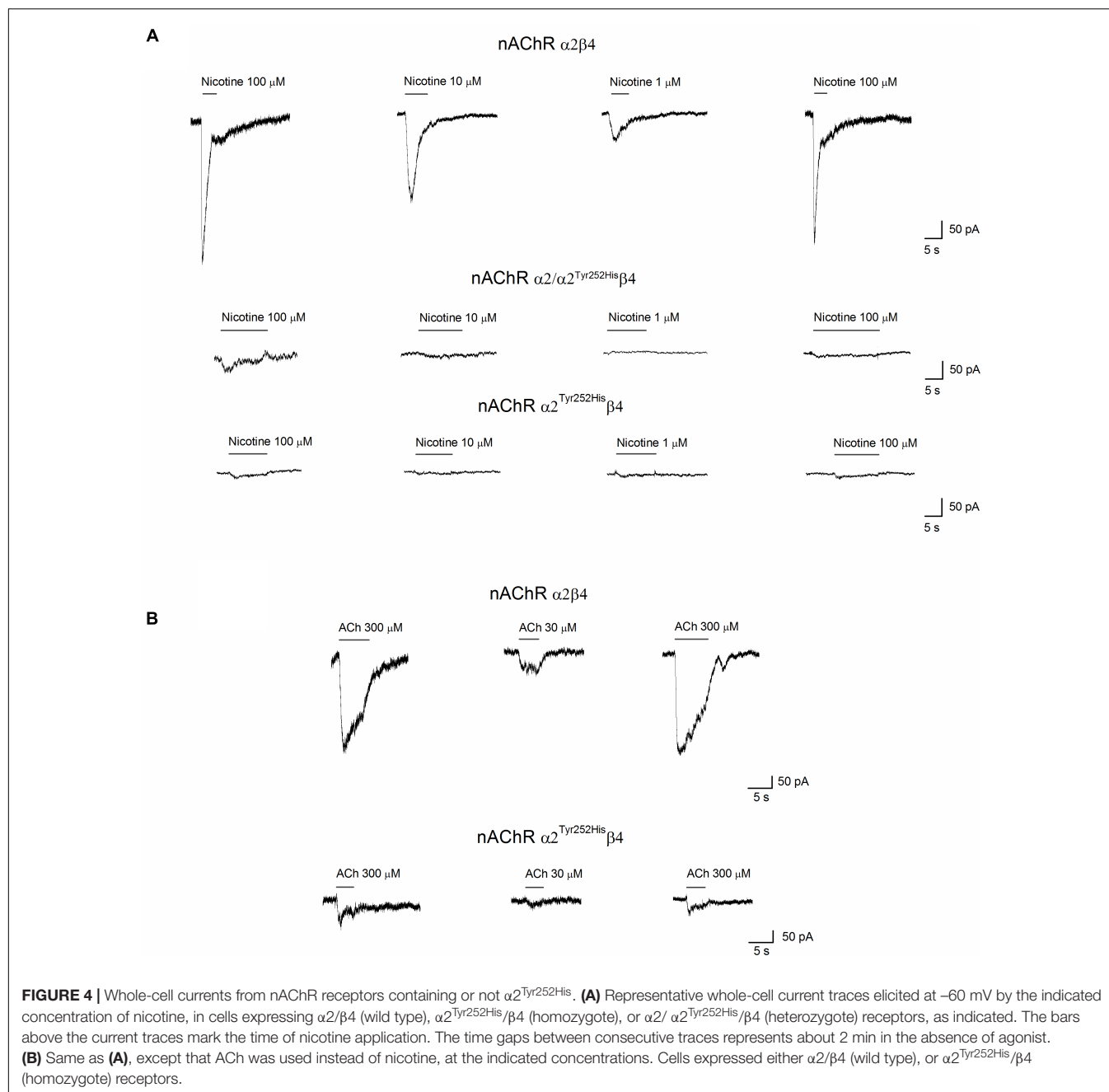
The Mutation Did Not Alter the Transcription Level of the Gene in HEK293 Cells

In order to evaluate the possible effects of the newly identified p.Tyr252His mutation in the *CHRNA2* gene, we engineered an F2A-based multicistronic plasmid encoding for the different

subunits of nAChR and a reporter gene for transfecting HEK293 cells. Firstly, we tested if the mutation could affect the transcription of the $\alpha 2$ subunit. To this extent, the correct transcription of the expression vectors in HEK293 cells was verified by RT-PCR. No differences in transcription levels were observed between the WT and mutant *CHRNA2* using both tricistronic vectors. In particular, the mRNA levels were 3.243 ± 1.249 (WT *CHRNA2*; $n = 3$) vs. 3.433 ± 0.864 (mutant *CHRNA2*; $n = 3$; $p > 0.05$, with unpaired *t*-test), in combination with *CHRNA4*. The corresponding values for the combination with *CHRNA2* were 2.860 ± 0.696 (WT *CHRNA2*; $n = 3$) vs. 2.760 ± 0.979 (mutant *CHRNA2*; $n = 3$, $p > 0.05$ with unpaired *t*-test). These results are shown in Figures 3A,B, and indicate that p.Tyr252His *CHRNA2* did not affect nAChR gene transcription and the plasmids gave similar levels of expression in our cells.

$\alpha 2^{Tyr252His}$ Did Not Alter Membrane Expression of $\alpha 2\beta 4$

In order to determine whether the mutation could affect different level of expression of receptor subtypes, we then performed Western Blotting (WB) analysis by loading on the gel the same amount of membrane proteins. Figure 3C shows the WB analysis



of two separate samples of $\alpha 2\beta 4$ (lanes 1 and 2), two samples of $\alpha 2^{\text{Tyr252His}}\beta 4$ (lanes 3 and 4) and two samples of untransfected HEK293 cells (lanes 5 and 6). The quantitative analysis of three independent preparations of WT $\alpha 2\beta 4$ and $\alpha 2^{\text{Tyr252His}}\beta 4$ showed that the $\alpha 2$ and $\beta 4$ subunit content was identical between cells transfected with $\alpha 2\beta 4$ or $\alpha 2^{\text{Tyr252His}}\beta 4$ (Figure 3C).

Patch-Clamp and Radioligand Assay Analysis

Whole-cell currents were elicited at -60 mV, by using nicotine or ACh. In Primate brain, the expression of $\alpha 2$ largely

overlaps with that of both $\beta 2$ and $\beta 4$ (Han et al., 2000; Quik et al., 2000). Moreover, there is evidence of *in vivo* expression of $\alpha 2\beta 2^*$ (Zoli et al., 2015), $\alpha 2\alpha 4\beta 2^*$ (Quik et al., 2005), and $\alpha 2\beta 4^*$ (Zoli et al., 1998). Therefore, we studied the functional effects of $\alpha 2^{\text{Tyr252His}}$ on both $\alpha 2\beta 4$ and $\alpha 2\beta 2$ receptors. Representative current traces obtained from cells expressing $\alpha 2\beta 4$ nAChRs are shown in Figure 4A (top panel). The maximal currents were repeatedly measured during the experiment, to check for possible activity rundown. Saturating nicotine concentrations (100–300 μM) elicited the typical inward current with desensitization. Consecutive agonist applications were spaced at least 2 min apart, to allow full channel

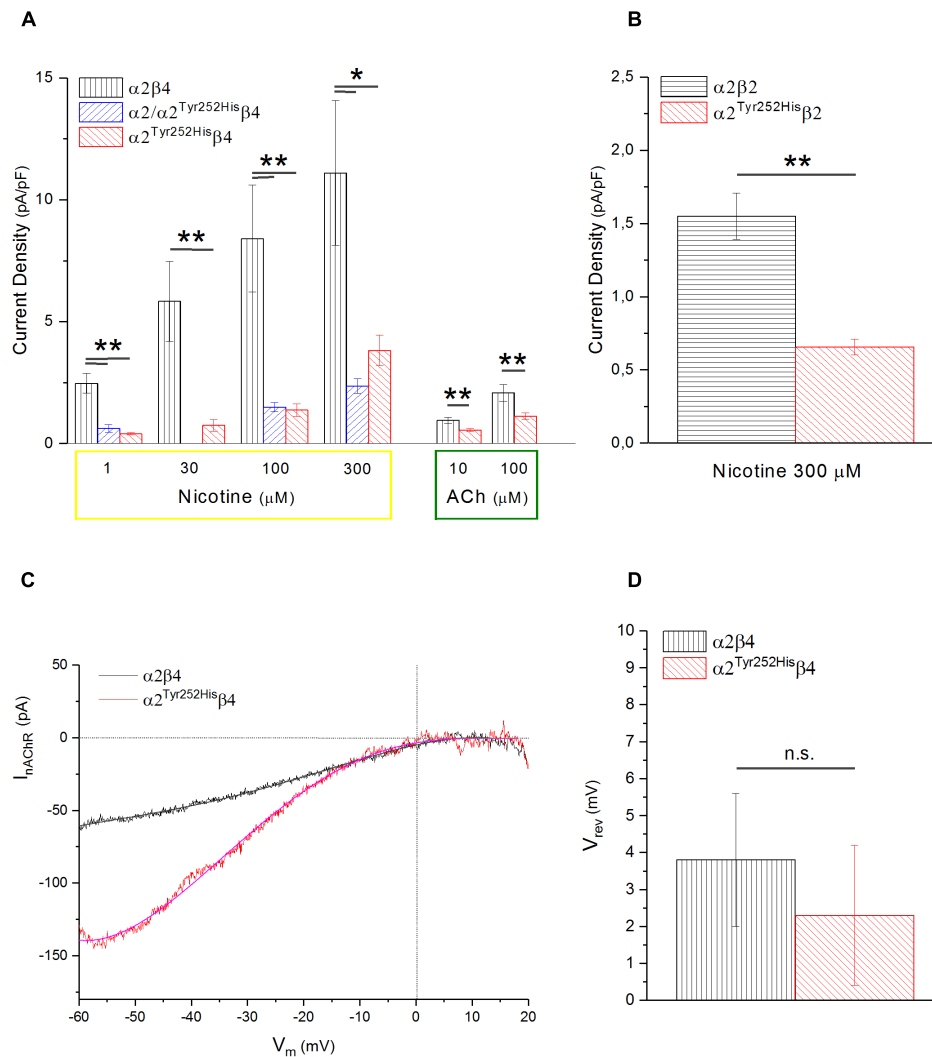


FIGURE 5 | $\alpha 2^{\text{Tyr252His}}$ decreases the maximal current density, without altering V_{rev} . **(A)** Bars represent average peak whole-cell current densities measured at the indicated concentrations of nicotine or ACh, in cells expressing $\alpha 2\beta 4$, $\alpha 2^{\text{Tyr252His}}\beta 4$, or $\alpha 2^{\text{Tyr252His}}\beta 4/\alpha 2\beta 4$. The results of representative measurements are shown for 1 μM nicotine ($p = 0.00005$ between WT, $n = 17$, and homozygotes, $n = 12$; $p = 0.0002$ between WT and heterozygotes, $n = 8$), 30 μM nicotine ($p = 0.0075$; $n = 9$ for WT and $n = 20$ for homozygotes), 100 μM nicotine ($p = 0.02$ between WT, $n = 9$, and homozygotes, $n = 22$; $p = 0.007$ between WT and heterozygotes, $n = 21$), 300 μM nicotine ($p = 0.02$ between WT, $n = 8$, and homozygotes, $n = 22$; $p = 0.01$ between WT and heterozygotes, $n = 21$), 10 μM ACh ($p = 0.0023$; $n = 17$ for WT and 15 for homozygotes), 100 μM ACh ($p = 0.010$; $n = 22$ for WT and $n = 19$ for homozygotes), $*p < 0.05$; $**p < 0.01$. **(B)** Same as **(A)**, but for $\alpha 2\beta 2$ and $\alpha 2^{\text{Tyr252His}}\beta 2$ receptors. For 1 μM nicotine ($p = 0.0004$; $n = 10$ for WT and $n = 7$ for homozygotes), 10 μM nicotine ($p = 0.0008$; $n = 11$ for WT and $n = 7$ for homozygotes), 300 μM nicotine ($p = 0.0006$; $n = 12$ for WT and $n = 11$ for homozygotes), $**p < 0.01$. **(C)** Representative current traces for the indicated receptor type, obtained by stimulating the cell with 1 s voltage ramps (-60 to $+20$ mV), in the presence or absence of 600 μM nicotine. The background current was subtracted to the one obtained in the presence of nicotine. V_{rev} was estimated by fitting the currents with a polynomial function. **(D)** Average V_{rev} values measured in WT ($n = 11$) and mutant ($n = 11$) receptors. The reported values were not significantly different between WT and mutant (with unpaired t -test).

recovery from desensitization. Lower agonist concentrations elicited smaller currents, with a slower desensitization. Similar experiments were carried out on cells expressing $\alpha 2^{\text{Tyr252His}}\alpha 2\beta 4$ receptors (simulated heterozygote; **Figure 4A**, middle panel), or $\alpha 2^{\text{Tyr252His}}\beta 4$ (homozygote; **Figure 4A**, bottom panel). The receptors containing $\alpha 2^{\text{Tyr252His}}$ generally presented much lower current amplitudes, compared to the WT. Similar results were obtained by using the physiological agonist ACh, instead of nicotine. Representative current traces are shown in **Figure 4B**.

When using ACh, atropine (1 μM) was added to the extracellular solution, to avoid the possible interference of muscarinic ACh receptors. To compare the current amplitudes obtained in cells with different surface areas, we report in **Figure 5A** the average peak whole-cell current densities (i.e., for each cell, the peak current was divided by the cell capacitance) obtained in the presence of the indicated concentrations of agonist, for the indicated $\alpha 2\beta 4$ nAChR subtypes. The current density observed in the presence of nicotine was decreased by approximately

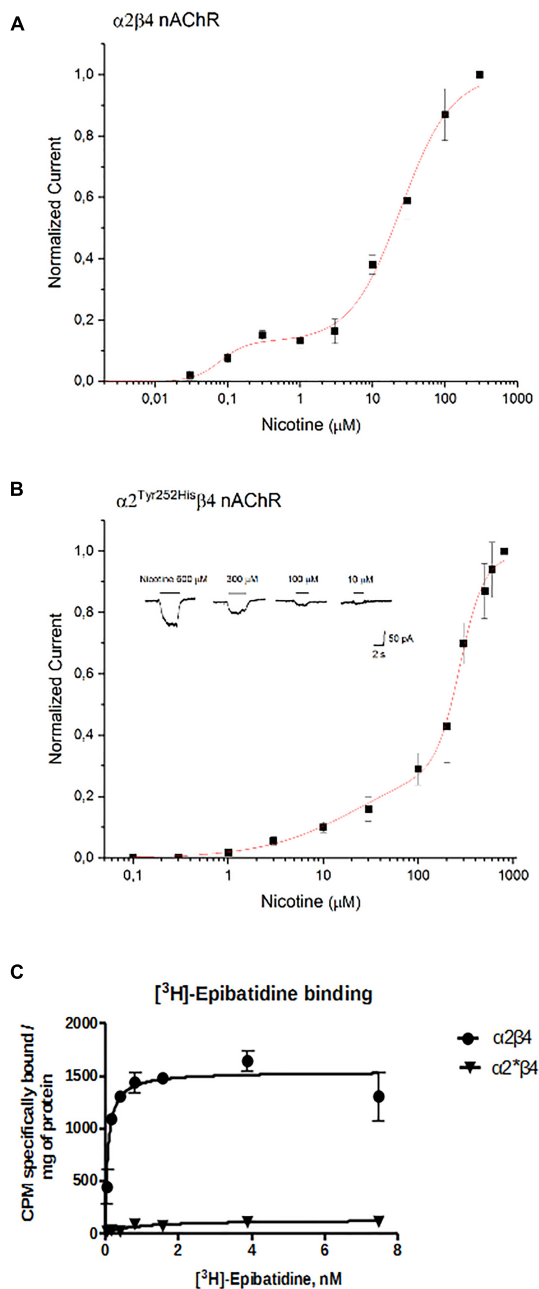


FIGURE 6 | Concentration-response analysis. **(A)** Concentration-response relation derived from patch-clamp results for $\alpha 2\beta 4$ receptors. Data points are average peak whole-cell currents, normalized to the current elicited by 300 μM nicotine in WT receptors. Continuous line is fit to equation (1). The relative estimated parameters were: $\text{EC}_{50\text{high}}$: $0.08 \pm 0.027 \mu\text{M}$; $\text{EC}_{50\text{low}}$: $24.7 \pm 2.76 \mu\text{M}$; nH1 : 2.41 ± 2.6 ; nH2 : 1.24 ± 0.15 . **(B)** Same as **(A)**, for $\alpha 2^{\text{Tyr252His}}\beta 4$. In this case, peak currents are normalized to the current elicited by 800 μM nicotine. Representative currents are shown in the inset. Continuous line is fit to equation (1). The relative estimated parameters were: $\text{EC}_{50\text{high}}$: $23.4 \pm 23 \mu\text{M}$; $\text{EC}_{50\text{low}}$: $275.7 \pm 12.5 \mu\text{M}$; nH1 : 0.87 ± 0.27 ; nH2 : 3.44 ± 0.81 . **(C)** Saturation binding experiments aimed to determine K_d and B_{max} of $[^3\text{H}]$ -Epibatidine in cells transfected with $\alpha 2\beta 4$, or $\alpha 2^{\text{Tyr252His}}\beta 4$ ($\alpha 2^*\beta 4$), or non-transfected. Curves were obtained from two independent saturation experiments using a non-linear least squares analysis program using GraphPad Prism version 6.

80% by $\alpha 2^{\text{Tyr252His}}$, in both homozygous and heterozygous condition. In agreement with previous reports (Di Resta et al., 2010; Conti et al., 2015), the $\alpha 2\beta 2$ nAChR subtype generally yielded lower functional expression in HEK293 cells, as compared to $\alpha 2\beta 4$. Therefore, the maximal current densities for $\alpha 2\beta 2$ receptors are reported for 300 μM nicotine (**Figure 5B**). In this case, the presence of $\alpha 2^{\text{Tyr252His}}$ brought the peak current density from $1.55 \pm 0.3 \text{ pA/pF}$ (WT; $n = 12$), to $0.67 \pm 0.1 \text{ pA/pF}$ (homozygote; $n = 11$). Similar results were obtained with the physiological agonist ACh. The average current densities measured at 10 and 100 μM ACh for WT and mutant receptors are shown in **Figure 5A**. Full statistics are given in the figure legend.

To study whether $\alpha 2^{\text{Tyr252His}}$ produced major alterations in the nAChR ion selectivity, we measured the reversal potential (V_{rev}) of $\alpha 2\beta 4$ and $\alpha 2^{\text{Tyr252His}}\beta 4$ receptors, as previously described (Conti et al., 2015). In brief, current-voltage relations were obtained by applying 1 s voltage ramps between -60 and $+20 \text{ mV}$, in the presence or absence of nicotine. Three ramps were usually averaged in either condition. Next, to isolate the nicotinic current, the background current obtained in the absence of nicotine was subtracted to the current recorded in the presence of nicotine. The resulting current-voltage relations were fit by polynomial functions, to estimate the nAChR V_{rev} . In general, V_{rev} turned out to be close to 0 mV for both $\alpha 2\beta 4$ and $\alpha 2^{\text{Tyr252His}}\beta 4$ receptors, in agreement with the typical V_{rev} observed in mammalian heteromeric nAChRs (Becchetti et al., 2015). Representative current traces and the average V_{rev} values estimated in a series of similar experiments are shown, respectively, in **Figures 5C,D**. These results suggest that major alterations in the ion selectivity are unlikely to be produced by $\alpha 2^{\text{Tyr252His}}$.

The concentration-response curves for nicotine were obtained by applying different concentrations of agonist at -60 mV . The peak currents thus obtained were normalized to the current obtained at 300 μM (for $\alpha 2\beta 4$), or 800 μM (for $\alpha 2^{\text{Tyr252His}}\beta 4$), and, respectively, plotted in **Figures 6A,B**. At higher agonist concentrations, the peak currents tended to decrease. This is also observed with other nAChR subtypes, and has been attributed to a blocked channel state at high concentrations of agonist (Maconochie and Knight, 1992). The presence of $\alpha 2^{\text{Tyr252His}}$ strongly decreased the amplitude of the currents activated by nicotine, which were barely detectable at concentrations lower than 10 μM . In fact, $\alpha 2^{\text{Tyr252His}}$ caused an approximately 10-fold right shift of the apparent EC_{50} of both the high and low affinity components of $\alpha 2\beta 4$ receptors. In particular, $\text{EC}_{50\text{high}}$ was $\sim 23 \mu\text{M}$ for $\alpha 2^{\text{Tyr252His}}\beta 4$, and $\sim 0.8 \mu\text{M}$ for $\alpha 2\beta 4$ receptors, while $\text{EC}_{50\text{low}}$ was $\sim 275 \mu\text{M}$ for $\alpha 2^{\text{Tyr252His}}\beta 4$, and $\sim 25 \mu\text{M}$ for $\alpha 2\beta 4$ receptors. Full statistics are given in the figure legend. The patch-clamp results can be compared with the measurements carried out with $[^3\text{H}]$ -Epibatidine (**Figure 6C**). The binding affinities (K_d) of $[^3\text{H}]$ -Epibatidine for transfected $\alpha 2\beta 4$ and $\alpha 2^{\text{Tyr252His}}\beta 4$ subtypes, were determined by saturation binding experiments. The affinity (K_d) of $[^3\text{H}]$ -Epibatidine for the $\alpha 2\beta 4$ or $\alpha 2^{\text{Tyr252His}}\beta 4$ nAChR subtypes were, respectively, 0.085 and

0.89 nM, and were derived from the average value of two independent [^3H]Epibatidine binding saturation experiments.

In addition to the difference in K_d , analysis of the saturation curves also showed that the B_{max} of [^3H]Epibatidine binding (expressed as cpm specifically bound/mg of protein) is much lower for $\alpha 2^{\text{Tyr252His}}\beta 4$ receptors than for $\alpha 2\beta 4$. In fact, fitting the saturation curves and calculating the cpm specifically bound by [^3H]Epibatidine/mg of protein gave 1535 cpm for $\alpha 2\beta 4$ and 127 for $\alpha 2^{\text{Tyr252His}}\beta 4$ (Figure 6C). Considering the WB results (Figure 3C), we conclude that the strong decrease produced by $\alpha 2^{\text{Tyr252His}}$ on both B_{max} and maximal whole-cell currents can be attributed to a conspicuous decrease in the number of channels bound to the agonist.

DISCUSSION

In the present work, we reported a new *CHRNA2* mutation detected in an ADNFLE patient. When expressed in HEK293 cells, the receptors containing $\alpha 2^{\text{Tyr252His}}$ displayed a marked reduction of whole-cell currents, as compared to WT receptors, in all experimental conditions. Such a decrease was paralleled by a B_{max} decrease with [^3H]-epibatidine. Moreover, the concentration-response curves determined by both methods showed that $\alpha 2^{\text{Tyr252His}}$ produced an approximate 10-fold decrease in the apparent affinity for the tested agonists of the $\alpha 2\beta 4$ subtype (Figure 6). The decrease in maximal current and B_{max} could be caused by a smaller single-channel conductance, a more negative V_{rev} , a decrease of the average number of active channels onto the plasma membrane, or a combination thereof. Because V_{rev} was not altered by $\alpha 2^{\text{Tyr252His}}$ and considering that Tyr252 is placed far from the pore region, we believe a major alteration of the channel's conductive properties is unlikely. Moreover, neither subunits' transcription nor membrane expression were altered by $\alpha 2^{\text{Tyr252His}}$ (Figure 3). Therefore, we attribute the overall reduction in the maximal response to the agonist, accompanied by a right-shift of the activation curve, to a strong decrease of the affinity of the ligand binding site for the agonist. Based on subunit sequence and what is known about the 3D structure of human $\alpha 4\beta 2$ nAChRs (Morales-Perez et al., 2016; Walsh et al., 2018), as well as the extracellular domain of human $\alpha 2$ subunits (Kouvatsos et al., 2016), Tyr252 results to be located in the pre-M1 functional loop C. A simple explanation of our results is that adding a positively charged histidine in the binding site would cause an electrostatic repulsion for the positively charged agonists, which would lead to a lower binding affinity. It is also possible that altering the local structure of the pre-M1 region could considerably increase the energy required to transduce the conformational change from the ligand binding site to the pore region. Fully discriminating between these (not mutually exclusive) possibilities would require

extensive single channel data. Regardless of the mechanistic details, our results suggest that, in the case of $\alpha 2^{\text{Tyr252His}}$, a dominant negative effect is probably responsible for the main pathophysiological consequences.

The functional features conferred to the nAChR by $\alpha 2^{\text{Tyr252His}}$ resemble those previously observed with p.Ile297Phe (Conti et al., 2015), and differ from those of p.Ile279Asn (Aridon et al., 2006). These results support the notion that loss of receptor function may be a more common epileptogenic mechanism for mutant $\alpha 2^*$ nAChRs, as compared to other nicotinic subunits. We hypothesize that the reasons for this difference may depend on the different distribution of nAChR subunits in the brain. The specific role of each subunit is still uncertain (Zoli et al., 2015), and particularly so in the case of $\alpha 2$ (Baddick and Marks, 2011), despite its relatively widespread expression in the mammalian brain (Wada et al., 1989; Marks et al., 1992). Recent work in the mouse neocortex suggested that $\alpha 2$ nAChR subunits are specifically expressed in the Martinotti cells that project to layer I and can synchronize the thick-tufted pyramidal cells in layer V (Hilscher et al., 2017). The present uncertainties about the distribution of $\alpha 2$ subunits at the cellular level in the human brain prevent to bring the comparison too far. Nonetheless, we can hypothesize that a decreased cholinergic response in Martinotti cells could facilitate inhibition of these interneurons, which could lead to pyramidal cell excitation through rebound excitation (Becchetti et al., 2015; Hilscher et al., 2017).

AUTHOR CONTRIBUTIONS

CV, GC, CG, RG, AB, and RC conceived and designed the experiments. CV, GC, SM, CG, MM, and EC performed the experiments. CV, GC, SM, CG, MM, AB, and RC analyzed the data. LF-S, CG, AB, and RC contributed to reagents, materials, and analysis tools. CV, GC, CG, LF-S, AB, and RC wrote the manuscript.

FUNDING

The present work was funded by the University of Milano-Bicocca (FAR 2017-ATE-0150 to AB and 2017-ATE-0009 to RC), and the Italian Ministry for University and Scientific Research (FFABR 2017-NAZ-0191 to AB, 2017-NAZ-0319 to RG and 2017-NAZ-0286 to RC).

ACKNOWLEDGMENTS

The authors thank Dr. Perota at Avantea for providing the pCX-EGFP plasmid.

REFERENCES

- Alkondon, M., Pereira, E. F., Eisenberg, H. M., and Albuquerque, E. X. (2000). Nicotinic receptor activation in human cerebral cortical interneurons: a mechanism for inhibition and disinhibition of neuronal networks. *J. Neurosci.* 20, 66–75. doi: 10.1523/JNEUROSCI.20-01-00066.2000
- Aracri, P., Amadeo, A., Pasini, M. E., Fascio, U., and Becchetti, A. (2013). Regulation of glutamate release by heteromeric nicotinic receptors in layer V of the secondary motor region (Fr2) in the dorsomedial shoulder of prefrontal cortex in mouse. *Synapse* 67, 338–357. doi: 10.1002/syn.21655
- Aracri, P., Consonni, S., Morini, R., Perrella, M., Rodighiero, S., Amadeo, A., et al. (2010). Tonic modulation of GABA release by nicotinic acetylcholine receptors,

- in layer V of the murine prefrontal cortex. *Cereb. Cortex* 20, 1539–1555. doi: 10.1093/cercor/bhp214
- Aracri, P., Meneghini, S., Coatti, A., Amadeo, A., and Becchetti, A. (2017). $\alpha 4\beta 2^*$ nicotinic receptors stimulate GABA release onto fast-spiking cells in layer V of mouse prefrontal (Fr2) cortex. *Neuroscience* 340, 48–61. doi: 10.1016/j.neuroscience.2016.10.045
- Aridon, P., Marini, C., Di Resta, C., Brilli, E., De Fusco, M., Politi, F., et al. (2006). Increased sensitivity of the neuronal nicotinic receptor $\alpha 2$ subunit causes familial epilepsy with nocturnal wandering and ictal fear. *Am. J. Hum. Genet.* 79, 342–350. doi: 10.1086/506459
- Baddick, C. G., and Marks, M. J. (2011). An autoradiographic survey of mouse brain nicotinic acetylcholine receptors defined by null mutants. *Biochem. Pharmacol.* 82, 828–841. doi: 10.1016/j.bcp.2011.04.019
- Becchetti, A., Aracri, P., Meneghini, S., Brusco, A., and Amadeo, A. (2015). The role of nicotinic acetylcholine receptors in autosomal dominant nocturnal frontal lobe epilepsy. *Front. Physiol.* 6:22. doi: 10.3389/fphys.2015.00022
- Brusco, S., Ambrosi, P., Meneghini, S., and Becchetti, A. (2015). Agonist and antagonist effects of tobacco-related nitrosamines on human $\alpha 4\beta 2$ nicotinic acetylcholine receptors. *Front. Pharmacol.* 6:201. doi: 10.3389/fphar.2015.00201
- Combi, R., Dalprà, L., Ferini-Strambi, L., and Tenchini, M. L. (2005a). Frontal lobe epilepsy and mutations in the corticotropin releasing hormone gene. *Ann. Neurol.* 58, 899–904. doi: 10.1002/ana.2066
- Combi, R., Ferini-Strambi, L., Montruccoli, A., Bianchi, V., Malcovati, M., Zucconi, M., et al. (2005b). Two new putative susceptibility loci for ADNFLE. *Brain Res. Bull.* 67, 257–263. doi: 10.1016/j.brainresbull.2005.06.032
- Combi, R., Ferini-Strambi, L., and Tenchini, M. L. (2009). CHRNA2 mutations are rare in the NFLE population: evaluation of a large cohort of Italian patients. *Sleep Med.* 10, 139–142. doi: 10.1016/j.sleep.2007.11.010
- Conti, V., Aracri, P., Chiti, L., Brusco, S., Mari, F., Marini, C., et al. (2015). Nocturnal frontal lobe epilepsy with paroxysmal arousals due to CHRNA2 loss of function. *Neurology* 84, 1520–1528. doi: 10.1212/WNL.0000000000001471
- Cooper, S. T., Harkness, P. C., Baker, E. R., and Millar, N. S. (1999). Up-regulation of cell-surface $\alpha 4\beta 2$ neuronal nicotinic receptors by lower temperature and expression of chimeric subunits. *J. Biol. Chem.* 274, 27145–27152. doi: 10.1074/jbc.274.38.27145
- Couey, J. J., Meredith, R. M., Spijker, S., Poorthuis, R. B., Smit, A. B., Brussaard, A. B., et al. (2007). Distributed network actions by nicotine increase the threshold for spike-timing dependent plasticity in prefrontal cortex. *Neuron* 54, 73–87. doi: 10.1016/j.neuron.2007.03.006
- Covernton, P. J., and Connolly, J. G. (2000). Multiple components in the agonist concentration-response relationship of neuronal nicotinic acetylcholine receptors. *J. Neurosci. Methods* 96, 63–70. doi: 10.1016/S0165-0270(99)00185-5
- Dani, J. A., and Bertrand, D. (2007). Nicotinic acetylcholine receptors and nicotinic cholinergic mechanisms of the central nervous system. *Annu. Rev. Pharmacol. Toxicol.* 47, 699–729. doi: 10.1146/annurev.pharmtox.47.120505.105214
- De Fusco, M., Becchetti, A., Patrignani, A., Annesi, G., Gambardella, A., Quattrone, A., et al. (2000). The nicotinic receptor $\beta 2$ subunit is mutant in nocturnal frontal lobe epilepsy. *Nat. Genet.* 26, 275–276. doi: 10.1038/81566
- De Giorgi, M., Cinti, A., Pelikant-Malecka, I., Chisci, E., Lavitrano, M., Giovannoni, R., et al. (2015). Co-expression of functional human Heme Oxygenase 1, Ecto-5'-Nucleotidase and ecto-nucleoside triphosphate diphosphohydrolase-1 by "self-cleaving" 2A peptide system. *Plasmid* 79, 22–29. doi: 10.1016/j.plasmid.2015.03.004
- Di Resta, C., Ambrosi, P., Curia, G., and Becchetti, A. (2010). Effect of carbamazepine and oxcarbazepine on wild-type and mutant neuronal nicotinic receptors linked to nocturnal frontal lobe epilepsy. *Eur. J. Pharmacol.* 643, 13–20. doi: 10.1016/j.ejphar.2010.05.063
- Ferini-Strambi, L., Sansoni, V., and Combi, R. (2012). Nocturnal frontal lobe epilepsy and the acetylcholine receptor. *Neurologist* 18, 343–349. doi: 10.1097/NRL.0b013e31826a99b8
- Han, Z. Y., Le Novère, N., Zoli, M., Hill, J. A., Champtiaux, N., and Changeux, J. P. (2000). Localization of nAChR subunit mRNAs in the brain of *Macaca mulatta*. *Eur. J. Neurosci.* 12, 3664–3674. doi: 10.1046/j.1460-9568.2000.00262.x
- Heron, S. E., Smith, K. R., Bahlo, M., Nobili, L., Kahana, E., Licchetta, L., et al. (2012). Missense mutations in the sodium-gated potassium channel gene KCNT1 cause severe autosomal dominant nocturnal frontal lobe epilepsy. *Nat. Genet.* 44, 1188–1190. doi: 10.1038/ng.2440
- Hilscher, M. M., Leão, R. N., Edwards, S. J., Leão, K. E., and Kullander, K. (2017). ChRNA2-Martinotti cells synchronize layer 5 type A pyramidal cells via rebound excitation. *PLoS Biol.* 15:e2001392. doi: 10.1371/journal.pbio.2001392
- Ishida, S., Picard, F., Rudolf, G., Noé, E., Achaz, G., Thomas, P., et al. (2013). Mutations of DEPDC5 cause autosomal dominant focal epilepsies. *Nat. Genet.* 45, 552–555. doi: 10.1038/ng.2601
- Kouvatsos, N., Giastas, P., Chroni-Tzartou, D., Pouloupoulou, C., and Tzartos, S. J. (2016). Crystal structure of a human neuronal nAChR extracellular domain in pentameric assembly: ligand-bound $\alpha 2$ homopentamer. *Proc. Natl. Acad. Sci. U.S.A.* 113, 9635–9640. doi: 10.1073/pnas.1602619113
- Lambe, E. K., Picciotto, M. R., and Aghajanian, G. K. (2003). Nicotine induces glutamate release from thalamocortical terminals in prefrontal cortex. *Neuropsychopharmacology* 28, 216–225. doi: 10.1038/sj.npp.13.00032
- Maconochie, D. J., and Knight, D. E. (1992). Markov modelling of ensemble current relaxations: bovine sdrenal nicotinic receptor currents analysed. *J. Physiol.* 454, 155–182. doi: 10.1113/jphysiol.1992.sp019258
- Marks, M. J., Pauly, J. R., Gross, S. D., Deneris, E. S., Hermans-Borgmeyer, I., Heinemann, S. F., et al. (1992). Nicotine binding and nicotinic receptor subunit RNA after chronic nicotine treatment. *J. Neurosci.* 12, 2765–2784. doi: 10.1523/JNEUROSCI.12-07-02765.1992
- Mazzo, F., Pistillo, F., Grazioso, G., Clementi, F., Borgese, N., Gotti, C., et al. (2013). Nicotine-modulated subunit stoichiometry affects stability and trafficking of $\alpha 3\beta 4$ nicotinic receptor. *J. Neurosci.* 33, 12316–12328. doi: 10.1523/JNEUROSCI.2393-13.2013
- Morales-Perez, C., Noviello, C. M., and Hibbs, R. E. (2016). X-ray structure of the human $\alpha 4\beta 2$ nicotinic receptor. *Nature* 538, 411–417. doi: 10.1038/nature19785
- Nobili, L., Proserpio, P., Combi, R., Provini, F., Plazzi, G., Bisulli, F., et al. (2014). Nocturnal frontal lobe epilepsy. *Curr. Neurol. Neurosci. Rep.* 14:424. doi: 10.1007/s11910-013-0424-6
- Phillips, H. A., Favre, I., Kirkpatrick, M., Zuberi, S. M., Goudie, D., Heron, S. E., et al. (2001). CHRN2 is the second acetylcholine receptor subunit associated with autosomal dominant nocturnal frontal lobe epilepsy. *Am. J. Hum. Genet.* 68, 225–231. doi: 10.1086/316946
- Porter, J. T., Cauli, B., Tsuzuki, K., Lambolez, B., Rossier, J., and Audinat, E. (1999). Selective excitation of subtypes of neocortical interneurons by nicotinic receptors. *J. Neurosci.* 19, 5228–5235. doi: 10.1523/JNEUROSCI.19-13-05228
- Quik, M., Polonskaya, Y., Gillespie, A., Jakowec, M., Lloyd, G. K., and Langston, J. W. (2000). Localization of nicotinic receptor subunit mRNAs in monkey brain by in situ hybridization. *J. Comp. Neurol.* 425, 58–69. doi: 10.1002/1096-9861(20000911)425:1<58::AID-CNE6>3.0.CO;2-X
- Quik, M., Vailati, S., Bordia, T., Kulak, J. M., Fan, H., McIntosh, J. M., et al. (2005). Subunit composition of nicotinic receptors in monkey striatum: effect of treatments with 1-methyl-4-phenyl-1,2,3,6-tetrahydropyridine or L-DOPA. *Mol. Pharmacol.* 67, 32–41. doi: 10.1124/mol.104.006015
- Ryan, M. D., and Drew, J. (1994). Foot-and-mouth disease virus 2A oligopeptide mediated cleavage of an artificial polyprotein. *EMBO J.* 13, 928–933. doi: 10.1002/j.1460-2075.1994.tb06337.x
- Sansoni, V., Forcella, M., Mozzi, A., Fusi, P., Ambrosini, R., Ferini-Strambi, L., et al. (2013). Functional characterization of a CRH missense mutation identified in an ADNFLE family. *PLoS One* 8:e61306. doi: 10.1371/journal.pone.0061306
- Steinlein, O. K., Mulley, J. C., Propping, P., Wallace, R. H., Phillips, H. A., Sutherland, G. R., et al. (1995). A missense mutation in the neuronal nicotinic acetylcholine receptor alpha 4 subunit is associated with autosomal dominant nocturnal frontal lobe epilepsy. *Nat. Genet.* 11, 201–203. doi: 10.1038/ng1095-201
- Tinuper, P., Bisulli, F., Cross, J. H., Hesdorffer, D., Kahane, P., Nobili, L., et al. (2016). Definition and diagnostic criteria of sleep-related hypermotor epilepsy. *Neurology* 86, 1834–1842. doi: 10.1212/WNL.0000000000002666
- Vidal, C., and Changeux, J. P. (1993). Nicotinic and muscarinic modulations of excitatory synaptic transmission in the rat prefrontal cortex in vitro. *Neuroscience* 56, 23–32. doi: 10.1016/0306-4522(93)90558-W
- Wada, E., Wada, K., Boulter, J., Deneris, E., Heinemann, S., Patrick, J., et al. (1989). Distribution of alpha 2, alpha 3, alpha 4, and beta 2 neuronal nicotinic receptor subunit mRNAs in the central nervous system: a hybridization histochemical

- study in the rat. *J. Comp. Neurol.* 284, 314–335. doi: 10.1002/cne.902840212
- Walsh, R. M. Jr., Roh, S. H., Gharpure, A., Morales-Perez, C. L., Teng, J., and Hibbs, R. E. (2018). Structural principles of distinct assemblies of the human $\alpha 4\beta 2$ nicotinic receptor. *Nature* 557, 261–265. doi: 10.1038/s41586-018-0081-7
- Zoli, M., Léna, C., Picciotto, M. R., and Changeux, J. P. (1998). Identification of four classes of brain nicotinic receptors using beta2 mutant mice. *J. Neurosci.* 18, 4461–4472. doi: 10.1523/JNEUROSCI.18-12-04461.1998
- Zoli, M., Pistillo, F., and Gotti, C. (2015). Diversity of native nicotinic receptor subtypes in mammalian brain. *Neuropharmacology* 96, 302–311. doi: 10.1016/j.neuropharm.2014.11.003

Conflict of Interest Statement: The authors declare that the research was conducted in the absence of any commercial or financial relationships that could be construed as a potential conflict of interest.

Copyright © 2019 Villa, Colombo, Meneghini, Gotti, Moretti, Ferini-Strambi, Chisci, Giovannoni, Becchetti and Combi. This is an open-access article distributed under the terms of the Creative Commons Attribution License (CC BY). The use, distribution or reproduction in other forums is permitted, provided the original author(s) and the copyright owner(s) are credited and that the original publication in this journal is cited, in accordance with accepted academic practice. No use, distribution or reproduction is permitted which does not comply with these terms.



Loss of Satb2 in the Cortex and Hippocampus Leads to Abnormal Behaviors in Mice

Qiong Zhang^{1,2†}, Ying Huang^{1,2†}, Lei Zhang^{1,2}, Yu-Qiang Ding^{1,2,3,4*} and Ning-Ning Song^{3*}

¹ Key Laboratory of Arrhythmias, Ministry of Education of China, East Hospital, Tongji University School of Medicine, Shanghai, China, ² Department of Anatomy and Neurobiology, Tongji University School of Medicine, Shanghai, China, ³ State Key Laboratory of Medical Neurobiology and MOE Frontiers Center for Brain Science, Institutes of Brain Science, Fudan University, Shanghai, China, ⁴ Department of Laboratory Animal Science, Fudan University, Shanghai, China

OPEN ACCESS

Edited by:

Xiao-Dong Wang,
Zhejiang University, China

Reviewed by:

Ismael Galve-Roperh,
Complutense University of Madrid,
Spain
Marta Nieto,
Spanish National Research Council
(CSIC), Spain

*Correspondence:

Yu-Qiang Ding
dingyuqiang@vip.163.com
Ning-Ning Song
songnn1982@outlook.com;
songnn@tongji.edu.cn

[†]These authors have contributed
equally to this work

Received: 11 November 2018

Accepted: 25 January 2019

Published: 12 February 2019

Citation:

Zhang Q, Huang Y, Zhang L,
Ding Y-Q and Song N-N (2019) Loss
of Satb2 in the Cortex
and Hippocampus Leads
to Abnormal Behaviors in Mice.
Front. Mol. Neurosci. 12:33.
doi: 10.3389/fnmol.2019.00033

Satb2-associated syndrome (SAS) is a genetic disorder that results from the deletion or mutation of one allele within the Satb2 locus. Patients with SAS show behavioral abnormalities, including developmental delay/intellectual disability, hyperactivity, and symptoms of autism. To address the role of Satb2 in SAS-related behaviors and generate an SAS mouse model, Satb2 was deleted in the cortex and hippocampus of Emx1-Cre; Satb2^{flox/flox} [Satb2 conditional knockout (CKO)] mice. Satb2 CKO mice showed hyperactivity, increased impulsivity, abnormal social novelty, and impaired spatial learning and memory. Furthermore, we also found that the development of neurons in cortical layer IV was defective in Satb2 CKO mice, as shown by the loss of layer-specific gene expression and abnormal thalamocortical projections. In summary, the abnormal behaviors revealed in Satb2 CKO mice may reflect the SAS symptoms associated with Satb2 mutation in human patients, possibly due to defective development of cortical neurons in multiple layers including alterations of their inputs/outputs.

Keywords: Satb2, cerebral cortex, hippocampus, Satb2-associated syndrome, mouse behavior

INTRODUCTION

Special AT-rich sequence-binding protein 2 (Satb2) is a transcription factor that regulates chromatin remodeling and gene expression via interactions with genomic nuclear matrix attachment regions, and it plays a pivotal role in the development of multiple organs. In skeletogenesis, Satb2 is essential for the craniofacial patterning and bone formation (Dobrev et al., 2006). In brain morphogenesis, Satb2 is required for the development of both callosal and subcortical projection neurons in the neocortex (Alcamo et al., 2008; Britanova et al., 2008; Leone et al., 2015; McKenna et al., 2015). In Satb2 conventional knockout mice and Satb2 CKO mice, most of callosal neurons do not send axons to the contralateral cortex (Alcamo et al., 2008; Leone et al., 2015). Recently, it has been reported that Satb2 is also required for the differentiation of a subset of spinal interneurons (Hilde et al., 2016).

In humans, the deletion or mutation of one allele within the Satb2 locus results in a disorder called Satb2-associated syndrome (SAS). Patients with SAS show craniofacial anomia, growth retardation, and behavioral abnormalities such as developmental delay/intellectual disability, hyperactivity, and symptoms of autism (Usui et al., 2013; Zarate and Fish, 2017; Zarate et al., 2018).

In addition, about 29% of patients with SAS show abnormal white matter and about 8% have a small corpus callosum, as revealed by brain imaging (Zarate et al., 2018), which may contribute to the behavioral abnormalities.

Available mouse models with a selective deletion of Satb2 in different neuronal types and brain regions have allowed researchers to explore the neurobiological basis of SAS in humans. Defective social, fear, and spatial memory have been reported in Satb2 conditional knockout (CKO) mice with a deletion of Satb2 in CamKII-Cre-expressing neurons and heterozygous Satb2 mice (Jaitner et al., 2016; Li et al., 2017). Unlike Satb2 KO mice, which die after birth with multiple defects (Dobrev et al., 2006), CKO mice can survive for at least 1 year and have normal gross appearance.

To better understand SAS, particularly its autistic and behavioral symptoms, we generated Satb2 CKO mice in which Satb2 was deleted in the cerebral cortex and hippocampus, which are two major brain regions with high levels of Satb2 expression (Huang et al., 2013a) and are likely to be involved in the SAS-related behavioral phenotypes. Here, we reported that the deletion of Satb2 in the mouse cerebral cortex and hippocampus resulted in hyperactivity, increased impulsivity, abnormal social novelty, and impaired spatial learning and memory. Thus, our Satb2 CKO mice may serve as a mouse model for studying the underlying mechanism of the SAS associated with Satb2 mutation in patients.

MATERIALS AND METHODS

Experimental Animals

Animal care practices and all experiments were reviewed and approved by the Animal Committee of Tongji University School of Medicine, Shanghai, China. We used Satb2-targeted embryonic stem cells (EPD0098_3_H05), purchased from the International Mouse Phenotyping Consortium, to generate the Satb2 knockout-first mice, which were initially crossed with FLP_{ER} mice to obtain floxed Satb2 mice. To delete Satb2 in the cerebral cortex and hippocampus, Emx1-Cre mice (Guo et al., 2000) were crossed with Satb2^{flox/flox} mice to obtain Emx1-Cre; Satb2^{flox/flox} mice (Satb2 CKO) mice. In the offspring, these genotypes (i.e., Satb2^{flox/+} or Satb2^{flox/flox}) were used as controls.

Immunohistochemistry, AuCl₃ Staining and *in situ* Hybridization

Mice were perfused with 4% paraformaldehyde (PFA) at different postnatal ages. All brains were fixed in 4% PFA overnight, cryoprotected in 30% sucrose in phosphate-buffered saline overnight and cut into 20 μ m-thick sections. For immunohistochemistry, brain sections were incubated with rabbit anti-Satb2 (1:300, Abcam) or goat anti-5-HTT antibody (1:1000, Immunostar) at 4°C overnight, and then incubated with biotinylated horse anti-rabbit IgG or horse anti-goat IgG (1:500, Jackson ImmunoResearch) at room temperature for 3 h followed by incubation with streptavidin-Cy3 (1:1000, Jackson ImmunoResearch) and counterstaining with Hoechst 33258 (1:2000, Sigma) at room temperature for 1 h.

The AuCl₃ staining was performed as a previous study (Wahlsten et al., 2003). The brain sections were stained with 0.2% gold chloride (AuCl₃) in phosphate buffer. The process was taken place in darkness. Once axonal staining became evident, the reaction was stopped by transferring sections to 2.5% sodium thiosulfate anhydrous for 5 min.

The antisense digoxigenin-labeled RNA probes of ROR β , Cux2, Ctbp2, and Tle4 were synthesized according to the Allen Brain Atlas website, and *in situ* hybridization was performed as described in our previous study (Song et al., 2011).

Behavioral Tests

Adult (3–6 months old) male mice were used in the following behavioral tests. All behavioral experiments were performed during the light phase of the light/dark cycle. Behavioral tests were conducted in a sound-proof room with a neutral environment. All mice were given a 30-min habituation time after transport to the behavioral test room. There were 2 or 3 days for resting between different tests. The experimenter was blind to the group identity of the tested mice. Some behavioral tests were recorded with a camera and a trained researcher analyzed these videos.

Open Field Test

The open field apparatus comprised a square arena, with a white floor divided into 9 squares (10 cm \times 10 cm) and enclosed by continuous 21 cm-high walls made of transparent plexiglass. The experiment lasted for 30 min. Average velocity, total distance traveled, ambulatory time, and average velocity were recorded by Activity Monitor software (Med Associates, St. Albans, VT, United States).

Cliff Avoidance Reaction

The cliff avoidance reaction (CAR) is based on the natural tendency of animals to avoid a potential fall from a height (Yamashita et al., 2013). The apparatus used in the CAR test included a round wooden platform (diameter, 20 cm) supported by a heavy rod (height, 50 cm). Two identical apparatus were used for the test. The test was initiated by placing mice on a platform such that the forelimbs approached its edge. If the mouse fell from the platform, it was immediately placed back on the platform and was considered to have impaired CAR. The experiment lasted for 30 min. The latency from the initial placement on the platform until falling was recorded. The incidence of impaired CAR was calculated as a percentage index for each group, as follows:

$$\% \text{ (CAR)} = [\text{the number of mice that did not fall from the platform} / \text{total numbers of tested mice}] \times 100.$$

Dark-Light Exploration Test

This test was performed to assess the anxiety-like behaviors of rodents, as described in our previous study (Zhang et al., 2016). The apparatus was a rectangular plexiglass box (45 cm length \times 20 cm width \times 20 cm height) divided into a smaller (1/3) black area with a lid and a larger (2/3) white area with an open-top. A black wall separated the two compartments and had an opening door (5 cm \times 5 cm) at floor level. The light intensity was about 500 lx in the white part. Each mouse was placed in the

center of the dark compartment and behavior was recorded over a 5-min period. The time spent in the white box and the number of transitions between dark and white compartments were recorded.

Elevated Plus-Maze Test

This test assesses anxiety-like behaviors in rodents, as described in our previous study (Zhang et al., 2016). The elevated plus-maze consisted of two open arms (30 cm × 5 cm), two enclosed arms (30 cm × 5 cm), and a central platform (5 cm × 5 cm). The maze was elevated 40 cm above the ground. Each mouse was placed in the central platform facing one of the enclosed arms and was observed for 5 min. The time spent in the open arms and the number of entries into the open arms were recorded. Open arm entry was defined as a mouse having entered an open arm with all four legs.

Pre-pulse Inhibition Test

The mouse was subjected to a pre-pulse inhibition (PPI) test in a startle chamber (SR-LAB; San Diego Instruments, San Diego, CA, United States) using the standard methods described previously (Geyer and Dulawa, 2003). The test sessions were started after an initial 5-min acclimation period in the chamber. Each PPI test session comprised 64 trials. Mice were subjected to one of the following five trials: (1) pulse alone, as a 40-ms burst (120 dB); a 40-ms pulse burst preceded by 100 ms with a 20-ms pre-pulse that was (2) 5 dB, (3) 13 dB, or (4) 22 dB over background (60 dB), namely, pre-pulse + pulse trials; and (5) background only (no-stimulus). Each test session began and ended with six presentations of the pulse-alone trial; between these, pre-pulse + pulse and no-stimulus trials were presented 10 times each, and the pulse-alone trials 12 times each, and in a pseudorandom order. The inter-trial interval was 7–23 s (15 s on average). The initial and final six pulse-alone trials were not included in the analysis. The amount of PPI was expressed as the percentage decrease in the amplitude of the startle reactivity caused by presentation of the pre-pulse, which was calculated as follows: % PPI = $100 - \{[(\text{startle response for pre-pulse} + \text{pulse}) / (\text{startle response for pulse alone})] \times 100\}$.

Three-Chamber Test

The three-chamber social test is an accepted and sensitive measure of social behavior in mice. The apparatus is a rectangular plexiglass box (90 cm length × 50 cm width × 30 cm height) divided into three equal chambers. Mice are allowed to access each compartment by crossing the door, which is a square opening (5 cm × 5 cm) located at floor level of the partition. Two inverted wire-mesh cylinders were placed at the corners of the two side chambers and a weighted bottle was placed on the top of the cylinders to prevent the animal from climbing on the top of them. The test was performed as described previously (Zhang et al., 2016) with minor modifications. The day before the test, all test mice were habituated to the apparatus for 20 min with the two empty cylinders inside, and all stranger mice were separately habituated inside the wire cylinders for 20 min at a time. On the test day, after a 10 min habituation period, all mice were tested in two conditions. In the first condition, an unfamiliar sex- and age-matched C57BL/6J mouse (stranger 1,

S1) was placed in one cylinder and an inanimate ball was placed in the other cylinder. The test mouse was placed in the middle chamber and was allowed to explore the three chambers for 10 min. In this phase (sociability phase), the test mouse had the choice to sniff the unfamiliar mouse (S1) or a novel object (ball). Ball and S1 preference, respectively, were calculated as follows: Ball preference % = $[\text{time spent to explore ball} / (\text{time spent exploring the ball} + \text{time spent to interact with S1})] \times 100$; S1 preference % = $[\text{time spent interacting with S1} / (\text{time spent to explore ball} + \text{time spent to interact with S1})] \times 100$. In the second condition, a novel mouse (stranger 2, S2) replaced the inanimate ball. The test mouse was then placed back into the middle chamber and was again allowed to explore the three chambers for 10 min. Thus, the test mouse had the choice to interact with S1 or S2 in this social novelty phase. S1 and S2 preference, respectively, were calculated as follows: S1 preference % = $[\text{time spent to interact with S1} / (\text{time spent to interact with S1} + \text{time spent to interact with S2})] \times 100$; S2 preference % = $[\text{time spent to interact with S2} / (\text{time spent to interact with S1} + \text{time spent to interact with S2})] \times 100$. Interaction time recordings began when test mice sniffed within 2 cm of the cages. The location of S1, S2 and the ball were changed between tests.

Direct Interaction Test

The direct interaction test was designed as described previously (Zhang et al., 2016), with some modifications. The experimental apparatus is a non-transparent, open-topped box (45 cm × 45 cm × 45 cm). One day before the test, all test mice and stranger mice were habituated to the arena for 20 min. On the test day, test mice were put in the box for a 5-min habituation period, and then a novel stimulus C57BL/6 J mouse (age- and sex-matched) was brought into the same box for 10 min. The following behaviors were recorded as social interaction: anogenital and nose-to-nose sniffing, following (within 2 cm), and allogrooming. Any aggressive behaviors between animals led to termination of the experiment and exclusion of the data from the analysis.

Morris Water Maze Test

The Morris water maze (MWM) test was used to evaluate spatial learning and memory in rodents. The test used a 1.2-m diameter circular blue pool, which was divided into four hypothetical, equal quadrants. A hidden circular platform (11 cm diameter) located in the middle of the target quadrant was submerged approximately 1.5 cm beneath the surface of the water. In this test, mice need to navigate to the hidden platform using spatial cues on the surrounding area across multiple trials. First, mice were trained to find the hidden platform during the learning phase. For this, four trials were conducted per day for 7 consecutive days. On the 8th day, the platform was removed and each mouse was allowed 60 s to search the pool for the platform. Noldus software (EthoVision XT 8.0, Noldus Technology) was used to monitor and track the movement of mice. Latency to find the platform, mean distance to platform, frequency of platform crosses, duration spent in the target quadrant,

and total distance traveled were measured automatically by the software.

Statistical Analysis

Statistical analyses were performed using IBM SPSS Statistics 19 software. Differences in weight between three groups (controls, Satb2 heterozygotes and Satb2 CKO mice) were analyzed by one-way ANOVA test. Differences between Satb2 CKO and control mice in the open field, dark-light exploration test, elevated plus-maze test, three-chamber test, direct interaction test and test phase of the MWM test were analyzed by Student's *t*-tests. Between genotype effects during the PPI test and the acquisition phase of the MWM task were analyzed by a repeated measures ANOVA, followed by a least significant difference test with genotype and pre-pulse intensities value, where genotype and days were the factors, respectively. Results were considered significant when *P*-value < 0.05.

RESULTS

Generation of Satb2 CKO Mice by Deletion of Satb2 in the Cerebral Cortex and Hippocampus

Our previous study has shown that Satb2 is abundantly expressed in the cerebral cortex and hippocampus (Huang et al., 2013a). To delete Satb2 in these two regions, we crossed Emx1-Cre mice (Guo et al., 2000) with Satb2^{flox/flox} mice to obtain Emx1-Cre; Satb2^{flox/flox} (Satb2 CKO) mice. Littermates with other genotypes (i.e., Satb2^{flox/+} and Satb2^{flox/flox}) showed no alterations examined below and were used as control mice. Deletion of Satb2 in the cerebral cortex of CKO mice was confirmed by immunostaining (Figures 1A,B). As Cre recombinase is exclusively active in the brain of Emx1-Cre mice (Guo et al., 2000), the cleft palate developed normally in Satb2 CKO mice (data not shown). Satb2 CKO mice showed normal body weight at birth (Figures 1C,D), but there was about a 20% reduction in body weight at adulthood compared with age-matched control mice (Figures 1C,D). The reduced body weight was first observed at around P15 in male and P20 in female Satb2 CKO mice (Figures 1C,D). Unlike conventional Satb2 mutant mice, which died at birth (Alcamo et al., 2008; Britanova et al., 2008), all the Satb2 CKO mice survived after birth and about 2/3 of CKO mice survived into adulthood (Figures 1E,F). Nevertheless, it is clear that Satb2 deletion in the cerebral cortex and hippocampus leads to growth retardation, which is present in patients with SAS (Zarate and Fish, 2017).

Hyperactivity and Increased Impulsivity in Satb2 CKO Mice

We noticed that Satb2 CKO mice showed hyperactivity in their home cages. To further examine locomotor activity, the open-field test was performed. We found that the total distance traveled was significantly greater in Satb2 CKO mice relative to controls (Figures 2A,B) and the ambulatory time of Satb2 CKO mice was also greater compared with that of control mice (Figure 2C).

These results indicated that hyperactivity was present in the Satb2 CKO mice.

To examine the phenotype of hyperactivity in more detail, we analyzed activity in the open field test every 5 min. The distance traveled gradually reduced in control mice, whereas it showed no obvious change in Satb2 CKO mice over time (Figures 2D,E). Although the total distance traveled was greater in Satb2 CKO mice compared to controls, the average velocity was less than that of control mice (Figure 2F). Hyperactivity is also observed in patients with attention-deficit/hyperactivity disorder (ADHD), which has a characteristic locomotor-related symptom called impulsive behavior (Willcutt, 2012). The cliff avoidance reaction (CAR) is widely used to assess impulsive behavior in rodents (Yamashita et al., 2013). During the 30-min test, about 80% of Satb2 CKO mice fell from the platform, whereas no control mice did so (Figures 2G,H). Taken together, Satb2 CKO mice showed hyperactivity and impulsivity behaviors.

Reduced Anxiety-Like Behaviors in Satb2 CKO Mice

The anxiety-like behaviors were examined in Satb2 CKO mice. First, the dark-light choice test showed that Satb2 CKO mice spent more time in the light box than did control mice (Figure 3A). However, the transition number of Satb2 CKO mice was comparable with control mice (Figure 3B), which may be a consequence of spending more time in the light box. Second, the elevated plus maze test showed that Satb2 CKO mice spent more time in the open arms than did control mice (Figure 3C). Satb2 CKO mice also exhibited more arm transitions than the control mice (Figure 3D). These data indicate reduced anxiety-like behaviors in Satb2 CKO mice.

Abnormal Sensorimotor Gating and Social Interaction in Satb2 CKO Mice

Pre-pulse inhibition of the acoustic startle response test, which is a measure of sensorimotor gating, was performed. The Satb2 CKO mice showed significant PPI deficits compared with control mice at 73 and 82 dB pre-pulse intensities, and showed an increased response tendency at 65 dB intensities (Figure 4A). The abnormal PPI reaction in Satb2 CKO mice indicates that the sensorimotor gating is disturbed in Satb2 CKO mice.

The social-related behaviors were then tested in the control and Satb2 CKO mice. The three-chamber social interaction test was first performed. Both control mice and Satb2 CKO mice showed a preference for S1 over the inanimate ball (Figure 4B), which indicates normal social ability in Satb2 CKO mice. In the social novelty phase, Satb2 CKO mice showed a similar preference for S2 and S1 mice, while the control mice showed a preference for the S2 mouse (Figure 4C), suggesting that social novelty is impaired in Satb2 CKO mice. In the direct social interaction test, however, Satb2 CKO mice spent more time interacting with the stranger mouse than did the control mice (Figure 4D). Taken together, these results indicate that sensorimotor gating is impaired and social interaction behaviors are altered in Satb2 CKO mice.

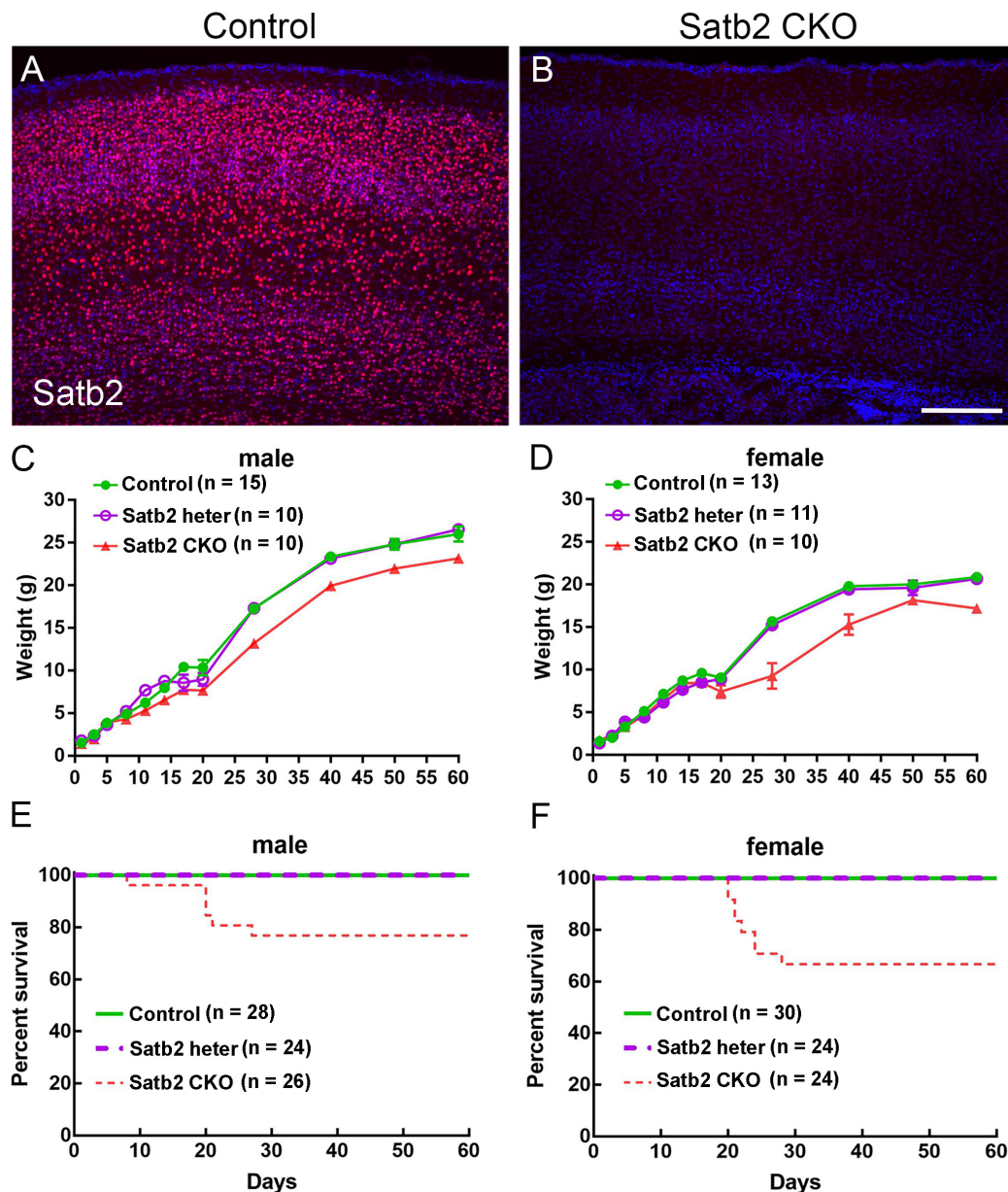


FIGURE 1 | Reduced body weight and survival rate in adult Satb2 CKO mice. **(A,B)** Satb2 immunostaining verified that Satb2 was deleted in the cerebral cortex in Satb2 CKO mice. **(C,D)** The growth curve of male **(C)** and female **(D)** control, Satb2 heterozygotes, and Satb2 CKO mice. Both male and female Satb2 heterozygotes (*Emx1-Cre; Satb2^{fllox/+}*) and CKO mice had a normal body weight until postnatal day 15 (P15). The one-way ANOVA test measured the significant differences between these groups appeared at P15 in male mice [$F_{[2,32]} = 14.55$, $P < 0.0001$; Tukey's multiple comparisons test showed $P = 0.7673$ (controls vs. Satb2 heterozygotes); $P < 0.0001$ (controls vs. Satb2 CKO mice); $P = 0.0008$ (Satb2 heterozygotes vs. Satb2 CKO mice)], and P20 in female mice [$F_{[2,31]} = 4.697$, $P = 0.0165$; Tukey's multiple comparisons test showed $P = 0.9858$ (controls vs. Satb2 heterozygotes); $P = 0.0225$ (controls vs. Satb2 CKO mice); $P = 0.0406$ (Satb2 heterozygotes vs. Satb2 CKO mice)]. **(E,F)** The survival rate of male **(E)** and female **(F)** wild-type, Satb2 heterozygotes, and Satb2 CKO mice. The survival rate of female Satb2 CKO mice was lower than male CKO mice. In **(C,D)**, data are presented as the mean \pm SEM. Scale bar = 200 μ m **(B)**.

Defective Spatial Learning and Memory in Satb2 CKO Mice

Deletion of Satb2 in the hippocampus with CamKII-Cre at the postnatal stage leads to impairment of long-term fear memory and object recognition memory (Jaitner et al., 2016). We examined whether spatial learning and memory was altered

in the CKO mice, in which Satb2 was deleted in the cortex and hippocampus at the embryonic stage. During the learning phase of the MWM, Satb2 CKO mice exhibited a longer latency in finding the platform than control mice (**Figure 5A**). The net decrease of the latency between days 1 and 7 in the control and Satb2 CKO mice were 21.33 ± 3.589 s and

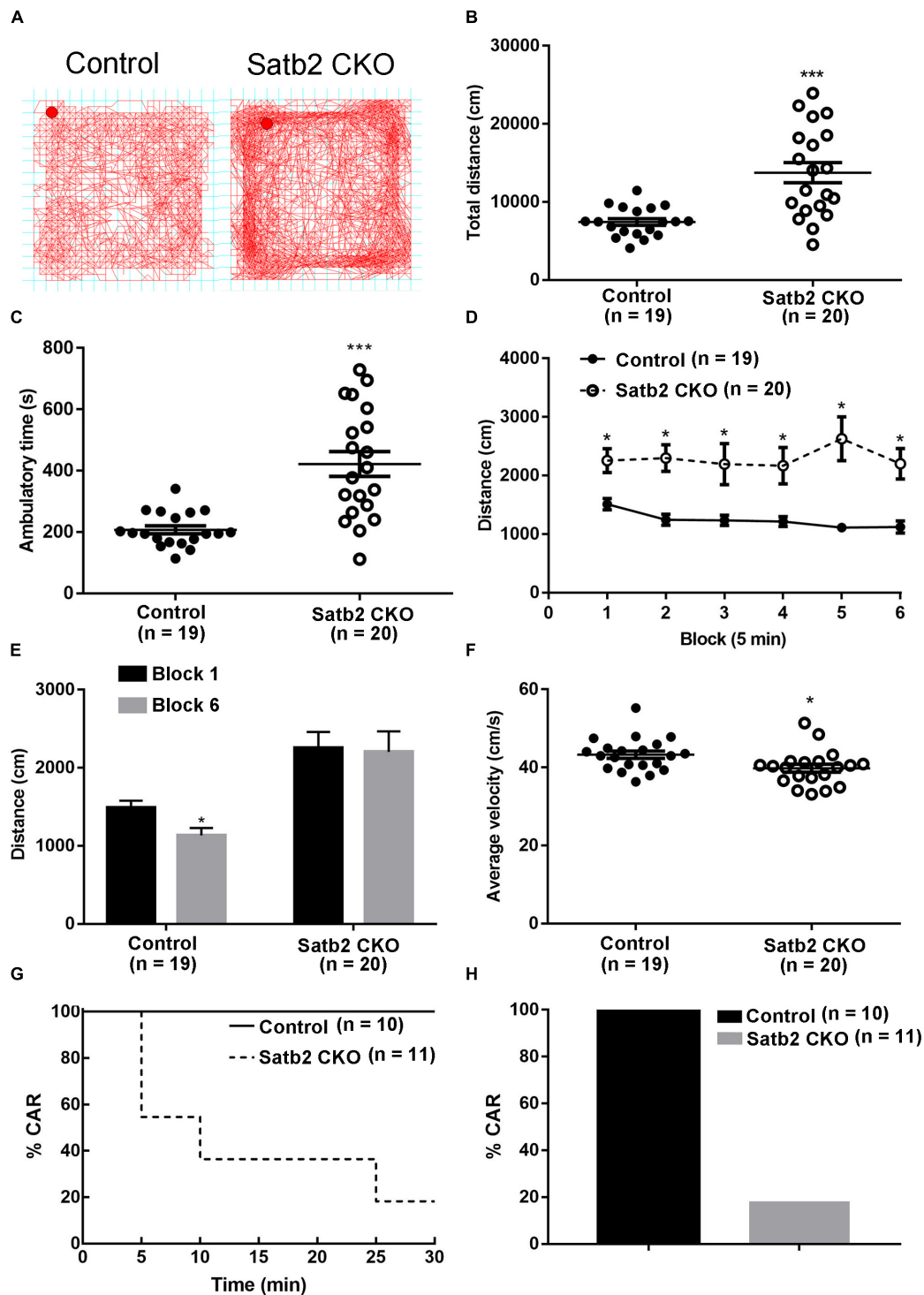
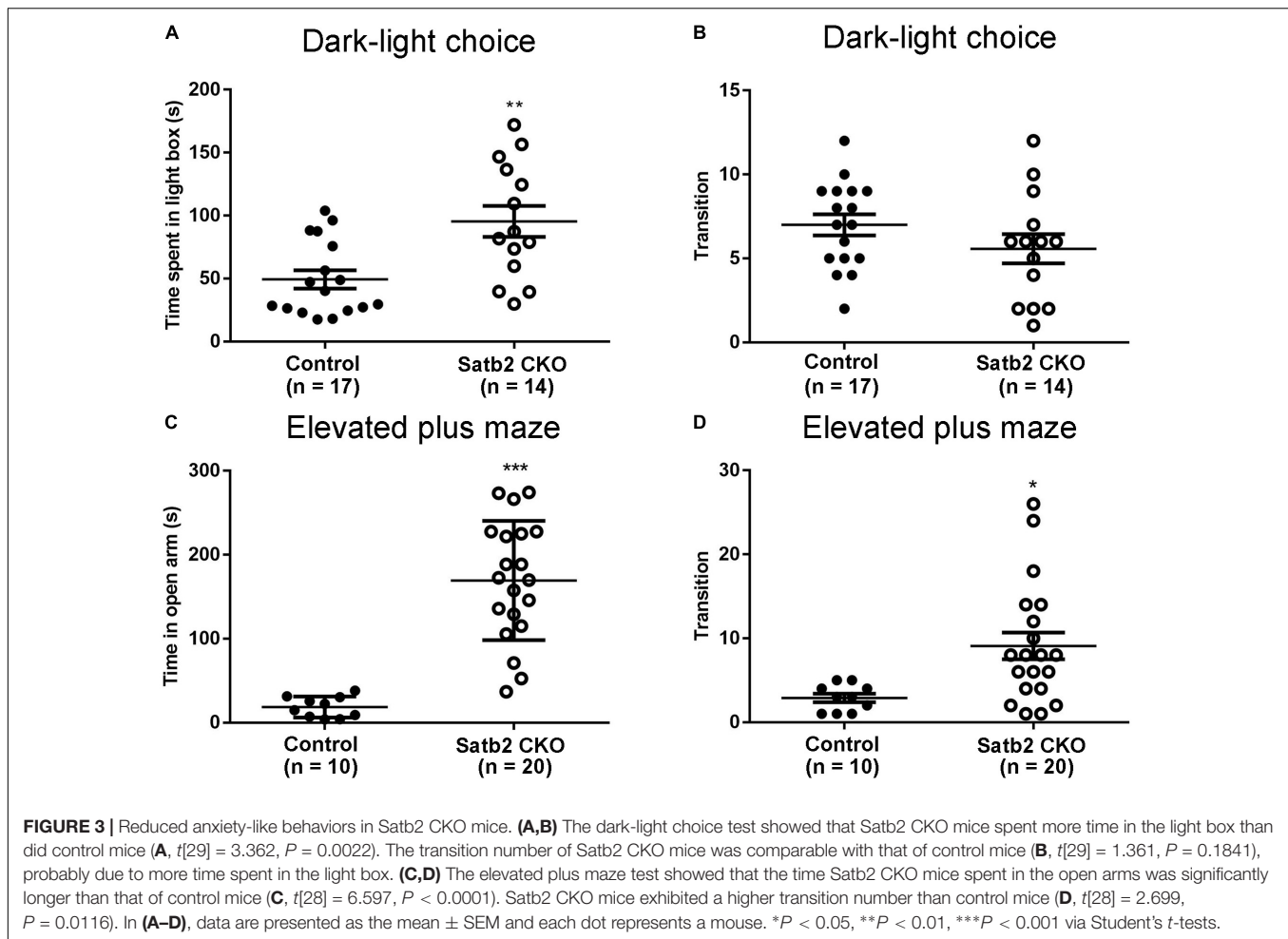


FIGURE 2 | Hyperactivity and increased impulsivity in Satb2 CKO mice. **(A)** The traveling trace in the open field of the control and Satb2 CKO mice. **(B)** The total distance traveled by Satb2 CKO mice in the open field was much higher than that of control mice ($t[37] = 4.553$, $P < 0.001$). **(C)** The ambulatory time of Satb2 CKO mice was longer than that of the control mice in the open field ($t[37] = 4.951$, $P < 0.001$). **(D,E)** The distance traveled was analyzed every 5 min; it gradually reduced in control mice over time, whereas this was not observed in Satb2 CKO mice as shown by persistent moving in the field **(D)**. The traveled distance in block 6 was significantly lower than that in block 1 in control mice and comparable with that in block 1 in Satb2 CKO mice (**E**, $t_{\text{control}[36]} = 2.687$, $P = 0.0108$; $t_{\text{CKO}[38]} = 0.1505$, $P = 0.8812$). **(F)** The average velocity of Satb2 CKO mice was lower than that of control mice ($t[37] = 2.196$, $P = 0.0345$). **(G,H)** The CAR test was performed to test impulsivity. During the 30-min test, more Satb2 CKO mice fell from the platform than did control mice, none of which fell **(G)**. In total, about 80% of Satb2 CKO mice fell from the platform **(F)**. In **(B–F)**, data are presented as the mean \pm SEM; each dot represents a mouse in **(B,C,F)**. * $P < 0.05$, *** $P < 0.001$ via Student's t -tests in **(B,C,E,F)**. Data were analyzed using a repeated measures ANOVA in **(D)**.



9.944 \pm 4.138 s, respectively. These results indicated that the Satb2 CKO mice may have impaired learning capacity during the consecutive 7-days training phase of the MWM task than their control counterparts. During the memory test, the latency to the location of platform and the mean distance to the platform was longer in Satb2 CKO mice compared with those in the control mice (**Figures 5B,C**). Consistently, the number of platform crossings and the duration spent in the target quadrant were lower in the Satb2 CKO mice compared to control mice (**Figures 5D,E**). These observed changes were not due to the different swimming abilities, as shown by the similar swimming distances between Satb2 CKO and control mice (**Figure 5F**). Thus, Satb2 CKO mice showed impaired spatial learning and memory.

Loss of “Barrels” in Layer IV in the Cerebral Cortex of Satb2 CKO Mice

In the morphogenesis of the cerebral cortex, Satb2 is known to regulate the development of both callosal projection neurons in layers II–III (Alcamo et al., 2008; Britanova et al., 2008) and subcerebral projection neurons in layer V (Leone et al., 2015; McKenna et al., 2015). We first examined if the corpus callosum is

affected in Satb2 CKO mice. As shown in **Figures 6A,A'**, although AuCl₃-labeled callosal axons were present in the midline region at the level around Bregma -0.94 mm in Satb2 CKO mice, their thickness was reduced relative to the control. At caudal level around Bregma -1.82 mm, AuCl₃-labeled corpus callosum was present in the control mice (**Figure 6B**) but absent in Satb2 CKO mice (arrowheads, **Figure 6B'**). Next, we moved to examine the expression of layer-specific genes in Satb2 CKO mice. Cux2 was expressed in layers II–IV in the control mice (**Figure 6C**), but its expression was much reduced in Satb2 CKO mice (**Figure 6C'**). Consistent with previous studies (Alcamo et al., 2008), Ctip2 was strongly expressed in layer V, but intense Ctip2 expression expanded into layers II–IV in Satb2 CKO mice at P6 (**Figures 6D,D'**). Tle4 is one of the deep layer markers, and mainly expressed in layer VI (**Figure 6E**) (Bin et al., 2005). However, Tle4 expression was increased in Satb2 CKO mice at P6 (**Figure 6E'**). Next, we examined whether the development of layer IV cortical neurons is affected in Satb2 CKO mice. ROR β is a specific marker for layer IV cortical neurons (Takeuchi et al., 2007) and we found that ROR β mRNA was dramatically reduced at P0 (**Figures 7A,A'**), more severely reduced at P6 (**Figure 7B'**), and totally lost in the Satb2 CKO mice at P15 (**Figure 7C'**). In addition, layer IV is the main target area

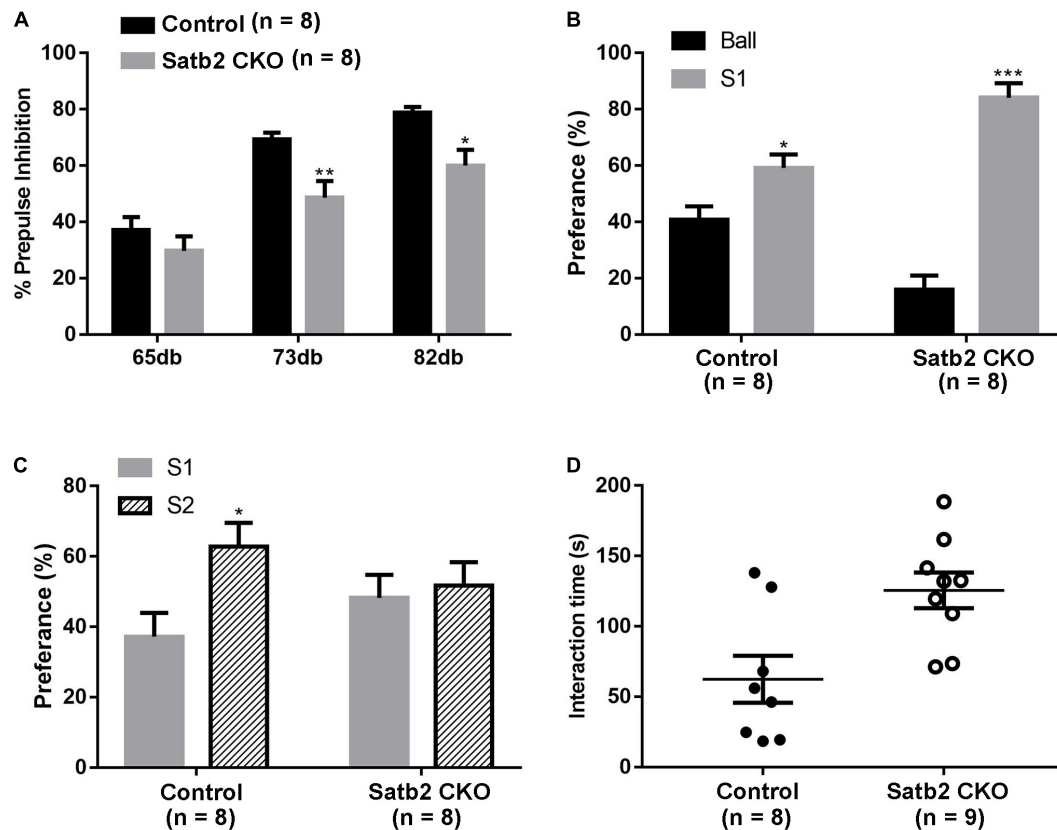


FIGURE 4 | Impaired sensorimotor gating and social novelty in Satb2 CKO mice. **(A)** The pre-pulse inhibition (PPI) test shows that Satb2 CKO mice had a significant PPI deficit compared with control mice at 73 and 82 dB pre-pulse intensities. The repeated measures ANOVA (2 genotypes \times 3 pre-pulse intensities with repeated measures on pre-pulse intensities) showed that both the genotypes and pre-pulse intensities affected response reactivity [genotypes effect: $F[1,42] = 17.76$, $P = 0.0001$; pre-pulse intensities effect: $F[2,42] = 33.52$, $P < 0.0001$; interaction: $F[2,42] = 1.246$, $P = 0.298$; $P = 0.0074$ (73dB); $P = 0.0165$ (82 dB); $P = 0.5856$ (65 dB)]. **(B,C)** The three-chamber social interaction test was performed. Satb2 CKO mice showed a preference for the animate stranger mouse (S1) over the inanimate ball, with no difference compared with control mice **(B)**, $t_{\text{control}}[14] = 2.755$, $P = 0.0155$; $t_{\text{CKO}}[14] = 9.409$, $P < 0.0001$. Satb2 CKO mice showed a similar preference to the S2 mouse and S1 mouse, while the control mice showed a preference for the S2 mouse **(C)**, $t_{\text{control}}[14] = 2.673$, $P = 0.0182$; $t_{\text{CKO}}[14] = 0.3878$, $P = 0.7040$. **(D)** In the direct social interaction test, the interaction time of Satb2 CKO mice was longer compared with control mice ($t[15] = 3.057$, $P = 0.0080$). In **(A–D)**, data are presented as the mean \pm SEM and each dot represents a mouse in **(D)**. * $P < 0.05$ via Student's *t*-tests in **(B–D)**, and repeated measures ANOVA in **(A)**. ** $P < 0.01$, *** $P < 0.001$.

for thalamocortical projections, and layer IV neurons together with thalamocortical projection axons, particularly those relaying sensory information from the whiskers, form “barrels” in the somatosensory cortex in rodents (Woolsey, 1990; Ding et al., 2003). The dense distribution of Hoechst-stained cells in the septal regions revealed the “barrels” in the control mice (arrows, **Figure 7E**). However, barrels were absent in Satb2 CKO mice, as shown by the homogenous distribution of Hoechst-stained cells in the somatosensory cortex (arrows, **Figure 7E'**). Meanwhile, the serotonin transporter (5-HTT) expressed by thalamocortical projection axons were densely located within individual barrels in layer IV of the wild-type somatosensory cortex (**Figures 7F,G**), but 5-HTT-positive axons were sparsely and homogeneously distributed in layer IV of Satb2 CKO mice (**Figures 7F',G'**), further supporting the loss of the somatosensory map in the cortex of Satb2 CKO mice. Furthermore, we examined whether the process of thalamocortical axons entering cortex is affected in Satb2 CKO mice. 5-HTT-positive fibers reached the deep layer

of cortex at P0 in Satb2 CKO mice as the control mice did (**Figures 7D,D'**). It should be noted that 5-HTT-positive fibers did not aggregate in layer IV in both control mice and Satb2 CKO mice at this stage (**Figures 7D,D'**). Previous studies have revealed impaired development of cortical neurons in layers II–III and V in the absence of Satb2 (Alcamo et al., 2008; Britanova et al., 2008). Furthermore, we demonstrated that the development of layer IV cortical neurons and the inputs from the thalamus are also impaired.

DISCUSSION

Satb2-associated syndrome, caused by the alteration in the Satb2 gene, is characterized by growth delay, intellectual disability, abnormal behaviors, and craniofacial and skeletal anomalies (Zarate and Fish, 2017). To investigate the fundamental basis of SAS-associated intellectual disability and abnormal

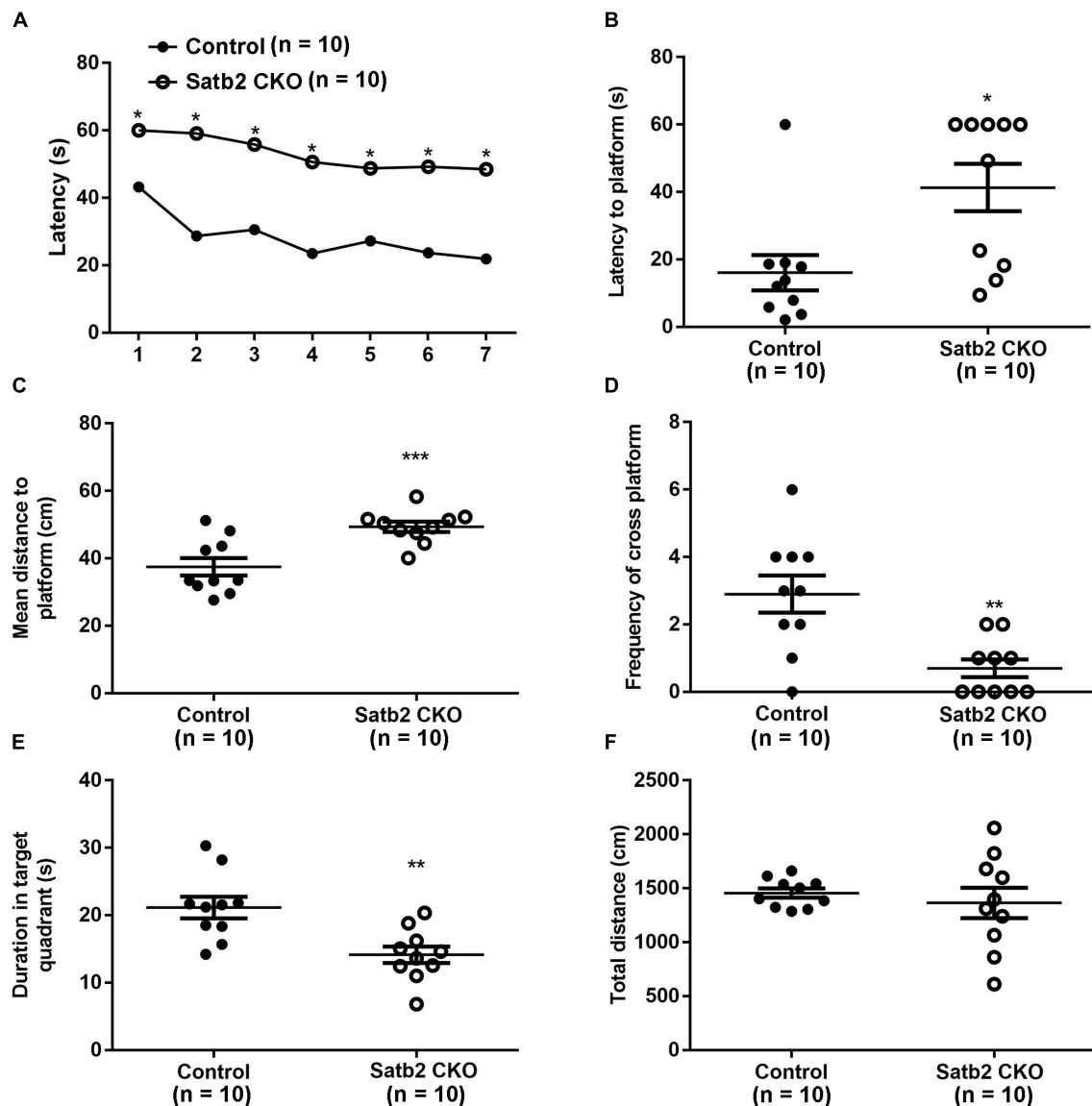
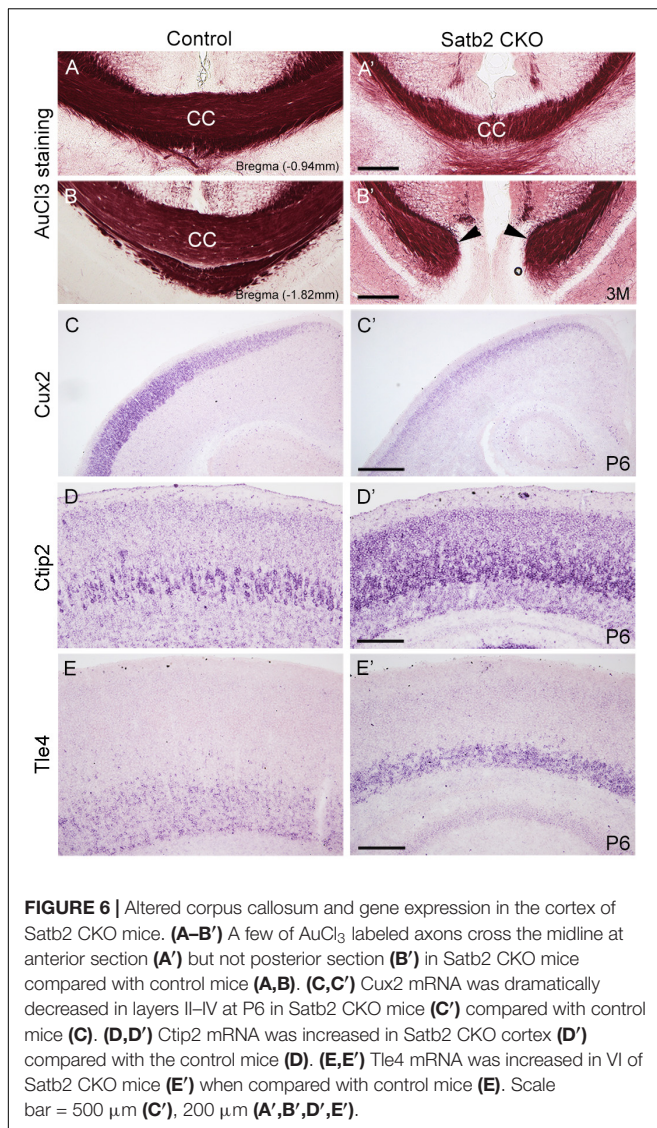


FIGURE 5 | Impaired spatial learning and memory in Satb2 CKO mice. The Morris water maze test was performed. **(A)** During the learning phase, the latency to the platform was significantly longer in Satb2 CKO mice than in the control mice. The analysis of the latency using a repeated measures ANOVA (2 genotypes \times 7 days with repeated measures on days) showed that both the genotypes and training days affected learning ability (genotype effect: $F[1,18] = 38.53$, $P < 0.0001$; days effect: $F[6,108] = 11.28$, $P < 0.0001$; and interaction: $F[6,108] = 1.59$, $P = 0.1571$). **(B)** During the memory trial, the latency to the platform was longer in Satb2 CKO mice compared with the control mice ($t[18] = 2.872$, $P = 0.0101$). **(C)** During the memory trial, the mean distance to the platform was higher in the Satb2 CKO mice compared with the control mice ($t[18] = 3.944$, $P = 0.0010$). **(D)** The duration in the target quadrant was shorter in Satb2 CKO mice compared to control mice ($t[18] = 3.493$, $P = 0.0026$). **(E)** The frequency of platform crossings was lower in Satb2 CKO mice compared to control mice ($t[18] = 3.633$, $P = 0.0019$). **(F)** Satb2 CKO mice showed a similar swimming velocity to control mice ($t[18] = 0.6638$, $P = 0.5153$). In **(A)**, data are presented as the mean and $*P < 0.05$ by a repeated measures ANOVA. In **(B–F)**, data are presented as the mean \pm SEM, and each dot represents a mouse. $*P < 0.05$, $**P < 0.01$, $***P < 0.001$ via Student's *t*-tests.

behaviors, and explore the behavioral consequences of Satb2-implicated behaviors, Satb2 was specifically deleted in the cerebral cortex and hippocampus in mice by crossing Emx1-Cre with Satb2^{flax/flax} mice. Unlike Satb2 KO and previous Satb2 CKO mice, which died at birth and juvenile period, respectively (Alcamo et al., 2008; Leone et al., 2015), about 2/3 of CKO mice in this study survived into adulthood. We found that the Satb2 CKO mice exhibited hyperactivity,

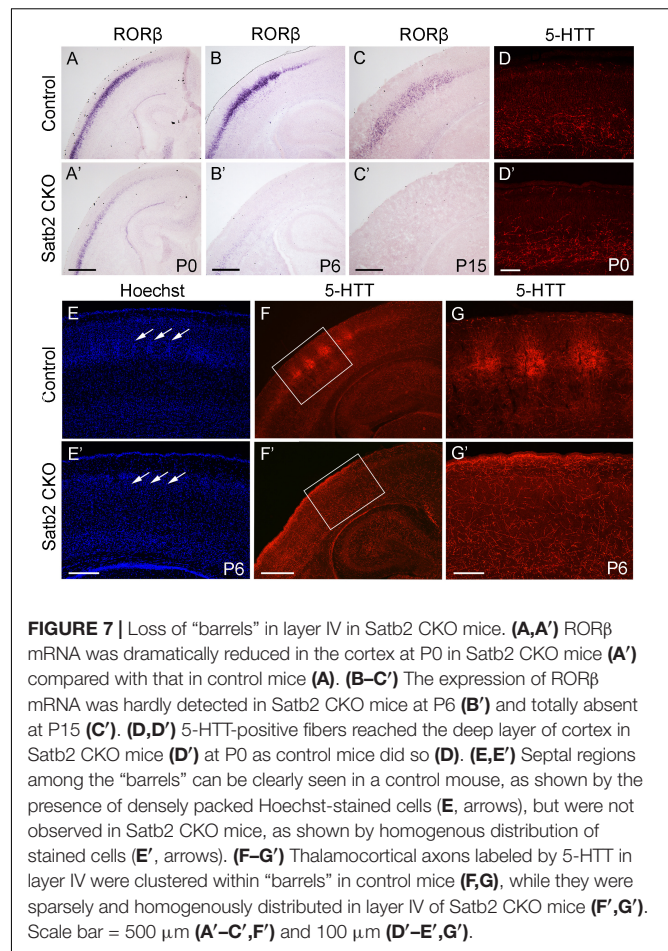
increased impulsivity, reduced anxiety-like behaviors, defective sensorimotor gating, and abnormal social interaction behaviors, which reflect most of the behavioral abnormalities observed in individuals with SAS.

Previous case reports have consistently reported the presence of developmental delay/intellectual disability in individuals with SAS (Zarate et al., 2017, 2018). In previous research, CamKII α -Cre;Satb2 CKO mice with postnatal deletion of Satb2



showed impairments in long-term memory in a contextual fear conditioning test and object location memory test (Jaitner et al., 2016), and in spatial learning and memory in the MWM test (Li et al., 2017). Our Satb2 CKO mice also displayed impaired spatial learning and memory (Figure 5). Furthermore, previous work has found that a deletion of Satb2 via AAV-Cre viral delivery to the hippocampus of adult Satb2^{flax/flax} mice also leads to impaired spatial learning and memory (Li et al., 2017). Thus, loss of Satb2 in the hippocampus alone is sufficient to disturb spatial learning and memory in mice.

It has been reported that over 80% of adult individuals with SAS have a jovial personality (Zarate et al., 2018). Although there are no standard behavioral paradigms to analyze this in mouse models of SAS, anxiety-like behaviors can, to some extent, reflect emotional states; we found reduced anxiety-like behaviors in Satb2 CKO mice compared to control mice (Figure 3). In addition, more than 20% of individuals with SAS show hyperactivity and distractibility (Zarate et al., 2017, 2018), which



are also symptoms of ADHD. Satb2 CKO mice were overactive in their home cages compared with the control mice, and exhibited hyperactivity in the open field (Figure 2). In the CAR test, Satb2 CKO mice were prone to falling from the platform, which may be caused by distractibility (Figure 2). Furthermore, about 20% of individuals with SAS exhibit autistic behaviors (Zarate et al., 2017, 2018). Using the three-chamber test and direct social interaction test, we found that Satb2 CKO mice showed normal social abilities; however, social novelty was disturbed (Figure 4). Finally, about 10% of individuals with SAS have social affective behaviors and sensory issues (Zarate et al., 2018), and Satb2 has been recognized as a risk gene for schizophrenia (Jaitner et al., 2016). Consistent with these findings, Satb2 CKO mice showed significant and distinct PPI deficits compared to control mice. Thus, most symptoms in patients with SAS were observed in our mouse model with the deletion of Satb2 in the cerebral cortex and hippocampus at embryonic stages, and it may therefore serve as an animal model for studying the neurobiological mechanisms underlying SAS.

Satb2 is a determinant gene for the cortical neuronal fate in layers II–III and layer V–VI (Alcamo et al., 2008; Britanova et al., 2008; Leone et al., 2015; McKenna et al., 2015). Consistent with results from a previous study (Alcamo et al., 2008), we confirmed RORβ mRNA was dramatically reduced at P0, more

severely reduced at P6, and totally lost at P15 in Satb2 CKO mice (**Figure 7**). In addition, loss of “barrels” in layer IV of the somatosensory cortex was found in Satb2 CKO mice. The formation of this unique structure is driven by whisker-related sensory inputs carried by thalamocortical projections during the early postnatal period (Killackey et al., 1990; Huang et al., 2013b). The loss of this somatosensory map strongly suggests that sensory information, including whisker-related information, cannot be processed properly within the cerebral cortex after deletion of Satb2. In addition, the corpus callosum is responsible for communication between the two hemispheres and therefore important for higher brain functions (Paul et al., 2007). In previous studies, Satb2 KO and Satb2 CKO mice have shown impairment of callosal development, with reduced axon projections across the midline (Alcamo et al., 2008; Leone et al., 2015). A similar phenotype has been observed in our Satb2 CKO mice. The corpus callosum was reduced at the anterior level and absent at the caudal level in Satb2 CKO mice (**Figure 6**). Data from gene expression and axonal connections demonstrate that the development of cortical neurons in multiple layers is impaired, and these defects may lead to behavioral abnormalities in Satb2 CKO mice. Besides, a large number of genes are differentially expressed in Satb2 CKO mice, and some of them are risk genes associated with schizophrenia and other neurodevelopmental disorders (Whitton et al., 2018). Moreover, the cortical layers II-III contain the major population of callosal neurons (Wang et al., 2007), and their neuronal identities are

severely affected in Satb2 CKO mice. Importantly, the excess of pyramidal neurons in cortical layers II-III caused autism-like behaviors in a mouse model (Fang et al., 2014). Thus, Satb2 may play some roles in the pathogenesis of these neurodevelopment-associated mental diseases.

AUTHOR CONTRIBUTIONS

QZ and YH conception and design, data acquisition, analysis and interpretation, and drafting and revising the article. LZ, N-NS, and Y-QD conception and design, data analysis and interpretation, supervision, funding acquisition, and drafting and revising the article.

FUNDING

This work was supported by grants from the National Natural Science Foundation of China (31671061 to LZ, 81571332 and 91232724 to Y-QD, and 31771134 to N-NS).

ACKNOWLEDGMENTS

We thank all of the participants for their commitment to this study.

REFERENCES

- Alcamo, E. A., Chirivella, L., Dautzenberg, M., Dobрева, G., Farinas, I., Grosschedl, R., et al. (2008). Satb2 regulates callosal projection neuron identity in the developing cerebral cortex. *Neuron* 57, 364–377. doi: 10.1016/j.neuron.2007.12.012
- Bin, C., Laura, R. S., and Susan, K. M. (2005). Fezl regulates the differentiation and axon targeting of layer 5 subcortical projection neurons in cerebral cortex. *Proc. Natl. Acad. Sci. U.S.A.* 102, 17184–17189.
- Britanova, O., de Juan Romero, C., Cheung, A., Kwan, K. Y., Schwark, M., Gyorgy, A., et al. (2008). Satb2 is a postmitotic determinant for upper-layer neuron specification in the neocortex. *Neuron* 57, 378–392. doi: 10.1016/j.neuron.2007.12.028
- Ding, Y. Q., Yin, J., Xu, H. M., Jacquin, M. F., and Chen, Z. F. (2003). Formation of whisker-related principal sensory nucleus-based lemniscal pathway requires a paired homeodomain transcription factor, Drg11. *J. Neurosci.* 23, 7246–7254.
- Dobрева, G., Chahrouh, M., Dautzenberg, M., Chirivella, L., Kanzler, B., Farinas, I., et al. (2006). SATB2 is a multifunctional determinant of craniofacial patterning and osteoblast differentiation. *Cell* 125, 971–986. doi: 10.1016/j.cell.2006.05.012
- Fang, W. Q., Chen, W. W., Jiang, L., Liu, K., Yung, W. H., Fu, A. Y., et al. (2014). Overproduction of upper-layer neurons in the neocortex leads to autism-like features in mice. *Cell Rep.* 9, 1635–1643. doi: 10.1016/j.celrep.2014.11.003
- Geyer, M. A., and Dulawa, S. C. (2003). Assessment of murine startle reactivity, prepulse inhibition, and habituation. *Curr. Protoc. Neurosci.* 24, 8.17.1–8.17.15. doi: 10.1002/0471142301.ns0817s24
- Guo, H., Hong, S., Jin, X. L., Chen, R. S., Avasthi, P. P., Tu, Y. T., et al. (2000). Specificity and efficiency of Cre-mediated recombination in Emx1-Cre knock-in mice. *Biochem. Biophys. Res. Commun.* 273, 661–665. doi: 10.1006/bbrc.2000.2870
- Hilde, K. L., Levine, A. J., Hinckley, C. A., Hayashi, M., Montgomery, J. M., Gullo, M., et al. (2016). Satb2 is required for the development of a spinal exteroceptive microcircuit that modulates limb position. *Neuron* 91, 763–776. doi: 10.1016/j.neuron.2016.07.014
- Huang, Y., Song, N. N., Lan, W., Hu, L., Su, C. J., Ding, Y. Q., et al. (2013a). Expression of transcription factor Satb2 in adult mouse brain. *Anat. Rec.* 296, 452–461. doi: 10.1002/ar.22656
- Huang, Y., Song, N. N., Lan, W., Zhang, Q., Zhang, L., Zhang, L., et al. (2013b). Sensory input is required for callosal axon targeting in the somatosensory cortex.pdf. *Mol. Brain* 6, 53–65. doi: 10.1186/1756-6606-6-53
- Jaitner, C., Reddy, C., Abentung, A., Whittle, N., Rieder, D., Delekate, A., et al. (2016). Satb2 determines miRNA expression and long-term memory in the adult central nervous system. *eLife* 5:17361. doi: 10.7554/eLife.17361
- Killackey, H. P., Jacquin, M. F., and Rhoades, R. W. (1990). “The somatosensory system,” in *Development of Sensory Systems in Mammals*, ed. J. R. Coleman (New York, NY: Wiley).
- Leone, D. P., Heavner, W. E., Ferenczi, E. A., Dobрева, G., Huguenard, J. R., Grosschedl, R., et al. (2015). Satb2 regulates the differentiation of both callosal and subcortical projection neurons in the developing cerebral cortex. *Cereb. Cortex* 25, 3406–3419. doi: 10.1093/cercor/bhu156
- Li, Y., You, Q. L., Zhang, S. R., Huang, W. Y., Zou, W. J., Jie, W., et al. (2017). Satb2 ablation impairs hippocampus-based long-term spatial memory and short-term working memory and immediate early genes (IEGs)-mediated hippocampal synaptic plasticity. *Mol. Neurobiol.* doi: 10.1007/s12035-017-0531-5 [Epub ahead of print].
- McKenna, W. L., Ortiz-Londono, C. F., Mathew, T. K., Hoang, K., Katzman, S., and Chen, B. (2015). Mutual regulation between Satb2 and Fezf2 promotes subcortical projection neuron identity in the developing cerebral cortex. *Proc. Natl. Acad. Sci. U.S.A.* 112, 11702–11707. doi: 10.1073/pnas.1504144112
- Paul, L. K., Brown, W. S., Adolphs, R., Tyszka, J. M., Richards, L. J., Mukherjee, P., et al. (2007). Agenesis of the corpus callosum: genetic, developmental and functional aspects of connectivity. *Nat. Rev. Neurosci.* 8, 287–299. doi: 10.1038/nrn2107
- Song, N. N., Xiu, J. B., Huang, Y., Chen, J. Y., Zhang, L., Gutknecht, L., et al. (2011). Adult raphe-specific deletion of Lmx1b leads to central serotonin deficiency. *PLoS One* 6:e15998. doi: 10.1371/journal.pone.0015998

- Takeuchi, A., Hamasaki, T., Litwack, E. D., and O'Leary, D. D. (2007). Novel IgCAM, MDGA1, expressed in unique cortical area- and layer-specific patterns and transiently by distinct forebrain populations of Cajal-Retzius neurons. *Cereb. Cortex* 17, 1531–1541. doi: 10.1093/cercor/bhl064
- Usui, D., Shimada, S., Shimojima, K., Sugawara, M., Kawasaki, H., Shigematu, H., et al. (2013). Interstitial duplication of 2q32.1-q33.3 in a patient with epilepsy, developmental delay, and autistic behavior. *Am. J. Med. Genet. A* 161A, 1078–1084. doi: 10.1002/ajmg.a.35679
- Wahlsten, D., Colbourne, F., and Pleus, R. (2003). A robust, efficient and flexible method for staining myelinated axons in blocks of brain tissue. *J. Neurosci. Methods* 123, 207–214.
- Wang, C. L., Zhang, L., Zhou, Y., Zhou, J., Yang, X. J., Duan, S. M., et al. (2007). Activity-dependent development of callosal projections in the somatosensory cortex. *J. Neurosci.* 27, 11334–11342. doi: 10.1523/jneurosci.3380-07.2007
- Whitton, L., Apostolova, G., Rieder, D., Dechant, G., Rea, S., Donohoe, G., et al. (2018). Genes regulated by SATB2 during neurodevelopment contribute to schizophrenia and educational attainment. *PLoS Genet.* 14:e1007515. doi: 10.1371/journal.pgen.1007515
- Willcutt, E. G. (2012). The prevalence of DSM-IV attention-deficit/hyperactivity disorder: a meta-analytic review. *Neurotherapeutics* 9, 490–499. doi: 10.1007/s13311-012-0135-8
- Woolsey, T. A. (1990). "Peripheral alteration and somatosensory development," in *Development of Sensory Systems in Mammals*, ed. J. R. Coleman (New York, NY: Wiley), 461–516.
- Yamashita, M., Sakakibara, Y., Hall, F. S., Numachi, Y., Yoshida, S., Kobayashi, H., et al. (2013). Impaired cliff avoidance reaction in dopamine transporter knockout mice. *Psychopharmacology* 227, 741–749. doi: 10.1007/s00213-013-3009-9
- Zarate, Y. A., and Fish, J. L. (2017). SATB2-associated syndrome: mechanisms, phenotype, and practical recommendations. *Am. J. Med. Genet. A* 173, 327–337. doi: 10.1002/ajmg.a.38022
- Zarate, Y. A., Kalsner, L., Basinger, A., Jones, J. R., Li, C., Szybowska, M., et al. (2017). Genotype and phenotype in 12 additional individuals with SATB2-associated syndrome. *Clin. Genet.* 92, 423–429. doi: 10.1111/cge.12982
- Zarate, Y. A., Smith-Hicks, C. L., Greene, C., Abbott, M. A., Siu, V. M., Calhoun, A., et al. (2018). Natural history and genotype-phenotype correlations in 72 individuals with SATB2-associated syndrome. *Am. J. Med. Genet. A* 176, 925–935. doi: 10.1002/ajmg.a.38630
- Zhang, J. B., Chen, L., Lv, Z. M., Niu, X. Y., Shao, C. C., Zhang, C., et al. (2016). Oxytocin is implicated in social memory deficits induced by early sensory deprivation in mice. *Mol. Brain* 9:98. doi: 10.1186/s13041-016-0278-3

Conflict of Interest Statement: The authors declare that the research was conducted in the absence of any commercial or financial relationships that could be construed as a potential conflict of interest.

Copyright © 2019 Zhang, Huang, Zhang, Ding and Song. This is an open-access article distributed under the terms of the Creative Commons Attribution License (CC BY). The use, distribution or reproduction in other forums is permitted, provided the original author(s) and the copyright owner(s) are credited and that the original publication in this journal is cited, in accordance with accepted academic practice. No use, distribution or reproduction is permitted which does not comply with these terms.



Glycine Regulates Neural Stem Cell Proliferation During Development *via* Lnx1-Dependent Notch Signaling

Abdelhamid Bekri^{1,2}, Meijiang Liao¹ and Pierre Drapeau^{1,3*}

¹Research Center of the University of Montreal Hospital Center (CRCHUM), University of Montreal, Montreal, QC, Canada,

²Department of Biochemistry, University of Montreal, Montreal, QC, Canada, ³Department of Neuroscience, University of Montreal, Montreal, QC, Canada

During development of the zebrafish embryo, glycine signaling promotes the differentiation of neural stem cells (NSCs). We found that glycine signaling suppresses the expression of Ligand of Numb X1 (*lnx1*, Ligand of numb protein-x1), a gene of unknown function during NSC differentiation that is selectively expressed in the embryonic central nervous system (CNS). As a consequence, Numb levels were stabilized and Notch activity (measured as *her4.1* expression) was reduced, promoting NSC differentiation. These consequent actions were blocked by knockdown of *lnx1*. In contrast, *lnx1* overexpression increased NSC proliferation and led to defects of neural tube closure at the early stages of development. Thus, our data provide evidence that glycine/*lnx1* signaling modulates NSC proliferation by regulation of Notch signaling.

Keywords: LNX1, NSCs, glycine signaling, neurogenesis, Notch activity

OPEN ACCESS

Edited by:

Abdul R. Asif,
University of Göttingen, Germany

Reviewed by:

Raman M. Das,
University of Manchester,
United Kingdom
Daniele Bottai,
University of Milan, Italy

*Correspondence:

Pierre Drapeau
p.drapeau@umontreal.ca

[†]Lead contact

Received: 23 November 2018

Accepted: 1 February 2019

Published: 18 February 2019

Citation:

Bekri A, Liao M and Drapeau P (2019) Glycine Regulates Neural Stem Cell Proliferation During Development *via* Lnx1-Dependent Notch Signaling. *Front. Mol. Neurosci.* 12:44. doi: 10.3389/fnmol.2019.00044

INTRODUCTION

During neuronal development an early spontaneous electrical activity is generated in neural stem cells (NSCs) as an essential step for their proliferation, migration and differentiation (Spitzer, 2006) and involves several neurotransmitters including glutamate, GABA and glycine (Demarque et al., 2002; Scaini et al., 2010). Here we investigated the role of glycine signaling during neuronal development in the zebrafish embryo. We demonstrated previously that glycine signaling regulates NSC proliferation (Mcdearnid et al., 2006) and differentiation (Cote and Drapeau, 2012) by promoting survival of a subpopulation of NSCs (Bekri and Drapeau, 2018). An RNA sequencing analysis revealed that glycine signaling regulates several pathways in NSC development (Samarut et al., 2016) as well as some outlying genes, with Ligand of numb protein-x1 (*lnx1*) among the most affected.

lnx1 protein is a RING-type E3 ubiquitin ligase (De Bie and Ciechanover, 2011; Flynn et al., 2011) that degrades Numb (Dho et al., 1998), a cell fate determinant (Uemura et al., 1989). Furthermore, Numb is associated with Shh signaling (Di Marcotullio et al., 2011) and P53 signaling (Colaluca et al., 2008), both participating in glycine-dependent neurogenesis in zebrafish models (Samarut et al., 2016; Bekri and Drapeau, 2018). Importantly, Numb is well-known to be an inhibitor of Notch signaling (Roegiers and Jan, 2004; McGill et al., 2009), but further elucidations are required to understand how Notch and *lnx1* activity correlates with other pathways to fine-tune neuronal development.

We report here that glycine signaling suppressed *lnx1* expression in NSCs and consequently modulated Notch activity by controlling Numb protein degradation.

MATERIALS AND METHODS

More information about materials and methods is provided in **Supplementary Materials**.

Zebrafish

Zebrafish (*Danio rerio*) were maintained at 28°C under a 12-h light/dark cycle in the crCHUM Zebrafish Facility and they were raised and manipulated as per guidelines of the Canadian Council for Animal Care and protocol approved (N15018PDz) by the crCHUM ethics committee. To knockdown gene expression, embryos were microinjected with morpholino (MO) as described previously (Bekri and Drapeau, 2018).

FACS and RT-qPCR

Tg(GFAP:GFP) embryos were injected with glycine receptor-MO (Glr-MO) or Ctrl-MO. At 20 hpf, GFAP-NSCs were sorted by FACS. Then, total RNA was extracted and gene expression was quantified as described previously (Samarut et al., 2016). Sequence of each primer was designed by Snapgene software®.

Whole-Mount *in situ* Hybridization and Immunostaining

Embryos were injected with Glr-MO or Ctrl-M, then subjected to *in situ* hybridization or immunostaining as described previously (Bekri and Drapeau, 2018).

Western Blotting

Embryos were injected with *lnx1-6myc* or *gal4* mRNA, then total protein was extracted at desired stages. Western blotting was performed as previously described (Swaminathan et al., 2018).

Probes and mRNA Synthesis

To make probes or mRNA, total RNA was extracted from 24 h post fertilization (hpf) of zebrafish embryos. Total RNA was reverse transcribed to cDNA. Then, used to make probes and full length *lnx1* as described previously (Brustein et al., 2013).

RESULTS

Glycine Signaling Suppresses *lnx1* Expression and Regulates Neural Tube Development

We identified that expression of *lnx1* was strongly suppressed by glycine signaling during zebrafish development (Samarut et al., 2016). To confirm our transcriptomic study, we analyzed the expression level of *lnx1* upon disruption of glycine signaling by RT-qPCR and *in situ* hybridization. We used the *tg(GFAP:GFP)* line that expresses GFP under the *gfap* promoter (Bernardos and Raymond, 2006), which is an early marker of NSCs. Embryos from this line were treated with a Glr-MO to disturb glycine signaling, or with control Ctrl-MO or in uninjected eggs as control conditions. Embryos at 18 hpf were dissociated and

GFP⁺ NSCs were sorted, total RNA was extracted and *lnx1* expression was analyzed by RT-qPCR. Disruption of glycine signaling confirmed a significant increase of *lnx1* expression compared with Ctrl-MO or uninjected embryos condition (Figure 1A). To further validate these results, *lnx1* expression was visualized by whole-mount *in situ* hybridization, revealing a strong expression of *lnx1* upon Glr knockdown especially in the central nervous system (CNS) at 18 and 24 hpf stages (Figure 1B; right side, asterisk), compared with control condition which showed only a slight expression of *lnx1* in the brain (Figure 1B; left side). Taken together, these results confirm that glycine signaling suppresses *lnx1* expression into NSC at early stage of development.

We next tested the effects of early overexpression of *lnx1*. First, due to the unavailability of efficient antibodies against *lnx1*, we created a construct which expressed *lnx1* with myc-tag (*lnx1-myc*) to reveal *lnx1* expression by myc-tag antibodies. Then, we overexpressed *lnx1* by injecting *lnx1-myc* mRNA. Result showed a low expression level at 3 hpf and strong expression at 6 hpf, followed by degradation from 12 to 18 hpf until 24 hpf (midway through embryonic development), when *lnx1* expression was no longer detected (Figure 1C). Based on these results, we defined 18 hpf, near the start of neurogenesis, as the best time point to analyze the effect of early *lnx1* expression on zebrafish development. Control embryos showed normal brain and neural tube development (Figure 1D, in the top), whereas those injected with *lnx1* mRNA showed a major defect of neural tube closure, especially during head development (Figure 1D, in the middle and bottom, asterisk). We then tested several doses of *lnx1* mRNA and determined that 40 pg was the lowest dose that consistently produced an effect. We classified the defective neural tube phenotype into three classes: normal, abnormal and severe (Figure 1D). Control embryos uninjected or injected with GFP mRNA or *lnx1*-MO showed normal development of the neural tube (Figure 1E). However, upon *lnx1* mRNA injection, many of the embryos showed defective neural tube closure (Figure 1E). To verify whether the defect of neural tube closure was caused by overexpression of *lnx1* and was not an artifact caused by toxicity of mRNA injections, we tested for rescue of the defect of neural tube closure by co-injection of *lnx1* mRNA with *lnx1*-MO to block translation of *lnx1* mRNA. The results revealed a partial rescue, with a doubling of the normal phenotype and reduction by half in the two classes of defective phenotypes (Figure 1E). Taken together, these results provide evidence that overexpression of *lnx1* induced a defect of neural tube closure, accruing in a major malformation of the head region during zebrafish embryogenesis.

Glycine/*lnx1* Signaling Regulates Notch Activity and NSCs Proliferation

Ln timers are E3 ubiquitin ligases which promote the degradation of Numb and modulate Numb/Notch signaling during neurogenesis (Nie et al., 2002; Kageyama et al., 2007), though the role of *lnx1* in NSCs is unknown. To test whether disruption of glycine signaling in zebrafish NSCs, with elevated *lnx1* expression (Figure 1), modulates Notch signaling, we injected

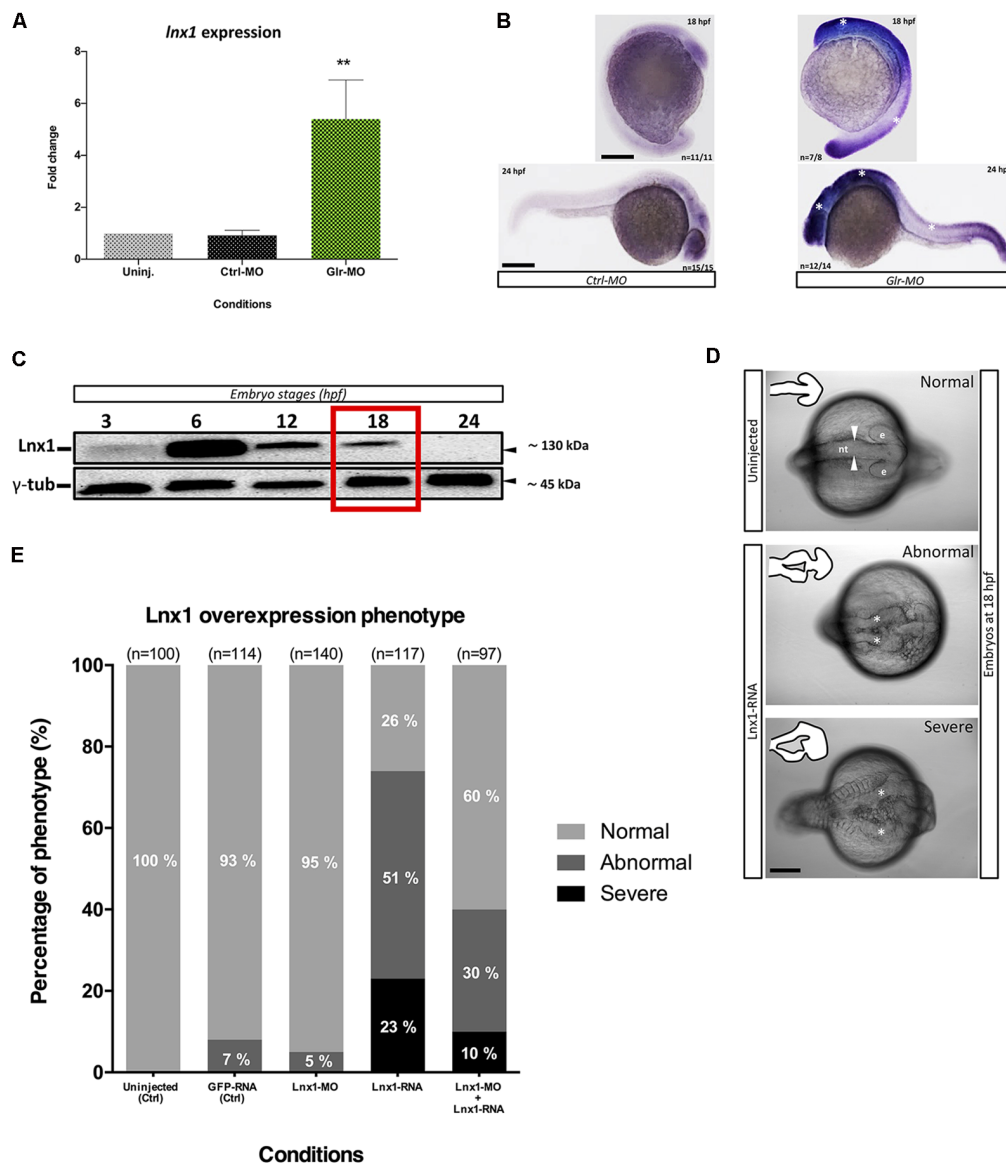


FIGURE 1 | Glycine signaling regulates Ligand of numb protein-x1 (*lnx1*) expression during neural tube development. **(A)** Quantification of *lnx1* expressions into sorted GFAP⁺-neural stem cell (NSC) by RT-qPCR revealed a significant up-regulation of *lnx1* expression upon glycine signaling disruption compared with uninjected and Ctrl-morpholino (MO) conditions. One-way ANOVA statistical analysis was performed ($n = 3$, $**p$ -value < 0.01). **(B)** Whole-mount *in situ* hybridization at 18 and 24 hours post fertilization (hpf) revealed that disruption of glycine signaling by glycine receptor morpholino (Glr-MO) induces an overexpression of *lnx1* into central nervous system (CNS; right) compared with control condition (left; Scale bar, 200 μ m). **(C)** Time course of transient *lnx1* overexpression revealed by Western blot; embryos were injected with *lnx1-6myc* RNA then *in vivo* expression of *lnx1* protein was detected by anti-myc antibodies and followed during five-time point including, 3, 6, 12, 18 and 24 hpf, and anti- γ -tub antibody was used as loading protein control. **(D)** Neural tube closes defects upon *lnx1* overexpression; embryos were injected with *lnx1-6myc* RNA, then neural tube was imaged at 18 hpf. Phenotype of neural tube defect closure caused by *lnx1* overexpression was divided into three classes: normal neural tube (arrowheads), abnormal neural tube and neural tube with severe defects (asterisks) from top to down respectively. Structure of neural tube was delineated in the corner of each image. (e, eye; nt, neural tube. Scale bar, 250 μ m). **(E)** Quantification of *lnx1* overexpression phenotype in each condition including uninjected, GFP-mRNA, *lnx1*-MO, *lnx1*-RNA or *lnx1*-MO and *lnx1*-RNA embryos.

Tg(gfap:GFP) embryos at the one-cell stage with Glr-MO or Ctrl-MO, which were then sorted at 18 hpf GFAP⁺-NSCs, followed by RNA extraction. Using RT-qPCR we quantified *Her4.1* expression, a reporter of Notch activity in zebrafish (Takke et al., 1999). The results showed a significant increase of *her4.1* expression in GFAP⁺-NSCs upon glycine disruption,

compared with uninjected and Ctrl-MO controls conditions (Figure 2A). This suggests that disruption of glycine signaling promotes Notch activity in NSCs.

We hypothesized that disruption of glycine signaling could modulate Numb protein expression, the main mediator between *lnx* and Notch signaling (Nie et al., 2002). We therefore used

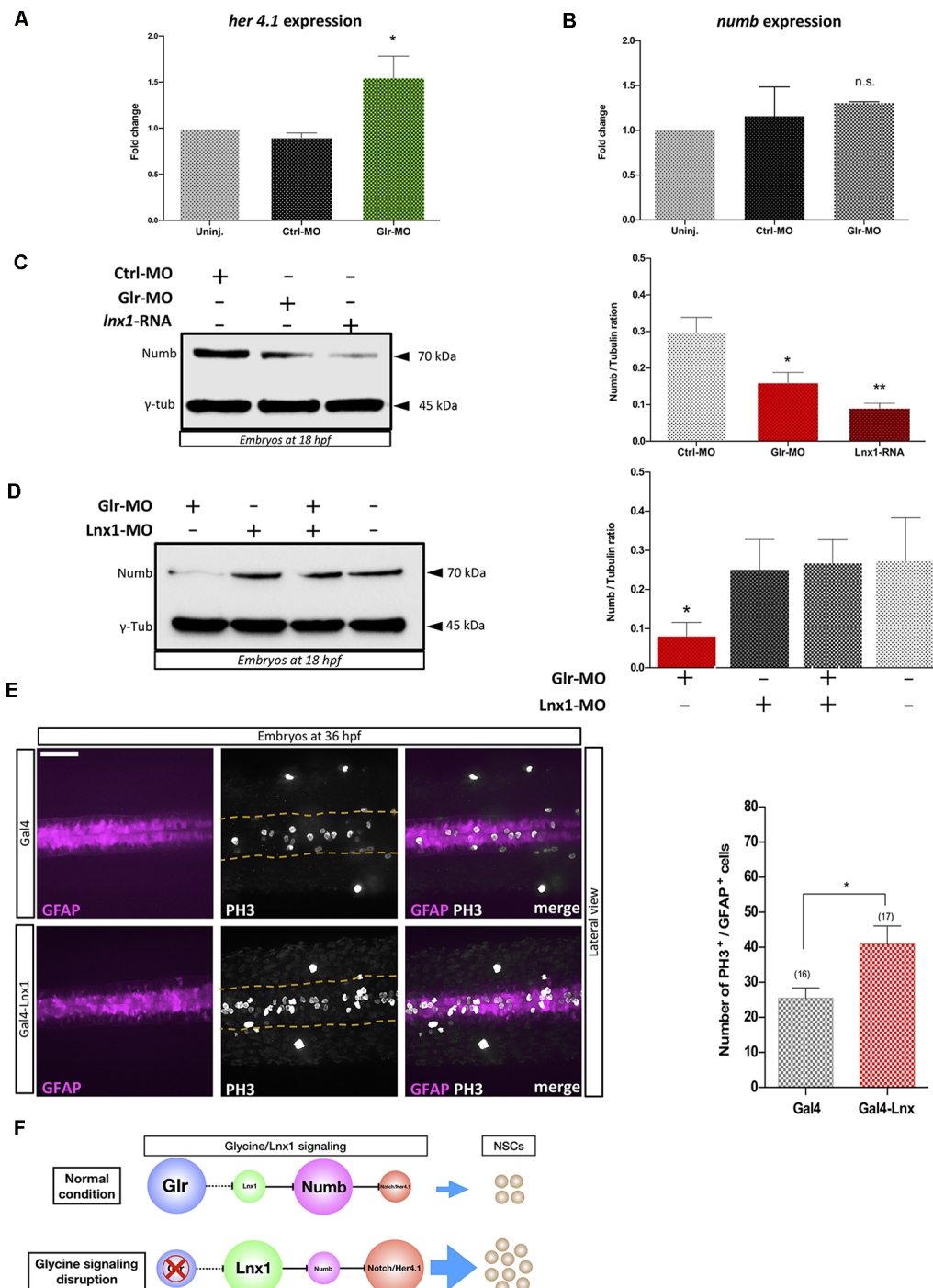


FIGURE 2 | Glycine signaling modulates Notch activity via *lnx1* expression and promotes NSCs proliferation. Quantification of *her4.1* mRNA (**A**) and *numb* mRNA (**B**) level into sorted GFAP⁺-NSC by RT-qPCR revealed a significant increase of *her4.1* expression upon disruption of glycine signaling by Glr-MO compared with uninjected and Ctrl-MO conditions. However, no significant changing of *numb* expression. One-way ANOVA statistical analysis was performed [$n = 3$, * p -value < 0.05, not significant (n.s.)]. (**C**) Expression of Numb protein was revealed by western blot at 18 hpf showing a significant degradation of numb protein upon disruption of glycine signaling by Glr-MO and overexpression of *lnx1* by *lnx1* mRNA injection compared with Ctrl-MO injections which were used as control condition. However, Co-injection of Glr-MO and *lnx1*-MO (**D**) rescued Numb protein degradation. One-way ANOVA statistical analysis was performed ($n = 3$, * p -value < 0.05, ** p -value < 0.01). (**E**) Proliferation of GFAP⁺-NSCs (pink) in spinal cord by PH3 immunostaining (white) into tg(GFAP:Gal4, UAS:RED; top panel), and tg(GFAP:Gal4, UAS, *lnx1*, UAS:RED; bottom panel) revealed a significant increase of GFAP⁺-NSCs proliferation in *lnx1* overexpression embryos (right panel). One-way ANOVA statistical analysis was performed ($n = 17$, ** p -value < 0.0001, scale bar, 250 μ m). (**F**) The schematic model of regulation of Notch activity by glycine/*lnx1* signaling into zebrafish NSCs during early development.

total RNA extracted from GFAP⁺-NSCs upon glycine signaling disruption to quantify *numb* expression by RT-qPCR. The results showed no significant change in *numb* mRNA level between disruption of glycine signaling (Glr-MO) and control conditions (Glr-MO or uninjected embryos) in NSCs (**Figure 2B**). However, analysis of Numb protein expression by western blot using anti-Numb antibody revealed a decrease in Numb protein level upon disruption of glycine signaling (Glr-MO) compared with control condition (Ctrl-MO; **Figure 2C**). This result suggests that while the *numb* mRNA level was unaffected by disruption of glycine signaling, Numb protein was degraded, likely *via* up-regulation of *lnx1* expression. To confirm that overexpression of *lnx1* in zebrafish embryos could mimic the disruption of glycine signaling and degrade Numb protein expression, we overexpressed *lnx1* and analyzed Numb protein expression at 18 hpf. The results showed an important decrease of Numb protein (**Figure 2C**). Finally, to verify whether degradation of Numb protein by glycine signaling was due specifically to *lnx1* overexpression, we tested whether down regulation of *lnx1* upon disruption of glycine signaling rescued Numb expression. To do so, we injected embryos with Glr-MO, *lnx1*-MO or both Glr-MO and *lnx1*-MO and evaluated Numb protein expression in each condition compared with uninjected embryos. The results showed a significant reduction of Numb protein level upon disruption of glycine signaling by Glr-MO compared with control whereas co-injection of Glr-MO and *lnx1*-MO together rescued the Numb protein level (**Figure 2D**). These results provide evidence that glycine/*lnx1* signaling modulates Notch activity by controlling Numb protein degradation in NSCs.

By analogy to *lnx2* (Won et al., 2015; Yin et al., 2015), we hypothesized that glycine/*lnx1* signaling controls NSC proliferation and that its disruption would cause a developmental phenotype with stabilized NSCs. To test this hypothesis, we expressed *lnx1* specifically in NSCs by generating a stable zebrafish line expressing *lnx1* (*UAS:lnx1*) in the *Tg(UAS:RFP)* reporter background, thus generating the double-*Tg(UAS:lnx1;UAS:RFP)* effector-line (**Supplementary Figure S1A**). First, to validate the transcriptional activation of *lnx1* in the *Tg(UAS:lnx1;UAS:RFP)* line, we induced ubiquitous expression of *lnx1* by injections of *Gal4*-activator mRNA (20 pg) into *Tg(UAS:lnx1;UAS:RFP)* or *Tg(UAS:RFP)* embryos, with the latter as controls. At 18 hpf, neural tube development was evaluated and *lnx1* mRNA level was analyzed by semi-quantitative RT-qPCR. The results showed a drastic defect of neural tube closure in *Tg(UAS:lnx1;UAS:RFP)* embryos compared with *Tg(UAS:RFP)* embryos, a phenotype similar to that of *lnx1* mRNA injection (data not shown). Moreover, quantification of *lnx1* mRNA levels demonstrated a strong transcriptional activity of *lnx1* in *Tg(UAS:lnx1;UAS:RFP)* compared with *Tg(UAS:RFP)* control. However, no significant change in transcriptional activity was observed in *rpl13a* and *ef1a*, used as reference genes (**Supplementary Figure S1B,C**). These results replicated the defect of neural tube closure observed by *lnx1* mRNA injections and confirmed the phenotype upon ubiquitous early expression of *lnx1* (**Figure 1**).

Next, in order to test the effect of *lnx1* overexpression on NSC proliferation, we specifically overexpressed *lnx1* in NSCs

by crossing *Tg(UAS:lnx1;UAS:RFP)* with *Tg(GFAP:Gal4)* adult zebrafish. Embryos were fixed at 36 hpf and proliferation was assayed by PH3 immunostaining. The results revealed similar GFAP⁺-NSC populations (pink color) in both conditions including *Tg(GFAP:Gal4;UAS:lnx1, UAS:RFP)* and *Tg(GFAP:Gal4;UAS:RFP)* (**Figure 2E**, in the left). However, *in vivo* overexpression of *lnx1* in NSCs in the *Tg(GFAP:Gal4;UAS:lnx1, UAS:RFP)* line revealed a large increase of PH3⁺-NSCs compared to the *Tg(UAS:RFP)* control line (**Figure 2E**, in the middle). This result indicates that early expression of *lnx1* in NSCs promotes their proliferation. Taken together, these results provide evidence that glycine/*lnx1* signaling modulates NSC proliferation through regulation of Notch activity (**Figure 2F**).

DISCUSSION

During neuronal development, several molecular changes take place in NSCs when glycine signaling is disrupted (Samarut et al., 2016). We demonstrated with different approaches that disruption of glycine signaling induced an overexpression of *lnx1* in NSCs (**Figure 1**). While regulation of *lnx2* transcription has been related to *Gli3* and *RunX2* (Pregizer et al., 2007; Wang et al., 2014), no transcription factors or pathways have been related to *lnx1* expression, leaving it as somewhat of an orphaned gene. However, increased *lnx1* expression reduces expression of the glycine transporter 2 (GlyT2) and impairs glycine transport in cortical neurons (Núñez et al., 2017). We showed that disruption of glycine signaling by knockdown of glycine receptors (Glr) induced an overexpression of *lnx1* in NSCs. Furthermore, we demonstrated that GFAP⁺-NSCs up-regulated *lnx1* upon disruption of glycine signaling (**Figure 1**). Thus, glycine signaling suppresses *lnx1*, which appears to increase GlyT2, possibly as a homeostatic mechanism to regulate glycine levels. On other hand, a few studies have highlighted the potential role of the *lnx* protein family during developmental stages. Investigation of the Shh signaling component “*Gli3*” revealed that in knockout mice (*Gli3*^{-/-}) there is an increased expression of *lnx2* and a dramatic decrease of Numb protein level in NSCs. These *Gli3*^{-/-} mice exhibit hydrocephaly and reduced cortical thickness as well (Wang et al., 2011, 2014). While *lnx2* signaling during neurogenesis is well explored, the role of *lnx1* in NSC development remained unknown. We demonstrated that transient expression of *lnx1* at an early stage of development caused a severe defect of neural tube closure in the head region, probably caused by the early loss of Numb proteins during embryogenesis. In support of our results, Numb^{-/-} null mice exhibit a severe defect in cranial neural tube closure and die around embryonic day 11.5 (E11.5; Zhong et al., 2000). These neural tube defects could be caused by disruption of neuronal development by affecting NSC proliferation.

We demonstrated that disruption of glycine signaling modulated Notch activity by increasing *her4.1* expression. While it did not affect *numb* transcription yet, it reduced the Numb protein level as a consequence of *lnx1* overexpression (**Figure 2**). We reported in zebrafish that disruption of glycine signaling increased NSC proliferation (Mcdearnid et al., 2006; Cote and Drapeau, 2012). Herein, by using a novel transgenic

Tg(UAS:lnx1;UAS;RFP), we showed that overexpression of *lnx1* in NSCs promotes their proliferation (Figure 2). These results provide compelling evidence that glycine signaling controls degradation of Numb via regulation of *lnx1* expression and modulate Notch activity and proliferation of NSCs. Over all, in this study we suggest that glycine/*lnx1* signaling controls NSC proliferation and differentiation by modulating the Notch pathway.

DATA AVAILABILITY

All datasets generated for this study are included in the manuscript and the supplementary files.

AUTHOR CONTRIBUTIONS

AB conceived and performed most of experiments, generated the transgenic line with assistance from ML, wrote the manuscript. ML provided expertise and feedback. AB and PD reviewed and

edited the manuscript. PD was responsible for supervision and funding acquisition.

FUNDING

This project was supported by funding from the Canadian Institutes of Health Research (Grant no: MOP-130448; to PD).

ACKNOWLEDGMENTS

We thank Dr. Karl Fernandes and Lamia Sid-otmane for their critical reading and valuable comments on the manuscript. we also thank Marina Drits for her assistance with fish maintenance.

SUPPLEMENTARY MATERIAL

The Supplementary Material for this article can be found online at: <https://www.frontiersin.org/articles/10.3389/fnmol.2019.00044/full#supplementary-material>

REFERENCES

- Bekri, A., and Drapeau, P. (2018). Glycine promotes the survival of a subpopulation of neural stem cells. *Front. Cell Dev. Biol.* 6:68. doi: 10.3389/fcell.2018.00068
- Bernardos, R. L., and Raymond, P. A. (2006). GFAP transgenic zebrafish. *Gene Expr. Patterns* 6, 1007–1013. doi: 10.1016/j.modgep.2006.04.006
- Brustein, E., Cote, S., Ghislain, J., and Drapeau, P. (2013). Spontaneous glycine-induced calcium transients in spinal cord progenitors promote neurogenesis. *Dev. Neurobiol.* 73, 168–175. doi: 10.1002/dneu.22050
- Colaluca, I. N., Tosoni, D., Nuciforo, P., Senic-Matuglia, F., Galimberti, V., Viale, G., et al. (2008). NUMB controls p53 tumour suppressor activity. *Nature* 451, 76–80. doi: 10.3410/f.1097644.553745
- Cote, S., and Drapeau, P. (2012). Regulation of spinal interneuron differentiation by the paracrine action of glycine. *Dev. Neurobiol.* 72, 208–214. doi: 10.1002/dneu.20972
- De Bie, P., and Ciechanover, A. (2011). Ubiquitination of E3 ligases: self-regulation of the ubiquitin system via proteolytic and non-proteolytic mechanisms. *Cell Death Differ.* 18, 1393–1402. doi: 10.1038/cdd.2011.16
- Demarque, M., Represa, A., Becq, H., Khalilov, I., Ben-Ari, Y., and Aniksztejn, L. (2002). Paracrine intercellular communication by a Ca²⁺- and SNARE-independent release of GABA and glutamate prior to synapse formation. *Neuron* 36, 1051–1061. doi: 10.1016/s0896-6273(02)01053-x
- Dho, S. E., Jacob, S., Wolting, C. D., French, M. B., Rohrschneider, L. R., and Mcglade, C. J. (1998). The mammalian numb phosphotyrosine-binding domain. Characterization of binding specificity and identification of a novel PDZ domain-containing numb binding protein, LNX. *J. Biol. Chem.* 273, 9179–9187. doi: 10.1074/jbc.273.15.9179
- Di Marcotullio, L., Greco, A., Mazza, D., Canettieri, G., Pietrosanti, L., Infante, P., et al. (2011). Numb activates the E3 ligase Itch to control Gli1 function through a novel degradation signal. *Oncogene* 30, 65–76. doi: 10.1038/onc.2010.394
- Flynn, M., Saha, O., and Young, P. (2011). Molecular evolution of the LNX gene family. *BMC Evol. Biol.* 11:235. doi: 10.1186/1471-2148-11-235
- Kageyama, R., Ohtsuka, T., and Kobayashi, T. (2007). The Hes gene family: repressors and oscillators that orchestrate embryogenesis. *Development* 134, 1243–1251. doi: 10.1242/dev.000786
- Mcdearmid, J. R., Liao, M., and Drapeau, P. (2006). Glycine receptors regulate interneuron differentiation during spinal network development. *Proc. Natl. Acad. Sci. U S A* 103, 9679–9684. doi: 10.1073/pnas.0504871103
- Mcgill, M. A., Dho, S. E., Weinmaster, G., and Mcglade, C. J. (2009). Numb regulates post-endocytic trafficking and degradation of Notch1. *J. Biol. Chem.* 284, 26427–26438. doi: 10.1074/jbc.m109.014845
- Nie, J., Mcgill, M. A., Dermer, M., Dho, S. E., Wolting, C. D., and Mcglade, C. J. (2002). LNX functions as a RING type E3 ubiquitin ligase that targets the cell fate determinant Numb for ubiquitin-dependent degradation. *EMBO J.* 21, 93–102. doi: 10.1093/emboj/21.1.93
- Núñez, E. A.-G. E., López-cordero, B., Aragón, C., and De Juan-Sanz, J. (2017). Ubiquitin ligase LNX1 is a major regulator of glycine recapture by the presynaptic transporter GlyT2. doi: 10.1101/233213
- Pregizer, S., Barski, A., Gersbach, C. A., Garcia, A. J., and Frenkel, B. (2007). Identification of novel Runx2 targets in osteoblasts: cell type-specific BMP-dependent regulation of Tram2. *J. Cell Biochem.* 102, 1458–1471. doi: 10.1002/jcb.21366
- Roegiers, F., and Jan, Y. N. (2004). Asymmetric cell division. *Curr. Opin. Cell Biol.* 16, 195–205. doi: 10.1016/j.ccb.2004.02.010
- Samarut, E., Bekri, A., and Drapeau, P. (2016). Transcriptomic Analysis of Purified Embryonic Neural Stem Cells from Zebrafish Embryos Reveals Signaling Pathways Involved in Glycine-Dependent Neurogenesis. *Front. Mol. Neurosci.* 9:22. doi: 10.3389/fnmol.2016.00022
- Scain, A. L., Le Corronc, H., Allain, A. E., Muller, E., Rigo, J. M., Meyrand, P., et al. (2010). Glycine release from radial cells modulates the spontaneous activity and its propagation during early spinal cord development. *J. Neurosci.* 30, 390–403. doi: 10.1523/JNEUROSCI.2115-09.2010
- Spitzer, N. C. (2006). Electrical activity in early neuronal development. *Nature* 444, 707–712. doi: 10.1038/nature05300
- Swaminathan, A., Hassan-Abdi, R., Renault, S., Siekierska, A., Riche, R., Liao, M., et al. (2018). Non-canonical mTOR-independent role of depdc5 in regulating gabaergic network development. *Curr. Biol.* 28, 1924.e5–1937.e5. doi: 10.1016/j.cub.2018.04.061
- Takke, C., Dornseifer, P., V Weizsacker, E., and Campos-Ortega, J. A. (1999). her4, a zebrafish homologue of the Drosophila neurogenic gene E(spl), is a target of NOTCH signalling. *Development* 126, 1811–1821.
- Uemura, T., Shepherd, S., Ackerman, L., Jan, L. Y., and Jan, Y. N. (1989). numb, a gene required in determination of cell fate during sensory organ formation in Drosophila embryos. *Cell* 58, 349–360. doi: 10.1016/0092-8674(89)90849-0
- Wang, H., Ge, G., Uchida, Y., Luu, B., and Ahn, S. (2011). Gli3 is required for maintenance and fate specification of cortical progenitors. *J. Neurosci.* 31, 6440–6448. doi: 10.1523/JNEUROSCI.4892-10.2011
- Wang, H., Kane, A. W., Lee, C., and Ahn, S. (2014). Gli3 repressor controls cell fates and cell adhesion for proper establishment of neurogenic niche. *Cell Rep.* 8, 1093–1104. doi: 10.1016/j.celrep.2014.07.006
- Won, M., Ro, H., and Dawid, I. B. (2015). Lnx2 ubiquitin ligase is essential for exocrine cell differentiation in the early zebrafish pancreas.

- Proc. Natl. Acad. Sci. U S A* 112, 12426–12431. doi: 10.1073/pnas.1517033112
- Yin, F. T., Futagawa, T., Li, D., Ma, Y. X., Lu, M. H., Lu, L., et al. (2015). Caspr4 interaction with LNX2 modulates the proliferation and neuronal differentiation of mouse neural progenitor cells. *Stem Cells Dev.* 24, 640–652. doi: 10.1089/scd.2014.0261
- Zhong, W., Jiang, M. M., Schonemann, M. D., Meneses, J. J., Pedersen, R. A., Jan, L. Y., et al. (2000). Mouse numb is an essential gene involved in cortical neurogenesis. *Proc. Natl. Acad. Sci. U S A* 97, 6844–6849. doi: 10.1073/pnas.97.12.6844

Conflict of Interest Statement: The authors declare that the research was conducted in the absence of any commercial or financial relationships that could be construed as a potential conflict of interest.

Copyright © 2019 Bekri, Liao and Drapeau. This is an open-access article distributed under the terms of the Creative Commons Attribution License (CC BY). The use, distribution or reproduction in other forums is permitted, provided the original author(s) and the copyright owner(s) are credited and that the original publication in this journal is cited, in accordance with accepted academic practice. No use, distribution or reproduction is permitted which does not comply with these terms.



Co-administration of Anti microRNA-124 and -137 Oligonucleotides Prevents Hippocampal Neural Stem Cell Loss Upon Non-convulsive Seizures

Pascal Bielefeld¹, Marijn Schouten¹, Guido M. Meijer¹, Marit J. Breuk¹, Karlijne Geijtenbeek¹, Sedef Karayel¹, Alisa Tiaglik¹, Anna H. Vuuregge¹, Ruth A.L. Willems¹, Diede Witkamp¹, Paul J. Lucassen¹, Juan M. Encinas^{2,3,4} and Carlos P. Fitzsimons^{1*}

¹ Neuroscience Program, Swammerdam Institute for Life Sciences, Faculty of Sciences, University of Amsterdam, Amsterdam, Netherlands, ² Achucarro Basque Center for Neuroscience, Bizkaia Science and Technology Park, Zamudio, Spain, ³ Ikerbasque Foundation, Bilbao, Spain, ⁴ University of the Basque Country (UPV/EHU), Leioa, Spain

OPEN ACCESS

Edited by:

Maria Llorens-Martin,
Autonomous University of Madrid,
Spain

Reviewed by:

Eva Maria Jimenez-Mateos,
Trinity College Dublin, Ireland
Luiz E. Mello,
Federal University of São Paulo, Brazil

*Correspondence:

Carlos P. Fitzsimons
c.p.fitzsimons@uva.nl

Received: 28 August 2018

Accepted: 24 January 2019

Published: 19 February 2019

Citation:

Bielefeld P, Schouten M, Meijer GM, Breuk MJ, Geijtenbeek K, Karayel S, Tiaglik A, Vuuregge AH, Willems RAL, Witkamp D, Lucassen PJ, Encinas JM and Fitzsimons CP (2019) Co-administration of Anti microRNA-124 and -137 Oligonucleotides Prevents Hippocampal Neural Stem Cell Loss Upon Non-convulsive Seizures. *Front. Mol. Neurosci.* 12:31. doi: 10.3389/fnmol.2019.00031

Convulsive seizures promote adult hippocampal neurogenesis (AHN) through a transient activation of neural stem/progenitor cells (NSPCs) in the subgranular zone (SGZ) of the dentate gyrus (DG). However, in a significant population of epilepsy patients, non-convulsive seizures (ncSZ) are observed. The response of NSPCs to non-convulsive seizure induction has not been characterized before. We here studied first the short-term effects of controlled seizure induction on NSPCs fate and identity. We induced seizures of controlled intensity by intrahippocampally injecting increasing doses of the chemoconvulsant kainic acid (KA) and analyzed their effect on subdural EEG recordings, hippocampal structure, NSPC proliferation and the number and location of immature neurons shortly after seizure onset. After establishing a KA dose that elicits ncSZ, we then analyzed the effects of ncSZ on NSPC proliferation and NSC identity in the hippocampus. ncSZ specifically triggered neuroblast proliferation, but did not induce proliferation of NSPCs in the SGZ, 3 days post seizure onset. However, ncSZ induced significant changes in NSPC composition in the hippocampus, including the generation of reactive NSCs. Interestingly, intrahippocampal injection of a combination of two anti microRNA oligonucleotides targeting microRNA-124 and -137 normalized neuroblast proliferation and prevented NSC loss in the DG upon ncSZ. Our results show for the first time that ncSZ induce significant changes in neuroblast proliferation and NSC composition. Simultaneous antagonism of both microRNA-124 and -137 rescued seizure-induced alterations in NSPC, supporting their coordinated action in the regulation of NSC fate and proliferation and their potential for future seizure therapies.

Keywords: non-convulsive seizures, kainic acid, adult hippocampal neurogenesis, neural stem cell fate, microRNA

INTRODUCTION

Convulsive seizures (cSZ) affect the hippocampus and promote adult hippocampal neurogenesis (AHN). A subset of adult-generated granule cells born after cSZ develop and integrate aberrantly in the hippocampus and have been implicated in circuit disinhibition, continued seizure formation, and epileptogenesis (Parent et al., 1997; Pun et al., 2012; Cho et al., 2015; Singh et al., 2015). Furthermore, the excessive activation of hippocampal Neural Stem/Progenitor Cells (NSPCs) that occurs shortly after seizure onset triggers their aberrant proliferation and may thereby deplete the neurogenic NSPC pool and limit AHN (Encinas et al., 2011; Sierra et al., 2015), contributing to some of the cognitive deficits that often accompany epilepsy (Hattiangady and Shetty, 2008; Cho et al., 2015).

Previous studies have suggested that the NSPC response to seizure stimulation may depend on seizure intensity, leading to differences in pathological outcome (Mohapel et al., 2004; Hung et al., 2012; Sierra et al., 2015; Uemori et al., 2017) (reviewed in Bielefeld et al., 2014). The induction of cSZ by kainic acid (KA) activates quiescent, radial glia-like NSCs in the hippocampus, promotes their proliferation, alters cell-fate decisions and results in a shift from a mainly neurogenic toward a strongly astrogenic fate (Lugert et al., 2010; Sierra et al., 2015). Importantly, a significant population of epilepsy patients never experience cSZ, but often suffer from milder, non-convulsive seizures (ncSZ) (Labovitz et al., 2001; Korff and Nordli, 2007; Rosenow et al., 2007), which have also been appreciated in rodent models (Kienzler-Norwood et al., 2017; Avdic et al., 2018). However, the effects of ncSZ on hippocampal NSPC proliferation and cell-fate decisions remains poorly characterized.

Neural stem cell fate choices depend on the expression of specific sets of co-regulated genes, that are often controlled by lineage-specific transcription factors and microRNAs (miRNAs) (Encinas and Fitzsimons, 2017; Llorens-Bobadilla and Martin-Villalba, 2017). miRNAs are short single-stranded non-coding RNAs, that post-transcriptionally repress target mRNAs through imperfect RNA-RNA binding (Bartel, 2004; Pasquinelli, 2012; Wilczynska and Bushell, 2015). miRNAs can act synergistically on the same gene targets, or on targets involved in the same biological process, creating an additional layer of regulatory complexity (Barca-Mayo and De Pietri Tonelli, 2014). Highly coordinated synergistic miRNA actions control neuronal fate in adult hippocampal NSPCs (Schouten et al., 2015; Pons-Espinal et al., 2017). The synergistic action of multiple miRNAs in NSPCs provides a possible mechanism that may render target genes more sensitive to relatively small changes in the level of individual miRNAs, thereby effectively reducing the number of biologically relevant targets (Barca-Mayo and De Pietri Tonelli, 2014; Schouten et al., 2015).

Here, we set out to study the effect of ncSZ on hippocampal NSPC proliferation and fate decisions and its regulation by the synergistic action of miR-124 and -137, which are upregulated in the mouse dentate gyrus (DG) shortly after KA-induced seizures (Schouten et al., 2015, 2016). To further characterize the synergistic role of miRNA-124 and -137 in NSPC *in vivo*, we used synthetic antimicroRNA oligonucleotides (AMOs)

(Weiler et al., 2006; Lennox et al., 2013) which bind specifically to miRNAs and block their action, thereby allowing a loss-of-function study of miRNA activity (Velu and Grimes, 2012; Li and Rana, 2014).

RESULTS

Seizure Intensity Conditions the Cellular Response in the Hippocampus

We first studied the effects on seizure activity recorded by subdural EEG of increasing intrahippocampal KA doses, within a range of previously established doses that induce interictal spiking (0.74 mM) (Sierra et al., 2015; Bielefeld et al., 2017), low-grade seizures (2.22 mM) (Bielefeld et al., 2017), and tonic-clonic seizures (20 mM) (Bouilleret et al., 1999; Sierra et al., 2015). We then analyzed granule cell dispersion and astrogliosis in the hippocampus. Injection of 0.74 mM KA elicited neuronal discharges in the form of single spikes compatible with epileptiform activity but no seizure activity was detected in subdural EEG recordings, as compared to saline injections (**Figure 1A**). Two point twenty two millimeter KA was the first dose to evoke seizures detectable by subdural EEG (**Figure 1A**). These seizures were also detected behaviorally, reaching stage 2 or 3 on a modified Racine scale, characterized by forelimb clonus (Kim et al., 1999) and were thereby classified as ncSZ (**Figure 1B**). ncSZ were associated with aberrant EEG patterns, showing high intensity individual spikes (**Figure 1A**). Administration of 20 mM KA resulted in strong seizures characterized by frequent spike-bursts (**Figure 1A**), reaching Racine stage 4–5 and were thereby classified as cSZ (**Figure 1B**). As seizures induced by 20 mM KA lasted longer than 5 min, these seizures were also classified as convulsive status epilepticus (cSE). Twenty eight days later, ncSZ had not induced detectable granule cell dispersion and only regional astrogliosis in the hippocampus (**Figures 1C–F**). In contrast, administration of 20 mM KA resulted in detectable granule cell dispersion and severe astrogliosis (**Figures 1C–F**). The effects of the seizures were limited to the ipsilateral hemisphere (**Figures 1C,E**, quantifications not shown). As seizures induced by 0.74 mM and 2.22 mM did not induce SE, one important factor discriminating ncSZ from cSZ in addition to seizure intensity in this manuscript may be the presence of isolated vs. generalized seizures. These results show that granule cell dispersion and astrogliosis induced by intrahippocampal injection of KA in the DG depend on the intensity, as assessed by EEG and a modified Racine scale, of the generated seizures indicating that they may represent meaningful cellular parameters to distinguish cSZ from ncSZ.

Seizure Intensity Conditions the Presence of Ectopic Immature Neurons in the DG

We next asked if NSPC proliferation was affected by seizure intensity. All the KA doses tested significantly increased proliferation in the hippocampus 3 days after administration, as measured by the expression of Ki67 (**Figure 2A**). This increase

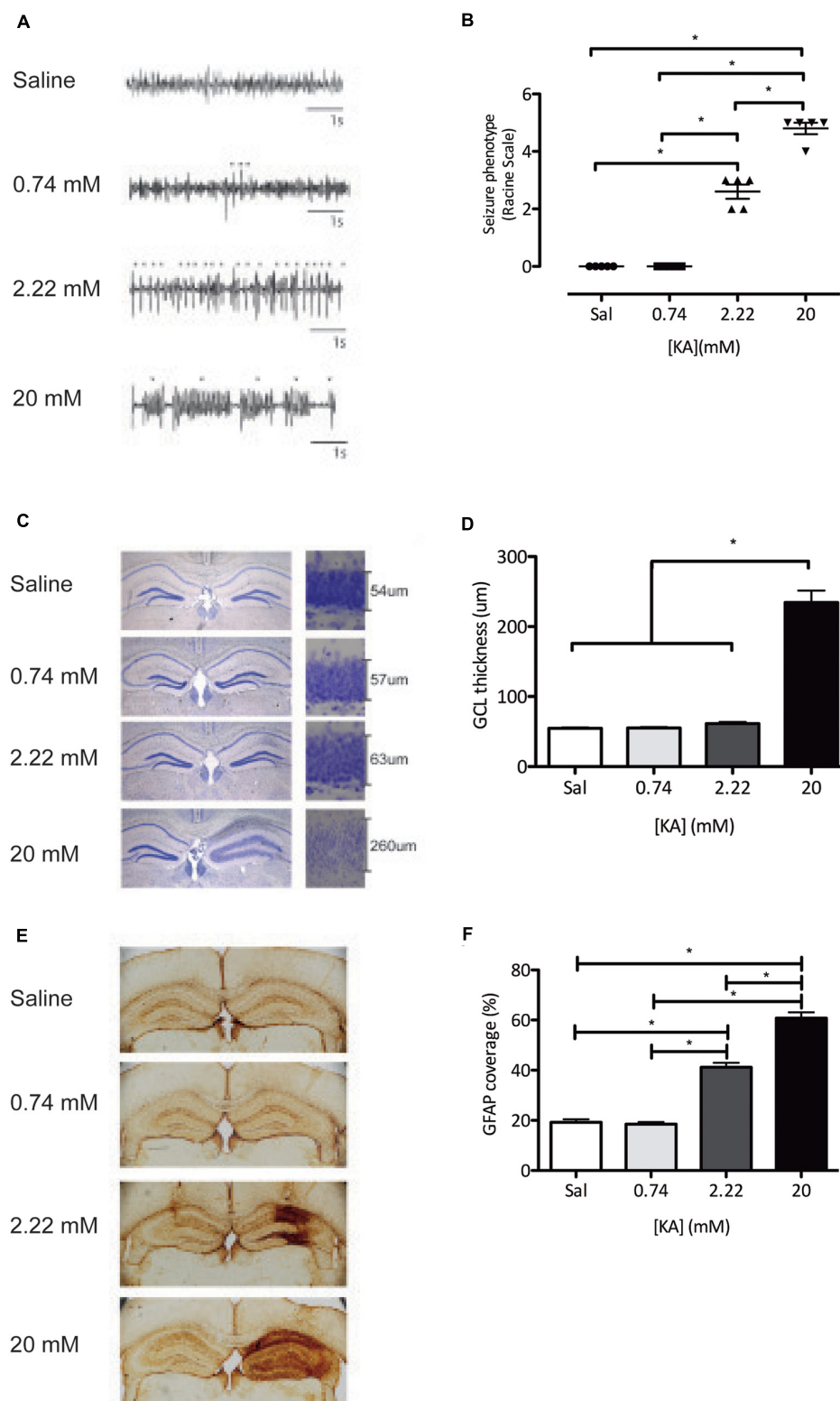


FIGURE 1 | Characterization of the intrahippocampal dose-dependent KA model. **(A)** EEG recordings during the first 4 h of status epilepticus show clear divergent patterns dependent on the KA dose, varying from single spikes(*) (0.74 mM) and repetitive single spikes (2.22 mM), to repetitive spike-bursts (▽) (20 mM). **(B)** Classification of behavioral seizures during the first 4 h of status epilepticus assessed using the Racine scale. **(C)** A Nissl staining shows dispersion of the granule cell layer. **(D)** Quantification of the granule dispersion 28 days after KA administration. **(E)** Immunohistochemistry against GFAP reveals KA dose-dependent induction of astrogliosis. **(F)** Quantification of GFAP coverage of the total hippocampus 28 days after KA administration. * $P < 0.05$.

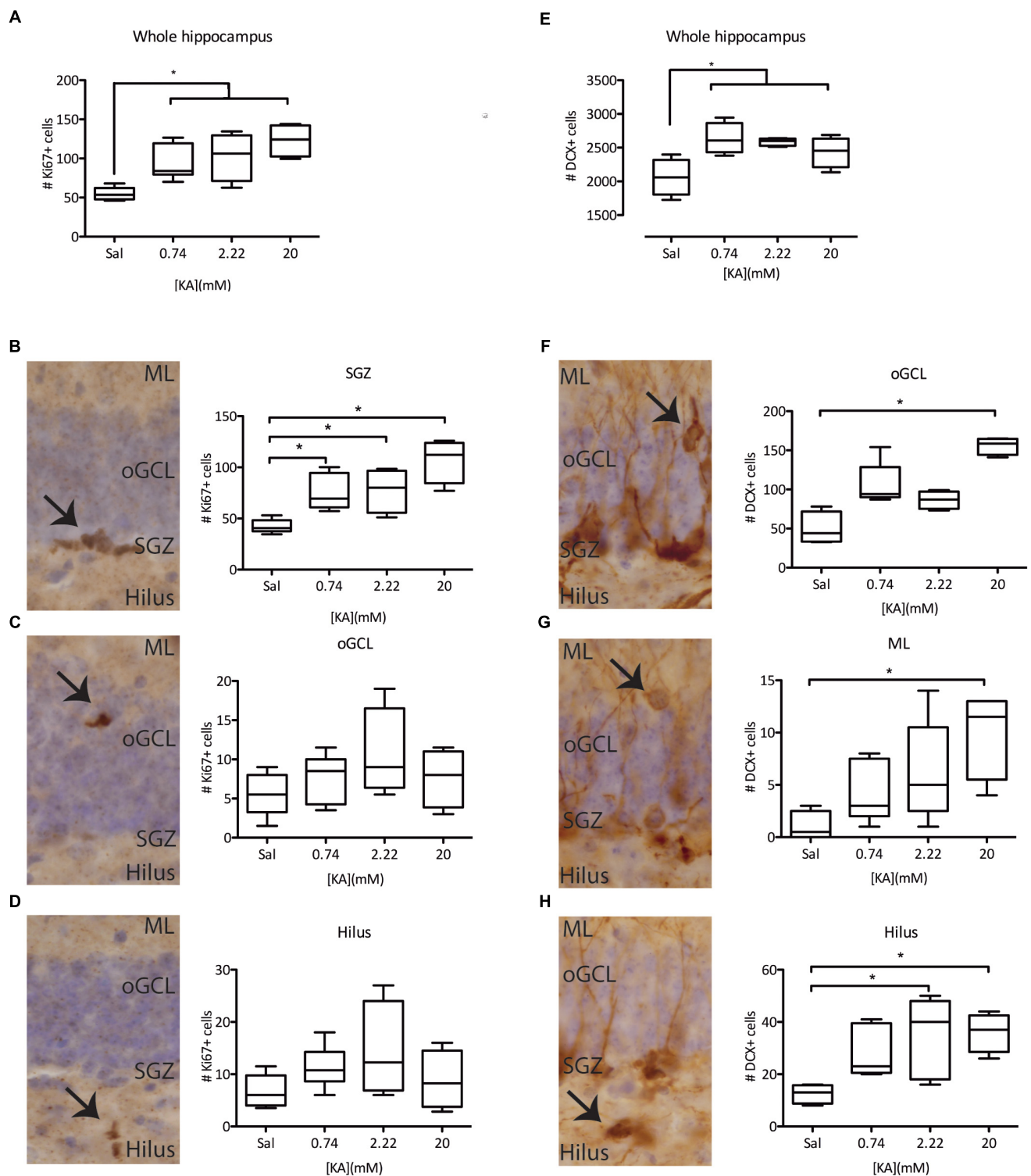


FIGURE 2 | Characterization of KA dose-dependency on proliferation and immature (DCX+) neurons. **(A)** Immunohistochemistry against Ki67 reveals an induction in the total proliferation in the whole hippocampus of the dentate gyrus, independent of KA dose. This effect is mainly driven by increased proliferation in the SGZ **(B)** of the DG, and not by ectopic proliferation in the oGCL **(C)** or the Hilus **(D)**. **(E)** Immunohistochemistry against DCX reveals an induction of DCX+ immature neurons in the whole hippocampus, irrespective of the KA dose. However, ectopic DCX+ immature neurons are only present in the oGCL **(F)**, the ML **(G)**, or the hilus **(H)** after higher KA doses. * $p < 0.05$ arrows indicate immunopositive cells at each studied location.

in proliferation was accounted by a significant increase in proliferation in the subgranular zone (SGZ), with no detectable effect on proliferation in the outer granule cell layer (oGCL) or the Hilus (**Figures 2B–D**). To understand the possible long-term effects of increased NSPC proliferation, we characterized the numbers of (ectopic) immature neurons, characterized by the expression of doublecortin (DCX) in the oGCL, the molecular layer (ML), and the Hilus 28 days after KA administration. In line with the increased proliferation of NSPCs, the total number of DCX+ immature neurons in the hippocampus was also increased following all KA doses (**Figure 2E**). In contrast, the numbers of ectopic DCX+ immature neurons present in each one of the quantified areas did not change after 0.74 mM KA (**Figures 2F–H**). However, the administration of 2.22 mM KA significantly increased the numbers of ectopic immature neurons in the Hilus, but not in the oGCL or the ML (**Figures 2F–H**), while 20 mM KA was associated with the presence of ectopic immature neurons in all three areas tested (**Figures 2F–H**). These results indicate that the induction of proliferation and increase in the numbers of immature neurons are more general effects of seizure induction in the DG, while the presence of ectopic immature neurons, particularly in the oGCL and hilus, depends on seizure intensity and may distinguish cSZ from ncSZ.

ncSZ Induces Neuroblast Proliferation in the DG

Previous observations have demonstrated a complex cell type-specific proliferative response to cSZ in the SGZ engaging quiescent NSC and early neuroblast populations (Jessberger et al., 2005; Lugert et al., 2010). To characterize the proliferative response to ncSZ, we focused on three main proliferative cell types present in Nestin-GFP mice, a well-characterized NSPC reporter model system (Mignone et al., 2004; Encinas et al., 2011) (**Figure 3B**). These were: (1) activated NSCs (aNSC), identified by co-expression of Nestin-GFP and Ki67, the absence of PSA-NCAM and the presence of a triangular soma in the SGZ and a radial process orientated perpendicular to the GCL (**Figure 3A**); (2) proliferating neural progenitor cells (pNPC), identified by the expression of Nestin-GFP and Ki67, the absence of PSA-NCAM, the presence of polygonal soma in the SGZ and the lack of radial processes (**Figure 3B**); and (3) proliferating early neuroblasts, identified by co-expression of Nestin-GFP, Ki67, and PSA-NCAM and the presence of polygonal soma in the SGZ (**Figure 3C**). We observed a significant increase in the numbers of proliferating neuroblasts and no differences in the numbers of aNSCs or pNPCs 3 days after the induction of ncSZ (**Figures 3D–F**). These results indicate that early neuroblast proliferation is specifically induced by ncSZ, as previously demonstrated for cSZ (Jessberger et al., 2005).

ncSZ Induces Changes in the Composition of the NSC Pool in the DG

Different NSC phenotypes have been identified in the DG based on marker expression and morphology (Kempermann et al., 2004; Sierra et al., 2015; Gebara et al., 2016). We first assessed the total numbers of Type A NSCs, detected as Nestin GFP+,

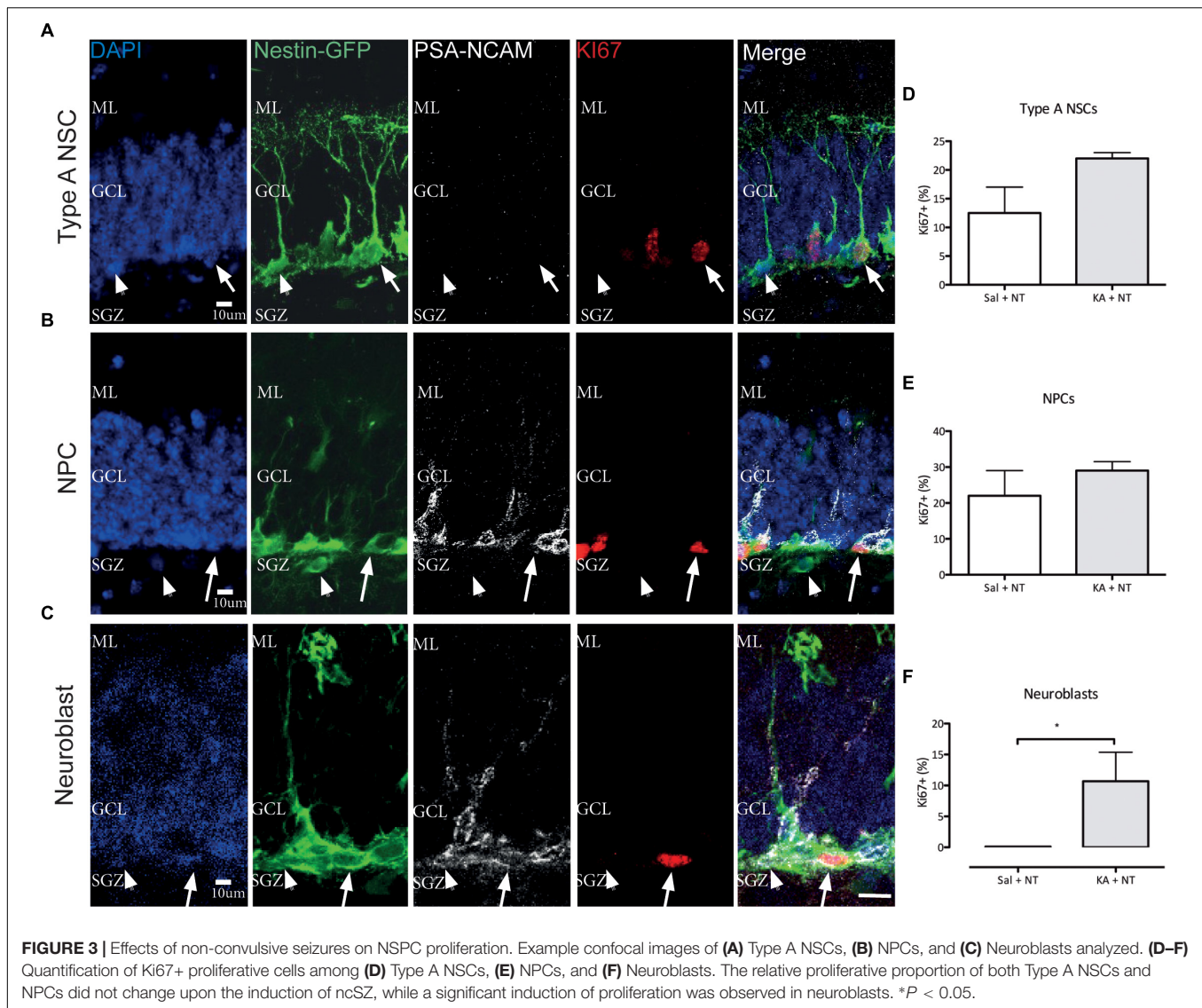
GFAP+, S100 β - cells with a triangular soma in the SGZ, a long radial process orientated perpendicular to the GCL and complex cellular processes reaching the ML (Kempermann et al., 2004) (**Figure 4A**); Type B NSC, detected as Nestin-GFP+, GFAP+, S100 β + cells with a triangular soma in the SGZ and a shorter radial process orientated perpendicular to the GCL (Gebara et al., 2016) (**Figure 4B**); and Reactive NSCs, detected as Nestin-GFP+, GFAP+ S100 β - cells, with an enlarged soma located in the SGZ a thicker radial process orientated perpendicular to the GCL and less branched cellular processes not reaching the ML as compared to Type A NSCs (Sierra et al., 2015) (**Figure 4C**) and then asked if ncSZ may affect these three populations in the DG. Three days after induction ncSZ decreased the number of Type A NSCs (**Figure 4D**); decreased the number of Type B NSCs (**Figure 4E**) and increased the total number of reactive NSCs and the ratio of rNSCs/Type A NSCs (**Figures 4F,G**). As Type B and reactive NSC may both derive from Type A NSCs (Sierra et al., 2015; Gebara et al., 2016), these results indicate that ncSZ induces significant changes in the composition of the NSC pool in the DG, possibly promoting the generation of reactive NSCs at the expense of other NSC types. Although the generation of reactive NSCs at the expense of Type A NSCs has been documented after cSZ (Sierra et al., 2015), this is the first report of a possible effect of ncSZ on Type A and B NSCs.

Co-administration of MiR-124 and -137 AMOs Prevents Neuroblast Proliferation in the DG Upon ncSZ

Previous observations indicate that miR-124 and -137 are upregulated after seizures in the DG and their synergistic action contributes to the regulation of NSPCs (Schouten et al., 2015, 2016). First, we confirmed that miR-124 and miR-137 are upregulated in the DG 72 h after intrahippocampal KA-induced ncSZ (**Figures 5A,B**). To address possible effects of both microRNAs after ncSZ, we administered an equimolar combination of miRNA-124 and -137, or non-targeting (NT) AMOs as experimental control, to the DG, 2 h after the induction of ncSZ. Treatment with AMOs against microRNA-124 and -137 successfully decreased expression levels of both miRs 3 days post seizure induction, without affecting the expression levels of an unrelated miR (miR-19a) (**Figures 5A–C**), which has been used previously as a control (Reschke et al., 2017). Furthermore, NT control AMOs did not affect the expression of miR-124 or -137 (**Figures 5A,B**), supporting the specificity of the AMOs used. Treatment with this equimolar combination of specific miRNA-124 and -137 AMOs significantly inhibited the neuroblast-specific proliferative response observed after ncSZ, without significant effects on the numbers of proliferating NSCs or NPCs in the DG (**Figures 5D–F**).

Co-administration of MiR-124 and -137 AMOs Prevents Changes in the Composition of the NSC Pool in the DG Upon ncSZ

Next, we asked if the co-administration of miR-124 and -137 AMOs could modify the NSC response to ncSZ in the DG.



Again, we administered to the DG an equimolar combination of miRNA-124 and -137 or NT AMOs as experimental control, 2 h after the induction of ncSZ. We found that treatment with the miRNA-124 and -137 AMO combination significantly reduced the loss of Type A and Type B NSCs observed after ncSZ (Figures 5G,H). Finally, administration of the miRNA-124 and -137 AMO combination had no significant effect on the induction of reactive NSCs (Figure 5I). However, it significantly prevented the increase of the reactive NSC/Type 1 A NSC ratio induced by ncSZ (Figure 5J). To address whether these effects were linked to the synergistic effect of both miR-124 and miR-137, we then applied individual AMOs against either miR-137 or miR-124 2 h post seizure induction. To allow for comparison between the data obtained from the animals infused with the combined AMOs all data were normalized against controls (saline + NT AMOs). Administration of individual AMOs against miR-124 failed to rescue both the loss of Type A NSCs (Figure 5K) and Type B NSCs (Figure 5L), while individual

AMOs against miR-137 prevented the loss of Type A NSCs (Figure 5K), but not the loss of Type B NSCs (Figure 5L). This indicates that the synergistic inhibition of both microRNAs plays a significant role in the preservation of NSCs after KA-induced ncSZ.

DISCUSSION

We show that intrahippocampal administration of increasing doses of KA results in a gradual increase in seizure intensity, induction of astrogliosis and ectopic immature neurons. In particular, ncSZ specifically induced proliferation of neuroblasts, increased the numbers of reactive NSC and resulted in a loss of Type A and Type B NSCs, thereby significantly altering the composition of the hippocampal NSC pool. Furthermore, we provide first evidence that a combination of specific AMOs directed against miR-124 and miR-137 administered locally to the

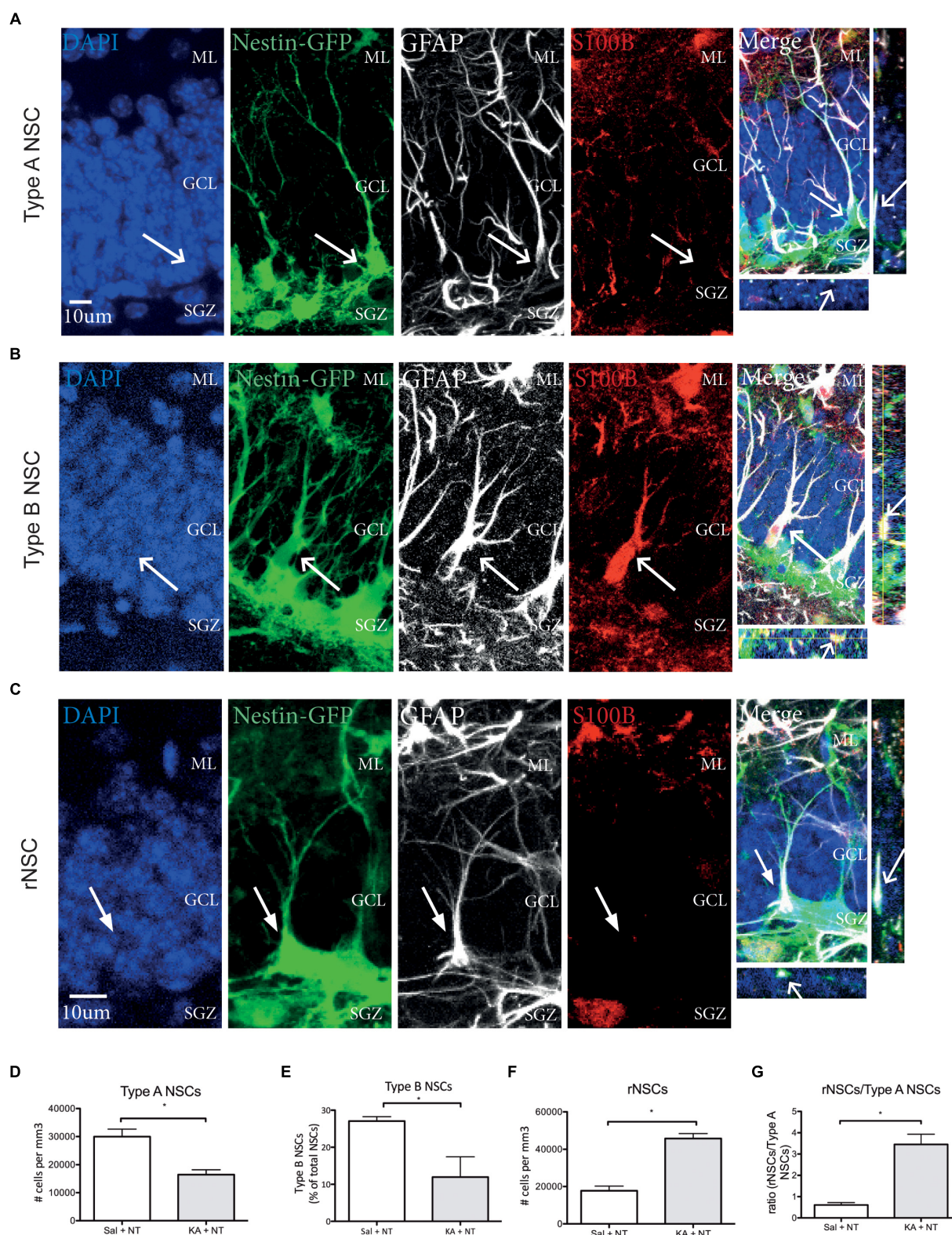


FIGURE 4 | Effects of non-convulsive seizures on NSC identity. Example confocal images of **(A)** Type A NSCs **(B)** Type B NSCs **(C)** reactive NSCs, as assessed by marker expression and morphology. **(D)** Upon induction of ncSZ a significant loss of Type A NSCs was found. **(E)** At the same time, the relative proportion of Type B NSCs in the NSC pool also decreases upon induction of ncSZ. **(F)** Simultaneously, a significant increase in the number of rNSCs occurs, an effect that becomes even more visible when comparing the rNSC/Type A NSC ratio **(G)**. * $P < 0.05$.

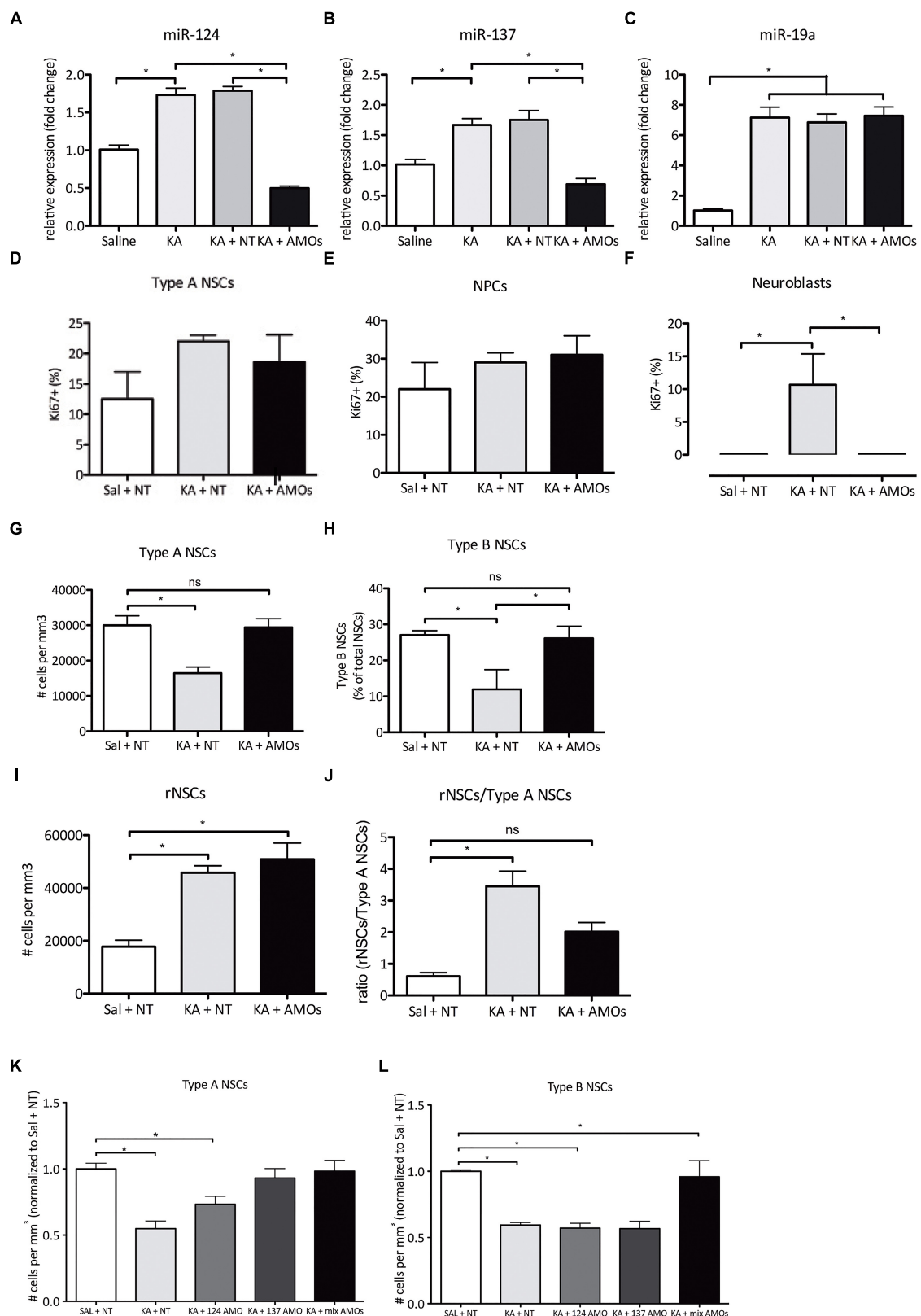


FIGURE 5 | Continued

FIGURE 5 | Combined treatment with anti miR-124 and -137 AMOs partially restores non-convulsive seizure-induced alterations in proliferation and NSC identity 3 days post SE onset. **(A)** Expression levels of miR-124 72 h post ncSZ and following AMO administration. **(B)** Expression levels of miR-137 72 h after ncSZ and following AMO administration. **(C)** Expression levels of the unrelated miR-19a 72 h after ncSZ, and following AMO administration. **(D–F)** combined AMO treatment successfully rescued the ncSZ-induced neuroblast proliferation, while not altering proliferation levels in Type A NSCs and NPCs. **(G)** The loss of Type A NSCs was rescued by the administration of the combined AMOs (Sal + NT vs. KA + AMOs, ns). **(H)** The decrease in the relative proportion of Type B NSCs among the NSC pool was also rescued by the AMO treatment (Sal + NT vs. KA + AMO, ns; KA + NT vs. KA + AMO, $P < 0.05$). **(I)** The induction of rNSCs upon ncSZ was not rescued by the AMO treatment; however, **(J)** as the number of Type A NSCs was restored, the rNSC/Type A NSC ratio was partially restored (Sal + NT vs. KA + AMO, ns). **(K)** Administration of individual AMOs 2 h post ncSZ partially prevents the loss of Type A NSCs. **(L)** Administration of individual AMOs 2 h post ncSZ did not prevent the loss of Type B NSCs. * $P < 0.05$.

DG shortly after the induction of ncSZ reverted the induction of neuroblast proliferation and the loss of Type A and Type B NSCs associated with ncSZ.

Most studies addressing the effects of seizures on the hippocampal NSC pool have used cSZ triggered by systemically administered chemoconvulsants like KA or pilocarpine (Parent et al., 1997; Bouillere et al., 1999; Parent et al., 2006; Jessberger et al., 2007; Sibbe et al., 2012; Miltiadous et al., 2013; Cho et al., 2015; Twele et al., 2015). This may represent a limitation in the translational power of these studies, since not all epilepsy patients experience cSZ (Labovitz et al., 2001; Korff and Nordli, 2007; Rosenow et al., 2007). Systemically applied KA is an extensively used model with unquestionable value (Lévesque and Avoli, 2013). However, it triggers an all-or-nothing response that is inherently uncontrollable and may result in several indirect effects that complicate a correct interpretation of the earliest changes induced in brain tissue (Kienzler-Norwood et al., 2017). We have recently adapted an experimental protocol that allows for the local injection of chemoconvulsants in the DG, thereby providing an opportunity to elicit ncSZ in mice (Schouten et al., 2015; Sierra et al., 2015; Abiega et al., 2016; Bielefeld et al., 2017), as it has been also shown in guinea pigs (Carriero et al., 2012). An added advantage of the intrahippocampal injection of KA at lower doses may be the absence of GCL dispersion we report here. GCL dispersion has been observed frequently in mice and human, while it has seldom been shown in rat models of epilepsy (Pirttilä et al., 2005), making it a complicating feature present in some cSZ mice models. Using this extensively validated protocol, we here show that some of the effects of ncSZ on NSPC diverge from those of cSZ. Theoretically, if the lowest dose of KA that we injected was saturating the cellular response, then the local effects of higher KA doses may not be different. However, our data show at least some of the cellular parameters that we studied were differentially affected by the increasing KA doses, indicating that seizure intensity is a meaningful parameter in the study of the regulation of AHN by epileptic seizures. We show for the first time that ncSZ induces proliferation of early neuroblasts, similarly to cSZ (Jessberger et al., 2005). In contrast to observations done after cSZ (Lugert et al., 2010; Sierra et al., 2015), we show that ncSZ did not induce significant differences in the proliferation of Type A NSCs. Thus, our results suggest that Type A NSCs may only respond to high seizure intensities, and therefore depletion of the hippocampal NSC pool after ncSZ could be less severe than anticipated from the use of cSZ. This could have clinical implications since a significant number of epileptic patients experience ncSZ (Drislane, 2000; Alroughani et al., 2009).

Under normal conditions, NSCs in the adult hippocampus undergo asymmetric divisions that generate both NPCs and NSCs. This mechanism favors a neuronal progeny, while slowing down the depletion of the NSC pool (Encinas et al., 2011). The neuronal hyperactivity associated with cSZ promotes a switch toward symmetric division. This switch in division mode generates reactive NSCs, thereby depleting the NSC pool and impairing AHN (Sierra et al., 2015). Here we report that ncSZ also induced a significant increase in the number of reactive NSCs in the DG. Interestingly, reactive NSCs may also contribute to astrogliosis, that is commonly observed in epilepsy models and mTLE patients (Robel et al., 2015; Sierra et al., 2015). In agreement with this, the increase in reactive NSCs shortly after ncSZ correlated with the extent of astrogliosis 28 days after seizure onset. However, further experiments are required to definitively demonstrate how reactive NSCs may contribute to hippocampal astrogliosis after ncSZ.

Further, we provide evidence supporting the conclusion that ncSZ affects NSC composition in the DG. ncSZ increased the numbers of reactive NSCs, while simultaneously decreasing the number of Type A and B NSCs. Type B NSCs are derived from Type A NSCs by asymmetric division under physiological conditions (Gebara et al., 2016), while reactive NSCs are derived from Type A NSCs by symmetric division after cSZ (Sierra et al., 2015). We here show for the first time that ncSZ leads to a decrease in the number of Type B NSCs in the DG, which may result from a loss of Type A NSCs, or through direct depletion of Type B NSCs. Our observations support the idea that ncSZ may affect the division mode of Type A NSCs without increasing their total proliferation rate, in contrast to what has been observed before after cSZ (Lugert et al., 2010). However, an alternative explanation for our observations is that seizures prevent the generation of Type B from Type A NSC through hitherto unidentified mechanisms that do not involve a change in their division mode. The validation of either of these hypotheses requires further experimental evidence.

Several miRNAs regulate multiple steps in AHN, and the expression profiles of some of these miRNAs are altered in the DG upon seizure induction [reviewed in (Schouten et al., 2012; Bielefeld et al., 2016)]. Adding an extra level of complexity to miRNA-mediated regulation, a synergistic action between multiple miRNAs may function to enforce and stabilize gene-regulatory networks converging on biological functions or pathways that determine the fate of adult hippocampal NSCs (Pons-Espinal et al., 2017). In particular, synergy between miR-124 and -137 in NSCs controls a significant number of common targets involved in neurogenesis (Santos et al., 2016).

Interestingly, miR-124 and -137 may regulate the division mode of NSCs (Gaiano and Fishell, 2002; Egger et al., 2010). Based on these previous observations, we explored the synergistic actions of miR-124 and -137 in NSC after ncSZ. AMOs (Weiler et al., 2006; Lennox et al., 2013), specifically inhibit miRNA actions *in vivo* and have shown therapeutic potential in treating epilepsy and concomitant cellular alterations in the hippocampus (Reschke et al., 2017; Beamer et al., 2018). We used a combination of AMOs targeting mir-124 and -137 administered locally to the DG to study possible cooperative functions. Strikingly, no proliferative neuroblasts were found 3 days after the onset of ncSZ in the combined AMO groups, indicating a crucial role for miR-124 and -137 synergy in the regulation of neuroblast proliferation upon ncSZ. Furthermore, the AMO treatment restored the numbers of Type A and Type B NSCs. Although the absolute number of reactive NSCs observed after ncSZ was unaffected by the AMO treatment, the reactive NSC/Type A NSC ratio was restored, indicating that prevention of Type A NSC loss is a main effect of the combined inhibition of miR-124 and miR-137 in the DG after ncSZ. To validate the functional role of microRNA cooperativity we administered individual AMOs against miR-124 or miR-137 2 h post ncSZ. Individual AMOs against miR-137 successfully prevented the loss of Type A NSCs, but not type B NSCs, while individual AMOs against miR-124 did not manage to prevent the loss of either type of NSCs. Since the combined administration of both AMOs did rescue the loss of Type B NSCs, these results indicate an action mediated by microRNA synergy, confirming the hypothesis that microRNA-124 and -137 act together to regulate many genes involved in the maintenance of NSCs after ncSZ.

MATERIALS AND METHODS

Animals

Six week-old male Nestin-GFP^{+/−} mice (Mignone et al., 2004), were used in all experiments. Mice were housed in groups for 1 week prior to the start of the experiment under a 12-h light/dark cycle (lights on at 08.00) in a temperature- and humidity controlled room, with *ad libitum* access to food and water. All experiments were approved by the committee of animal health and care, University of Amsterdam (DED protocol #296 and #314, CCD 4925) and were performed in accordance with the guidelines and regulations of the European Union for the use of animals for scientific purposes. All mice were randomly assigned to experimental groups.

Intrahippocampal KA and AMO Infusions

At post-natal day 42, mice were anesthetized in an airtight container using 5% isoflurane and placed in a stereotaxic apparatus. Anesthesia was maintained using 2% isoflurane during surgery. The intrahippocampal injection of KA was performed as described before (Bielefeld et al., 2017). In short, a small hole was drilled in the skull above both the hippocampi at the following coordinates: anteroposterior (AP) −2.0, mediolateral (ML) +1.5/−1.5. A pulled microcapillary was inserted and positioned at dorsoventral (DV) −2.0 and

50 nL of Saline (SAL) or KA (0.74, 2.22, or 20 mM) was infused into the DG using a microinjector (Nanoject II, Drummond Scientific). A second cohort of animals underwent the same stereotaxic procedure. Using the same bregma coordinates and a pulled microcapillary, 1.0 μ L of an equimolar (50 μ M) mix of microRNA-124 and -137 AMOs (Mirvana miRNA inhibitors, miRNA-124: CGUGUUCACAGCGGACCUUGAU; miRNA-137: ACGGGUAUUCUUGGGUGGAUAAU) was infused (50 μ M, 0.2 μ L/minute) using a microinjector (Nanoject II, Drummond Scientific). When necessary, mice were given intraperitoneal physiological saline injections to prevent dehydration after seizure onset.

Electrode Implantation and EEG Recording

A separate cohort of mice underwent similar KA infusions and was additionally implemented with subdural goldplated stainless steel screw electrodes. The electrode implantation and EEG recordings were performed as described before (Schouten et al., 2015; Bielefeld et al., 2017). In short, electrodes were placed beneath the dura in the holes drilled for KA infusion. An additional dual reference and ground electrode was placed above the frontal cortex (AP−0.1, ML +0.1). All electrodes were attached to the skull using dental cement (Simplex Rapid, Kemdent), and attached to a wireless EEG recording system (Neurologger, TSE) allowing 72 h non-stop EEG acquisition.

Seizure Classification

Seizures were scored using both EEG data and behavioral assessment based on a modified Racine scale (Racine, 1972; Schouten et al., 2015). We classified seizures to be non-convulsive based on behavioral assessment, with seizures not reaching higher than three on the Racine scale. Seizures reaching Racine scale 4 or higher were classified as cSZ. Seizures reaching Racine scale 4 or higher and lasting longer than 5 min were classified as cSE as in agreement with the official guidelines of the International League Against Epilepsy (Trinka et al., 2015). EEG data was analyzed separately, and both single spikes as well as spike bursts were manually identified.

Tissue Collection

Seventy two hours or 28 days post KA infusion mice were sacrificed by transcardial perfusion with PBS followed by 4% paraformaldehyde (pH 7.4). Brains were extracted and stored overnight in paraformaldehyde at 4°C, followed by long-term storage in PBS containing 0.01% azide at 4°C. Serial 40 μ m-thick coronal sections were obtained using a microtome (Jung). A second cohort of animals was sacrificed by decapitation 3 days post ncSZ and the DG was microdissected and snap frozen.

Immunohistochemistry

All fluorescent immunohistochemical experiments were performed following a standard procedure. Sections were incubated with a blocking and permeabilization solution (PBS containing 0.3% Triton-100X and 2% serum) for 30 min at room temperature, followed by incubation with primary antibodies

in the same solution for 1 h at room temperature followed by overnight incubation at 4°C. After thorough washing with PBS, sections were incubated with fluorochrome-conjugated secondary antibodies for 2 h at room temperature. All sections were again thoroughly washed in PBS and PB and subsequently mounted on slides. Slides were enclosed using vectashield containing DAPI and dried. The following antibodies were used: Chicken anti GFP, mouse anti GFAP, mouse anti PSA-NCAM, Rabbit anti S100B, rabbit anti Ki67.

DAB-based immunohistochemistry was performed as described previously (Oomen et al., 2010; Schouten et al., 2015) using the following antibodies: goat anti DCX (Santa Cruz, 1:500), rabbit anti Ki67 (Abcam, 1:500), mouse anti GFAP (Millipore, 1:1000). Nissl staining was performed using Cresyl violet, as previously described (Heinrich et al., 2006).

Image Acquisition and Quantification

All fluorescent images were acquired using a Zeiss LSM 510 confocal microscope and the corresponding manufacturer software. From each animal, every eighth serial coronal slice containing the dorsal hippocampus was analyzed. Per slice, four 30 μ M-thick z-stack images of the dorsal hippocampus were obtained equally distributed along the suprapyramidal and infrapyramidal blade of the DG using a 40 \times magnification and transferred into ImageJ software for editing and analysis.

Quantitative analysis of cell populations was performed by manual counting of cell populations based on the coexpression of cell-type specific markers as described in the results section and corrected for the analyzed volume of the measured area. Images of all DAB-based immunohistochemistry were acquired using a Nikon Eclipse fluorescence microscope and transferred to ImageJ for analysis. Ki67+ cells were counted manually and assigned to one of the following locations: SGZ, outer GCL, or the Hilus. Per hippocampus, eight coronal, 40 μ m thick sections were sampled along the rostro-caudal axis (corresponding with Bregma: -1.34, -1.70, -2.06, -2.46, -2.92, -3.16, -3.52, -3.80) as described before (Abbink et al., 2017).

Total DCX+ cells were assessed using a stereological approach as described before (Oomen et al., 2010; Schouten et al., 2015). Ectopic DCX+ cells were counted manually and assigned to one of three anatomical locations: outer GCL, ML, or Hilus. The SGZ was defined as two cell bodies distance from the GCL, while the

outer GCL was here defined as the outer half of the GCL. Gliosis was analyzed by measuring GFAP surface area coverage in the whole hippocampus using ImageJ. GCL dispersion was assessed by measuring the total thickness of the GCL using ImageJ.

microRNA Expression Analysis

RNA was isolated from snap frozen fresh micro dissected DG tissue and subsequently transcribed into cDNA using a taqman microRNA reverse transcription kit combined with specific miR-reverse transcription primers. MicroRNA expression levels were determined using taqman microRNA assays specific for miR-124 (assay ID:001182), miR-137 (assay ID:001129), and miR-19a (assay ID:002544) and levels were normalized to RNU6b (assay ID:001093) as described before (Schouten et al., 2015).

Statistical Analysis

All statistical analyses were carried out using Graphpad Prism 5.0. All data are shown as mean \pm SEM and $p < 0.05$ was considered significant. All comparisons were tested using a 1-way ANOVA and Tukey *post hoc* analysis, unless specifically stated otherwise.

AUTHOR CONTRIBUTIONS

PB, MS, GM, MB, KG, SK, AT, AV, RW, and DW performed experiments and analyzed data. PL, JE, and CF participated in experimental design, result discussion, interpretation, and manuscript preparation. PB and CF conceived the study, designed experiments, analyzed and interpreted results, and wrote the manuscript.

FUNDING

This work was supported in part by the grant H64.09.016 from the Innovational Research Incentives Scheme VIDI, The Netherlands Organization for Scientific Research (NWO) to CF as well as a grant by Alzheimer Netherlands to CF and by a grant from the Spanish Ministry of Economy and Competitiveness (MINECO) with FEDER funds to JE (SAF2012-40085) and with MINECO Ramón y Cajal contracts to JE (RyC-2012-11185). PL was supported by Alzheimer Netherlands.

REFERENCES

- Abbink, M. R., Naninck, E. F. G., Lucassen, P. J., and Korosi, A. (2017). Early-life stress diminishes the increase in neurogenesis after exercise in adult female mice. *Hippocampus* 27, 839–844. doi: 10.1002/hipo.22745
- Abiega, O., Beccari, S., Diaz-Aparicio, I., Nadjar, A., Layé, S., Leyrolle, Q., et al. (2016). Neuronal hyperactivity disturbs ATP microgradients, impairs microglial motility, and reduces phagocytic receptor expression triggering apoptosis/microglial phagocytosis uncoupling. *PLoS Biol.* 14:e1002466. doi: 10.1371/journal.pbio.1002466
- Alroughani, R., Javidan, M., Qasem, A., and Alotaibi, N. (2009). Non-convulsive status epilepticus; the rate of occurrence in a general hospital. *Seizure* 18, 38–42. doi: 10.1016/j.seizure.2008.06.013
- Avdic, U., Ahl, M., Chugh, D., Ali, I., Chary, K., Sierra, A., et al. (2018). Nonconvulsive status epilepticus in rats leads to brain pathology. *Epilepsia* 59, 945–958. doi: 10.1111/epi.14070
- Barca-Mayo, O., and De Pietri Tonelli, D. (2014). Convergent microRNA actions coordinate neocortical development. *Cell Mol. Life Sci.* 71, 2975–2995. doi: 10.1007/s00018-014-1576-5
- Bartel, D. P. (2004). MicroRNAs: genomics, biogenesis, mechanism, and function. *Cell* 116, 281–297. doi: 10.1016/S0092-8674(04)00045-5
- Beamer, E. H., Jurado-Arjona, J., Jimenez-Mateos, E. M., Morgan, J., Reschke, C. R., Kenny, A., et al. (2018). MicroRNA-22 controls aberrant neurogenesis and changes in neuronal morphology after status epilepticus. *Front. Mol. Neurosci.* 11:442. doi: 10.3389/fnmol.2018.00442

- Bielefeld, P., Mooney, C., Henshall, D. C., and Fitzsimons, C. P. (2016). miRNA-mediated regulation of adult hippocampal neurogenesis; implications for epilepsy. *Brain Plast.* 3, 43–59. doi: 10.3233/BPL-160036
- Bielefeld, P., Sierra, A., Encinas, J. M., Maletic-Savatic, M., Anderson, A., and Fitzsimons, C. P. (2017). A standardized protocol for stereotaxic intrahippocampal administration of kainic acid combined with electroencephalographic seizure monitoring in mice. *Front. Neurosci.* 11:160. doi: 10.3389/fnins.2017.00160
- Bielefeld, P., van Vliet, E. A., Gorter, J. A., Lucassen, P. J., and Fitzsimons, C. P. (2014). Different subsets of newborn granule cells: a possible role in epileptogenesis? *Eur. J. Neurosci.* 39, 1–11. doi: 10.1111/ejn.12387
- Bouilleret, V., Ridoux, V., Depaulis, A., Marescaux, C., Nehlig, A., and Le Gal La Salle, G. (1999). Recurrent seizures and hippocampal sclerosis following intrahippocampal kainate injection in adult mice: electroencephalography, histopathology and synaptic reorganization similar to mesial temporal lobe epilepsy. *Neuroscience* 89, 717–729. doi: 10.1016/S0306-4522(98)00401-1
- Carriero, G., Arcieri, S., Cattalini, A., Corsi, L., Gnatkovsky, V., and de Curtis, M. (2012). A guinea pig model of mesial temporal lobe epilepsy following nonconvulsive status epilepticus induced by unilateral intrahippocampal injection of kainic acid. *Epilepsia* 53, 1917–1927. doi: 10.1111/j.1528-1167.2012.03669.x
- Cho, K.-O., Lybrand, Z. R., Ito, N., Brulet, R., Tafacory, F., Zhang, L., et al. (2015). Aberrant hippocampal neurogenesis contributes to epilepsy and associated cognitive decline. *Nat. Commun.* 6:6606. doi: 10.1038/ncomms7606
- Driscoll, F. W. (2000). Presentation, evaluation, and treatment of nonconvulsive status epilepticus. *Epilepsy Behav.* 1, 301–314. doi: 10.1006/ebep.2000.0100
- Egger, B., Gold, K. S., and Brand, A. H. (2010). Notch regulates the switch from symmetric to asymmetric neural stem cell division in the *Drosophila* optic lobe. *Development* 137, 2981–2987. doi: 10.1242/dev.051250
- Encinas, J. M., and Fitzsimons, C. P. (2017). Gene regulation in adult neural stem cells. Current challenges and possible applications. *Adv. Drug Deliv. Rev.* 120, 118–132. doi: 10.1016/j.addr.2017.07.016
- Encinas, J. M., Michurina, T. V., Peunova, N., Park, J. H., Tordo, J., Peterson, D. A., et al. (2011). Division-coupled astrocytic differentiation and age-related depletion of neural stem cells in the adult hippocampus. *Cell Stem Cell* 8, 566–579. doi: 10.1016/j.stem.2011.03.010
- Gaiano, N., and Fishell, G. (2002). The role of notch in promoting glial and neural stem cell fates. *Annu. Rev. Neurosci.* 25, 471–490. doi: 10.1146/annurev.neuro.25.030702.130823
- Gebara, E., Bonaguidi, M. A., Beckervordersandforth, R., Sultan, S., Udry, F., Gijss, P.-J., et al. (2016). Heterogeneity of radial glia-like cells in the adult hippocampus. *Stem Cells* 34, 997–1010. doi: 10.1002/stem.2266
- Hattiangady, B., and Shetty, A. K. (2008). Implications of decreased hippocampal neurogenesis in chronic temporal lobe epilepsy. *Epilepsia* 49(Suppl. 5), 26–41. doi: 10.1111/j.1528-1167.2008.01635.x
- Heinrich, C., Nitta, N., Flubacher, A., Müller, M., Fahrner, A., Kirsch, M., et al. (2006). Reelin deficiency and displacement of mature neurons, but not neurogenesis, underlie the formation of granule cell dispersion in the epileptic hippocampus. *J. Neurosci.* 26, 4701–4713. doi: 10.1523/JNEUROSCI.5516-05.2006
- Hung, Y.-W., Yang, D.-I., Huang, P.-Y., Lee, T.-S., Kuo, T. B. J., Yiu, C.-H., et al. (2012). The duration of sustained convulsive seizures determines the pattern of hippocampal neurogenesis and the development of spontaneous epilepsy in rats. *Epilepsy Res.* 98, 206–215. doi: 10.1016/j.eplepsyres.2011.09.015
- Jessberger, S., Römer, B., Babu, H., and Kempermann, G. (2005). Seizures induce proliferation and dispersion of doublecortin-positive hippocampal progenitor cells. *Exp. Neurol.* 196, 342–351. doi: 10.1016/j.expneurol.2005.08.010
- Jessberger, S., Zhao, C., Toni, N., Clemenson, G. D., Li, Y., and Gage, F. H. (2007). Seizure-associated, aberrant neurogenesis in adult rats characterized with retrovirus-mediated cell labeling. *J. Neurosci.* 27, 9400–9407. doi: 10.1523/JNEUROSCI.2002-07.2007
- Kempermann, G., Jessberger, S., Steiner, B., and Kronenberg, G. (2004). Milestones of neuronal development in the adult hippocampus. *Trends Neurosci.* 27, 447–452. doi: 10.1016/j.tins.2004.05.013
- Kienzler-Norwood, F., Costard, L., Sadangi, C., Müller, P., Neubert, V., Bauer, S., et al. (2017). A novel animal model of acquired human temporal lobe epilepsy based on the simultaneous administration of kainic acid and lorazepam. *Epilepsia* 58, 222–230. doi: 10.1111/epi.13579
- Kim, C. H., Lisman, J. E., Smith, K., Swann, J., Rothman, S. M., and Wong, M. (1999). A role of actin filament in synaptic transmission and long-term potentiation. *J. Neurosci.* 19, 4314–4324. doi: 10.1523/JNEUROSCI.19-11-04314.1999
- Korff, C. M., and Nordli, D. R. (2007). Diagnosis and management of nonconvulsive status epilepticus in children. *Nat. Clin. Pract. Neurol.* 3, 505–516. doi: 10.1038/ncpneuro0605
- Labovitz, D. L., Hauser, W. A., and Sacco, R. L. (2001). Prevalence and predictors of early seizure and status epilepticus after first stroke. *Neurology* 57, 200–206. doi: 10.1212/WNL.57.2.200
- Lennox, K. A., Owczarzy, R., Thomas, D. M., Walder, J. A., and Behlke, M. A. (2013). Improved performance of Anti-miRNA oligonucleotides using a novel non-nucleotide modifier. *Mol. Ther. Nucleic Acids* 2:e117. doi: 10.1038/mtna.2013.46
- Lévesque, M., and Avoli, M. (2013). The kainic acid model of temporal lobe epilepsy. *Neurosci. Biobehav. Rev.* 37(10 Pt 2), 2887–2899. doi: 10.1016/j.neubiorev.2013.10.011
- Li, Z., and Rana, T. M. (2014). Therapeutic targeting of microRNAs: current status and future challenges. *Nat. Rev. Drug Discov.* 13, 622–638. doi: 10.1038/nrd4359
- Llorens-Bobadilla, E., and Martin-Villalba, A. (2017). Adult NSC diversity and plasticity: the role of the niche. *Curr. Opin. Neurobiol.* 42, 68–74. doi: 10.1016/j.conb.2016.11.008
- Lugert, S., Basak, O., Knuckles, P., Haussler, U., Fabel, K., Götz, M., et al. (2010). Quiescent and active hippocampal neural stem cells with distinct morphologies respond selectively to physiological and pathological stimuli and aging. *Cell Stem Cell* 6, 445–456. doi: 10.1016/j.stem.2010.03.017
- Mignone, J. L., Kukekov, V., Chiang, A.-S., Steindler, D., and Enikolopov, G. (2004). Neural stem and progenitor cells in nestin-GFP transgenic mice. *J. Comp. Neurol.* 469, 311–324. doi: 10.1002/cne.10964
- Miliadous, P., Kouroupi, G., Stamatakis, A., Koutsoudaki, P. N., Matsas, R., and Stylianopoulou, F. (2013). Subventricular zone-derived neural stem cell grafts protect against hippocampal degeneration and restore cognitive function in the mouse following intrahippocampal kainic acid administration. *Stem Cells Transl. Med.* 2, 185–198. doi: 10.5966/sctm.2012-0074
- Mohapel, P., Ekdahl, C. T., and Lindvall, O. (2004). Status epilepticus severity influences the long-term outcome of neurogenesis in the adult dentate gyrus. *Neurobiol. Dis.* 15, 196–205. doi: 10.1016/j.nbd.2003.11.010
- Oomen, C. A., Soeters, H., Audureau, N., Vermunt, L., van Hasselt, F. N., Manders, E. M. M., et al. (2010). Severe early life stress hampers spatial learning and neurogenesis, but improves hippocampal synaptic plasticity and emotional learning under high-stress conditions in adulthood. *J. Neurosci.* 30, 6635–6645. doi: 10.1523/JNEUROSCI.0247-10.2010
- Parent, J. M., Elliott, R. C., Pleasure, S. J., Barbaro, N. M., and Lowenstein, D. H. (2006). Aberrant seizure-induced neurogenesis in experimental temporal lobe epilepsy. *Ann. Neurol.* 59, 81–91. doi: 10.1002/ana.20699
- Parent, J. M., Yu, T. W., Leibowitz, R. T., Geschwind, D. H., Sloviter, R. S., and Lowenstein, D. H. (1997). Dentate granule cell neurogenesis is increased by seizures and contributes to aberrant network reorganization in the adult rat hippocampus. *J. Neurosci.* 17, 3727–3738. doi: 10.1523/JNEUROSCI.17-10-03727.1997
- Pasquinelli, A. E. (2012). MicroRNAs and their targets: recognition, regulation and an emerging reciprocal relationship. *Nat. Rev. Genet.* 13, 271–282. doi: 10.1038/nrg3162
- Pirttilä, T. J., Manninen, A., Jutila, L., Nissinen, J., Kälviäinen, R., Vapalahti, M., et al. (2005). Cystatin C expression is associated with granule cell dispersion in epilepsy. *Ann. Neurol.* 58, 211–223. doi: 10.1002/ana.20545
- Pons-Espinal, M., de Luca, E., Marzi, M. J., Beckervordersandforth, R., Armiorotti, A., Nicassio, F., et al. (2017). Synergic functions of miRNAs determine neuronal fate of adult neural stem cells. *Stem Cell Rep.* 8, 1046–1061. doi: 10.1016/j.stemcr.2017.02.012
- Pun, R. Y. K., Rolle, I. J., Lasarge, C. L., Hosford, B. E., Rosen, J. M., Uhl, J. D., et al. (2012). Excessive activation of mTOR in postnatally generated granule cells is sufficient to cause epilepsy. *Neuron* 75, 1022–1034. doi: 10.1016/j.neuron.2012.08.002

- Racine, R. J. (1972). Modification of seizure activity by electrical stimulation. II. Motor seizure. *Electroencephalogr. Clin. Neurophysiol.* 32, 281–294. doi: 10.1016/0013-4694(72)90177-0
- Reschke, C. R., Silva, L. F. A., Norwood, B. A., Senthilkumar, K., Morris, G., Sanz-Rodriguez, A., et al. (2017). Potent anti-seizure effects of locked nucleic acid antagomirs targeting miR-134 in multiple mouse and rat models of epilepsy. *Mol. Ther. Nucleic Acids* 6, 45–56. doi: 10.1016/j.omtn.2016.11.002
- Robel, S., Buckingham, S. C., Boni, J. L., Campbell, S. L., Danbolt, N. C., Riedemann, T., et al. (2015). Reactive astrogliosis causes the development of spontaneous seizures. *J. Neurosci.* 35, 3330–3345. doi: 10.1523/JNEUROSCI.1574-14.2015
- Rosenow, F., Hamer, H. M., and Knake, S. (2007). The epidemiology of convulsive and nonconvulsive status epilepticus. *Epilepsia* 48(Suppl. 8), 82–84. doi: 10.1111/j.1528-1167.2007.01359.x
- Santos, M. C. T., Tegge, A. N., Correa, B. R., Mahesula, S., Kohnke, L. Q., Qiao, M., et al. (2016). miR-124, -128, and -137 orchestrate neural differentiation by acting on overlapping gene sets containing a highly connected transcription factor network. *Stem Cells* 34, 220–232. doi: 10.1002/stem.2204
- Schouten, M., Bielefeld, P., Fratantoni, S. A., Hubens, C. J., Piersma, S. R., Pham, T. V., et al. (2016). Multi-omics profile of the mouse dentate gyrus after kainic acid-induced status epilepticus. *Sci. Data* 3:160068. doi: 10.1038/sdata.2016.68
- Schouten, M., Buijink, M. R., Lucassen, P. J., and Fitzsimons, C. P. (2012). New neurons in aging brains: molecular control by small non-coding RNAs. *Front. Neurosci.* 6:25. doi: 10.3389/fnins.2012.00025
- Schouten, M., Fratantoni, S. A., Hubens, C. J., Piersma, S. R., Pham, T. V., Bielefeld, P., et al. (2015). MicroRNA-124 and -137 cooperativity controls caspase-3 activity through BCL2L13 in hippocampal neural stem cells. *Sci. Rep.* 5:12448. doi: 10.1038/srep12448
- Sibbe, M., Häussler, U., Dieni, S., Althof, D., Haas, C. A., and Frotscher, M. (2012). Experimental epilepsy affects Notch1 signalling and the stem cell pool in the dentate gyrus. *Eur. J. Neurosci.* 36, 3643–3652. doi: 10.1111/j.1460-9568.2012.08279.x
- Sierra, A., Martín-Suárez, S., Valcárcel-Martín, R., Pascual-Brazo, J., Aelvoet, S.-A., Abiega, O., et al. (2015). Neuronal hyperactivity accelerates depletion of neural stem cells and impairs hippocampal neurogenesis. *Cell Stem Cell* 16, 488–503. doi: 10.1016/j.stem.2015.04.003
- Singh, S. P., LaSarge, C. L., An, A., McAuliffe, J. J., and Danzer, S. C. (2015). Clonal analysis of newborn hippocampal dentate granule cell proliferation and development in temporal lobe epilepsy. *eNeuro* 2:ENEURO.0087-15.2015. doi: 10.1523/ENEURO.0087-15.2015
- Trinka, E., Cock, H., Hesdorffer, D., Rossetti, A. O., Scheffer, I. E., Shinnar, S., et al. (2015). A definition and classification of status epilepticus - report of the ILAE task force on classification of status epilepticus. *Epilepsia* 56, 1515–1523. doi: 10.1111/epi.13121
- Twele, F., Bankstahl, M., Klein, S., Römermann, K., and Löscher, W. (2015). The AMPA receptor antagonist NBQX exerts anti-seizure but not antiepileptogenic effects in the intrahippocampal kainate mouse model of mesial temporal lobe epilepsy. *Neuropharmacology* 95, 234–242. doi: 10.1016/j.neuropharm.2015.03.014
- Uemori, T., Toda, K., and Seki, T. (2017). Seizure severity-dependent selective vulnerability of the granule cell layer and aberrant neurogenesis in the rat hippocampus. *Hippocampus* 27, 1054–1068. doi: 10.1002/hipo.22752
- Velu, C. S., and Grimes, H. L. (2012). Utilizing antagomiR (antisense microRNA) to knock down microRNA in murine bone marrow cells. *Methods Mol. Biol.* 928, 185–195. doi: 10.1007/978-1-62703-008-3_15
- Weiler, J., Hunziker, J., and Hall, J. (2006). Anti-miRNA oligonucleotides (AMOs): ammunition to target miRNAs implicated in human disease? *Gene Ther.* 13, 496–502. doi: 10.1038/sj.gt.3302654
- Wilczynska, A., and Bushell, M. (2015). The complexity of miRNA-mediated repression. *Cell Death Differ.* 22, 22–33. doi: 10.1038/cdd.2014.112

Conflict of Interest Statement: The authors declare that the research was conducted in the absence of any commercial or financial relationships that could be construed as a potential conflict of interest.

Copyright © 2019 Bielefeld, Schouten, Meijer, Breuk, Geijtenbeek, Karayel, Tiaglik, Vuuregge, Willems, Witkamp, Lucassen, Encinas and Fitzsimons. This is an open-access article distributed under the terms of the Creative Commons Attribution License (CC BY). The use, distribution or reproduction in other forums is permitted, provided the original author(s) and the copyright owner(s) are credited and that the original publication in this journal is cited, in accordance with accepted academic practice. No use, distribution or reproduction is permitted which does not comply with these terms.



BDNF Induced Translation of Limk1 in Developing Neurons Regulates Dendrite Growth by Fine-Tuning Cofilin1 Activity

Sreenath Ravindran^{1,2}, Vijayalaxmi C. Nalavadi¹ and Ravi S. Muddashetty^{1*}

¹Center for Brain Development and Repair (CBDR), Institute for Stem Cell Biology and Regenerative Medicine (inStem), Bangalore, India, ²Manipal Academy of Higher Education, Manipal, India

Dendritic growth and branching are highly regulated processes and are essential for establishing proper neuronal connectivity. There is a critical phase of early dendrite development when these are heavily regulated by external cues such as trophic factors. Brain-derived neurotrophic factor (BDNF) is a major trophic factor known to enhance dendrite growth in cortical neurons, but the molecular underpinnings of this response are not completely understood. We have identified that BDNF induced translational regulation is an important mechanism governing dendrite development in cultured rat cortical neurons. We show that BDNF treatment for 1 h in young neurons leads to translational up-regulation of an important actin regulatory protein LIM domain kinase 1 (Limk1), increasing its level locally in the dendrites. Limk1 is a member of serine/threonine (Ser/Thr) family kinases downstream of the Rho-GTPase pathway. BDNF induced increase in Limk1 levels leads to increased phosphorylation of its target protein cofilin1. We observed that these changes are maintained for long durations of up to 48 h and are mediating increase in number of primary dendrites and total dendrite length. Thus, we show that BDNF induced protein synthesis leads to fine-tuning of the actin cytoskeletal reassembly and thereby mediate dendrite development.

Keywords: BDNF, cofilin1, dendrite growth, early neurodevelopment, Limk1, translation

OPEN ACCESS

Edited by:

Enrico Tongiorgi,
University of Trieste, Italy

Reviewed by:

Petra Wahle,
Ruhr-Universität Bochum, Germany
Ana Luisa Carvalho,
University of Coimbra, Portugal

*Correspondence:

Ravi S. Muddashetty
ravism@instem.res.in

Received: 27 October 2018

Accepted: 26 February 2019

Published: 20 March 2019

Citation:

Ravindran S, Nalavadi VC and Muddashetty RS (2019) BDNF Induced Translation of Limk1 in Developing Neurons Regulates Dendrite Growth by Fine-Tuning Cofilin1 Activity. *Front. Mol. Neurosci.* 12:64. doi: 10.3389/fnmol.2019.00064

INTRODUCTION

During neuronal development, dendritic growth and patterning lay down the basic architecture of the neuronal network. This important phase is regulated by various cell-intrinsic and external cues (Scott and Luo, 2001). The temporal profile of dendrite development *in vivo* typically is non-linear (Wu et al., 1999). In the early phase of perinatal development, the dendrite branches are highly dynamic and are affected significantly by different cues. This dynamic phase of development is a critical time window which later is replaced with a stable phase where dendritic branches show minimal growth and pruning. This developmental profile is recapitulated in *in vitro* systems as well. Dendrites of cultured neurons have an initial slow phase (which also shows fast axonal growth), followed by an active phase of dendritic growth and pruning, and then a late phase of slow growth and pruning (Dotti et al., 1988). Although a large number of studies have focussed on understanding spine formation, pruning and plasticity in mature dendrites, the molecular details governing early dendrite development is not completely understood. This understanding is imperative in the context of several neurodevelopmental disorders, as defects in this critical window lead to long term and irreversible changes in the neuronal connectivity.

Similar to axons, dendrite growth and spine development also require extensive cytoskeletal re-arrangements involving both actin and microtubule filaments (Ferreira et al., 2010; Ohtani et al., 2014). Actin network, being peripherally present in the filopodia, responds to several external cues, initiating the reassembly (Scott and Luo, 2001; Da Silva and Dotti, 2002). The microtubule cytoskeleton is involved in the stabilization of the new branches initiated due to actin reassembly (Zhou et al., 2002; Hu et al., 2008; Gu and Zheng, 2009). External cues activated signaling cascades converge on these cytoskeletal elements bringing about dendrite growth (Whitford et al., 2002). Brain-derived neurotrophic factor (BDNF), a member of the neurotrophin family of proteins promotes neuronal survival and dendritic growth in the cerebral cortex and hippocampus (McAllister et al., 1995; Labelle and Leclerc, 2000; Horch and Katz, 2002). BDNF-TrkB signaling is also critical for dendritic spine enlargement and maintenance of LTP, mediated partly through mTOR dependent activation of protein synthesis (Schratt et al., 2004, 2006; Kuipers et al., 2016). Dendritic spines are actin-rich structures and spine dynamics are driven mainly by actin remodeling, thus sharing several molecular pathways with dendrite growth. Reports have shown that BDNF induced changes in spine morphology, as well as trophic factor responses in growing axons, are mediated *via* translational regulation of actin modulator proteins (Leung et al., 2006; Schratt et al., 2006; Spillane et al., 2012). These studies clearly indicate that trophic factors affect the translational profile of actin modulator proteins in neuronal compartments involving structural alterations.

Microarray-based studies have identified that translation of an actin modulator protein LIM domain kinase 1 (Limk1) is enhanced on BDNF treatment in mature as well as immature rat cortical neuronal cultures (Schratt et al., 2004). We were interested in understanding the role of BDNF mediated Limk1 translation in young neurons during the critical period of dendritic growth, and its physiological role in dendrite development. Cultured neurons are a good model system as the neurite growth profile is well characterized (Kaech and Banker, 2006) and the system is amenable to both long term and short term drug treatments. Our results show that BDNF causes translational up-regulation of Limk1 and increases its level in the dendrites. This effect persists for long period and enhances dendrite growth *via* modulating the activity of the actin-binding protein cofilin1.

MATERIALS AND METHODS

Ethics Statement

All animal work was done with due approval from the Institutional Animal Ethics committee (IAEC) constituting Prof. Sumantra Chattarji as the chairperson and Dr. P. Krishnamurthy as the CPCSEA nominee (external member) and the Institutional Biosafety Committee (IBSC), InStem, Bangalore, India.

Primary Neuronal Culture

Primary neuronal culture was prepared from cerebral cortices of E18 rats (Sprague-Dawley) according to an established protocol

(Kaech and Banker, 2006). For biochemical studies, high-density neuronal cultures (~38,000 cells per square cm) were plated on poly-L-lysine (0.2 mg/ml in borate buffer, pH 8.5) coated dishes. For the immunostaining experiments, dissociated cells were plated at lower density (~2,500 cells per square cm) on poly-L-lysine coated coverslips. Neurons were attached to the substrate in minimal essential medium with 10% fetal bovine serum (FBS, Sigma F2442) for 3 h, and coverslips were inverted onto 6-well plates containing astroglia, and grown in defined Neurobasal Medium (Invitrogen, Carlsbad, CA, USA) with GlutaMAXTM supplement (GibcoTM) and B-27 supplements (Invitrogen, Carlsbad, CA, USA). Neurons were cultured for 5 days at 37°C in a 5% CO₂ environment.

Polysome Profiling

Polysome assay was done from cell lysate as described previously (Muddashetty et al., 2007). In brief, cell lysate was separated on 15%–45% linear sucrose gradient in presence of cycloheximide (CHX) by centrifugation at 39,000 rpm in SW41 rotor for 90 min. The sample was fractionated in 11 1.0 mL fractions with continuous UV absorbance measurement (A254). Fractions were further analyzed by western blots. Fractions were pooled (1–7 and 8–11) according to puromycin sensitivity, as assessed by UV absorbance profile and the distribution of ribosomal protein RPLP0 in western blots. Total RNA isolated from the pooled fractions using Trizol LS method according to the company protocol. Quantitative PCRs (qPCRs) performed with primers for *Limk1*, *β-Actin*, *cofilin1*, *Arc*, *Arcp3*, from the two pools.

Quantitative PCR and Primers

	Forward	Reverse
<i>Limk1</i>	GTAACCCCTACTGGATGGCG	AGTTTGGTGGACAGTAGCGG
<i>Arc</i>	AAGTTC AAGCGCTTTCTGCG	GACTCGCTGGTAAGAGCAGG
<i>Arcp3</i>	GAGACCGGACTGAGGCTTTG	CACCTCAATGCGATGCTGAC
<i>cofilin1</i>	GGCTCTGTTCTTCTGTAGCTCT	CAGTGCCTTCTTGCGTTTCTT
<i>β-actin</i>	GGCTCTAGCACCATGAAGAT	AAACGCAGCTCAGTAACAGTC

Arbitrary copy numbers calculated from a standard curve drawn from Ct values obtained from serial dilutions of cDNA.

Immunostaining

Rat primary cortical neurons were stimulated at days *in vitro* (DIV) 5 with 50 ng/ml BDNF for 1 h. Cells were fixed with 4% PFA and processed for imaging as described before (Muddashetty et al., 2011). In brief, cells were permeabilized using TBS₅₀T (0.3%) [50 mM Tris-Cl (pH 7.4) + 150 mM NaCl + 0.3% TritonX-100]. This was followed by treatment with Tris-Glycine solution (0.5 M Tris and 0.2 M Glycine) for background reduction before blocking with blocking buffer [TBS₅₀T (0.1%) + 2% BSA + 2% FBS]. Primary antibodies were incubated in TBS₅₀T (0.1%) + 1% BSA overnight at 4°C which was followed by washes. Alexa Fluor 488 coupled anti-mouse and Alexa Fluor 555 coupled anti-rabbit secondary antibodies were incubated for 1 h at room temperature. Finally, coverslips were mounted for imaging using Mowiol[®] 4-88 mounting media. Images were

acquired on FV3000 confocal microscope (Olympus) using Plan Apo 60 \times , NA 1.42, oil immersion objective. Z-series of 6–10 stacks with XY sampling density of 0.094 $\mu\text{m}/\text{pixel}$ were taken at 0.5 micron step size from all dendrites. Imaging conditions were kept constant across experiments. Antibodies against p-ser3-cofilin1 (ab12866), p-thr508-Limk1 (ab38508) and total Limk1 (ab119084) were purchased from Abcam. Total cofilin1 (WH0001072M4) and alpha-tubulin (T9026) from Sigma.

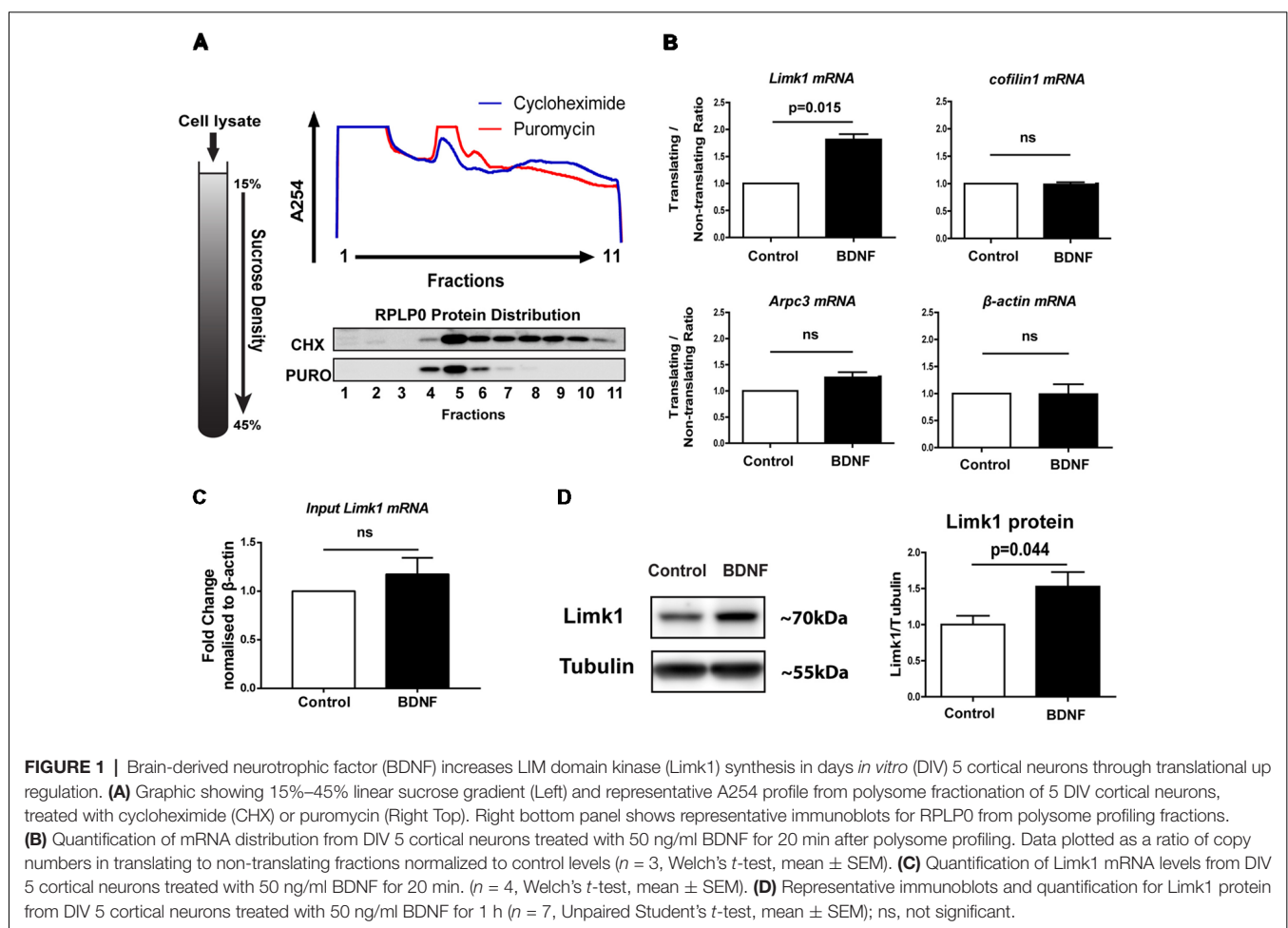
Neurite Growth Assays

Rat primary cortical neurons were stimulated at DIV 5 with 50 ng/ml BDNF for 48 h. Cells were fixed with 4% PFA and immunostained for microtubule-associated protein2 (Map2) and Microtubule-associated protein Tau (Tau) proteins with respective antibodies (Map2-Sigma M9942, Tau- Abcam ab76128). Dendrites (Map2 positive and Tau negative) were traced using the NeuronJ plugin in ImageJ software as described (Meijering et al., 2004). The threshold was set up manually for the images and Sholl analysis was carried out using the sholl plugin in ImageJ (Ferreira et al., 2014) with 10 micron steps. For Limk1 knockdown experiments, DIV 5 cortical neurons were transfected with scrambled or Limk1 siRNA (Thermo Fisher,

Waltham, MA, USA, s134717) along with EGFP, followed by BDNF treatment for 48 h. Dendrites were identified based on their short, distally tapering branches from the cell body and traced using NeuronStudio software (CNIC, v 0.9.92; Wearne et al., 2005). All the analysis were done with experimenter blind to the condition.

Live Imaging to Quantitate Dendrite Growth

Rat primary cortical neurons were cultured on Nunc glass bottom Petri dishes at a density of 200,000 cells per dish. Cells were transfected at DIV 4 using Lifeact-mCherry (Addgene, Watertown, MA, USA) vector by magnetofection as per the company protocol. Images were acquired on FV3000 confocal microscope (Olympus) using Plan Apo 60 \times , NA 1.42, oil immersion objective, with 37°C temperature and 5% CO₂ maintenance. Dendrites were identified as short, distally tapering branches from the cell body. Images were captured as Z-series of 6–10 stacks with XY sampling density of 0.090 $\mu\text{m}/\text{pixel}$ at 0.5 micron step size from all dendrites at 5 min interval using a high sensitivity PMT detector. Cells were imaged for a period of 1 h after which 50 ng/ml BDNF was added and imaging was continued for one more hour. For analysis, the



Z stacks were compressed by maximum intensity projection using ImageJ and imported into Imaris software (Bitplane AG, x64, v 9.0.1). The FilamentTracer tool in Imaris was used for automatic tracing of dendrites and identification of dendrite tips. Tip trajectories were traced and quantified for the entire imaging duration.

Fixed Cell F-Actin Measurement

F-actin visualization, Alexa Fluor 488 phalloidin (Invitrogen, Carlsbad, CA, USA) was added to the secondary antibody solution (1:50 dilution) during immunostaining and incubated for 1 h. F-actin levels were quantified as an intensity ratio of phalloidin to Map2 fluorescence. As an alternate method, rat primary cortical neurons were transfected at DIV 4 with equimolar concentrations of Lifeact-mCherry and EGFP C1 vectors and treated at DIV 5 with 50 ng/ml for 48 h. Cells were fixed at DIV 7 and F-actin measured as mean intensity ratio of mCherry to EGFP.

Statistical Analysis

Statistical significance was calculated using unpaired Student's *t*-test for biochemical experiments. For immunostaining based quantifications, Mann Whitney test was used. Data plotted as mean \pm SEM unless described otherwise. Value of $p < 0.05$ was considered statistically significant.

RESULTS

BDNF Activates Limk1 Translation in Immature Neurons in Culture

We used primary neurons cultured from embryonic (E18) rat cerebral cortex for this study. We have conducted our experiments on DIV-5 neurons which are in their stage four growth phase and do not possess mature synapses (Dotti et al., 1988; Kaech and Banker, 2006). To study the influence of BDNF on translation of actin modulators in these young neurons, we used the translational assay of polysome profiling (Schratt et al., 2004; Muddashetty et al., 2007). In this assay, post-nuclear cell lysates were subjected to ultracentrifugation on a linear sucrose gradient (Figure 1A). Fractions were collected with measurement of UV absorbance at 254 nm to identify various ribosomal pools. UV absorbance profile, as well as ribosomal protein RPLP0 distribution in puromycin vs. CHX treated cells, were used to identify the fractions containing actively translating polysomes (Figure 1A). Based on puromycin sensitivity, fractions were pooled into translating (8–11) and non-translating (1–7) pools. DIV 5 cortical neurons were treated with 50 ng/ml BDNF for 20 min and distribution of selected mRNAs in these pools were assayed by qPCR (Figure 1B). We screened for several candidates previously reported as actin cytoskeletal modulators in mature synapses or growing axons (Leung et al., 2006; Messaoudi et al., 2007; Spillane et al., 2012). Among the candidates, *Limk1* mRNA showed a significant increase in polysomal distribution on BDNF treatment compared to control; suggesting that translation of *Limk1* mRNA is up-regulated on BDNF treatment (Figure 1B). Other mRNAs that we examined include β -

actin, *cofilin1*, and *Arpc3* which did not show significant change in their polysomal distribution (Figure 1B). To measure the transcriptional contribution, we examined the total levels of *Limk1* mRNA on BDNF treatment. We did not observe a significant increase in total *Limk1* mRNA levels as quantitated by qPCR. (Figure 1C). To validate the change in translation at the protein level, we quantified *Limk1* levels by immunoblotting and found that 1 h of BDNF treatment resulted in $53 \pm 20\%$ increase in *Limk1* levels compared to control (Figure 1D). Thus, the change in mRNA translational profile for *Limk1* is reflected in the protein levels. Both polysome profiling and immunoblotting results confirm that BDNF causes translational up-regulation of *Limk1* in immature neurons. Next, we studied whether this newly synthesized protein is functionally active.

BDNF Induces Phosphorylation of Cofilin1 in a Translation-Dependent Manner

Limk1 is a serine/threonine (Ser/Thr) kinase downstream of Rho-GTPase signaling pathway that plays a key role in actin filament dynamics. Phosphorylated *Limk1* (active form) phosphorylates the actin-binding protein cofilin1 at Ser-3 (Arber et al., 1998; Yang et al., 1998; Figure 2A). Cofilin1 is a member of ADF/cofilin family of proteins. As shown in the illustration (Figure 2A), cofilin1 has multiple effects on actin polymerization depending on the stoichiometry of binding. At lower concentration, it binds to F-actin and leads to depolymerization as well as filament breaks. At higher concentrations, it can stabilize F-actin and cause nucleation (Andrianantoandro and Pollard, 2006; Van Troys et al., 2008). Phosphorylated cofilin1 loses its actin binding ability and becomes inactive. As both *Limk1* and cofilin1 are important for neurite growth (Meberg and Bamberg, 2000; Endo et al., 2003, 2007; Lee-Hoeflich et al., 2004), we looked at the phosphorylation status of cofilin1, a *Limk1* target protein following BDNF treatment. We found that BDNF induces a robust increase in phosphorylation of cofilin1 in DIV 5 neurons (Figure 2B) with no change in the total cofilin1 levels (Figure 2B). This is in accordance with the translational profiling which showed that translation of cofilin1 mRNA was unaffected on BDNF treatment (Figure 1B). The change in phosphorylation of cofilin1 was abrogated by blocking new protein synthesis using CHX or anisomycin (Figures 2C,D). This indicates that BDNF induced cofilin1 phosphorylation is dependent on BDNF induced translation. To test if these changes are dependent on TrkB activation, we used the tyrosine protein kinase inhibitor K252a to block TrkB phosphorylation. Both BDNF mediated *Limk1* synthesis, as well as cofilin1 phosphorylation was completely blocked by inhibiting TrkB activation (Figure 2E). These results suggest that BDNF induced TrkB phosphorylation is required for *Limk1* synthesis and cofilin1 phosphorylation. However, we did not any change in *Limk1* and p-cofilin1 levels on treatment with the second TrkB ligand Neurotrophin-4 (NT4) (Supplementary Figure S1), indicating the specificity of this response. Our

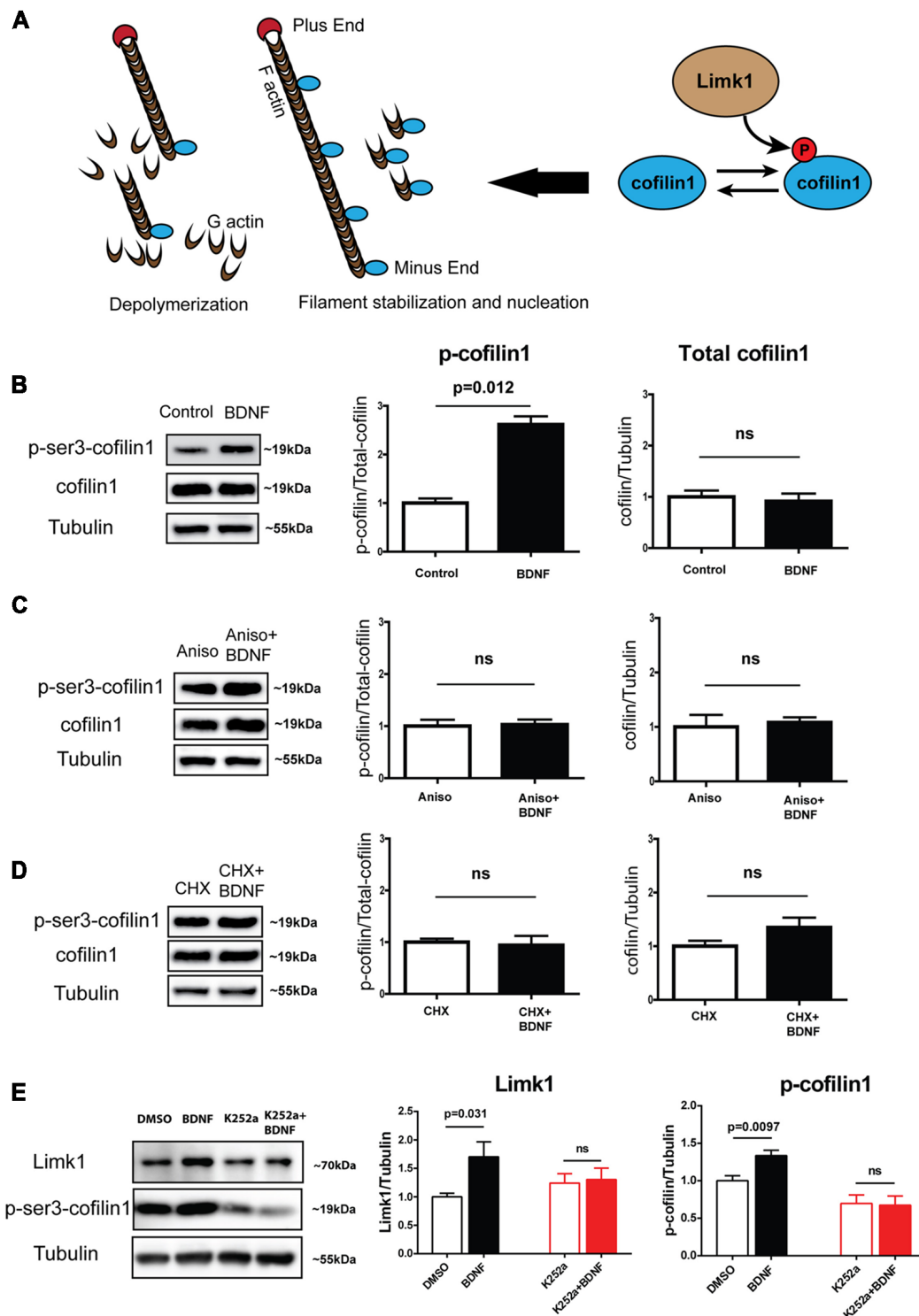


FIGURE 2 | BDNF leads to increase in phosphorylation of cofilin1 in a protein synthesis-dependent manner. **(A)** Schematic showing Limk1 and cofilin1 function. **(B)** Representative immunoblots (Left) and quantification of phosphorylated (Center) and total cofilin (Right) from DIV 5 cortical neurons with BDNF treatment for 1 h. **(C)** Representative immunoblots (Left) and quantification of phosphorylated (Center) and total cofilin (Right) from DIV 5 cortical neurons with BDNF treatment for 1 h in the presence of 40 μ M anisomycin. **(D)** Representative immunoblots (Left) and quantification of phosphorylated (Center) and total cofilin (Right) from DIV 5 cortical neurons with BDNF treatment for 1 h in the presence of 100 μ M CHX. **(E)** Representative immunoblots (Left) and quantification of Limk1 (Center) and phosphorylated cofilin (Right) from DIV 5 cortical neurons with BDNF treatment for 1 h in the presence of 200 nM K252a ($n = 3-5$, Unpaired Student's t -test, mean \pm SEM), ns, not significant.

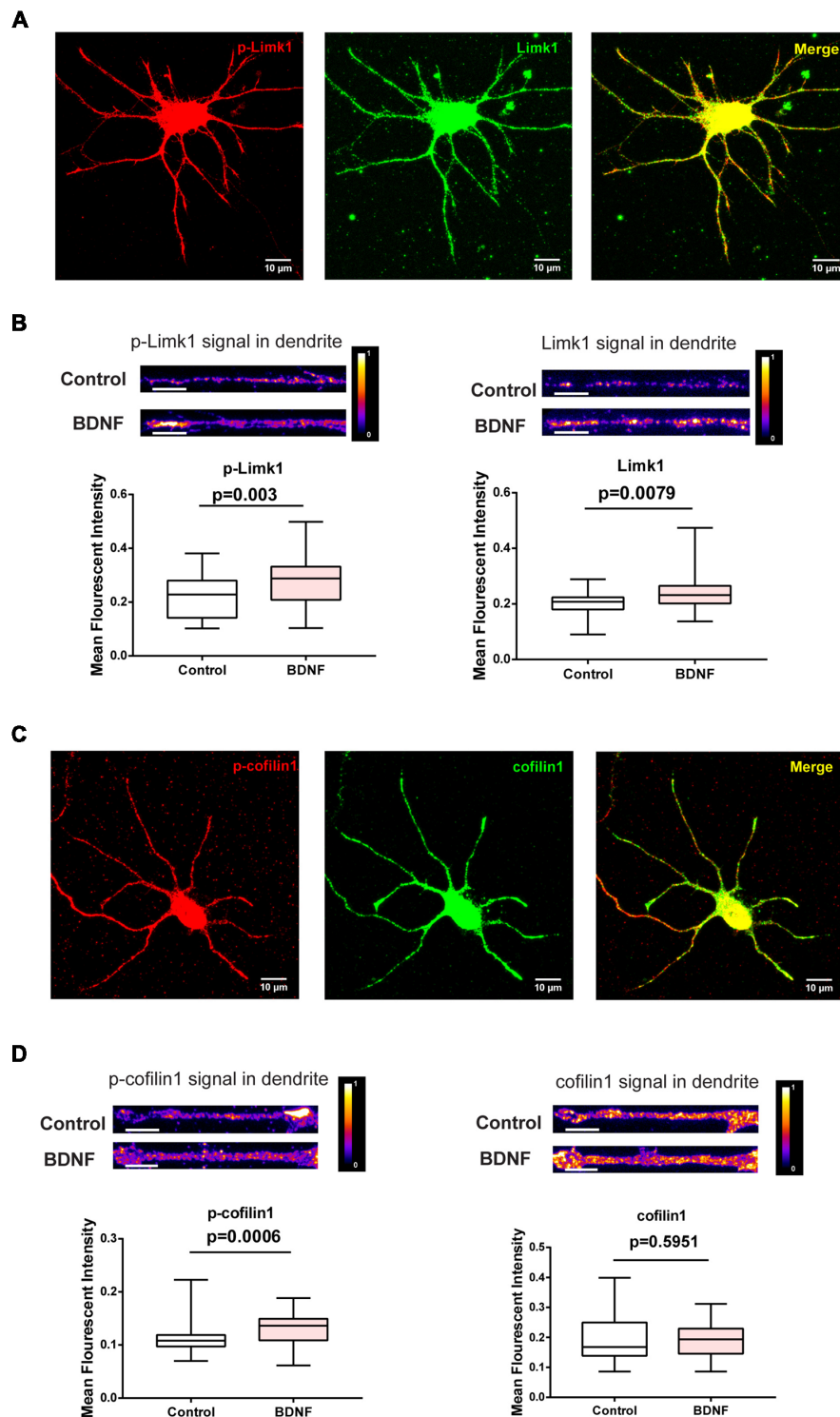


FIGURE 3 | BDNF leads to increased dendritic Limk1 levels and phosphorylation of cofilin1. **(A)** Immunofluorescence images showing phosphorylated (Red) and total Limk1 (Green) distribution in the dendrites of DIV 5 cortical neurons. **(B)** Representative intensity profiles (Top) and quantification (Bottom) of mean fluorescent intensities from the entire dendrite for p-Limk1 (Left) and Limk1 (Right) from DIV 5 cortical neurons treated with 50 ng/ml BDNF for 1 h ($n = 38$ – 39 neurons from three independent experiments). **(C)** Immunofluorescence images showing phosphorylated (Red) and total cofilin1 (Green) distribution in the dendrites of DIV 5 cortical neurons. **(D)** Representative intensity profiles (Top) and quantification (Bottom) of mean fluorescent intensities from the entire dendrite for p-cofilin1 (Left) and cofilin1 (Right) from DIV 5 cortical neurons treated with 50 ng/ml BDNF for 1 h ($n = 34$ – 46 neurons from three independent experiments). Box and whisker plots show median, first and third quartiles with error bars representing the minimum and maximum data points (Mann-Whitney test).

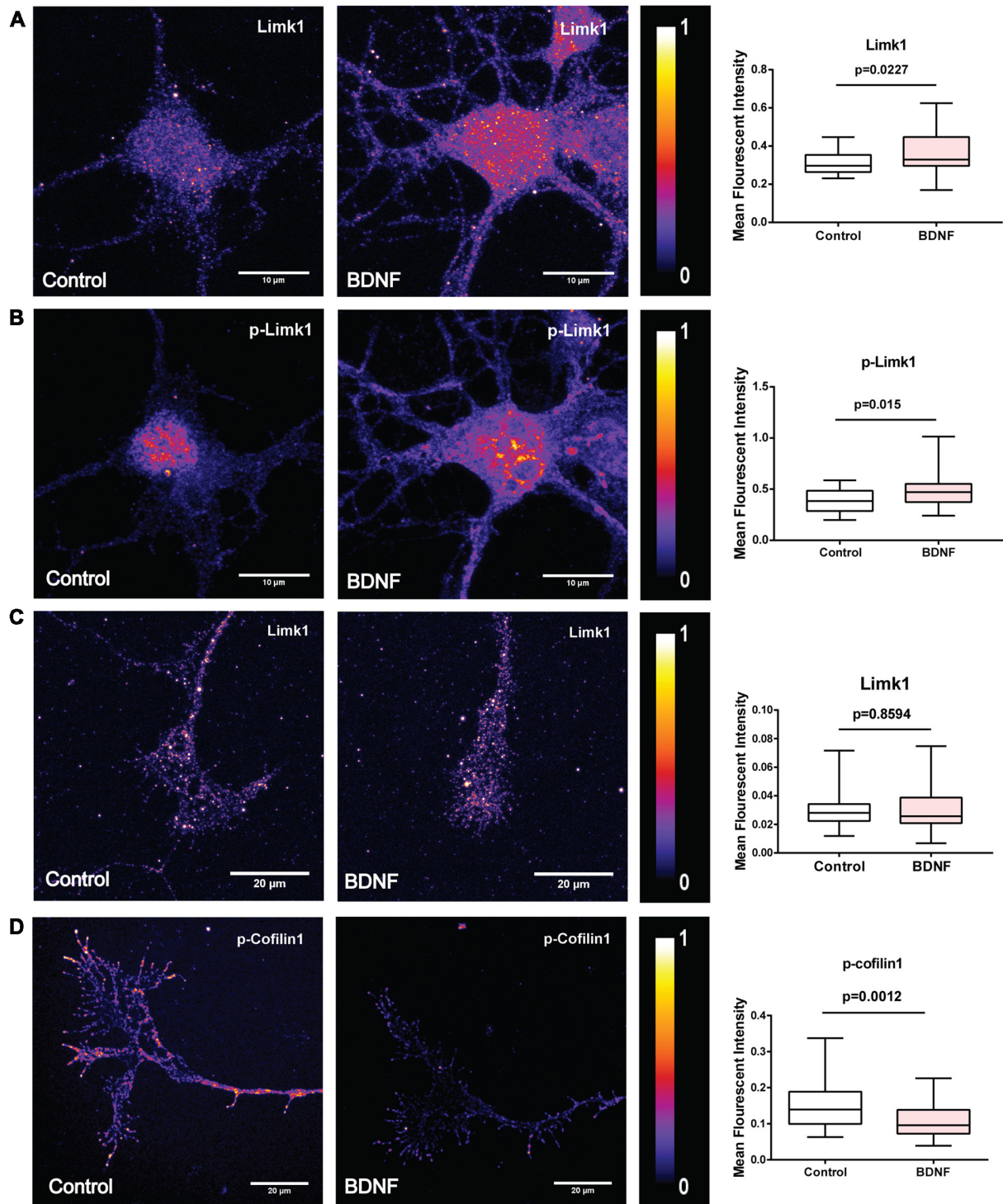


FIGURE 4 | BDNF leads to increased Limk1 levels in the cell body. In the axonal growth cones BDNF did not affect Limk1 levels, but reduced phosphorylation of cofilin1. **(A)** Representative heat map images of control (Left) and BDNF treated (Center) cortical neurons immunostained for Limk1. Right panel shows the quantification of the signal from the cell body. **(B)** Representative heat map images of control (Left) and BDNF treated (Center) cortical neurons immunostained for p-Limk1. Right panel shows the quantification of the signal from the cell body. **(C)** Representative heat map images of axonal growth-cones from control (Left) and BDNF treated (Center) cortical neurons immunostained for Limk1. Right panel shows the quantification of the signal. **(D)** Representative heat map images of axonal growth-cones from control (Left) and BDNF treated (Center) cortical neurons immunostained for p-cofilin1. Right panel shows the quantification of the signal ($n = 30$ – 36 neurons from three independent experiments. Box and whisker plots show median, first and third quartiles with error bars representing the minimum and maximum data points. Mann-Whitney test).

data so far shows that similar to its role in dendritic spines (Schratt et al., 2006), BDNF is involved in translational fine-tuning of some key actin modulators in immature neurons. Since the majority of the cell volume is contributed by the somatodendritic compartment, this implies that dendrite development is regulated by this process. Considering that BDNF is a well-known factor regulating dendrite growth and that actin cytoskeletal changes are indispensable in mediating neurite growth, we tested whether BDNF induced Limk1 synthesis

and consequent cofilin phosphorylation is important for dendrite growth.

BDNF Leads to Increase in Limk1 Levels and Phosphorylation of Cofilin1 in the Dendrites

To check if BDNF affects Limk1 levels locally in dendrites, we measured Limk1 levels in the dendrites of DIV 5 neurons

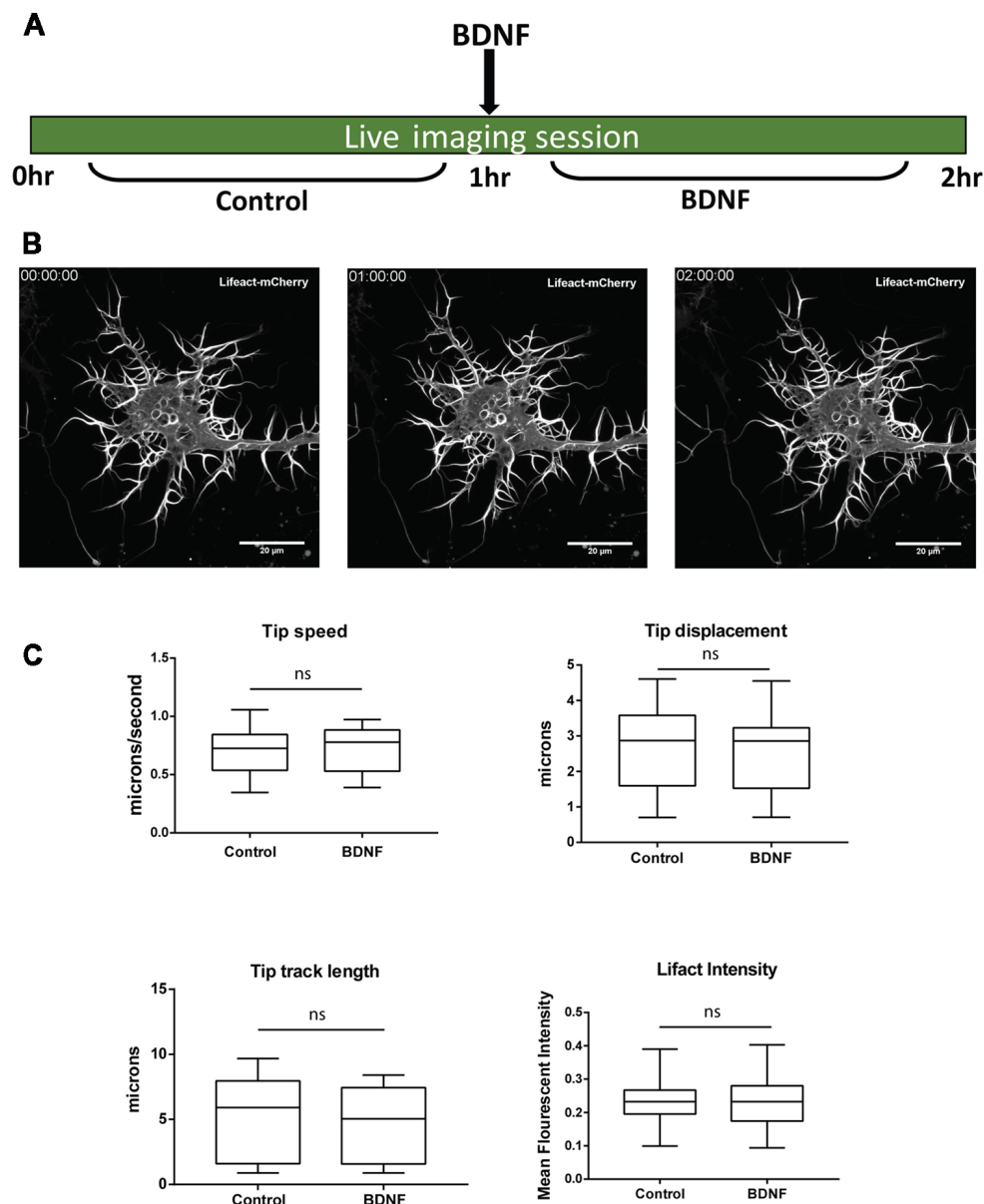


FIGURE 5 | One hour BDNF treatment did not lead to detectable changes in dendrite growth visualized by live imaging. **(A)** Schematic showing live imaging paradigm. Cortical neurons are transfected with Lifact-mCherry at DIV 4 and imaged at DIV 5 for 1 h before and after BDNF addition. **(B)** Representative images from Lifact-mCherry transfected cortical neurons at time points of 0, 1 and 2 h as indicated. **(C)** Quantification of dendrite tip speed (Top Left), displacement (Top Right), track length (Bottom Left) and Lifact intensity in dendritic filopodia (Bottom Right) from control and BDNF treated conditions as described in **(A,B)** ($n = 14$ neurons from three independent experiments. Box and whisker plots show median, first and third quartiles with error bars representing minimum and maximum data points. Mann-Whitney test), ns, not significant.

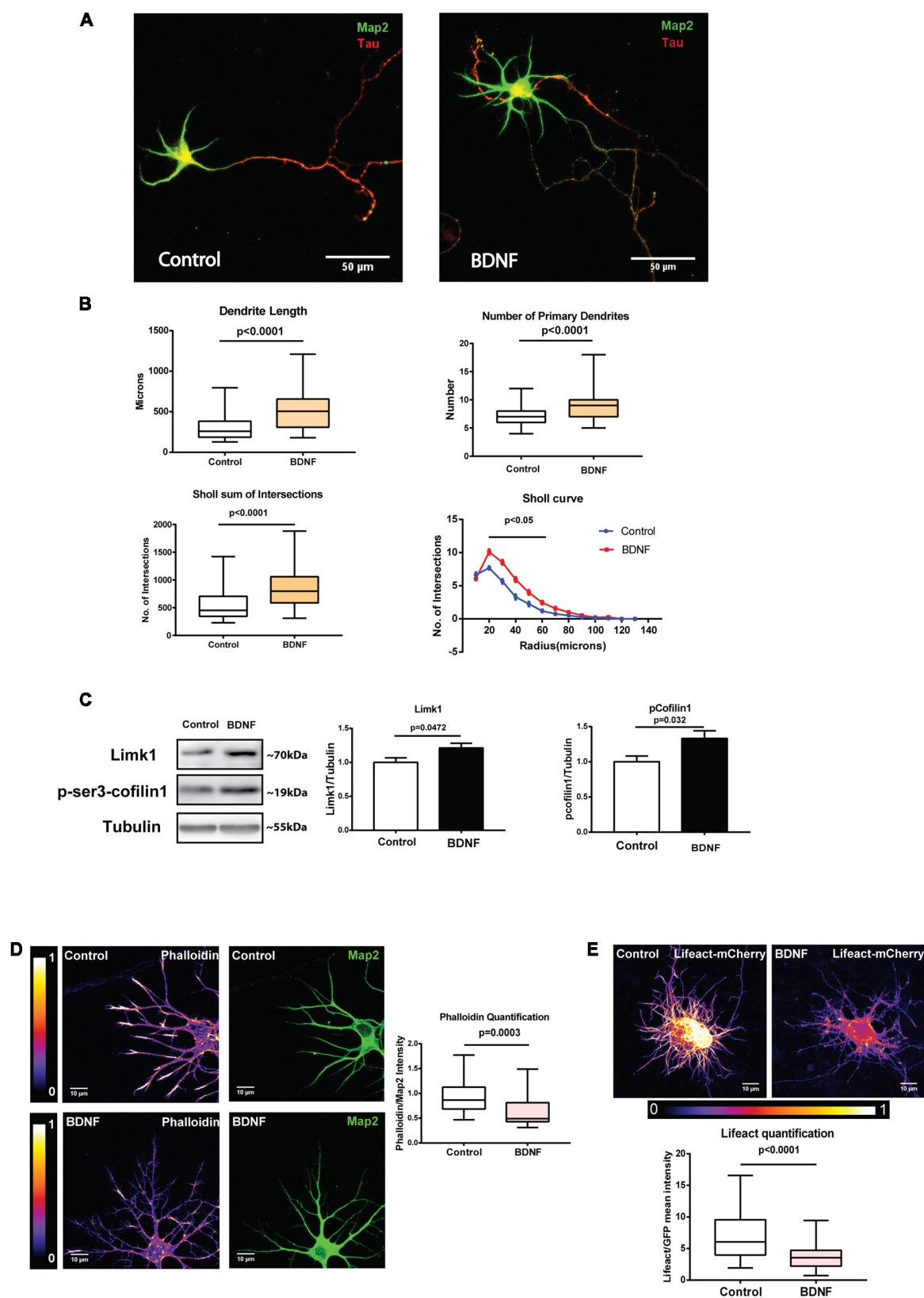


FIGURE 6 | Continued

FIGURE 6 | BDNF-induced Limk1 synthesis is sustained for 48 h and is associated with dissolution of F-actin and dendritic growth.

(A) Representative images of neurons treated with or without 50 ng/ml BDNF for 48 h, fixed and immunostained for microtubule-associated protein2 (Map2; Green) and Tau (Red). **(B)** Quantification of total dendritic length (Top Left), number of primary dendrites (Top Right) total intersections by Sholl analysis (Bottom Left) and Sholl curves (Bottom Right) from control and BDNF treated cortical neurons from the experiment described in **Figure 6A** ($n = 49$ – 61 neurons across three independent experiments, Box and whisker plots show median, first and third quartiles with error bars representing minimum and maximum data points, Mann Whitney test). **(C)** Representative immunoblots (Left) and quantification of Limk1 (Center) and p-cofilin1 (Right) levels from control or 48 h BDNF treated cortical neurons ($n = 7$, Unpaired Student's *t*-test, mean \pm SEM). **(D)** Representative images (Left) and quantification (Center) of phalloidin from neurons treated with or without 50 ng/ml BDNF for 48 h. Mean intensity of phalloidin normalized to Map2 ($n = 23$ neurons from two independent experiments, Mann Whitney test). **(E)** Representative images (Top) and quantification of F-actin (Bottom) from neurons treated with or without 50 ng/ml BDNF for 48 h (Right) transfected with Lifeact-mCherry. Mean intensity of mCherry normalized to EGFP ($n = 49$ – 50 neurons from three independent experiments, Mann-Whitney test).

by quantitative immunofluorescence. Both total and phosphorylated Limk1 are present in the cell body as well as throughout the length of the dendrite (**Figure 3A**). We observed a significant increase in total as well as phosphorylated Limk1 levels in the whole dendrites following 1 h of BDNF treatment (**Figure 3B**). Next, we checked the levels of phosphorylation of cofilin1 in the dendrites. Similar to Limk1 distribution, both total and phosphorylated cofilin1 is present throughout dendrites (**Figure 3C**). Corresponding to the increase in Limk1 levels, the phosphorylated cofilin1 levels were increased in the dendrites in response to BDNF treatment (**Figure 3D**). Similar to the immunoblot data, total cofilin1 levels were unaffected by BDNF treatment (**Figure 3D**). We also found that total and phosphorylated Limk1 levels in the cell body increased on BDNF treatment (**Figures 4A,B**) showing that this is a somatodendritic effect. Contrary to the dendritic increase of Limk1, there was no change in Limk1 levels in the axonal growth cones (**Figure 4C**). Similarly, the phosphorylation of cofilin1 on BDNF treatment was not observed in the axonal compartment. As reported previously (Marsick et al., 2010) with positive trophic factors, we observed a reduction in cofilin1 phosphorylation on BDNF treatment in axonal growth cones (**Figure 4D**) while proximal axonal segments did not show a significant change (data not shown). Thus, our data show that BDNF mediated rise in Limk1 levels is present in the cell body and dendrites, which mediates the phosphorylation of cofilin1. This translational response is not observed in the axons. To test whether these molecular changes are present in the later stages of dendrite development, we quantified dendritic levels of Limk1 and p-cofilin1 in DIV10 neurons following BDNF treatment by quantitative immunofluorescence. Similar to DIV5 data, we observed a significant increase in Limk1 as well as phosphorylated cofilin1 levels in the DIV10 dendrites following 1 h of BDNF treatment (**Supplementary Figure S2**), showing that these responses are preserved in later stages of dendritic growth as well.

BDNF-Induced Limk1 Synthesis Is Sustained for 48 h and Mediate Dendrite Growth

Next, we investigated whether newly synthesized Limk1 is important for mediating dendrite growth induced by BDNF. We studied the physiological response after 1 h of BDNF treatment, which brings about some key actin modulator protein changes. We standardized a short-term live imaging assay to visualize dendrite growth through labeling filamentous actin with mCherry tagged Lifeact. Cortical neurons were transfected by Lifeact-mCherry at DIV 4 and imaged at DIV 5. Growing dendritic filopodia were identified based on their morphology and imaged for a period of 1 h before and after BDNF addition (**Figure 5A**). Using this method we observed growth and retractions in the dendrite tips during this period (**Figure 5B**). The filopodial length and tip dynamics were tracked using FilamentTracer in Imaris software and was quantitated as parameters of tip track length, displacement and speed (**Figure 5C**) before and after BDNF addition. The F-actin content was also quantified by measuring Lifeact intensity (**Figure 5C**). Dendritic filopodia showed a high rate of dynamicity during the imaging period, but we did not find the difference statistically significant for the measured parameters between control and BDNF treated neurons. This points out that the BDNF induces morphological changes in dendrites could not be captured at shorter time scales but needed longer periods.

To confirm this, we measured total dendrite length after long term BDNF treatment. DIV 5 neurons treated with BDNF for 48 h were fixed and immunostained for Map2 to visualize the entire dendritic arbor (**Figure 6A**). All dendrites were traced semi-automatically using NeuronJ plugin in ImageJ software. Tau-positive axons were excluded from the analysis. As reported before (McAllister et al., 1996), this long term BDNF treatment caused a robust increase in total dendrite length and number of primary dendrites in cultured neurons compared to the controls (**Figure 6B**). An increase in the number of intersections was also observed in the Sholl analysis (**Figure 6B**). Together, the above results show that even though we can detect the molecular changes in Limk1 translation and cofilin1 phosphorylation as early as 1 h, morphological changes are detected only after a long term BDNF treatment. One possible explanation could be that these molecular changes are sustained longer to bring about detectable morphological changes. To check this possibility, we measured Limk1 and p-cofilin1 levels after 48 h of BDNF treatment by immunoblotting. In accordance with our hypothesis, we found that both Limk1 and p-cofilin levels remain elevated after 48 h of BDNF treatment (**Figure 6C**). Although correlative at this stage, our data suggests that sustained higher levels of Limk1 is important in mediating BDNF induced dendritic growth. To find the effect of this on actin polymerization, we measured F-actin levels by phalloidin staining as well as Lifeact quantification. In both assays, we found that 48 h BDNF treatment led to a significant reduction in F-actin levels in the dendrites (**Figures 6D,E**). This shows that the primary role of cofilin1 in the dendrites is either stabilization of actin filaments or actin nucleation. BDNF leads to deactivation of

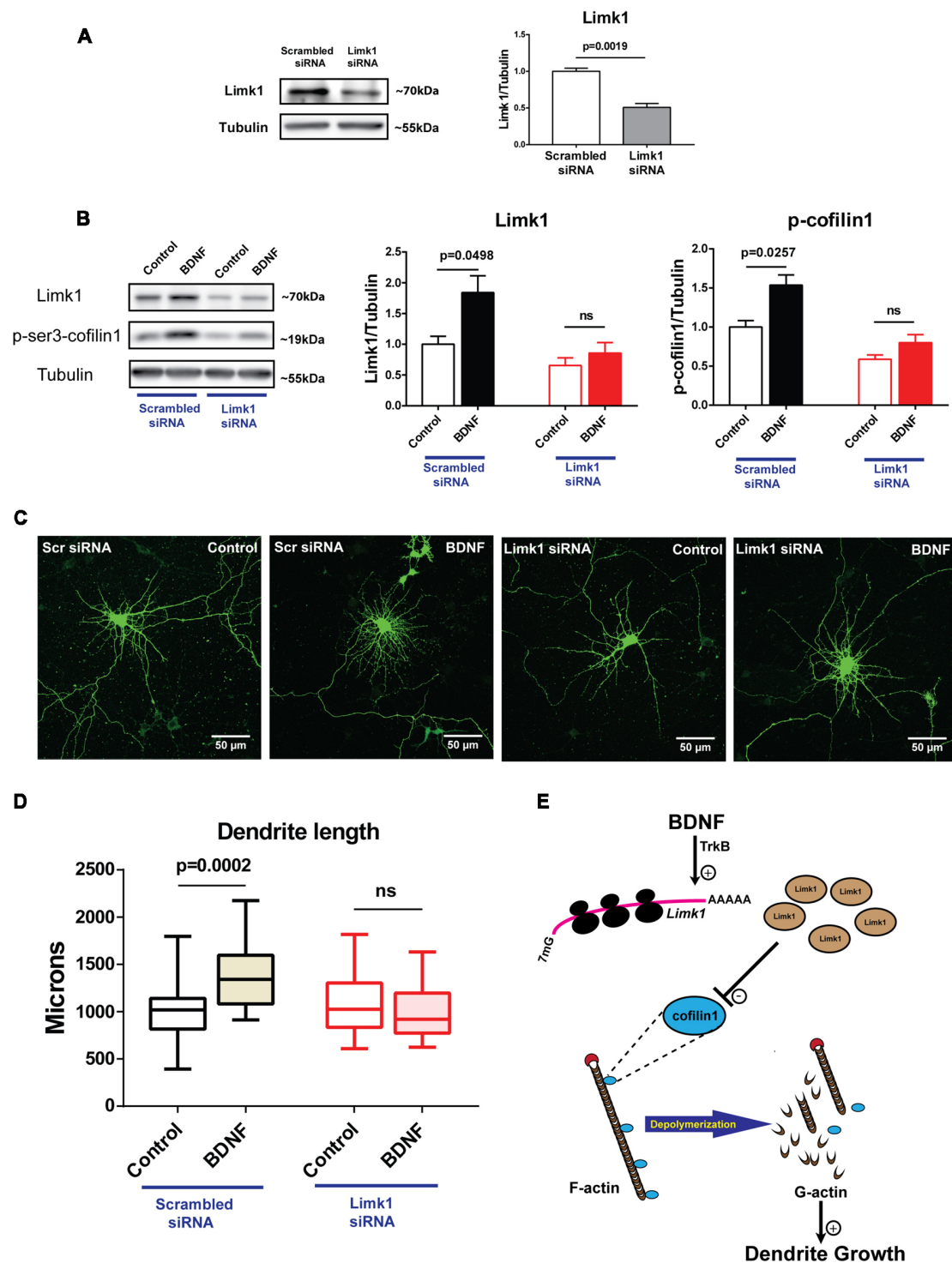


FIGURE 7 | Acute knockdown of Limk1 affects BDNF mediated dendrite growth. **(A)** Representative immunoblots (Left) and quantification (Right) of Limk1 from Neuro 2a cells transfected with Limk1 or scrambled siRNA ($n = 3$, Unpaired Student's t -test, mean \pm SEM). **(B)** Representative immunoblots (Left) and quantification of Limk1 (Center) and p-cofilin1 (Right) from DIV5 neurons transfected with Limk1 or scrambled siRNA and treated with or without 50 ng/ml BDNF for 48 h ($n = 3$, Unpaired Student's t -test, mean \pm SEM). **(C)** Representative images of DIV5 neurons co-transfected with Limk1 or scrambled siRNA and EGFP and treated with or without 50 ng/ml BDNF for 48 h. **(D)** Quantification of total dendritic length from control and BDNF treated cortical neurons from the experiment described in **(C)**; $n = 23$ –26 neurons across two independent experiments, Box and whisker plots show median, first and third quartiles with error bars representing minimum and maximum data points, Mann Whitney test). **(E)** Model showing BDNF activated Limk1 synthesis leading to phosphorylation of cofilin1 and reduced dendritic F-actin level, thus playing important role in dendrite growth, ns, not significant.

cofilin1 through Limk1 synthesis, thus causing a reduction in the F-actin pool.

To confirm the role of new Limk1 synthesis on BDNF mediated dendrite growth, we performed an acute Limk1 knockdown just prior to BDNF treatment. We used a specific siRNA against *Limk1* mRNA for this experiment. Limk1 knockdown was validated at the protein level compared to scrambled siRNA transfection by immunoblots (**Figure 7A**). To test the role for Limk1 synthesis on dendrite growth, we transfected DIV 5 cortical neurons with Limk1 or scrambled siRNA followed immediately by BDNF treatment for 48 h. Such a paradigm was used so that basal levels of Limk1 is only minimally perturbed, but any new Limk1 synthesis is inhibited. Using immunoblots, we verified that Limk1 siRNA effectively prevented BDNF mediated increased Limk1 levels as well as phosphorylation of cofilin1 (**Figure 7B**). This confirms that new Limk1 synthesis on BDNF stimulation is required for phosphorylation of cofilin1. For quantifying dendrite length, neurons were visualized by co-transfection of EGFP. We observed that Limk1 siRNA transfection prevented BDNF induced increase in total dendrite length, while scrambled siRNA did not have any effect (**Figures 7C,D**). This shows that BDNF mediated increase in Limk1 levels plays a critical role in BDNF mediated-dendrite growth.

DISCUSSION

Defects in activity-mediated protein synthesis are thought to be a primary cause of pathophysiology for several neurodevelopmental disorders (Kelleher and Bear, 2008; Liu-Yesucevitz et al., 2011). The role of activity mediated translation is well studied in the context of spine development and synaptic signaling (Fernandez-Moya et al., 2014). It is also established that synaptic protein synthesis is critical for long term plasticity (Kang and Schuman, 1996; Costa-Mattioli et al., 2009). But its role in dendrite morphogenesis remains largely overlooked in the field of neurodevelopment, studies are largely confined to axonal growth cones. In the current study, we focused on the role activity mediated translation regulation at this critical juncture of neuronal development which could be important in many neurodevelopmental disorders.

We demonstrate that activity-mediated translation plays an important role at the stage of robust dendritic growth and arborization. Multiple reports show that actin modulator proteins are important targets for this mode of translational regulation (Leung et al., 2006; Spillane et al., 2012; Choi et al., 2018). Our study shows this mode of regulation fine tune the local proteome of growing dendrites, thereby significantly affecting dendrite growth. We show that BDNF, a key neurotropic factor, affects dendrite growth, partially through driving translation of a Ser/Thr kinase Limk1. Exogenous BDNF stimulation in DIV5 neurons caused increased translation of Limk1 which is a key actin modulator protein. We validated this BDNF mediated translation of Limk1 mRNA by polysome profiling as well as increased Limk1 protein by immunoblot. As depicted in the model (**Figure 7E**), up-regulation of translation on BDNF treatment results in an increase in Limk1 in the dendrites and

increased phosphorylation of its target, cofilin1. Phosphorylation of cofilin1 reduces its actin binding activity, leading to a decrease in the F-actin pool in dendrites. Interestingly we observed these specific molecular changes in dendrites and cell bodies, but not in the axons, suggesting there could be different molecular cascades activated in the axons and dendrites in response to the same trophic factor. This observation also suggests that the basal function of cofilin1 is likely to be different in axons and dendrites. Dendritic cofilin1 could be primarily mediating filament stabilization or actin nucleation. BDNF induced cofilin1 phosphorylation and subsequent dissolution of actin filaments could be important for microtubule invasion to the filopodia leading to branch stabilization and eventual increase in the dendrite length (Poulain and Sobel, 2010). These molecular change that we observed persists for durations up to 48 h and is important for mediating the physiological effect of enhanced dendritic growth.

In this study, we focussed primarily of exogenous BDNF on the pyramidal neurons in the rat cerebral cortical cultures. It remains to be studied whether other neuronal subtypes also show a similar response. We have also not explored the role of endogenous BDNF in the cultures. Further studies are required to address these questions as well as to understand the mechanism of this translational regulation. Exploring the pathways involved in such regulation would provide key insights into understanding the pathophysiology of several neurodevelopmental disorders in which dysregulation of translation is reported. Previous studies on such disorders have focussed mainly on synaptic dysfunction. Considering that both dendrite and spine development share molecular pathways pertaining to actin rearrangement, dendritic growth defects are largely overlooked in such disorders. Studying the dendritic arbor at later developmental stages might not reveal significant deficits, probably due to compensatory mechanisms. Our study indicates strongly the need to study the early developmental stages of dendritic arborization.

DATA AVAILABILITY

The datasets generated for this study are available on request to the corresponding author.

AUTHOR CONTRIBUTIONS

SR and RM designed the experiments, analyzed the results and wrote the manuscript. SR carried out the experiments. VN optimized the primary neuronal culture and contributed to the image analysis.

FUNDING

The work has been funded by the Indo-Danish NeuroStem grant (BT/IN/Denmark/07/RSM/2015-2016) and RNAi grant from Department of Biotechnology, India (BT/PR8723/AGR/36/776/2013) to RM. SR was funded by the CSIR-SPM fellowship [Award No: SPM-07/860(0202)/2014]. Animal work in the NCBS/inStem Animal Care and Resource Center was partially supported by the National Mouse Research

Resource (NaMoR) grant# BT/PR5981/MED/31/181/2012;2013-2016 & 102/IFD/SAN/5003/2017-2018 from the Indian Department of Biotechnology.

ACKNOWLEDGMENTS

We would like to thank Central Imaging Facility (CIFF) and animal house facility at NCBS-inStem for the technical support. We are grateful to Prof. Sumantra Chattarji, CBDR, inStem

for providing resources for image analysis. We thank Sindhu Lakshmanan, Ananya Dash, and Shobana Murali for help with image analysis.

SUPPLEMENTARY MATERIAL

The Supplementary Material for this article can be found online at: <https://www.frontiersin.org/articles/10.3389/fnmol.2019.00064/full#supplementary-material>

REFERENCES

- Andrianantoandro, E., and Pollard, T. D. (2006). Mechanism of actin filament turnover by severing and nucleation at different concentrations of ADF/cofilin. *Mol. Cell* 24, 13–23. doi: 10.1016/j.molcel.2006.08.006
- Arber, S., Barbayannis, F. A., Hanser, H., Schneider, C., Stanyon, C. A., Bernard, O., et al. (1998). Regulation of actin dynamics through phosphorylation of cofilin by LIM-kinase. *Nature* 393, 805–809. doi: 10.1038/31729
- Choi, J., Wang, W., Park, D., Kim, S., Kim, K., and Min, K. (2018). IRES-mediated translation of cofilin regulates axonal growth cone extension and turning. *EMBO J.* 37:e95266. doi: 10.15252/embj.201695266
- Costa-Mattioli, M., Sossin, W. S., Klann, E., and Sonenberg, N. (2009). Translational control of long-lasting synaptic plasticity and memory. *Neuron* 61, 10–26. doi: 10.1016/j.neuron.2008.10.055
- Da Silva, J. S., and Dotti, C. G. (2002). Breaking the neuronal sphere: regulation of the actin cytoskeleton in neuritogenesis. *Nat. Rev. Neurosci.* 3, 694–704. doi: 10.1038/nrn918
- Dotti, C. G., Sullivan, C. A., and Banker, G. A. (1988). The establishment of polarity by hippocampal neurons in culture. *J. Neurosci.* 8, 1454–1468. doi: 10.1523/JNEUROSCI.08-04-01454.1988
- Endo, M., Ohashi, K., and Mizuno, K. (2007). LIM kinase and slingshot are critical for neurite extension. *J. Biol. Chem.* 282, 13692–13702. doi: 10.1074/jbc.m610873200
- Endo, M., Ohashi, K., Sasaki, Y., Goshima, Y., Niwa, R., Uemura, T., et al. (2003). Control of growth cone motility and morphology by LIM kinase and Slingshot via phosphorylation and dephosphorylation of cofilin. *J. Neurosci.* 23, 2527–2537. doi: 10.1523/JNEUROSCI.23-07-02527.2003
- Fernandez-Moya, S. M., Bauer, K. E., and Kiebler, M. A. (2014). Meet the players: local translation at the synapse. *Front. Mol. Neurosci.* 7:84. doi: 10.3389/fnmol.2014.00084
- Ferreira, T. A., Blackman, A. V., Oyrer, J., Jayabal, S., Chung, A. J., Watt, A. J., et al. (2014). Neuronal morphometry directly from bitmap images. *Nat. Methods* 11, 982–984. doi: 10.1038/nmeth.3125
- Ferreira, T. A., Iacono, L. L., and Gross, C. T. (2010). Serotonin receptor 1A modulates actin dynamics and restricts dendritic growth in hippocampal neurons. *Eur. J. Neurosci.* 32, 18–26. doi: 10.1111/j.1460-9568.2010.07283.x
- Gu, J., and Zheng, J. Q. (2009). Microtubules in dendritic spine development and plasticity. *Open Neurosci. J.* 3, 128–133. doi: 10.2174/1874082000903010128
- Horch, H. W., and Katz, L. C. (2002). BDNF release from single cells elicits local dendritic growth in nearby neurons. *Nat. Neurosci.* 5, 1177–1184. doi: 10.1038/nn927
- Hu, X., Viesselmann, C., Nam, S., Merriam, E., and Dent, E. W. (2008). Activity-dependent dynamic microtubule invasion of dendritic spines. *J. Neurosci.* 28, 13094–13105. doi: 10.1523/JNEUROSCI.3074-08.2008
- Kaech, S., and Banker, G. (2006). Culturing hippocampal neurons. *Nat. Protoc.* 1, 2406–2415. doi: 10.1038/nprot.2006.356
- Kang, H., and Schuman, E. M. (1996). A requirement for local protein synthesis in neurotrophin-induced hippocampal synaptic plasticity. *Science* 273, 1402–1406. doi: 10.1126/science.273.5280.1402
- Kelleher, R. J. III., and Bear, M. F. (2008). The autistic neuron: troubled translation? *Cell* 135, 401–406. doi: 10.1016/j.cell.2008.10.017
- Kuipers, S. D., Trentani, A., Tiron, A., Mao, X., Kuhl, D., and Bramham, C. R. (2016). BDNF-induced LTP is associated with rapid Arc/Arg3.1-dependent enhancement in adult hippocampal neurogenesis. *Sci. Rep.* 6:1222. doi: 10.1038/srep21222
- Labelle, C., and Leclerc, N. (2000). Exogenous BDNF, NT-3 and NT-4 differentially regulate neurite outgrowth in cultured hippocampal neurons. *Dev. Brain Res.* 123, 1–11. doi: 10.1016/s0165-3806(00)00069-9
- Lee-Hoeflich, S. T., Causing, C. G., Podkowa, M., Zhao, X., Wrana, J. L., and Attisano, L. (2004). Activation of LIMK1 by binding to the BMP receptor, BMPRII, regulates BMP-dependent dendritogenesis. *EMBO J.* 23, 4792–4801. doi: 10.1038/sj.emboj.7600418
- Leung, K. M., van Horck, F. P. G., Lin, A. C., Allison, R., Standart, N., and Holt, C. E. (2006). Asymmetrical β -actin mRNA translation in growth cones mediates attractive turning to netrin-1. *Nat. Neurosci.* 9, 1247–1256. doi: 10.1038/nn1775
- Liu-Yesucevitz, L., Bassell, G. J., Gitler, A. D., Hart, A. C., Klann, E., Richter, J. D., et al. (2011). Local RNA translation at the synapse and in disease. *J. Neurosci.* 31, 16086–16093. doi: 10.1523/JNEUROSCI.4105-11.2011
- Marsick, B. M., Flynn, K. C., Santiago-Medina, M., Bamburg, J. R., and Letourneau, P. C. (2010). Activation of ADF/cofilin mediates attractive growth cone turning toward nerve growth factor and netrin-1. *Dev. Neurobiol.* 70, 565–588. doi: 10.1002/dneu.20800
- McAllister, A. K., Katz, L. C., and Lo, D. C. (1996). Neurotrophin regulation of cortical dendritic growth requires activity. *Neuron* 17, 1057–1064. doi: 10.1016/s0896-6273(00)80239-1
- McAllister, A. K., Lo, D. C., and Katz, L. C. (1995). Neurotrophins regulate dendritic growth in developing visual cortex. *Neuron* 15, 791–803. doi: 10.1016/0896-6273(95)90171-x
- Meberg, P. J., and Bamburg, J. R. (2000). Increase in neurite outgrowth mediated by overexpression of actin depolymerizing factor. *J. Neurosci.* 20, 2459–2469. doi: 10.1523/JNEUROSCI.20-07-02459.2000
- Meijering, E., Jacob, M., Sarria, J. C. F., Steiner, P., Hirling, H., and Unser, M. (2011). Design and validation of a tool for neurite tracing and analysis in fluorescence microscopy images. *Cytometry A* 58A, 167–176. doi: 10.1002/cyto.a.20022
- Messaoudi, E., Kanhema, T., Soule, J., Tiron, A., Dagyte, G., da Silva, B., et al. (2007). Sustained Arc/Arg3.1 synthesis controls long-term potentiation consolidation through regulation of local actin polymerization in the dentate gyrus *in vivo*. *J. Neurosci.* 27, 10445–10455. doi: 10.1523/JNEUROSCI.2883-07.2007
- Muddashetty, R. S., Kelić, S., Gross, C., Xu, M., and Bassell, G. J. (2007). Dysregulated metabotropic glutamate receptor-dependent translation of AMPA receptor and postsynaptic density-95 mRNAs at synapses in a mouse model of fragile X syndrome. *J. Neurosci.* 27, 5338–5348. doi: 10.1523/JNEUROSCI.0937-07.2007
- Muddashetty, R. S., Nalavadi, V. C., Gross, C., Yao, X., Xing, L., Laur, O., et al. (2011). Reversible inhibition of PSD-95 mRNA translation by miR-125a, FMRP phosphorylation and mGluR signaling. *Mol. Cell* 42, 673–688. doi: 10.1016/j.molcel.2011.05.006
- Ohtani, A., Kozono, N., Senzaki, K., and Shiga, T. (2014). Serotonin 2A receptor regulates microtubule assembly and induces dynamics of dendritic growth cones in rat cortical neurons *in vitro*. *Neurosci. Res.* 81–82, 11–20. doi: 10.1016/j.neures.2014.03.006
- Poulain, F. E., and Sobel, A. (2010). The microtubule network and neuronal morphogenesis: dynamic and coordinated orchestration through multiple players. *Mol. Cell. Neurosci.* 43, 15–32. doi: 10.1016/j.mcn.2009.07.012

- Schratt, G. M., Nigh, E. A., Chen, W. G., Hu, L., and Greenberg, M. E. (2004). BDNF regulates the translation of a select group of mRNAs by a mammalian target of rapamycin-phosphatidylinositol 3-kinase-dependent pathway during neuronal development. *J. Neurosci.* 24, 7366–7377. doi: 10.1523/JNEUROSCI.1739-04.2004
- Schratt, G. M., Tuebing, F., Nigh, E. A., Kane, C. G., Sabatini, M. E., Kiebler, M., et al. (2006). A brain-specific microRNA regulates dendritic spine development. *Nature* 439, 283–289. doi: 10.1038/nature04367
- Scott, E. K., and Luo, L. (2001). How do dendrites take their shape? *Nat. Neurosci.* 4, 359–365. doi: 10.1038/86006
- Spillane, M., Ketschek, A., Donnelly, C. J., Pacheco, A., Twiss, J. L., and Gallo, G. (2012). Nerve growth factor-induced formation of axonal filopodia and collateral branches involves the intra-axonal synthesis of regulators of the actin-nucleating Arp2/3 complex. *J. Neurosci.* 32, 17671–17689. doi: 10.1523/JNEUROSCI.1079-12.2012
- Van Troys, M., Huyck, L., Leyman, S., Dhaese, S., Vandekerckhove, J., and Ampe, C. (2008). Ins and outs of ADF/cofilin activity and regulation. *Eur. J. Cell Biol.* 87, 649–667. doi: 10.1016/j.ejcb.2008.04.001
- Wearne, S. L., Rodriguez, A., Ehlenberger, D. B., Rocher, A. B., Henderson, S. C., and Hof, P. R. (2005). New techniques for imaging, digitization and analysis of three-dimensional neural morphology on multiple scales. *Neuroscience* 136, 661–680. doi: 10.1016/j.neuroscience.2005.05.053
- Whitford, K. L., Dijkhuizen, P., Polleux, F., and Ghosh, A. (2002). Molecular control of cortical dendrite development. *Annu. Rev. Neurosci.* 25, 127–149. doi: 10.1146/annurev.neuro.25.112701.142932
- Wu, G. Y., Zou, D. J., Rajan, I., and Cline, H. (1999). Dendritic dynamics *in vivo* change during neuronal maturation. *J. Neurosci.* 19, 4472–4483. doi: 10.1523/JNEUROSCI.19-11-04472.1999
- Yang, N., Higuchi, O., Ohashi, K., Nagata, K., Wada, A., Kangawa, K., et al. (1998). Cofilin phosphorylation by LIM-kinase 1 and its role in Rac-mediated actin reorganization. *Nature* 393, 809–812. doi: 10.1038/31735
- Zhou, F. Q., Waterman-Storer, C. M., and Cohan, C. S. (2002). Focal loss of actin bundles causes microtubule redistribution and growth cone turning. *J. Cell Biol.* 157, 839–849. doi: 10.1083/jcb.200112014

Conflict of Interest Statement: The authors declare that the research was conducted in the absence of any commercial or financial relationships that could be construed as a potential conflict of interest.

Copyright © 2019 Ravindran, Nalavadi and Muddashetty. This is an open-access article distributed under the terms of the Creative Commons Attribution License (CC BY). The use, distribution or reproduction in other forums is permitted, provided the original author(s) and the copyright owner(s) are credited and that the original publication in this journal is cited, in accordance with accepted academic practice. No use, distribution or reproduction is permitted which does not comply with these terms.



The Autism and Angelman Syndrome Protein Ube3A/E6AP: The Gene, E3 Ligase Ubiquitination Targets and Neurobiological Functions

Natasha Khatri^{1,2} and Heng-Ye Man^{1,2*}

¹Department of Biology, Boston University, Boston, MA, United States, ²Department of Pharmacology and Experimental Therapeutics, Boston University School of Medicine, Boston, MA, United States

OPEN ACCESS

Edited by:

Markus Wöhr,
University of Marburg, Germany

Reviewed by:

Gerhard Schratt,
ETH Zürich, Switzerland
Jill L. Silverman,
MIND Institute, UC Davis,
United States

*Correspondence:

Heng-Ye Man
hman@bu.edu

Received: 16 January 2019

Accepted: 12 April 2019

Published: 30 April 2019

Citation:

Khatri N and Man HY (2019) The Autism and Angelman Syndrome Protein Ube3A/E6AP: The Gene, E3 Ligase Ubiquitination Targets and Neurobiological Functions. *Front. Mol. Neurosci.* 12:109. doi: 10.3389/fnmol.2019.00109

UBE3A is a gene implicated in neurodevelopmental disorders. The protein product of UBE3A is the E3 ligase E6-associated protein (E6AP), and its expression in the brain is uniquely regulated via genetic imprinting. Loss of E6AP expression leads to the development of Angelman syndrome (AS), clinically characterized by lack of speech, abnormal motor development, and the presence of seizures. Conversely, copy number variations (CNVs) that result in the overexpression of E6AP are strongly associated with the development of autism spectrum disorders (ASDs), defined by decreased communication, impaired social interest, and increased repetitive behavior. In this review article, we focus on the neurobiological function of Ube3A/E6AP. As an E3 ligase, many functional target proteins of E6AP have been discovered, including p53, Arc, Ephexin5, and SK2. On a neuronal level, E6AP is widely expressed within the cell, including dendritic arbors, spines, and the nucleus. E6AP regulates neuronal morphological maturation and plays an important role in synaptic plasticity and cortical development. These molecular findings provide insight into our understanding of the molecular events underlying AS and ASDs.

Keywords: neurodevelopment, UBE3A (E6AP), autism (ASD), Angelman syndrome (AS), ubiquitination, dendritic pruning, synaptic plasticity

INTRODUCTION

The human brain consists of 86 billion neurons, which are connected via trillions of synapses (Azevedo et al., 2009). The proper development of neurons and their connections, therefore, is critical for normal brain function. The establishment of brain structure and cortical layers begins during prenatal neuronal development, when neurons produced in the ventricular zone migrate radially out into the developing neocortex to form six distinct layers (Huang, 2009). After initial migration, neurons undergo extensive morphological change to form specific synaptic connections with target neurons via axon formation and dendritic arbor elaboration. Synaptic formation and refinement occur during prenatal and early postnatal periods in an activity-dependent manner, and brain circuitry can continue to be modified into adolescence and early adulthood. Disruption in any of these developmental processes can cause abnormalities in overall brain connectivity and lead to neurodevelopmental disorders.

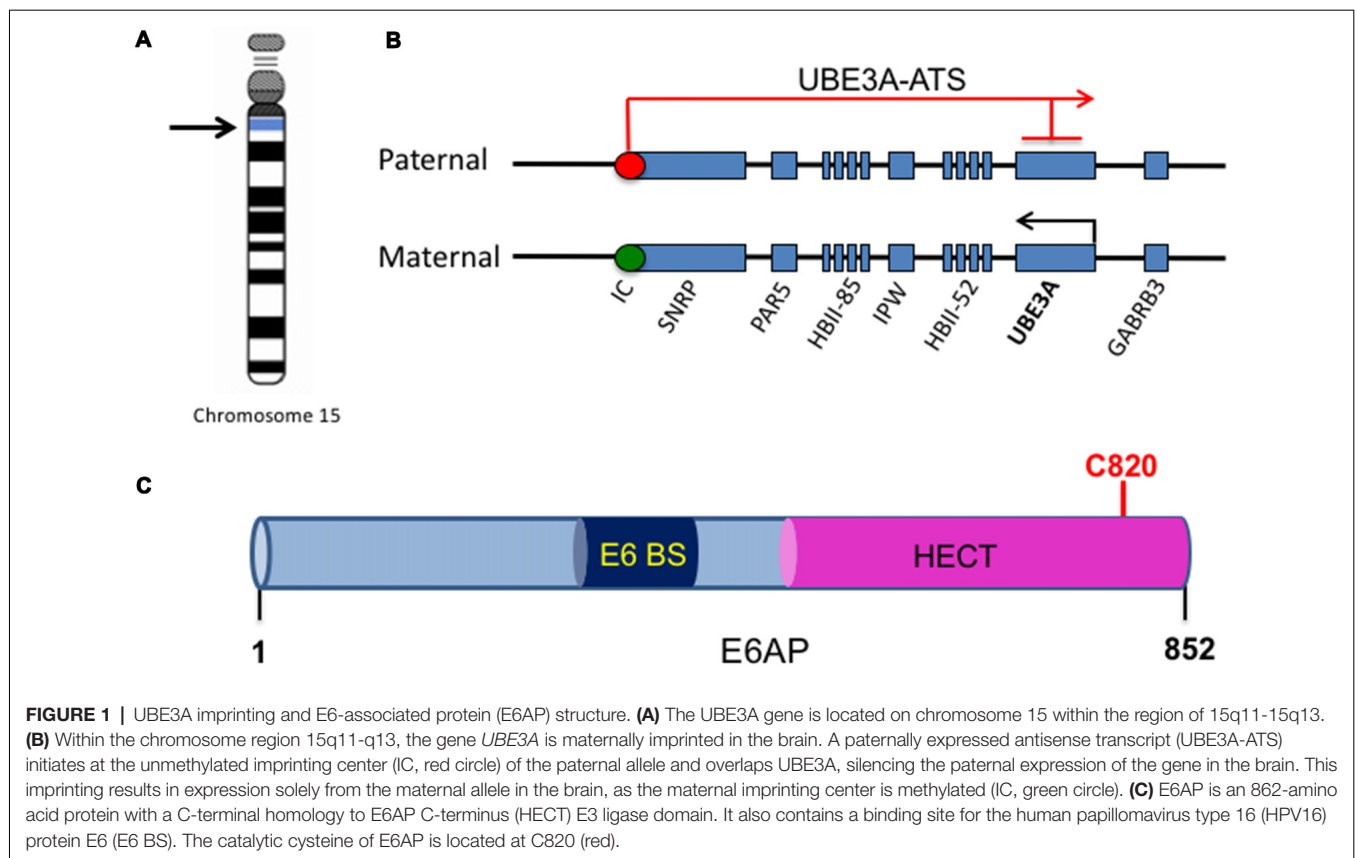
Autism spectrum disorders (ASDs) are a heterogeneous class of neurodevelopmental disorders characterized by three main behavioral traits: impaired social interactions, lack of communication, and increased repetitive behaviors (Levy et al., 2009). However, these core clinical symptoms are often accompanied by other symptoms and disorders. Developmental comorbidities may include cognitive and intellectual disability, language deficits, attention problems, hyperactivity, and motor delays (Newschaffer et al., 2007; Levy et al., 2009). Psychiatric and related behavioral comorbidities include anxiety, depression, obsessive-compulsive disorder, defiant and aggressive behavior, and self-injurious behavior (Hartley et al., 2008; Simonoff et al., 2008). Other common comorbid features are seizures and epilepsy, gastrointestinal difficulties, and sleep disruption (Limoges et al., 2005; Rapin and Tuchman, 2008; Nikolov et al., 2009).

The genetic basis of ASDs is highly heterogeneous, as hundreds of different genes have been implicated in their cause. Interestingly, most of the genes show expression profiles at the stage of early development, and their functionalities share strong enrichment in cell adhesion and mobility, cytoskeleton regulation, synapse formation and kinase signaling (Pinto et al., 2010; Gilbert and Man, 2017). These ASD genes include FMR1, LIS1, MECP2, PTEN, SHANK1/2/3, TAOK2, TSC1/2, Neuroligins, Neurexins, KIAA2022/KIDLIA (Gilbert and Man, 2016) and UBE3A/E6-associated protein (E6AP). Pathological studies of ASD

patients have revealed neurodevelopmental defects such as abnormal brain growth, impaired neuron morphology and brain cytoarchitecture, along with impaired synapse formation (Chen et al., 2015). The vast genetic landscape of ASDs and the resulting variability in pathology and causative pathways have made studying and treating ASDs a great challenge.

GENOMIC IMPRINTING AND REGULATION OF UBE3A/E6AP

One of the major genes implicated in ASDs is the Ubiquitin Protein Ligase E3A, *UBE3A*, the gene that encodes E6AP, a protein that is expressed in an imprinted manner in the brain. From here onwards, *UBE3A* will refer to the gene, and E6AP will refer to its protein product. Genomic imprinting marks the parental origin of chromosomal subregions and results in allele-specific differences in DNA methylation, transcription, and replication. Within the chromosome region 15q11-q13, the gene *UBE3A* is imprinted specifically in the brain, resulting in maternal expression of E6AP in human fetal brain and adult cortex, while the paternal copy is silenced (Figures 1A,B; Rougeulle et al., 1997; Vu and Hoffman, 1997). Similar imprinting in *UBE3A* also exists in rats and mice (Albrecht et al., 1997). Although the mechanism of tissue-specific *UBE3A* imprinting is not fully understood, its expression in general has been found to be



mediated by the presence of an antisense transcript, *UBE3A-ATS*, which is paternally expressed (Rougeulle et al., 1998). *UBE3A-ATS* is a ~460-kb noncoding RNA that initiates in the 15q11-q13 region of the paternal allele and overlaps *UBE3A*, silencing the paternal expression of the gene in the brain (Figure 1B; Runte et al., 2001). Similarly, the murine *Ube3A-ATS* is also observed to be paternal-specific and restricted to the brain (Chamberlain and Brannan, 2001). Interestingly, *UBE3A* imprinting occurs only in neurons in the brain; both alleles are active in glial cells and other peripheral tissues (Yamasaki et al., 2003).

The *UBE3A* gene encodes three potential E6AP protein isoforms generated by differential splicing (Yamamoto et al., 1997). The coding region of E6AP is 2,700 bp long and consists of 10 exons, encoding for 865 amino acids (Huibregtse et al., 1993a). Isoforms 2 and 3 have an additional 20 and 23 amino acids, respectively, at their amino-terminus. Although isoforms 2/3 have similar E3 ligase catalytic function, it is unknown whether the variable amino terminus could account for differential ubiquitination substrate specificity (Yamamoto et al., 1997). Interestingly, a recent study reported that Ube3A isoform 1 RNA is encoded by a truncated sequence of the gene and does not include the E3 catalytic domain sequence (Valluy et al., 2015). Interestingly, while it is not detectably translated into protein, its expression is involved in the regulation of dendritic complexity and spine maturation. It was suggested that Ube3A1 RNA might be a target for microRNA miR-134, providing a novel protein expression-independent function of Ube3A (Valluy et al., 2015).

Neuronal activity can alter expression of E6AP (Greer et al., 2010). Specifically, expression of E6AP mRNA in cultured neurons is increased by either membrane depolarization or glutamate receptor activation, while blocking activity with NMDA receptor, sodium channel, or AMPA receptor (AMPA) inhibitors decreased E6AP mRNA expression. In addition, E6AP expression is induced in response to environmental stimuli that trigger experience-dependent synaptic development, as shown in mice that received an enriched environment compared to those in a standard cage. This increase was found to be regulated by the binding of the activity-regulated transcription factor myocyte enhancer factor 2 (MEF2) to *UBE3A* promoters 1 and 3 (Greer et al., 2010). Interestingly, MEF2 has previously been shown to control synapse development and regulates a number of genes that have been implicated in ASDs (Flavell et al., 2006; Morrow et al., 2008). Further involvement of synaptic activity on the levels of E6AP was reported in another study (Filonova et al., 2014). Levels of nuclear and cytoplasmic E6AP were increased after neuronal depolarization in primary neuron culture, and upregulation of E6AP was observed in mice with an E6AP-YFP reporter following fear conditioning (Filonova et al., 2014). Additionally, a lack of E6AP led to deficits in the increased activity-dependent phosphorylation of the kinase ERK1/2, a process that is important in synaptic plasticity and memory formation (Thomas and Huganir, 2004; Filonova et al., 2014). These studies suggest that E6AP levels are regulated by synaptic activity and that loss of experience and activity-dependent

induction of E6AP expression during postnatal development may contribute to ASDs.

ROLE OF *UBE3A*/E6AP GENE DOSAGE AND PROTEIN LEVELS IN ANGELMAN SYNDROME AND ASD

Proper gene dosage of *UBE3A* is crucial to normal brain development, as evidenced by the neurodevelopmental disorders associated with deletions, mutations, and copy number variations (CNVs) of *UBE3A*. Angelman syndrome (AS) was characterized behaviorally by Harry Angelman to consist of “puppet”-like behavior, a distinctive feature of AS (Angelman, 1965). AS manifests itself as a severe developmental delay with a virtual absence of speech and abnormal gait (Williams et al., 1995). In addition, patients exhibit coordination difficulties, a contagiously happy demeanor, prominent laughing, tongue protrusion, and a seizure disorder (Williams et al., 1995). Some characteristics of AS may be seen on the spectrum of autistic features, such as impaired communication, absence of speech, attentional deficits, hyperactivity, feeding and sleeping problems, and delay of motor development (Williams et al., 2001, 2006).

AS is primarily caused by deletions and mutations in *UBE3A*, and its specific genetic causes are differentiated by five molecular classes (Lossie et al., 2001; Clayton-Smith and Laan, 2003). Class I accounts for 65%–70% of AS cases and is caused by a *de novo* deletion of the maternal chromosome 15q11-q13, causing a loss of all E6AP expression in the brain (Clayton-Smith and Laan, 2003). Class II patients have uniparental disomy (UPD) for chromosome 15 and therefore fail to inherit a maternal copy of *UBE3A* (Clayton-Smith and Laan, 2003). Class III patients are those without deletions or UPD, but with abnormal methylation of the chromosome 15 maternal allele, resulting in a defect in maternal expression (Reis et al., 1994). Class IV patients are those who have mutations within *UBE3A* (Kishino et al., 1997; Matsuura et al., 1997). Point mutations in AS patients have been found throughout the entire coding region with clusters in exon 9, which contains the E6AP homology to E6AP C-terminus (HECT) domain. Many mutations, including frameshift, nonsense, and splice mutations, have been found to be located within the region encoding the catalytic cleft between the two lobes of the HECT domain (Cooper et al., 2004). Finally, Class V patients are designated as those with a clinical phenotype of AS with no chromosome 15 abnormality (Lossie et al., 2001).

A potential treatment for the imprinting defects in AS may be to unsilence the dormant paternal allele in neurons and restore E6AP expression despite the loss of maternal expression (Mabb et al., 2011). Indeed, an unbiased, high throughput screen in neurons from AS mice lead to the discovery of 12 topoisomerase I inhibitors and four topoisomerase II inhibitors that unsilence the paternal *UBE3A* allele (Huang et al., 2011). One of the drugs found, topotecan, upregulated levels of active E6AP by downregulating the paternal *UBE3A-ATS*. Expression of the paternal *UBE3A* allele was unsilenced by topotecan in the hippocampus, neocortex, striatum, cerebellum, and spinal cord, suggesting that silencing the *UBE3A-ATS* and reactivating

paternal expression of E6AP may serve as a potential therapeutic strategy for patients with AS (Huang et al., 2011). Similarly, it has been shown that expression of a truncated Ube3A-ATS unsilenced paternal E6AP and was able to ameliorate behavioral deficits in AS mice (Meng et al., 2013). More importantly, reactivation of Ube3A expression in a Cre-dependent manner during early development was shown to rescue behavioral phenotypes, while reinstatement during adulthood improved the electrophysiological deficits in layer 5 pyramidal neurons (Silva-Santos et al., 2015; Rotaru et al., 2018). Consistent with the beneficial effect of Ube3A reinstatement, a study in AS mice showed that restoring Ube3A expression in GABAergic neurons suppressed the occurrence of epileptic activity (Gu et al., 2019).

ASDs, on the other hand, are caused by CNVs in the *UBE3A* gene. Individuals with an additional maternal copy of *UBE3A* (dup15), due to duplication of the 15q11.2–11.3 chromosomal region, and those with two extra copies from an isodicentric chromosome 15 (idic15) both display autism penetrance, with the two extra copies resulting in a more severe phenotype (Borgatti et al., 2001; Hogart et al., 2010). Consistent with the imprinted expression of *UBE3A*, ASDs arise from maternally, but not paternally, derived 15q11-q13 duplications (Cook et al., 1997). These genetic studies suggest a role for *UBE3A* dosage in neuronal development.

ANIMAL MODELS OF ANGELMAN SYNDROME AND *UBE3A*-DEPENDENT ASD

The *UBE3A* maternal deficient mouse model of AS (*Ube3A^{m-/p+}*), in which a deletion mutation in exon 2 of *UBE3A* inhibits maternal expression of the gene, successfully captures many of the classical features associated with AS and is the most widely used AS mouse model (Jiang et al., 1998). *Ube3A^{m-/p+}* mice exhibit reduced brain weight, ataxia, motor impairments, abnormal EEG, and audiogenic seizures. These mice also display context-dependent learning and memory impairments, and deficits in hippocampal long-term potentiation (LTP; Jiang et al., 1998). Importantly, the degree of behavioral EEG activity phenotypes varies based on the genetic background of *Ube3A^{m-/p+}* mice (Born et al., 2017). Mice on a C57BL/6J background displayed robust behavioral impairments, such as decreased activity and marble burying, increased anxiety, and altered novel object recognition, along with spontaneous EEG polypikes and increased spectral power. Mice on a 129 background performed poorly on a wire hand test and contextual fear conditions and had a lower seizure threshold. Mice on a F1 hybrid background showed milder behavioral impairments, and fewer EEG polypikes and spectral power alterations, raising the awareness that small genetic variances in mice could lead to discrepancies in observed phenotypes (Born et al., 2017).

Increased gene dosage of *UBE3A* has been modeled in mice to mimic the *UBE3A* CNVs in ASDs. The Ube3A 2X transgenic (Tg) mouse model exhibits a tripling of the normal Ube3A gene dosage in neurons, replicating idic15 in patients with

autism (Smith et al., 2011). Ube3A 2XTg mice show typical autistic behavioral deficits, including impaired social behavior, as measured by social preference tests, decreased communication, measured by vocalizations, and increased repetitive behavior, shown by excessive grooming. In addition, recordings in hippocampal slices showed reduced strength in excitatory synaptic transmission, both in frequency and amplitude, suggesting that E6AP may regulate glutamate transmission at both pre- and post-synaptic sites (Smith et al., 2011). More recently, it was found that E6AP regulates levels of the synaptic protein Cbln1 in these mice and that recurrent seizures led to increased *Cbln1* mRNA in the ventral tegmental area (VTA; Krishnan et al., 2017). Importantly, restoring *Cbln1* levels in neurons of the VTA reversed the impaired sociability behavioral phenotype of Ube3A 2X mice, suggesting that Cbln1 levels play a key role in E6AP-dependent ASD behavior (Krishnan et al., 2017). Interestingly, the activity of the VTA, specifically the VTA-to-nucleus accumbens (NAc) dopaminergic projections, is sufficient and necessary to control key features of social behavior, as demonstrated by optogenetic modulation of the pathway (Gunaydin et al., 2014).

BRAIN AND CELLULAR DISTRIBUTION OF E6AP

Knowledge of the imprinting and expression pattern of E6AP in the brain has come from studying various brain regions and tissues in the maternally-deficient *Ube3A^{m-/p+}* mice. It has been shown that maternal E6AP is expressed in the hippocampus, hypothalamus, olfactory bulb, cerebral cortex, striatum, midbrain, and cerebellum (Gustin et al., 2010). Expression is seen primarily in neurons, both excitatory and inhibitory neurons (Gustin et al., 2010). Within neurons, E6AP is enriched in the nucleus and dendrites in mouse brain tissue (Dindot et al., 2008). In cultured hippocampal neurons, E6AP also localizes to the nucleus and to presynaptic and postsynaptic compartments (Dindot et al., 2008).

The expression of imprinted E6AP in the brain also seems to be temporally regulated. To study imprinting and the resulting expression, mouse models lacking either the paternal or maternal copy of *UBE3A* have been utilized (*UBE3A^{m+/-p-}* or *UBE3A^{m-/p+}*). In the visual cortex, low levels of expression of paternal E6AP remain during early postnatal development at postnatal day 6 (P6), indicating that the paternal allele is not completely silenced at this stage (Sato and Stryker, 2010). Conversely, expression of E6AP at later developmental time points, around P27–P29, stem primarily from the maternal allele expression (Sato and Stryker, 2010). Although paternal E6AP expression becomes undetectable in neurons beyond the first postnatal week in mice, maternal E6AP is expressed throughout postnatal development and into adulthood (Judson et al., 2014). However, this imprinting may not occur similarly throughout the brain. Although cortical lysates show residual expression of E6AP in *Ube3A^{m-/p+}* mice at birth that is diminished by adulthood, presumably from expression of the paternal allele, sub-cortical and cerebellar tissues express levels of E6AP at birth that are comparable to those in adult mice (Grier et al., 2015).

Late-onset silencing of paternal Ube3A has also been observed in induced pluripotent stem cells (iPSCs) derived from an AS patient (Stanurova et al., 2016). These findings suggest that in AS mice and AS patients, normal development of neurons may occur while paternal E6AP expression remains, but developmental deficits begin to arise as paternal expression diminishes and the lack of maternal expression leads to a complete loss of E6AP function in the brain. The timing of this imprinting pattern suggests that deficits in AS may occur during a postnatal critical period of experience-dependent neuronal development.

E6AP STRUCTURE AND FUNCTION

E6AP was first discovered as the ubiquitin protein ligase involved in the degradation of the tumor repressor p53 (Scheffner et al., 1993). Human papillomavirus type 16 (HPV16) viral infections are associated with malignant lesions leading to cervical cancer and encode the oncoprotein E6 (zur Hausen, 1991). The E6 protein leads to degradation of the tumor repressor p53 in cells infected with HPV16, which was mediated by the involvement of a 100 kDa protein (Huibregtse et al., 1991). Indeed, that protein was termed E6AP and was found to be a necessary component in the ubiquitination and degradation of p53 in cancer cells (Scheffner et al., 1993). The binding region for E6 is localized to the N-terminal of E6AP, from amino acid 391–408, while the p53 binding domain consists of 500 amino acids. Additionally, the last 84 amino acids of E6AP were required for p53 degradation (Huibregtse et al., 1993b). The COOH-terminal 350 amino acids of E6AP comprise the HECT domain, a region shared by several E3 ligases structurally similar to E6AP, and this domain is required for the ubiquitination function of E6AP (Huibregtse et al., 1993a, 1995; **Figure 1C**). Furthermore, the catalytic active site of E6AP is localized to a cysteine at position 833, as mutating this cysteine to alanine renders the E3 ligase unable to form a thioester bond with ubiquitin (Scheffner et al., 1995). E6AP can also self-ubiquitinate in HPV16-positive cells and mediate its own degradation (Kao et al., 2000). This requires the binding of E6 to E6AP and is mediated by the intramolecular transfer of ubiquitin from the active cysteine site of E6AP to one of its own lysine residues, possibly acting as a multimer in order to achieve self-ubiquitination (Kao et al., 2000).

Crystal structure of E6AP showed that the HECT domain consists of two lobes that pack loosely across a small interface and are connected by a three-residue hinge (residues 738–740). The larger NH₂-terminal lobe of the HECT domain (residues 495–737) has a mostly α -helical structure, while the smaller COOH-terminal lobe (residues 741–852) has an α/β structure and contains the catalytic Cys⁸²⁰ (Huang et al., 1999). Notably, many E6AP mutations in AS patients are located in the HECT domain and around the catalytic site (Nawaz et al., 1999; Cooper et al., 2004). Several AS mutations that affect E6AP substrate ubiquitination inhibit the E3 ligase from forming a thioester bond with ubiquitin (Cooper et al., 2004). In addition, an autism-linked missense mutation disrupts E6AP phosphorylation by protein kinase A (PKA) at residue T485 and leads to an

enhancement of its activity towards other substrates (Yi et al., 2015). Thus, there is a strong link between the E3 ligase function of E6AP and its involvement in neurodevelopmental disorders, suggesting that E3 ligase function is essential to the role of E6AP in normal brain development.

Another function of E6AP has been discovered as coactivator for the nuclear hormone receptor superfamily. Nuclear hormone receptors are ligand-induced transcription factors that require coactivators to achieve optimal function (Shibata et al., 1997). Coactivators enhance receptor function by acting as a bridge between DNA-bound receptors and basal transcription factors (Chen et al., 1997). E6AP contains a nuclear localization signal that allows it to be localized to the nucleus, and three LXXL motifs, which are important for receptor interaction (Hatakeyama et al., 1997; Heery et al., 1997). E6AP was found to interact with the liganded form of the progesterone receptor and increase its transcriptional activity (Nawaz et al., 1999). Interestingly, its function as a receptor coactivator is independent from its function as a ubiquitin protein ligase. However, further evidence is needed to support the contribution of the nuclear hormone receptor in Ube3A-dependent AS and ASD pathogenesis.

PRIMARY UBIQUITINATION TARGETS OF E6AP E3 LIGASE

The proteolysis of specific substrates *via* the ubiquitin-proteasome pathway (UPS) is essential to neuronal development and synaptic plasticity (Hegde and DiAntonio, 2002). Proteasome-mediated degradation of proteins involves the addition of ubiquitin to specific target molecules followed by their trafficking to the proteasome for degradation into small peptides and amino acids. This process occurs *via* coordinated actions of three classes of enzymes: E1, E2, and E3 (**Figure 2**). E1, the ubiquitin-activating enzyme, activates the free ubiquitin in an ATP-dependent manner. The conjugating enzyme E2 then carries the transfer of the activated ubiquitin, and a substrate-specific E3 ligase attaches the ubiquitin molecule to a target protein. Once a ubiquitin molecule has attached to a protein, another ubiquitin can be attached to an internal lysine residue of the first ubiquitin, and this can go on to form a polyubiquitin chain on the target protein. Polyubiquitination tags a protein substrate for degradation and causes it to be trafficked to the 26S proteasome (Hegde, 2004). At the synapse, ubiquitination can modulate neurotransmitter receptors, as well as components of the postsynaptic density (Ehlers, 2003). The UPS also plays an important role in cell growth, neurite extension, structural remodeling, and synaptic formation and plasticity (d'Azzo et al., 2005; Hurley et al., 2006; Nandi et al., 2006; Shearwin-Whyatt et al., 2006; Segref and Hoppe, 2009). Impairments in ubiquitin-mediated protein degradation can, therefore, lead to deficits in neuronal development and the maintenance of synaptic connections.

As the primary function of E6AP is that of an E3 ligase and its function is mediated *via* protein ubiquitination, it is critical to identify its downstream targets. To date, several

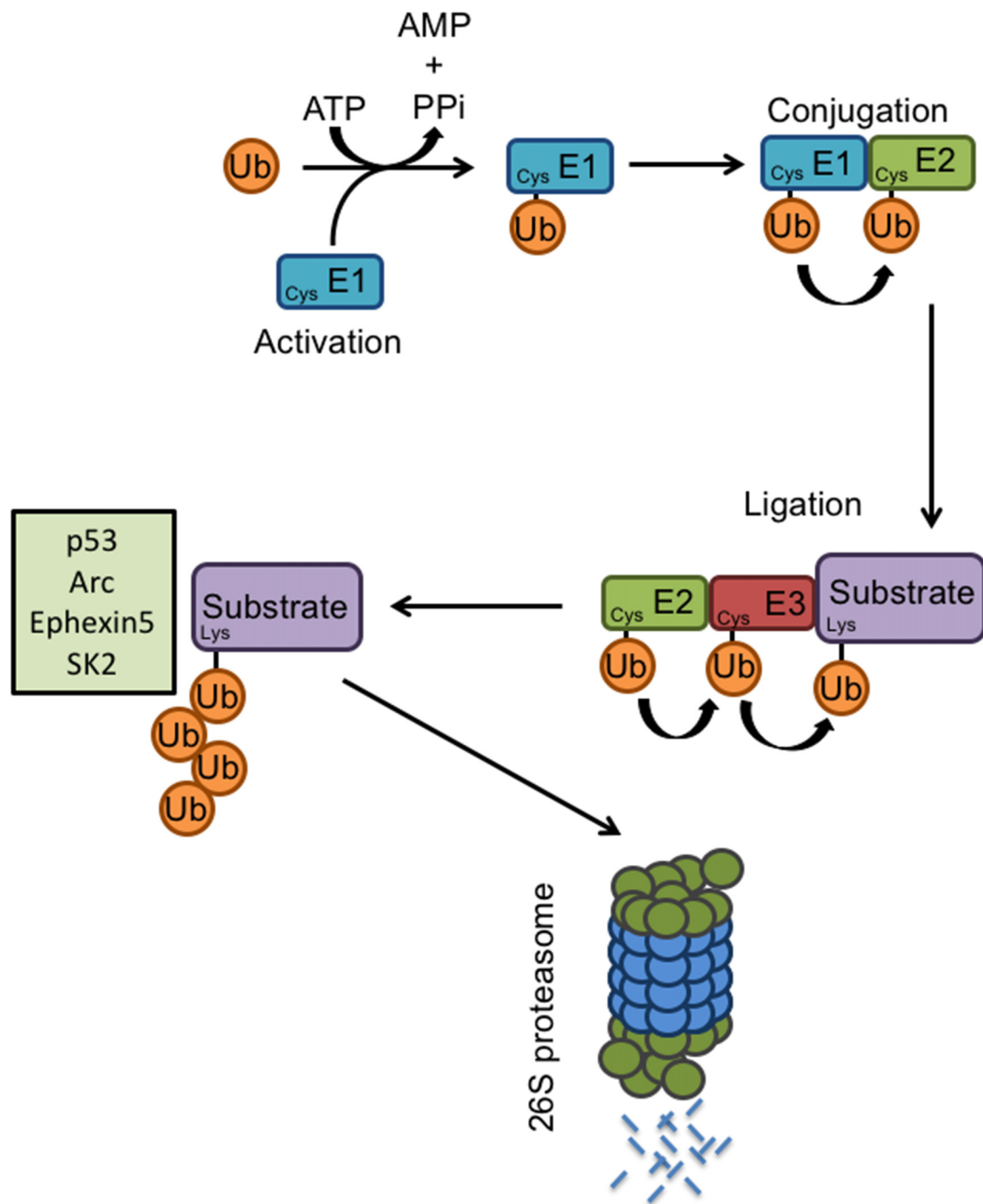


FIGURE 2 | E3 ligases and the ubiquitin proteasome system. Proteasome-mediated degradation of proteins involves the addition of ubiquitin to specific target molecules followed by their trafficking to the proteasome for degradation into small peptides and amino acids. This process occurs *via* coordinated actions of three classes of enzymes: E1, E2, and E3. The ubiquitin-activating enzyme E1, activates the free ubiquitin in an ATP-dependent manner. The conjugating enzyme E2 then carries the transfer of the activated ubiquitin, and a substrate-specific E3 ligase attaches the ubiquitin molecule to a target protein. Once a ubiquitin molecule has attached to a protein, another ubiquitin can be attached to an internal lysine residue of the first ubiquitin, and this can go on to form a polyubiquitin chain on the target protein. Known E6AP targets include p53, Arc, Ephexin5, and SK2. Polyubiquitination tags a protein substrate for degradation and causes it to be trafficked to the 26S proteasome.

E6AP ubiquitination targets have been identified, including the tumor suppressor p53, the PDZ-containing protein Scribble, the transcriptional repressor NFX1-91, the DNA-repair protein

HHR23A, the AMPAR-trafficking regulator Arc, the RhoA guanine nucleotide exchange factor Ephexin5, and the small-conductance potassium channel SK2.

The Tumor Repressor p53

The tumor repressor p53 was one of the first ubiquitination targets discovered for E6AP in the context of viral infection by HPV16. Although most of the studies on the interaction between E6AP and p53 have focused on its role in cancer, p53 has also been studied in the context of AS. In mice maternally deficient for E6AP, increased cytoplasmic p53 was found in Purkinje and hippocampal cells compared to wild type (WT) mice (Jiang et al., 1998). No differences in p53 transcripts were found between the mice, suggesting that the change in p53 levels was due to a posttranscriptional effect. In addition, increased p53 immunoreactivity was found in Purkinje cells of a patient with clinical diagnosis of AS, suggesting that E6AP can regulate levels of p53 in the absence of the E6 viral protein (Jiang et al., 1998). Although these *UBE3A^{m-/p+}* mice display impaired contextual learning and hippocampal LTP, it is unclear whether the changes in p53 contribute to the behavioral phenotype of AS mice. Furthermore, how the ubiquitination of p53 by E6AP affects neuronal developmental or morphology in the context of AS or ASD remains to be studied.

The Human Homolog of the Yeast DNA Report Protein Rad 23 (HHR23A)

One of the substrates identified with the normal cellular function of E6AP, as opposed to its role in cancer cells, is HHR23A, the human homolog of the yeast DNA repair protein Rad23 (Kumar et al., 1999). HHR23A levels are increased in response to DNA damage, and its levels are also regulated in a cell-cycle dependent manner, with specific degradation occurring during the S phase. HHR23A binds E6AP and is ubiquitinated *in vitro* in a cell-cycle and E6AP-dependent manner, which is enhanced with the overexpression of WT E6AP, but not the E3 ligase mutant E6AP C833A (Kumar et al., 1999). Although this study provides important information on the cellular function of E6AP in DNA repair and cell cycle progression *via* regulation of HHR23A levels, the role of this ubiquitination target has not been studied in the context of AS and ASD.

The Synaptic Protein Arc

Arc is an immediate early gene protein with its expression tightly regulated by neuronal activity (Link et al., 1995; Lyford et al., 1995). Arc has been shown to play important roles in AMPAR trafficking and synaptic plasticity (Chowdhury et al., 2006; Rial Verde et al., 2006; Shepherd et al., 2006). In elucidating the molecular mechanisms underlying AS, Arc was shown to be a target for E6AP-mediated ubiquitination (Greer et al., 2010). Arc regulates the trafficking of AMPARs at the synapse by accelerating endocytosis and reducing surface expression (Chowdhury et al., 2006). In mouse brain extracts, Arc was associated with E6AP. Increased expression of E6AP, but not the E3 ligase mutant E6AP C833A, led to increased Arc ubiquitination (Greer et al., 2010). Under the conditions of increased neuronal activity, either by kainic acid or an enriched environment, *Ube3A^{m-/p+}* AS mice have higher levels of Arc than WT animals. Neurons transfected with E6AP shRNA have reduced levels of the AMPAR subunit GluA1, which was caused by increased endocytosis of GluA1 and resulted in

decreased miniature excitatory postsynaptic currents (mEPSCs). The reduction in GluA1 was mediated by E6AP-dependent ubiquitination of Arc, and *Ube3A^{m-/p+}* mice also had decreased levels of AMPARs (Greer et al., 2010). Further supporting this work was the finding that seizure-like activity in the AS mouse model could be attenuated by reducing Arc expression (Mandel-Brehm et al., 2015). However, the ubiquitination-dependent degradation of Arc by E6AP has been challenged. Another study demonstrated a lack of interaction between full-length Arc and E6AP, and Arc ubiquitination and its total protein levels seemed not affected by increased E6AP expression (Kuhnle et al., 2013). Furthermore, they showed that down-regulation of E6AP expression stimulates estradiol-induced transcription of the Arc gene, suggesting that Arc protein levels are controlled by E6AP at the transcriptional rather than post-translational level (Kuhnle et al., 2013).

The RhoA Guanine Nucleotide Exchange Factor Ephexin5

EphB receptors are expressed on developing axons and dendrites and regulate actin cytoskeleton remodeling critical for excitatory synapse development *via* binding to their ligand EphrinBs and the subsequent activation of guanine nucleotide exchange factors (GEFs; Klein, 2009). Activation of EphBs in hippocampal neurons leads to an increase in dendritic spines and functional excitatory synapses, whereas disruption of EphB function leads to defects in spine morphogenesis and a decrease in excitatory synapse number (Ethell et al., 2001; Henkemeyer et al., 2003; Penzes et al., 2003; Kayser et al., 2006). Ephexin5, a RhoA GEF expressed in the brain, negatively regulates excitatory synapse development until EphrinB binding to the EphB receptor tyrosine kinase triggers Ephexin5 (E5) phosphorylation, ubiquitination, and degradation. The degradation of E5 promotes EphB-dependent excitatory synapse development and was found to be mediated by E6AP (Margolis et al., 2010). A Ube3A binding domain (UBD) sequence, corresponding to the E6AP-binding sequence of HHR23A, was identified in Ephexin5. Furthermore, immunoprecipitation showed binding between E6AP and E5. E5 levels were decreased in the presence of E6AP, but not the E3 ligase mutant E6AP C833A, and E5 degradation was attenuated by shRNA-mediated knockdown of E6AP (Margolis et al., 2010). Additionally, E5 levels in the brains of *Ube3A^{m-/p+}* mice were significantly higher and E5 ubiquitination levels were reduced, supporting the role of E6AP in mediating E5 degradation by ubiquitination and potentially regulating excitatory synapse formation (Margolis et al., 2010).

Small-Conductance Potassium Channel 2 (SK2)

Small-conductance potassium channels (SKs) are involved in synaptic transmission by contributing to the hyperpolarization after an action potential or repolarization after EPSCs (Adelman et al., 2012). In hippocampal neurons, synaptic SK channels become active upon NMDAR activation, leading to membrane repolarization and thus suppression of the NMDAR activity, a function that is important in regulating neuronal excitability

for LTP, a well-studied form of synaptic plasticity important for learning and memory (Nicoll and Malenka, 1999; Malinow and Malenka, 2002). In turn, LTP induction regulates levels of synaptic SK2 by triggering endocytosis (Lin et al., 2008). Recently, it was discovered that E6AP ubiquitinates SK2 and facilitates its internalization (Sun et al., 2015). Specifically, ubiquitination by E6AP was found to occur at the C-terminal K506/K514/K550 residues of SK2. Furthermore, synaptic SK2 levels were increased in the hippocampus of Ube3A^{m-/P+} mice, along with decreased ubiquitination of SK2. This resulted in impaired synaptic plasticity and decreased NMDAR function, suggesting that E6AP can modulate synaptic plasticity by regulating SK2 channel levels *via* ubiquitination and endocytosis (Sun et al., 2015).

Additional new targets have been continuously discovered in recent studies, such as the mTORC1 regulating protein p18 and the inhibitor of apoptosis XIAP (Khatri et al., 2018; Sun et al., 2018). Ube3A has been shown to regulate mTORC1 signaling by targeting the Ragulator complex subunit p18 for proteasomal degradation (Sun et al., 2018). Ube3A deficiency increases lysosomal localization of p18 and the Ragulator complex, and leads to increased mTORC1 activity and eventual improvement in dendritic spine maturation and learning performance. This study provides a novel mechanism by which Ube3A can modulate synaptic activity *via* its function as an E3 ligase (Sun et al., 2018). In our recent study, we have identified XIAP as a Ube3A target for ubiquitination and degradation, which is involved in aberrant dendritic arborization in Ube3A-dependent ASD (Khatri et al., 2018).

ROLE OF UBE3A/E6AP IN NEURITE GROWTH AND NEURONAL MATURATION

The signs and symptoms of ASDs often appear before 3 years of life, a time window when social, emotional, and cognitive skills are developing (Walsh et al., 2008). This period correlates with a development phase of brain architecture, including the generation of new neurons, dendritic growth, synaptogenesis, neuron circuit formation, and experience-dependent remodeling (Fox et al., 2010).

A growing number of studies have revealed a role for E6AP in neuron structural development. Alterations in E6AP levels have led to changes in dendritic and spine morphology. Ube3A^{m-/P+} AS mice have dendritic spines with inconsistent morphology, including variability in spine neck length and head size (Dindot et al., 2008). Hippocampal dendritic spines were lower in density and shorter in length in Ube3A^{m-/P+} mice than in WT mice (Dindot et al., 2008). When E6AP was downregulated in mice *via in utero* electroporation of shRNA, changes in the polarity of dendrites was observed (Miao et al., 2013). Specifically, at P7, the orientation property of the apical dendrite relative to the line perpendicular to the pial surface in layer 2/3 neurons was impaired in neurons with E6AP shRNA. The length of the apical dendrite was also reduced compared to control neurons, both in cortical and hippocampal neurons. These deficits were attributed to the regulation of Golgi apparatus distribution; control neurons had Golgi enriched within the apical dendrite,

whereas E6AP shRNA-transfected neurons had Golgi clustered near the nucleus. Interestingly, these deficits were rescued by the overexpression of shRNA-resistant E6AP isoform 2, the primary E6AP isoform expressed in the brain from embryonic to adult stages in mice (Miao et al., 2013). Furthermore, stunted apical dendrites and decreased dendritic polarity were observed in Ube3A^{m-/P+} mice (Miao et al., 2013). Supporting the role for Golgi dysfunction in AS, another study reported structural disruption of cisternal swelling of the Golgi apparatus in Ube3A^{m-/P+} cortical neurons (Condon et al., 2013). Golgi were found to be severely under-acidified, leading to osmotic swelling, and resulting in a marked reduction in protein sialylation, a process dependent on Golgi pH (Condon et al., 2013).

Morphological deficits have also been found in *Drosophila* with a loss of dUBE3A, the homolog for Ube3A/E6AP. In the absence of dUBE3A, the number of terminal dendritic branches in class IV da sensory neurons was reduced (Lu et al., 2009). Da neurons in dUBE3A-null neurons fail to completely prune their dendrites during early metamorphosis, suggesting a pruning defect. Strikingly, overexpression of dUBE3A in da neurons decreased dendritic branching, implicating an important role for the dosage of E6AP in neuronal development (Lu et al., 2009).

Abnormalities in dopamine signaling have been found in Ube3A^{m-/P+} mice. Although the number of dopaminergic cells and dopamine synthesis are normal in these AS mice, increased dopamine release was observed in the mesolimbic pathway, while the nigrostriatal pathway exhibited decreased dopamine release (Riday et al., 2012). Decreased GABA co-release was also found as a result of E6AP loss from tyrosine hydroxylase-expressing dopaminergic neurons in the VTA, leading to enhanced reward-seeking behavior (Berrios et al., 2016). Interestingly, clinical administration of levodopa (L-DOPA) in a small number of AS patients dramatically improved resting tremor and rigidity symptoms (Harbord, 2001). These studies suggest that although defects in the dopaminergic pathway may not account for all neurodevelopmental effects of E6AP loss, it may be involved in causing some of the symptoms arising from dopaminergic signaling.

More recently, our own work showed that in cultured hippocampal neurons, ASD-related overexpression of Ube3A led to a drastic remodeling of dendritic arborization, mainly by a reduction in dendrite number and length (Khatri et al., 2018). This remodeling effect was mediated by the ubiquitination and degradation of XIAP by E6AP, which led to the activation of caspase-3 and subsequent cleavage of microtubules (Khatri et al., 2018). Strikingly, the Ube3A 2X ASD mouse model displayed a similar reduction in dendritic branching in cortical neurons, along with decreased XIAP levels, increased caspase-3 activation, and elevated levels of tubulin cleavage. Spine morphology was also affected by overexpression of Ube3A, as decreased spine density and increased spine length were observed both *in vitro* and *in vivo* (Khatri et al., 2018). These findings reveal an important mechanism for increased Ube3A gene dosage in ASD-related neurodevelopmental alterations, and further implicate the role of Ube3A/E6AP in neuronal morphology growth and maturation. Interestingly, in some studies, reduced Ube3A expression also leads to a reduction in dendritic

arborization (Miao et al., 2013; Valluy et al., 2015), suggesting that an opposite change in Ube3A gene dosage may trigger distinct signaling cascades, which nevertheless cause similar changes in dendritic development.

THE ROLE OF E6AP IN NEURAL AND SYNAPTIC PLASTICITY

Ube3A^{m-/p+} mice were shown to have impaired experience-dependent synaptic plasticity in the visual cortex (Yashiro et al., 2009). Specifically, Ube3A^{m-/p+} do not exhibit ocular dominance plasticity induced by monocular deprivation, and visual cortex neurons show decreased mEPSCs in response to visual experience (Yashiro et al., 2009). Cortical circuitry and retinotopic maps form normally, with no obvious defects seen in cell density and overall cortical development in the visual cortex. However, spine density in the basal dendrites of the Layer V visual cortex neurons is reduced in Ube3A^{m-/p+} mice (Sato and Stryker, 2010). The time for ocular dominance formation represents a critical period for experience-dependent visual cortex maturation, and UBE3A maternal allele expression is increased during this critical period, suggesting that E6AP plays a role in postnatal experience-dependent neuronal development (Sato and Stryker, 2010). Interestingly, in Ube3A^{m-/p+} mice, reinstatement of E6AP expression at birth and at 3 weeks of age was able to rescue motor deficits, while reinstatement in adults failed to show rescue effects, suggesting the existence of a developmental time window with high sensitivity to E6AP activities (Silva-Santos et al., 2015).

E6AP has also been implicated in the expression of LTP. In the hippocampus of Ube3A^{m-/p+} mice, increased levels of inhibitory phosphorylation at Thr305 of CaMKII were found, thereby decreasing the activity of the protein, which is important in the induction of LTP (Weeber et al., 2003; Lisman et al., 2012). This change in CaMKII function was thought to be responsible for some of the learning impairments in Ube3A^{m-/p+} mice, as the behavioral and learning deficits were reversed when a mutation was introduced to block the inhibitory phosphorylation of CaMKII (van Woerden et al., 2007). E6AP was also shown to modulate NMDAR-mediated synaptic plasticity by ubiquitinating and internalizing SK2 channels (Sun et al., 2015).

An alteration in the excitatory/inhibitory (E/I) balance is increasingly considered a key feature in ASD pathogenesis (Nelson and Valakh, 2015). Indeed, a loss of E6AP leads to an E/I imbalance in the brains of Ube3A^{m-/p+} mice, which may contribute to seizure susceptibility in AS (Wallace et al., 2012). Inhibitory GABAergic drive onto layer 2/3 pyramidal neurons in the visual cortex is decreased with loss of maternal E6AP, which arises from an accumulation of clathrin-coated vesicles at

inhibitory axon terminals in interneurons. However, excitatory interneuron input is not affected, suggesting that the E/I balance is neuron-specific (Wallace et al., 2012). Furthermore, selective loss of E6AP in GABAergic neurons causes AS-like neocortical EEG patterns, enhancing seizure susceptibility, and leads to presynaptic accumulation of clathrin-coated vesicles, whereas specific glutamatergic loss has no effect on EEG patterns (Judson et al., 2016). Decreased tonic inhibition has also been found in cerebellar granule cells of E6AP-deficient mice (Egawa et al., 2012). E6AP was found to control the degradation of the GABA transporter 1 (GAT1) in cerebellar granule cells, leading to an increase in GAT1 with loss of E6AP and resulting in decreased GABA concentrations in the extrasynaptic space. Additionally, treatment of a selective GABA_A receptor agonist improved the firing properties of cerebellar cells in brain slices and reduced cerebellar ataxia in Ube3A^{m-/p+} mice, further supporting the role of neuron-specific effects of E6AP loss resulting in the manifestation of various behavioral phenotypes in AS (Egawa et al., 2012). More recently, it was shown that increased sensitivity to seizures in AS mice was attributed to Ube3A deletion in GABAergic but not glutamatergic neurons, and the epileptic behavior was rescued by reinstatement of Ube3A in the GABAergic cells during development (Gu et al., 2019).

CONCLUSION

Loss of function of Ube3A/E6AP results in the manifestation of AS, whereas duplication and triplication of the gene cause autism, suggesting the sensitivity of neurodevelopmental processes to the E6AP dosage. As an E3 ligase, the discovery of specific ubiquitination targets and their neuronal function is critical to the understanding of AS and E6AP-dependent ASDs. Many studies using mouse models have elucidated a mechanism by which E6AP alters dendrite and spine formation, and synaptic plasticity during an experience-dependent critical window in brain development. E6AP targets may be widely distributed in a neuron including the nucleus, neurites and the spines, but the exact subcellular location of E6AP activity execution remains less clear. Future work will elucidate the specific contribution of cellular and molecular alterations to the aberrant brain development and behavioral phenotype in AS and ASD.

AUTHOR CONTRIBUTIONS

NK and HYM wrote the manuscript.

FUNDING

This work was supported by National Institute of Mental Health NIH grant R01 MH079407 (HYM).

REFERENCES

Adelman, J. P., Maylie, J., and Sah, P. (2012). Small-conductance Ca²⁺-activated K⁺ channels: form and function. *Annu. Rev. Physiol.* 74, 245–269. doi: 10.1146/annurev-physiol-020911-153336

Albrecht, U., Sutcliffe, J. S., Cattanach, B. M., Beechey, C. V., Armstrong, D., Eichele, G., et al. (1997). Imprinted expression of the murine Angelman syndrome gene, Ube3a, in hippocampal and Purkinje neurons. *Nat. Genet.* 17, 75–78. doi: 10.1038/ng0997-57

- Angelman, H. (1965). 'Puppet' children a report on three cases. *Dev. Med. Child Neurol.* 7, 681–688. doi: 10.1111/j.1469-8749.1965.tb07844.x
- Azevedo, F. A., Carvalho, L. R., Grinberg, L. T., Farfel, J. M., Ferretti, R. E., Leite, R. E., et al. (2009). Equal numbers of neuronal and nonneuronal cells make the human brain an isometrically scaled-up primate brain. *J. Comp. Neurol.* 513, 532–541. doi: 10.1002/cne.21974
- Berrios, J., Stamatakis, A. M., Kantak, P. A., McElligott, Z. A., Judson, M. C., Aita, M., et al. (2016). Loss of UBE3A from TH-expressing neurons suppresses GABA co-release and enhances VTA-NAc optical self-stimulation. *Nat. Commun.* 7:10702. doi: 10.1038/ncomms10702
- Borgatti, R., Piccinelli, P., Passoni, D., Dalprà, L., Miozzo, M., Micheli, R., et al. (2001). Relationship between clinical and genetic features in "inverted duplicated chromosome 15" patients. *Pediatr. Neurol.* 24, 111–116. doi: 10.1016/s0887-8994(00)00244-7
- Born, H. A., Dao, A. T., Levine, A. T., Lee, W. L., Mehta, N. M., Mehra, S., et al. (2017). Strain-dependence of the angelman syndrome phenotypes in Ube3a maternal deficiency mice. *Sci. Rep.* 7:8451. doi: 10.1038/s41598-017-08825-x
- Chamberlain, S. J., and Brannan, C. I. (2001). The Prader-Willi syndrome imprinting center activates the paternally expressed murine Ube3a antisense transcript but represses paternal Ube3a. *Genomics* 73, 316–322. doi: 10.1006/geno.2001.6543
- Chen, H., Lin, R. J., Schiltz, R. L., Chakravarti, D., Nash, A., Nagy, L., et al. (1997). Nuclear receptor coactivator ACTR is a novel histone acetyltransferase and forms a multimeric activation complex with P/CAF and CBP/p300. *Cell* 90, 569–580. doi: 10.1016/s0092-8674(00)80516-4
- Chen, J. A., Penagarikano, O., Belgard, T. G., Swarup, V., and Geschwind, D. H. (2015). The emerging picture of autism spectrum disorder: genetics and pathology. *Annu. Rev. Pathol.* 10, 111–144. doi: 10.1146/annurev-pathol-012414-040405
- Chowdhury, S., Shepherd, J. D., Okuno, H., Lyford, G., Petralia, R. S., Plath, N., et al. (2006). Arc/Arg3.1 interacts with the endocytic machinery to regulate AMPA receptor trafficking. *Neuron* 52, 445–459. doi: 10.1016/j.neuron.2006.08.033
- Clayton-Smith, J., and Laan, L. (2003). Angelman syndrome: a review of the clinical and genetic aspects. *J. Med. Genet.* 40, 87–95. doi: 10.1136/jmg.40.2.87
- Condon, K. H., Ho, J., Robinson, C. G., Hanus, C., and Ehlers, M. D. (2013). The Angelman syndrome protein Ube3a/E6AP is required for Golgi acidification and surface protein sialylation. *J. Neurosci.* 33, 3799–3814. doi: 10.1523/JNEUROSCI.1930-11.2013
- Cook, E. H. Jr., Lindgren, V., Leventhal, B. L., Courchesne, R., Lincoln, A., Shulman, C., et al. (1997). Autism or atypical autism in maternally but not paternally derived proximal 15q duplication. *Am. J. Hum. Genet.* 60, 928–934.
- Cooper, E. M., Hudson, A. W., Amos, J., Wagstaff, J., and Howley, P. M. (2004). Biochemical analysis of Angelman syndrome-associated mutations in the E3 ubiquitin ligase E6-associated protein. *J. Biol. Chem.* 279, 41208–41217. doi: 10.1074/jbc.m401302200
- d'Azzo, A., Bongiovanni, A., and Nastasi, T. (2005). E3 ubiquitin ligases as regulators of membrane protein trafficking and degradation. *Traffic* 6, 429–441. doi: 10.1111/j.1600-0854.2005.00294.x
- Dindot, S. V., Antalffy, B. A., Bhattacharjee, M. B., and Beaudet, A. L. (2008). The Angelman syndrome ubiquitin ligase localizes to the synapse and nucleus and maternal deficiency results in abnormal dendritic spine morphology. *Hum. Mol. Genet.* 17, 111–118. doi: 10.1093/hmg/ddm288
- Egawa, K., Kitagawa, K., Inoue, K., Takayama, M., Takayama, C., Saitoh, S., et al. (2012). Decreased tonic inhibition in cerebellar granule cells causes motor dysfunction in a mouse model of Angelman syndrome. *Sci. Transl. Med.* 4:163ra157. doi: 10.1126/scitranslmed.3004655
- Ehlers, M. D. (2003). Activity level controls postsynaptic composition and signaling via the ubiquitin-proteasome system. *Nat. Neurosci.* 6, 231–242. doi: 10.1038/nn1013
- Ethell, I. M., Irie, F., Kalo, M. S., Couchman, J. R., Pasquale, E. B., and Yamaguchi, Y. (2001). EphB/syndecan-2 signaling in dendritic spine morphogenesis. *Neuron* 31, 1001–1013. doi: 10.1016/s0896-6273(01)00440-8
- Filonova, I., Trotter, J. H., Banko, J. L., and Weeber, E. J. (2014). Activity-dependent changes in MAPK activation in the Angelman Syndrome mouse model. *Learn. Mem.* 21, 98–104. doi: 10.1101/lm.032375.113
- Flavell, S. W., Cowan, C. W., Kim, T. K., Greer, P. L., Lin, Y., Paradis, S., et al. (2006). Activity-dependent regulation of MEF2 transcription factors suppresses excitatory synapse number. *Science* 311, 1008–1012. doi: 10.1126/science.1122511
- Fox, S. E., Levitt, P., and Nelson, C. A. III. (2010). How the timing and quality of early experiences influence the development of brain architecture. *Child Dev.* 81, 28–40. doi: 10.1111/j.1467-8624.2009.01380.x
- Gilbert, J., and Man, H. Y. (2016). The X-linked autism protein KIAA2022/KIDLIA regulates neurite outgrowth via N-cadherin and delta-catenin signaling. *eNeuro* 3:ENEURO.0238-16.2016. doi: 10.1523/eneuro.0238-16.2016
- Gilbert, J., and Man, H. Y. (2017). Fundamental elements in autism: from neurogenesis and neurite growth to synaptic plasticity. *Front. Cell. Neurosci.* 11:359. doi: 10.3389/fncel.2017.00359
- Greer, P. L., Hanayama, R., Bloodgood, B. L., Mardinly, A. R., Lipton, D. M., Flavell, S. W., et al. (2010). The Angelman Syndrome protein Ube3A regulates synapse development by ubiquitinating arc. *Cell* 140, 704–716. doi: 10.1016/j.cell.2010.01.026
- Grier, M. D., Carson, R. P., and Lagrange, A. H. (2015). Toward a broader view of Ube3a in a mouse model of angelman syndrome: expression in brain, spinal cord, sciatic nerve and glial cells. *PLoS One* 10:e0124649. doi: 10.1371/journal.pone.0124649
- Gu, B., Carstens, K. E., Judson, M. C., Dalton, K. A., Rougie, M., Clark, E. P., et al. (2019). Ube3a reinstatement mitigates epileptogenesis in Angelman syndrome model mice. *J. Clin. Invest.* 129, 163–168. doi: 10.1172/jci120816
- Gunaydin, L. A., Grosenick, L., Finkelstein, J. C., Kauvar, I. V., Fenno, L. E., Adhikari, A., et al. (2014). Natural neural projection dynamics underlying social behavior. *Cell* 157, 1535–1551. doi: 10.1016/j.cell.2014.05.017
- Gustin, R. M., Bichell, T. J., Bubser, M., Daily, J., Filonova, I., Mrelashvili, D., et al. (2010). Tissue-specific variation of Ube3a protein expression in rodents and in a mouse model of Angelman syndrome. *Neurobiol. Dis.* 39, 283–291. doi: 10.1016/j.nbd.2010.04.012
- Harbord, M. (2001). Levodopa responsive Parkinsonism in adults with Angelman Syndrome. *J. Clin. Neurosci.* 8, 421–422. doi: 10.1054/jocn.2000.0753
- Hartley, S. L., Sikora, D. M., and McCoy, R. (2008). Prevalence and risk factors of maladaptive behaviour in young children with Autistic disorder. *J. Intellect. Disabil. Res.* 52, 819–829. doi: 10.1111/j.1365-2788.2008.01065.x
- Hatakeyama, S., Jensen, J. P., and Weissman, A. M. (1997). Subcellular localization and ubiquitin-conjugating enzyme (E2) interactions of mammalian HECT family ubiquitin protein ligases. *J. Biol. Chem.* 272, 15085–15092. doi: 10.1074/jbc.272.24.15085
- Heery, D. M., Kalkhoven, E., Hoare, S., and Parker, M. G. (1997). A signature motif in transcriptional co-activators mediates binding to nuclear receptors. *Nature* 387, 733–736. doi: 10.1038/42750
- Hegde, A. N. (2004). Ubiquitin-proteasome-mediated local protein degradation and synaptic plasticity. *Prog. Neurobiol.* 73, 311–357. doi: 10.1016/j.pneurobio.2004.05.005
- Hegde, A. N., and DiAntonio, A. (2002). Ubiquitin and the synapse. *Nat. Rev. Neurosci.* 3, 854–861. doi: 10.1038/nnrn961
- Henkemeyer, M., Itkis, O. S., Ngo, M., Hickmott, P. W., and Ethell, I. M. (2003). Multiple EphB receptor tyrosine kinases shape dendritic spines in the hippocampus. *J. Cell Biol.* 163, 1313–1326. doi: 10.1083/jcb.2003.06033
- Hogart, A., Wu, D., LaSalle, J. M., and Schanen, N. C. (2010). The comorbidity of autism with the genomic disorders of chromosome 15q11.2–q13. *Neurobiol. Dis.* 38, 181–191. doi: 10.1016/j.nbd.2008.08.011
- Huang, Z. (2009). Molecular regulation of neuronal migration during neocortical development. *Mol. Cell. Neurosci.* 42, 11–22. doi: 10.1016/j.mcn.2009.06.003
- Huang, H. S., Allen, J. A., Mabb, A. M., King, I. F., Miriyala, J., Taylor-Blake, B., et al. (2011). Topoisomerase inhibitors unsilence the dormant allele of Ube3a in neurons. *Nature* 481, 185–189. doi: 10.1038/nature10726
- Huang, L., Kinnucan, E., Wang, G., Beaudenon, S., Howley, P. M., Huijbregtse, J. M., et al. (1999). Structure of an E6AP-UbcH7 complex: insights into ubiquitination by the E2-E3 enzyme cascade. *Science* 286, 1321–1326. doi: 10.1126/science.286.5443.1321

- Huibregtse, J. M., Scheffner, M., Beaudenon, S., and Howley, P. M. (1995). A family of proteins structurally and functionally related to the E6-AP ubiquitin-protein ligase. *Proc. Natl. Acad. Sci. U S A* 92, 2563–2567. doi: 10.1073/pnas.92.11.5249a
- Huibregtse, J. M., Scheffner, M., and Howley, P. M. (1991). A cellular protein mediates association of p53 with the E6 oncoprotein of human papillomavirus types 16 or 18. *EMBO J.* 10, 4129–4135. doi: 10.1002/j.1460-2075.1991.tb04990.x
- Huibregtse, J. M., Scheffner, M., and Howley, P. M. (1993a). Cloning and expression of the cDNA for E6-AP, a protein that mediates the interaction of the human papillomavirus E6 oncoprotein with p53. *Mol. Cell. Biol.* 13, 775–784. doi: 10.1128/mcb.13.2.775
- Huibregtse, J. M., Scheffner, M., and Howley, P. M. (1993b). Localization of the E6-AP regions that direct human papillomavirus E6 binding, association with p53, and ubiquitination of associated proteins. *Mol. Cell. Biol.* 13, 4918–4927. doi: 10.1128/mcb.13.8.4918
- Hurley, J. H., Lee, S., and Prag, G. (2006). Ubiquitin-binding domains. *Biochem. J.* 399, 361–372. doi: 10.1042/BJ20061138
- Jiang, Y. H., Armstrong, D., Albrecht, U., Atkins, C. M., Noebels, J. L., Eichele, G., et al. (1998). Mutation of the Angelman ubiquitin ligase in mice causes increased cytoplasmic p53 and deficits of contextual learning and long-term potentiation. *Neuron* 21, 799–811. doi: 10.1016/s0896-6273(00)80596-6
- Judson, M. C., Sosa-Pagan, J. O., Del Cid, W. A., Han, J. E., and Philpot, B. D. (2014). Allelic specificity of Ube3a expression in the mouse brain during postnatal development. *J. Comp. Neurol.* 522, 1874–1896. doi: 10.1002/cne.23507
- Judson, M. C., Wallace, M. L., Sidorov, M. S., Burette, A. C., Gu, B., van Woerden, G. M., et al. (2016). GABAergic neuron-specific loss of Ube3a causes angelman syndrome-Like EEG abnormalities and enhances seizure susceptibility. *Neuron* 90, 56–69. doi: 10.1016/j.neuron.2016.02.040
- Kao, W. H., Beaudenon, S. L., Talis, A. L., Huibregtse, J. M., and Howley, P. M. (2000). Human papillomavirus type 16 E6 induces self-ubiquitination of the E6AP ubiquitin-protein ligase. *J. Virol.* 74, 6408–6417. doi: 10.1128/jvi.74.14.6408-6417.2000
- Kayser, M. S., McClelland, A. C., Hughes, E. G., and Dalva, M. B. (2006). Intracellular and trans-synaptic regulation of glutamatergic synaptogenesis by EphB receptors. *J. Neurosci.* 26, 12152–12164. doi: 10.1523/JNEUROSCI.3072-06.2006
- Khatri, N., Gilbert, J. P., Huo, Y., Sharafli, R., Nee, M., Qiao, H., et al. (2018). The autism protein Ube3A/E6AP remodels neuronal dendritic arborization via caspase-dependent microtubule destabilization. *J. Neurosci.* 38, 363–378. doi: 10.1523/JNEUROSCI.1511-17.2017
- Kishino, T., Lalande, M., and Wagstaff, J. (1997). UBE3A/E6-AP mutations cause Angelman syndrome. *Nat. Genet.* 15, 70–73. doi: 10.1038/ng0497-411d
- Klein, R. (2009). Bidirectional modulation of synaptic functions by Eph/ephrin signaling. *Nat. Neurosci.* 12, 15–20. doi: 10.1038/nn.2231
- Krishnan, V., Stoppel, D. C., Nong, Y., Johnson, M. A., Nadler, M. J., Ozkaynak, E., et al. (2017). Autism gene Ube3a and seizures impair sociability by repressing VTA Cbln1. *Nature* 543, 507–512. doi: 10.1038/nature21678
- Kuhnle, S., Mothes, B., Matentzoglou, K., and Scheffner, M. (2013). Role of the ubiquitin ligase E6AP/UBE3A in controlling levels of the synaptic protein Arc. *Proc. Natl. Acad. Sci. U S A* 110, 8888–8893. doi: 10.1073/pnas.1302792110
- Kumar, S., Talis, A. L., and Howley, P. M. (1999). Identification of HHR23A as a substrate for E6-associated protein-mediated ubiquitination. *J. Biol. Chem.* 274, 18785–18792. doi: 10.1074/jbc.274.26.18785
- Levy, S. E., Mandell, D. S., and Schultz, R. T. (2009). Autism. *Lancet* 374, 1627–1638. doi: 10.1016/S0140-6736(09)61376-3
- Limoges, E., Mottron, L., Bolduc, C., Berthiaume, C., and Godbout, R. (2005). Atypical sleep architecture and the autism phenotype. *Brain* 128, 1049–1061. doi: 10.1093/brain/awh425
- Lin, M. T., Lujan, R., Watanabe, M., Adelman, J. P., and Maylie, J. (2008). SK2 channel plasticity contributes to LTP at Schaffer collateral-CA1 synapses. *Nat. Neurosci.* 11, 170–177. doi: 10.1038/nn2041
- Link, W., Konietzko, U., Kauselmann, G., Krug, M., Schwanke, B., Frey, U., et al. (1995). Somatodendritic expression of an immediate early gene is regulated by synaptic activity. *Proc. Natl. Acad. Sci. U S A* 92, 5734–5738. doi: 10.1073/pnas.92.12.5734
- Lisman, J., Yasuda, R., and Raghavachari, S. (2012). Mechanisms of CaMKII action in long-term potentiation. *Nat. Rev. Neurosci.* 13, 169–182. doi: 10.1038/nrn3192
- Lossie, A. C., Whitney, M. M., Amidon, D., Dong, H. J., Chen, P., Theriaque, D., et al. (2001). Distinct phenotypes distinguish the molecular classes of Angelman syndrome. *J. Med. Genet.* 38, 834–845. doi: 10.1136/jmg.38.12.834
- Lu, Y., Wang, F., Li, Y., Ferris, J., Lee, J. A., and Gao, F. B. (2009). The *Drosophila* homologue of the Angelman syndrome ubiquitin ligase regulates the formation of terminal dendritic branches. *Hum. Mol. Genet.* 18, 454–462. doi: 10.1093/hmg/ddn373
- Lyford, G. L., Yamagata, K., Kaufmann, W. E., Barnes, C. A., Sanders, L. K., Copeland, N. G., et al. (1995). Arc, a growth factor and activity-regulated gene, encodes a novel cytoskeleton-associated protein that is enriched in neuronal dendrites. *Neuron* 14, 433–445. doi: 10.1016/0896-6273(95)90299-6
- Mabb, A. M., Judson, M. C., Zylka, M. J., and Philpot, B. D. (2011). Angelman syndrome: insights into genomic imprinting and neurodevelopmental phenotypes. *Trends Neurosci.* 34, 293–303. doi: 10.1016/j.tins.2011.04.001
- Malinow, R., and Malenka, R. C. (2002). AMPA receptor trafficking and synaptic plasticity. *Annu. Rev. Neurosci.* 25, 103–126. doi: 10.1146/annurev.neuro.25.112701.142758
- Mandel-Brehm, C., Salogiannis, J., Dhamne, S. C., Rotenberg, A., and Greenberg, M. E. (2015). Seizure-like activity in a juvenile Angelman syndrome mouse model is attenuated by reducing Arc expression. *Proc. Natl. Acad. Sci. U S A* 112, 5129–5134. doi: 10.1073/pnas.1504809112
- Margolis, S. S., Salogiannis, J., Lipton, D. M., Mandel-Brehm, C., Wills, Z. P., Mardinly, A. R., et al. (2010). EphB-mediated degradation of the RhoA GEF Ephexin5 relieves a developmental brake on excitatory synapse formation. *Cell* 143, 442–455. doi: 10.1016/j.cell.2010.09.038
- Matsuura, T., Sutcliffe, J. S., Fang, P., Galjaard, R. J., Jiang, Y. H., Benton, C. S., et al. (1997). *De novo* truncating mutations in E6-AP ubiquitin-protein ligase gene (UBE3A) in Angelman syndrome. *Nat. Genet.* 15, 74–77. doi: 10.1038/ng0197-74
- Meng, L., Person, R. E., Huang, W., Zhu, P. J., Costa-Mattioli, M., and Beaudet, A. L. (2013). Truncation of Ube3a-ATS unsilences paternal Ube3a and ameliorates behavioral defects in the Angelman syndrome mouse model. *PLoS Genet.* 9:e1004039. doi: 10.1371/journal.pgen.1004039
- Miao, S., Chen, R., Ye, J., Tan, G. H., Li, S., Zhang, J., et al. (2013). The Angelman syndrome protein Ube3a is required for polarized dendrite morphogenesis in pyramidal neurons. *J. Neurosci.* 33, 327–333. doi: 10.1523/JNEUROSCI.2509-12.2013
- Morrow, E. M., Yoo, S. Y., Flavell, S. W., Kim, T. K., Lin, Y., Hill, R. S., et al. (2008). Identifying autism loci and genes by tracing recent shared ancestry. *Science* 321, 218–223. doi: 10.1126/science.1157657
- Nandi, D., Tahliliani, P., Kumar, A., and Chandu, D. (2006). The ubiquitin-proteasome system. *J. Biosci.* 31, 137–155. doi: 10.1007/BF02705243
- Nawaz, Z., Lonard, D. M., Smith, C. L., Lev-Lehman, E., Tsai, S. Y., Tsai, M. J., et al. (1999). The Angelman syndrome-associated protein, E6-AP, is a coactivator for the nuclear hormone receptor superfamily. *Mol. Cell. Biol.* 19, 1182–1189. doi: 10.1128/mcb.19.2.1182
- Nelson, S. B., and Valakh, V. (2015). Excitatory/inhibitory balance and circuit homeostasis in autism spectrum disorders. *Neuron* 87, 684–698. doi: 10.1016/j.neuron.2015.07.033
- Newschaffer, C. J., Croen, L. A., Daniels, J., Giarelli, E., Grether, J. K., Levy, S. E., et al. (2007). The epidemiology of autism spectrum disorders. *Annu. Rev. Public Health* 28, 235–258. doi: 10.1146/annurev.publhealth.28.021406.144007
- Nicol, R. A., and Malenka, R. C. (1999). Expression mechanisms underlying NMDA receptor-dependent long-term potentiation. *Ann. N Y Acad. Sci.* 868, 515–525. doi: 10.1111/j.1749-6632.1999.tb11320.x
- Nikolov, R. N., Bearss, K. E., Lettinga, J., Erickson, C., Rodowski, M., Aman, M. G., et al. (2009). Gastrointestinal symptoms in a sample of children with pervasive developmental disorders. *J. Autism Dev. Disord.* 39, 405–413. doi: 10.1007/s10803-008-0637-8
- Penzes, P., Beaser, A., Chernoff, J., Schiller, M. R., Eipper, B. A., Mains, R. E., et al. (2003). Rapid induction of dendritic spine morphogenesis by trans-synaptic ephrinB-EphB receptor activation of the Rho-GEF kalirin. *Neuron* 37, 263–274. doi: 10.1016/s0896-6273(02)01168-6

- Pinto, D., Pagnamenta, A. T., Klei, L., Anney, R., Merico, D., Regan, R., et al. (2010). Functional impact of global rare copy number variation in autism spectrum disorders. *Nature* 466, 368–372. doi: 10.1038/nature09146
- Rapin, I., and Tuchman, R. F. (2008). Autism: definition, neurobiology, screening, diagnosis. *Pediatr. Clin. North Am.* 55, 1129–1146, viii. doi: 10.1016/j.pcl.2008.07.005
- Reis, A., Dittrich, B., Greger, V., Buiting, K., Lalande, M., Gillissen-Kaesbach, G., et al. (1994). Imprinting mutations suggested by abnormal DNA methylation patterns in familial Angelman and Prader-Willi syndromes. *Am. J. Hum. Genet.* 54, 741–747.
- Rial Verde, E. M., Lee-Osbourne, J., Worley, P. F., Malinow, R., and Cline, H. T. (2006). Increased expression of the immediate-early gene *arc/arg3.1* reduces AMPA receptor-mediated synaptic transmission. *Neuron* 52, 461–474. doi: 10.1016/j.neuron.2006.09.031
- Riday, T. T., Dankoski, E. C., Krouse, M. C., Fish, E. W., Walsh, P. L., Han, J. E., et al. (2012). Pathway-specific dopaminergic deficits in a mouse model of Angelman syndrome. *J. Clin. Invest.* 122, 4544–4554. doi: 10.1172/jci61888
- Rotaru, D. C., van Woerden, G. M., Wallaard, I., and Elgersma, Y. (2018). Adult Ube3a gene reinstatement restores the electrophysiological deficits of prefrontal cortex layer 5 neurons in a mouse model of Angelman syndrome. *J. Neurosci.* 38, 8011–8030. doi: 10.1523/jneurosci.0083-18.2018
- Rougeulle, C., Cardoso, C., Fontes, M., Colleaux, L., and Lalande, M. (1998). An imprinted antisense RNA overlaps UBE3A and a second maternally expressed transcript. *Nat. Genet.* 19, 15–16. doi: 10.1038/ng0598-15
- Rougeulle, C., Glatt, H., and Lalande, M. (1997). The Angelman syndrome candidate gene, UBE3A/E6-AP, is imprinted in brain. *Nat. Genet.* 17, 14–15. doi: 10.1038/ng0997-14
- Runte, M., Hüttenhofer, A., Gross, S., Kieffmann, M., Horsthemke, B., and Buiting, K. (2001). The IC-SNURF-SNRPN transcript serves as a host for multiple small nucleolar RNA species and as an antisense RNA for UBE3A. *Hum. Mol. Genet.* 10, 2687–2700. doi: 10.1093/hmg/10.23.2687
- Sato, M., and Stryker, M. P. (2010). Genomic imprinting of experience-dependent cortical plasticity by the ubiquitin ligase gene Ube3a. *Proc. Natl. Acad. Sci. U S A* 107, 5611–5616. doi: 10.1073/pnas.1001281107
- Scheffner, M., Huibregtse, J. M., Vierstra, R. D., and Howley, P. M. (1993). The HPV-16 E6 and E6-AP complex functions as a ubiquitin-protein ligase in the ubiquitination of p53. *Cell* 75, 495–505. doi: 10.1016/0092-8674(93)90384-3
- Scheffner, M., Nuber, U., and Huibregtse, J. M. (1995). Protein ubiquitination involving an E1–E2–E3 enzyme ubiquitin thioester cascade. *Nature* 373, 81–83. doi: 10.1038/373081a0
- Segref, A., and Hoppe, T. (2009). Think locally: control of ubiquitin-dependent protein degradation in neurons. *EMBO Rep.* 10, 44–50. doi: 10.1038/embor.2008.229
- Shearwin-Whyatt, L., Dalton, H. E., Foot, N., and Kumar, S. (2006). Regulation of functional diversity within the Nedd4 family by accessory and adaptor proteins. *Bioessays* 28, 617–628. doi: 10.1002/bies.20422
- Shepherd, J. D., Rumbaugh, G., Wu, J., Chowdhury, S., Plath, N., Kuhl, D., et al. (2006). Arc/Arg3.1 mediates homeostatic synaptic scaling of AMPA receptors. *Neuron* 52, 475–484. doi: 10.1016/j.neuron.2006.08.034
- Shibata, H., Spencer, T. E., Onate, S. A., Jenster, G., Tsai, S. Y., Tsai, M. J., et al. (1997). Role of co-activators and co-repressors in the mechanism of steroid/thyroid receptor action. *Recent Prog. Horm. Res.* 52, 141–164; discussion 164–165.
- Silva-Santos, S., van Woerden, G. M., Bruinsma, C. F., Mientjes, E., Jolfaei, M. A., Distel, B., et al. (2015). Ube3a reinstatement identifies distinct developmental windows in a murine Angelman syndrome model. *J. Clin. Invest.* 125, 2069–2076. doi: 10.1172/jci80554
- Simonoff, E., Pickles, A., Charman, T., Chandler, S., Loucas, T., and Baird, G. (2008). Psychiatric disorders in children with autism spectrum disorders: prevalence, comorbidity, and associated factors in a population-derived sample. *J. Am. Acad. Child Adolesc. Psychiatry* 47, 921–929. doi: 10.1097/chi.0b013e318179964f
- Smith, S. E., Zhou, Y. D., Zhang, G., Jin, Z., Stoppel, D. C., and Anderson, M. P. (2011). Increased gene dosage of Ube3a results in autism traits and decreased glutamate synaptic transmission in mice. *Sci. Transl. Med.* 3:103ra197. doi: 10.1126/scitranslmed.3002627
- Stanurova, J., Neureiter, A., Hiber, M., de Oliveira Kessler, H., Stolp, K., Goetzke, R., et al. (2016). Angelman syndrome-derived neurons display late onset of paternal UBE3A silencing. *Sci. Rep.* 6:30792. doi: 10.1038/srep30792
- Sun, J., Liu, Y., Jia, Y., Hao, X., Lin, W. J., Tran, J., et al. (2018). UBE3A-mediated p18/LAMTOR1 ubiquitination and degradation regulate mTORC1 activity and synaptic plasticity. *Elife* 7:e37993. doi: 10.7554/elifesciences.37993
- Sun, J., Zhu, G., Liu, Y., Standley, S., Ji, A., Tunuguntla, R., et al. (2015). UBE3A regulates synaptic plasticity and learning and memory by controlling SK2 channel endocytosis. *Cell Rep.* 12, 449–461. doi: 10.1016/j.celrep.2015.06.023
- Thomas, G. M., and Hagan, R. L. (2004). MAPK cascade signalling and synaptic plasticity. *Nat. Rev. Neurosci.* 5, 173–183. doi: 10.1038/nrn1346
- Valluy, J., Bicker, S., Aksoy-Aksel, A., Lackinger, M., Sumer, S., Fiore, R., et al. (2015). A coding-independent function of an alternative Ube3a transcript during neuronal development. *Nat. Neurosci.* 18, 666–673. doi: 10.1038/nn.3996
- van Woerden, G. M., Harris, K. D., Hojjati, M. R., Gustin, R. M., Qiu, S., de Avila Freire, R., et al. (2007). Rescue of neurological deficits in a mouse model for Angelman syndrome by reduction of α CaMKII inhibitory phosphorylation. *Nat. Neurosci.* 10, 280–282. doi: 10.1038/nn1845
- Vu, T. H., and Hoffman, A. R. (1997). Imprinting of the Angelman syndrome gene, UBE3A, is restricted to brain. *Nat. Genet.* 17, 12–13. doi: 10.1038/ng0997-12
- Wallace, M. L., Burette, A. C., Weinberg, R. J., and Philpot, B. D. (2012). Maternal loss of Ube3a produces an excitatory/inhibitory imbalance through neuron type-specific synaptic defects. *Neuron* 74, 793–800. doi: 10.1016/j.neuron.2012.03.036
- Walsh, C. A., Morrow, E. M., and Rubenstein, J. L. (2008). Autism and brain development. *Cell* 135, 396–400. doi: 10.1016/j.cell.2008.10.015
- Weeber, E. J., Jiang, Y. H., Elgersma, Y., Varga, A. W., Carrasquillo, Y., Brown, S. E., et al. (2003). Derangements of hippocampal calcium/calmodulin-dependent protein kinase II in a mouse model for Angelman mental retardation syndrome. *J. Neurosci.* 23, 2634–2644. doi: 10.1523/jneurosci.23-07-02634.2003
- Williams, C. A., Angelman, H., Clayton-Smith, J., Driscoll, D. J., Hendrickson, J. E., Knoll, J. H., et al. (1995). Angelman syndrome: consensus for diagnostic criteria. *Am. J. Med. Genet.* 56, 237–238. doi: 10.1002/ajmg.1320560224
- Williams, C. A., Beaudet, A. L., Clayton-Smith, J., Knoll, J. H., Kyllerman, M., Laan, L. A., et al. (2006). Angelman syndrome 2005: updated consensus for diagnostic criteria. *Am. J. Med. Genet. A* 140, 413–418. doi: 10.1002/ajmg.a.31074
- Williams, C. A., Lossie, A., Driscoll, D., and Unit, R. C. P. (2001). Angelman syndrome: mimicking conditions and phenotypes. *Am. J. Med. Genet.* 101, 59–64. doi: 10.1002/ajmg.1316
- Yamamoto, Y., Huibregtse, J. M., and Howley, P. M. (1997). The human E6-AP gene (UBE3A) encodes three potential protein isoforms generated by differential splicing. *Genomics* 41, 263–266. doi: 10.1006/geno.1997.4617
- Yamasaki, K., Joh, K., Ohta, T., Masuzaki, H., Ishimaru, T., Mukai, T., et al. (2003). Neurons but not glial cells show reciprocal imprinting of sense and antisense transcripts of Ube3a. *Hum. Mol. Genet.* 12, 837–847. doi: 10.1093/hmg/ddg106
- Yashiro, K., Riday, T. T., Condon, K. H., Roberts, A. C., Bernardo, D. R., Prakash, R., et al. (2009). Ube3a is required for experience-dependent maturation of the neocortex. *Nat. Neurosci.* 12, 777–783. doi: 10.1038/nn.2327
- Yi, J. J., Berrios, J., Newbern, J. M., Snider, W. D., Philpot, B. D., Hahn, K. M., et al. (2015). An autism-linked mutation disables phosphorylation control of UBE3A. *Cell* 162, 795–807. doi: 10.1016/j.cell.2015.06.045
- zur Hausen, H. (1991). Human papillomaviruses in the pathogenesis of anogenital cancer. *Virology* 184, 9–13. doi: 10.1016/0042-6822(91)90816-t

Conflict of Interest Statement: The authors declare that the research was conducted in the absence of any commercial or financial relationships that could be construed as a potential conflict of interest.

Copyright © 2019 Khatri and Man. This is an open-access article distributed under the terms of the Creative Commons Attribution License (CC BY). The use, distribution or reproduction in other forums is permitted, provided the original author(s) and the copyright owner(s) are credited and that the original publication in this journal is cited, in accordance with accepted academic practice. No use, distribution or reproduction is permitted which does not comply with these terms.



Scn2a Haploinsufficiency in Mice Suppresses Hippocampal Neuronal Excitability, Excitatory Synaptic Drive, and Long-Term Potentiation, and Spatial Learning and Memory

Wangyong Shin^{1†}, Hanseul Kweon^{1†}, Ryeonghwa Kang^{1†}, Doyoun Kim², Kyungdeok Kim¹, Muwon Kang¹, Seo Yeong Kim¹, Sun Nam Hwang², Jin Yong Kim³, Esther Yang³, Hyun Kim³ and Eunjoon Kim^{1,2*}

¹ Department of Biological Sciences, Korea Advanced Institute of Science and Technology (KAIST), Daejeon, South Korea,

² Center for Synaptic Brain Dysfunctions, Institute for Basic Science, Daejeon, South Korea, ³ Department of Anatomy and Division of Brain Korea 21, Biomedical Science, College of Medicine, Korea University, Seoul, South Korea

OPEN ACCESS

Edited by:

Yi-Ping Hsueh,
Institute of Molecular Biology,
Academia Sinica, Taiwan

Reviewed by:

Carlo Sala,
Institute of Neuroscience (IN), Italy
Hyunsoo Shawn Je,
Duke-NUS Medical School,
Singapore

*Correspondence:

Eunjoon Kim
kime@kaist.ac.kr

[†] These authors have contributed
equally to the work

Received: 11 April 2019

Accepted: 17 May 2019

Published: 04 June 2019

Citation:

Shin W, Kweon H, Kang R, Kim D, Kim K, Kang M, Kim SY, Hwang SN, Kim JY, Yang E, Kim H and Kim E (2019) Scn2a Haploinsufficiency in Mice Suppresses Hippocampal Neuronal Excitability, Excitatory Synaptic Drive, and Long-Term Potentiation, and Spatial Learning and Memory. *Front. Mol. Neurosci.* 12:145. doi: 10.3389/fnmol.2019.00145

Nav1.2, a voltage-gated sodium channel subunit encoded by the *Scn2a* gene, has been implicated in various brain disorders, including epilepsy, autism spectrum disorder, intellectual disability, and schizophrenia. Nav1.2 is known to regulate the generation of action potentials in the axon initial segment and their propagation along axonal pathways. Nav1.2 also regulates synaptic integration and plasticity by promoting back-propagation of action potentials to dendrites, but whether Nav1.2 deletion in mice affects neuronal excitability, synaptic transmission, synaptic plasticity, and/or disease-related animal behaviors remains largely unclear. Here, we report that mice heterozygous for the *Scn2a* gene (*Scn2a*^{+/-} mice) show decreased neuronal excitability and suppressed excitatory synaptic transmission in the presence of network activity in the hippocampus. In addition, *Scn2a*^{+/-} mice show suppressed hippocampal long-term potentiation (LTP) in association with impaired spatial learning and memory, but show largely normal locomotor activity, anxiety-like behavior, social interaction, repetitive behavior, and whole-brain excitation. These results suggest that Nav1.2 regulates hippocampal neuronal excitability, excitatory synaptic drive, LTP, and spatial learning and memory in mice.

Keywords: sodium channel, neuronal excitability, synaptic transmission, synaptic plasticity, learning and memory, autism, intellectual disability, schizophrenia

INTRODUCTION

Voltage-gated sodium channels play critical roles in the regulation of action potential initiation and propagation (Catterall, 2017). Mutations in the *SCN2A* gene encoding the Nav1.2 subunit of the voltage-gated sodium channel α subunit have been strongly implicated in multiple neurodevelopmental disorders (Sanders et al., 2018), including forms of epileptic disorders such as infantile epileptic encephalopathy and benign familial infantile seizures (Sugawara et al., 2001; Heron et al., 2002; Berkovic et al., 2004; Kamiya et al., 2004; Ogiwara et al., 2009; Klassen et al., 2011; Carvill et al., 2013; Epi4K Consortium et al., 2013; Nakamura et al., 2013; Touma et al., 2013; Baasch et al., 2014; Howell et al., 2015; Parrini et al., 2017; Wolff et al., 2017), autism spectrum

disorders (ASD) (Weiss et al., 2003; Kamiya et al., 2004; Buxbaum et al., 2012; Sanders et al., 2012; Jiang et al., 2013; De Rubeis et al., 2014; Iossifov et al., 2014; Tavassoli et al., 2014; Codina-Sola et al., 2015; D’Gama et al., 2015; Deciphering Developmental Disorders Study, 2015; Krumm et al., 2015; Tammimies et al., 2015; Yuen et al., 2015; Turner et al., 2016; Wang T. et al., 2016; Geisheker et al., 2017; Krupp et al., 2017; Li et al., 2017; Stessman et al., 2017; Trujillano et al., 2017; Wolff et al., 2017), intellectual disability (Kamiya et al., 2004; de Ligt et al., 2012; Rauch et al., 2012; Bowling et al., 2017; Hamdan et al., 2017; Stessman et al., 2017; Wolff et al., 2017; Cherot et al., 2018; Yokoi et al., 2018), and schizophrenia (Fromer et al., 2014; Carroll et al., 2016). SCN2A mutations that lead to a gain of Nav1.2 function are thought to induce early onset epilepsy, whereas those that lead to a loss of Nav1.2 function induce ASD and intellectual disability (Ben-Shalom et al., 2017; Wolff et al., 2017; Sanders et al., 2018). However, the underlying pathophysiology, particularly for ASD and intellectual disability, remains largely unclear.

Nav1.2 is strongly expressed in the brain together with Nav1.1, Nav1.3, and Nav1.6 (Trimmer and Rhodes, 2004; Vacher et al., 2008; Catterall, 2017), and displays distinct spatiotemporal distribution patterns in various brain regions and at subcellular sites (Westenbroek et al., 1989; Gong et al., 1999; Boiko et al., 2001, 2003; Van Wart and Matthews, 2006; Kole et al., 2008; Hu et al., 2009; Liao et al., 2010; Li et al., 2014; Tian et al., 2014; Yamagata et al., 2017). For instance, Nav1.2 is mainly expressed in excitatory neurons in brain regions including the neocortex, hippocampus, and cerebellum (Trimmer and Rhodes, 2004; Vacher et al., 2008). Although Nav1.2 is primarily localized to axonal and nerve terminal regions, it is also detected in apical dendrites of neocortical and hippocampal pyramidal neurons (Westenbroek et al., 1989; Gong et al., 1999), as well as in the postsynaptic density of CA1 pyramidal synapses (Johnson et al., 2017).

At the neonatal stage, Nav1.2 serves as the main sodium channel subunit concentrated in the axon and axon initial segment (AIS) – a membrane specialization in proximal axons responsible for action potential generation (Bender and Trussell, 2012; Kole and Stuart, 2012). At later stages, its expression decreases in favor of Nav1.6 (Boiko et al., 2001, 2003; Kaplan et al., 2001; Liao et al., 2010; Gazina et al., 2015), which localizes to the distal side of the AIS and plays a critical role in action potential generation. At this stage, Nav1.2 comes to reside in the proximal side of the AIS and contributes to back-propagation of action potentials to dendritic and synaptic compartments (Hu et al., 2009), known to promote synaptic integration and plasticity (Magee and Johnston, 1997; Bi and Poo, 1998; Koester and Sakmann, 1998; Larkum et al., 1999; Johnston et al., 2003; Feldman, 2012; Kim et al., 2015).

Recent studies have shown that mice with a heterozygous deletion of *Scn2a* display absence-like seizure (Ogiwara et al., 2018) and impaired spatial working and reference memory, effects that are associated with altered hippocampal replay content (Middleton et al., 2018). However, although a recent study has suggested a novel role for Nav1.2 in regulating dendritic GABA release in granule cells in the olfactory bulb (Nunes and Kuner, 2018), *in vivo* evidence supporting the dendritic and

synaptic roles of Nav1.2 is limited. In addition, whether mice heterozygous for *Scn2a* display behavioral phenotypes related to ASD and intellectual disability remains unclear.

In the present study, we generated a new heterozygous *Scn2a* mutant mouse line in which one allele contains a deletion of exons 4–6. We found that these mice display decreases in neuronal excitability, excitatory synaptic drive, and long-term potentiation (LTP) in the hippocampus. They also show decreased hippocampus-dependent spatial learning and memory, but largely normal locomotor activity, anxiety-like behavior, social interaction, repetitive behavior, and whole-brain excitation.

MATERIALS AND METHODS

Animals

Floxed *Scn2a* mice in a C57BL/6J genetic background carrying a deletion of exons 4–6 of the *Scn2a* gene (encompassing the 5′ untranslated region and the first 158 amino acids of the protein) flanked by loxP sites and a neomycin cassette (*Scn2a^{cassette/+}*) were designed and generated by Biocytogen. The neomycin cassette was removed by crossing *Scn2a^{cassette/+}* mice with protamine-Flp mice (C57BL/6J), yielding floxed heterozygous mice (*Scn2a^{f/+}*). *Scn2a^{+/-}* mice were subsequently obtained by *in vitro* fertilization of eggs from female *Scn2a^{f/+}* mice with sperm from male C57BL/6J mice. To accelerate the generation of *Scn2a^{+/-}* mice, we treated fertilized eggs at the two-cell embryo stage with purified HTNC, a cell-permeable Cre recombinase (see below for details), in media at a final concentration of 0.3 μM for 30–40 min. After treating with HTNC, the embryos were washed and transferred to surrogate ICR female mice. *Scn2a^{+/+}*, *Scn2a^{+/-}*, and *Scn2a^{-/-}* mice were genotyped by polymerase chain reaction (PCR) using the following primer sets: set 1, 5′-TGG AGC GCT GAA GTT CCT ATT-3′ (forward 1) and 5′-ATG CTG TGC TAG GGG TTG GA-3′ (reverse 1); and set 2, 5′-TGT TGG CAT TCT GCA TGA CAT T-3′ (forward 2) and 5′-AGG CAG TAC CAT TCC AAT CCA-3′ (reverse 2). Young mice were weaned at approximately postnatal day 21–27 (P21–27). After weaning, a maximum of eight littermates of mixed genotype were group-housed before experiments. Animals were housed under a 12-h (13:00–01:00) dark/light cycle and were fed *ad libitum*. All animals were bred and maintained according to the Requirements of Animal Research at KAIST, and all procedures were approved by the Committees of Animal Research at KAIST (KA2016-31).

Expression and Purification of HTNC

The pTriEx-HTNC construct encoding HTNC (histidine-TAT-NLS-Cre), a His₆-tagged Cre recombinase rendered cell permeable by incorporation of the cell-penetrating TAT peptide (Peitz et al., 2002), was a kind gift from Dr. Klaus Rajewsky (AddGene plasmid #13763). *Escherichia coli* strain BL21 (DE3) (Enzynomics) was transformed with the HTNC construct and cultured in Luria-Bertani (LB) medium containing 50 μg/ml ampicillin to an optical density at 600 nm (OD₆₀₀) of 0.5–0.6, at which point expression of recombinant HTNC protein was induced by addition of 0.5 mM isopropyl-β-D-thiogalactoside

(IPTG). After culturing for an additional 4 h at 37°C in the presence of IPTG, cells were harvested and resuspended in a buffer consisting of 50 mM Tris-HCl (pH 8.0), 500 mM NaCl, and 30 mM imidazole, and then lysed by sonication. HTNC proteins were initially purified using a histidine affinity column (GE Healthcare). Thereafter, the HTNC buffer was changed to an imidazole-free, low-salt buffer (50 mM Tris-HCl pH 8.0, 100 mM NaCl), and HTNC proteins were further purified by cation exchange chromatography using an SP column (GE Healthcare). Purified proteins were then exchanged into phosphate-buffered saline (PBS) using a PD-10 desalting column (GE Healthcare) and concentrated using a Centricon-YM10 centrifugal concentrator (Millipore).

Brain Homogenates and Immunoblotting

Brain homogenates from *Scn2a*^{+/+}, *Scn2a*^{+/-}, and *Scn2a*^{-/-} mice were prepared as described previously (Lee et al., 2015). Briefly, mouse brains (2 months for *Scn2a*^{+/+} and *Scn2a*^{+/-} mice; embryonic day 20.5 for *Scn2a*^{-/-}) were homogenized in ice-cold homogenization buffer (0.32 M sucrose, 10 mM HEPES, pH 7.4, 2 mM EDTA, protease inhibitors and phosphatase inhibitors). Brain lysates were immunoblotted with Nav1.2 antibodies (Alomone, ASC-002, 1:200 or NeuroMab, K69/3, 1:500).

Immunohistochemistry

After cardiac perfusion of adult mice (3 months) using 1% heparin and subsequent 4% paraformaldehyde (PFA), brains were stored in 4% PFA for more than 1 day. Coronal sections (40 μm), prepared using a vibratome (Leica), were blocked with 5% goat serum, 0.2% TritonX-100 for 1 h and incubated with primary antibodies (1:500 for NeuN) for 24 h. After washing with PBS three times, sections were incubated with fluorophore-conjugated secondary antibodies (1:1000) in PBS with 0.2% Triton X-100 (Jackson ImmunoResearch). After washing with PBS, sections were mounted with VECTASHIELD (Vector Laboratory), and images were acquired using an LSM-780 confocal microscope (Zeiss).

Radioisotope *in situ* Hybridization

Mouse brain sections (14 μm thick) at embryonic day (E18) and postnatal days (P0, P7, P14, P21, and P56) were prepared using a cryostat (Leica CM 1950). Hybridization probes specific for mouse *Scn2a* mRNAs were prepared using the following regions: nt 181–480 (N-term) and nt 6060–6359 (C-term) of *Scn2a* (NM_001099298.2). Antisense riboprobes were generated using ³⁵S-uridine triphosphate (UTP) and the Riboprobe system (Promega).

Fluorescence *in situ* Hybridization

Frozen mouse brain sections (14 μm thick) were cut coronally through the hippocampal formation. Sections were thaw-mounted onto Superfrost Plus Microscope Slides (Fisher Scientific 12-550-15). The sections were fixed in 4% PFA for 10 min, dehydrated in increasing concentrations of ethanol for 5 min, and finally air-dried. Tissues were then pretreated

for protease digestion for 10 min at room temperature. For RNA detection, incubations with different amplifier solutions were performed in a HybEZ hybridization oven (ACDBio) at 40°C. The probes used in this study were three synthetic oligonucleotides complementary to the nucleotide (nt) sequence 2973–4072 of Mm-Scn2a-C1, nt 464–1415 of Mm-Slc17a7/Vglut1-C2, nt 1986–2998 of Mm-Slc17a6/Vglut2-C3, nt 62–3113 of Mm-Gad1-C3, nt 552–1506 of Mm-Gad2-C2, nt 2–885 of Mm-Pvalb, nt 18–407 of Mm-SST-C3, and nt 124–1280 of Mm-VIP-C3 (ACDBio, Newark, CA, United States). The labeled probes were conjugated to Atto 550 (C1), Alexa Fluor 488 (C2), and Atto 647 (C3). The sections were hybridized at 40°C with labeled probe mixtures (C1 + C2 + C3) per slide for 2 h. Then the nonspecifically hybridized probes were removed by washing the sections, three times each in 1× wash buffer at room temperature for 2 min. Amplification steps involved sequential incubations with Amplifier 1-FL for 30 min, Amplifier 2-FL for 15 min, Amplifier 3-FL for 30 min, and Amplifier 4 Alt B-FL at 40°C for 15 min. Each amplifier solutions were removed by washing three times with 1× wash buffer for 2 min at room temperature. Fluorescent images were acquired using TCS SP8 Dichroic/CS (Leica), and the ImageJ program (NIH) was used to analyze the images.

Brain Slices for Electrophysiology

For hippocampal electrophysiology experiments, acute sagittal brain slices (300 μm thickness for whole-cell patch and 400 μm for field recordings) of *Scn2a*^{+/+} and *Scn2a*^{+/-} mice were obtained using a vibratome (Leica VT1200) after anesthetizing animals with isoflurane (Terrell). Brains were extracted and sliced in ice-cold dissection buffer containing (in mM) 212 sucrose, 25 NaHCO₃, 5 KCl, 1.25 NaH₂PO₄, 0.5 CaCl₂, 3.5 MgSO₄, 10 D-glucose, 1.25 L-ascorbic acid, and 2 Na-pyruvate bubbled with 95% O₂/5% CO₂. The slices were transferred to a recovery chamber at 32°C with normal ACSF (in mM: 125 NaCl, 2.5 KCl, 1.25 NaH₂PO₄, 25 NaHCO₃, 10 glucose, 2.5 CaCl₂, and 1.3 MgCl₂, oxygenated with 95% O₂/5% CO₂). After 30-min recovery at 32°C, slices were recovered for additional 30 min at 20–25°C. For the recording, a single slice was transferred to a submerged-type chamber at 27–28°C with circulating ACSF (2 ml/min) saturated with 95% O₂ and 5% CO₂. Stimulation and recording pipettes were pulled from thin-walled borosilicate glass capillaries (30–0065, Harvard Apparatus) with resistance 2.5–3.5 MΩ using a micropipette electrode puller (PC-10, Narishege).

Whole-Cell Patch

Whole-cell patch-clamp recordings of hippocampal CA1 pyramidal neurons were made using a MultiClamp 700B amplifier (Molecular Devices) and Digidata 1550 (Molecular Devices). During whole-cell patch-clamp recordings, series resistance was monitored each sweep by measuring the peak amplitude of the capacitance currents in response to short hyperpolarizing step pulse (5 mV, 40 ms); only cells with a change in <20% were included in the analysis. To measure the intrinsic excitability of hippocampal CA1 cells, recording pipettes (2.5–3.5 MΩ) were filled with an internal solution containing (in mM) 137 K-gluconate, 5 KCl, 10 HEPES, 0.2

EGTA, 10 Na-phosphocreatine, 4 Mg-ATP, and 0.5 Na-GTP, with pH 7.2, 280 mOsm. To inhibit postsynaptic responses, picrotoxin (100 μ M), NBQX (10 μ M) and D-AP5 (50 μ M) were added. After rupturing the cell, currents were clamped, and resting membrane potential (RMP) was measured. Cells with RMP larger than -60 mV were not used. After stabilizing cells, RMP was adjusted by -65 mV. Current inputs were increased from 0 to 330 pA in increments of 30 pA per sweep. Each current was injected with the time interval of 15 s. For mEPSCs in hippocampal CA1 pyramidal neurons, recording pipettes (2.5–3.5 M Ω) were filled with an internal solution containing (in mM) 100 CsMeSO₄, 10 TEA-Cl, 8 NaCl, 10 HEPES, 5 QX-314-Cl, 2 Mg-ATP, 0.3 Na-GTP, and 10 EGTA, with pH 7.25, 295 mOsm. Whole-cell recordings of mEPSCs were obtained in neurons at a holding potential of -70 mV. TTX (1 μ M) and picrotoxin (100 μ M) were added to ACSF to inhibit spontaneous action potential-mediated synaptic currents and inhibitory postsynaptic currents (IPSCs), respectively. For recordings of spontaneous excitatory postsynaptic currents (sEPSCs), only picrotoxin (100 mM) were added to ACSF. For hippocampal CA1 pyramidal neuron mIPSCs, recording pipettes (2.5–3.5 M Ω) were filled with an internal solution containing (in mM) 120 CsCl, 10 TEA-Cl, 8 NaCl, 10 HEPES, 5 QX-314-Cl, 4 Mg-ATP, 0.3 Na-GTP and 10 EGTA, with pH 7.35, 280 mOsm. TTX (1 μ M), NBQX (10 μ M) and D-AP5 (50 μ M) were added to ACSF to inhibit spontaneous action potential-mediated synaptic currents, AMPAR-mediated currents and *N*-methyl-*D*-aspartate receptor (NMDAR)-mediated currents, respectively. For the recording of spontaneous inhibitory postsynaptic currents (sIPSCs), NBQX (10 μ M) and D-AP5 (50 μ M) were added to ACSF. For measuring NMDAR/AMPA ratio, CA1 pyramidal neurons were voltage clamped at -70 mV, and EPSCs were evoked at every 15 s. AMPAR-mediated EPSCs were recorded at -70 mV, and 20 consecutive responses were recorded after stable baseline. After recording AMPAR-mediated EPSCs, holding potential was changed to $+40$ mV to record NMDAR-mediated EPSCs. NMDA component was measured at 60 ms after the stimulation. The NMDA/AMPA ratio was determined by dividing the mean value of 20 NMDA components of EPSCs by the mean value of 20 AMPAR-mediated EPSC peak amplitudes. Data were acquired by Clampex 10.2 (Molecular Devices) and analyzed by Clampfit 10 (Molecular Devices). Drugs were purchased from Abcam (TTX), Tocris (NBQX, D-AP5), and Sigma (picrotoxin).

Field Recording

In field recordings, fEPSPs were recorded in the stratum radiatum of the hippocampal CA1 region using pipettes filled with ACSF. fEPSPs were amplified (MultiClamp 700B, Molecular Devices) and digitized (Digidata 1550, Molecular Devices) for measurements. The Schaffer collateral pathway was stimulated, and baseline responses were collected every 20 s with a stimulation intensity that yielded a half-maximal response. For input/output experiments, after acquiring a stable baseline, a series of increasing input stimuli were given to evoke output signals. Measured fEPSP slopes and fiber volleys were then interpolated by linear fits to plot input/output relationships.

For paired-pulse ratio experiments, stimuli with indicated inter-pulse intervals (25, 50, 75, 100, 200, 300 ms) were given, pairs of peak amplitudes were recorded, and the ratio of that amplitudes was calculated. To induce LTP and long-term depression (LTD) at Schaffer collateral synapses on CA1 pyramidal neurons, high-frequency stimulation (100 Hz, 1 s), theta-burst stimulation (10 trains of 4 pulses at 100 Hz), or low-frequency stimulation (1 Hz, 15 min), was applied. Data were acquired by Clampex 10.2 (Molecular Devices) and analyzed by Clampfit 10 (Molecular Devices).

Animal Behavioral Tests

All behavioral assays were performed using littermates or age-matched male animals during light-off periods, except for automated 48-h movement analyses in LABORAS cages. All behavioral test results were performed and analyzed in a blinded manner.

Three-Chamber Social Interaction Test

The three-chamber test (Silverman et al., 2010) was performed as described previously (Won et al., 2012; Chung et al., 2015). Briefly, a subject mouse was placed in the center region of the three-chamber apparatus, which contains a center and two side chambers. In the first session, the subject mouse was allowed to freely move around the whole three chambers for 10 min. The mouse was then gently confined in the center chamber while a novel “Object” and a wild-type (WT) stranger mouse “Stranger 1 (129Sv strain)” was placed in the containers in the two side chambers. The subject mouse was then allowed to freely explore all three chambers for 10 min. In the third session, the subject mouse was again gently guided to the center chamber while the “Object” was replaced with a WT “Stranger 2” mouse. The subject mouse was again allowed to freely explore all three chambers for 10 min.

Direct Interaction Test and Juvenile Play Test

Each mouse was habituated in a direct social interaction box for 30 min on the day before the experiment. On test day, pairs of mice in the same age, sex, and genotype that have not met before were placed in a direct interaction box, and their interactions were recorded for 10 min. For the juvenile play test, subject mice were habituated in a new home cage with bedding for 1 h, after isolation from their mothers and siblings, on test day. Pairs of mice in the same age, sex, and genotype that have not met before were placed in a new home cage without bedding, and their interactions were recorded for 10 min. Nose-to-nose sniffing, following, mounting, and allo-grooming were quantified manually and pooled to calculate total social interaction.

Ultrasonic Vocalization Test

An ultrasound microphone (Avisoft) and Avisoft Recorder software were used to record mice ultrasonic vocalizations (USVs). For recording adult USVs, subject male mice were placed in a home cage with an age-matched unfamiliar C57BL/6J female counterpart, and USVs were recorded for 5 min. For

pup USVs, pups at the age of postnatal day 4, 6, 8, and 10 were separated from dams and placed in a glass container, and USVs were recorded for 3 min. Recorded USVs were analyzed as previously described (Kim et al., 2018). Briefly, Avisoft SASLab Pro software (RRID:SCR_014438) was used to analyze USVs. Signals were filtered from 1 Hz to 100 kHz and digitized with a sampling frequency of 250 kHz, 16 bits per sample (Avisoft UltraSoundGate 116H). To generate spectrograms, the following parameters were used: FFT length, 256; frame size, 100; window, FlatTop; overlap, 75%, which resulted in a frequency resolution of 977 Hz and a temporal resolution of 0.256 ms. Frequencies lower than 45 kHz were filtered out to reduce background white noises.

Repetitive Behaviors Test

For repetitive behaviors tests using adult mice, a subject mouse was placed in a novel and transparent grooming chamber (40 cm × 15 cm × 15 cm), and their behaviors were recorded through transparent side faces for 20 min. Self-grooming and rearing behaviors from the last 10 min were quantified manually. For juvenile repetitive behaviors, subject mice were placed in a new home cage without bedding, and their behaviors were recorded for 15 min. Self-grooming behavior from the last 10 min was quantified manually.

Open-Field Test

Mice were placed in an open field box (40 cm × 40 cm × 40 cm) and recorded for 60 min (20 min for juvenile open-field test). The center zone line was 10 cm apart from the edge. The testing room was illuminated at ~100 lux. Mice movements were analyzed using EthoVision XT 10 program (Noldus).

Automated 48-h Movement Analysis (LABORAS Test)

For a long-term and real-time movement analysis, we used the LABORAS system (Metris), designed to detect and analyze vibrations delivered from a cage to a carbon-fiber vibration-sensitive plate placed underneath the cage with a mouse. Each mouse was placed in the LABORAS cage without habituation. After recording for 96 h, the data from all 96 h were analyzed using LABORAS software.

Elevated Plus-Maze Test

The elevated plus-maze consisted of two open arms, two closed arms, and a center zone, and was elevated to a height of 50 cm above the floor. Mice were placed in the center zone and allowed to explore the space for 8 min. The data was analyzed using EthoVision XT 10 program (Noldus).

Light-Dark Chamber Test

The apparatus for the light-dark test consisted of light (~300 lux) and dark (~0 lux) chambers adhered to each other. The size of the light chamber was 20 cm × 30 cm × 20 cm, and that of the dark chamber was 20 cm × 13 cm × 20 cm. An entrance enabled mice to freely move across the light and dark chambers. Mice were introduced to the center of the light chamber and allowed to explore the apparatus freely for 10 min. The time spent in dark

and light chambers and the number of transitions were measured using EthoVision XT 10 program (Noldus).

Seizure Susceptibility Test

Immediately before behavioral tests, the subject mouse received an intraperitoneal injection of pentylenetetrazol (PTZ) (40 mg/kg), or the same volume of saline, and was then allowed to acclimate to a novel cage with bedding for 10 min under low-light (60 lux) conditions. Seizure susceptibility was measured in a blinded manner based on the following behaviors: movement slowing (Phase 1), myoclonic jerk (Phase 2), clonic and generalized tonic seizure (Phase 3), and death (Phase 4). A seizure-susceptibility score was determined according to a modified Racine scale (Ferraro et al., 1999; Naydenov et al., 2014).

Morris Water Maze Test

Mice were trained to find the hidden platform (10 cm diameter) in a white plastic tank (120 cm diameter). Mice were given three trials per day with an inter-trial interval of 30 min. The learning phase of the water maze was performed for seven consecutive days, followed by the probe test on day 8 where mice were given 1 min to find the removed platform. For reversal training (days 9–11), the location of the platform was switched to the opposite position from the previously trained position, and mice were trained to learn the new position of the platform. Target quadrant occupancy and the exact number of crossings over the former platform location during the probe test were measured using EthoVision 10 program (Noldus).

Rotarod Test

Mice were placed on the rotating rod for 10 s, followed by the start of rod rotation. The rotating speed of rod was gradually increased from 4 to 40 rpm over 5 min. The assay was performed for two consecutive days and three times per day, while measuring the latencies of mice falling from the rod or showing 360-degree rotation on the rod twice.

Novel Object Recognition Test

Object recognition test was performed in the open field box. On the first day, mice were allowed to explore two identical objects for 10 min. Twenty-four hours later, mice were placed the same box where one of the two objects was replaced with a new one. Exploration time for each object was measured. Object exploration was defined by the mouse's nose being oriented toward the object and came within 2 cm of it as measured by EthoVision XT 10 program (Noldus).

Contextual Fear Conditioning Test

All experiments were carried out in a fear conditioning system (Coulbourn Instruments). Training and testing were performed in a Plexiglas chamber with a stainless steel grid floor. On the training day, mice were placed in the fear chamber and allowed to freely move around the chamber for 2 min before they received five foot shocks (2 s, 0.8 mA, 1 min apart). To measure fear conditioning, mice were re-exposed the same

chamber for 5 min without foot shock 24 h, or 7 days (in a separate cohort), after training.

Maternal Homing Test

Maternal homing test was performed as previously described (Jung et al., 2018). Juvenile mice were separated from their mothers for at least 30 min before testing. The testing consists of a nest homing phase followed by a maternal homing phase. For the nest homing phase, bedding materials from the original home cage (Home) and fresh bedding (New) were placed in the opposite corner of open field box, previously described. Subject mice were placed in one empty corner, and their behaviors were recorded for 3 min. For the maternal homing phase, an empty container and container with the mother of the subject mice were placed in the two opposite empty corners of the box after finishing 3 min nest homing phase. Subject mice were placed in corner of bedding from home cage, and their behaviors were recorded for 5 min. Time spent with bedding and time spent sniffing containers was quantified using EthoVision XT 10 program (Noldus).

Statistics

Statistical analyses were performed using GraphPad Prism 7. Normally distributed data were analyzed using Student's *t*-test, whereas data that did not conform to a normal distribution were analyzed using the non-parametric Mann-Whitney test. For data that were normally distributed but exhibited a significant difference in variance in the *F*-test, Welch's correction was used. Outliers were determined using ROUT test. All details of statistical analyses, including the sex, age and number of mice, are described in **Supplementary Table 1**.

RESULTS

Generation of *Scn2a*^{+/-} Mice and Characterization of *Scn2a* mRNA Expression

To determine whether *Scn2a* haploinsufficiency in mice leads to any changes in synaptic, neuronal or behavioral phenotypes, we generated *Scn2a*^{+/-} mice carrying a heterozygous deletion of the *Scn2a* gene (exons 4–6 covering aa 159–300 of Nav1.2; **Figures 1A,B**). This region also contains two exon 5 splice variants – 5N/neonatal and 5A/adult – that are known to show a neonatal-to-adult shift during postnatal brain development in mice and rats and are thought to differentially regulate neuronal excitability (Gustafson et al., 1993; Gazina et al., 2010, 2015). After removal of the neomycin cassette by crossing with a flippase-expressing mouse, the region containing exons 4–6 of the *Scn2a* gene was deleted by incubating fertilized eggs at the two-cell stage with purified, recombinant, cell-permeable HTNC (histidine-TAT-NLS-Cre) recombinase (Peitz et al., 2002) (see section “Materials and Methods” for details).

Immunoblot analyses of whole-brain lysates from 2-month-old mice using an anti-Nav1.2 antibody directed against aa 467–485 of Nav1.2 showed that Nav1.2 protein levels in the

resulting *Scn2a*^{+/-} mice were approximately ~60% of those in WT mice (**Figure 1C**). The gross morphology of the *Scn2a*^{+/-} mouse brain was normal, as determined by immunostaining for NeuN (neuronal marker) (**Figure 1D**). Homozygous *Scn2a*^{-/-} mice showed near complete elimination of Nav1.2 proteins and exhibited perinatal lethality, consistent with a previous report (Planells-Cases et al., 2000).

To determine the distribution pattern of *Scn2a* mRNA in the mouse brain at various developmental stages [embryonic day 18 (E18), P0, P7, P14, P21, and P56], we performed *in situ* hybridization experiments using horizontal and sagittal mouse brain sections and two independent radiolabeled probes targeting 5' and 3' regions of the *Scn2a* mRNA. These experiments revealed *Scn2a* mRNA signals in various brain regions, including the neocortex, hippocampus, striatum, thalamus, and cerebellum; similar results were obtained for 5' and 3' probes, although signals were stronger using the 5' probe (**Figure 1E**).

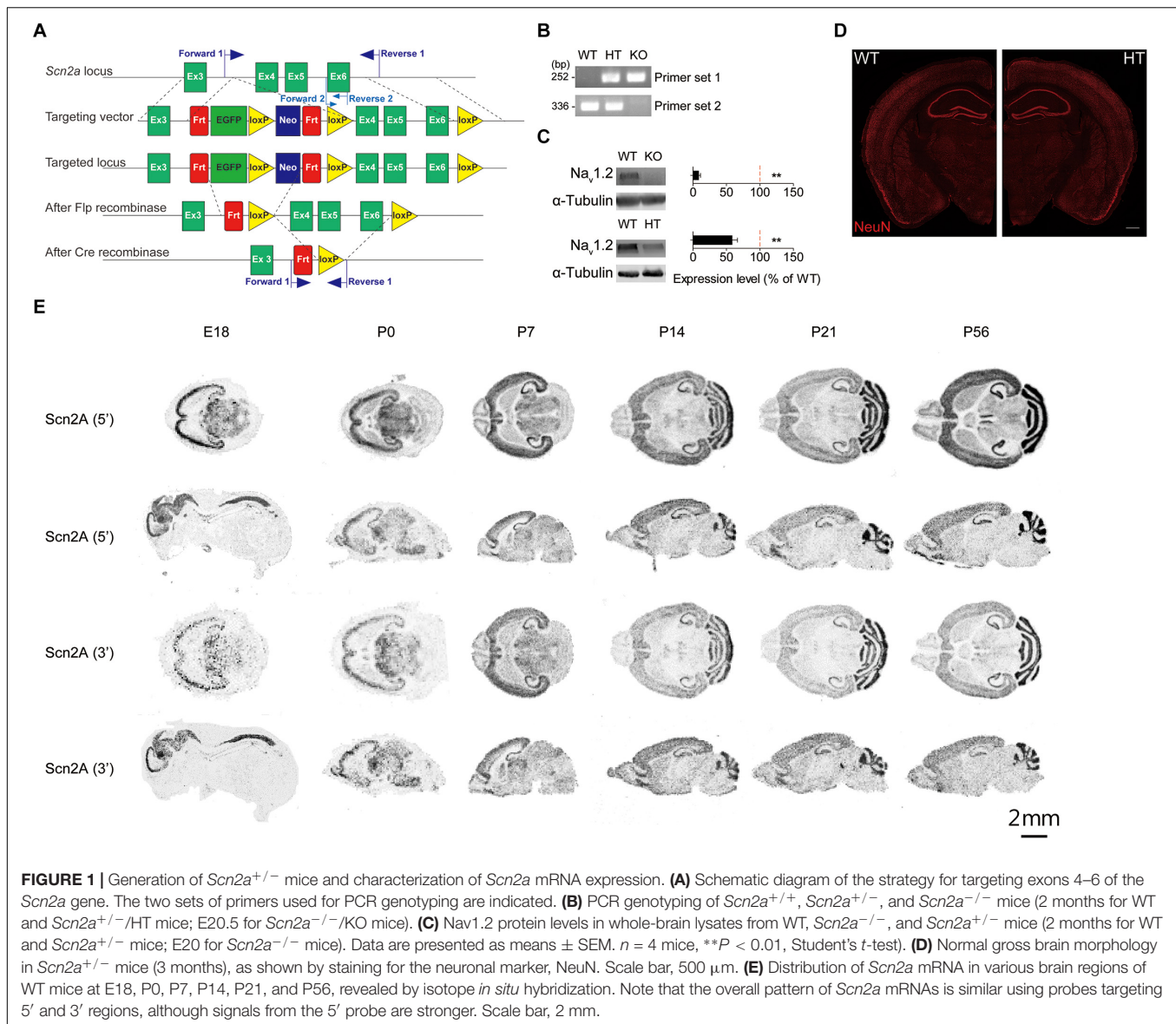
Scn2a Expression in Glutamatergic and GABAergic Neurons

Previous studies reported that Nav1.2 proteins are detected in glutamatergic neurons (Trimmer and Rhodes, 2004; Vacher et al., 2008) and GABAergic neurons with a caudal ganglionic eminence origin, such as vasoactive intestinal polypeptide (VIP)-positive neurons and reelin-positive/somatostatin (SST)-negative neurons in the neocortex and hippocampus (Yamagata et al., 2017). Another study, however, has reported that Nav1.2 is expressed in SST-positive, but not parvalbumin (PV)-positive, neurons in the neocortex (Li et al., 2014). To gain additional insights into the expression of *Scn2a* in glutamatergic and GABAergic neurons in mice at the mRNA level, we attempted double/triple fluorescence *in situ* hybridization for *Scn2a* and markers of glutamatergic (Vglut1/2) and GABAergic (Gad1/2) neurons using the RNA Scope method, which is known to substantially enhance signal amplification and suppress background (Wang et al., 2012).

Scn2a mRNA was detected in both glutamatergic and GABAergic neurons in the neocortex and hippocampus of the mouse brain at P56 (**Figures 2A,B**). *Scn2a* mRNA was also detected in various subtypes of GABAergic neurons, including those expressing SST and VIP, although signals in PV-positive neurons were largely absent in the cortex and weak in the hippocampus (**Figures 2C–E**). These mRNA analysis results are partly similar to the previous reports (Li et al., 2014; Yamagata et al., 2017), although our results are from mRNA analysis. These results suggest that *Scn2a* is expressed in both glutamatergic and GABAergic neurons in the mouse brain at least at the mRNA level.

Decreased Neuronal Excitability and Suppressed Excitatory Synaptic Transmission in the Presence of Network Activity in the *Scn2a*^{+/-} Hippocampus

Nav1.2 regulates action potential initiation and propagation in the AIS in neonatal neurons (Catterall, 2017) and



back-propagation of action potentials to somatic and dendritic compartments to regulate synaptic integration and plasticity in more mature neurons (Hu et al., 2009), suggesting that *Scn2a* haploinsufficiency in mice might alter neuronal properties or synaptic functions.

To test this, we first measured the excitability of *Scn2a*^{+/-} pyramidal neurons in the hippocampal CA1 region. *Scn2a*^{+/-} neurons showed reduced input resistance, suggesting modestly decreased intrinsic excitability, but the current-firing relationship showed only a tendency toward a decrease (Figures 3A,B).

Notably, in the presence of network activity, achieved by omitting tetrodotoxin in the recording solution, the frequency and amplitude of sEPSCs in *Scn2a*^{+/-} CA1 pyramidal neurons were significantly reduced (Figure 3C). In contrast, sIPSCs were normal in *Scn2a*^{+/-} neurons (Figure 3D). These results suggest that, in the presence of network activity, *Scn2a* haploinsufficiency

suppresses intrinsic excitability and excitatory transmission, but not inhibitory synaptic transmission, in hippocampal neurons in the presence of network activity.

In contrast to these changes, miniature excitatory and inhibitory postsynaptic currents (mEPSCs and mIPSCs, respectively) were normal in *Scn2a*^{+/-} CA1 pyramidal neurons (Figures 3E,F). These results collectively suggest that excitatory network activity is strongly decreased in the hippocampus of *Scn2a*^{+/-} mice.

Scn2a Haploinsufficiency Suppresses Long-Term Potentiation

Back-propagation of action potentials regulates dendritic excitability and synaptic integration and plasticity (Magee and Johnston, 1997; Bi and Poo, 1998; Koester and Sakmann, 1998; Larkum et al., 1999; Johnston et al., 2003; Feldman, 2012;

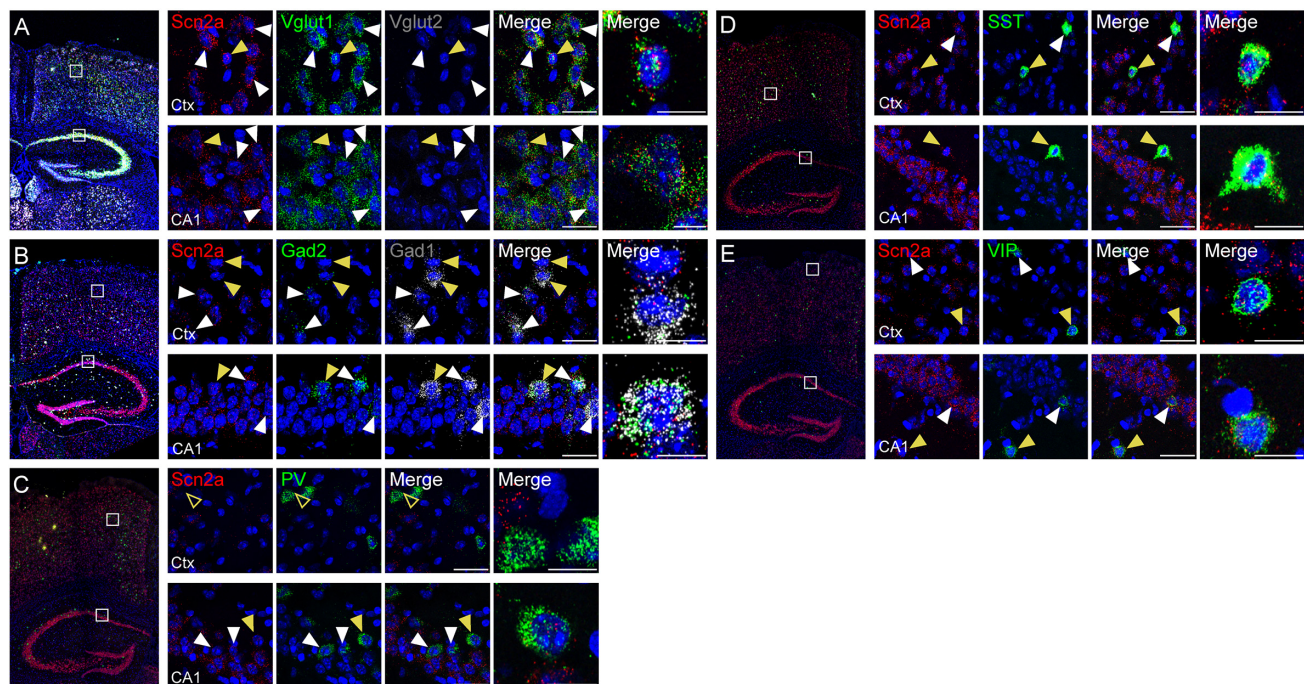


FIGURE 2 | Expression of *Scn2a* mRNA in both glutamatergic and GABAergic neurons. **(A,B)** Expression of *Scn2a* mRNAs in Vglut1/2-positive glutamatergic neurons **(A)** and Gad1/2-positive GABAergic neurons **(B)** in the neocortex and hippocampus in the mouse brain (P56), as detected by fluorescence *in situ* hybridization. Coronal brain sections were triply stained for *Scn2a*, Vglut1/2 or Gad1/2, and DAPI (nuclear stain; blue). Images at right show enlarged views of white boxes in the images at left. Arrowheads indicate neurons that express both *Scn2a* and neuronal markers; cells indicated by yellow arrowheads were further enlarged to highlight coexpression of the markers. Scale bar, 20 and 10 μ m for left and right scale bars, respectively, in each row. **(C–E)** Expression of *Scn2a* mRNA in PV-, SST-, or VIP-expressing GABAergic neurons in the neocortex and hippocampus in the mouse brain (P56), as detected by fluorescence *in situ* hybridization. Scale bar, 20 and 10 μ m for left and right scale bars, respectively, in each row.

Kim et al., 2015), suggesting the possibility that *Scn2a*^{+/-} SC-CA1 synapses may display altered synaptic plasticity.

Levels of basal excitatory synaptic transmission in the Schaffer collateral-CA1 pathway (SC-CA1) were normal in the *Scn2a*^{+/-} hippocampus, as shown by the input-output relationship between fiber volley and fEPSP slope in field recordings (**Figure 4A**). In addition, these synapses showed normal levels of paired-pulse facilitation (**Figure 4B**), suggestive of unaltered presynaptic release.

An assessment of synaptic plasticity showed that LTP induced by high-frequency stimulation was suppressed at *Scn2a*^{+/-} SC-CA1 synapses (**Figure 4C**). Similarly, LTP-induced by theta-burst stimulation was suppressed at *Scn2a*^{+/-} SC-CA1 synapses (**Figure 4D**). In contrast, LTD at *Scn2a*^{+/-} SC-CA1 synapses was normal (**Figure 4E**).

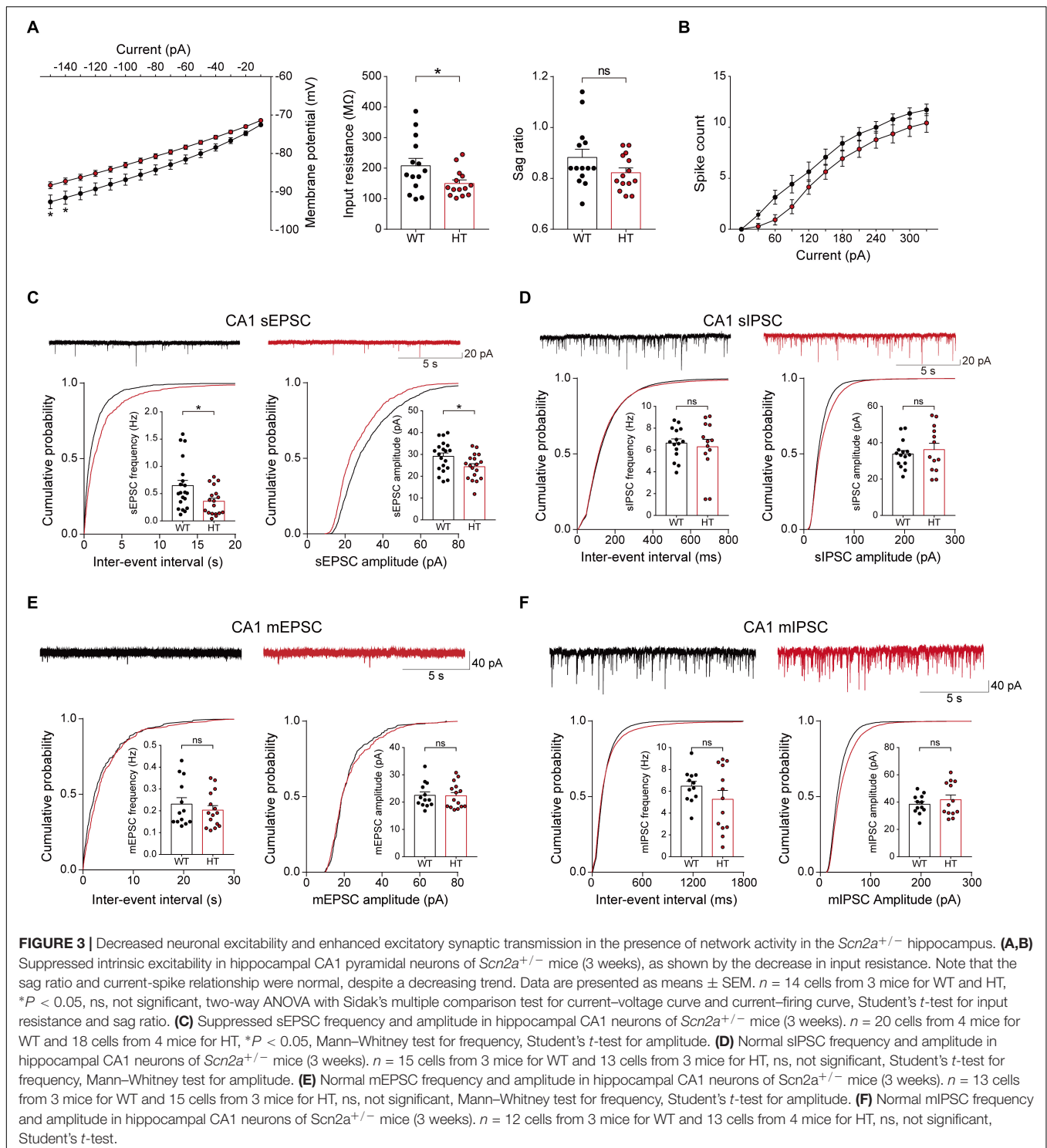
Given that both LTP and LTD are mediated by NMDARs (Malenka and Bear, 2004; Collingridge et al., 2010), the suppressed LTP, which contrasts with the normal LTD, is unlikely to involve a decrease in NMDAR function. Indeed, in patch-clamp recordings, *Scn2a*^{+/-} SC-CA1 synapses showed a normal ratio of NMDAR- to AMPA (α -amino-3-hydroxy-5-methyl-4-isoxazolepropionic acid) receptor (AMPA)-mediated synaptic transmission (**Figure 4F**). Taken together with the normal AMPAR-mediated synaptic transmission, implied by the results of spontaneous (mEPSC) and evoked (input-output)

excitatory transmission (**Figures 3E, 4A**), this indicates that NMDAR-mediated synaptic transmission at *Scn2a*^{+/-} SC-CA1 synapses is normal. Collectively, these results suggest that *Scn2a* haploinsufficiency suppresses LTP without affecting LTD through mechanisms independent of NMDAR-mediated synaptic transmission.

Scn2a^{+/-} Mice Display Impaired Spatial Learning and Memory but Enhanced Fear Memory

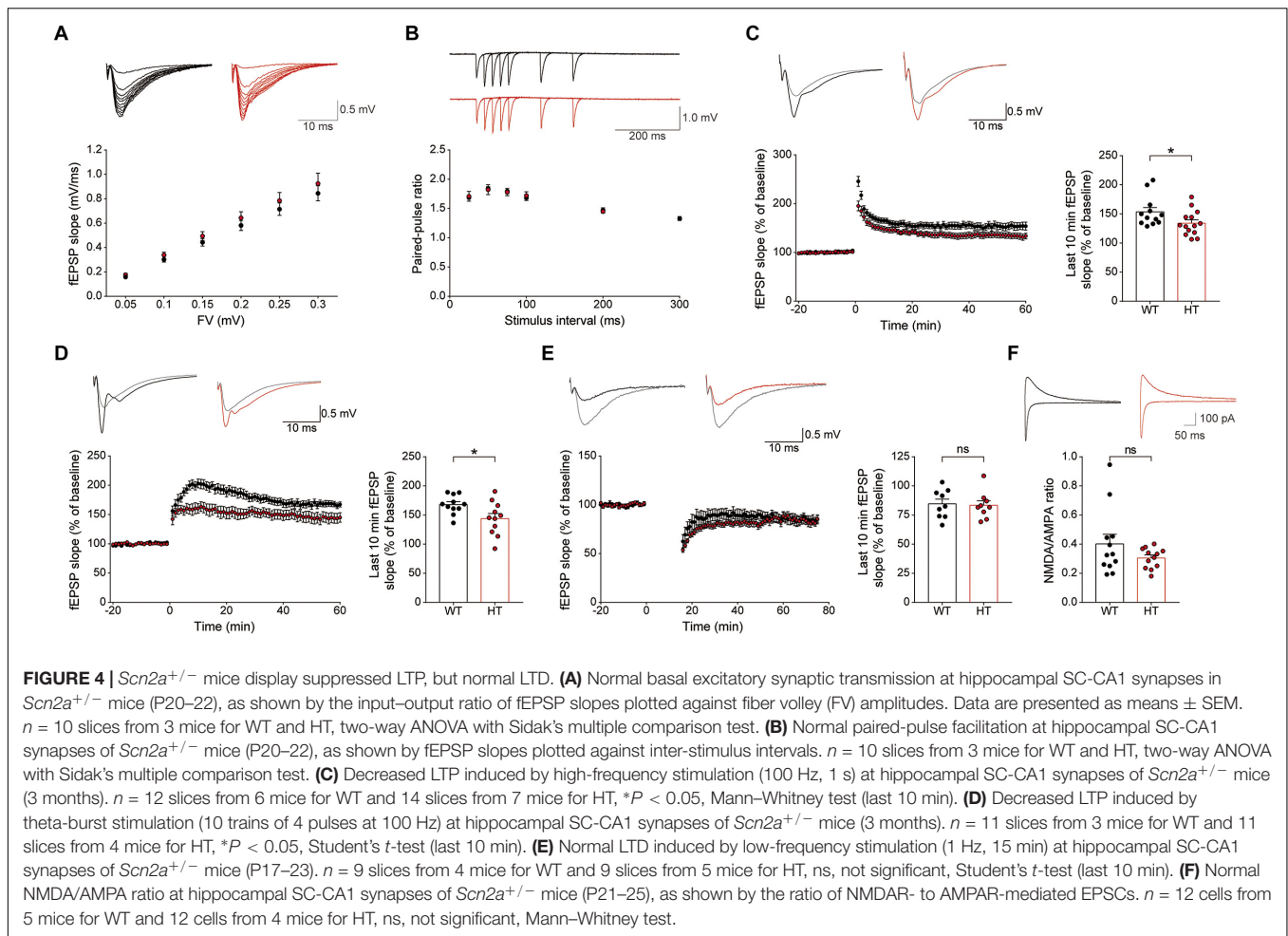
Because hippocampal LTP is known to be associated with associative learning and memory (Bliss and Collingridge, 1993), we next subjected *Scn2a*^{+/-} mice to a battery of learning and memory tests. *Scn2a*^{+/-} mice displayed suppressed spatial learning and memory in the learning and probe phases of the Morris water-maze test compared with WT mice (**Figures 5A,B**). In addition, *Scn2a*^{+/-} mice performed poorly in the reversal phase of the Morris water-maze test in both learning and probe sessions (**Figures 5A,C**).

In the novel object-recognition test, *Scn2a*^{+/-} mice displayed novel object-recognition memory comparable to that of WT mice (**Figure 5D**). In the contextual fear-conditioning test, *Scn2a*^{+/-} mice showed normal memory immediately and 24 h after fear memory acquisition (**Figure 5E**). Intriguingly,



however, these mice showed enhanced fear memory 7 days after fear memory acquisition. Therefore, these mice seem to have normal fear memory acquisition and short-term fear memory, but enhanced long-term fear memory. Lastly, *Scn2a*^{+/-} mice showed normal motor coordination and learning in the rotarod test (Figure 5F).

These results collectively suggest that *Scn2a* haploinsufficiency impairs spatial learning and memory while enhancing long-term fear memory, but does not affect object-recognition memory. In addition, *Scn2a* haploinsufficiency has mixed effects on fear memory, enhancing long-term fear memory while leaving fear-memory acquisition and short-term fear memory unaffected.



Scn2a^{+/-} Mice Show Abnormally Enhanced Direct Social Interaction but Normal Social Approach, Social Communication, and Repetitive Behavior

Given the strong association of *SCN2A* with ASD (Sanders et al., 2018), we next tested whether *Scn2a*^{+/-} mice display autistic-like impairments in social and repetitive behaviors. In the three-chamber test, known to measure social approach and social novelty-recognition behaviors in rodents (Crawley, 2004; Nadler et al., 2004; Silverman et al., 2010), *Scn2a*^{+/-} mice showed normal levels of social approach, as measured by sniffing time and time spent in the chamber (Figures 6A,C). *Scn2a*^{+/-} mice also showed normal social-novelty recognition (Figures 6B,D). In a direct social-interaction test using freely moving pairs of WT or *Scn2a*^{+/-} mice, *Scn2a*^{+/-} mice showed abnormally increased total social interaction (Figure 6E).

In tests measuring USVs, a form of social communication in rodents frequently impaired in mouse models of ASD (Scattoni et al., 2009; Wohr, 2014), *Scn2a*^{+/-} mice showed normal levels of USVs during encounters with a novel female mouse, as shown by the number of USV calls, duration of each call, and the latency to the first call (Figure 6F).

In tests measuring repetitive behaviors, *Scn2a*^{+/-} mice displayed normal levels of self-grooming and rearing (Figure 6G). These results collectively suggest that *Scn2a* haploinsufficiency induces abnormally enhanced direct social interaction, but does not affect social approach, social communication, or repetitive behavior in mice.

Scn2a^{+/-} Mice Show Suppressed Locomotion in a Familiar Environment but Normal Susceptibility to Induced Seizure

Because disorders associated with *SCN2A* (epilepsy, ASD, intellectual disability, and schizophrenia) involve hyperactivity, anxiety, and seizure as important symptoms and comorbidities, we next tested locomotor behavior, anxiety-like behavior, and seizure susceptibility in *Scn2a*^{+/-} mice.

In the open-field test, *Scn2a*^{+/-} mice showed normal levels of locomotor activity and time spent in the center of the open-field arena (a measure of anxiety-like behavior) compared with WT mice (Figures 7A,B).

In LABORAS cages, in which mouse movements are measured for four consecutive days and thus represent a familiar

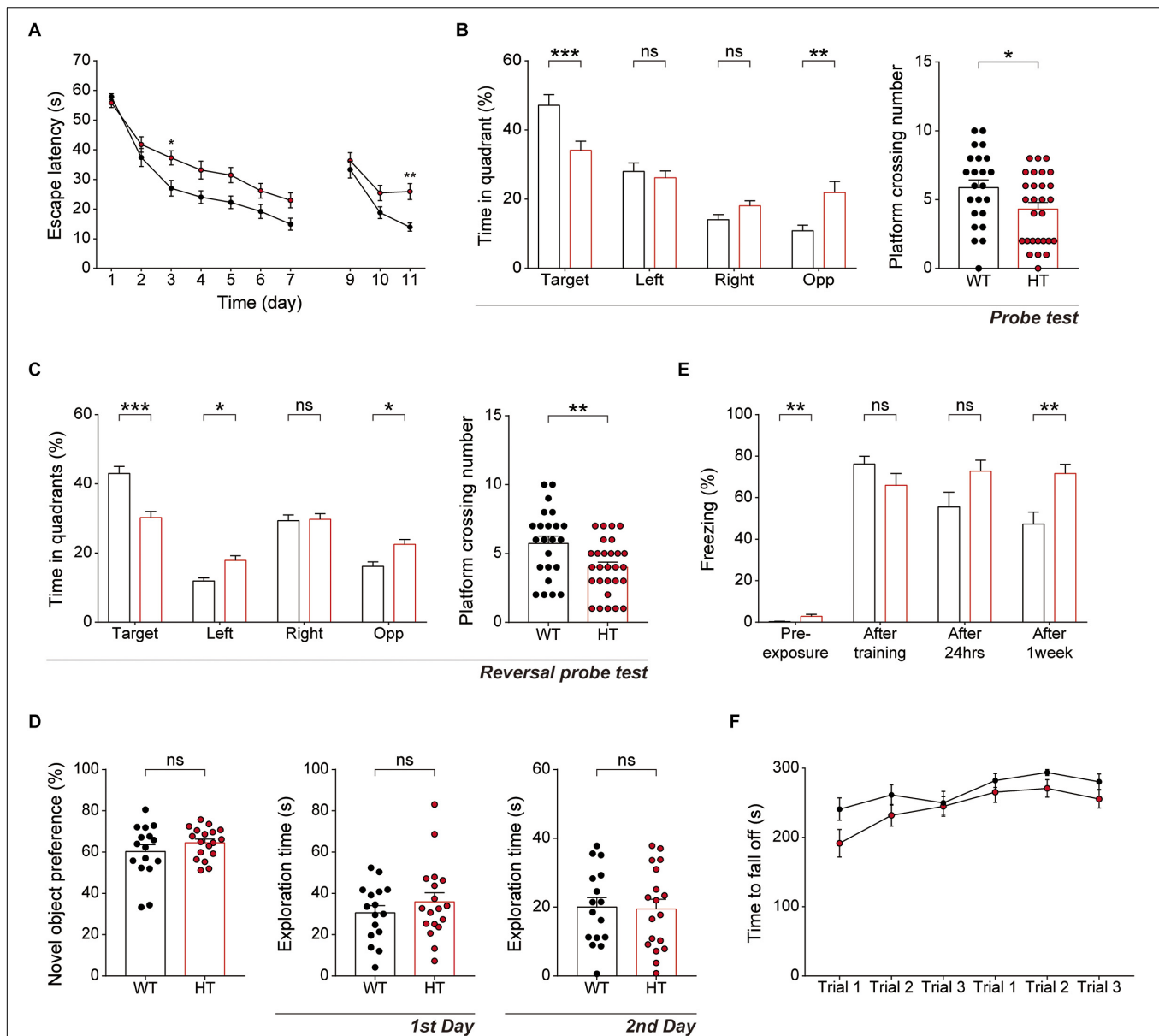


FIGURE 5 | *Scn2a*^{+/-} mice show impaired spatial learning and memory and enhanced long-term fear memory. **(A–C)** Impaired spatial learning and memory in both the initial and reversal phases of the Morris water-maze test in *Scn2a*^{+/-} mice (3–4 months), as shown by escape latency, time spent in quadrant, and number of exact platform crossings in the learning phase (day 1–7), reversal phase (day 9–11), and respective probe tests (days 8 and 12). Data are presented as means \pm SEM. $n = 23$ mice for WT and 28 for HT, * $P < 0.05$, ** $P < 0.01$, *** $P < 0.001$, ns, not significant, two-way ANOVA with Sidak's multiple comparison test, Mann–Whitney test, and Student's *t*-test. **(D)** Normal behavior of *Scn2a*^{+/-} mice (2–3 months) in novel object-recognition test, as shown by novel-object preference. Note object exploration times are normal on both first and second days. $n = 16$ mice for WT and 18 for HT, ns, not significant, Student's *t*-test. **(E)** Normal contextual fear memory acquisition and 24-h memory in *Scn2a*^{+/-} mice (2–3 months), but enhanced 7-day fear memory in contextual fear-conditioning tests, as shown by freezing levels. Note that the 7-day experiment was performed directly after fear memory acquisition (no 24-h retrieval experiment). $n = 13$ mice for WT and 10 for HT, ** $P < 0.01$, ns, not significant, Mann–Whitney test and Student's *t*-test. **(F)** Normal motor learning of *Scn2a*^{+/-} mice (3–4 months) in the rotarod test, as shown by latency to fall from the rotating rod. $n = 8$ mice for WT and 12 for HT, two-way ANOVA with Sidak's multiple comparison test.

environment (Quinn et al., 2003; Quinn et al., 2006), *Scn2a*^{+/-} mice showed decreased levels of total distance moved and time spent rearing, but normal levels of self-grooming and climbing (Figures 7C,D). Notably, the decreased locomotion became more evident as the number of days in the LABORAS cage increased, suggesting that habituation to this environment exacerbates

the decreased locomotion. These results suggest that *Scn2a*^{+/-} mice display normal locomotor activity in a novel environment, but suppressed locomotor activity and repetitive behavior in a familiar environment.

Scn2a^{+/-} mice were then subjected to tests measuring anxiety-like behaviors. In the elevated plus-maze test, *Scn2a*^{+/-}

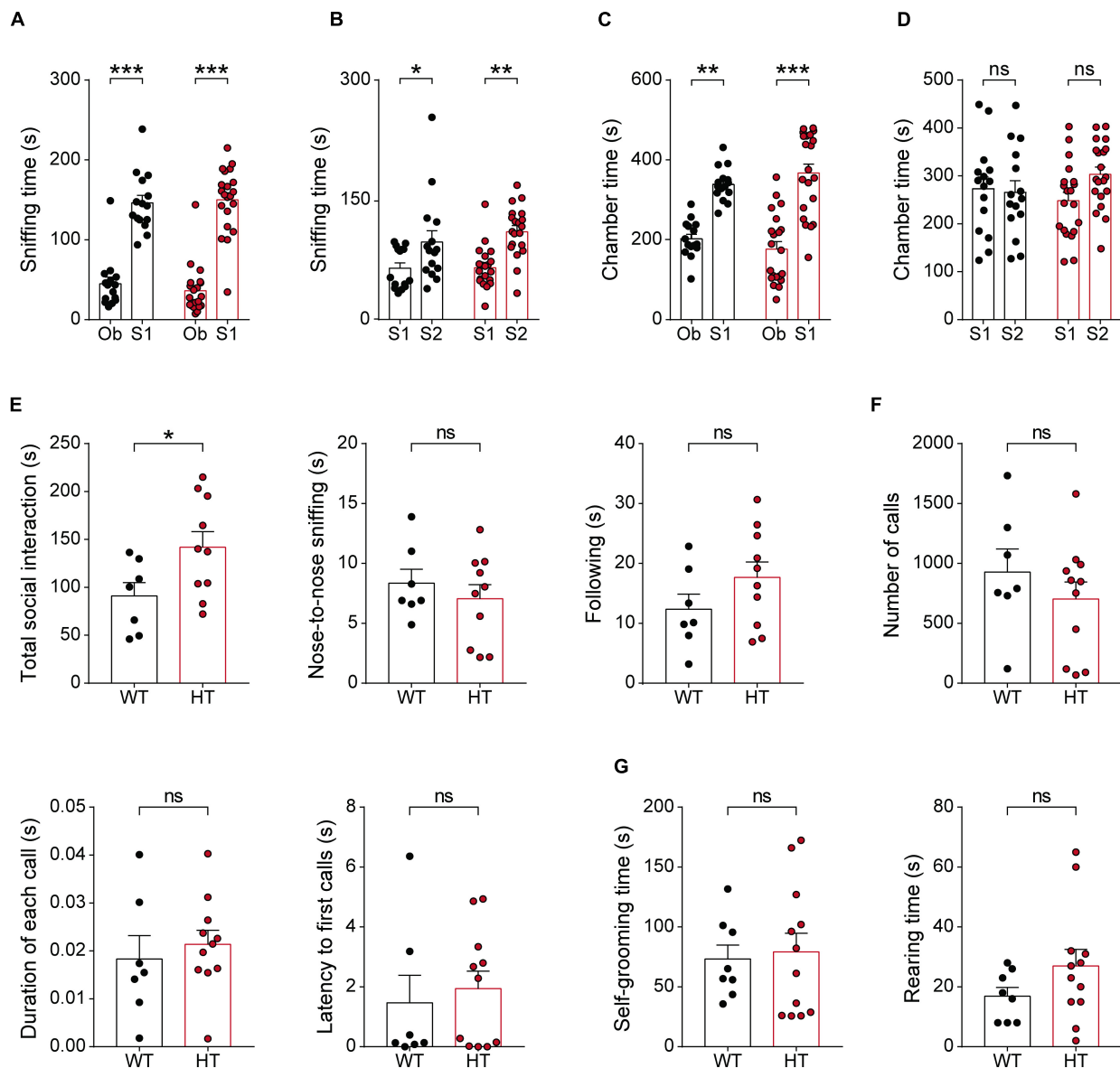


FIGURE 6 | *Scn2a*^{+/−} mice show abnormally enhanced direct social interaction but normal social approach, social communication, and repetitive behavior. **(A–D)** Normal social approach in *Scn2a*^{+/−} mice (3–4 months) in the three-chamber test, as shown by time spent sniffing or in the chamber. Ob, object; S1, familiar stranger; S2, novel stranger. Data are presented as means ± SEM. *n* = 15 mice for WT and 21 for HT, **P* < 0.05, ***P* < 0.01, ****P* < 0.001, ns, not significant, two-way ANOVA with Sidak's multiple comparison test. **(E)** Enhanced social interaction in *Scn2a*^{+/−} mice (3–4 months) in the direct social-interaction test, using pairs of WT or *Scn2a*^{+/−} mice. Note that, although the total social interaction was increased, a subset of individual parameters (nose-to-nose interaction and following) was normal in *Scn2a*^{+/−} mice. *n* = 7 pairs of mice for WT and 10 for HT, **P* < 0.05, ns, not significant, Student's *t*-test. **(F)** Normal USVs induced by a stranger female in *Scn2a*^{+/−} mice (3–4 months), as shown by the number of USV calls, duration of each call, and latency to first call. *n* = 7 mice for WT and 11 for HT, ns, not significant, Student's *t*-test and Mann–Whitney test. **(G)** Normal repetitive behaviors in *Scn2a*^{+/−} mice (2–3 months), as shown by time spent self-grooming and rearing. *n* = 8 mice for WT and 12 for HT, ns, not significant, Student's *t*-test.

mice showed unaltered time spent in open or closed arms and number of closed/open arm entries compared with WT mice (Figure 7E). Similarly, in the light–dark chamber test, the time spent by *Scn2a*^{+/−} mice in light/dark chambers was comparable to that of WT mice, although *Scn2a*^{+/−} mice showed mild hypoactivity in the light chamber under intense illumination (300 lux) (Figure 7F), suggestive of light-induced hypoactivity. These

results suggest that *Scn2a* haploinsufficiency minimally affects anxiety-like behaviors.

Visual inspection revealed no overt evidence of seizures in *Scn2a*^{+/−} mice, an observation similar to that previously reported using an independent *Scn2a*^{+/−} mouse line with a deletion of *Scn2a* exon 1 (Planells-Cases et al., 2000; Ogiwara et al., 2018). However, because the *Scn2a*^{+/−} hippocampus

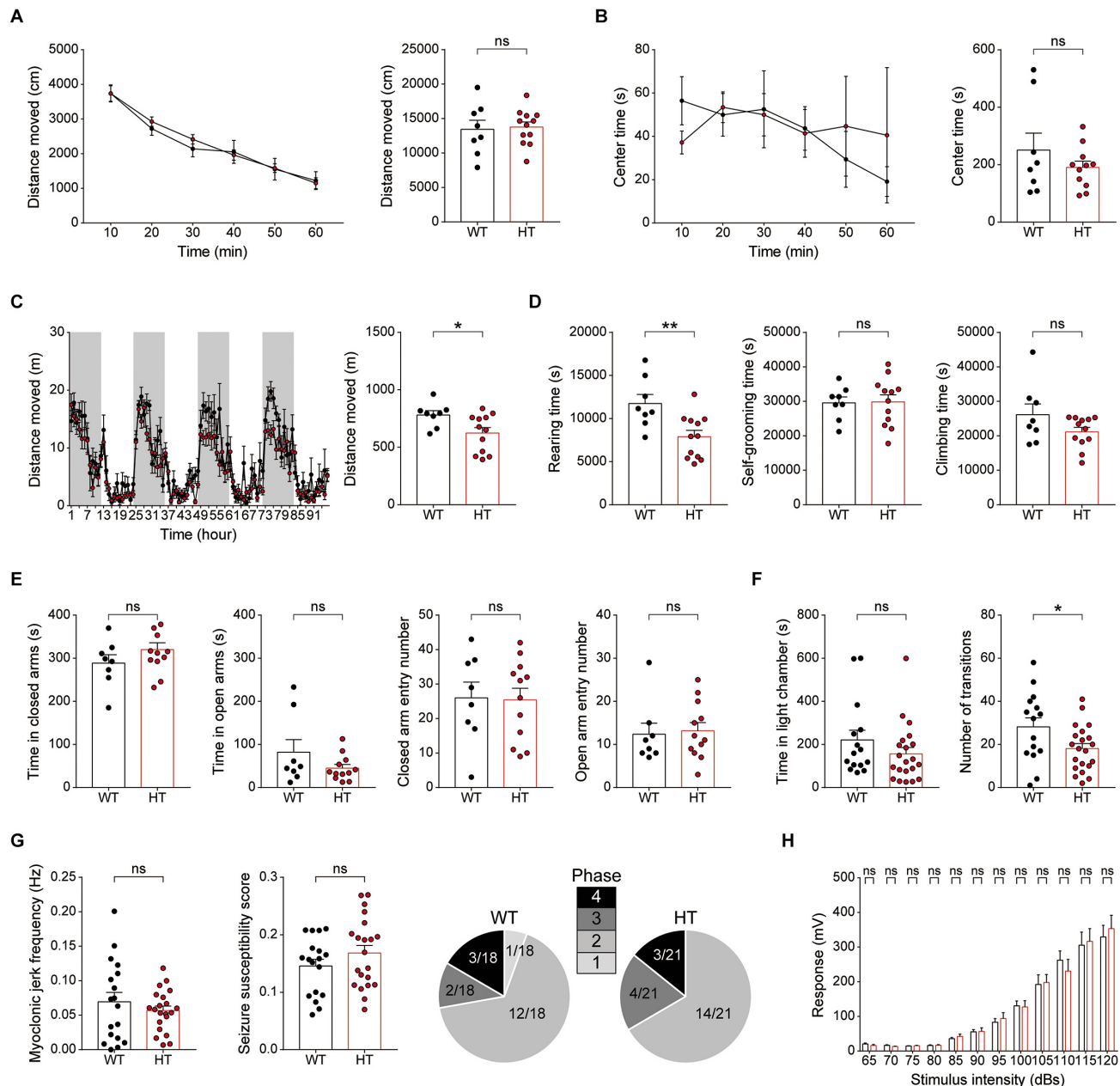


FIGURE 7 | *Scn2a*^{+/-} mice show suppressed locomotion in a familiar environment, but normal anxiety-like behavior and susceptibility to induced seizure. **(A,B)** Normal locomotor activity of *Scn2a*^{+/-} mice (2–3 months) in the open-field test. Data are presented as means ± SEM. *n* = 8 mice for WT and 11 for HT, ns, not significant, Two-way ANOVA with Sidak's multiple comparison test, Student's *t*-test and Mann-Whitney test. **(C,D)** Decreased distance moved and rearing time, but normal self-grooming and climbing, in *Scn2a*^{+/-} mice (2–3 months) in the LABORAS test, in which mouse movements are continuously monitored for four consecutive days. Note that the extent of the decrease in distance moved became more evident as the time in LABORAS cages increased. The shaded regions indicate light-off periods. *n* = 8 mice for WT and 12 for HT, **P* < 0.05, ***P* < 0.01, ns, not significant, two-way ANOVA with Sidak's multiple comparison test, and Student's *t*-test. **(E)** Normal anxiety-like behavior of *Scn2a*^{+/-} mice (2–3 months) in the elevated plus-maze test, as shown by time in closed/open arms and number of entries into each arm. *n* = 8 mice for WT and 12 for HT, ns, not significant, Student's *t*-test and Mann-Whitney test. **(F)** Normal anxiety-like behavior of *Scn2a*^{+/-} mice (2–3 months) in the light-dark chamber test, as shown by time spent in the light chamber. Note that the number of transitions into the light chamber was decreased, indicative of mild hypoactivity in the light-dark apparatus. *n* = 15 mice for WT and 21 for HT, **P* < 0.05, ns, not significant, Mann-Whitney test and Student's *t*-test. **(G)** Normal susceptibility to PTZ-induced seizures in *Scn2a*^{+/-} mice (4 months), as shown by myoclonic jerk frequency, seizure susceptibility score, and terminal seizure stage reached. *n* = 18 mice for WT and 21 for HT, ns, not significant, Student's *t*-test, and Chi-square test. **(H)** Normal acoustic startle response of *Scn2a*^{+/-} mice (2–3 months), as shown by the responses to different intensities of acoustic stimuli. *n* = 13 mice for WT and 10 for HT, ns, not significant, two-way ANOVA with Sidak's multiple comparison test.

showed suppressed neuronal excitability and excitatory synaptic transmission in the presence of network activity (**Figure 3**), we measured the susceptibility of *Scn2a*^{+/-} mice to induced seizure. *Scn2a*^{+/-} mice injected intraperitoneally with PTZ (40 mg/kg) showed a similar susceptibility to induced seizures as WT mice, as measured by myoclonic jerk frequency, seizure susceptibility score, and terminal seizure stage reached (**Figure 7G**). Lastly, *Scn2a*^{+/-} mice showed normal levels of acoustic startle in all sound intensity ranges tested (**Figure 7H**).

Newborn and Juvenile *Scn2a*^{+/-} Mice Show Modestly Increased Direct Social Interaction and Moderately Decreased Locomotion but Normal Social Communication and Mother-Attachment Behavior

Because neurodevelopmental psychiatric disorders frequently involve early symptoms and pathophysiology, and *Scn2a* expression reaches a high level at early postnatal stages (**Figure 1E**), similar to results in rats (Shah et al., 2001), we subjected newborn and juvenile *Scn2a*^{+/-} mice to a set of behavioral tests.

Newborn *Scn2a*^{+/-} mice (P4–10) separated from their mother emitted USVs at levels comparable to those of WT mice, as shown by the number of USV calls and duration of each call (**Figure 8A**), suggesting that social communication is normal in these mice.

Juvenile *Scn2a*^{+/-} mice (~3 weeks of age) subjected to a direct social-interaction test (also known as juvenile play) displayed moderately increased levels of direct social interaction, as shown by the significant increase in nose-to-nose sniffing (**Figure 8B**), similar to adult *Scn2a*^{+/-} mice, which showed increased total direct social interaction (**Figure 6E**). Juvenile *Scn2a*^{+/-} mice separated from their mothers for 30 min and then allowed to reunite, spent comparable amounts of time with the reunited mothers compared with WT mice (**Figure 8C**). Juvenile WT and *Scn2a*^{+/-} mice also showed no genotype differences in the self-grooming test (**Figure 8D**).

Notably, juvenile *Scn2a*^{+/-} mice showed moderately decreased locomotor activity in the open-field test (**Figure 8E**), a finding that contrasts with the normal open-field locomotor activity in adult *Scn2a*^{+/-} mice (**Figure 7A**). This suggests that the mild hypoactivity induced in juvenile *Scn2a*^{+/-} mice by a novel environment spontaneously resolves as these mice grow into adulthood. Lastly, *Scn2a*^{+/-} mice showed no anxiety-like behavior, as measured by the time spent in the center region of the open-field arena (**Figure 8F**).

Collectively, these results indicate that newborn and juvenile *Scn2a*^{+/-} mice show moderately increased direct social interaction and moderately decreased open-field locomotion, but normal social communication and mother-attachment behavior. In addition, the decreased open-field locomotion in young *Scn2a*^{+/-} mice contrasts with the normal open-field locomotion in adult *Scn2a*^{+/-} mice.

DISCUSSION

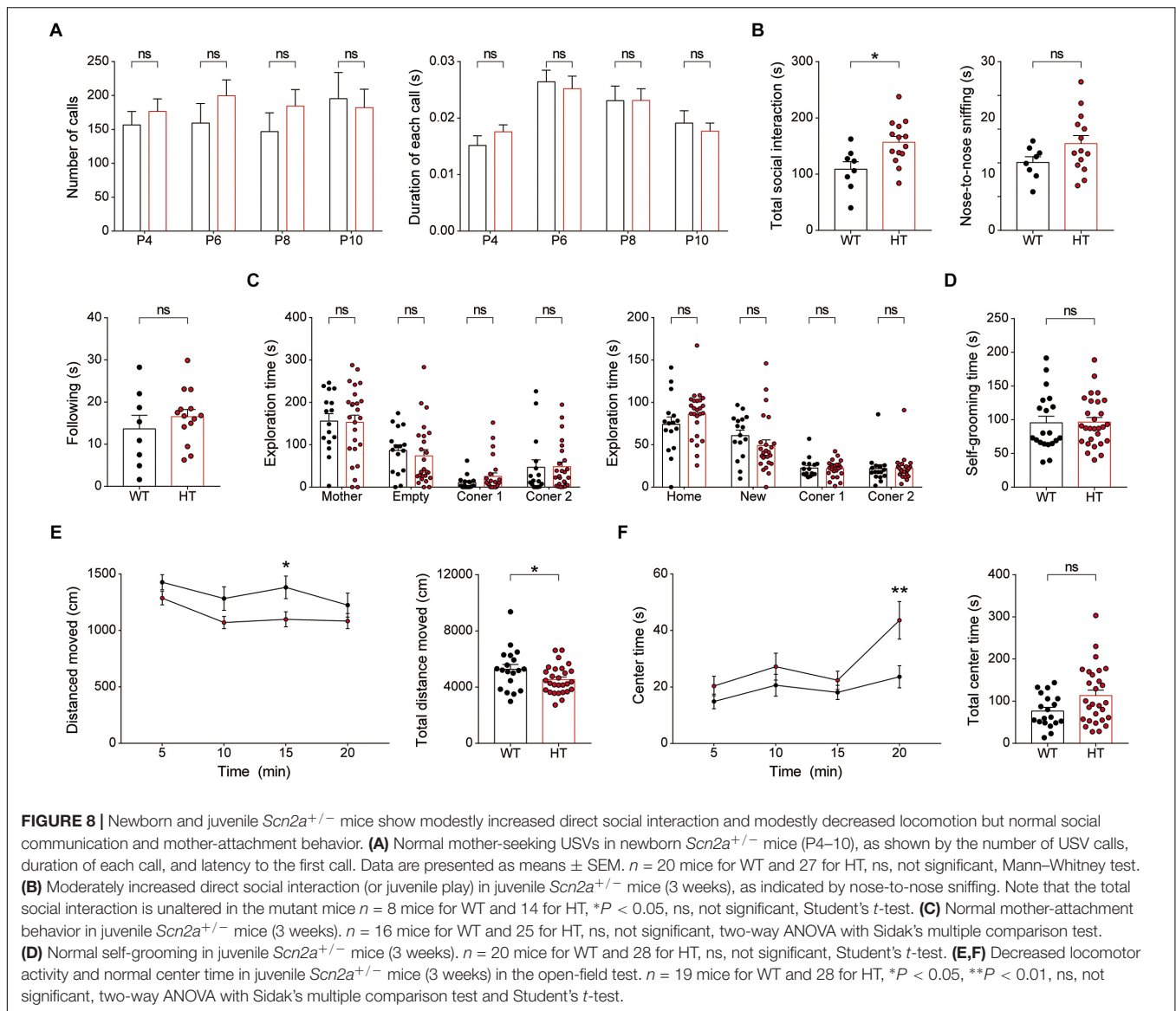
Our study demonstrates that *Scn2a* haploinsufficiency in mice leads to decreases in neuronal activity, excitatory synaptic transmission in the presence of network activity, and LTP in the hippocampus that are associated with impaired spatial learning and memory.

In support of these conclusions, our data indicate that *Scn2a*^{+/-} hippocampal CA1 neurons show moderately decreased neuronal excitability at about postnatal week 3 (**Figures 3A,B**). Whether this decrease is attributable to a decrease in action potential initiation or back-propagation remains unclear. Nevertheless, because Nav1.2 promotes back-propagation of action potentials, whereas Nav1.6 promotes action potential initiation in pyramidal neurons of the prefrontal cortex in P16–20 rats (Hu et al., 2009), a decrease in the back-propagation of action potentials is a possible contributor to the decreased neuronal excitability in *Scn2a*^{+/-} hippocampal neurons.

The decreased neuronal excitability in *Scn2a*^{+/-} hippocampal CA1 neurons is likely to suppress the output function of these neurons. Similar changes might also occur in neurons that lie upstream of CA1 neurons, such as CA3 and dentate gyrus neurons, as well as neocortical neurons. These changes might explain why *Scn2a*^{+/-} CA1 pyramidal neurons display a markedly decreased frequency of sEPSCs in the presence of network activity (**Figures 3C,D**). However, this effect does not seem to involve a decrease in excitatory synapse number because mEPSC frequency and amplitude in *Scn2a*^{+/-} CA1 pyramidal neurons was unchanged (**Figure 3E**).

In contrast to the normal basal excitatory synaptic transmission observed in the *Scn2a*^{+/-} hippocampus (**Figures 4A,B**), LTP induced by high-frequency, or theta-burst stimulation, was suppressed at *Scn2a*^{+/-} SC-CA1 synapses (**Figures 4C,D**). This change does not seem to involve a decrease in NMDAR function, because there was no change in NMDAR-mediated currents (**Figure 4F**) or LTD induced by low-frequency stimulation (**Figure 4E**), which, like LTP, requires NMDAR activation (Malenka and Bear, 2004; Collingridge et al., 2010). Along the same lines, the suppressed LTP is unlikely to involve post-translational modifications of NMDARs, which are known to affect NMDAR channel properties (Lussier et al., 2015). Instead, the decreased LTP likely reflects the operation of mechanisms that do not involve NMDAR-mediated synaptic currents *per se*. Importantly, back-propagation of action potentials is known to act together with dendritic sodium, calcium, and potassium channels and NMDARs to regulate the activity of dendritic properties and synaptic integration and plasticity (Magee and Johnston, 1997; Bi and Poo, 1998; Koester and Sakmann, 1998; Larkum et al., 1999; Johnston et al., 2003; Feldman, 2012; Kim et al., 2015). Therefore, the reduced Nav1.2 function in *Scn2a*^{+/-} hippocampal CA1 neurons may suppress these back-propagation processes and related synaptic plasticity.

It has been shown that distal dendrites of CA1 pyramidal neurons display local sodium spikes that are independent



of back-propagating action potentials and are capable of contributing to the postsynaptic depolarization and calcium entry needed for LTP induction (Golding et al., 2002; Spruston, 2008). More recently, it has been shown that distal dendrites in freely behaving animals display local dendritic spikes and fluctuations of subthreshold membrane potentials independent of back-propagating action potentials (Moore et al., 2017). In addition, Nav1.2 signals are detectable in apical dendrites of neocortical and hippocampal pyramidal neurons (Westenbroek et al., 1989; Gong et al., 1999) as well as in the postsynaptic density of CA1 pyramidal synapses (Johnson et al., 2017). Importantly, our data indicate moderately suppressed neuronal excitability of *Scn2a*^{+/-} pyramidal neurons in the hippocampal CA1 region (Figures 3A,B). These results collectively suggest the possibility that suppressed sodium spikes and dendritic hyperpolarization in *Scn2a*^{+/-} dendrites might contribute to the suppressed LTP independent of back-propagating action potentials.

The decreased LTP in the *Scn2a*^{+/-} hippocampus is in line with the suppressed spatial learning and memory of *Scn2a*^{+/-} mice in the Morris water-maze test (Figures 5A–C). This result is also in agreement with the recently reported impairments in tasks requiring spatial working and reference memory in an independent *Scn2a*^{+/-} mouse line (deletion of exon 1 vs. deletion of exons 4–6 in our mice) (Planells-Cases et al., 2000), which are associated with altered hippocampal replay content (Middleton et al., 2018). In contrast, novel object-recognition memory was unaltered in our *Scn2a*^{+/-} mice (Figure 5D), although it should be noted that brain structures in addition to the hippocampus, such as the perirhinal cortex, have been suggested to be involved (Warburton and Brown, 2015).

Our *Scn2a*^{+/-} mice also show normal contextual-fear learning and 24-h memory (Figure 5E); these findings are seemingly at odds with Morris water-maze result, possibly reflecting differences in neural pathways or stimulus

contexts/intensities between the two assays. Notably, however, *Scn2a*^{+/-} mice show abnormally enhanced 7-day fear memory (Figure 5E), suggesting that these mice are more vulnerable to strong noxious stimuli, a vulnerability that might stem from enhanced fear memory or suppressed fear memory extinction.

Behaviors associated with an autistic-like phenotype, including social interaction/communication and repetitive behaviors, were largely normal in *Scn2a*^{+/-} mice (Figure 6), a surprising result considering the strong association of SCN2A with ASD. It is possible that *Scn2a* haploinsufficiency in mice does not elicit autistic-like behaviors because of fundamental differences between human and mouse brains, or because the behavioral assays used are not sensitive enough to detect subtle changes in social interaction or repetitive behavior. Notably, however, *Scn2a*^{+/-} adult and juvenile mice showed increased direct social interaction (Figure 6E), a result often observed in other mouse models of autism that lack, i.e., the excitatory postsynaptic scaffolding protein Shank3 (Wang X. et al., 2016; Yoo et al., 2018). One of these studies on *Shank3*-mutant mice carrying a deletion of exons 4–22 reported that the increased social-interaction phenotype involves normal social interest but unsuccessful repetitive attempts for social interaction toward a mouse under a different genetic background (Wang X. et al., 2016), although our study used pairs of *Scn2a*^{+/-} mice in the same genetic background, making a similar analysis of unidirectional social interaction not feasible.

Lastly, susceptibility to induced seizure and acoustic startle responses were unaltered in *Scn2a*^{+/-} mice (Figures 7G,H), a finding that contrasts with the decreased neuronal excitability and excitatory synaptic drive observed in the *Scn2a*^{+/-} hippocampus. This result is similar to that obtained in a previous study using a different *Scn2a*^{+/-} mouse line (exon 1 deleted), in which seizure behaviors could not be detected by visual inspection (Planells-Cases et al., 2000). On the other hand, a recent study on this latter *Scn2a*^{+/-} mouse line employing long-term electrocorticography-electromyography recordings reported the presence of absence-like seizures with short bursts of spike-wave discharges and behavioral arrests (Ogiwara et al., 2018). This study further showed that conditional, heterozygous *Scn2a*^{+/-} mice in which deletion of yet another *Scn2a* exon (exon 2) restricted to excitatory neurons leads to similar absence-like seizures. Thus, the prediction is that electrocorticography-electromyography recordings in our mouse line might also reveal absence-like seizures, although deletion of different exons in the *Scn2a* gene might lead to different seizure phenotypes.

In conclusion, our study demonstrates that *Scn2a* haploinsufficiency in mice leads to decreases in neuronal excitability, excitatory drive, and LTP in the hippocampus that are associated with suppressed spatial learning and memory.

DATA AVAILABILITY

The raw data supporting the conclusions of this manuscript will be made available by the authors, without undue reservation, to any qualified researcher.

ETHICS STATEMENT

All animals were bred and maintained according to the Requirements of Animal Research at KAIST, and all procedures were approved by the Committees of Animal Research at KAIST (KA2016-31).

AUTHOR CONTRIBUTIONS

WS, HSK, RK, KK, and MK performed the behavioral experiments. WS and RK performed the immunoblot experiments. WS, HSK, and RK performed the electrophysiological experiments. DK, SK, and SH performed the HTNC experiments. JK and EY performed *in situ* hybridization experiments. WS, HK, and EK designed the experiments and wrote the manuscript.

FUNDING

This work was supported by the National Research Foundation of Korea (NRF), funded by the Ministry of Science, ICT and Future Planning (2017M3C7A1079692 to HK, NRF Global Ph.D. Fellowship Program Grant NRF-2017H1A2A1043768 to HSK), and the Institute for Basic Science (IBSR002-D1 to EK).

SUPPLEMENTARY MATERIAL

The Supplementary Material for this article can be found online at: <https://www.frontiersin.org/articles/10.3389/fnmol.2019.00145/full#supplementary-material>

REFERENCES

- Baasch, A. L., Huning, I., Gilissen, C., Klepper, J., Veltman, J. A., Gillessen-Kaesbach, G., et al. (2014). Exome sequencing identifies a de novo SCN2A mutation in a patient with intractable seizures, severe intellectual disability, optic atrophy, muscular hypotonia, and brain abnormalities. *Epilepsia* 55, e25–e29. doi: 10.1111/epi.12554
- Bender, K. J., and Trussell, L. O. (2012). The physiology of the axon initial segment. *Annu. Rev. Neurosci.* 35, 249–265. doi: 10.1146/annurev-neuro-062111-150339
- Ben-Shalom, R., Keeshen, C. M., Berrios, K. N., An, J. Y., Sanders, S. J., and Bender, K. J. (2017). Opposing effects on Nav1.2 function underlie differences between SCN2A variants observed in individuals with autism spectrum disorder or infantile seizures. *Biol. Psychiatry* 82, 224–232. doi: 10.1016/j.biopsych.2017.01.009
- Berkovic, S. F., Heron, S. E., Giordano, L., Marini, C., Guerrini, R., Kaplan, R. E., et al. (2004). Benign familial neonatal-infantile seizures: characterization of a new sodium channelopathy. *Ann. Neurol.* 55, 550–557. doi: 10.1002/ana.20029
- Bi, G. Q., and Poo, M. M. (1998). Synaptic modifications in cultured hippocampal neurons: dependence on spike timing, synaptic strength, and postsynaptic cell type. *J. Neurosci.* 18, 10464–10472. doi: 10.1523/jneurosci.18-24-10464.1998
- Bliss, T. V., and Collingridge, G. L. (1993). A synaptic model of memory: long-term potentiation in the hippocampus. *Nature* 361, 31–39. doi: 10.1038/361031a0

- Boiko, T., Rasband, M. N., Levinson, S. R., Caldwell, J. H., Mandel, G., Trimmer, J. S., et al. (2001). Compact myelin dictates the differential targeting of two sodium channel isoforms in the same axon. *Neuron* 30, 91–104. doi: 10.1016/S0896-6273(01)00265-3
- Boiko, T., Van Wart, A., Caldwell, J. H., Levinson, S. R., Trimmer, J. S., and Matthews, G. (2003). Functional specialization of the axon initial segment by isoform-specific sodium channel targeting. *J. Neurosci.* 23, 2306–2313. doi: 10.1523/jneurosci.23-06-02306.2003
- Bowling, K. M., Thompson, M. L., Amaral, M. D., Finnila, C. R., Hiatt, S. M., Engel, K. L., et al. (2017). Genomic diagnosis for children with intellectual disability and/or developmental delay. *Genome Med.* 9:43. doi: 10.1186/s13073-017-0433-1
- Buxbaum, J. D., Daly, M. J., Devlin, B., Lehner, T., Roeder, K., State, M. W., et al. (2012). The autism sequencing consortium: large-scale, high-throughput sequencing in autism spectrum disorders. *Neuron* 76, 1052–1056. doi: 10.1016/j.neuron.2012.12.008
- Carroll, L. S., Woolf, R., Ibrahim, Y., Williams, H. J., Dwyer, S., Walters, J., et al. (2016). Mutation screening of SCN2A in schizophrenia and identification of a novel loss-of-function mutation. *Psychiatr. Genet.* 26, 60–65. doi: 10.1097/YPG.0000000000000110
- Carvill, G. L., Heavin, S. B., Yendle, S. C., McMahon, J. M., O'Roak, B. J., Cook, J., et al. (2013). Targeted resequencing in epileptic encephalopathies identifies de novo mutations in CHD2 and SYNGAP1. *Nat. Genet.* 45, 825–830. doi: 10.1038/ng.2646
- Catterall, W. A. (2017). Forty Years of sodium channels: structure, function, pharmacology, and epilepsy. *Neurochem. Res.* 42, 2495–2504. doi: 10.1007/s11064-017-2314-9
- Cherot, E., Keren, B., Dubourg, C., Carré, W., Fradin, M., Lavillaureix, A., et al. (2018). Using medical exome sequencing to identify the causes of neurodevelopmental disorders: Experience of 2 clinical units and 216 patients. *Clin. Genet.* 93, 567–576. doi: 10.1111/cge.13102
- Chung, W., Choi, S. Y., Lee, E., Park, H., Kang, J., Park, H., et al. (2015). Social deficits in IRSp53 mutant mice improved by NMDAR and mGluR5 suppression. *Nat. Neurosci.* 18, 435–443. doi: 10.1038/nn.3927
- Codina-Sola, M., Rodriguez-Santiago, B., Homs, A., Santoyo, J., Rigau, M., Aznar-Lain, G., et al. (2015). Integrated analysis of whole-exome sequencing and transcriptome profiling in males with autism spectrum disorders. *Mol. Autism* 6:21. doi: 10.1186/s13229-015-0017-0
- Collingridge, G. L., Peineau, S., Howland, J. G., and Wang, Y. T. (2010). Long-term depression in the CNS. *Nat. Rev. Neurosci.* 11, 459–473.
- Crawley, J. N. (2004). Designing mouse behavioral tasks relevant to autistic-like behaviors. *Ment. Retard. Dev. Disabil. Res. Rev.* 10, 248–258. doi: 10.1002/mrdd.20039
- de Ligt, J., Willemsen, M. H., van Bon, B. W., Kleefstra, T., Yntema, H. G., Kroes, T., et al. (2012). Diagnostic exome sequencing in persons with severe intellectual disability. *N. Engl. J. Med.* 367, 1921–1929. doi: 10.1056/NEJMoa1206524
- De Rubeis, S., He, X., Goldberg, A. P., Poultney, C. S., Samocha, K., Cicek, A. E., et al. (2014). Synaptic, transcriptional and chromatin genes disrupted in autism. *Nature* 515, 209–215. doi: 10.1038/nature13772
- Deciphering Developmental Disorders Study (2015). Large-scale discovery of novel genetic causes of developmental disorders. *Nature* 519, 223–228. doi: 10.1038/nature14135
- D'Gama, A. M., Pochareddy, S., Li, M., Jamuar, S. S., Reiff, R. E., Lam, A. N., et al. (2015). Targeted DNA sequencing from autism spectrum disorder brains implicates multiple genetic mechanisms. *Neuron* 88, 910–917. doi: 10.1016/j.neuron.2015.11.009
- Epi4K Consortium, Epilepsy Phenome/Genome Project, Allen, A. S., Berkovic, S. F., Cossette, P., Delanty, N., et al. (2013). De novo mutations in epileptic encephalopathies. *Nature* 501, 217–221. doi: 10.1038/nature12439
- Feldman, D. E. (2012). The spike-timing dependence of plasticity. *Neuron* 75, 556–571. doi: 10.1016/j.neuron.2012.08.001
- Ferraro, T. N., Golden, G. T., Smith, G. G., St Jean, P., Schork, N. J., Mulholland, N., et al. (1999). Mapping loci for pentylenetetrazol-induced seizure susceptibility in mice. *J. Neurosci.* 19, 6733–6739. doi: 10.1523/jneurosci.19-16-06733.1999
- Fromer, M., Pocklington, A. J., Kavanagh, D. H., Williams, H. J., Dwyer, S., Gormley, P., et al. (2014). De novo mutations in schizophrenia implicate synaptic networks. *Nature* 506, 179–184. doi: 10.1038/nature12929
- Gazina, E. V., Leaw, B. T., Richards, K. L., Wimmer, V. C., Kim, T. H., Aumann, T. D., et al. (2015). 'Neonatal' Nav1.2 reduces neuronal excitability and affects seizure susceptibility and behaviour. *Hum. Mol. Genet.* 24, 1457–1468. doi: 10.1093/hmg/ddu562
- Gazina, E. V., Richards, K. L., Mokhtar, M. B., Thomas, E. A., Reid, C. A., and Petrou, S. (2010). Differential expression of exon 5 splice variants of sodium channel alpha subunit mRNAs in the developing mouse brain. *Neuroscience* 166, 195–200. doi: 10.1016/j.neuroscience.2009.12.011
- Geisheker, M. R., Heymann, G., Wang, T., Coe, B. P., Turner, T. N., Stessman, H. A. F., et al. (2017). Hotspots of missense mutation identify neurodevelopmental disorder genes and functional domains. *Nat. Neurosci.* 20, 1043–1051. doi: 10.1038/nn.4589
- Golding, N. L., Staff, N. P., and Spruston, N. (2002). Dendritic spikes as a mechanism for cooperative long-term potentiation. *Nature* 418, 326–331. doi: 10.1038/nature00854
- Gong, B., Rhodes, K. J., Bekele-Arcuri, Z., and Trimmer, J. S. (1999). Type I and type II Na(+) channel alpha-subunit polypeptides exhibit distinct spatial and temporal patterning, and association with auxiliary subunits in rat brain. *J. Comp. Neurol.* 412, 342–352. doi: 10.1002/(sici)1096-9861(19990920)412:2<342::aid-cne11>3.0.co;2-2
- Gustafson, T. A., Clevinger, E. C., O'Neill, T. J., Yarowsky, P. J., and Krueger, B. K. (1993). Mutually exclusive exon splicing of type III brain sodium channel alpha subunit RNA generates developmentally regulated isoforms in rat brain. *J. Biol. Chem.* 268, 18648–18653.
- Hamdan, F. F., Myers, C. T., Cossette, P., Lemay, P., Spiegelman, D., Laporte, A. D., et al. (2017). High rate of recurrent de novo mutations in developmental and epileptic encephalopathies. *Am. J. Hum. Genet.* 101, 664–685. doi: 10.1016/j.ajhg.2017.09.008
- Heron, S. E., Crossland, K. M., Andermann, E., Phillips, H. A., Hall, A. J., Bleasel, A., et al. (2002). Sodium-channel defects in benign familial neonatal-infantile seizures. *Lancet* 360, 851–852. doi: 10.1016/S0140-6736(02)09968-3
- Howell, K. B., McMahon, J. M., Carvill, G. L., Tambunan, D., Mackay, M. T., Rodriguez-Casero, V., et al. (2015). SCN2A encephalopathy: a major cause of epilepsy of infancy with migrating focal seizures. *Neurology* 85, 958–966. doi: 10.1212/WNL.0000000000001926
- Hu, W., Tian, C., Li, T., Yang, M., Hou, H., and Shu, Y. (2009). Distinct contributions of Na(v)1.6 and Na(v)1.2 in action potential initiation and backpropagation. *Nat. Neurosci.* 12, 996–1002. doi: 10.1038/nn.2359
- Iossifov, I., O'Roak, B. J., Sanders, S. J., Ronemus, M., Krumm, N., Levy, D., et al. (2014). The contribution of de novo coding mutations to autism spectrum disorder. *Nature* 515, 216–221. doi: 10.1038/nature13908
- Jiang, Y. H., Yuen, R. K., Jin, X., Wang, M., Chen, N., Wu, X., et al. (2013). Detection of clinically relevant genetic variants in autism spectrum disorder by whole-genome sequencing. *Am. J. Hum. Genet.* 93, 249–263. doi: 10.1016/j.ajhg.2013.06.012
- Johnson, K. W., Herold, K. F., Milner, T. A., Hemmings, H. C. Jr., and Platholi, J. (2017). Sodium channel subtypes are differentially localized to pre- and post-synaptic sites in rat hippocampus. *J. Comp. Neurol.* 525, 3563–3578. doi: 10.1002/cne.24291
- Johnston, D., Christie, B. R., Frick, A., Gray, R., Hoffman, D. A., Schexnayder, L. K., et al. (2003). Active dendrites, potassium channels and synaptic plasticity. *Philos. Trans. R. Soc. Lond. B. Biol. Sci.* 358, 667–674. doi: 10.1098/rstb.2002.1248
- Jung, H., Park, H., Choi, Y., Kang, H., Lee, E., Kweon, H., et al. (2018). Sexually dimorphic behavior, neuronal activity, and gene expression in Chd8-mutant mice. *Nat. Neurosci.* 21, 1218–1228. doi: 10.1038/s41593-018-0208-z
- Kamiya, K., Kaneda, M., Sugawara, T., Mazaki, E., Okamura, N., Montal, M., et al. (2004). A nonsense mutation of the sodium channel gene SCN2A in a patient with intractable epilepsy and mental decline. *J. Neurosci.* 24, 2690–2698. doi: 10.1523/jneurosci.3089-03.2004
- Kaplan, M. R., Cho, M. H., Ullian, E. M., Isom, L. L., Levinson, S. R., and Barres, B. A. (2001). Differential control of clustering of the sodium channels Na(v)1.2 and Na(v)1.6 at developing CNS nodes of ranvier. *Neuron* 30, 105–119. doi: 10.1016/S0896-6273(01)00266-5
- Kim, R., Kim, J., Chung, C., Ha, S., Lee, S., Lee, E., et al. (2018). Cell-type-specific shank2 deletion in mice leads to differential synaptic and behavioral phenotypes. *J. Neurosci.* 38, 4076–4092. doi: 10.1523/JNEUROSCI.2684-17.2018

- Kim, Y., Hsu, C. L., Cembrowski, M. S., Mensh, B. D., and Spruston, N. (2015). Dendritic sodium spikes are required for long-term potentiation at distal synapses on hippocampal pyramidal neurons. *eLife* 4:e06414. doi: 10.7554/eLife.06414
- Klassen, T., Davis, C., Goldman, A., Burgess, D., Chen, T., Wheeler, D., et al. (2011). Exome sequencing of ion channel genes reveals complex profiles confounding personal risk assessment in epilepsy. *Cell* 145, 1036–1048. doi: 10.1016/j.cell.2011.05.025
- Koester, H. J., and Sakmann, B. (1998). Calcium dynamics in single spines during coincident pre- and postsynaptic activity depend on relative timing of back-propagating action potentials and subthreshold excitatory postsynaptic potentials. *Proc. Natl. Acad. Sci. U.S.A.* 95, 9596–9601. doi: 10.1073/pnas.95.16.9596
- Kole, M. H., Ilshner, S. U., Kampa, B. M., Williams, S. R., Ruben, P. C., and Stuart, G. J. (2008). Action potential generation requires a high sodium channel density in the axon initial segment. *Nat. Neurosci.* 11, 178–186. doi: 10.1038/nn2040
- Kole, M. H., and Stuart, G. J. (2012). Signal processing in the axon initial segment. *Neuron* 73, 235–247. doi: 10.1016/j.neuron.2012.01.007
- Krumm, N., Turner, T. N., Baker, C., Vives, L., Mohajeri, K., Witherspoon, K., et al. (2015). Excess of rare, inherited truncating mutations in autism. *Nat. Genet.* 47, 582–588. doi: 10.1038/ng.3303
- Krupp, D. R., Barnard, R. A., Duffourd, Y., Evans, S. A., Mulqueen, R. M., Bernier, R., et al. (2017). Exonic mosaic mutations contribute risk for autism spectrum disorder. *Am. J. Hum. Genet.* 101, 369–390. doi: 10.1016/j.ajhg.2017.07.016
- Larkum, M. E., Zhu, J. J., and Sakmann, B. (1999). A new cellular mechanism for coupling inputs arriving at different cortical layers. *Nature* 398, 338–341. doi: 10.1038/18686
- Lee, E. J., Lee, H., Huang, T. N., Chung, C., Shin, W., Kim, K., et al. (2015). Trans-synaptic zinc mobilization improves social interaction in two mouse models of autism through NMDAR activation. *Nat. Commun.* 6:7168. doi: 10.1038/ncomms8168
- Li, J., Wang, L., Guo, H., Shi, L., Zhang, K., Tang, M., et al. (2017). Targeted sequencing and functional analysis reveal brain-size-related genes and their networks in autism spectrum disorders. *Mol. Psychiatry* 22, 1282–1290. doi: 10.1038/mp.2017.140
- Li, T., Tian, C., Scalmani, P., Frassoni, C., Mantegazza, M., Wang, Y., et al. (2014). Action potential initiation in neocortical inhibitory interneurons. *PLoS Biol.* 12:e1001944. doi: 10.1371/journal.pbio.1001944
- Liao, Y., Deprez, L., Maljevic, S., Pitsch, J., Claes, L., Hristova, D., et al. (2010). Molecular correlates of age-dependent seizures in an inherited neonatal-infantile epilepsy. *Brain* 133, 1403–1414. doi: 10.1093/brain/awq057
- Lussier, M. P., Sanz-Clemente, A., and Roche, K. W. (2015). Dynamic regulation of N-Methyl-D-aspartate (NMDA) and alpha-Amino-3-hydroxy-5-methyl-4-isoxazolepropionic acid (AMPA) receptors by posttranslational modifications. *J. Biol. Chem.* 290, 28596–28603. doi: 10.1074/jbc.R115.652750
- Magee, J. C., and Johnston, D. (1997). A synaptically controlled, associative signal for hebbian plasticity in hippocampal neurons. *Science* 275, 209–213. doi: 10.1126/science.275.5297.209
- Malenka, R. C., and Bear, M. F. (2004). LTP and LTD: an embarrassment of riches. *Neuron* 44, 5–21.
- Middleton, S. J., Kneller, E. M., Chen, S., Ogiwara, I., Montal, M., Yamakawa, K., et al. (2018). Altered hippocampal replay is associated with memory impairment in mice heterozygous for the Scn2a gene. *Nat. Neurosci.* 21, 996–1003. doi: 10.1038/s41593-018-0163-8
- Moore, J. J., Ravassard, P. M., Ho, D., Acharya, L., Kees, A. L., Vuong, C., et al. (2017). Dynamics of cortical dendritic membrane potential and spikes in freely behaving rats. *Science* 355:eaaj1497. doi: 10.1126/science.aaj1497
- Nadler, J. J., Moy, S. S., Dold, G., Trang, D., Simmons, N., Perez, A., et al. (2004). Automated apparatus for quantitation of social approach behaviors in mice. *Genes Brain Behav.* 3, 303–314. doi: 10.1111/j.1601-183x.2004.00071.x
- Nakamura, K., Kato, M., Osaka, H., Yamashita, S., Nakagawa, E., Haginoya, K., et al. (2013). Clinical spectrum of SCN2A mutations expanding to ohtahara syndrome. *Neurology* 81, 992–998. doi: 10.1212/WNL.0b013e3182a43e57
- Naydenov, A. V., Horne, E. A., Cheah, C. S., Swinney, K., Hsu, K. L., Cao, J. K., et al. (2014). ABHD6 blockade exerts antiepileptic activity in PTZ-induced seizures and in spontaneous seizures in R6/2 mice. *Neuron* 83, 361–371. doi: 10.1016/j.neuron.2014.06.030
- Nunes, D., and Kuner, T. (2018). Axonal sodium channel NaV1.2 drives granule cell dendritic GABA release and rapid odor discrimination. *PLoS Biol.* 16:e2003816. doi: 10.1371/journal.pbio.2003816
- Ogiwara, I., Ito, K., Sawaishi, Y., Osaka, H., Mazaki, E., Inoue, I., et al. (2009). De novo mutations of voltage-gated sodium channel alphaII gene SCN2A in intractable epilepsies. *Neurology* 73, 1046–1053. doi: 10.1212/WNL.0b013e3181b9cebc
- Ogiwara, I., Miyamoto, H., Tatsukawa, T., Yamagata, T., Nakayama, T., Atapour, N., et al. (2018). Nav1.2 haploinsufficiency in excitatory neurons causes absence-like seizures in mice. *Commun. Biol.* 1:96. doi: 10.1038/s42003-018-0099-2
- Parrini, E., Marini, C., Mei, D., Galuppi, A., Cellini, E., Pucatti, D., et al. (2017). Diagnostic targeted resequencing in 349 patients with drug-resistant pediatric epilepsies identifies causative mutations in 30 different genes. *Hum. Mutat.* 38, 216–225. doi: 10.1002/humu.23149
- Peitz, M., Pfannkuche, K., Rajewsky, K., and Edenhofer, F. (2002). Ability of the hydrophobic FGF and basic TAT peptides to promote cellular uptake of recombinant Cre recombinase: a tool for efficient genetic engineering of mammalian genomes. *Proc. Natl. Acad. Sci. U.S.A.* 99, 4489–4494. doi: 10.1073/pnas.032068699
- Planells-Cases, R., Caprini, M., Zhang, J., Rockenstein, E. M., Rivera, R. R., Murre, C., et al. (2000). Neuronal death and perinatal lethality in voltage-gated sodium channel alphaII-deficient mice. *Biophys. J.* 78, 2878–2891. doi: 10.1016/s0006-3495(00)76829-9
- Quinn, L. P., Stean, T. O., Chapman, H., Brown, M., Vidgeon-Hart, M., Upton, N., et al. (2006). Further validation of LABORAS using various dopaminergic manipulations in mice including MPTP-induced nigro-striatal degeneration. *J. Neurosci. Methods* 156, 218–227. doi: 10.1016/j.jneumeth.2006.03.013
- Quinn, L. P., Stean, T. O., Trail, B., Duxon, M. S., Stratton, S. C., Billinton, A., et al. (2003). LABORAS: initial pharmacological validation of a system allowing continuous monitoring of laboratory rodent behaviour. *J. Neurosci. Methods* 130, 83–92. doi: 10.1016/s0165-0270(03)00227-9
- Rauch, A., Wiczorek, D., Graf, E., Wieland, T., Ende, S., Schwarzmayr, T., et al. (2012). Range of genetic mutations associated with severe non-syndromic sporadic intellectual disability: an exome sequencing study. *Lancet* 380, 1674–1682. doi: 10.1016/S0140-6736(12)61480-9
- Sanders, S. J., Campbell, A. J., Cottrell, J. R., Moller, R. S., Wagner, F. F., Auldridge, A. L., et al. (2018). Progress in understanding and treating SCN2A-mediated disorders. *Trends Neurosci.* 41, 442–456. doi: 10.1016/j.tins.2018.03.011
- Sanders, S. J., Murtha, M. T., Gupta, A. R., Murdoch, J. D., Raubeson, M. J., Willsey, A. J., et al. (2012). De novo mutations revealed by whole-exome sequencing are strongly associated with autism. *Nature* 485, 237–241.
- Scattoni, M. L., Crawley, J., and Ricceri, L. (2009). Ultrasonic vocalizations: a tool for behavioural phenotyping of mouse models of neurodevelopmental disorders. *Neurosci. Biobehav. Rev.* 33, 508–515. doi: 10.1016/j.neubiorev.2008.08.003
- Shah, B. S., Stevens, E. B., Pinnock, R. D., Dixon, A. K., and Lee, K. (2001). Developmental expression of the novel voltage-gated sodium channel auxiliary subunit beta3, in rat CNS. *J. Physiol.* 534, 763–776. doi: 10.1111/j.1469-7793.2001.t01-1-00763.x
- Silverman, J. L., Yang, M., Lord, C., and Crawley, J. N. (2010). Behavioural phenotyping assays for mouse models of autism. *Nat. Rev. Neurosci.* 11, 490–502. doi: 10.1038/nrn2851
- Spruston, N. (2008). Pyramidal neurons: dendritic structure and synaptic integration. *Nat. Rev. Neurosci.* 9, 206–221. doi: 10.1038/nrn2286
- Stessman, H. A., Xiong, B., Coe, B. P., Wang, T., Hoekzema, K., Fencikova, M., et al. (2017). Targeted sequencing identifies 91 neurodevelopmental-disorder risk genes with autism and developmental-disability biases. *Nat. Genet.* 49, 515–526. doi: 10.1038/ng.3792
- Sugawara, T., Tsurubuchi, Y., Agarwala, K. L., Ito, M., Fukuma, G., Mazaki-Miyazaki, E., et al. (2001). A missense mutation of the Na⁺ channel alpha II subunit gene Na(v)1.2 in a patient with febrile and afebrile seizures causes channel dysfunction. *Proc. Natl. Acad. Sci. U.S.A.* 98, 6384–6389. doi: 10.1073/pnas.111065098
- Tammimies, K., Marshall, C. R., Walker, S., Kaur, G., Thiruvahindrapuram, B., Lionel, A. C., et al. (2015). Molecular diagnostic yield of chromosomal

- microarray analysis and whole-exome sequencing in children with autism spectrum disorder. *JAMA* 314, 895–903.
- Tavassoli, T., Kolevzon, A., Wang, A. T., Curchack-Lichtin, J., Halpern, D., Schwartz, L., et al. (2014). De novo SCN2A splice site mutation in a boy with autism spectrum disorder. *BMC Med. Genet.* 15:35. doi: 10.1186/1471-2350-15-35
- Tian, C., Wang, K., Ke, W., Guo, H., and Shu, Y. (2014). Molecular identity of axonal sodium channels in human cortical pyramidal cells. *Front. Cell. Neurosci.* 8:297. doi: 10.3389/fncel.2014.00297
- Touma, M., Joshi, M., Connolly, M. C., Grant, P. E., Hansen, A. R., Khwaja, O., et al. (2013). Whole genome sequencing identifies SCN2A mutation in monozygotic twins with ohtahara syndrome and unique neuropathologic findings. *Epilepsia* 54, e81–e85. doi: 10.1111/epi.12137
- Trimmer, J. S., and Rhodes, K. J. (2004). Localization of voltage-gated ion channels in mammalian brain. *Annu. Rev. Physiol.* 66, 477–519. doi: 10.1146/annurev.physiol.66.032102.113328
- Trujillano, D., Bertoli-Avella, A. M., Kandaswamy, K. K., Weiss, M. E. R., Köster, J., Marais, A., et al. (2017). Clinical exome sequencing: results from 2819 samples reflecting 1000 families. *EJHG* 25, 176–182. doi: 10.1038/ejhg.2016.146
- Turner, T. N., Hormozdiani, F., Duyzend, M. H., McClymont, S. A., Hook, P. W., Iossifov, I., et al. (2016). Genome sequencing of autism-affected families reveals disruption of putative noncoding regulatory DNA. *Am. J. Hum. Genet.* 98, 58–74. doi: 10.1016/j.ajhg.2015.11.023
- Vacher, H., Mohapatra, D. P., and Trimmer, J. S. (2008). Localization and targeting of voltage-dependent ion channels in mammalian central neurons. *Physiol. Rev.* 88, 1407–1447. doi: 10.1152/physrev.00002.2008
- Van Wart, A., and Matthews, G. (2006). Impaired firing and cell-specific compensation in neurons lacking nav1.6 sodium channels. *J. Neurosci.* 26, 7172–7180. doi: 10.1523/jneurosci.1101-06.2006
- Wang, F., Flanagan, J., Su, N., Wang, L. C., Bui, S., Nielson, A., et al. (2012). RNAscope: a novel in situ RNA analysis platform for formalin-fixed, paraffin-embedded tissues. *J. Mol. Diagn.* 14, 22–29. doi: 10.1016/j.jmoldx.2011.08.002
- Wang, T., Guo, H., Xiong, B., Stessman, H. A. F., Wu, H., Coe, B. P., et al. (2016). De novo genic mutations among a Chinese autism spectrum disorder cohort. *Nat. Commun.* 7:13316. doi: 10.1038/ncomms13316
- Wang, X., Bey, A. L., Katz, B. M., Badea, A., Kim, N., David, L. K., et al. (2016). Altered mGluR5-homer scaffolds and corticostriatal connectivity in a Shank3 complete knockout model of autism. *Nat. Commun.* 7:11459. doi: 10.1038/ncomms11459
- Warburton, E. C., and Brown, M. W. (2015). Neural circuitry for rat recognition memory. *Behav. Brain Res.* 285, 131–139. doi: 10.1016/j.bbr.2014.09.050
- Weiss, L. A., Escayg, A., Kearney, J. A., Trudeau, M., MacDonald, B. T., Mori, M., et al. (2003). Sodium channels SCN1A, SCN2A and SCN3A in familial autism. *Mol. Psychiatry* 8, 186–194. doi: 10.1038/sj.mp.4001241
- Westenbroek, R. E., Merrick, D. K., and Catterall, W. A. (1989). Differential subcellular localization of the RI and RII Na⁺ channel subtypes in central neurons. *Neuron* 3, 695–704. doi: 10.1016/0896-6273(89)90238-9
- Wohr, M. (2014). Ultrasonic vocalizations in shank mouse models for autism spectrum disorders: detailed spectrographic analyses and developmental profiles. *Neurosci. Biobehav. Rev.* 43C, 199–212. doi: 10.1016/j.neubiorev.2014.03.021
- Wolff, M., Johannesen, K. M., Hedrich, U. B. S., Masnada, S., Rubboli, G., Gardella, E., et al. (2017). Genetic and phenotypic heterogeneity suggest therapeutic implications in SCN2A-related disorders. *Brain* 140, 1316–1336. doi: 10.1093/brain/awx054
- Won, H., Lee, H. R., Gee, H. Y., Mah, W., Kim, J. I., Lee, J., et al. (2012). Autistic-like social behaviour in shank2-mutant mice improved by restoring NMDA receptor function. *Nature* 486, 261–265. doi: 10.1038/nature11208
- Yamagata, T., Ogiwara, I., Mazaki, E., Yanagawa, Y., and Yamakawa, K. (2017). Nav1.2 is expressed in caudal ganglionic eminence-derived disinhibitory interneurons: mutually exclusive distributions of Nav1.1 and Nav1.2. *Biochem. Biophys. Res. Commun.* 491, 1070–1076. doi: 10.1016/j.bbrc.2017.08.013
- Yokoi, T., Enomoto, Y., Tsurusaki, Y., Naruto, T., and Kurosawa, K. (2018). Nonsyndromic intellectual disability with novel heterozygous SCN2A mutation and epilepsy. *Hum. Genome Var.* 5:20. doi: 10.1038/s41439-018-0019-5
- Yoo, T., Cho, H., Lee, J., Park, H., Yoo, Y. E., Yang, E., et al. (2018). GABA neuronal deletion of shank3 exons 14–16 in mice suppresses striatal excitatory synaptic input and induces social and locomotor abnormalities. *Front. Cell. Neurosci.* 12:341. doi: 10.3389/fncel.2018.00341
- Yuen, R. K., Thiruvahindrapuram, B., Merico, D., Walker, S., Tammimies, K., Hoang, N., et al. (2015). Whole-genome sequencing of quartet families with autism spectrum disorder. *Nat. Med.* 21, 185–191. doi: 10.1038/nm.3792

Conflict of Interest Statement: The authors declare that the research was conducted in the absence of any commercial or financial relationships that could be construed as a potential conflict of interest.

Copyright © 2019 Shin, Kweon, Kang, Kim, Kim, Kang, Kim, Hwang, Kim, Yang, Kim and Kim. This is an open-access article distributed under the terms of the Creative Commons Attribution License (CC BY). The use, distribution or reproduction in other forums is permitted, provided the original author(s) and the copyright owner(s) are credited and that the original publication in this journal is cited, in accordance with accepted academic practice. No use, distribution or reproduction is permitted which does not comply with these terms.



Developmental Regulation of KCC2 Phosphorylation Has Long-Term Impacts on Cognitive Function

Yvonne E. Moore¹, Leslie C. Conway², Heike J. Wobst³, Nicholas J. Brandon³, Tarek Z. Deeb¹ and Stephen J. Moss^{1,2,4*}

¹Department of Neuroscience, Tufts University School of Medicine, Boston, MA, United States, ²AstraZeneca-Tufts University Laboratory for Basic and Translational Neuroscience Research, Tufts University School of Medicine, Boston, MA, United States, ³Neuroscience, R&D Biopharmaceuticals, AstraZeneca, Boston, MA, United States, ⁴Department of Neuroscience, Physiology and Pharmacology, University College London, London, United Kingdom

OPEN ACCESS

Edited by:

Verena Tretter,
Medical University of Vienna, Austria

Reviewed by:

Henry Lee,
Boston Children's Hospital, Harvard
Medical School, United States
Michal Hershfinkel,
Ben-Gurion University of the Negev,
Israel

*Correspondence:

Stephen J. Moss
stephen.moss@tufts.edu

Received: 16 January 2019

Accepted: 01 July 2019

Published: 23 July 2019

Citation:

Moore YE, Conway LC, Wobst HJ, Brandon NJ, Deeb TZ and Moss SJ (2019) Developmental Regulation of KCC2 Phosphorylation Has Long-Term Impacts on Cognitive Function. *Front. Mol. Neurosci.* 12:173. doi: 10.3389/fnmol.2019.00173

GABA_A receptor-mediated currents shift from excitatory to inhibitory during postnatal brain development in rodents. A postnatal increase in KCC2 protein expression is considered to be the sole mechanism controlling the developmental onset of hyperpolarizing synaptic transmission, but here we identify a key role for KCC2 phosphorylation in the developmental E_{GABA} shift. Preventing phosphorylation of KCC2 *in vivo* at either residue serine 940 (S940), or at residues threonine 906 and threonine 1007 (T906/T1007), delayed or accelerated the postnatal onset of KCC2 function, respectively. Several models of neurodevelopmental disorders including Rett syndrome, Fragile X and Down's syndrome exhibit delayed postnatal onset of hyperpolarizing GABAergic inhibition, but whether the timing of the onset of hyperpolarizing synaptic inhibition during development plays a role in establishing adulthood cognitive function is unknown; we have used the distinct KCC2-S940A and KCC2-T906A/T1007A knock-in mouse models to address this issue. Altering KCC2 function resulted in long-term abnormalities in social behavior and memory retention. Tight regulation of KCC2 phosphorylation is therefore required for the typical timing of the developmental onset of hyperpolarizing synaptic inhibition, and it plays a fundamental role in the regulation of adulthood cognitive function.

Keywords: KCC2, depolarizing GABA, autism, cognition, social behavior, memory, phosphorylation

INTRODUCTION

Cl⁻-permeable Glycine and GABA_A receptors are the exclusive mediators of fast synaptic inhibition in the central nervous system. Maintaining low intraneuronal Cl⁻ levels, and thus an inwardly directed electrochemical driving force for Cl⁻, is essential for the inhibitory efficacy of these receptors (Bormann et al., 1987). However, during the early postnatal period, neurons have a high [Cl⁻]_i, resulting in depolarizing responses to GABA_A receptor activation, demonstrated through studies on the rodent brain (Ben-Ari et al., 1989, 2007; Owens et al., 1996). A progressive increase in Cl⁻ extrusion as development proceeds is responsible for the conversion of GABA_A currents

from depolarizing to hyperpolarizing (Rivera et al., 1999). This increase in Cl^- extrusion is widely considered to be due to the functional upregulation of the neuron-specific K^+/Cl^- cotransporter type 2 (KCC2), which couples the outwardly directed K^+ gradient to extrude Cl^- from the cell against its concentration gradient (Li et al., 2002; Uvarov et al., 2006). KCC2 activity is therefore essential for establishing the developmental onset of hyperpolarizing GABA_A receptor currents.

An upregulation of KCC2 gene expression and protein production are currently thought to be the primary driver of the increase in KCC2 function during development. However, we have previously demonstrated a critical role for the phosphorylation of several KCC2 residues within its intracellular C-terminal domain that regulate its function in the mature brain. Phosphorylation of residue serine 940 (KCC2-S940) is necessary for maintaining KCC2 function under pathological conditions in the adult brain (Lee et al., 2007, 2011; Silayeva et al., 2015). In contrast, phosphorylation of threonine residues 906 and 1007 (KCC2-T906/T1007) decreases during development (Rinehart et al., 2009; Friedel et al., 2015), and simultaneous alanine substitution at both residues increases KCC2 function in cell lines and mature neurons (Rinehart et al., 2009; de Los Heros et al., 2014; Titz et al., 2015; Moore et al., 2018). But it is unknown whether phosphorylation of these residues similarly regulates KCC2 function during development, and subsequently the timing of the developmental onset of hyperpolarizing fast synaptic inhibition.

Importantly, KCC2 dysfunction and dysregulation of Cl^- homeostasis occurs in neurodevelopmental disorders including Down syndrome (Deidda et al., 2015), fragile \times syndrome (He et al., 2014), and Rett syndrome (Duarte et al., 2013; Tang et al., 2016). Postnatal E_{GABA} hyperpolarization is delayed in these disorders, but whether this contributes to any of the cognitive deficits characteristic of these pleiotropic disorders is unknown. We, therefore, sought to identify whether the amount of KCC2 function and the timing of the developmental onset of fast synaptic inhibition plays a determining role in cognitive function in adulthood, particularly in the context of behaviors associated with autism-spectrum disorders.

MATERIALS AND METHODS

Animal Care

All animal studies were performed with protocols approved by the Institutional Animal Care and Use committee of Tufts New England Medical Center. Animals live in temperature-controlled rooms on a 12 h day/light cycle, fed *ad libitum*, with cage changes performed twice weekly.

Tissue Preparations

Cultured Mouse Hippocampal Neurons

Electrophysiology experiments were performed on hippocampal neurons cultured from P1 mouse pups. Pups were cooled on ice before decapitation and brain removal. Brains were submerged in ice-cold HEPES-buffered saline solution, meninges removed from the brain surface, and hippocampi dissected out.

Hippocampi were transferred to 10 mL of 0.25% trypsin in HBSS at 37°C for 9 min to dissociate the tissue. Trypsin was then removed from the hippocampi, which were then washed three times with HBSS to remove any residual trypsin. Ten milliliters of fresh media was then added to the cells, and the cells were triturated with a 10 mL pipette, by gently pipetting up and down 15 times. Cells were then filtered to remove non-dissociated tissue. Four-hundred thousand cells were plated onto each pre-prepared PLL coated 30 mm dish each containing 3 mL culture media [Neurobasal A media containing B27 (2%), glucose (0.6%), Glutamax (1%), and penicillin/streptomycin (1%)]. Cells were maintained at 37°C in a humidified 5% CO₂ incubator.

Cultured Rat Hippocampal Neurons

Cultured hippocampal neurons obtained from Sprague-Dawley rat embryonic day 18 embryos. Neuronal preparation was carried out as described above for the mouse neurons. Cells were then plated onto pre-prepared PLL coated 6cl dishes, each containing 6 mL of culture media [Neurobasal media containing B27 (2%), glucose (0.6%), Glutamax (1%), and penicillin/streptomycin (1%)]. Cells were maintained at 37°C in a humidified 5% CO₂ incubator. Hippocampal neurons were lysed in RIPA Buffer (2% Triton-X-100, 0.5% deoxycholic acid, 5 mM EDTA, 5 mM EGTA, 1 mM sodium orthovanadate, 25 mM sodium fluoride, 10 mM sodium pyrophosphate, 100 mM NaCl, 10 mM sodium phosphate monobasic, pH7.4) containing protease inhibitors by rotating samples for 30 min at 4°C. Insoluble material was removed by centrifugation for 15 min at 15,700× g.

Whole Hippocampal Dissection

Mice were deeply anesthetized with isoflurane before decapitation at the second cervical vertebrae. Brains were carefully removed and rinsed in ice-cold phosphate buffered saline. The hippocampus were then dissected with forceps, and immediately put into ice-cold RIPA lysis buffer (2% Triton-X-100, 0.5% deoxycholic acid, 5 mM EDTA, 5 mM EGTA, 1 mM sodium orthovanadate, 25 mM sodium fluoride, 10 mM sodium pyrophosphate, 100 mM NaCl, 10 mM sodium phosphate monobasic, pH7.4) containing protease inhibitors. Here, the tissue was dissociated with a 26G needle and rotated at 4°C for 30 min to lyse. The samples were then centrifuged at 15,700× g for 15 min at 4°C to pellet all insoluble material. The supernatant was used for western blotting.

Biochemistry

SDS-PAGE and Western Blotting

Lysate samples were separated by SDS-PAGE and transferred to nitrocellulose membrane. Following the transfer, membranes were blocked at room temperature for 1 h in 5% milk, 1% BSA in PBS-Tween. Membranes were then incubated with primary antibody diluted in blocking solution overnight at 4°C to detect total KCC2 (Millipore 07-432), KCC2 pS940 [PhosphoSolutions, previously characterized (Lee et al., 2011)], and α -tubulin (Abcam 7291). Membranes were then washed three times in PBS-Tween and incubated with the respective HRP-conjugated secondary antibody. Secondary antibody

incubations were carried out in blocking solution for 1 h at room temperature. Membranes were then washed three times in PBS-Tween, followed by one wash in PBS. Chemiluminescence signal was detected using SuperSignal West Dura Extended Duration Substrate (Thermo Scientific). Quantification of chemiluminescence signal was carried out using Image Lab 5.0 (BioRad).

Patch Clamp Electrophysiology

All electrophysiology experiments were performed on hippocampal mouse neurons cultured from P1 pups. All data incorporates Ns from a minimum of three separate neuronal dissections per genotype.

Solutions and Set Up

Recordings were conducted at 32° C in bath saline containing (in mM) NaCl 140, KCl 2.5, CaCl₂ 2, MgCl₂ 1.5, Hepes 10, glucose 11, pH 7.4 NaOH. TTX was used at a concentration of 500 nM. Muscimol was used at 1 μM and applied through a three-barrel microperfusion system (700 μm, Warner Instruments, Hamden, CT, USA) closely positioned above the cell, at a rate of 0.5 mL/min and we used a computer-controlled perfusion fast-step device (Warner Instruments, Hamden, CT, USA) to ensure fast and complete exchange of solutions. Perforated patch clamp experiments were performed with gramicidin (50 μg/mL) inside a patch pipette (3–6 mohm) containing (in mM) KCl 140, HEPES 10, pH 7.4 KOH, and experiments began once adequate perforation had been achieved, classed as a series resistance <50 mohm.

E_{GABA} Measurements

E_{GABA} was measured by application of muscimol (1 μM) during positive going voltage ramps (10 mV or 20 mV, 1 s duration), and subsequent calculation of the reversal potential of the leak-subtracted muscimol currents. Data were acquired at 10 kHz with an Axopatch 200B amplifier and Clampex 10 software (Molecular Devices, Sunnyvale, CA). Once E_{GABA} values were obtained, these were used to determine the intracellular Cl[−] concentration of the cells. This was done using the Nernst equation: $E_{Cl^-} = RT/zF \times \ln[Cl^-]_o/[Cl^-]_i$.

Behavior

For all behavioral experiments, mice were habituated in the testing rooms for 1 h prior to testing. Testing was performed at similar times of the day (between 9 and 11 am), in temperature-controlled rooms (70–74°C). Littermates were always tested at the same time. Following completion of each experiment, mice were returned to their home cage. Equipment was cleaned between each mouse using 70% ethanol, followed by Clidox (chlorine dioxide based sterilant). Male mice were used for all experiments.

3-Chamber Social Interaction Assay

Mice were tested in this assay between 6 and 7 weeks of age. A 3-chamber set up, each chamber measuring 40 cm × 40 cm, was used. Mice were placed in the center chamber, and allowed to explore all chambers for 10 min. Metal cages, measuring 4 cm × 4 cm × 5 cm with 1 cm gaps between each vertical bar, were then placed in the center of the left and right chambers,

and a juvenile unfamiliar male mouse (3–4 weeks old) placed under one of the cages. The test mice were then allowed to explore the arena for 10 min and time spent in the chamber with the mouse vs. the empty cage was calculated. An additional unfamiliar juvenile male mouse was then placed under the previously empty cage, and the test mice were again allowed to explore the arena for 10 min and the time spent in the chamber with the familiar vs. the novel mouse was calculated. An overhead camera and Ethovision software was used to detect time spent in each region of the arena, and to generate heat maps of the data.

Barnes Maze Assay

Mice were tested in this assay between 8 and 10 weeks of age. The maze was a circular platform, measuring 1.5 m in diameter, with 40 holes at the perimeter each measuring 2.5 cm in diameter. An escape tunnel was placed under one hole. Different shapes drawn onto article were used as spatial cues around the maze. Mice were placed onto the center of the maze under a wire cage and allowed to orient themselves for 10 s. The cage was then lifted and the mice were given 3 min to explore the maze and find the escape hole, and latency to exit the maze through this escape tunnel was recorded. If the mice did not enter the escape within 3 min they were removed from the maze and their time was recorded as the maximum 180 s. This was repeated twice on each day, with a 30 min delay between each trial, and the average of these trials was used as the final value. This process was completed on six consecutive days. To assess memory, on day 7 the escape hole was removed, and the mice were given 3 min to explore the arena. The time spent at each hole was measured, and each hole assigned to a 45° bin each composed of five holes, with 0° relating to the goal hole and the two holes either side of this hole. The 45° bins then continued in a clockwise direction around the perimeter of the maze. This was also repeated on day 14 to memory after 1 week of no exposure to the maze. An overhead camera and Ethovision software was used to detect time spent in each region of the arena, and to generate heat maps of the data.

Statistical Analysis

All data are presented as the mean ± standard error of the mean (SEM). Biochemistry data were analyzed using the one-way analysis of variance (ANOVA) test. Electrophysiology data were analyzed using the unpaired *T*-test. Behavioral data were analyzed using the unpaired *T*-test to compare between genotypes, and the paired *T*-test to compare data obtained on individual mice across different trials. *P* values < 0.05 are considered statistically significant.

RESULTS

Phosphorylation of KCC2 Residues S940 and T906/T1007 Control the Timing of the Postnatal Onset of Hyperpolarizing Inhibition

Phosphorylation of KCC2 residue serine 940 (S940) regulates KCC2 function in the adult brain (Lee et al., 2007;

Silayeva et al., 2015), and we sought to examine the developmental profile of S940 phosphorylation. We measured total KCC2 expression and KCC2 S940 phosphorylation in cultured rat hippocampal neurons at 5, 10, 15 and 20 days *in vitro* (DIV) and detected phosphorylation of this residue at each of these time points. Total KCC2 expression increased linearly over-development, with significantly lower expression at 5 DIV (Mean: 0.19 a.u. \pm 0.02., compared to 20 DIV, $P < 0.0001$, $N = 3$), 10 DIV (Mean: 0.48 a.u. \pm 0.05., compared to 20 DIV, $P < 0.0001$, $N = 3$) and 15 DIV (Mean: 0.64 a.u. \pm 0.05., compared to 20 DIV, $P = 0.0003$, $N = 3$). We detected a decrease in S940 phosphorylation between 5 and 10 DIV, followed by maintenance at this level as the neurons further matured (**Figure 1A**; 5 DIV Mean: 1.96 a.u. \pm 0.18, $P = 0.0012$ compared to 20 DIV, $N = 3$; 10 DIV Mean: 1.06 a.u. \pm 0.03, $P = 0.96$ compared to 20 DIV, $N = 3$; 15 DIV Mean: 1.03 a.u. \pm 0.15, $P = 1.00$ compared to 20 DIV $N = 3$). Given that S940 phosphorylation scales with the developmental increase in total KCC2 expression between 10 and 20 DIV, we hypothesized that S940 phosphorylation plays a role in the developmental regulation of KCC2 function. To answer this question, we performed gramicidin perforated patch-clamp experiments to measure E_{GABA} values between 4 and 22 DIV on hippocampal neurons cultured from phospho-mutant knock-in mice, in which residue S940 is mutated to an alanine residue (S940A) to prevent its phosphorylation (Silayeva et al., 2015; **Figure 1B**). Compared to WT, the developmental onset of hyperpolarizing GABAergic inhibition was delayed in the S940A neurons, deviating from WT values between 4 and 6 DIV and 14 and 18 DIV (**Supplementary Table S1**), but displayed similar E_{GABA} values to WT neurons by 21–22 DIV (**Figure 1C**; **Supplementary Table S2**). $[\text{Cl}^-]_i$ values were calculated using the Nernst equation (**Figure 1D**; **Supplementary Table S2**), and S940A neurons had higher $[\text{Cl}^-]_i$ levels between 4 and 6 DIV and 10 and 18 DIV. This indicates that S940 phosphorylation plays an important role in regulating KCC2 function at several stages of postnatal development and highlights a critical role for KCC2-S940 phosphoregulation for the appropriate timing of the developmental onset of hyperpolarizing synaptic inhibition. Resting membrane potentials were also measured across development and no differences were detected between WT and S940A neurons (**Supplementary Figure S1**; **Supplementary Table S3**).

KCC2 can also be phosphorylated at threonine residues 906 and 1007 (T906/T1007; Rinehart et al., 2009). Phosphorylation of these residues decreases during development which may contribute to the developmental upregulation of KCC2 function (Rinehart et al., 2009; Friedel et al., 2015). Using an additional phospho-mutant knock-in mouse model, in which KCC2-T906/T1007 residues are mutated to alanine to prevent their phosphorylation (T906A/T1007A; Moore et al., 2018), we were able to directly assess the role of these phosphorylation sites in the regulation of KCC2 function during development. We performed gramicidin perforated patch-clamp experiments on hippocampal neurons cultured

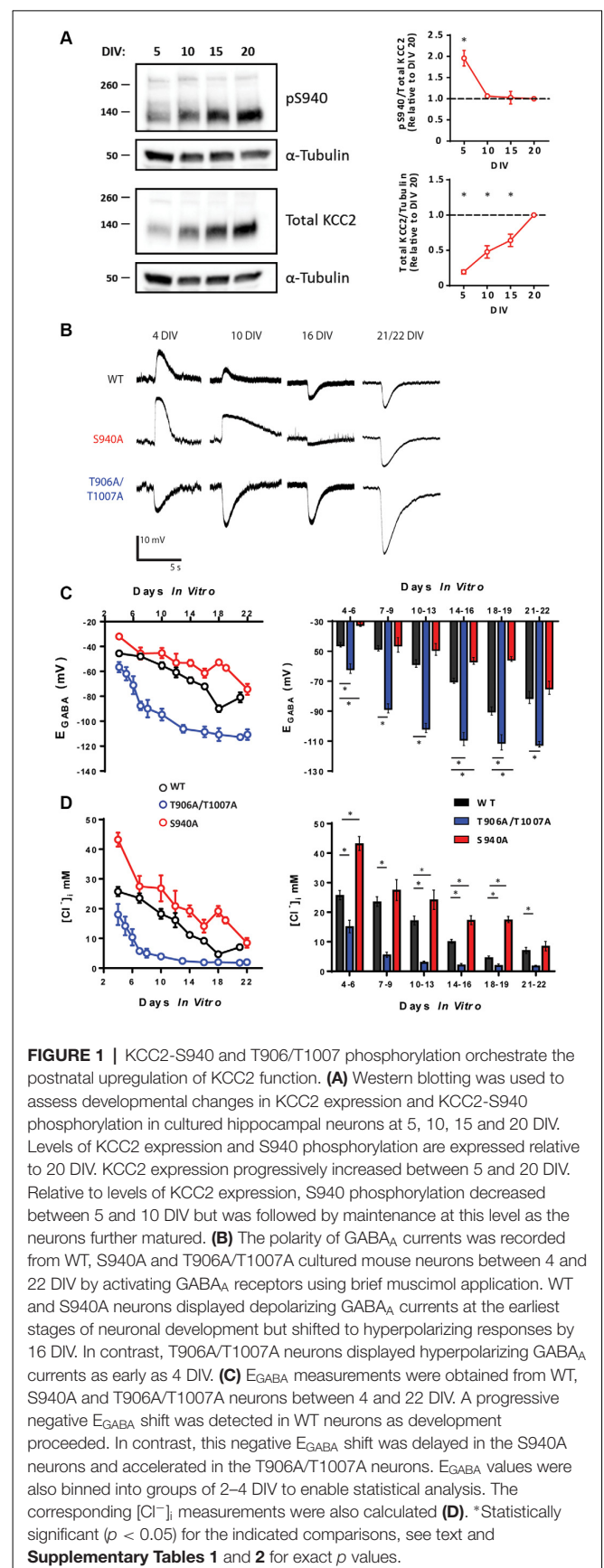


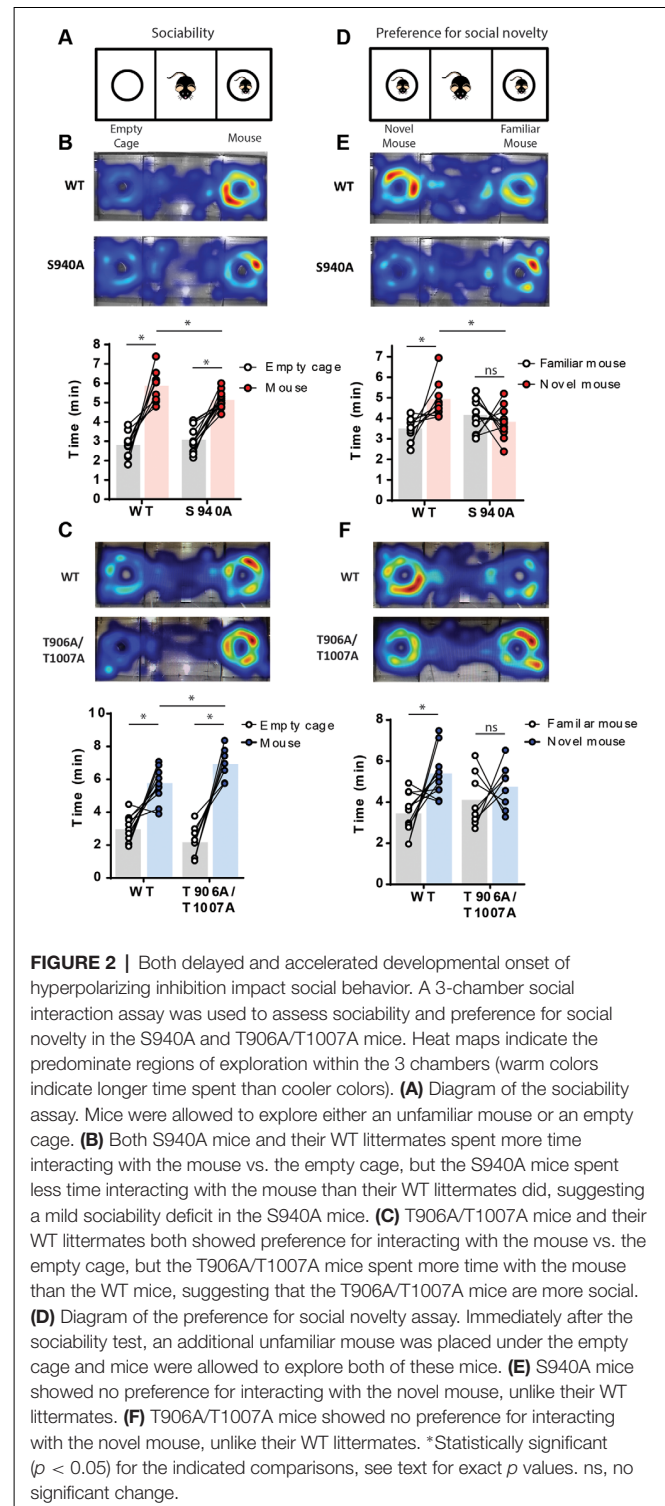
FIGURE 1 | KCC2-S940 and T906/T1007 phosphorylation orchestrate the postnatal upregulation of KCC2 function. **(A)** Western blotting was used to assess developmental changes in KCC2 expression and KCC2-S940 phosphorylation in cultured hippocampal neurons at 5, 10, 15 and 20 DIV. Levels of KCC2 expression and S940 phosphorylation are expressed relative to 20 DIV. KCC2 expression progressively increased between 5 and 20 DIV. Relative to levels of KCC2 expression, S940 phosphorylation decreased between 5 and 10 DIV but was followed by maintenance at this level as the neurons further matured. **(B)** The polarity of GABA_A currents was recorded from WT, S940A and T906A/T1007A cultured mouse neurons between 4 and 22 DIV by activating GABA_A receptors using brief muscimol application. WT and S940A neurons displayed depolarizing GABA_A currents at the earliest stages of neuronal development but shifted to hyperpolarizing responses by 16 DIV. In contrast, T906A/T1007A neurons displayed hyperpolarizing GABA_A currents as early as 4 DIV. **(C)** E_{GABA} measurements were obtained from WT, S940A and T906A/T1007A neurons between 4 and 22 DIV. A progressive negative E_{GABA} shift was detected in WT neurons as development proceeded. In contrast, this negative E_{GABA} shift was delayed in the S940A neurons and accelerated in the T906A/T1007A neurons. E_{GABA} values were also binned into groups of 2–4 DIV to enable statistical analysis. The corresponding $[\text{Cl}^-]_i$ measurements were also calculated **(D)**. *Statistically significant ($p < 0.05$) for the indicated comparisons, see text and **Supplementary Tables 1 and 2** for exact p values.

from T906A/T1007A mice and measured E_{GABA} between 4 and 22 DIV (**Figure 1B**). E_{GABA} values were strongly hyperpolarized in T906A/T1007A neurons compared to WT neurons across all stages of neuronal development (**Supplementary Table S1**). The corresponding $[Cl^-]_i$ values were also measured, demonstrating $[Cl^-]_i$ levels were lower in the T906A/T1007A neurons at all time points (**Figure 1C**; **Supplementary Table S2**). This indicates that preventing phosphorylation of these sites significantly accelerates the postnatal onset of hyperpolarizing inhibition, largely eliminating postnatal depolarizing GABAergic signaling. Resting membrane potentials were also measured across development and no differences were detected between WT and T906A/T1007A neurons (**Supplementary Figure S1**; **Supplementary Table S3**).

KCC2-T906A/T1007A and KCC2-S940A mutations altered KCC2 function independently of KCC2 protein expression in mature neurons. To determine if this is also the case in immature neurons, we compared KCC2 expression in total hippocampal lysate of P5 WT (Mean: 2.99 ± 0.27 a.u.; $N = 3$), T906A/T1007A (Mean: 3.69 ± 0.35 a.u.; $N = 3$) and S940A (Mean: 2.82 ± 0.37 a.u.; $N = 3$) mice (**Supplementary Figure S2**). No difference in KCC2 expression levels was detected between WT and T906A/T1007A ($P = 0.19$) or between WT and S940A ($P = 0.73$) suggesting that these mutations are specifically enhancing the surface activity of KCC2 rather than by altering KCC2 expression during this time period.

KCC2 Function Alters Social Interaction Behaviors

Delayed timing of the developmental onset of fast synaptic inhibition has been detected in several models of neurodevelopmental disorders associated with autism-like behaviors (Duarte et al., 2013; He et al., 2014; Deidda et al., 2015; Tang et al., 2016). Social interaction deficits that persist into adulthood are a core feature of autism-spectrum disorders, and so we assessed the impact of the S940A or the T906A/T1007A mutations on social behavior in adult mice (6–7 weeks old). Social interaction was assessed using a 3-chamber social interaction test. Firstly, sociability was examined by measuring time spent interacting with an unfamiliar mouse vs. an empty cage (**Figure 2A**). S940A mice, and their WT littermates, both spent more time interacting with the mouse vs. the empty cage (**Figure 2B**; WT: Empty 2.81 ± 0.20 min, Mouse 5.88 ± 0.25 min, $p < 0.0001$, $N = 10$; S940A: Empty 3.1 ± 0.2 min, Mouse 5.1 ± 0.1 min, $p < 0.0001$, $N = 13$). However, the S940A mice spent less total time interacting with the mouse compared to their WT littermates (WT: 5.9 ± 0.3 min; S940A: 5.1 ± 0.1 min; $p = 0.0075$), indicating that S940A mice have a reduced preference for social interaction. Although, time spent near the empty cage was not significantly different between WT and S940A mice (WT: 2.81 ± 0.2 min; S940A: 3.08 ± 0.2 min; $p = 0.3135$). T906A/T1007A mice also spent more time interacting with the mouse vs. the empty cage (**Figure 2B**; Empty: 2.2 ± 0.4 min, Mouse: 7.0 ± 0.3 min; $p = 0.0002$, $N = 8$), as did their WT littermates (Empty: 3.0 ± 0.3 min, Mouse: 5.8 ± 0.3 min; $p = 0.0005$, $N = 11$). Interestingly,



the T906A/T1007A showed increased sociability compared to WT mice, demonstrated by an increase in the total time spent with the mouse compared to WT (**Figure 2C**; WT: 5.8 ± 0.3 min; T906A/T1007A: 7.0 ± 0.3 min; $p = 0.0247$). Moreover, T906A/T1007A mice trended toward spending less time near the empty cage than WT mice, but not to

a significant degree (WT: 2.98 ± 0.2 min; T906A/T1007A: 2.18 ± 0.3 min; $p = 0.0688$).

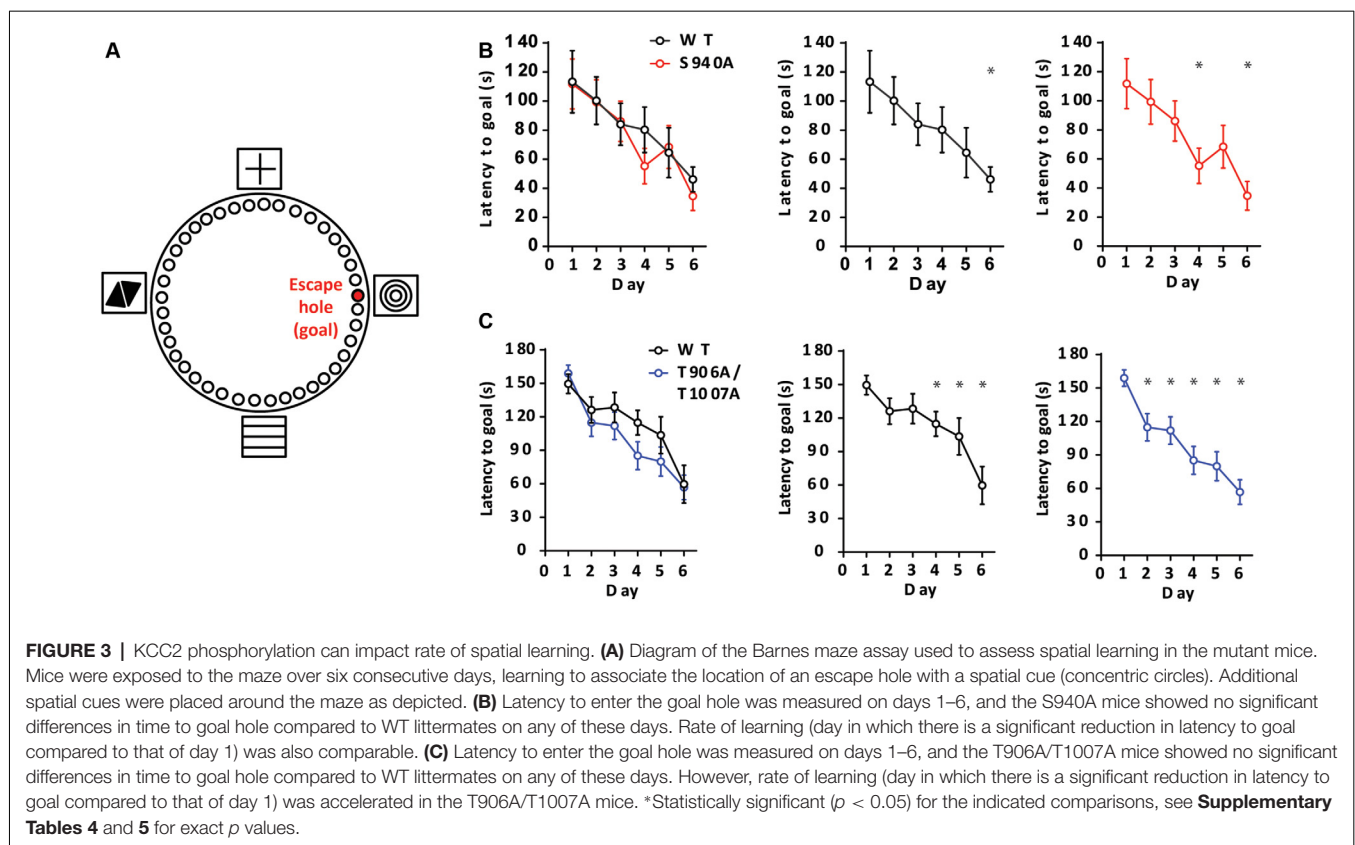
A novel mouse was then placed in the empty cage to assess preference for social novelty (**Figure 2D**). S940A mice showed no preference for interacting with the novel mouse compared to the familiar mouse (Familiar: 4.13 ± 0.02 min, Novel: 3.8 ± 0.2 min; $P = 0.42$, $N = 12$), in contrast to their WT littermates which did show preference for the novel mouse (**Figure 2E**; Familiar: 3.5 ± 0.6 min, Novel: 4.9 ± 0.3 min; $P = 0.0160$, $N = 9$). WT mice also spent greater total time interacting with the novel mouse compared to S940A mice (WT: 4.9 ± 0.3 min; S940A: 3.8 ± 0.2 min; $P < 0.0063$). Similarly, the T906A/T1007A mice showed no preference for the novel mouse (Familiar: 4.1 ± 0.5 min, Novel: 4.7 ± 0.4 min; $p = 0.46$, $N = 8$), while their WT littermates did show preference for the novel mouse (**Figure 2F**; Familiar: 3.4 ± 0.3 min, Novel: 5.38 ± 0.01 min; $P = 0.0112$, $N = 11$). These data demonstrate that either delaying or accelerating the developmental E_{GABA} shift results in altered social behaviors, indicating that the postnatal onset of KCC2 function must be finely orchestrated to establish typical social behaviors in adulthood.

KCC2 Function Impacts Spatial Memory

We next sought to determine if altered timing of developmental E_{GABA} hyperpolarization impacts learning and memory, as intellectual disabilities are frequently present in patients with autism-spectrum disorders. To assess learning and memory we used a Barnes maze assay, and latency to enter the escape hole

over six consecutive days was recorded (**Figure 3A**). The S940A mice showed comparable escape latencies to their WT littermates over the 6-day learning period (WT: $N = 11$; S940A: $N = 12$ for all days; **Figure 3B**; **Supplementary Table S4**). Similarly, the T906A/T1007A mice did not exhibit differences in the latency to find the goal hole compared to WT littermates (WT: $N = 14$; T906A/T1007A: $N = 15$ for all days; **Figure 3C**; **Supplementary Table S5**). However, the T906A/T1007A mice did show a significant improvement over their day 1 escape latencies by training day 2. In comparison, their WT littermates which did not show significantly improved performance over their day 1 escape latencies until training day 4. This suggests that rate of spatial learning was mildly improved in the T906A/T1007A mice (**Figure 3C**; **Supplementary Table S5**).

Long term memory was then assessed over increasing periods of time after the learning portion of the Barnes maze assay. We removed the escape chamber on day 7 and 14 and then measured the time spent in the space where the escape hole was originally located. Time spent at the goal hole was comparable between WT and S940A mice on both day 7 (WT: $N = 11$; S940A: $N = 12$; **Figures 4A,B**) and day 14 (WT: $N = 8$; S940A: $N = 11$; **Figures 4E,F**) which would initially suggest no memory impairment is present in S940A mice. However, when memory retention is normal, mice will spend significantly more time investigating the goal hole than any of the remaining holes in the maze. In other words, they will display a specific interest in the goal hole over all other holes. Interestingly, by day 14 S940A mice spent equal amounts of time at the non-goal regions as they



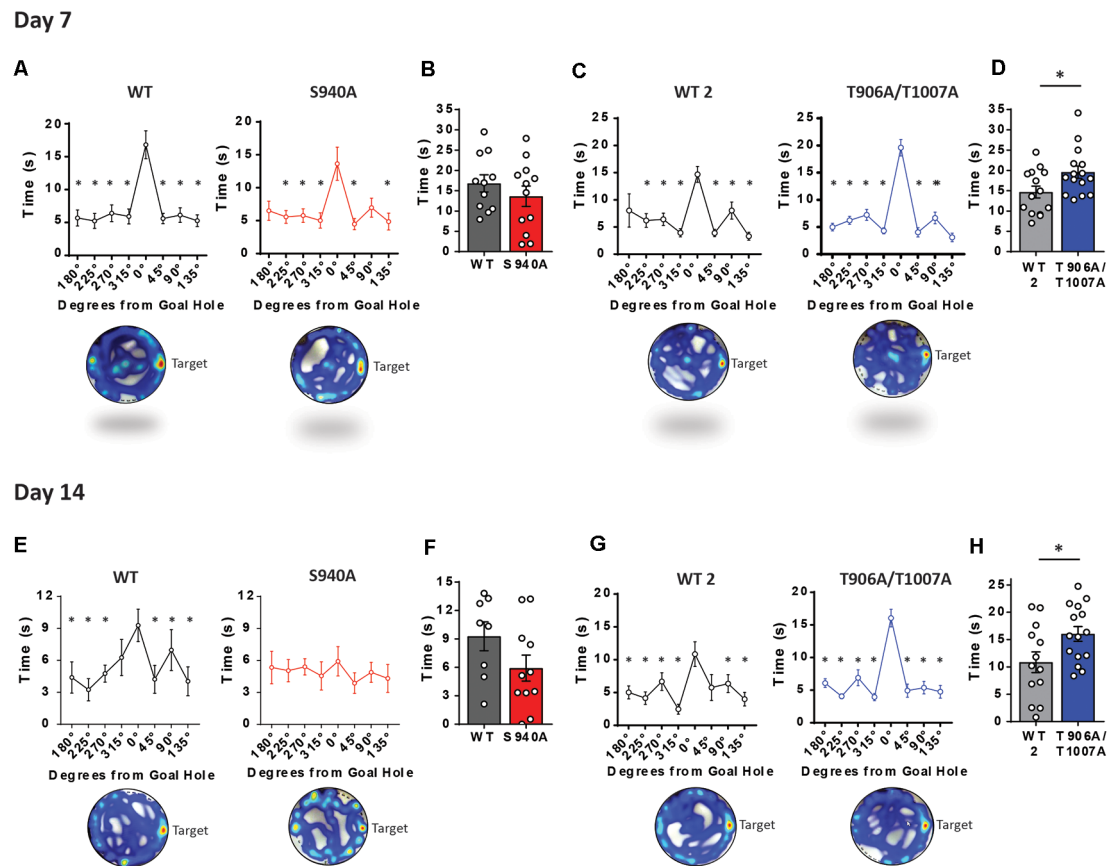


FIGURE 4 | KCC2-S940A and KCC2-T906A/T1007A mutations have bidirectional effects on spatial memory retention. Spatial memory was assessed using a Barnes maze assay. After 6 days of learning the location of an escape hole (see **Figure 3**) time spent at each of the holes was measured on day 7 and day 14 upon removal of the escape tunnel, and data binned into 45° groups. **(A)** S940A mice and their WT littermates both show preference for the goal area on day 7, and spent comparable time at the goal area as their WT littermates **(B)**. **(C)** T906A/T1007A mice and their WT littermates both show preference for the goal area on day 7, but T906A/T1007A mice spent more time at the goal than their WT littermates **(D)**. **(E)** S940A mice show no preference for the goal hole on day 14, but time spent at the goal was comparable to their WT littermates **(F)**. **(G)** T906A/T1007A mice show enhanced specificity of the spatial memory on day 14 compared to their WT littermates, and T906A/T1007A mice spent more time at the goal than their WT littermates **(H)**, indicating that the T906A/T1007A mutations enhance spatial memory retention. *Statistically significant ($p < 0.05$) for the indicated comparisons, see **Supplementary Table 6** for exact p values. ns, no significant change.

did at the goal region demonstrating a lack of spatial memory specificity compared to their WT littermates, suggesting that S940A mice have a deficit in memory retention (**Figure 4E**; **Supplementary Table S6**). In contrast, T906A/T1007A mice spent more time at the goal hole position at both day 7 (WT: $N = 14$; T906A/T1007A: $N = 15$; **Figures 4C,D**) and day 14 (WT: $N = 13$; T906A/T1007A: $N = 15$; **Figures 4E,F**) compared to their WT littermates (**Supplementary Table S6**), suggesting that increasing KCC2 function may improve memory retention.

DISCUSSION

KCC2 is heavily phospho-regulated in the adult brain (Silayeva et al., 2015; Moore et al., 2017, 2018) and we have now identified a critical role for phosphorylation in regulating KCC2 function during postnatal brain development. We have determined that

KCC2 phospho-regulation at sites S940 and T906/T1007 plays differential roles in cognition. Our data suggest a prolonged postnatal period of depolarizing GABA that may contribute to behavioral manifestations of neurodevelopmental disorders, specifically abnormalities in social behavior and memory retention. Unexpectedly, accelerating the postnatal onset of KCC2 function also resulted in social abnormalities, indicating that postnatal depolarizing GABA may be necessary for the development of typical social behavior. However, KCC2 gain-of-function mice excelled at spatial memory tasks suggesting that increasing KCC2 activity can also positively impact cognitive function.

The time-course of the developmental E_{GABA} shift we observed in WT hippocampal neurons matches the timing of the disappearance of giant depolarizing potentials in CA3 slices (Ben-Ari et al., 1989), the E_{GABA} shift in CA1 neurons in slices (Zhang et al., 1991) and cortical neurons of the

rat (Owens et al., 1996), all of which indicate that the mechanisms underlying the E_{GABA} shift is preserved in culture. By preventing the phosphorylation of endogenous KCC2 *in vivo* at sites S940 and T906/T1007 we were able to precisely establish the postnatal periods during which phosphorylation of these residues plays a role in the developmental onset of hyperpolarizing synaptic inhibition. KCC2 was most heavily phosphorylated at site S940 during the 1st postnatal week, and the largest deficit in KCC2 function in the S940A neurons was detected at this time period. This indicates that S940 phosphorylation plays an important role in shaping the timing of the postnatal onset of hyperpolarizing inhibition. The S940A mutation had less impact on basal KCC2 function as the neurons matured and had no detrimental impact by the most mature stages of development. Interestingly, the impact of the S940A mutation on KCC2 function followed a biphasic pattern, with no effect on basal KCC2 function detected between WT and S940A neurons at both 7–9 DIV and 21–22 DIV, despite deficits detected at all other developmental time points. Interpreting this finding is complicated by our lack of understanding of the signaling cascades that regulate S940 phosphorylation during development, and whether or not these pathways also change during development. S940 is phosphorylated by protein kinase C in mature neurons (Lee et al., 2007), which may provide a starting point for future investigations into the signaling cascades that impinge on KCC2-S940 and affect its function. G-protein-coupled receptor (GPCR) signaling through group 1 metabotropic glutamate receptors, metabotropic Zn(2+) receptors, 5-HT_{2A} serotonin receptors and A_{3A}-type adenosine receptors can regulate KCC2 function in neurons (Mahadevan and Woodin, 2016), and so examining these signaling cascades in the context of developmental KCC2 regulation may be informative. In contrast, phosphorylation of KCC2 at sites T906/T1007 appears to play a key role in regulating KCC2 function at all stages of neuronal development. Interestingly, elimination of depolarizing GABA occurred as early as 4 DIV in the T906A/T1007A neurons. KCC2 protein expression is still very low at such early stages of development which strongly suggests that the phosphorylation state of KCC2 is the major determinant of the efficacy of KCC2-mediated Cl[−] transport, surpassing the importance of KCC2 protein expression levels.

Recent work has identified that GABA is depolarizing for an extended period of time in several neurodevelopmental disorders associated with autism-like behaviors (He et al., 2014; Deidda et al., 2015; Tang et al., 2016). Whether this delayed E_{GABA} shift plays any role in the behavioral consequences of these pleiotropic disorders has not previously been assessed, but using the S940A mice we were able to address this question. Abnormal social behavior is a core feature of autism-spectrum disorders, and we detected profound social interaction abnormalities in the S940A mice. This interesting finding suggests that the delayed onset of hyperpolarizing synaptic inhibition detected in various models of neurodevelopment disorders associated with social interaction deficits may, in fact, be responsible for this abnormal behavior. Correcting this delay in established models of autism-spectrum disorders

would determine whether this delay is solely responsible for the abnormal social behavior.

It was particularly interesting that premature onset of KCC2 function also results in abnormal social behavior, but increased preference in social interaction in contrast to a reduced preference seen in the S940A mice. This suggests that reduced vs. increased KCC2 activity alters the function of neuronal networks involved in social behaviors in different ways. However, T906A/T1007A mice did display deficient preference for social novelty, which is a characteristic behavior seen in mouse models of autism-spectrum disorders (Takumi et al., 2019). This was an unexpected finding as no previous studies have linked excessive KCC2 function to the onset of autism-like behaviors. This is especially important as enhancing KCC2 function has been proposed as a novel mechanism for treating seizures (Moore et al., 2018), but our finding here raises some questions regarding the potential safety of using pharmacological activators of KCC2 in healthy individuals during early brain development.

In addition to the impact of the S940A and T906A/T1007A mutations on social behaviors, we also detected deficient or improved memory retention in the S940A and T906A/T1007A mice, respectively. The contrasting impact of the S940A and T906A/T1007A mutations on memory retention detected in this study is interesting in light of the fact that both deficient and improved memory retention is associated with autism-spectrum disorders (Gras-Vincendon et al., 2008; Treffert, 2009). Our observation that S940A mice show deficits in spatial memory retention suggests that there may be a pathological link between the delayed E_{GABA} shift detected in several neurodevelopmental disorders and the often co-morbid intellectual disability present in these patients. Interestingly, several studies suggest that adulthood regulation of KCC2 can impact memory retention. Reduced KCC2 expression and depolarizing GABA has been detected in aged mouse brains, which is suggested to reduce synapse specificity of LTP and contribute to cognitive decline in old age (Ferando et al., 2016). Moreover, KCC2 deficits have been detected in several neurodegenerative disorders (Fuchs et al., 2010) and reducing intracellular Cl[−] levels can rescue memory deficits in a mouse model of Huntington's disease (Dargaei et al., 2018), suggesting that increasing KCC2 function may be therapeutically beneficial for disorders associated with memory deficits. In support of this, T906A/T1007A mice performed better in the spatial memory tasks compared to their WT littermates, suggesting that increasing KCC2 function may improve memory retention.

It is possible that rapid transient neuronal Cl[−] loading may play a role in memory retention, rather than a specific impact of altered GABAergic signaling during development. Adulthood manipulation of KCC2 function would be required to differentiate the developmental vs. the mature alteration in KCC2 function as the cause of the observed differences in memory retention between the S940A and T906A/T1007A mutant mice. Moreover, whether autism-associated memory impairments can be rescued in adulthood through KCC2 manipulation, or whether any potential benefit

of enhancing KCC2 function is limited to a critical period during development, is unknown; a lack of pharmacological KCC2 activators prevents this question from being addressed (Cardarelli et al., 2017).

We do not know how these developmental changes in KCC2 function could lead to altered cognitive function, but we can speculate that aberrant network formation during a critical period of brain development is responsible. Interestingly, premature E_{GABA} hyperpolarization through KCC2 overexpression in cortical neurons impairs their morphological maturation (Cancedda et al., 2007). Additionally, premature overexpression of KCC2 results in a permanent decrease in excitatory synaptic signaling (Akerman and Cline, 2006). However, many previous studies have established a role for KCC2 in regulating spine formation and maturation through a mechanism independent of its transport function and is instead regulated by KCC2 protein expression levels (Li et al., 2007; Gauvain et al., 2011; Fiumelli et al., 2013; Blaesse and Schmidt, 2015; Llano et al., 2015; Awad et al., 2018). As S940A and T906A/T1007A neurons have comparable KCC2 protein expression to WT neurons at early and late developmental periods (Silayeva et al., 2015; Moore et al., 2018) it is possible that neuronal morphology and synapse formation would not be impacted in this same way and therefore is likely not responsible for the behavioral changes seen in these KCC2 phospho-mutant mice. However, we have not examined whether the S940A or T906A/T1007A mutations impact KCC2 surface stability at the early postnatal period as we were not able to generate enough material to measure this parameter at early time points using biotinylation. Still, it is important to note that published studies have shown that mutation of either S940 or T906/1007 do not alter plasma membrane levels of KCC2 in mature neurons (Silayeva et al., 2015; Moore et al., 2018), which suggests that the impact of the respective mutations on Cl^- levels is not related to KCC2 surface expression levels *per se*. This could also explain why we do not see any changes in motor learning in our phospho-mutant mice (Silayeva et al., 2015; Moore et al., 2018) despite a previous study documenting that rates of motor learning are improved when KCC2 is overexpressed (Nakamura et al., 2019).

Blocking early depolarizing GABA using a pharmacological inhibitor of NKCC1 also impairs excitatory synaptic signaling (Akerman and Cline, 2006; Wang and Kriegstein, 2011). However, as NKCC1 is also present in glia, deficits in glial function may be responsible for these synaptic abnormalities rather than a specific impact of altered Cl^- homeostasis. Interestingly, however, migrating interneurons expressing KCC2 show reduced motility in response to GABA application (Bortone and Polleux, 2009) suggesting that higher levels of KCC2 function can terminate interneuron migration which supports a role for the Cl^- transport function of KCC2 in neuronal network formation. It is, therefore, possible that premature/delayed termination of interneuron migration may occur in the T906A/T1007A and S940A mice, respectively; as autism-spectrum disorders have been associated with altered interneuron placement this would be an interesting question to address (Katsarou et al., 2017). It is also important to consider

that these KCC2 mutations may be altering GABAergic signaling in newborn granule cells in the dentate gyrus of the adult hippocampus, as knocking-down NKCC1 results in a premature hyperpolarizing onset of hyperpolarizing GABA currents in the newborn neurons in the adult brain which leads to defective dendritic development and synapse formation (Ge et al., 2006). However, altered NKCC1 function in glia may be responsible for these dendritic and synaptic deficits.

Ultimately, this work suggests that KCC2 phosphorylation and thus the polarity of synaptic inhibition is finely orchestrated during a critical period of postnatal development, which may be necessary for ensuring normal brain function in adulthood. These findings further our insight into molecular events that regulate KCC2 function and GABA_A receptor activity that may go awry in autism-spectrum disorders, and suggest a potential role of altered timing of postnatal E_{GABA} hyperpolarization in the behavioral manifestations of these disorders. Examining the phosphorylation state of KCC2 in neurodevelopmental disorders would, therefore, be informative. How social behaviors and memory retention are specifically vulnerable to altered KCC2 function in the phospho-mutant mice, despite other behaviors such as motor function and anxiety-like behaviors being unaffected (Silayeva et al., 2015; Moore et al., 2018), also requires further investigation but may be due to differential regulation of KCC2 phosphorylation in different brain regions. We chose to perform our biochemical and electrophysiological studies on hippocampal neurons as these are some of the most homogeneous neuronal populations in the brain and would, therefore, avoid any variability that may result from exploring other brain regions which are composed of a much more heterogeneous population of neurons. Additionally, given the known role of the hippocampus for spatial memory, the hippocampus is potentially the most relevant region of the brain to examine for our study. Examination of additional brain regions would indeed be interesting in light of our identification of social interaction abnormalities, but the array of different brain regions contributing to social behavior, including PFC, Amygdala, VTA and Accumbens (Gunaydin et al., 2014), make this a large undertaking.

We propose that potentiating KCC2 function during development to rescue the delayed E_{GABA} shift detected in several neurodevelopmental disorders (Duarte et al., 2013; He et al., 2014; Deidda et al., 2015; Tang et al., 2016) may alleviate the complex cognitive deficits characteristic of these disorders. This adds to the already promising prospects of KCC2 activators for other neurological disorders such as for the treatment of seizures (Moore et al., 2017, 2018), a common co-morbidity of autism-spectrum disorders. Further investigations into the signaling cascades that regulate KCC2 phosphorylation may help identify novel therapeutic targets for these disorders. However, given our finding that loss of depolarizing GABA in development disrupts establishment of normal social behavior, caution may be needed in increasing KCC2 function in healthy children to prevent complete elimination of depolarizing GABA in the immature brain. Nevertheless, this work suggests that KCC2 may be a promising novel

therapeutic target for alleviating some of the symptoms of these complex disorders.

ETHICS STATEMENT

All mice were handled according to protocols approved by the Institutional Animal Care and Use Committee (IACUC).

AUTHOR CONTRIBUTIONS

YM, NB, TD and SM designed the research. YM, LC and HW performed the research. YM, LC and TD analyzed the data. YM, TD and SM wrote the article.

REFERENCES

- Akerman, C. J., and Cline, H. T. (2006). Depolarizing GABAergic conductances regulate the balance of excitation to inhibition in the developing retinotectal circuit *in vivo*. *J. Neurosci.* 26, 5117–5130. doi: 10.1523/JNEUROSCI.0319-06.2006
- Awad, P. N., Amegandjin, C. A., Szczurkowska, J., Carriço, J. N., Fernandes do Nascimento, A. S., Baho, E., et al. (2018). KCC2 regulates dendritic spine formation in a brain-region specific and BDNF dependent manner. *Cereb. Cortex* 28, 4049–4062. doi: 10.1093/cercor/bhy198
- Ben-Ari, Y., Cherubini, E., Corradetti, R., and Gaiarsa, J. L. (1989). Giant synaptic potentials in immature rat CA3 hippocampal neurones. *J. Physiol.* 416, 303–325. doi: 10.1113/jphysiol.1989.sp017762
- Ben-Ari, Y., Gaiarsa, J. L., Tyzio, R., and Khazipov, R. (2007). GABA: a pioneer transmitter that excites immature neurons and generates primitive oscillations. *Physiol. Rev.* 87, 1215–1284. doi: 10.1152/physrev.00017.2006
- Blaesse, P., and Schmidt, T. (2015). K-Cl cotransporter KCC2—a moonlighting protein in excitatory and inhibitory synapse development and function. *Pflugers Arch.* 467, 615–624. doi: 10.1007/s00424-014-1547-6
- Bormann, J., Hamill, O. P., and Sakmann, B. (1987). Mechanism of anion permeation through channels gated by glycine and γ -aminobutyric acid in mouse cultured spinal neurones. *J. Physiol.* 385, 243–286. doi: 10.1113/jphysiol.1987.sp016493
- Bortone, D., and Polleux, F. (2009). KCC2 expression promotes the termination of cortical interneuron migration in a voltage-sensitive calcium-dependent manner. *Neuron* 62, 53–71. doi: 10.1016/j.neuron.2009.01.034
- Cancedda, L., Fiumelli, H., Chen, K., and Poo, M. M. (2007). Excitatory GABA action is essential for morphological maturation of cortical neurons *in vivo*. *J. Neurosci.* 27, 5224–5235. doi: 10.1523/JNEUROSCI.5169-06.2007
- Cardarelli, R. A., Jones, K., Pisella, L. I., Wobst, H. J., McWilliams, L. J., Sharpe, P. M., et al. (2017). The small molecule CLP257 does not modify activity of the K^+ - Cl^- co-transporter KCC2 but does potentiate GABAA receptor activity. *Nat. Med.* 23, 1394–1396. doi: 10.1038/nm.4442
- Dargaei, Z., Bang, J. Y., Mahadevan, V., Khademullah, C. S., Bedard, S., Parfitt, G. M., et al. (2018). Restoring GABAergic inhibition rescues memory deficits in a Huntington's disease mouse model. *Proc. Natl. Acad. Sci. U S A* 115, E1618–E1626. doi: 10.1073/pnas.1716871115
- de Los Heros, P., Alessi, D. R., Gourlay, R., Campbell, D. G., Deak, M., Macartney, T. J., et al. (2014). The WNK-regulated SPAK/OSR1 kinases directly phosphorylate and inhibit the K^+ - Cl^- co-transporters. *Biochem. J.* 458, 559–573. doi: 10.1042/bj20131478
- Deidda, G., Parrini, M., Naskar, S., Bozarth, I. F., Contestabile, A., and Cancedda, L. (2015). Reversing excitatory GABAAR signaling restores synaptic plasticity and memory in a mouse model of Down syndrome. *Nat. Med.* 21, 318–326. doi: 10.1038/nm.3827
- Duarte, S. T., Armstrong, J., Roche, A., Ortez, C., Pérez, A., O'Callaghan Mdel, M., et al. (2013). Abnormal expression of cerebrospinal fluid cation chloride cotransporters in patients with Rett syndrome. *PLoS One* 8:e68851. doi: 10.1371/journal.pone.0068851

FUNDING

This work was supported by funding from National Institutes of Health-National Institute of Neurological Disorders and Stroke (NIH-NINDS) Grants NS101888 (TD, SM), NS081735 (SM), and NS087662 (SM); National Institute of Mental Health (NIMH) Grants MH097446 and MH106954 (SM).

SUPPLEMENTARY MATERIAL

The Supplementary Material for this article can be found online at: <https://www.frontiersin.org/articles/10.3389/fnmol.2019.00173/full#supplementary-material>

- Ferando, I., Faas, G. C., and Mody, I. (2016). Diminished KCC2 confounds synapse specificity of LTP during senescence. *Nat. Neurosci.* 19, 1197–1200. doi: 10.1038/nn.4357
- Fiumelli, H., Briner, A., Puskarjov, M., Blaesse, P., Belem, B. J., Dayer, A. G., et al. (2013). An ion transport-independent role for the cation-chloride cotransporter KCC2 in dendritic spinogenesis *in vivo*. *Cereb. Cortex* 23, 378–388. doi: 10.1093/cercor/bhs027
- Friedel, P., Kahle, K. T., Zhang, J., Hertz, N., Pisella, L. I., Buhler, E., et al. (2015). WNK1-regulated inhibitory phosphorylation of the KCC2 cotransporter maintains the depolarizing action of GABA in immature neurons. *Sci. Signal.* 8:ra65. doi: 10.1126/scisignal.aaa0354
- Fuchs, A., Ringer, C., Bilkei-Gorzo, A., Weihe, E., Roeper, J., and Schütz, B. (2010). Downregulation of the potassium chloride cotransporter KCC2 in vulnerable motoneurons in the SOD1-G93A mouse model of amyotrophic lateral sclerosis. *J. Neuropathol. Exp. Neurol.* 69, 1057–1070. doi: 10.1097/nen.0b013e3181f4dcef
- Gauvain, G., Chamma, I., Chevy, Q., Cabezas, C., Irinopoulou, T., Bodrug, N., et al. (2011). The neuronal K-Cl cotransporter KCC2 influences postsynaptic AMPA receptor content and lateral diffusion in dendritic spines. *Proc. Natl. Acad. Sci. U S A* 108, 15474–15479. doi: 10.1073/pnas.1107893108
- Ge, S., Goh, E. L., Sailor, K. A., Kitabatake, Y., Ming, G. L., and Song, H. (2006). GABA regulates synaptic integration of newly generated neurons in the adult brain. *Nature* 439, 589–593. doi: 10.1038/nature04404
- Gras-Vincendon, A., Bursztejn, C., and Danion, J. M. (2008). [Functioning of memory in subjects with autism]. *Encephale* 34, 550–556. doi: 10.1016/j.encep.2007.10.010
- Gunaydin, L. A., Grosenick, L., Finkelstein, J. C., Kauvar, I. V., Fenno, L. E., Adhikari, A., et al. (2014). Natural neural projection dynamics underlying social behavior. *Cell* 157, 1535–1551. doi: 10.1016/j.cell.2014.05.017
- He, Q., Nomura, T., Xu, J., and Contractor, A. (2014). The developmental switch in GABA polarity is delayed in fragile X mice. *J. Neurosci.* 34, 446–450. doi: 10.1523/JNEUROSCI.4447-13.2014
- Katsarou, A. M., Moshé, S. L., and Galanopoulou, A. S. (2017). Interneuronopathies and their role in early life epilepsies and neurodevelopmental disorders. *Epilepsia Open* 2, 284–306. doi: 10.1002/epi4.12062
- Lee, H. H., Deeb, T. Z., Walker, J. A., Davies, P. A., and Moss, S. J. (2011). NMDA receptor activity downregulates KCC2 resulting in depolarizing GABAA receptor-mediated currents. *Nat. Neurosci.* 14, 736–743. doi: 10.1038/nn.2806
- Lee, H. H., Walker, J. A., Williams, J. R., Goodier, R. J., Payne, J. A., and Moss, S. J. (2007). Direct protein kinase C-dependent phosphorylation regulates the cell surface stability and activity of the potassium chloride cotransporter KCC2. *J. Biol. Chem.* 282, 29777–29784. doi: 10.1074/jbc.m705053200
- Li, H., Khirug, S., Cai, C., Ludwig, A., Blaesse, P., Kolikova, J., et al. (2007). KCC2 interacts with the dendritic cytoskeleton to promote spine development. *Neuron* 56, 1019–1033. doi: 10.1016/j.neuron.2007.10.039
- Li, H., Tornberg, J., Kaila, K., Airaksinen, M. S., and Rivera, C. (2002). Patterns of cation-chloride cotransporter expression during embryonic rodent CNS

- development. *Eur. J. Neurosci.* 16, 2358–2370. doi: 10.1046/j.1460-9568.2002.02419.x
- Llano, O., Smirnov, S., Soni, S., Golubtsov, A., Guillemin, I., Hotulainen, P., et al. (2015). KCC2 regulates actin dynamics in dendritic spines via interaction with β -PIX. *J. Cell Biol.* 209, 671–686. doi: 10.1083/jcb.201411008
- Mahadevan, V., and Woodin, M. A. (2016). Regulation of neuronal chloride homeostasis by neuromodulators. *J. Physiol.* 594, 2593–2605. doi: 10.1113/jp271593
- Moore, Y. E., Deeb, T. Z., Chadchankar, H., Brandon, N. J., and Moss, S. J. (2018). Potentiating KCC2 activity is sufficient to limit the onset and severity of seizures. *Proc. Natl. Acad. Sci. U S A* 115, 10166–10171. doi: 10.1073/pnas.1810134115
- Moore, Y. E., Kelley, M. R., Brandon, N. J., Deeb, T. Z., and Moss, S. J. (2017). Seizing control of KCC2: a new therapeutic target for epilepsy. *Trends Neurosci.* 40, 555–571. doi: 10.1016/j.tins.2017.06.008
- Nakamura, K., Moorhouse, A. J., Cheung, D. L., Eto, K., Takeda, I., Rozenbroek, P. W., et al. (2019). Overexpression of neuronal $K^+ - Cl^-$ co-transporter enhances dendritic spine plasticity and motor learning. *J. Physiol. Sci.* 69, 453–463. doi: 10.1007/s12576-018-00654-5
- Owens, D. F., Boyce, L. H., Davis, M. B., and Kriegstein, A. R. (1996). Excitatory GABA responses in embryonic and neonatal cortical slices demonstrated by gramicidin perforated-patch recordings and calcium imaging. *J. Neurosci.* 16, 6414–6423. doi: 10.1523/JNEUROSCI.16-20-06414.1996
- Rinehart, J., Maksimova, Y. D., Tanis, J. E., Stone, K. L., Hodson, C. A., Zhang, J., et al. (2009). Sites of regulated phosphorylation that control K-Cl cotransporter activity. *Cell* 138, 525–536. doi: 10.1016/j.cell.2009.05.031
- Rivera, C., Voipio, J., Payne, J. A., Ruusuvuori, E., Lahtinen, H., Lamsa, K., et al. (1999). The K^+ / Cl^- co-transporter KCC2 renders GABA hyperpolarizing during neuronal maturation. *Nature* 397, 251–255. doi: 10.1038/16697
- Silayeva, L., Deeb, T. Z., Hines, R. M., Kelley, M. R., Munoz, M. B., Lee, H. H., et al. (2015). KCC2 activity is critical in limiting the onset and severity of status epilepticus. *Proc. Natl. Acad. Sci. U S A* 112, 3523–3528. doi: 10.1073/pnas.1415126112
- Takumi, T., Tamada, K., Hatanaka, F., Nakai, N., and Bolton, P. F. (2019). Behavioral neuroscience of autism. *Neurosci. Biobehav. Rev.* doi: 10.1016/j.neubiorev.2019.04.012 [Epub ahead of print].
- Tang, X., Kim, J., Zhou, L., Wengert, E., Zhang, L., Wu, Z., et al. (2016). KCC2 rescues functional deficits in human neurons derived from patients with Rett syndrome. *Proc. Natl. Acad. Sci. U S A* 113, 751–756. doi: 10.1073/pnas.1524013113
- Titz, S., Sammler, E. M., and Hormuzdi, S. G. (2015). Could tuning of the inhibitory tone involve graded changes in neuronal chloride transport? *Neuropharmacology* 95, 321–331. doi: 10.1016/j.neuropharm.2015.03.026
- Treffert, D. A. (2009). The savant syndrome: an extraordinary condition. A synopsis: past, present, future. *Philos. Trans. R. Soc. Lond. B Biol. Sci.* 364, 1351–1357. doi: 10.1098/rstb.2008.0326
- Uvarov, P., Ludwig, A., Markkanen, M., Rivera, C., and Airaksinen, M. S. (2006). Upregulation of the neuron-specific K^+ / Cl^- cotransporter expression by transcription factor early growth response 4. *J. Neurosci.* 26, 13463–13473. doi: 10.1523/JNEUROSCI.4731-06.2006
- Wang, D. D., and Kriegstein, A. R. (2011). Blocking early GABA depolarization with bumetanide results in permanent alterations in cortical circuits and sensorimotor gating deficits. *Cereb. Cortex* 21, 574–587. doi: 10.1093/cercor/bhq124
- Zhang, L., Spigelman, I., and Carlen, P. L. (1991). Development of GABA-mediated, chloride-dependent inhibition in CA1 pyramidal neurones of immature rat hippocampal slices. *J. Physiol.* 444, 25–49. doi: 10.1113/jphysiol.1991.sp018864

Conflict of Interest Statement: NB and HW were full-time employees and shareholders of AstraZeneca at the time the studies were conducted. SM serves as a consultant for SAGE therapeutics and AstraZeneca, relationships that are regulated by Tufts University.

The remaining authors declare that the research was conducted in the absence of any commercial or financial relationships that could be construed as a potential conflict of interest.

Copyright © 2019 Moore, Conway, Wobst, Brandon, Deeb and Moss. This is an open-access article distributed under the terms of the Creative Commons Attribution License (CC BY). The use, distribution or reproduction in other forums is permitted, provided the original author(s) and the copyright owner(s) are credited and that the original publication in this journal is cited, in accordance with accepted academic practice. No use, distribution or reproduction is permitted which does not comply with these terms.



The Orphan Cytokine Receptor CRLF3 Emerged With the Origin of the Nervous System and Is a Neuroprotective Erythropoietin Receptor in Locusts

Nina Hahn^{1*}, Luca Büschgens¹, Nicola Schwedhelm-Domeyer¹, Sarah Bank², Bart R. H. Geurten¹, Pia Neugebauer¹, Bitu Massih¹, Martin C. Göpfert¹ and Ralf Heinrich^{1*}

¹ Department of Cellular Neurobiology, Institute for Zoology and Anthropology, Georg-August University of Göttingen, Göttingen, Germany, ² Department of Animal Evolution and Biodiversity, Institute for Zoology & Anthropology, Georg-August University of Göttingen, Göttingen, Germany

OPEN ACCESS

Edited by:

Vsevolod V. Gurevich,
Vanderbilt University, United States

Reviewed by:

Dietmar Benke,
University of Zurich, Switzerland
Philip Forsyth Copenhaver,
Oregon Health & Science University,
United States

*Correspondence:

Nina Hahn
nina.hahn@uni-goettingen.de
Ralf Heinrich
rheinri1@gwdg.de

Received: 13 August 2019

Accepted: 27 September 2019

Published: 11 October 2019

Citation:

Hahn N, Büschgens L, Schwedhelm-Domeyer N, Bank S, Geurten BRH, Neugebauer P, Massih B, Göpfert MC and Heinrich R (2019) The Orphan Cytokine Receptor CRLF3 Emerged With the Origin of the Nervous System and Is a Neuroprotective Erythropoietin Receptor in Locusts. *Front. Mol. Neurosci.* 12:251. doi: 10.3389/fnmol.2019.00251

The orphan cytokine receptor-like factor 3 (CRLF3) was identified as a neuroprotective erythropoietin receptor in locust neurons and emerged with the evolution of the eumetazoan nervous system. Human CRLF3 belongs to class I helical cytokine receptors that mediate pleiotropic cellular reactions to injury and diverse physiological challenges. It is expressed in various tissues including the central nervous system but its ligand remains unidentified. A CRLF3 ortholog in the holometabolous beetle *Tribolium castaneum* was recently shown to induce anti-apoptotic mechanisms upon stimulation with human recombinant erythropoietin. To test the hypothesis that CRLF3 represents an ancient cell-protective receptor for erythropoietin-like cytokines, we investigated its presence across metazoan species. Furthermore, we examined CRLF3 expression and function in the hemimetabolous insect *Locusta migratoria*. Phylogenetic analysis of CRLF3 sequences indicated that CRLF3 is absent in Porifera, Placozoa and Ctenophora, all lacking the traditional nervous system. However, it is present in all major eumetazoan groups ranging from cnidarians over protostomians to mammals. The CRLF3 sequence is highly conserved and abundant amongst vertebrates. In contrast, relatively few invertebrates express CRLF3 and these sequences show greater variability, suggesting frequent loss due to low functional importance. In *L. migratoria*, we identified the transcript *Lm-crlf3* by RACE-PCR and detected its expression in locust brain, skeletal muscle and hemocytes. These findings correspond to the ubiquitous expression of *crlf3* in mammalian tissues. We demonstrate that the sole addition of double-stranded RNA to the culture medium (called soaking RNA interference) specifically interferes with protein expression in locust primary brain cell cultures. This technique was used to knock down *Lm-crlf3* expression and to abolish its physiological function. We confirmed that recombinant human erythropoietin rescues locust brain neurons from hypoxia-induced apoptosis and showed that this neuroprotective effect is absent after knocking down *Lm-crlf3*. Our results affirm the erythropoietin-induced neuroprotective

function of CRLF3 in a second insect species from a different taxonomic group. They suggest that the phylogenetically conserved CRLF3 receptor may function as a cell protective receptor for erythropoietin or a structurally related cytokine also in other animals including vertebrate and mammalian species.

Keywords: neuroprotection, erythropoietin, cytokine receptor, *Locusta migratoria*, soaking RNA interference, nervous system, ancient receptor, orphan receptor

INTRODUCTION

The cytokine receptor-like factor 3 (CRLF3) is a largely uncharacterized orphan cytokine receptor with unknown function and endogenous ligand. The human *crlf3* gene (NCBI Accession No. NM_015986.4, synonyms *Cremer9*, *Cytor4*, *p48.2*, *p48.6*) is located on chromosome 17 and spans 2873 base pairs. The human CRLF3 spans 442 amino acids comprising the conserved cytokine receptor motif WSXWS, a single transmembrane segment and an intracellular Janus kinase (JAK) docking site. These characteristics identify CRLF3 as a member of the group 1 in the prototypic class I cytokine receptors that typically bind class 1 helical cytokines (Boulay et al., 2003; Liongue and Ward, 2007). Group 1 also contains the classical erythropoietin receptor (EpoR), the thrombopoietin receptor, the prolactin receptor and the growth hormone receptor. They typically function as homo- or hetero-dimers or associate to multimeric receptor complexes (Boulay et al., 2003). CRLF3 is expressed in various human tissues, including pancreas, kidney, and brain amongst others (Yang et al., 2009). In addition, freshly isolated tumor tissues and some tumor cell lines show elevated CRLF3 expression (Dang et al., 2006; Yang et al., 2009). CRLF3 has been associated with signal transducer and activator of transcription 3 (STAT3) activation, cell cycle regulation, neuronal morphology, and amyotrophic lateral sclerosis (Yang et al., 2009; Hashimoto et al., 2012; Cirulli et al., 2015). However, its physiological function is yet to be determined. Given its structural similarities to EpoR, we have investigated the potential involvement of CRLF3 in erythropoietin (Epo)-mediated neuroprotection.

Even though *epo* and *epoR* are not present in invertebrate genomes, previous *in vitro* and *in vivo* studies demonstrated neuroprotective and neuroregenerative effects of recombinant human erythropoietin (rhEpo) in the insects *Locusta migratoria* and *Tribolium castaneum* (Ostrowski et al., 2011; Miljus et al., 2014; Hahn et al., 2017). We found several parallels between Epo-mediated neuroprotection in mammals and insects including activation of JAK/STAT intracellular signaling, induction of anti-apoptotic proteins, initiation of receptor endocytosis after Epo-binding, and sensitivity to the non-erythropoietic human Epo splice variant EV-3 (Miljus et al., 2014, 2017; Hahn et al., 2017; Heinrich et al., 2017). These findings supported the hypothesis (Brines and Cerami, 2005; Ostrowski et al., 2011; Ghezzi and Conklin, 2013) that Epo signaling originally functioned as an adaptation mechanism to challenging physiological conditions (e.g., infections, metabolic stress, injury, hypoxia) and only later evolved to regulate vertebrate red blood cell production (summarized by Jelkmann, 2011). Since cytokines commonly

activate different receptors and cytokine receptors often respond to several cytokine ligands, we explored the hypothesis that CRLF3 serves as the neuroprotective receptor stimulated by rhEpo in insects.

We previously demonstrated that CRLF3 is crucial for Epo-mediated neuroprotection in hypoxia-exposed neurons from the beetle *T. castaneum* (Hahn et al., 2017). In contrast, Epo showed no cell protective effects in *in vitro* studies using macrophage-like Schneider (S2) cells and neuron-like BG2-c2 cells derived from the fruit fly *Drosophila melanogaster* (unpublished data). *Drosophila* lacks a *crlf3* gene (Wyder et al., 2007; Hahn et al., 2017, this study) supporting the hypothesis that CRLF3 may function as a neuroprotective receptor for Epo. Investigating CRLF3 as a neuroprotective Epo receptor contributes to the understanding of Epo as a neuroprotective agent and may support the development of alternative, safe treatments for neurological and neurodegenerative diseases that, unlike Epo itself, do not stimulate adverse side effects (Leist et al., 2004; Unger et al., 2010).

To the present, studies on CRLF3 involvement in Epo-mediated cell protection have only been performed in the beetle *T. castaneum* (Coleoptera). Here, we study locust primary brain cells (*L. migratoria*, Orthoptera) to confirm the hypothesis that CRLF3 represents an evolutionary ancient cell protective receptor. *In vivo* cellular functions can best be modeled *in vitro* by primary cell cultures, since their cellular development took place in natural environment. *In vitro* loss of function studies with mammalian cells require electroporation, lipid-mediated or viral-mediated transfection in order to induce gene targeted RNA interference (RNAi) and are prone to low efficiency. Locust primary brain neurons have the advantage that they spontaneously take up double-stranded RNA from the medium. This initiates the RNAi machinery, specifically suppressing the production of a protein of interest (called soaking RNAi). We applied soaking RNAi for a loss of function study in order to investigate the function of *Lm*-CRLF3 in primary locust brain cells.

The present study provides further evidence for the importance of CRLF3 in Epo-mediated neuroprotection using locust neurons. Moreover, we show *Lm*-*crlf3* expression in a variety of locust tissues, arguing for a general cell protective function of CRLF3. Phylogenetic analysis resulted in 293 eumetazoan species expressing CRLF3 with the earliest appearance in the last common ancestor of Cnidaria and Bilateria. This indicates that its original function might have been related to the eumetazoan nervous system. Later in evolution, CRLF3 was coopted for functions also in other tissues leading to frequent expression and high sequence conservation amongst

vertebrate species. We furthermore validate soaking RNAi in locust neurons as an appropriate technique for robust loss of function studies *in vitro*.

MATERIALS AND METHODS

Primers

TABLE 1 | Summary of oligonucleotides.

Name	DNA sequence (5'–>3')
UPM long T3	5' ATTAACCCCTCACTAAAGGGAAA GCAGTGGTATCAACGCAGAGT 3'
UPM short T3	5' ATTAACCCCTCACTAAAGGGA 3'
RACE_Lm-crlf3_for	5' GGTTTCATGCTGTTGAGAGGGTTGGCAG 3'
RACE_Lm-crlf3_rev	5' CTGCCAACCCCTCTCAACAGCATGAACC 3'
Lm-crlf3 F1 Fw	5' GTGTGATAGGTTGCCAGCAGTC 3'
Lm-crlf3 F1 Rv	5' CGTATAAGGTGGTGACATTCAGGTC 3'
Lm-crlf3 F2 Fw	5' GGAACCAAGTCATCTGCGAG 3'
Lm-crlf3 F2 Rv	5' CGAATATTACCCAGGCTGGAG 3'
Lm-rpt3 full Fw	5' TTGGGGATCGGTGCGTCAG 3'
Lm-rpt3 full Rv	5' TTATTATAGAATTCATGCTCTGATTCATCC 3'
Lm-rpt3 Fw	5' GATGAGCAGCGCAATTTGAAAA 3'
Lm-rpt3 Rv	5' CACATCTGGCTTTTCATCTGC 3'
qLm-gapdh Fw	5' GTCTGATGACAAAGTGCAT 3'
qLm-gapdh Rv	5' GTCCATCAGCCACAACCTTC 3'
qLm-CRLF3 Fw	5' GTCTGGCTCTTGCCGATCACC 3'
qLm-CRLF3 Rv	5' GTAGTCTTTCCCTTGCCATCCACAAACACAC 3'
M13F	5' GTAAACGACGCGCCAGT 3'
M13R-T7	5' taatacgaactcactataggCAGGAAACAGCTATGAC 3'

Plasmids

The plasmid pDsRed (GB0100) was a gift from Diego Orzaez (Addgene plasmid # 68202¹; RRID:Addgene_68202) (Sarrion-Perdigones et al., 2013). *Lm-crlf3* fragment 1 and fragment 2 were designed as two non-overlapping fragments. They were inserted into the pCRII vector (TA Cloning® Kit Dual Promoter with pCR™II vector, Thermo Fisher Scientific, Germany) by TA-cloning, respectively. Then, pCRII-*Lm-crlf3_F1* and pCRII-*Lm-crlf3_F2* plasmids were transformed into XL1-Blue competent cells (#200249, Agilent, United States) and purified with the NucleoBond® Xtra Midi kit (Macherey-Nagel, Germany) according to the user manual. The plasmid DNA was eluted in 500 µl H₂O. *Lm-rpt3* was identified using BLAST and the LocustBase official gene set (OGS CDS V2.4.1)² (Altschul et al., 1990). The sequence LOCMI02241 was determined as *Lm-rpt3*: the full-length CDS (submitted to GenBank with Accession No. MN245517) and a fragment of *Lm-rpt3* were cloned into the pCRII vector as described above. All sequences are summarized in **Supplementary File S1**.

¹<http://n2t.net/addgene:68202>

²<http://www.locustmine.org/viroblast/viroblast.php>

Animals

Locusts (*L. migratoria*) were purchased from Feeders & more (Au i.d. Hallertau, Germany) and HW-Terra (Herzogenaurach, Germany). They were kept in groups at 24°C, 55% air humidity and 12 h/12 h dark/light cycle for up to 1 week. Food was composed of organic lettuce leaves and reed *ad libitum*. Since this study was conducted exclusively with insects, it does not require a special permission. All experiments comply with the German laws for animal welfare (“Deutsches Tierschutzgesetz”).

Phylogenetic Analysis

We searched for CRLF3 sequences with the blastp algorithm and default settings using the Geneious® 11.1.5 (Biomatters, Ltd.) BLAST tool and the human CRLF3 sequence (Q8IU18.2) as query sequence. The NCBI accession numbers of the resulting hits are listed in **Supplementary File S2**. The CRLF3 sequence of *L. migratoria* was obtained by RACE PCR (rapid amplification of cDNA-ends with polymerase chain reaction) and submitted to GenBank (Accession No. MN245516). The CRLF3 sequence of *Gryllus bimaculatus* was obtained by using the tblastn search on the ASgard data base³. The resulting hit GB-isotig00932 was translated into all possible reading frames. We used the translated sequence of reverse frame 3 since it comprises the CRLF3 characteristic motif WSXWS and an appropriate stop codon. All amino acid sequences were aligned using ClustalW version 2.1 implemented in Geneious® with default settings. Subsequently, we removed all columns that consisted of more than 50% missing data from the alignment resulting in a length of 438 amino acids. The phylogenetic tree was inferred with IQ-TREE version 1.6.8 (Nguyen et al., 2015) using the suggested substitution model JTT + R6 (Wong et al., 2017). Support values were computed using the implemented ultrafast bootstrap approximation and 1000 replicates (Minh et al., 2013; Hoang et al., 2018). The tree was rooted with the Cnidaria cluster.

First Strand cDNA Synthesis and RACE PCR

First-strand cDNA was synthesized from 1 µg total RNA of brain tissue using SMARTer® RACE 5'/3' Kit (Clontech, Takara, France) according to the user manual. Subsequently 5'- and 3'-rapid amplification of cDNA ends (5' and 3' RACE) was performed. The respective primers are summarized in **Table 1**. Gene-specific primers were designed on the partial sequences available at LocustBase² and i5k⁴. The RACE PCR was performed with the following touchdown program and Advantage® 2 Polymerase Mix (Takara, France): initial step at 94°C for 2 min, 5 cycles at 94°C for 30 s and 72°C for 5 min, 10 cycles at 94°C for 30 s, 70°C for 30 s and 72°C for 5 min, 25 cycles at 94°C for 30 s, 68°C for 30 s and 72°C for 5 min, and a final step at 72°C for 5 min. PCR products were analyzed by 1% agarose gel electrophoresis and purified with the NucleoSpin® Gel and PCR Clean-up kit (#740609.50, Macherey-Nagel, Germany). Afterwards, they were cloned into

³<http://asgard.rc.fas.harvard.edu/blast.html>

⁴<http://i5k.nal.usda.gov/locusta-migratoria>

the pCRII vector (#K207040, TA Cloning® Kit Dual Promoter with pCRTMII vector, Thermo Fisher Scientific, Germany), transformed into XL1-Blue competent cells (#200249, Agilent, United States), purified and sequenced with M13 primers. The obtained full length mRNA sequence of *Lm-crlf3* was submitted to GenBank (Accession No. MN245516) and used for gene specific primer design.

Dissection of Locust Tissue and RNA Isolation

2–4 adult or 4 juvenile locusts were used for total RNA extraction. Brain, muscle and hemocytes RNA was isolated using the ZR Tissue & Insect RNA MicroPrepTM Kit (#R2030, Zymo Research). Hemolymph (final amount 1.5 ml) was collected by injecting 500 µl anticoagulant solution (98 mM NaOH, 186 mM NaCl, 17 mM Na₂EDTA, 41 mM citric acid, pH 4.5) into the abdomen of a locust. After 1 min, the hemolymph was collected with a pipette through an abdominal incision and stored on ice until further usage. Hemocytes were spun down, resuspended in 800 µl RNA lysis buffer and transferred to a ZR BashingBeadTM Lysis Tube. Brains were dissected as described in Miljus et al. (2014). Skeletal muscle originated from 4 to 6 large wing muscle strands. Tissue from either brain or muscle was directly collected in 800 µl RNA lysis buffer in a ZR BashingBeadTM Lysis Tube on ice. The following steps were performed according to the user manual including the on-column DNase I treatment.

Total RNA from primary brain cell cultures was purified using the Monarch® Total RNA Miniprep Kit (#T2010S, New England BioLabs® GmbH, Germany) according to the user manual including the recommended on-column DNase I treatment. Cells were mechanically detached from the coverslips and directly transferred into 300 µl lysis buffer. Finally, RNA was eluted twice with 20 µl nuclease free water and stored at –80°C.

cDNA Synthesis, Reverse Transcription PCR (RT-PCR), and Quantitative Real-Time PCR (qRT-PCR)

cDNA was synthesized from 1 µg total RNA using QuantiTect Reverse Transcription Kit (#205311, Qiagen, Germany) according to the user manual. RT-PCR was performed with 100 ng cDNA template, 0.4 µM forward and reverse primers targeting *Lm-crlf3* F1 and GoTaq® Green Master Mix (Promega, Germany) in a 25 µl reaction volume. The PCR program consisted of an initial denaturing step at 95°C for 3 min, 30 cycles of 95°C for 30 s, 58°C for 30 s and 72°C for 45 s and a final step at 72°C for 3 min. Amplicons were analyzed by 1% agarose gel electrophoresis. qRT-PCR was conducted with the MyiQTM Single-Color Real-Time PCR Detection System (#170-9740, Bio-Rad, Germany) in 96-well plates (#HSS9665, Bio-Rad, Germany) covered with a seal (#MSB1001, Bio-Rad, Germany). The final reaction volume was 10 µl containing 5 µl of iTaqTM Universal SYBR® Green Supermix (#1725121, Bio-Rad, Germany), 0.1 µM primers and 10 ng cDNA. Primers were tested for efficiency and stability. *Lm-gapdh* was used as a reference gene (Van Hiel et al., 2009). Amplification was performed with this program: 95°C for

3 min followed by 40 cycles of 95°C for 10 s, 60°C for 30 s and 72°C for 30 s, and a final step at 95°C for 1 min. Afterwards, melting curve analysis was performed starting at 55°C for 1 min and increasing the temperature in 81 cycles for 0.5°C every 10 s up to 95°C. Data were analyzed by the comparative C_T method (Livak and Schmittgen, 2001).

Synthesis of Double-Stranded RNA (dsRNA)

Template DNA was amplified by PCR using M13F and M13R-T7 primers (M13R attached with an additional T7 promotor) using the following program: denaturation at 98°C for 3 min, 30 cycles of 98°C for 30 s, 60°C for 30 s and 72°C for 30 s, and a final step of 72°C for 5 min. *In vitro* transcription of dsRNA was performed using a T7 transcription kit (MEGAscriptTM T7 Transcription Kit, Thermo Fisher Scientific, Germany) and 400–600 ng template DNA. RNA was purified by lithium chloride precipitation and resuspended in injection buffer (1.4 mM NaCl, 0.07 mM Na₂HPO₄, 0.03 mM, KH₂PO₄, 4 mM KCl). RNA strands were annealed using a thermocycler and the following program: 60°C for 20 min, 95°C for 5 min, decrease to 20°C in steps of 0.1°C/s. Size and quality of the dsRNA was checked with 1% agarose gel electrophoresis. Prior to usage, dsRNA was filtered through a sterile filter by centrifugation (Millex®-HV Syringe Filter Unit, 0.45 µm, #SLHV004SL, Millipore, Germany).

Locust Primary Brain Cell Cultures

Locust primary brain cell cultures were established from 4th stage juvenile locusts as previously described (Ostrowski et al., 2011; Miljus et al., 2014). Complete growth medium consisted of L15 (Leibovitz's L-15 Medium, #11415049, Thermo Fisher Scientific, Germany), 5% FBSG (Fetal Bovine Serum Gold, PAA Laboratories GmbH, Austria), 1x Penicillin-Streptomycin (Penicillin-Streptomycin, 10,000 units penicillin and 10 mg streptomycin/ml, #P4333, Sigma-Aldrich®, Germany) and 1% Amphotericin B (GibcoTM Amphotericin B, 250 µg/ml, #15290018, Thermo Fisher Scientific, Germany). Dissected brains were pooled (see below), enzymatically digested with 2 mg/ml Collagenase/Dispase solution for 30–45 min at 27°C and mechanically dissociated by trituration with a 100 µl tip of an Eppendorf pipette. The primary brain cells were cultured on ConcanavalinA-coated (Sigma-Aldrich®, Germany) round glass cover slips (Ø 10mm, Corning, Inc., Sigma-Aldrich®, Germany) in 4-well NUNC plates (#176740, NuncTM Delta Surface, Thermo Fisher Scientific, Germany) filled with 500 µl of complete growth medium at 27°C in a humidified atmosphere. The medium was changed every 2 days. Based on previous studies (Gocht et al., 2009), locust brain cultures are estimated to contain approximately 3% glia and 97% neurons after 7 days *in vitro* under normoxic conditions.

Soaking RNAi

Soaking RNAi describes the supplementation of standard growth medium with dsRNA to initiate a target-specific degradation of the respective transcripts. In order to investigate the applicability of soaking RNAi in locust primary brain cell cultures, we exposed

cultures derived from the same pool of brain cells to dsRNA (final concentration 10 ng/ μ l) targeting various transcripts. Fresh dsRNA was added with every medium change. Cells were fixed on day 5 and stained in order to assess the effect on cell viability as described below. dsRNA targeting *Lm-rpt3* and *dsRed* were tested in this study. *Lm-RPT3* is a proteosomal regulatory protein that is essential for cellular survival and served as a positive control for RNAi efficacy. dsRNA targeting *dsRed* served as a negative control as *dsRed* is not naturally expressed in *L. migratoria*. Additionally, dsRNA targeting *Lm-crlf3* fragment 1 and *Lm-crlf3* fragment 2 was applied to otherwise untreated cultures during neuroprotection assays (see below) in order to exclude effects on cellular survival of the CRLF3 knock-down itself.

Neuroprotection Assay and Pharmacological Treatment

Neuroprotection assays compared cellular survival in cultures exposed to normoxia, hypoxia and rhEpo with or without previous knock-down of *Lm-crlf3* expression. Each experiment compared differently treated cultures that derived from the same pool of locust brain cells (two brains per culture/treatment). One experiment consisted of one culture at normoxic conditions (control), a hypoxia-treated culture (challenged, reduction to < 90% cell survival), a hypoxia- and Epo-treated culture (positive control for neuroprotective effect) and a hypoxia- and Epo-treated culture that was previously subjected to RNAi-induced *Lm-CRLF3* knock-down (experimental group) (Figure 5). In some experiments, potential effects of dsRNA targeting *Lm-crlf3* were also determined in normoxic conditions. Control cultures were always incubated with the same medium and at the same temperature as experimental cultures. In order to knock down *Lm-CRLF3*, growth medium was supplemented with 10 ng/ μ l dsRNA (*Lm-crlf3* fragment 1 or fragment 2) from day 0 to day 7. After 4 days, complete growth medium was replaced by growth medium without serum. On day 5, *in vitro* cultures were treated with 32 ng/ml (\triangleq 4 U/ml) rhEpo (NeoRecormon, Roche, Welwyn Garden City, United Kingdom) 12 h prior to 36 h hypoxia exposure.

Hypoxia (O_2 level < 0.5%) was maintained in a hypoxic chamber (Hypoxia Incubator Chamber, #27310, STEMCELL,™ Germany) flooded with nitrogen. After hypoxic treatment, the cells were fixed for 30 min with 4% paraformaldehyde and stained with DAPI (1:1000) without agitation as described elsewhere to assess cell viability (Miljus et al., 2014; Hahn et al., 2017). The evaluation of cell viability (at the time of fixation) was performed on the basis of the DAPI-labeled nuclear morphology (Gocht et al., 2009). Photographs were taken with a Spot CCD camera (Invisitron, Germany) mounted on an epifluorescence microscope (Zeiss Axioskop; 40x objective, Germany). Numbers of alive and dead nuclei were evaluated using Fiji (Version 1.52.i) as described elsewhere (Schindelin et al., 2012; Hahn et al., 2017). The portion of living cells was determined for each culture and normalized to the portion of living cells in the normoxic control culture (set to 1). The experimenter was blinded with respect to the identity of the cultures while cell viability evaluation.

Statistical Analysis

Data analysis and statistics were performed with R (version 3.6.0) using R Studio (version 1.2.1335) (RStudio Team, 2018; R Core Team, 2019). Boxplots depict the median, the upper and lower quartile, and whiskers represent 1.5 times the interquartile range and outliers. Black circles represent the data of individual experiments. Statistics were calculated using the pairwise permutation test included within the packages “coin” and “rcompanion” (Hothorn et al., 2006, 2008; Mangiafico, 2019). The false discovery rate was controlled using the Benjamini–Hochberg procedure (Benjamini and Hochberg, 1995).

RESULTS

Identification of *Lm-crlf3*

The sequence of the full length *Lm-crlf3* transcript was obtained by RACE PCR from locust brain tissue. It comprises 2522 bp and includes a 253 bp 5' UTR, a 1320 bp coding sequence (CDS) and 949 bp 3' UTR (Figure 1). The CDS determined in Geneious® refers to the translation of frame 2 and codes for 439 amino acids (see Supplementary File S1). The *Lm-crlf3* sequence was used to transcribe double-stranded RNA targeting two non-overlapping fragments for RNAi experiments, for qRT-PCR to detect *crlf3* expression in locust tissues and for phylogenetic analysis.

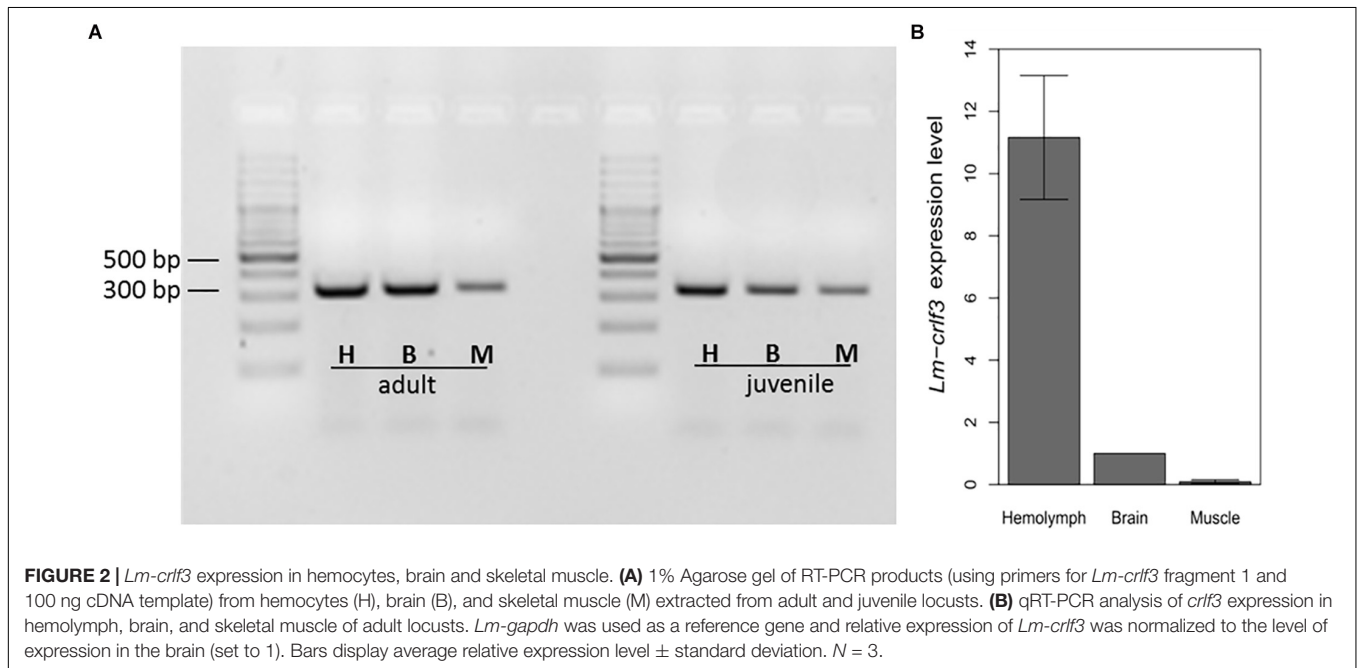
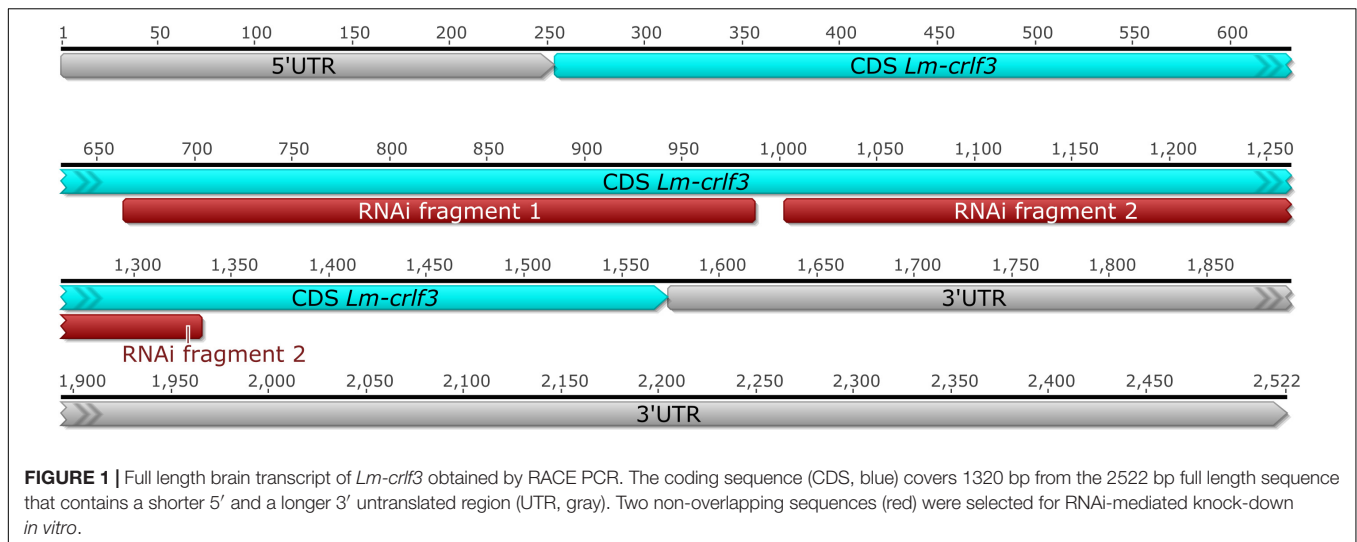
Lm-crlf3 Expression

In mammals, *crlf3* is expressed in various tissues including the nervous system, reproductive organs, bone marrow and immune system. For comparison, *crlf3* expression was determined in brain tissue, skeletal muscle and hemolymph. As determined by RT-PCR amplifying *Lm-crlf3* fragment 1 (displayed in Figure 1), all three tissues expressed *Lm-crlf3* in detectable amounts in both adult and juvenile locusts (Figure 2A). In both developmental stages, hemolymph seemed to contain the most and muscle the least amount of *crlf3* transcripts. These semi-quantitative *crlf3* expression levels were confirmed by qRT-PCR analysis of adult locust tissues using *gapdh* as reference. With respect to brain *crlf3* expression (normalized to 1) hemolymph contained 11.16 (\pm 1.99 STDV) fold *crlf3* transcripts while muscle contained only 0.09 (\pm 0.06 STDV) fold (Figure 2B).

Gene Tree of CRLF3

BLAST searches with the human CRLF3 query detected CRLF3 sequences with reliable e-values ranging from 0 to 6.43E-07. Coverage of the human query varied between 16% (*Pan troglodytes*) and 100%, with a median of 97.29%. The minimum sequence length was 86 amino acids (aa) (*Pan troglodytes*, Mammalia), the maximum 625 aa (*Daphnia magna*, Crustacea), whereas the median sequence length was 438 aa.

CRLF3 was shown to be present in 293 eumetazoan species ranging from Cnidaria to Mammalia. No hits were found in the basal metazoan taxa Porifera, Placozoa, and Ctenophora. A collapsed version of the CRLF3-based gene tree is shown in Figure 3, while the detailed version depicting all included species is presented as Supplementary Figure S1 and

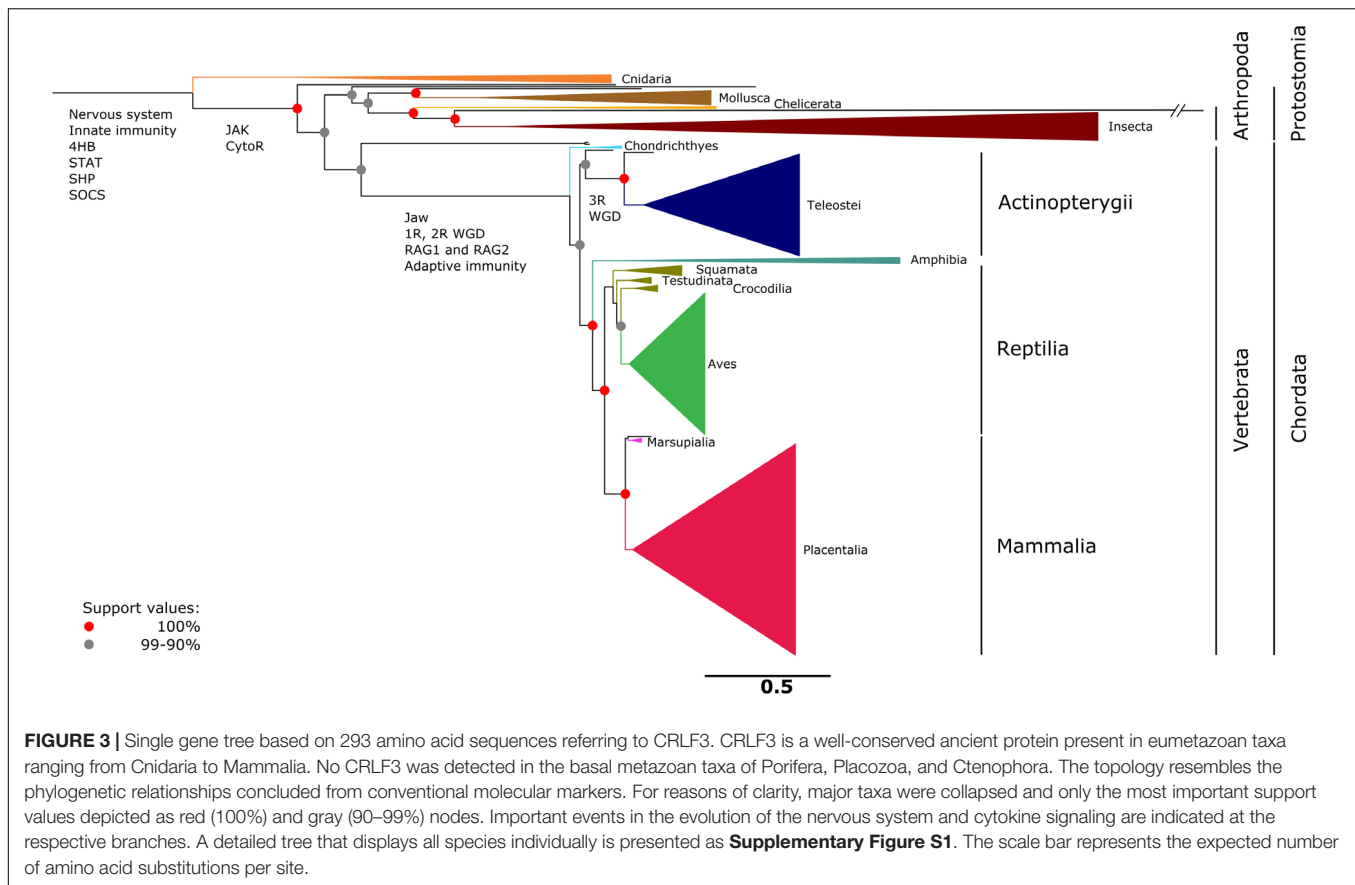


Supplementary File S3. CRLF3 is present in only 34 invertebrate species while 259 hits were detected among vertebrate species. Branches are considerably longer in invertebrates than in vertebrates. Speciation events for major taxa are very well-supported (>90%).

Soaking RNAi in Locust Primary Brain Cells

We initially conducted control experiments to verify that cultured locust brain neurons take up dsRNA from the medium and initiate an RNAi response. We furthermore tested that soaking RNAi as such has no negative impact on cell survival. For these means, two dsRNA constructs (applied at 10 ng/ μ l concentration for 5 days) were evaluated in

respect to their effect on neuronal cell survival. The first one targeted dsRed, a protein that is not naturally expressed in *L. migratoria*. As shown in **Figure 4**, dsRNA targeting dsRed had no significant effect on cell survival. In contrast, dsRNA targeting the expression of the proteasomal protein rpt3 caused a significant reduction of cellular survival ($p = 0.0008$; median survival 74.8% compared to untreated controls from the same pool of cells). In addition, dsRNA targeting CRLF3 had no significant effect on cellular survival compared to untreated control cultures in both unchallenged and challenged cell cultures (**Figure 5** and **Supplementary Figure S3**). These results indicate the functionality of soaking RNAi to suppress the translation of target proteins and serve as a control for the negligible impact of unspecific dsRNA and its solvent on cell viability.



Involvement of *Lm*-CRLF3 in Epo-Mediated Neuroprotection

After demonstrating a robust knock-down of *Lm-rpt3* following 5 days of exposure to dsRNA, we knocked down *Lm-crlf3* expression to investigate its importance for Epo-mediated neuroprotection. In these experiments, we applied dsRNA with the same protocol (exposure to 10 ng/μl dsRNA for 5 days before experiments started) targeting two non-overlapping fragments of *Lm-crlf3* to exclude off-target effects. qRT-PCR analysis proved that after 5 days of soaking RNAi the expression levels dropped by half compared to controls (**Supplementary Figure S2**). The involvement of CRLF3 in Epo-mediated neuroprotection of locust neurons was tested in a neuroprotection assay. Following identical protocols, two series of experiments were conducted, in which *Lm*-CRLF3 expression was suppressed by two different dsRNA constructs (fragment 1 and fragment 2). The results of experiments with fragment 1 are shown in **Figure 5** whereas the results of experiments with fragment 2 are displayed in **Supplementary Figure S3**. Cells were stressed by hypoxia (<0.5% O₂) and a normoxic group was used as control (cell viability was set to 1). Cell viability was significantly decreased by hypoxia, however, pre-treatment with 32 ng/μl rhEpo protected cells from hypoxia-induced apoptosis. Knock-down of CRLF3 abolished Epo's neuroprotective effect and cell viability was not significantly different to sole hypoxia-treated cells. The phenotypes observed by soaking RNAi using dsRNA constructs

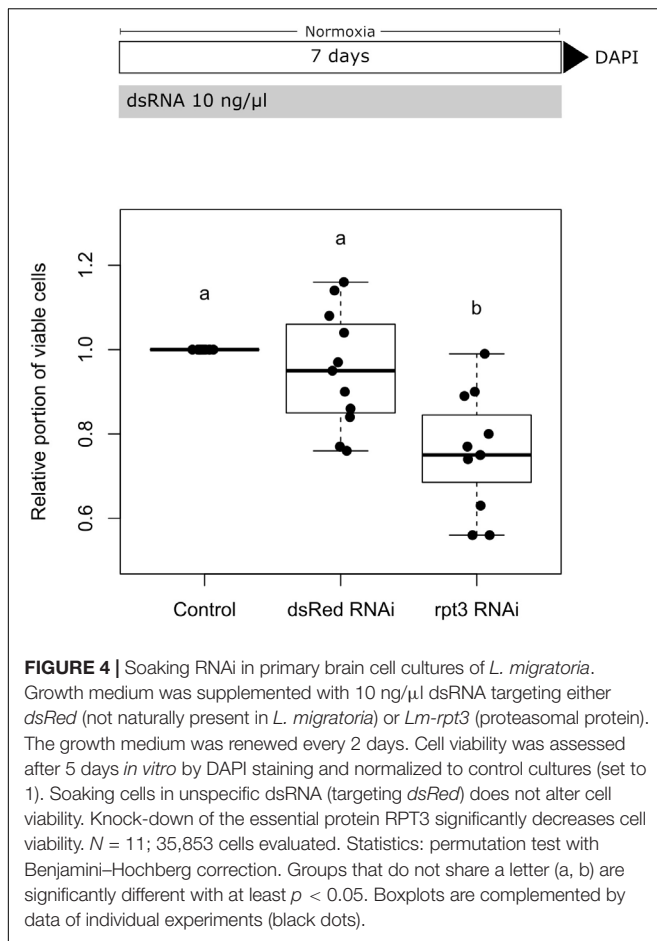
targeting *Lm-crlf3* fragment 1 or fragment 2 are similar (compare **Figure 5** and **Supplementary Figure S3**). Hence, unspecific off-target effects resulting from interference with the expression of another protein are unlikely.

DISCUSSION

Lm-CRLF3 consists of 439 amino acids (aa) which is similar to the size of other insect CRLF3 sequences ranging from 391 to 504 aa. The size of all CRLF3 sequences included into the analysis varies between 86 and 625 aa. CRLF3 found in *Gryllus bimaculatus*, another orthopteran species, is the closest to *Lm*-CRLF3 (51% identity). Similar to *Lm*-CRLF3, the *T. castaneum* CRLF3 receptor (*Tc*-CRLF3) has previously been described as an Epo-responsive receptor involved in neuroprotection (Hahn et al., 2017). Both receptors share 35% similarity of their sequences while the similarity between the locust and the human sequence is 29%.

Phylogenetic Analysis of CRLF3 and Potential Functions

CRLF3 sequences were identified in 293 species and included in the phylogenetic analysis. The single gene tree mirrors the phylogenetic relationships of major metazoan taxa concluded from studies using conventional molecular markers or



transcriptomes with remarkable detail (Dunn et al., 2014; Misof et al., 2014; Irie et al., 2018; Laumer et al., 2019). However, minor exceptions are present. The chordate *Ciona intestinalis* is represented as a sister group to all bilaterians but has been shown to be the sister group to vertebrates (Berná et al., 2009). The misplacement of *Ciona* might be explained by its particularly fast evolving genome (Berná et al., 2009). Furthermore, *Latimeria chalumnae* appears as sister to ray-finned fish (Actinopterygii). For decades, the phylogenetic position of *Latimeria* was subject to debate, but recent studies provide evidence for a closer relationship of *Latimeria* to tetrapods (Takezaki and Nishihara, 2016; Yoshida et al., 2019).

The high conservation of CRLF3 in vertebrates, reflected by short branches, suggests an important role for the organisms. Since the phylogenetic tree of CRLF3 resembles the molecular metazoan tree of life, CRLF3 seems to be subjected to rather high selective pressure leading to a fairly low evolutionary rate. The fact that no matches were found in Porifera, Placozoa and Ctenophora but in Cnidaria, suggests that CRLF3 might have evolved for some function in eumetazoan nervous systems (Grimmelikhuijzen et al., 1996; Westfall, 1996; Bosch et al., 2017). Porifera and Placozoa lack nervous systems. Nervous systems of Ctenophora are fundamentally different from eumetazoan counterparts (with respect to the presence of typical transmitters,

gap-junctional proteins, expression of *elav*, large number of specific neuropeptides and others) (Moroz and Kohn, 2016). Thus, an independent evolutionary origin of ctenophoran and eumetazoan nervous systems is intensely debated (Jékely et al., 2015; Moroz and Kohn, 2016). Cnidaria possess extended neuronal networks that are regarded as homologous to the bilaterian nervous system. The presence of CRLF3 in Eumetazoa but not in Ctenophora matches the hypothesis that the nervous systems of both taxa have evolved convergently (Jékely et al., 2015; Moroz and Kohn, 2016). Main components of the CRLF3-initiated signaling cascades were already present in ancestors of Cnidarians, including the four-helix-bundle (characteristic of class-I cytokines), SHP, STAT, and SOCS. These might have been complemented by JAK and CytoR in Bilateria forming the JAK/STAT signaling pathway (Babonis and Martindale, 2016; Liongue et al., 2016).

Although many invertebrate genomes (626 in NCBI) are available, CRLF3 is only sparsely present. Furthermore, the branch lengths amongst invertebrate taxa are comparably long indicating a lower conservation and higher diversification of this gene (Supplementary Figure S1). In order to exclude that the sparse representation of CRLF3 in insects is due to sequence unavailability and poor quality, we performed an additional analysis restricted to insects (data not shown). We analyzed the transcriptomes published by Misof and colleagues, who provided a robust phylogenetic tree based on high quality transcriptomes covering all extant insect orders and some other arthropods (144 in total) (Misof et al., 2014). Evaluation of this data set confirmed the low abundance of CRLF3 in insects (5 species out of 128). Hence, we hypothesize that CRLF3 has been lost in many invertebrates but was strictly maintained in vertebrates. Potential involvement in further physiological processes outside the nervous system, for instance within adaptive immunity, might have increased the selective pressure. In contrast to the innate immune system, which has already been present in early eukaryotes, the adaptive immune system, relying on V(D)J recombination, emerged in jawed vertebrates 450 million years ago (Rast et al., 1997; Dzik, 2010). It has been suggested that this adaptive immune system is an offshoot of the nervous system or that both derived from an ancestral neuro-immune cell (Bayne, 2003; Kioussis and Pachnis, 2009).

Both, the nervous and adaptive immune system share a variety of signaling molecules including neurotrophic factors, cytokines, chemokines (Habibi et al., 2009; Kerschensteiner et al., 2009; Ransohoff, 2009) and their receptors (Atwal et al., 2008; Levite, 2008; Ben Baruch-Morgenstern et al., 2014). Some molecules have initially been assigned as neurospecific and were later found to be involved in immune functions. For instance, the neuropeptide Y (orthologs are already present in insects) was first discovered as one of the most abundant neuropeptides in the central nervous system but has additional effects on immune cells (Brown et al., 1999; Wheway et al., 2007). In addition, the proteoglycan agrin was known to be required for the formation of the neuromuscular junction but is present on lymphocytes, too (Gautam et al., 1996; Khan et al., 2001; Zhang et al., 2006). In contrast, interleukin 2 was introduced as an immunoregulatory cytokine but more recent

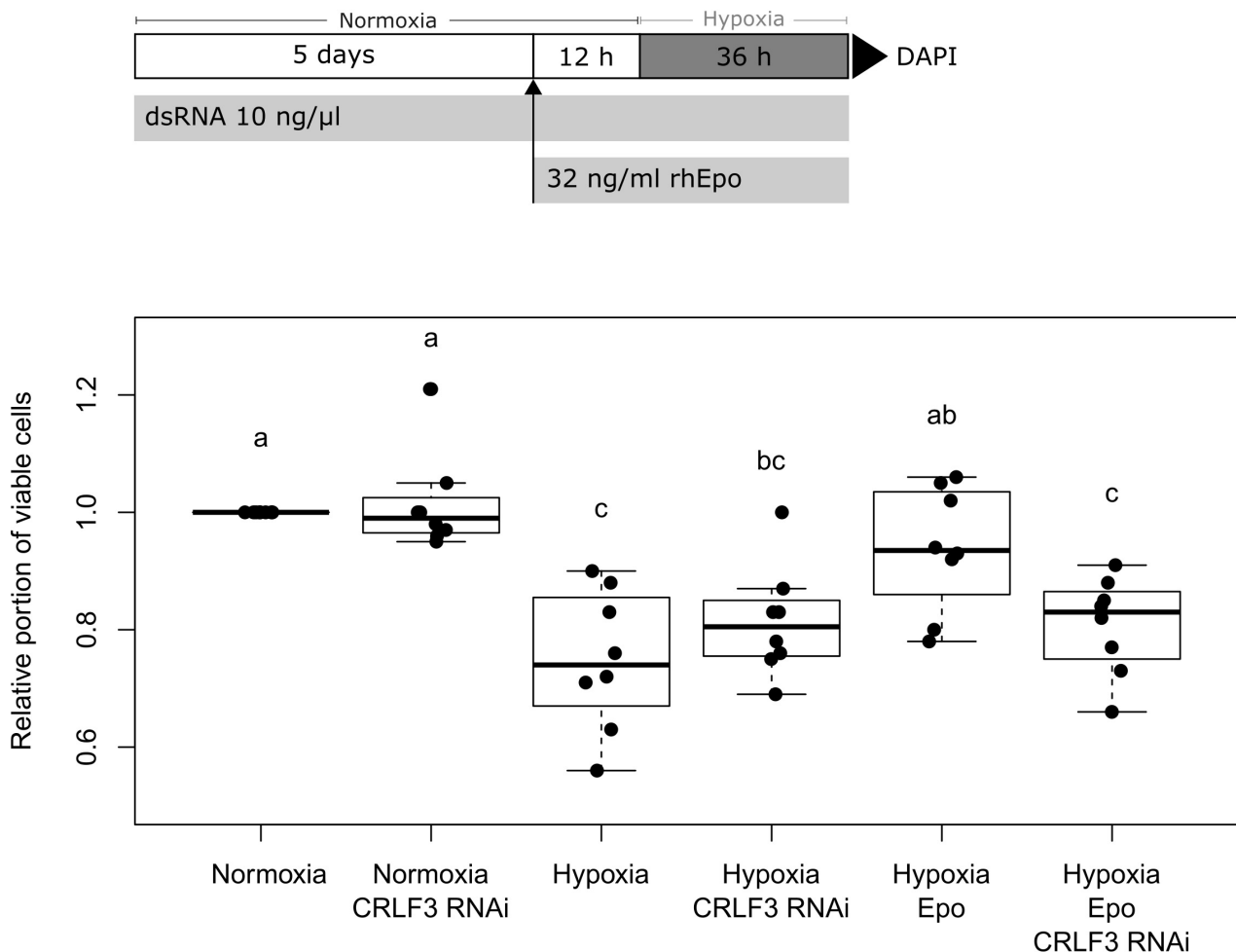


FIGURE 5 | Survival of *L. migratoria* primary brain neurons in normoxia, hypoxia, and after knock-down of *Lm*-CRLF3 expression with fragment 1. Cellular survival was assessed by DAPI staining at day 7 to evaluate the impact of hypoxia (36 h), rhEpo (32 ng/ml) and RNAi-mediated knock-down of *Lm*-CRLF3 (10 ng/μl dsRNA targeting fragment 1). Hypoxia significantly decreases cell viability but treatment with rhEpo prevents neurons from hypoxia-induced apoptosis. The neuroprotective effect of rhEpo is absent following knock-down of *Lm*-*crlf3* expression. Knocking down *Lm*-CRLF3 *per se* has no impact on cell viability, neither in normoxia nor in hypoxia. $N = 8$; 131,792 cells evaluated. Statistics: permutation test with Benjamini-Hochberg correction. Groups that do not share a letter (a, b, c) are significantly different with at least $p < 0.05$. Boxplots are complemented by data of individual experiments (black dots).

studies detected interleukin 2 production by neurons (Muraguchi et al., 1985; Meola et al., 2013). These shared chemical molecules involved in cell-to-cell communication support the hypothesis of an evolutionary common origin of the nervous and adaptive immune system.

Besides functional and physiological similarities, they also share morphological similarities. Both systems function via intimate associations, called synapses, at interfaces between homologous and heterologous cells. The term immunological synapse refers to the similarity to neural synapses and describes the contact between a T cell and an antigen presenting cell. The neural synapse and the immunological synapse share structural (e.g., adhesion molecules, cytokine secretion, receptor clustering) and functional (e.g., memory storage, exchange of information)

commonalities (Donnadieu et al., 2001; Habibi et al., 2009). For instance, the proteoglycan agrin plays an important role in the construction and regulation of synapse formation in both synapse types (Gautam et al., 1996; Khan et al., 2001).

A major trigger for the development of this offshoot could have been two rounds of whole genome duplications (WGDs) that occurred after the split of invertebrates and the evolution toward jawed vertebrates (Gnathostomata) (Figure 3 and Supplementary Figure S1). According to the 2R hypothesis, the first WGD took place within early chordates and the second in the last common ancestor of gnathostomes (Kasahara, 2007). WGDs facilitate the adaptation of genes and molecules to new functions and cooption into new tasks. After WGD, one copy becomes redundant lowering the selection pressure on the

maintenance of its original function. This copy might either accumulate adverse mutations or gain beneficial modifications that enable the acquisition of new functions.

Furthermore, a horizontal gene transfer of a bacterial transposon after the second WGD might have led to the incorporation of the recombination activating genes (RAGs) *RAG1* and *RAG2* providing the basis for somatic V(D)J recombination within the adaptive immune system (Oettinger et al., 1990; Agrawal et al., 1998; Schatz, 2004; Kapitonov and Koonin, 2015). The V(D)J recombination occurs only in lymphocyte development generating the diverse repertoire of antigen receptors that are required for adaptive immunity (Oettinger et al., 1990). In this context, the orphan cytokine receptor might have been adapted to new functions of the adaptive immune system of jawed vertebrates. This hypothesis is supported by data indicating that WGDs diversified the functions of Tyrosine receptor kinases (Brunet et al., 2016). Furthermore, other class I cytokine receptors besides CRLF3 are also involved in the immune system (Holdsworth and Gan, 2015). The lack of this adaptive immunity in invertebrates might have altered the selective pressure on CRLF3. This hypothesis would explain the sparse occurrence as well as the high diversity seen in these species.

***Lm-crlf3* Is Expressed in Various Tissues**

In mammals, CRLF3 is expressed in a variety of tissues including the kidney, pancreas, and brain (Yang et al., 2009). Cell protective functions of Epo have also been reported in various tissues including the hematopoietic system, kidney, skeletal and heart muscle, pancreas, and others all of which also express CRLF3 (Brines and Cerami, 2006; Noguchi et al., 2008; Yang et al., 2009; Ogunshola and Bogdanova, 2013). This supports the hypothesis that CRLF3 might be a cell protective Epo receptor in mammals. In addition, similar expression patterns have been detected in various locust tissues including the nervous system, hemolymph, and skeletal muscle. Since hemocytes display adhesive properties, it cannot be excluded that low levels of *crlf3* transcripts detected in wing muscle may result from contamination with adherent hemocytes that circulate throughout the hemocoel. This data suggests that CRLF3 is an ancient receptor that in the beginning had a function in general cell protective mechanisms and has been adapted to various tissues during evolution.

Soaking RNAi for Loss of Function Studies in Locust Neurons

We supplemented cell culture medium with dsRNA and let locust primary brain cells spontaneously take up dsRNA for 5 days. Medium and dsRNA were refreshed every 2 days to maintain a constant supply of dsRNA and nutrients. In order to assess the applicability of soaking RNAi in locust neuron cultures, we targeted the proteasomal protein RPT3 that is essential for cellular survival. The reduction of cellular survival to 75%, compared to untreated control cultures, indicates that the neurons take up dsRNA and process it to small interfering RNA (siRNA) initiating mRNA degradation. dsRNA targeting dsRed, a protein that is not expressed in locusts, showed no significant

reduction in cellular survival. By this we show that cell death was caused by the absence of RPT3 and not due to effects that were associated with dsRNA uptake. Moreover, dsRNA-mediated knock-down of *Lm-crlf3* expression had no significant impact on neuronal survival, neither in normoxic nor hypoxic conditions. These results indicate that changes in cellular survival depended on the absence of specifically downregulated proteins [RPT3 and CRLF3 during hypoxia/Epo treatment (see below)] rather than on unspecific effects of dsRNA exposure.

RNAi in insects has been reported by various studies (reviewed in Vogel et al., 2019). Many of them focused on RNAi as a tool for pest control (Mamta and Rajam, 2017; Niu et al., 2018). However, the efficiency and success of RNAi varies tremendously between species and targeted tissues. Presumably, this depends on differences in dsRNA uptake and the ability to process dsRNA to siRNA (Ren et al., 2014; Wang et al., 2016; Singh et al., 2017). *In vivo*, dsRNA is typically delivered by feeding or injection into the hemocoel. It has been shown that dsRNases are more abundant in the digestive system than in hemolymph. This is in line with observations showing that feeding dsRNA is often less effective than injecting dsRNA (Wang et al., 2016; Singh et al., 2017; Song et al., 2019). In locusts, feeding of dsRNA is not successful whereas injecting dsRNA leads to a robust systemic RNAi response (Luo et al., 2013; Song et al., 2019; Xie et al., 2019). The efficacy of RNAi differs between tissues. Injection of dsRNA into the hemocoel induces RNAi in the brain but not in ovaries (Ma et al., 2011; Ren et al., 2014). We herein introduce a new and convenient RNAi application method for loss of function studies in locust primary brain cell cultures. We termed it soaking RNAi since it requires no additional manipulations (e.g., lipofection, electroporation, viral delivery) to suppress specific protein expression as in mammalian cells. Soaking RNAi has been successfully applied in primary brain cell cultures from the beetle *T. castaneum* (Hahn et al., 2017). It has now been adapted to locust primary brain neurons, offering a new tool for *in vitro* loss of function studies in *L. migratoria*. The RNAi effect observed in *L. migratoria* is slightly lower than in the beetle *T. castaneum* (Hahn et al., 2017). Four days exposure of *T. castaneum* brain cells to 10 ng/ μ l dsRNA targeting *rpt3* expression reduced cell survival to approximately 34–67% while 5 days exposure reduced *L. migratoria* median brain cell survival to approximately 75%. In line with these observations, coleoptera, including *T. castaneum*, exhibit a generally higher RNAi susceptibility in comparison to *L. migratoria* (Wang et al., 2016; Singh et al., 2017). However, the RNAi response of *L. migratoria* is sufficiently robust and useful for loss of function studies.

***Lm*-CRLF3 Is Crucial for Epo-Mediated Neuroprotection**

Selective neuroprotective activity (without stimulation of erythropoiesis) by EV-3 and other Epo-like ligands (e.g., carbamylated Epo, asialo-Epo, helix B surface peptide, Epo mimetic peptide 1) provided clear evidence for alternative cell protective Epo-receptors other than (EpoR)₂ (Erbayraktar et al., 2003; Brines et al., 2004, 2008; Leist et al., 2004; Bonnas et al., 2017). Several receptors and receptor complexes have been

associated with Epo-induced neuroprotection in mammals, including homodimeric (EpoR)₂, heteromeric EpoR/ β -common receptor and Ephrin B4 receptor (Brines et al., 2004; Um et al., 2007; Pradeep et al., 2016). However, Epo-mediated neuroprotection remains only partially understood. Hence, we investigated a potential neuroprotective involvement of CRLF3 in locust primary brain neurons.

Our experiments indicate that *Lm*-CRLF3 represents an Epo-binding receptor, or alternatively constitutes an essential component of an Epo-binding receptor complex, whose activation can fully prevent hypoxia-induced apoptosis in locust primary brain cell cultures. RNAi against *Lm-crlf3* does not generally affect the cell viability of locust primary brain neurons, neither in unchallenged nor in challenged conditions. This implies that *Lm*-CRLF3 is not involved in physiological maintenance of differentiated neurons, but specifically induces protective mechanisms upon Epo stimulation. However, *Lm*-CRLF3 is crucial for Epo-induced neuroprotection *in vitro* since a knock-down by RNAi abolished the neuroprotective effect of Epo in locust primary brain cell cultures. Our previous study focused on the holometabolous beetle *T. castaneum* and saw similar results concerning CRLF3 involvement. Given that locusts are hemimetabolous, these findings lead to the assumption that the last common ancestor of hemi- and holometabolous insects already employed CRLF3 as a neuroprotective receptor. However, its endogenous ligand is yet unknown. Since insects do not possess *epo* genes, the endogenous ligand has to be different from Epo but might share structural features with Epo and other class-I helical cytokines. The artificial activation of insect CRLF3 receptors by rhEpo is not surprising, because CRLF3 and EpoR both belong to group 1 of class I cytokine receptors and EpoR has already been shown to crossreact with thrombopoietin, the typical ligand of another receptor of that group (Rouleau et al., 2004).

In contrast to vertebrates, only few cytokines or cytokine-like peptides have been identified in insects (Duressa et al., 2015; Schrag et al., 2017; Matsumura et al., 2018). Expression of CRLF3 by locust hemocytes and brain cells may indicate multiple production sites of its endogenous ligand, since blood-brain-barriers restrict the exchange of ions and soluble molecules (reviewed in DeSalvo et al., 2011). Potential production sites, that release the ligand into the circulation, are certain types of hemocytes, neurosecretory organs including the corpora allata as well as the corpora cardiaca, and the fat body. They contain and release also other cytokines involved in stress responses (Duressa et al., 2015; Matsumura et al., 2018).

As documented for many species from different orders, insects achieve extraordinary resistance to hypoxia by switching to anaerobic metabolic pathways and reduction of basal metabolic rates amongst other adaptations (reviewed by Hoback and Stanley, 2001). Hypoxia tolerance has also been reported for locusts (Arieli and Lehrer, 1988; Wegener and Moratzky, 1995; Greenlee and Harrison, 2004) and *T. castaneum* (Donahaye, 1990; Kharel et al., 2019), the two species in which CRLF3-mediated neuroprotection has been demonstrated. In comparison to mammalian neurons, where rather brief hypoxic episodes are sufficient to induce apoptosis, survival of locust and beetle neurons *in vitro* decreases only 20–30% even when

challenged by prolonged (36 h) and severe (<0.3% oxygen) hypoxia (this study; Miljus et al., 2014; Hahn et al., 2017). However, similar degrees of hypoxia tolerance have also been reported for specially adapted vertebrates (such as turtles and naked mole-rats; reviewed by Larson et al., 2014) and for some mammalian cell types *in vitro* (human SH-SY5Y neuroblastoma cells, Reich et al., 2008). Since DAPI nuclear staining, trypan blue accumulation and immunocytochemical detection of pro-apoptotic activated caspase-3 consistently identified dead or dying locust neurons (Gocht et al., 2009; Miljus et al., 2014; Heinrich et al., 2017), hypoxia-induced cell death is most likely not underestimated by our analysis of DAPI-labeled nuclear morphology. Whether and how CRLF3-induced adaptations may contribute to hypoxia tolerance *in vivo* will be a subject of our future studies.

The neuroprotective effect of rhEpo on locust neurons challenged by hypoxia, by the cellular toxin H-7 or by serum deprivation has been characterized earlier. Its anti-apoptotic mechanisms involve activation of JAK/STAT signaling, translation of anti-apoptotic factors and interference with caspase-activation but are independent of PI3K signaling (Miljus et al., 2014; Heinrich et al., 2017). At that time, the receptor mediating this effect was not known. It can be assumed, that these insights are transferable to neuroprotective CRLF3 signaling since the knock-down of CRLF3 in beetles and locusts brain cell cultures abolished Epo-mediated neuroprotection completely, suggesting that CRLF3 is the only neuroprotective Epo-receptor in these insect neurons. Furthermore, it is likely that even the neuroprotective but non-erythropoietic Epo variants (e.g., EV-3) and Epo like ligands activate CRLF3. Epo-induced endocytosis is reduced by pre-incubation to EV-3 indicating that EV-3 and Epo bind to the same receptor on locust neurons (Miljus et al., 2017).

Its sensitivity toward Epo treatment in insects and its high conservation throughout metazoans suggests CRLF3 as a potential mammalian neuroprotective Epo-receptor. The neuroprotective function of Epo has been well-investigated in vertebrates and Epo is even used in clinical trials as a treatment after ischemic stroke (Ehrenreich et al., 2009; Subiras et al., 2012; Habib et al., 2019; Simon et al., 2019). However, Epo treatment leads to various adverse side effects (e.g., thromboembolism, cardiovascular events) that mainly arise from its erythropoietic function in vertebrates (Jelkmann et al., 2008; Noguchi et al., 2008; Ehrenreich et al., 2009; Souvenir et al., 2015). Hence, developing drugs that specifically target CRLF3 might improve neuroprotective therapies.

Outlook

Current experiments focus on the identification of the endogenous ligand of CRLF3 and the characterization of mammalian CRLF3. Cytokines typically share low sequence and overall structural similarity which complicates analyses of their evolutionary origins (Beschin et al., 2001; Liongue and Ward, 2007). Instead of bioinformatic approaches based on sequence similarity, endogenous CRLF3 ligands may rather be identified by functional studies with fractionated tissue extracts from which potential ligands can be separated and molecularly identified (Watari et al., 2019). In addition, potential neuro- and

cell protective functions of CRLF3 in Mammalia should be investigated also considering a putative involvement in the adaptive immune system.

DATA AVAILABILITY STATEMENT

Nucleotide sequences were submitted to GenBank with the submission numbers MN245516 and MN245517.

AUTHOR CONTRIBUTIONS

NH, LB, NS-D, BM, PN, and RH collected the experimental data. NH, LB, BG, and RH conducted the data analysis and interpretation. NH and SB performed the phylogenetic analysis. NH, MG, and RH wrote the manuscript. NH and RH designed and supervised the study. All authors discussed the results and commented on the manuscript.

FUNDING

The project was funded by Deutsche Forschungsgemeinschaft (DFG) – Projekt Nummer 398214842. NH was partially supported

by a grant from the Deutsche Forschungsgemeinschaft (DFG CRC 889, A1) to MG. SB was supported by a grant from the Deutsche Forschungsgemeinschaft (DFG 2930\3-1) to Sven Bradler.

ACKNOWLEDGMENTS

We thank Steffi Pauls for technical assistance, Sven Bradler for scientific advice and Debba Y. Knorr for proofreading and language editing of the manuscript. Furthermore, we thank Gregor Bucher for introducing us to RNAi in *Tribolium castaneum* and Natascha Zhang for assistance with RACE PCR. We acknowledge the support by the Open Access Publication Funds of the Göttingen University. Finally, we owe our thanks to the reviewers for constructive comments which greatly improved the quality of the manuscript.

SUPPLEMENTARY MATERIAL

The Supplementary Material for this article can be found online at: <https://www.frontiersin.org/articles/10.3389/fnmol.2019.00251/full#supplementary-material>

REFERENCES

- Agrawal, A., Eastman, Q. M., and Schatz, D. G. (1998). Implications of transposition mediated by V(D)J-recombination proteins RAG1 and RAG2 for origins of antigen-specific immunity. *Nature* 394, 744–751. doi: 10.1038/29457
- Altschul, S. F., Gish, W., Miller, W., Myers, E. W., and Lipman, D. J. (1990). Basic local alignment search tool. *J. Mol. Biol.* 215, 403–410. doi: 10.1006/jmbi.1990.9999
- Arieli, R., and Lehrer, C. (1988). Recording of locust breathing frequency by barometric method exemplified by hypoxic exposure. *J. Insect Physiol.* 34, 325–328. doi: 10.1016/0022-1910(88)90143-6
- Atwal, J. K., Julie, P. G., Josh, S., Scott, S., Yan, W., Carla, S., et al. (2008). PirB is a functional receptor for myelin inhibitors of axonal regeneration. *Science* 322, 967–970. doi: 10.1126/science.1161151
- Babonis, L. S., and Martindale, M. Q. (2016). Phylogenetic evidence for the modular evolution of metazoan signalling pathways. *Philos. Trans. B* 372:20150477. doi: 10.1098/rstb.2015.0477
- Bayne, C. J. (2003). Origins and evolutionary relationships between the innate and adaptive arms of immune systems. *Integr. Comp. Biol.* 43, 293–299. doi: 10.1093/icb/43.2.293
- Ben Baruch-Morgenstern, N., Shik, D., Moshkovits, I., Itan, M., Karo-Atar, D., Bouffi, C., et al. (2014). Paired immunoglobulin-like receptor A is an intrinsic, self-limiting suppressor of IL-5-induced eosinophil development. *Nat. Immunol.* 15, 36–44. doi: 10.1038/ni.2757
- Benjamini, Y., and Hochberg, Y. (1995). Controlling the False discovery rate: a practical and powerful approach to multiple testing. *J. R. Stat. Soc. Ser. B* 57, 289–300. doi: 10.1111/j.2517-6161.1995.tb02031.x
- Berná, L., Alvarez-Valín, F., and D'Onofrio, G. (2009). How fast is the sessile Ciona? *Comp. Funct. Genomics* 2006:875901. doi: 10.1155/2009/875901
- Beschin, A., Bilej, M., Torreele, E., and De Baetselier, P. (2001). Cellular and molecular life sciences On the existence of cytokines in invertebrates. *Cell. Mol. Life Sci.* 58, 801–814. doi: 10.1007/pl00000901
- Bonnas, C., Wüstefeld, L., Winkler, D., Kronstein-Wiedemann, R., Dere, E., Specht, K., et al. (2017). EV-3, an endogenous human erythropoietin isoform with distinct functional relevance. *Sci. Rep.* 7, 1–15. doi: 10.1038/s41598-017-03167-0
- Bosch, T. C. G., Klimovich, A., Domazet-Lošo, T., Gründer, S., Holstein, T. W., Jékely, G., et al. (2017). Back to the basics: cnidarians start to fire. *Trends Neurosci.* 40, 92–105. doi: 10.1016/j.tins.2016.11.005
- Boulay, J. L., O'Shea, J. J., and Paul, W. E. (2003). Molecular phylogeny within type I cytokines and their cognate receptors. *Immunity* 19, 159–163. doi: 10.1016/s1074-7613(03)00211-5
- Brines, M., and Cerami, A. (2005). Emerging biological roles for erythropoietin in the nervous system. *Nat. Rev. Neurosci.* 6, 484–494. doi: 10.1038/nrn1687
- Brines, M., and Cerami, A. (2006). Discovering erythropoietin's extra-hematopoietic functions: biology and clinical promise. *Kidney Int.* 70, 246–250. doi: 10.1038/sj.ki.5001546
- Brines, M., Grasso, G., Fiordaliso, F., Sfacteria, A., Ghezzi, P., Fratelli, M., et al. (2004). Erythropoietin mediates tissue protection through an erythropoietin and common -subunit heteroreceptor. *Proc. Natl. Acad. Sci. U.S.A.* 101, 14907–14912. doi: 10.1073/pnas.0406491101
- Brines, M., Patel, N. S. A., Villa, P., Brines, C., Mennini, T., De Paola, M., et al. (2008). Nonerythropoietic, tissue-protective peptides derived from the tertiary structure of erythropoietin. *Proc. Natl. Acad. Sci. U.S.A.* 105, 10925–10930. doi: 10.1073/pnas.0805594105
- Brown, M. R., Crim, J. W., Arata, R. C., Cai, H. N., Chun, C., and Shen, P. (1999). Identification of a *Drosophila* brain-gut peptide related to the neuropeptide Y family. *Peptides* 20, 1035–1042. doi: 10.1016/s0196-9781(99)00097-2
- Brunet, F. G., Volff, J. N., and Scharl, M. (2016). Whole genome duplications shaped the receptor tyrosine kinase repertoire of jawed vertebrates. *Genome Biol. Evol.* 8, 1600–1613. doi: 10.1093/gbe/evw103
- Cirulli, E. T., Lasseigne, B. N., Petrovski, S., Sapp, P. C., Dion, P. A., Leblond, C. S., et al. (2015). Exome sequencing in amyotrophic lateral sclerosis identifies risk genes and pathways. *Science* 347, 1436–1441. doi: 10.1126/science.aaa3650
- Dang, C., Gottschling, M., Manning, K., O'Curraín, E., Schneider, S., Sterry, W., et al. (2006). Identification of dysregulated genes in cutaneous squamous cell carcinoma. *Oncol. Rep.* 16, 513–519.
- DeSalvo, M. K., Mayer, N., Mayer, F., and Bainton, R. J. (2011). Physiologic and anatomic characterization of the brain surface glia barrier of *Drosophila*. *Glia* 59, 1322–1340. doi: 10.1002/glia.21147

- Donahaye, E. (1990). Laboratory selection of resistance by the red flour beetle, *Tribolium castaneum* (Herbst), to an atmosphere of low oxygen concentration. *Phytoparasitica* 18, 189–202. doi: 10.1007/BF02980989
- Donnadieu, E., Revy, P., and Trautmann, A. (2001). Imaging T-cell antigen recognition and comparing immunological and neuronal synapses. *Immunology* 103, 417–425. doi: 10.1046/j.1365-2567.2001.01268.x
- Dunn, C. W., Giribet, G., Edgecombe, G. D., and Hejnol, A. (2014). Animal phylogeny and its evolutionary implications. *Annu. Rev. Ecol. Evol. Syst.* 45, 371–395. doi: 10.1146/annurev-ecolsys-120213-091627
- Duressa, T. F., Boonen, K., Hayakawa, Y., and Huybrechts, R. (2015). Identification and functional characterization of a novel locust peptide belonging to the family of insect growth blocking peptides. *Peptides* 74, 23–32. doi: 10.1016/j.peptides.2015.09.011
- Dzik, J. M. (2010). The ancestry and cumulative evolution of immune reactions. *Acta Biochim. Pol.* 57, 443–466.
- Ehrenreich, H., Weissenborn, K., Prange, H., Schneider, D., Weimar, C., Wartenberg, K., et al. (2009). Recombinant human erythropoietin in the treatment of acute ischemic stroke. *Stroke* 40, e647–e656. doi: 10.1161/STROKEAHA.109.564872
- Erbayraktar, S., Grasso, G., Sfacteria, A., Xie, Q., Coleman, T., Kreilgaard, M., et al. (2003). Asialoerythropoietin is a nonerythropoietic cytokine with broad neuroprotective activity in vivo. *Proc. Natl. Acad. Sci. U.S.A.* 100, 6741–6746. doi: 10.1073/pnas.1031753100
- Gautam, M., Noakes, P. G., Moscoso, L., Rupp, F., Scheller, R. H., Merlie, J. P., et al. (1996). Defective neuromuscular synaptogenesis in agrin-deficient mutant mice. *Cell* 85, 525–535. doi: 10.1016/s0092-8674(00)81253-2
- Ghezzi, P., and Conklin, D. (2013). Tissue-protective cytokines: structure and evolution. *Methods Mol. Biol.* 982, 43–58. doi: 10.1007/978-1-62703-308-4_3
- Gocht, D., Wagner, S., and Heinrich, R. (2009). Recognition, presence, and survival of locust central nervous glia in situ and in vitro. *Microsc. Res. Tech.* 72, 385–397. doi: 10.1002/jemt.20683
- Greenlee, K. J., and Harrison, J. F. (2004). Development of respiratory function in the American locust *Schistocerca americana*. *J. Exp. Biol.* 207, 509–517. doi: 10.1242/jeb.00766
- Grimmelikhuijzen, C. J. P., Leviev, I., and Carstensen, K. (1996). Peptides in the nervous systems of cnidarians: structure, function, and biosynthesis. *Int. Rev. Cytol.* 167, 37–89. doi: 10.1016/s0074-7696(08)61345-5
- Habib, P., Stamm, A. S., Zeyen, T., Noristani, R., Slowik, A., Beyer, C., et al. (2019). EPO regulates neuroprotective Transmembrane BAX Inhibitor-1 Motif-containing (TMBIM) family members GRINA and FAIM2 after cerebral ischemia-reperfusion injury. *Exp. Neurol.* 320:112978. doi: 10.1016/j.expneurol.2019.112978
- Habib, L., Ebtakar, M., and Jameie, S. B. (2009). Immune and nervous systems share molecular and functional similarities: memory storage mechanism. *Scand. J. Immunol.* 69, 291–301. doi: 10.1111/j.1365-3083.2008.02215.x
- Hahn, N., Knorr, D., Liebig, J., Wüstefeld, L., Peters, K., Büscher, M., et al. (2017). The human orphan cytokine receptor CRLF3 is a neuroprotective erythropoietin receptor in insects. *Front. Mol. Neurosci.* 10:223. doi: 10.3389/fnmol.2017.00223
- Hashimoto, Y., Muramatsu, K., Kunii, M., Yoshimura, S. I., Yamada, M., Sato, T., et al. (2012). Uncovering genes required for neuronal morphology by morphology-based gene trap screening with a revertible retrovirus vector. *FASEB J.* 26, 4662–4674. doi: 10.1096/fj.12-207530
- Heinrich, R., Guenther, V., and Miljus, N. (2017). Erythropoietin-mediated neuroprotection in insects suggests a prevertebrate evolution of erythropoietin-like signaling. *Vitam. Horm.* 105, 181–196. doi: 10.1016/bs.vh.2017.02.004
- Hoang, D. T., Chernomor, O., von Haeseler, A., Minh, B. Q., and Vinh, L. S. (2018). UFBoot2: improving the ultrafast bootstrap approximation. *Mol. Biol. Evol.* 35, 518–522. doi: 10.1093/molbev/msx281
- Hoback, W. W., and Stanley, D. W. (2001). Insects in hypoxia. *J. Insect Physiol.* 47, 533–542. doi: 10.1016/s0022-1910(00)00153-0
- Holdsworth, S. R., and Gan, P. Y. (2015). Cytokines: names and numbers you should care about. *Clin. J. Am. Soc. Nephrol.* 10, 2243–2254. doi: 10.2215/CJN.07590714
- Hothorn, T., Hornik, K., van de Wiel, M. A., and Zeileis, A. (2006). A lego system for conditional inference. *Am. Stat.* 60, 257–263. doi: 10.1198/000313006x118430
- Hothorn, T., Hornik, K., van de Wiel, M. A., and Zeileis, A. (2008). Implementing a class of permutation tests: the coin package. *J. Stat. Softw.* 28, 1–23. doi: 10.18637/jss.v028.i08
- Irie, N., Satoh, N., and Kuratani, S. (2018). The phylum Vertebrata: a case for zoological recognition. *Zool. Lett.* 4:32. doi: 10.1186/s40851-018-0114-y
- Jékely, G., Paps, J., and Nielsen, C. (2015). The phylogenetic position of ctenophores and the origin(s) of nervous systems. *Evodevo* 6:1. doi: 10.1186/2041-9139-6-1
- Jelkmann, W. (2011). Regulation of erythropoietin production. *J. Physiol.* 589, 1251–1258. doi: 10.1113/jphysiol.2010.195057
- Jelkmann, W., Bohlius, J., Hallek, M., and Sytkowski, A. J. (2008). The erythropoietin receptor in normal and cancer tissues. *Crit. Rev. Oncol. Hematol.* 67, 39–61. doi: 10.1016/j.critrevonc.2008.03.006
- Kapitonov, V. V., and Koonin, E. V. (2015). Evolution of the RAG1-RAG2 locus: both proteins came from the same transposon. *Biol. Direct* 10:20. doi: 10.1186/s13062-015-0055-8
- Kasahara, M. (2007). The 2R hypothesis: an update. *Curr. Opin. Immunol.* 19, 547–552. doi: 10.1016/j.coi.2007.07.009
- Kerschensteiner, M., Mehl, E., and Hohlfeld, R. (2009). Neuro-immune crosstalk in CNS diseases. *Neuroscience* 158, 1122–1132. doi: 10.1016/j.neuroscience.2008.09.009
- Khan, A. A., Bose, C., Yam, L. S., Soloski, M. J., and Rupp, F. (2001). Physiological regulation of the immunological synapse by agrin. *Science* 292, 1681–1686. doi: 10.1126/science.1056594
- Kharel, K., Mason, L. J., Murdock, L. L., and Baributsa, D. (2019). Efficacy of hypoxia against *Tribolium castaneum* (Coleoptera: Tenebrionidae) throughout ontogeny. *J. Econ. Entomol.* 112, 1463–1468. doi: 10.1093/jeet/toz019
- Kioussis, D., and Pachnis, V. (2009). Immune and nervous systems: more than just a superficial similarity? *Immunity* 31, 705–710. doi: 10.1016/j.immuni.2009.09.009
- Larson, J., Drew, K. L., Folkow, L. P., Milton, S. L., and Park, T. J. (2014). No oxygen? No problem! Intrinsic brain tolerance to hypoxia in vertebrates. *J. Exp. Biol.* 217, 1024–1039. doi: 10.1242/jeb.085381
- Laumer, C. E., Fernández, R., Lemer, S., Combosch, D., Kocot, K. M., Riesgo, A., et al. (2019). Revisiting metazoan phylogeny with genomic sampling of all phyla. *Proc. R. Soc. B Biol. Sci.* 286:20190831. doi: 10.1098/rspb.2019.0831
- Leist, M., Ghezzi, P., Grasso, G., Bianchi, R., Villa, P., Fratelli, M., et al. (2004). Derivatives of erythropoietin not erythropoietic. *Science* 305, 239–243.
- Levite, M. (2008). Neurotransmitters activate T-cells and elicit crucial functions via neurotransmitter receptors. *Curr. Opin. Pharmacol.* 8, 460–471. doi: 10.1016/j.coph.2008.05.001
- Liongue, C., Sertori, R., and Ward, A. C. (2016). Evolution of cytokine receptor signaling. *J. Immunol.* 197, 11–18. doi: 10.4049/jimmunol.1600372
- Liongue, C., and Ward, A. C. (2007). Evolution of class I cytokine receptors. *BMC Evol. Biol.* 7:120. doi: 10.1186/1471-2148-7-120
- Livak, K. J., and Schmittgen, T. D. (2001). Analysis of relative gene expression data using real-time quantitative PCR and the 2[−]ΔΔCT method. *Methods* 25, 402–408. doi: 10.1006/meth.2001.1262
- Luo, Y., Wang, X., Wang, X., Yu, D., Chen, B., and Kang, L. (2013). Differential responses of migratory locusts to systemic RNA interference via double-stranded RNA injection and feeding. *Insect Mol. Biol.* 22, 574–583. doi: 10.1111/imb.12046
- Ma, Z., Guo, W., Guo, X., Wang, X., and Kang, L. (2011). Modulation of behavioral phase changes of the migratory locust by the catecholamine metabolic pathway. *Proc. Natl. Acad. Sci. U.S.A.* 108, 3882–3887. doi: 10.1073/pnas.1015098108
- Mamta, B., and Rajam, M. V. (2017). RNAi technology: a new platform for crop pest control. *Physiol. Mol. Biol. Plants* 23, 487–501. doi: 10.1007/s12298-017-0443-x
- Mangiafico, S. (2019). *rcompanion: Functions to Support Extension Education Program Evaluation. Package Version 2.1.7.*
- Matsumura, T., Nakano, F., Matsumoto, H., Uryu, O., and Hayakawa, Y. (2018). Identification of a cytokine combination that protects insects from stress. *Insect Biochem. Mol. Biol.* 97, 19–30. doi: 10.1016/j.ibmb.2018.04.002
- Meola, D., Huang, Z., and Petitto, J. M. (2013). Selective neuronal and brain regional expression of IL-2 in IL2P 8-GFP transgenic mice: relation to sensorimotor gating. *J. Alzheimers Dis. Park.* 3:1000127. doi: 10.4172/2161-0460.1000127

- Miljus, N., Heibeck, S., Jarrar, M., Micke, M., Ostrowski, D., Ehrenreich, H., et al. (2014). Erythropoietin-mediated protection of insect brain neurons involves JAK and STAT but not PI3K transduction pathways. *Neuroscience* 258, 218–227. doi: 10.1016/j.neuroscience.2013.11.020
- Miljus, N., Massih, B., Weis, M. A., Rison, J. V., Bonnas, C. B., Sillaber, I., et al. (2017). Neuroprotection and endocytosis: erythropoietin receptors in insect nervous systems. *J. Neurochem.* 141, 63–74. doi: 10.1111/jnc.13967
- Minh, B. Q., Nguyen, M. A. T., and Von Haeseler, A. (2013). Ultrafast approximation for phylogenetic bootstrap. *Mol. Biol. Evol.* 30, 1188–1195. doi: 10.1093/molbev/mst024
- Misof, B., Liu, S., Meusemann, K., Peters, R. S., Donath, A., Mayer, C., et al. (2014). Phylogenomics resolves the timing and pattern of insect evolution. *Science* 346, 763–767. doi: 10.1126/science.1257570
- Moroz, L. L., and Kohn, A. B. (2016). Independent origins of neurons and synapses: insights from ctenophores. *Philos. Trans. R. Soc. B Biol. Sci.* 371:20150041. doi: 10.1098/rstb.2015.0041
- Muraguchi, B. Y. A., Kehl, J. H., Longo, D. A. N. L., Volkman, D. J., Smith, K. A., and Fauci, A. S. (1985). Interleukin 2 receptors on human B cells. Implications for the role of interleukin 2 in human B cell function. *J. Exp. Med.* 161, 181–197. doi: 10.1084/jem.161.1.181
- Nguyen, L. T., Schmidt, H. A., Von Haeseler, A., and Minh, B. Q. (2015). IQ-TREE: a fast and effective stochastic algorithm for estimating maximum-likelihood phylogenies. *Mol. Biol. Evol.* 32, 268–274. doi: 10.1093/molbev/msu300
- Niu, J., Taning, C. N. T., Christiaens, O., Smagghe, G., and Wang, J. J. (2018). “Rethink RNAi in Insect Pest Control: Challenges and Perspectives,” in *Advances in Insect Physiology*, Vol. 55, ed. G. Smagghe, (Cambridge, MA: Elsevier Ltd.), 1–7. doi: 10.1016/bs.aiip.2018.07.003
- Noguchi, C. T., Wang, L., Rogers, H. M., Teng, R., and Jia, Y. (2008). Survival and proliferative roles of erythropoietin beyond the erythroid lineage. *Expert Rev. Mol. Med.* 10, 1–27. doi: 10.1017/S1462399408000860
- Oettinger, M. A., Schatz, D. G., Gorka, C., and Baltimore, D. (1990). RAG-1 and RAG-2, adjacent genes that synergistically activate V(D)J recombination. *Science* 248, 1517–1523. doi: 10.1126/science.2360047
- Ogunshola, O. O., and Bogdanova, A. Y. (2013). Tissue-protective cytokines. *Methods Mol. Biol.* 982, 13–41.
- Ostrowski, D., Ehrenreich, H., and Heinrich, R. (2011). Erythropoietin promotes survival and regeneration of insect neurons in vivo and in vitro. *Neuroscience* 188, 95–108. doi: 10.1016/j.neuroscience.2011.05.018
- Pradeep, S., Huang, J., Mora, E. M., Nick, A. M., Cho, M. S., Wu, S. Y., et al. (2016). Erythropoietin stimulates tumor growth via EphB4. *Cancer Cell* 28, 610–622. doi: 10.1016/j.ccell.2015.09.008
- R Core Team, (2019). *R: A Language and Environment for Statistical Computing*. Vienna: R Foundation for Statistical Computing.
- Ransohoff, R. M. (2009). Chemokines and chemokine receptors: standing at the crossroads of immunobiology and neurobiology. *Immunity* 31, 711–721. doi: 10.1016/j.immuni.2009.09.010
- Rast, J. P., Anderson, M. K., Strong, S. J., Luer, C., Litman, R. T., and Litman, G. W. (1997). α , β , γ , δ T cell antigen receptor genes arose early in vertebrate phylogeny. *Immunity* 6, 1–11. doi: 10.1016/S1074-7613(00)80237-X
- Reich, D. M., Hau, S., Stahl, T., Scholz, M., Naumann, W., Emmrich, F., et al. (2008). Neuronal hypoxia in vitro: investigation of therapeutic principles of HUCB-MNC and CD133+ stem cells. *BMC Neurosci.* 9:91. doi: 10.1186/1471-2202-9-91
- Ren, D., Cai, Z., Song, J., Wu, Z., and Zhou, S. (2014). DsRNA uptake and persistence account for tissue-dependent susceptibility to RNA interference in the migratory locust, *Locusta migratoria*. *Insect Mol. Biol.* 23, 175–184. doi: 10.1111/imb.12074
- Rouleau, C., Cui, K., and Feldman, L. (2004). A functional erythropoietin receptor is necessary for the action of thrombopoietin on erythroid cells lacking c-mpl. *Exp. Hematol.* 32, 140–148. doi: 10.1016/j.exphem.2003.10.015
- RStudio Team, (2018). *RStudio: Integrated Development for R*. Boston, MA: RStudio, Inc.
- Sarrion-Perdigones, A., Vazquez-Vilar, M., Palaci, J., Castelijns, B., Forment, J., Ziaresolo, P., et al. (2013). GoldenBraid 2.0: a comprehensive DNA assembly framework for plant synthetic biology. *Plant Physiol.* 162, 1618–1631. doi: 10.1104/pp.113.217661
- Schatz, D. G. (2004). Antigen receptor genes and the evolution of a recombinase. *Semin. Immunol.* 16, 245–256. doi: 10.1016/j.smim.2004.08.004
- Schindelin, J., Arganda-Carreras, I., Frise, E., Kaynig, V., Longair, M., Pietzsch, T., et al. (2012). Fiji: an open-source platform for biological-image analysis. *Nat. Methods* 9, 676–682. doi: 10.1038/nmeth.2019
- Schrag, L. G., Cao, X., Herrera, A. I., Wang, Y., Jiang, H., and Prakash, O. (2017). Solution structure and expression profile of an insect cytokine: *Manduca sexta* stress response peptide-2. *Protein Pept. Lett.* 24, 3–11. doi: 10.2174/0929866524666161121142840
- Simon, F., Floros, N., Ibing, W., Schelzig, H., and Knapsis, A. (2019). Neurotherapeutic potential of erythropoietin after ischemic injury of the central nervous system. *Neural Regen. Res.* 14, 1309–1312. doi: 10.4103/1673-5374.253507
- Singh, I. K., Singh, S., Mogilicherla, K., Shukla, J. N., and Palli, S. R. (2017). Comparative analysis of double-stranded RNA degradation and processing in insects. *Sci. Rep.* 7:17059. doi: 10.1038/s41598-017-17134-2
- Song, H., Fan, Y., Zhang, J., Cooper, A. M. W., Silver, K., Li, D., et al. (2019). Contributions of dsRNases to differential RNAi efficiencies between the injection and oral delivery of dsRNA in *Locusta migratoria*. *Pest Manag. Sci.* 75, 1707–1717. doi: 10.1002/ps.5291
- Souvenir, R., Doycheva, D., Zhang, J., and Tang, J. (2015). Erythropoietin in stroke therapy: friend or foe. *Curr. Med. Chem.* 22, 1205–1213. doi: 10.2174/0929867322666150114152134
- Subiras, N., Del Barco, D. G., and Coro-Antich, R. M. (2012). Erythropoietin: still on the neuroprotection road. *Ther. Adv. Neurol. Disord.* 5, 161–173. doi: 10.1177/1756285611434926
- Takezaki, N., and Nishihara, H. (2016). Resolving the phylogenetic position of coelacanth: the closest relative is not always the most appropriate outgroup. *Genome Biol. Evol.* 8, 1208–1221. doi: 10.1093/gbe/evw071
- Um, M., Gross, A. W., and Lodish, H. F. (2007). A “classical” homodimeric erythropoietin receptor is essential for the antiapoptotic effects of erythropoietin on differentiated neuroblastoma SH-SY5Y and pheochromocytoma PC-12 cells. *Cell. Signal.* 19, 634–645. doi: 10.1016/j.cellsig.2006.08.014
- Unger, E. F., Thompson, A. M., Blank, M. J., and Temple, R. (2010). Erythropoiesis-stimulating agents — time for a reevaluation. *N. Engl. J. Med.* 362, 189–192. doi: 10.1056/nejmp0912328
- Van Hiel, M. B., Van Wielendaele, P., Temmerman, L., Van Soest, S., Vuerinckx, K., Huybrechts, R., et al. (2009). Identification and validation of housekeeping genes in brains of the desert locust *Schistocerca gregaria* under different developmental conditions. *BMC Mol. Biol.* 10:56. doi: 10.1186/1471-2199-10-56
- Vogel, E., Santos, D., Mingels, L., Verdonck, T. W., and Broeck, J. V. (2019). RNA interference in insects: protecting beneficials and controlling pests. *Front. Physiol.* 10:1912. doi: 10.3389/fphys.2018.01912
- Wang, K., Peng, Y., Pu, J., Fu, W., Wang, J., and Han, Z. (2016). Variation in RNAi efficacy among insect species is attributable to dsRNA degradation in vivo. *Insect Biochem. Mol. Biol.* 77, 1–9. doi: 10.1016/j.ibmb.2016.07.007
- Watari, H., Nakajima, H., Atsuumi, W., Nakamura, T., Nanya, T., Ise, Y., et al. (2019). A novel sponge-derived protein thrombocortin is a new agonist for thrombopoietin receptor. *Comp. Biochem. Physiol. Part C Toxicol. Pharmacol.* 221, 82–88. doi: 10.1016/j.cbpc.2019.04.003
- Wegener, G., and Moratzky, T. (1995). Hypoxia and anoxia in insects: microcalorimetric studies on two species (*Locusta migratoria* and *Manduca sexta*) showing different degrees of anoxia tolerance. *Thermochim. Acta* 251, 209–218. doi: 10.1016/0040-6031(94)02009-d
- Westfall, I. A. (1996). Ultrastructure of synapses in the first-evolved nervous systems. *J. Neurocytol.* 25, 735–746. doi: 10.1007/bf02284838
- Wheway, J., Herzog, H., and Mackay, F. (2007). NPY and receptors in immune and inflammatory diseases. *Curr. Top. Med. Chem.* 7, 1743–1752. doi: 10.2174/156802607782341046
- Wong, T. K. F., Jermini, L. S., Minh, B. Q., Kalyaanamoorthy, S., and von Haeseler, A. (2017). ModelFinder: fast model selection for accurate phylogenetic estimates. *Nat. Methods* 14, 587–589. doi: 10.1038/nmeth.4285
- Wyder, S., Kriventseva, E. V., Schröder, R., Kadowaki, T., and Zdobnov, E. M. (2007). Quantification of ortholog losses in insects and vertebrates. *Genome Biol.* 8:R242. doi: 10.1186/gb-2007-8-11-r242

- Xie, J., Li, S., Zhang, W., and Xia, Y. (2019). RNAi-knockdown of the *Locusta migratoria* nuclear export factor protein results in insect mortality and alterations in gut microbiome. *Pest Manag. Sci.* 75, 1383–1390. doi: 10.1002/ps.5258
- Yang, F., Xu, Y.-P., Li, J., Duan, S.-S., Fu, Y.-J., Zhang, Y., et al. (2009). Cloning and characterization of a novel intracellular protein p48.2 that negatively regulates cell cycle progression. *Int. J. Biochem. Cell Biol.* 41, 2240–2250. doi: 10.1016/j.biocel.2009.04.022
- Yoshida, R., Fukumizu, K., and Vogiatzis, C. (2019). Multilocus phylogenetic analysis with gene tree clustering. *Ann. Oper. Res.* 276, 293–313. doi: 10.1007/s10479-017-2456-9
- Zhang, J., Wang, Y., Chu, Y., Su, L., Gong, Y., Zhang, R., et al. (2006). Agrin is involved in lymphocytes activation that is mediated by α -dystroglycan. *FASEB J.* 20, 50–58. doi: 10.1096/fj.04-3303com

Conflict of Interest: RH is a consultant for Epomedics GmbH, Göttingen, Germany.

The remaining authors declare that the research was conducted in the absence of any commercial or financial relationships that could be construed as a potential conflict of interest.

Copyright © 2019 Hahn, Büschgens, Schwedhelm-Domeyer, Bank, Geurten, Neugebauer, Massih, Göpfert and Heinrich. This is an open-access article distributed under the terms of the Creative Commons Attribution License (CC BY). The use, distribution or reproduction in other forums is permitted, provided the original author(s) and the copyright owner(s) are credited and that the original publication in this journal is cited, in accordance with accepted academic practice. No use, distribution or reproduction is permitted which does not comply with these terms.

Advantages of publishing in Frontiers



OPEN ACCESS

Articles are free to read
for greatest visibility
and readership



FAST PUBLICATION

Around 90 days
from submission
to decision



HIGH QUALITY PEER-REVIEW

Rigorous, collaborative,
and constructive
peer-review



TRANSPARENT PEER-REVIEW

Editors and reviewers
acknowledged by name
on published articles

Frontiers

Avenue du Tribunal-Fédéral 34
1005 Lausanne | Switzerland

Visit us: www.frontiersin.org

Contact us: frontiersin.org/about/contact



REPRODUCIBILITY OF RESEARCH

Support open data
and methods to enhance
research reproducibility



DIGITAL PUBLISHING

Articles designed
for optimal readership
across devices



FOLLOW US

@frontiersin



IMPACT METRICS

Advanced article metrics
track visibility across
digital media



EXTENSIVE PROMOTION

Marketing
and promotion
of impactful research



LOOP RESEARCH NETWORK

Our network
increases your
article's readership